Using Lunar In-Situ Resources for the Production of Solar Conversion Devices

Jürgen G. Schleppi, B.Eng., M.Sc.

A thesis submitted in fulfilment of the requirements for the degree of Doctor of Philosophy

Heriot-Watt University Edinburgh
Institute of Mechanical, Process and Energy Engineering

February 2020

Supervisor: Dr. Nick Bennett
Second Supervisor: Dr. Tadhg O'Donovan

Heriot Watt University
Edinburgh
Scotland

Abstract

The European Space Agency's vision is to establish a permanent research outpost on the lunar surface in the coming years. For building and establishing such an outpost, the overall mass/equipment, which can directly be transported from Earth to the Moon's surface, is limited by physics and hence are such a mission's capabilities. To expand these capabilities, it will be required to free up mass on the re-supply flights from Earth, this can be done by using lunar regolith material to augment building and operating an outpost on the lunar surface. At present, a burden of proof exists on technologies using such in-situ resources and mission designers are conservative in their integration of such technologies and methodologies for future exploration missions. To change that, by advancing the technology readiness level (TRL) of such technologies, one of the heaviest systems of a lunar outpost, the energy system, was targeted to be augmented by means of using local resources. This was done by first, finding and analysing suitable (analogue) building material, second, how these materials can be used to manufacture glasses and third, how power harvesting systems can be build from these glasses. To successfully complete all three steps, characterisation of analogue regolith materials (simulants) by means of XRD, XRF, SEM/EDX and microscopy as well as characterisation of all manufactured devices by means of analysis of surface quality, reflectivity, transmission, I-V curves, EQE and efficiencies was required.

Analysis showed that no commercially available simulant is mineralogically and geochemically reassembling all aspects of the lunar regolith. Thus, to maximize the possibility that manufacturing will work using actual lunar regolith, a variety of up to six different simulants was used and in some cases magnetically beneficiated. Next, the key challenge was how to using these six to manufacture a stable glass substrate with a defect free and flat surface, suitable for further manufacturing. After successfully manufacturing such substrates; transparent glass, mirrors, solar concentrators and solar cells were built. By characterising the substrates surface quality, reflectivity and transmission as well as the devices' I-V curves, EQE and efficiencies, it could be concluded that all manufactured devices show a similar performance compared to off-the-shelf components. Best solar cells devices achieved efficiencies of > 3 %, about 35 % lower than reference cells. The conducted investigations have shown for the first time, that it is possible to manufacture: glass substrates, mirrors, solar concentrators, solar cells and transparent glass by exploiting lunar resources. Next steps will require testing under lunar like conditions, to show how it may be possible to advance these devices into becoming technologies to be used on an actual lunar mission.

Keep Exploring

Acknowledgements

First thanks is to my supervisor, Dr. Nick Bennett, for guiding, advising and pushing this thesis to completion. I appreciated the calm supervision and the vast knowledge and experience, it was his flexibility and support for my ideas which made it possible for this thesis to come as far as it did.
Special thanks goes to Dr. Aidan Cowley and Dr. Matthias Maurer for recommending me for this thesis as well as supporting it during the whole time. My gratitude also extends to ESA for cosponsoring this thesis.
Further thanks to Dr. Tadhg O'Donovan for co-supervision and facilitating testing at the Heriot-Watt Campus in Dubai, as well as to Dr. Gudrun Kocher for her PV support.
The list of people who provided help, support and knowledge to me in the various instances over the years is long, nonetheless thanks goes to all of them. The manufacturing portion of my Ph.D. would have been impossible without the contributions of Dr. Geoffrey Bromiley. By providing access to his laboratories and passing on so much of his knowledge he enabled me to progress further than I could have hoped for. Dr. Linda A. Kirstein enabled me to manufacture transparent glass by introducing me to magnetic beneficiation. Discussion on the design of solar concentrator systems with Dr. Faisal Ghani and Immo Weidner were key to manufacturing a working system. Building actual solar cells was only possible due to the tireless efforts of Dr. Vladimir Smirnov who did not give up trying until it worked. Accomplishing to build a fully ISRU built mirror from just an idea was made possible by Philipp Nieke and his team in Bayreuth.
Sample analysis was essential to the success of this thesis, support in that area was provided by Dr. Jim Buckman (SEM/EDX/CL and geological guidance), Dr. Nicholas Odling and Bernard Charlier (XRF/XRD), Dr. Christian Schroeder (Mösbauer spectroscopy), Dr. Gary Nichol (TGA/DSC) and Dr. Gylen Odling and the Neil Robertson Group (UV-vis). Ingrid Phillips, thanks for introducing me to how to work with hot/cold glass as well as creative glass work. Mike Hall, enabled me to grind and polish to the required quality and precision, it would have been impossible without his help and experience. The best logistical and procurement support one could hope for was provided by Cameron Smith. Prior and during my thesis, Pablo López Soriano has taught me much on graphic design and editing, which was extremely useful writing a thesis.
One of the best experiences during my Ph.D. was working with the incredibly skilled people at NASA/Swamp Works and UCF/CLASS at Cape Canaveral and Orlando. Being part of the Robotic Mining Challenge organisational team, as well as the research teams at SWAMP works and UCF taught me invaluable things on space science, history and the future of humankind. Special thanks goes to Robert P. Mueller, Dr. Phil Metzger and Dr. Laurent Sibille.
Support on side projects working on basaltic fibres, was provided by Dr. Ferry Melchels and Hanna Läkk. Further collaboration on beneficiation of regolith for the use as soil and 3D printing material was based on works with Benjamin Lehner, Dr. Advenit Makaya and Dr. Martin Schwentenwein.
Thanks also goes to my fellow postgraduates Joseph Gibbons and Alexander Groetsch as well as to Emily Mullen for scientific and logistical support.
Special thanks goes to Dr. Theo Lim and Dr. Mahesh Anand for their roles as examiners.
Last but definitely not least my dear wife, Dr. Wiebke Schleppi, who enabled me to finish this thesis under the best possible conditions. Without her help and support, writing the thesis would have been a much longer and definitely more unpleasant experience!

Special Thanks to: esa

ACADEMIC REGISTRY

Research Thesis Submission

Please note this form should be bound into the submitted thesis.

Name:	Jürgen Gerhard Schleppi		
School:	Institute of Mechanical, Process and Energy Engineering		
Version: *(i.e. First, Resubmission, Final)*	Final	Degree Sought:	Doctor of Philosophy

Declaration

In accordance with the appropriate regulations I hereby submit my thesis and I declare that:

1. The thesis embodies the results of my own work and has been composed by myself
2. Where appropriate, I have made acknowledgement of the work of others
3. Where the thesis contains published outputs under Regulation 6 (9.1.2) these are accompanied by a critical review which accurately describes my contribution to the research and, for multi-author outputs, a signed declaration indicating the contribution of each author (complete Inclusion of Published Works Form – see below)
4. The thesis is the correct version for submission and is the same version as any electronic versions submitted*.
5. My thesis for the award referred to, deposited in the Heriot-Watt University Library, should be made available for loan or photocopying and be available via the Institutional Repository, subject to such conditions as the Librarian may require
6. I understand that as a student of the University I am required to abide by the Regulations of the University and to conform to its discipline.
7. Inclusion of published outputs under Regulation 6 (9.1.2) shall not constitute plagiarism.
8. I confirm that the thesis has been verified against plagiarism via an approved plagiarism detection application e.g. Turnitin.

* *Please note that it is the responsibility of the candidate to ensure that the correct version of the thesis is submitted.*

Signature of Candidate:		Date:	10.02.2020

Submission

Submitted By *(name in capitals):*	
Signature of Individual Submitting:	
Date Submitted:	

For Completion in the Student Service Centre (SSC)

Received in the SSC by *(name in capitals):*			
Method of Submission *(Handed in to SSC; posted through internal/external mail):*			
E-thesis Submitted ***(mandatory for final theses)***			
Signature:		Date:	

Contents

List of Tables

List of Figures

Abbreviations

3D	Three Dimensional
A %	Area percent
a-Si	amorphous-Silicon
AAC	Automated Additive Construction
Ab	Albite
AD	Aerosol Deposition
AD	Anno Domini
Ad	Andesine
Aeg	Agerine
Afs	Alkali Feldspar
Al	Aluminium
Alt	Alterations
AM	Air Mass (Coefficient)
An	Anorthite
Ann	Annite
Ap	Apatite
ap	aperture area
AU	Astronomical Unit
Au	Gold
Aug	Augite
avg	average
AvgSurf	Average Surface Composition
AZO	Aluminium doped Zinc Oxide
BFRPC	Basalt Fibre Reinforced Polymer Composites
BG	Basaltic Glass
BOL	Beginning Of-Life
BP-1	Black Point 1
BSE	Backscattered Electrons
By	Bytownite
C	Carbon
Ca	Calcium
CAD	Computer Aided Design
Cal	Calcite
CdTe	Cadmium Tellurium
Chl	Chlorite
CHN	Carbon, Hydrogen and Nitrogen Analyser
CIGS	Copper Indium Gallium Selenide
CIS	Copper Indium Selenium
CL	Cathodoluminescence
Cl	Chlorine
CLASS	Center for Lunar and Asteroid Surface Sciences
CME	Coronal Mass Ejection
Co	Cobalt
CPx	Clinopyroxene
CSA	Canadian Space Agency
csv	comma separated values
CTR	Carbothermic Reduction
Cu	Copper
CuInAlS	Copper Indium Aluminium Sulfur
CuInGaSe	Copper Indium Gallium Selenium
CuInS	Copper Indium Sulfur
CuInSe	Copper Indium Selenium
CVD	Chemical Vapour Deposition
CZ-Si	Czochralski-Silicon
da	designated Illumination area
Di	Diopside

DSC	Differential Scanning Calorimetry
EAC-1	European Astronaut Centre 1
EDS/EDX	Energy-dispersive X-ray Spectroscopy
EG-Si	Electronic Grade Silicon
EMW	Electromagnetic Wave
En	Enstatite
ENVISAT	Environmental Satellite
EQE	External Quantum Efficiency
ESA	European Space Agency
ESEM	Environmental Scanning Electron Microscope
EVA	Extravehicular Activities
F	Fluorine
Fa	Fayalite
Fe	Iron
FF	Fill Factor
FJS-1	Fuji Japanese Simulant 1
fltr	from left to right
Fo	Forsterite
Fs	Ferrosilite
Fsp	Feldspar
FWHM	Full Width at Half Maximum
GaAs	Gallium Arsenide
GaInP	Gallium Indium Phosphorus
Ge	Germanium
GEO	Geostationary Orbit
GER	Global Exploration Roadmap
Hbl	Hornblende
Hd	Hedenbergite
He	Helium
Hem	Haematite
HF	Hydrofluoric Acid
HRI	Human-Robot Interaction
HST	Hubble Space Telescope
Hz	Hertz
ICDD	International Centre for Diffraction Data
Ill	Illite
Ilm	Ilmenite
IMM	Inverted Metamorphic Multijunction
In	Indium
IR	Infrared
IS	Isomer Shift
ISECG	International Space Exploration Coordination Group
ISRU	In-Situ Resource Utilisation
ISS	International Space Station
JAXA	Japan Aerospace Exploration Agency
JSC	Johnson Space Centre
JSC-1A	Johnson Space Center 1A
JSC-MARS-1A	Johnson Space Center 1A MARS
JSC-2A	Johnson Space Center 2A
JSC-2A-TG	Johnson Space Center 2A Technical Grade
JSC-AF	Johnson Space Center A Fine
JWST	James Web Space Telescope
K	Potassium
KF	Potassium Fluoride
Kln	Kaolinite
KSC	Kennedy Space Centre
La	Labradorite
LEO	Low Earth Orbit
LOI	Loss on Ignition
LST	Lithium polytungstate
Mag	Magnetite
MBE	Molecular Beam Epitaxy
Mc	Microcline
mc-Si	multicrystalline-Silicon

Mca	Mica
Med	Median
Mg	Magnesium
MG-Si	Metallurgical Grade Silicon
MJ	Multijunction
MLI	Multilayer Insulation
Mn	Manganese
MOCVD	Metal-Organic Chemical-Vapour Deposition
MPP	Maximum Power Point
MRE	Molten Regolith Electrolysis
Ms	Muscovite
Na	Sodium
na	not available
NASA	National Aeronautics and Space Administration
Nb	Niobium
nc-Si	nanocrystalline Silicon
Ne	Nepheline
NEA	Near Earth Asteroids
NGO	Non-Governmental Organisation
Ni	Nickel
NIR	Near Infra Red
NSTS	National Space Technology Strategy
NU-LHT-2	NASA/USGS-Lunar Highland Type - 2 Medium
NU-LHT-3	NASA/USGS-Lunar Highland Type - 3 Medium
O	Oxygen
Ol	Olivine
Oli	Oligioclase
OM	Oxide Mineral
OPx	Orthopyroxene
Or	Orthoclase
PE	Polyethylene
PECVD	Plasma Enhanced Chemical Vapour Deposition
Pgt	Pigeonite
Phl	Phlogopite
Pl	Plagioclase
PlFsp	Plagioclase Feldspar
PPL	Plain-Polarised light
ppm	parts per million
PR	Public Relations
PV	Photovoltaic
PVA	Poly-Vinyl Acetate
PVD	Physical Vapour Deposition
Px	Pyroxene
QA	Quality Assurance
QE	Quantum Efficiency
QS	Quadrupole Splitting/Shift
Qtz	Quartz
Rb	Rubidium
RF	Radio Frequency
Rh	Rhodium
RMS	Root Mean Square
ROSCOSMOS	Roscosmos State Corporation for Space Activities
Sa	Sanidine
sccm	Standard Cubic Centimeters per Minute
SE	Secondary Electron
Se	Selenium
SEM	Scanning Electron Microscope
SEU	Single Event Upsets
SG-Si	Solar Grade Silicon
Si	Silicon
SiC	Silicon Carbide
SLM	Selective Laser Melting
SOTA	State of The Art
SoW	Statement of Work

Sr	Strontium
SW	Solar Wind
TA	Technology Area
TAS	Total Alkali-Silica (diagram)
TCO	Transparent Conducting Oxides
tbd	to be determined
TGA	Thermogravimetric Analysis
Ti	Titanium
TJ	Tripple Junction
TMag	Titanomagnetite
TMB	Trimethylboron
TRL	Technology Readiness Level
UAV	Unmanned Aerial Vehicle
UCF	University of Central Florida
UHV	Ultra High Vacuum
USA	United States of America
USGS	United States Geological Survey
UV	Ultra Violet
Vis	Visible
vol %	volume percent
WP	Work Package
wt %	weight percent
XPL	Crossed Polarised Light
XRD	X-ray (Powder) Diffraction
XRF	X-ray Fluorescence
Y	Yttrium
Zn	Zinc
Zo	Zircon
Zr	Zirconium

Variables

Symbol	**Description\Units**
Å	Angstrom Å
I	Current A
ϵ	Emissivity -
η	Efficiency %
f	Frequency Hz
λ	Wavelength nm
P	Power W
R	Resistance Ω
V	Voltage V

Publications

Manufacture of Glass and Mirrors from Lunar Regolith Simulant
Schleppi, J., Gibbons, J., Groetsch, A., Buckman, J., Cowley, A. and Bennett, N. - Journal of Materials Science, 54(5),2019, pp.3726-3747 https://doi.org/10.1007/s10853-018-3101-y

Theoretical Bioreactor Design to Perform Microbial Mining Activities on Mars
R. Volger, M.J. Timmer, **J. Schleppi**, C. N. Haenggi, A.S. Meyer, C. Picioreanu, A. Cowley and B. A. E. Lehner - Acta Astronautica, accepted 25.01.2020

Fibrous Habitat Structure from Lunar Basalt Fibre
Hanna Läkk, **Jürgen Schleppi**, Aidan Cowley, Lauren Vasey , Maria Yablonina , Achim Menges - 69^th International Astronautical Congress (IAC), Bremen, Germany, 1-5 October 2018. IAC-18-E5.1.8 x48245

An ISRU-Based Architecture for Human Habitats on Mars: the 'Lava Hive' Concept
Cowley, A., Imhof, B., Teeney, L., Waclavicek, R., Spina, F., Canals, A., **Schleppi, J.**, Soriano Lopez, P. - Acta Futura Vol. 10, Dec.2016, pages 109-119 https://doi.org/10.5281/zenodo.202220

1 Introduction

Earliest attempts to study the universe began with the Greeks and their first astronomical theories. Famous early scientists like Ptolemy, Aristarchus of Samos, Eratosthenes of Cyrene and Hipparchus of Nicaea used geometry to provide first numbers for distances and sizes in the Solar System [1]. Many famous names followed in the footsteps of these researchers, but as good and correct as their research was, it was always limited by the fact that they could all only make Earth based observations and conduct terrestrial measurements. It was not until 1946 [2], when space based measurements suddenly became available, when the first flights to space were made possible. In 1957, with Sputnik 1, the area of satellite remote sensing began and until 2002 when the so far biggest Earth observation satellite was launched with the European Space Agency's (ESA) - ENVISAT (ENVIronmental SATellite) [3]. With the Great Observatories program [4], in the time in-between 1990 and 2003, a series of four telescopes with different wavelength (visible, gamma rays, X-rays and infra red) was sent into space. Those, amongst others, have helped in the past decades to characterise the space surrounding Earth. Future missions like the James Web Space Telescope (JWST) [5] will continue to do so in the years to come.

Although observations by space based telescopes are important in understanding the origin of the universe, they are limited by only being able to detect a certain part of the electromagnetic wave spectrum hitting the sensors at a certain point in time. This limitation can be overcome by looking at parts of the Solar System that have been mostly untouched and have the history of the Solar System conserved. The age of Earth's Moon is assumed to be in-between 4.6 [6] and 4.4 [7] billion years, which is similar to the age of Earth [8]. However, the Moon's environment differs significantly from Earth's (more in section 2.1) with the major differences being the lack of an atmosphere and magnetic field. On Earth, most Solar System history is lost or not "recorded" since Earth has an atmosphere and a magnetic field protecting the planet from solar radiation. Moreover, weathering effects on Earth allow only for comparably short sedimentation periods which can provide clues about Earth's history. On the Moon however, the solar wind can directly hit the lunar surface and no environmental conditions erase the information about the history of our Solar System. Although, the lunar surface is still subject to change, such as space weathering, meteoroid impacts and cosmic radiation, some information that was lost on Earth may be preserved on the Moon.

Due to the Moon being volcanically active in the past, multiple layers of lava and regolith[1] form a "history book" of the activities in the Solar System, which was

[1] lose rocks/sand formed on the lunar surface by effects of space weathering - More in section 2.2.1.

stored on the surface of the Moon. The impact introduction of solar wind particles can be analysed in order to find cosmogenic isotopes like Argon (Ar), Neon (Ne) or Helium (He). The ratio of those isotopes can then be used to determine the history of the Solar System [9]. To get a full picture of the Solar System's history, samples of different ages need to be analysed. The amount of lunar material that is currently available on Earth for analysis is limited to >400 kg [10] - brought back by the Apollo missions, sample return missions, and lunar meteorites - and is only taken from a few different locations on the lunar surface. To get a better understanding of the history of the Solar System, more samples are required. Those samples should ideally be taken at different locations all over the Moon and would ideally be taken by drilling through different layers of regolith. More easily accessible samples can be gathered at the edge of craters or the rims of collapsed lava tubes and will deliver a greater timespan of the history.

To find out more about the history of the Solar System is one reason to return to the Moon but not the only one. Other reasons to return to the Moon may be: to inspire, the human need to explore, coming closer to solving the world's energy problems [2], preparation for potential manned missions to Mars or beyond or to build commercial bases on the Moon. Additionally most of these reasons might stimulate the economy and research on Earth. These and others are reasons for the worlds agencies to work on common roadmaps for space exploration like the Global Exploration Roadmap (GER) [11], shown in figure 1.1 and published by the International Space Exploration Coordination Group (ISECG). These roadmaps determine the direction of global space exploration in the coming decades and shall be a guideline for the development of national space programs and research.

From the Saturn V rocket flight manual [13] the actual "payload-to-lunar-surface" mass, which has been taken to the Moon during the Apollo missions, can be derived to about 6 metric tons (6,000 kg). This is the mass of the lunar lander after touch down (fuel of decent stage fully burnt). Future space exploration missions outlined in the ISECG's GER, such as human missions to the Moon and Mars, will have increasingly demanding payload requirements [14, 15]. Although advances have been made on technologies used during the Apollo area, the overall mass-to-surface has not increased drastically since the physical principles governing a direct landing with a launch from the Earth's surface have not changed. Physically speaking, that the amount of kinetic energy required to reach the Moon and to escape Earth's gravitational field has remained constant. So, even if it is possible to increase the mass to several tens of metric tons, this is still imposing constraints on the mission and equipment design. The number of resupply flights to a lunar landing site will be limited, thus typically all safety relevant equipment and payload for a mission needs to be included within the mass constraints. In the 1960s, In-Situ Resource Utilisation (ISRU) has been suggested to make a significant contribution to a space mission and open-up new approaches to mission design.

[2] by developing new, more efficient and more sustainable energy harvesting approaches

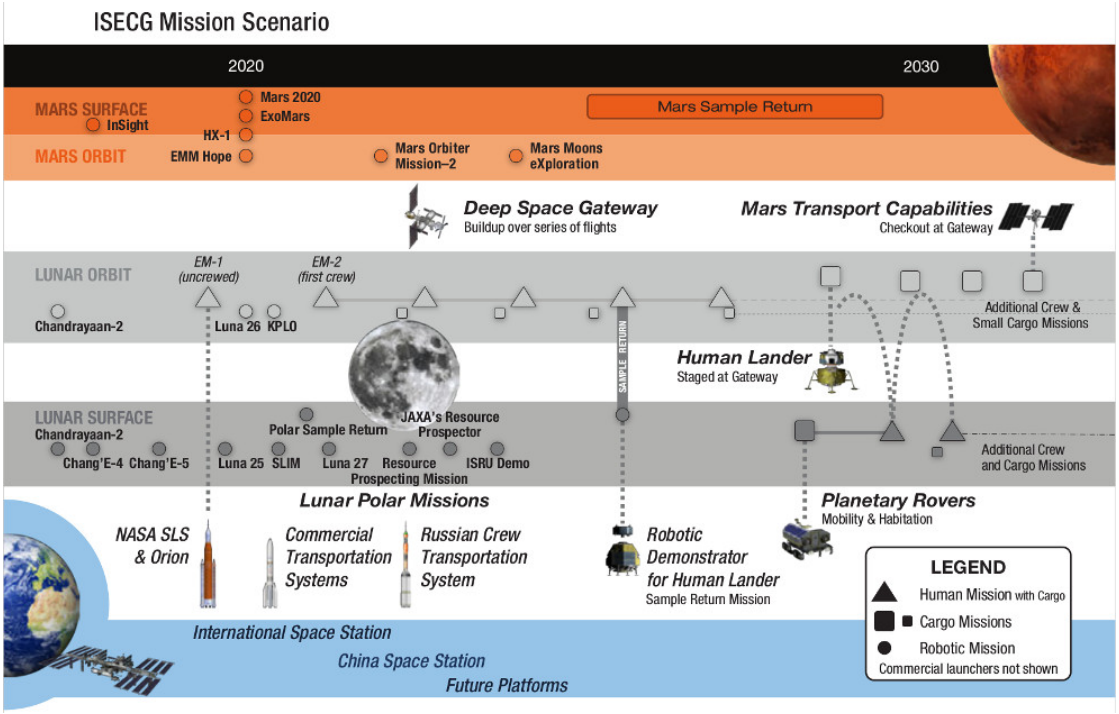

Figure 1.1: The ISECG's roadmap combining international plans for space exploration [12].

In space mission design ISRU refers to the possibility of using in-situ resources, found on other celestial bodies, to augment mission capabilities by replacing material which would be brought from Earth otherwise [16]. Such augmentation will reduce the number of re-supply flights needed and therefore significantly reduce the overall cost of human space exploration. Research conducted in the recent years showed how regolith can potentially be used as building material [17], and has been identified in the National Space Technology Strategy (NSTS[3]) the "NASA Strategic Space Technology Investment Plan - 2015" and ESA's "Space Exploration Strategy - 2015" as a field of interest. At present, a burden of proof exists on ISRU-related technology and mission designers are conservative in their integration of such technologies and methodologies for future exploration missions. However, a range of potential resources exists on the Moon, including minerals found in rocks and regolith and exploiting these resources via modifications to conventional extraction techniques may therefore be possible.

More specifically the technology roadmaps identified that augmentation by ISRU can make a difference ind the field of "Space Power and Energy Systems". Whether using lunar resources - by means of ISRU - to help satisfy power demand on the lunar surface, is feasible was the starting point for this work. The following elaborates on investigations into using lunar in-situ resources for the production of solar conversion devices.

[3]written by the UK National Space Technology Steering Group

1.1 Future Space Exploration

The first known mentioning of space exploration is referred back to Lucien of Samosata who wrote in his book *Lucian's True History* [18] in 175 AD about his journey to the Moon. This was pointed out by Greg Grewell in 2001 [19] and after Lucien of Samosata, many other authors followed in the coming centuries with their vision of what the Moon would be like or how we would get there (e.g. Jules Verne [20]). Finally, on July 20, 1969, at 20:18 UTC the Apollo 11 lunar module *Eagle* landed on the lunar surface and humans were walking on the Moon for the very first time. Another five lunar modules followed until on December 14 1972, at 5:55 pm EST the last one left the surface. Ever since, humanity has not returned to the Moon.

After the Moon landings the world was dreaming of exploring space and many proposals for long term settlements in space and planetary bases were made. Back in 1979, the National Aeronautics and Space Administration (NASA) in the United States of America (USA) filed a report [21], related to this topic, based on the outcome of the *Summer Study on Space Settlements and Industrialization Using Nonterrestrial Materials*. The report addresses five major topics relevant for long term space exploration:

1. Life support systems and controlled agriculture
2. Efficient space habitats
3. Asteroids as material sources
4. Electromagnetic mass drivers for use as interorbital engines
5. Chemical processing of nonterrestrial material in space

These topics mark one of the starting points for the "Post Apollo Era" of space exploration. The topics show in particular how much interest was given to the utilisation of extraterrestrial material already after the Apollo missions. What was true by the time the report was written, is still true today - bringing mass to space is expensive. Although improvements in the fields of rocket engines, launcher structure and light weight manufacturing brought the overall cost down, ever since Apollo the amount of energy required to bring one kilogram of mass into orbit is still the same. Which is exactly why it seems a logical step to utilise as much material as possible in-situ on the Moon itself, for example.

Since the late 70s, space agencies around the world have been working on common goals, like the exploration of the Solar System and bringing humans to the martian surface. Next will be shown, how current plans of the world's largest agencies plan to achieve these goals and which critical technologies they identified for these goals to be developed. Lastly, it will be addressed what are potential power sources, that are available for future exploration missions, as well as how these mission can be augmented by means of ISRU.

1.1.1 Human Exploration Goals

The current global future space exploration goals, of sending humans to the Moon and/or asteroids and/or Mars, create the necessity for humans and robots to,

once more, fly beyond the Low Earth Orbit (LEO). Missions like the International Space Station (ISS) or the Hubble Space Telescope (HST) are essential stepping stones to achieving the ultimate goal - a human mission to the surface of Mars. Benefits arising from such a mission to Mars can lead from cultural inspiration to solutions for global problems faced on Earth in the form of innovations [22].

One of the reasons why humanity is interested in space is that resources on Earth are limited. Whether it is material or energy, there is a limit to what can be obtained on Earth. For many years it is acknowledged that extraterrestrial resources exist and could be potentially harvested [23]. This only being one idea, the most prominent and comprehensive plan for space exploration has been issued by NASA with its "NASA Technology Roadmaps" [24] and the "NASA Strategic Space Technology Investment Plan" [25]. Since 2012, NASA therefore has an agency-wide structured plan for near and far-term space technology development, synchronised in-between the government and the needs of the scientists. Other agencies like ESA [15, 26, 27], the Japan Aerospace Exploration Agency (JAXA), the Roscosmos State Corporation for Space Activities (ROSCOSMOS), or the Canadian Space Agency (CSA) have similar plans. Plans of most of the world's agencies have been summarised in the ISECG's GER [12] shown in figure 1.1. The GER aims at expanding human/robotic exploration mission collaboration opportunities [28].

The mission scenario depicted in the roadmap in figure 1.1 outlines stepping stones and technologies required to send humans to Mars. This includes a "humans to the lunar surface" mission as a step towards flying to Mars. Although humanity has been to the Moon already before; this time it is about using the Moon as a test bed, rather than landing on the surface for a few hours or days only. A long-term lunar base will provide an ideal test bed for technologies, operations and "planetary" surface science. The information gathered during such a mission will be vital to achieving the overarching goal of flying to Mars. Technologies required for the ISECG mission scenario are discussed in the next section.

1.1.2 Key Technologies Required

In the recent years, multiple different designs, concepts for a lunar habitat or base have been developed, such as for example [29–33]. To be able to build such base designs, NASA has, as mentioned before, developed its "NASA Technology Roadmaps" wherein it identified 15 key technology areas necessary to be investigated, to push the boundaries and capabilities in aeronautics, science, and space. These 15 branches are shown in figure 1.2 and represent NASA's work in all fields, not only in space.

Within these areas, possibilities for mission augmentations, by using local resources at the destination, have been identified. Future missions will require better understanding on how to use indigenous resources. Using natural resources like metals or minerals as well as else discarded materials (recycling) can play a crucial role in succeeding. Technology Areas (TA), which could be enhanced by ISRU are:

Figure 1.2: NASA roadmap technology areas [24].

TA3, TA4, TA6, TA7, TA13, and TA14. Moreover, ISRU can be an enabler in the following areas: TA2, TA3, TA4, TA6, TA7, TA12, and TA14 [24].

This thesis will focus on augmenting TA3 - Space Power and Energy Storage and TA7 - Human Exploration Destination Systems.

1.1.3 Space Power Systems

Each space mission will require power, no matter whether it is a satellite orbiting Earth, a deep space probe, or a human planetary base. Mission designers choose the type of power device deployed according to the mission scenario. Main criteria for selecting a space power system are:

1. Power demands
2. Location
3. Lifetime requirements

The **power demand** is usually driven by the payloads, as depicted in figure 1.3. Different types of spacecraft have different loads and bus voltages. For example, Skylab had a load of about 10 kW, or the ISS has a maximum load of around 100 kW. Future space stations (space or planetary based) will have higher demands of up to 250 kW [34].

The **location** of a power system, located on a spacecraft, space station or planetary base is important to consider when choosing the type of power supply. When using solar cells, for example, it is important for the cells to be fully illuminated and and further, their power output is higher the closer they are to the Sun. With increasing distance from the Sun, the available solar power (W/m^2) is decreases, hence, the power that can be harvested by solar panels decreases

as well. A Moon base is approximately at the same distance from the Sun as Earth is, therefore enough solar power is considered to be available on the lunar surface. Potentially even more solar energy is available on the lunar surface, due to the lack of an atmosphere on the Moon, which is the reason for attenuation on Earth.

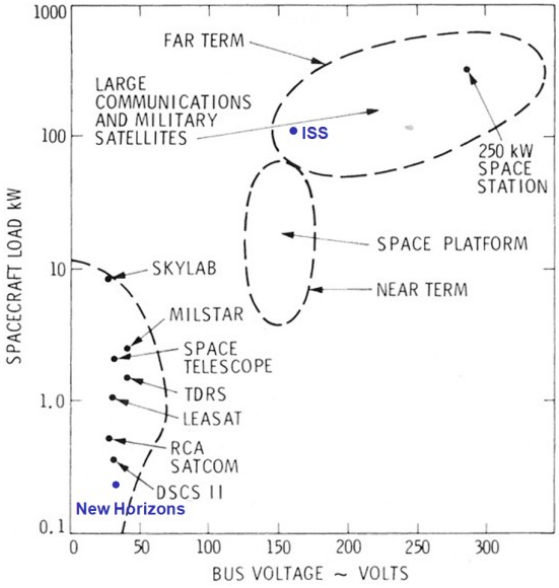

Figure 1.3: Trends in spacecraft power [34].

The **lifetime requirements** are determined by the mission duration. While at one end of the spectrum, there are the space shuttle and Apollo missions (short duration), and on the other end, missions like Voyager or Cassini (long duration). The duration of the mission will set requirements for power storage and consumables, thus narrow done the available power systems that can be used.

Types of power devices available for space missions in general are:

- Fuel cells
- Batteries
- Solar arrays
- Nuclear reactors
- Radioisotopic Thermal Generators (RTGs)

In figure 1.4, these devices are shown with respect to their use aboard spacecraft. The larger a spacecraft gets, the more power it will require to operate. The same is true for a lunar or planetary base, the larger it gets, the higher the power demand of the station will be. Concepts for power systems for a lunar outpost have been reviewed in [35] and outline the technologies and development required for a lunar outpost. Depending on the scenario, different devices are used for different durations and serve different purposes:

Fuel Cells are most often used for short duration missions like the Apollo missions or space shuttle missions, but have also been analysed for their uses in surface applications [36]. Fuel cells are, however, not only used and developed for space

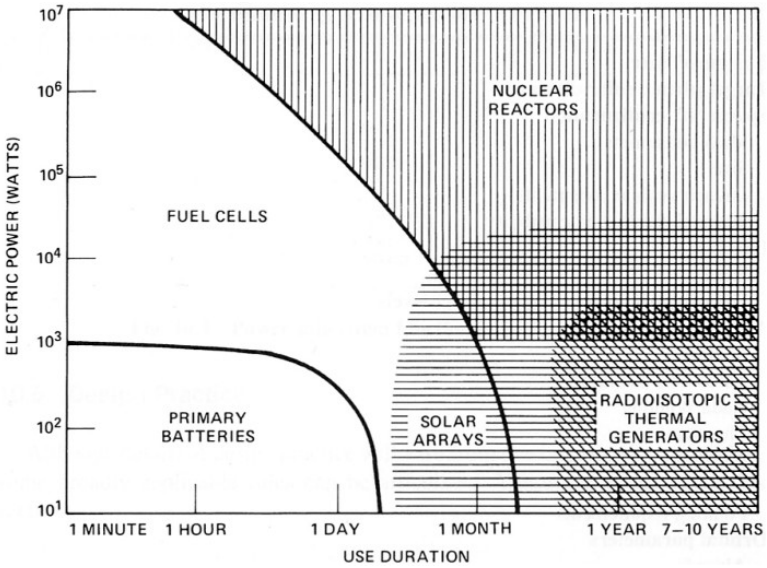

Figure 1.4: Operating regimes of spacecraft power systems [34]

anymore but also for terrestrial applications, such as the use in UAVs (Unmanned Aerial Vehicle), for example, is getting more common [37]. A current State Of The Art (SOTA) regenerative fuel cell system offers a power-to-weight[4] ratio of 500 $^{W}/_{kg}$ - for comparison historic values are shown in table 1.1. These numbers need to be reviewed, bearing in mind that a fuel cell does not run without fuel and hence the weight of the fuel cell system including fuel and storage tanks tends to be higher. If, however, the fuel can be re-utilised by electrolysing the exhaust product water, the power to weight ratio can be stabilised.

Table 1.1: Performance summary of fuel cells for space use [39].

Specific	**System Power** ($\frac{W}{kg}$)	**Operation**
Gemini	33	
Apollo	25	
Shuttle	275	2500 hr at P_{avg}
SPE Technology	10-146	>40000 hr
Alkaline Technology	367	>3000 hr
Alkaline Technology	110	>40000 hr
Goal (Light Weight Cell)	550	

Batteries in combination with solar arrays are most commonly used on spacecraft, such as communication or Earth observation satellites placed in LEO or Geostationary Orbit (GEO), which require medium power. However, solar arrays have also been used for missions beyond Earth's orbit like in the Rosetta mission

[4]One of the metrics important for space based power systems, also called specific power (unit $^{W}/_{kg}$). It defines how much power a system can generate per kilogram overall system mass. A high power generation by at the same time little weight, is an ideal value for space applications. A theoretical power system with 1000 $^{W}/_{kg}$ specific power can therefore deliver $1^{kW}/_{hkg}$. Further reading in [38]

[40]. Batteries and solar arrays can also be used in combination with fuel cells to form an off-grid power supply that can power a planetary base during day and night time. Most locations on Earth's Moon have a day and night cycle of about two Earth weeks. Hence, at most locations the Sun is not shining for a duration of about 350 h. This poses the challenge of supplying a lunar base with power during the night, and required power storage. To achieve this with only batteries does not seem likely, therefore, including fuel cells in the system design can overcome these challenges. Hydrogen and oxygen can be produced during the day by converting solar power into electricity and using it for electrolysing water. Storing hydrogen and oxygen produced from electrolysing water during the day allows to use it for a fuel cell system during the night. Even with the best fuel cells available at the moment, the weight of the overall power system is estimated to be 6.7 metric tons [41, 42] and therefore, only the power system would approximately take up all the payload mass (to lunar surface) of one Saturn V rocket.

Solar Arrays have been analysed for their use in a stationary setup for a lunar base located at the lunar south pole [43]. Due to permanently lit areas found in that region on the Moon, it may be possible to use only solar cells for power supply, since they would permanently be illuminated. Other design and power considerations for lunar bases have been conducted in the past, and further highlight potential advantages and disadvantages of photovoltaic power systems [44–48]. All pointing out that, solar energy is the only energy directly and almost infinitely available on the lunar surface, and should therefore be included in any system design.

Nuclear Reactors offer high power for long durations and would be ideal for a human planetary surface mission since they can deliver constant power independent of illumination conditions [49, 50]. This advantage might be outweighed by the need for radiation protection material (increase of mass) to keep the payload and/or humans safe [41]. Moreover, in case of total failure of the launch system during the first seconds of launch, radioactive material will be spread over large surface areas on the ground, increasing the risk of using nuclear reactors.

Radioisotope Thermoelectric Generators (RTGs) are typically deployed for long duration missions with comparably low power demands, further away from the Sun than Earth or Mars. Examples are Cassini or Voyager, but also the curiosity rover [51] on Mars, which is currently using an RTG. Researchers at NASA are working on using an energy conversion process - such as the Stirling process - rather than a thermoelectric process which could yield a better power-to-weight-ratio [52] for RTGs and thus expands its uses to other mission types. Currently, however, the output power and specific power of these devices is too low to be considered for a planetary base with power demand of about 250 kW.

Other Options, such as wind as a source for energy, for example, which could only be utilised on Mars [53] but not on the Moon, or other alternative power sources are not evaluated in this work. However, novel and unconventional [54] energy storage methods as, for example, using ISRU to work as a thermal energy storage

[41, 55, 56], are promising concepts which may become more relevant in the future.

The estimated required specific power for future exploration missions, undertaken by NASA, are more than 500 $^{W}/_{kg}$ [57]. The following table (1.2) shows an overview of some power devices available for space missions. The list is by no means extensive nor is the mass of fuel - for the fuel cells, for example - considered, as well as batteries, for example, will need to be recharged. However, the table provides an indication to the general potential capabilities of a technology.

Table 1.2: Summary of specific power of selected power systems only some examples shown.

Power Supply	Specific Power $^{W}/_{kg}$	Reference
Fuel Cell	500	[42]
Multijunction Solar Cells	1000 /1400+	[58, 59]
Thin-Film Solar Cells	2000	[60]
RTG	5	[61]
Batteries	2000	[62]
Nuclear Reactor	(700 $^{kW}/_{dm^3}$)	[38]

The numbers listed in table 1.2 show, that solar cells and batteries can have higher specific power values than the 500 $^{W}/_{kg}$, specified by NASA [57]. In addition to that, as discussed, it is however likely, that solar cells will not be used as a standalone system, but would be augmented with fuel cells and batteries. Despite other metrics that could be considered as well, the specific power gives a good indication of which power systems are most promising. Although RTGs perform poorly, considering the specific power metric only, is not showing other benefits RTGs have. Thus an overviews and further information on RTGs is provided in [61, 62]. Considering the selection of a specific type of solar cell, trade-off analyses for space solar cells can be found in [63, 64]. These may provide a basis for choosing a solar cell type, once other parameters such as a lunar landing site are known.

In conclusion, photovoltaic (PV) systems employing solar modules/cells are considered a good choice for a lunar base power system in general. Hence, investigations into augmenting solar cell technology with lunar in-situ resources will be conducted in this work.

1.1.4 In-Situ Resource Utilisation - ISRU

Gaining knowledge on how to utilise indigenous resources is vital to any extended human presence and operations on an extraterrestrial body. Locating, harnessing, utilising and recycling resources on the exploration site - to create new products - is the purpose of ISRU. Aforementioned, space resources can include (but are not limited to) regolith, water, metals, discarded hardware, and solar energy. By using these resources, ISRU is ultimately aiming at reducing the overall system weight

and cost of exploration missions, as well as providing a second layer of safety in case resupplies fail.

As pointed out in the previous sections, space missions are significantly constrained by their payload mass. Which is why, already early after the Apollo missions ended, scientists and engineers started thinking about using extraterrestrial material to augment space missions [21]. Manufacturing equipment outside Earth's atmosphere, on another celestial bodies will significantly lower the launch mass, and therefore provide more space for scientific equipment and astronauts, for example. The use of regolith on the lunar surface, for such uses, seems a first choice, since it is the abundant material on the Moon. Ideas for technologies using regolith in-situ are for example using fuel extracted from space propulsion [65], or manufacturing of regolith-derived reentry heat shields [66].

ISRU in general can be defined as a multi-stage process; which is schematically depicted in the flow diagram in figure 1.5. This flow chart identifies four main stages:

1. Use of source material without beneficiation
2. Production of resources
3. Use of source material by use of energy
4. Use of source material by introducing additives

The complexity and technology required for each stage varies depending on the final product. Some applications only require power as a resource where as others need consumables in the form of gases for example. Further extracting water on the lunar surface seems comparably easy to extracting elemental silicon [67]. Finding smart and resource saving applications for lunar resources is considered to be the goal of any ISRU application. Since ISRU can make a significant difference for mission design, it is essential that more practical validation of ideas is carried out, to determine what is achievable within the technical constraints.

Before ISRU technologies achieve the required Technology Readiness Level (TRL [68]), they will not be deployed on an actual space mission. Currently only a few technologies have been practically validated [69–77] and, considering the number of potential applications for ISRU identified in 1.1.2, these works seem to be rather little. Further, none of these technologies has reached the required TRL to fly on a space mission as a mission critical system yet. Hence, it seems vital, that the TRL of such technologies is advanced further within the next years, to realistically consider these new technologies for a lunar surface mission. In the context of these findings, work conducted for this thesis is aiming at advancing the TRL of producing solar conversion devices by means of ISRU.

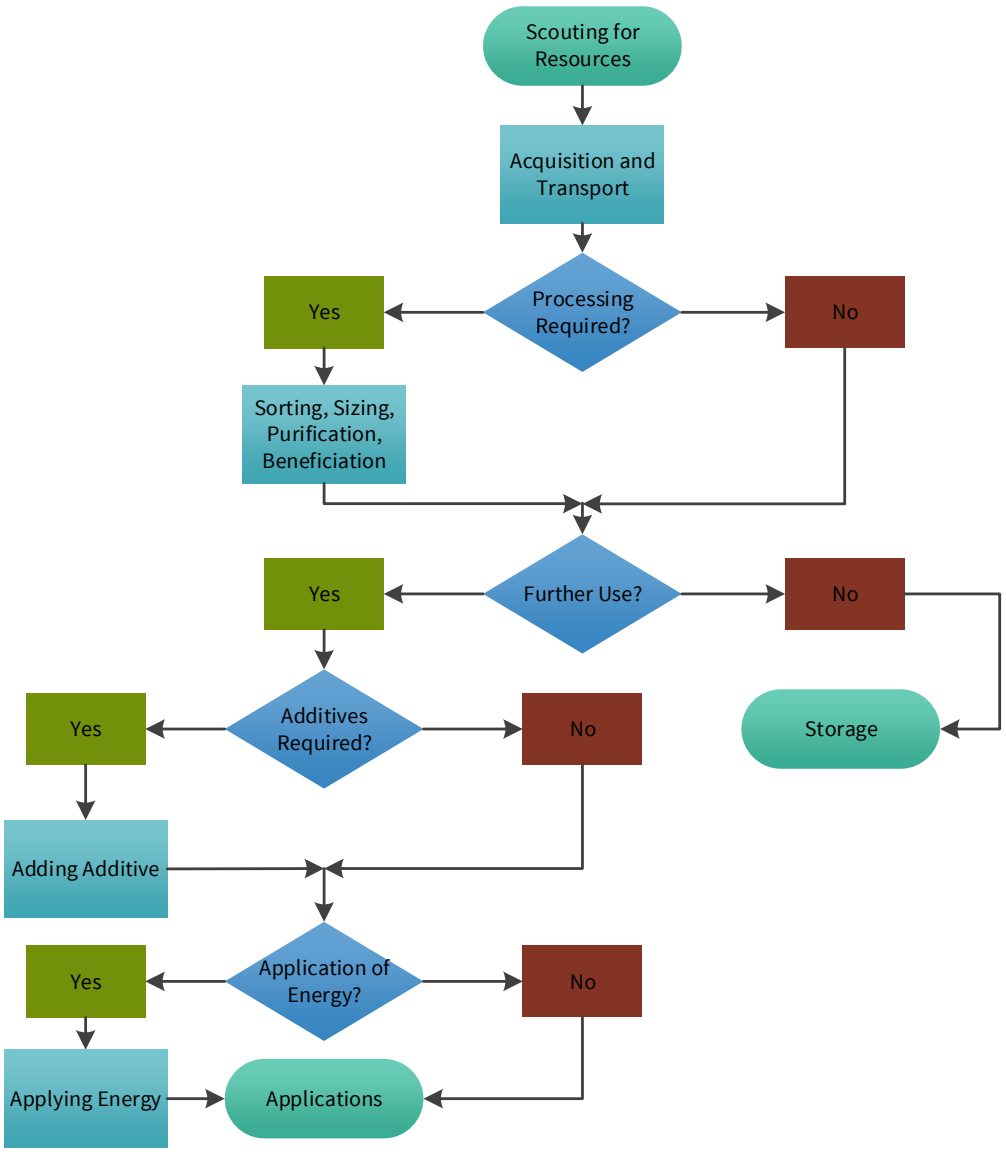

Figure 1.5: A schematic overview of the steps necessary for manufacturing mission relevant components in-situ.

1.2 Research Objectives

Based on gaps in humankind's knowledge, the key objectives of this thesis are:

1. Determine suitable raw materials for manufacturing and testing, using lunar surface like materials.
2. Demonstrate manufacturing of glass like substrates for use as back-plate, and cover glass for solar conversion device production.
3. Demonstrate manufacturing of solar conversion devices from primarily lunar analogue material.
4. Use experimental methods to determine the quality of the substrates and determine the performance of built solar conversion devices, corresponding to space exploration technology roadmaps.

1.3 Novelty Statement

This thesis demonstrates for the first time how lunar regolith simulant can be used to manufacture basaltic glass substrates. For future lunar/planetary surface missions this glass as resource can be particularly interesting. Further, beneficiation techniques have been investigated, which alter the optical properties of this glass and open it up to a variety of uses. One field of usage for this glass, the field of power generation, was investigated in detail by, for the first time, manufacturing working solar conversion devices using mostly lunar like materials.

1.4 Thesis Outline

The remainder of this thesis is structured as follows:

Chapter 2 provides a review of the latest literature in the fields of lunar environment, regolith, regolith simulant (regolith analogue material) and basaltic glass, extraction and purification processes, ISRU manufacturing techniques and solar conversion devices. It also establishes the context and goals for the research undertaken in this thesis.

Chapter 3 describes the experimental approach and conditions under which solar test devices were manufactured.

Chapter 4 discusses methods used for testing and characterisation of manufactured devices and measurement samples.

Chapter 5 elaborates testing of basaltic raw material used for manufacturing, testing of basaltic glasses, mirrors, mirror concentrator devices and solar cells.

Chapter 6, the conclusion, summarises key findings, draws conclusions from the conducted research undertaken and identifies areas for future exploration.

2 Literature Review

Current exploration plans of the world's space agencies as well as the potential of ISRU has been outlined in the first chapter and showed the need for developing new space exploration technologies. Interesting in particular is the idea of building power generation systems on the lunar surface, using local resources. Thus, this chapter focuses on aspects relevant to this idea by, reviewing the environmental conditions and available materials on the lunar surface, lunar analogue materials available on Earth, manufacturing and purification methods used to process lunar (analogue) regolith and energy harvesting technologies. Reviewing the latest relevant research in these areas shall provide a start for building solar conversion devices from lunar analogue material on Earth and ultimately in-situ on the lunar surface. The review concludes with a plan on how to fulfil the research objectives listed prior.

2.1 Lunar Environment and Resources

The lunar environment is necessary to be considered for the design and testing of surface mission equipment. Further, it will be relevant to understand what resources are available on the lunar surface to be used as building/manufacturing materials.

2.1.1 Lunar Environment

The lunar environment is different from Earth's in many ways, the following provides a brief overview of the most prominent differences between Earth and the Moon.

Atmosphere and Magnetic Field

Planet Earth is protected from the hostile space environment by an atmosphere (1 bar pressure at sea level) and a magnetic field (25 - 65 μT magnetic field strength [78]), both of which the Moon does not have. The pressure on the lunar surface at night is as low as $3 * 10^{-15}$ bar [79] and the magnetic field is less than $2 * 10^{-8}$ of Earth's dipole moment [80, 81]. Local maxima of > 40 nT [82] can, however, be found in some areas on the Moon. Although a global magnetic field does not exist on the Moon, there are regions with so called crustal magnetic anomalies [83, 84]. The current understanding is that these anomalies occur at the same locations where lunar swirls are found [81], and a global map of such can be found in [85]. Although the Moon does not have a global magnetic field, local magnetic field strength maps [82] of the Moon might be relevant for landing site selection. Local magnetic fields may be beneficial for a lunar base since they may offer some radiation protection or navigational guidance. As mentioned, the Moon does not have an atmosphere, thus, natural convection due to atmospheric gases, as well as erosion caused by winds,

is non-existent. As a consequence, the missing atmosphere and largely reduced magnetic field will impose higher doses of radiations on humans and equipment than on experienced on Earth.

Space Weather

The weather in space is primarily determined by the Solar Wind (SW) which is a plasma mainly consisting of ionized hydrogen[1], details are shown in table 2.1 [86]. The SW is not constant and its parameters are dependent on the 11 year solar cycle. Due to the lack of an atmosphere on the Moon, space weather, and therefore the SW, has a high impact on a lunar surface mission.

Table 2.1: Measured properties of the SW near the orbit of the Earth (1 AU) [86]

Parameter	Value
Proton Density	6.6 cm^{-3}
Electron Density	7.1 cm^{-3}
He^{2+} Density	0.25 cm^{-3}
Flow Speed (Nearly Radial)	450 $^{km}/_{s}$
Proton Temperature	1.2 * 10^5 K
Electron Temperature	1.4 * 10^5 K
Magnetic Field (Induction)	7 * 10^{-9} T

The solar wind speed is an indicator for the activity of the Sun. Its speed is usually in-between 260 $^{km}/_{s}$ to 750 $^{km}/_{s}$. The all-time high was recorded on 29 - 30 October 2003 with a peak of 1850 $^{km}/_{s}$ [87]. These high speeds are a result of Coronal Mass Ejections (CMEs) which even in the vicinity of Earth under the protection of an atmosphere and a magnetic field can lead to system failures and significantly impact the habitability of a celestial body [88]. Not least, this also impacts the solar irradiance [89] and therefore the performance of solar panels deployed in space or on the Moon.

Moon's missing atmosphere is also the cause for gamma rays, X-rays and full spectrum Ultra Violet (UV) light directly hitting the surface. Earth's atmosphere protects its inhabitants and technology from gamma radiation and X-rays [90, 91], as well as 100 % of the UV-C (280 - 100 nm) and 90 % of the UV-B (315 - 280 nm) light [92]. The UV-A (400 - 315 nm) part penetrates fully down to the surface. This abundance of radiation on the lunar surface shall be taken into account for the system design as, for example, the design of radiation tolerant solar cells [57].

All types of radiation can lead to long term degradation of a solar cell in space. Figure 2.1 shows the effect of degradation on a solar cell by looking at a voltage vs. current diagram. It can be observed, that current and voltage decrease, from Beginning Of Lifetime (BOL) until the End Of Lifetime (EOL). Power requirements

[1] protons and electrons in nearly equal numbers, as well as approximately 2 - 4 % of He^{2+}

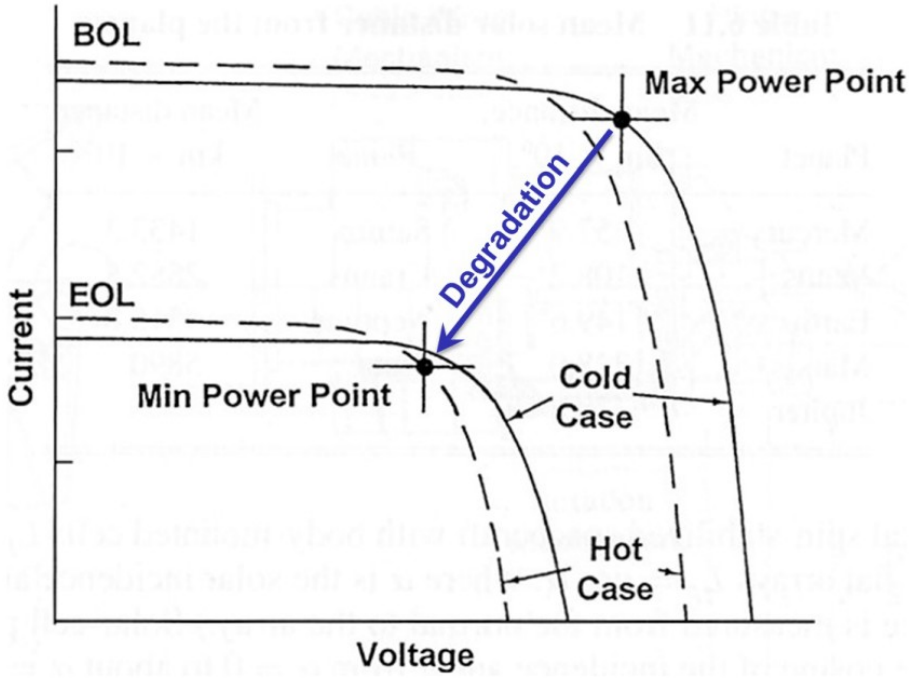

Figure 2.1: Diagram showing voltage versus current plot of the BOL and EOL of a solar cell for the hot and cold case [34].

should always take degradation into account, when designing the solar array system according to the EOL power delivered by the cells. Moreover, radiation protection in the form of a glass shield covering the radiation facing side of the panels should be considered. Radiation protection will also influence the overall weight of the system and decrease the specific power value of the devices. Parts of the system which need to be illuminated, such as solar cells, could therefore be protected by transparent glass, ideally manufactured using local resources. Parts of the system which do not need to be illuminated directly can be protected by utilising regolith, or regolith in combination with polymers and/or water [93, 94]. However, such a radiative protection might weather and break down [95], thus may require maintenance after a certain time.

Gravitational Force and Temperature

The average maximum and minimum temperature around the equator on the lunar surface is found to be in-between 94.3 - 392.3 K (mean average 215.5 K) and 50 - 202 K (mean average 104 K) around the poles ($> 85°$ latitude) [96–98]. Temperature changes are linked to illumination conditions (day/night) and are important to be considered for the analysis and design of a lunar outpost, including its power and thermal systems [99, 100]. Permanently lit and shadowed areas [101, 102] can be found around the poles which will deliver stable conditions from a thermal perspective, but also in terms of availability of sunlight, and hence power. Further considerations of the lunar environmental conditions with respect to a potential lunar landing sites selection, can be found in [103].

The surface acceleration on the Moon is only 1.62 $^{m}/_{s^2}$ [79] compared to 9.78 $^{m}/_{s^2}$ on Earth. The reduced gravity environment is expected to have long term impact on the human locomotion, physiology and behaviour [104–106] which will create challenges for day-to-day operations and Extravehicular Activities (EVAs) [107]. On the bright side, bulkiness and mass of equipment manufactured on the lunar surfaces can be up to six times higher than on Earth. This could be beneficial for producing large parts like glass plates or mirrors since it would make transport and handling easier.

Lunar Dust

The very fine dust on the lunar surface can be a significant problem for operations and hardware. Lessons learned from the Apollo missions [108] are that the lunar dust is important to be considered in equipment design due to its health and safety risk [109, 110]. The effect of dust on the Apollo space suits has been studied [111, 112] and potential electrostatic removal systems [113] as well as filtration systems [114] have been developed to minimise that risk. Dust mitigation was not only studied for space suits but for all equipment deployed on a planetary surface [115–117], and potential counter measures like electrostatic curtains have been investigated [118–120]. Since the Moon does not have an atmosphere, dust transportation via wind does not occur. However, charged dust particles are known to appear in cloud form near the surface of atmosphere-less bodies such as the Moon or asteroids, which might be caused by electric discharges on the surface [95, 121]. A comprehensive summary of the effects of dust on solar cells and reflectors can be found in [122] and shows that dust coverage can lead to significant reduction of a solar cells performance.

2.1.2 Solar Radiation

The Sun in our Solar System radiates in a certain wavelength spectrum (yellow area in figure 2.2) which gets attenuated on Earth due to the Earth's atmosphere or air mass (red area). This attenuation is typically represented by a coefficient called Air Mass (AM) coefficient. The air mass is exactly 1.0, if the Sun is directly above (zenith) the solar cell/spectator, and it is 1.5 at 48.2°, and 2.0 at 60° [123]. Hence, the red area in figure 2.2 corresponds to AM 1.0 and AM 1.5 and 2.0 would be respectively lower/smaller. Note the "valleys" or attenuations in the red coloured part are caused by atmospheric interaction in-between the sunlight and the atmospheric gases. Additionally, a thorough explanation on AM values and spectra is provided in [124].

On Earth, certain wavelength regimes are specifically targeted for energy harvesting, since, due to attenuation effects in the Earth's atmosphere, not all of the emitted sunlight hits the surface. Hence, not all sunlight which would be available in space, is available for energy harnessing on Earth. Typical power per surface area levels, outside the Earth's atmosphere at 1 Astronomical Unit (1 AU = 1.496 * 10^8 km [126]) distance from the Sun, are about 1367 $^{W}/_{m^2}$ [127, 128] for a wavelength spectrum of 250 - 2500 nm. This value is called, the solar constant [129] and is based on spectral irradiance measurements (depicted in figure 2.2). Compared to that, for standard testing of solar devices under the Earth's atmosphere, 1 Sun is

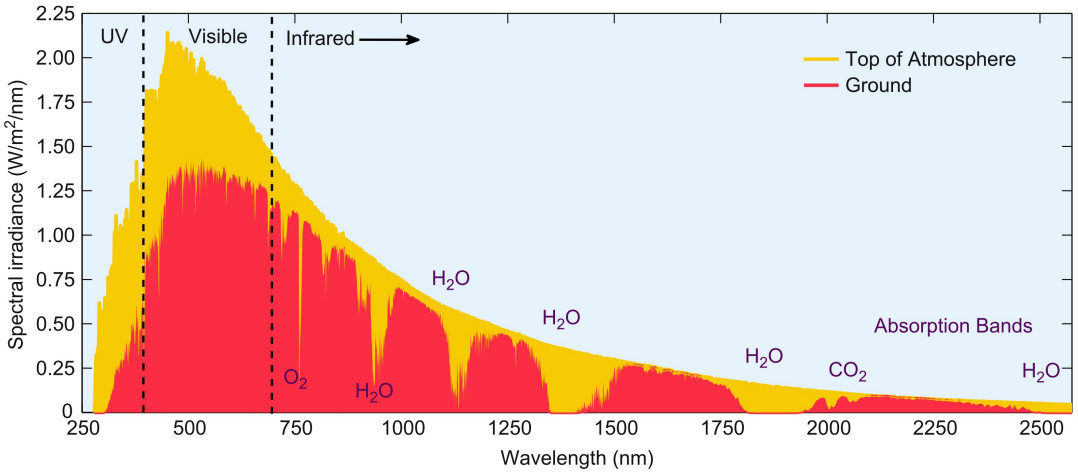

Figure 2.2: Spectral Irradiance of the Sun dependent on the wavelength [125].

used which corresponded to 1000 $^{W}/_{m^2}$, which accounts for the attenuation. The difference between these two values is made visible graphically in figure 2.2, and is the difference in-between the surface area of the yellow and the red area.

This gives a space based solar devices an advantage compared to a Earth based one, since the same surface area of solar panels has more power available for harvesting, thus produces more electrical energy. At this point it needs to be understood that each solar cell type can only harvest energy from a certain wavelength band and although the irradiance in space is higher for all wavelength, only a fraction of the 1367 $^{W}/_{m^2}$ can be converted by each type of solar cell.

The total solar radiation power outside of Earth's atmosphere is almost constant, but energy harvesting on the lunar surface might be impacted by other factors as well, such as:

- The position (latitude) on the Moon
- The time in the year, such as date and time
- The incident angle on a collecting surface
- The reflection from the lunar surface

These will impact the decision at which location and at which orientation solar panels are mounted on the Moon.

2.1.3 Potential Resources

Reviews about potential resources on the Moon and how they could theoretically be utilised are provided by [21, 67, 130–133]. However, none to little practical validations or testing of these ISRU approaches was conducted and poses a gap in knowledge. Furthermore, these authors show that there is a number of different elements which can be found on the Moon which may be exploited. However, the authors also show that none of them can be extracted with simple technology and the most practical resource to extract seems to be water (H_2O)

[67]. Water has independently been confirmed to occur around the Moon's poles [134–136] and it seems that water trapped in the lunar regolith is recently getting more attention [137]. This interest may not at least be based on the idea of using regenerative fuel cell systems in combination with PV. Other elements abundant on the lunar surface are oxygen, silicon, aluminium, iron, calcium, magnesium, titanium and smaller amounts of other elements (more will follow in table 2.2).

The mineralogical and chemical composition of the Moon has been measured by means of analysing samples[2] or remote sensing [138, 139]. Remote sensing seems to be prone to more sources of error [140] than direct sample analysis [141], due to the distance between sample and measurement instrument. With remote sensing it is however possible to create a map of the composition of the Moon's surface. On top of the chemical elements which could be gained from the lunar regolith, other trace elements, such as nitrogen [142], phosphorous [143] or hydrogen [144] (from SW or micrometeorites [145]) can be found in the lunar environment. It might be viable to harvest some of these resources and utilise them for in-situ production of consumables or devices such as solar panels. This, however, does not seem feasible since the abundant amounts on the lunar surface are to little for small scale mining/exploiting. Excavation prototypes, suitable for gathering regolith were already reviewed in [146] and harvesting of lunar resources can be assumed possible in general. Lastly, as an alternative to sourcing material from the lunar surface, it is worth mentioning, that in the long run it might be viable to harness Near Earth Asteroids (NEA) for resources as well. These NEA harvesting missions could be launched from the lunar surface as well, rather than from Earth [147].

2.1.4 Conclusion Lunar Environment

Lunar conditions and resources have shown to be different from the Earth's. Understanding these differences before deploying newly developed systems on the lunar surface will be essential. Hence, after successfully manufacturing devices on Earth, by using lunar analogue materials, testing whether these devices will withstand the lunar environment will be a next step. Since, however, the path from "regolith-to-solar-cell" seems rather long, environmental testing is not considered a priority, as long as no working devices are built. Thus, the following recommendations for environmental testing only apply once working devices have been built.

After successful manufacturing, extensive testing for lunar environmental conditions will be required. The conditions to be considered for testing are:

- Vacuum environment
- Unfiltered solar wavelength spectrum (AM 0) exposure
- Thermal environment
- Radiation effects
- Reduced gravity environment
- Dust contamination

[2] Apollo, sample return missions and lunar meteoroids

These should be tested either individually and/or in combination. Although, lunar environmental testing may not be conducted within this thesis, environmental conditions on the lunar surface will be considered for the design of any equipment to be manufactured on Earth, to ultimately enable manufacturing on the lunar surface.

2.2 Regolith, Regolith Simulant and Basaltic Glass

Addressed in the previous chapter already, the lunar surface has resources to offer, which can be used and made available for building and manufacturing by means of ISRU. Before using any material for manufacturing or processing, an overview of the available actual lunar regolith, lunar analogue regolith (simulant), as well as (basaltic) glasses is provided. Selected works in these fields are shown and provide a direction for manufacturing solar conversion devices from regolith.

2.2.1 Regolith

The lunar surface can generally be divided in two different areas, the mare areas, which appear darker to the human eye, and the highland (terrae) areas which appear brighter. The lunar surface is covered with a layer of fine dust, the so called regolith, depicted in figure 2.3 on the left. It is up to 10 meters thick in the highland regions and up to 5 meters in the mare regions [148]. Schematically depicted on the right in figure 2.3 are the first 25 km of the lunar crust, where these 5 - 10 meters of regolith are depicted on top.

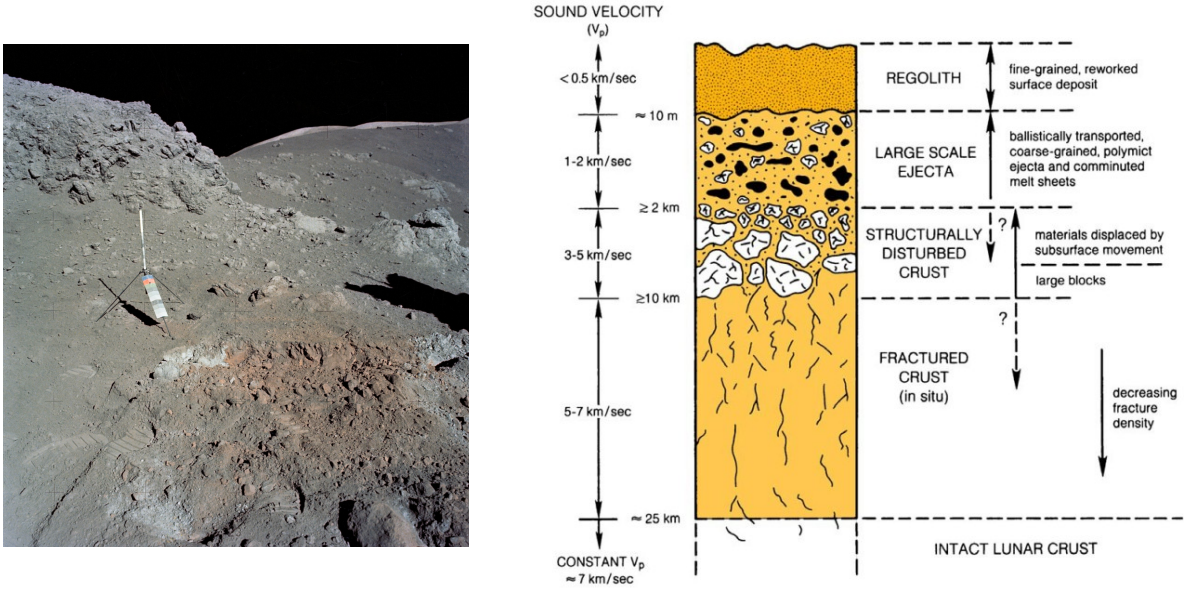

Figure 2.3: (Left, a photograph taken by Apollo 17 astronauts during an EVA (credits: NASA). Right, a schematic cross-section of the structure of the upper lunar crust, taken from [149], originally published in [148], and modified by [103].

Although the bulk part of the regolith is fine grey soil, it also contains rock fragments from the bedrock (depicted on the right in figure 2.3). The bulk of this

fine grey regolith is a soil with a density of about 1.5 g/cm^3 [150]. Further, half of the weight of the lunar regolith is made up of grains, smaller than 60 to 80 microns [150]. Many studies on the lunar regolith's characteristics have been conducted such as, its thermal behaviour [151–153] or grain size distribution [154–158], for example. Overviews of the regoliths' characteristics are provided in [159, 160] and comprehensive works on lunar regolith can be found in [161, 162]. All lunar samples NASA gathered so far are catalogued online in the, Lunar Sample and Photo Catalogue [163].

Regolith characteristics of particular importance for manufacturing are its geochemistry and mineralogy. Not only will these characteristics define processing temperatures, or suitable materials used to process regolith, but also give clues to how regolith can be made useful for building solar conversion devices, such as mirrors or solar cells in general. Thus, next, a closer look is taken at these two characteristics.

Geochemical Composition

An average (geo)chemical composition of the lunar regolith is shown in table 2.2 provided by [164]. Other measurements of more specific samples can be found in [165] and a comparison of remote sensed and real values can be found in [166].

Table 2.2: Average (geo)chemical composition of lunar regolith and Earth's crust in weight percent (wt %) [164].

	Percent of Atoms			**Oxides**	**Percent of Atoms**
Element	Maria	Terrae	Average Surface	Average Surface	Earth's Crust
Oxygen (O)	60.6	61.1	61.1	-	45.2
Silicon (Si)	16.8	16.2	16.3	45.0	27.2
Aluminium (Al)	6.6	10.2	9.5	22.3	8.0
Magnesium (Mg)	5.3	4.0	4.3	8.0	2.8
Calcium (Ca)	4.7	6.3	6.0	15.5	5.1
+ Potassium (K)					1.7
Iron (Fe)	4.5	1.6	2.3	7.6	5.8
Titanium (Ti)	1.0	0.1	0.3	1.1	0.9
Sodium (Na)	0.4	0.4	0.4	0.6	2.3

The composition listed in table 2.2 shows estimated amounts of chemical elements contained in the lunar soil, which are based on samples from eleven landing sites, collected during the six Apollo and three Luna missions. Although the listed average composition of the lunar surface regolith may not be accurate, since it is only averaged using elven landing sites, it still gives an indication to what elements are likely to be found at a landing site. After oxygen, silicon seems to be the most abundant element, which suggests that enough of it would be available to consider manufacturing silicon based solar cells of it. However, all elements (including silicon) occur in their very stable oxide form and first need to be freed

of their oxygen, by processes which are non-trivial. Thus, in the next section these processes will be reviewed as well, to determine whether silicon extraction on the lunar surface could be a viable option.

Comparing the lunar composition, with the composition of Earth's crust, both listed in table 2.2, both appear similar. Therefore, it seems possible to find a (geo)chemical analogue material (similar to lunar regolith) on Earth. The first and most obvious choice are basaltic sands found on Earth, some of which have shown to be adequate simulants in terms of their composition. Regolith simulants will be discussed in more detail in section 2.2.2 after a brief look is taken at the lunar regolith's mineralogy.

Mineralogy

The geology and mineralogy of lunar material has been studied intensively since the 60s, which is why it is impossible to provide a full overview in this literature review. Therefore, this section merely provides a minimum overview. However, an in-depth study will only need to be conducted once a landing site will have been selected. Despite a project specific in-depth study of lunar geology not being conducted, some of the most recent works provide an overview of the geology, geochemistry and geophysics of lunar regolith [167]. Further geological studies can be found in [168–170], the lunar source book [148], and a few further examples of mineralogical studies [171–175].

The mineralogical composition from the Apollo and Luna mission is summarised in table A.2 in the appendix, from which can be seen that pyroxene, plagioclase and olivine are the dominant minerals on the lunar surface. These minerals are mainly consisting of oxygen, silicon, aluminium, calcium, iron, sodium and magnesium, which correspond to the chemical composition shown previously. Rocks or sand with this composition, which have formed during cooling and solidification of lava or magma, are called igneous rock [176]. Geology has been studied for many years and so has the evolution of igneous rock [177] and the melting points, and behaviour of minerals [178]. Since then geological research has come far, for example, thin sections of lunar rock [179], melt compositions in lunar regoliths [180], or iron oxide [181] bearing minerals contained in the lunar regolith [182], have been studied.

For this work, however, only those minerals are relevant which are either contained in regolith simulants, or in actual lunar regolith. Most of these minerals are formed from a combination of elements contained in magma, which form a number of silicate minerals and some oxides (in addition to other minor phases). The most common of these silicate minerals found in terrestrial basalts are (adapted from [176]):

Essential minerals
- Clinopyroxene (augite)
- Plagioclase (e.g. anorthite, bytownite, labradorite)

Common minerals
- Enstatite, pigeonite (low-Ca pyroxenes)

- Olivine
- Feldspathoid (nepheline)

Common accessory minor minerals and alteration products

- Ilmenite or titanomagnetite (oxide mineral), often a major mineral too
- Chlorite (replacing pyroxene)
- Mica (muscovite, biotite)
- Basaltic glass
- Clay minerals
- Hornblende (amphibole)

Further, an introduction to the terminology used in terrestrial and lunar geology can be found in [183], an introduction to mineralogy (and petrology) can be found in [184] and are assumed foreknowledge. Minerals discussed in this work, may be abbreviated with the abbreviations listed in the nomenclature, and a compact overview of these abbreviations can be found in the mineral overview table A.1 in the appendix.

To determine which minerals are contained in a regolith (simulant) will be key to understanding the behaviour of this input material during processing. Therefore, melting behaviour is an important characteristic to consider since depending on which mineral endmember is contained in which quantities, the melting point of the bulk may differ significantly. For example, the two plagioclase endmembers albite and anorthite have different melting points with albite as low as 1100° [185], and anorthite as high as 1550°C [186]. These individual temperatures do only provide a rough orientation for the temperature range, since in reality regolith contains a multitude of different minerals, which will all impact the melting behaviour of each mineral contained. Therefore, the melting behaviour of igneous rock in general [187], as well as the melting behaviour of plagioclase [188], pyroxene [189] and olivine [190] may be of more interest for processing. This overview is considered enough to start first manufacturing trials, and other sources may be consulted where required.

The mineralogy of actual lunar samples shown in table A.2 in the appendix, shows mineral proportions of nine sampling sites on the lunar surface. Drastic variations in-between samples are observed, such as 12.9 to 69.1 volume percent (vol %) of plagioclase content, for example. Thus mineralogical composition is expected to significantly fluctuate between different landing sites and will need to be accounted for by any ISRU application. Once more, before a landing site is selected, it is of little use to design processes only capable of handling a specific type of regolith or mineral. The approach for this work will be to design a manufacturing process capable of tolerating a wide variety of mineral compositions.

2.2.2 Regolith Simulants

As aforementioned, on Earth so called regolith simulants are used to simulate the lunar regolith. The use of simulants is critical for the planned return missions to the lunar surface, since all equipment and technologies developed will require testing. This testing will need to be conducted using suitable regolith simulants. The use of simulants instead of actual lunar regolith is required since only about 400 kg of real regolith is available on Earth [191–193], which is not nearly enough to be used for studies, such as, for example, the sinkage of rover wheels in regolith [194].

Over the past 15 years interest in development of high fidelity (lunar) regolith simulants has gained momentum again [195–197]. This momentum led to considerations [198], requirements [199] and recommendations [200, 201], on how to manufacture [202, 203] simulants, as well as how to characterise [204] them. NASA even has a program dedicated to simulants [205], which underlines how important simulants are for future surface missions.

Summaries and evaluations of (some) available simulants have been summarised in [206, 207], and a functional comparison of real regolith and simulants was provided by [208]. Furthermore, a characterisation of lunar dust and a synopsis of current lunar simulants is summarised in [209], additionally, a regolith simulant user's guide has been developed [210]. Nevertheless, no actual standards and/or requirements for simulants exist, neither for testing nor for quality assurance. Without these, it is inevitable that for each new project, which requires regolith simulant for testing, new tests are conducted on project relevant parameters. These parameters then need to be compared to the actual lunar regolith and a conclusion needs to be drawn whether or not the analysed simulant is suitable for the required testing. This leads to numerous studies being conducted on individual parameters of individual simulants, such as for example thermal, strength and stress-strain properties [211–213], drilling behaviour [214], compressive deformation [215], soil mechanics in vacuum [216], dust erosive wear [217], discharge analysis [218], dielectric properties [219] or 3D shape analysis [220]. A larger study analysing composition, structure and physics of some lunar simulants was conducted in [221]. These few examples show already how complex the field of lunar regolith simulants is. Without regulations and coordination a work needs to be conducted multiple times although sometimes even only for slightly different use-cases of a simulants. Since these regulations or standards are missing, individual testing is one of the two solutions available at the moment, to use simulants for scientific testing.

Another solution of finding a simulant suitable for required testing is to develop and manufacture a simulant. This has been done in the form of many new simulants, such as (amongst others), BHLD20 [222], CLDS-i [223], BP-1 [224], NU-LHT-1M and -2M [225], GRC-1 [226], OB-1 [227], JSC-1A [228], NAO-1 [229], CAS-1 [230] and FJS-1 [231]. Although in some cases it is inevitable to develop a new simulant, for example, conducting NEA research, it is a time and resources consuming task. Hence, if possible it would be ideal to avoid a new development of a simulant.

In general, the high number of tests conducted on regolith simulants, and the increasing number of newly developed regolith simulants suggests, that the demand for regolith simulants is increasing. This observation is further supported by, ESA establishing a collection and curation facility [232, 233] for regolith source materials, which could help to manufacture a simulant on demand, according the requirements of the customer. Further it may help to establish standards for assessing and manufacturing regolith simulants, which has been suggested before [234–237].

Since no standards are established yet, it will however also be required to analyse all simulants, utilised for this study, individually. Choosing simulants for this investigation was necessary to be able to start analysing these simulants, prior to manufacturing and testing could commence. Drastically visible is the need for individual analysis off-the-shelf simulants from looking at the manufacturer data provided with the simulants. Table 2.3 lists the geochemical compositions of eight simulants, which are, or have been provided of off-the-shelf. For all simulants containing "JSC" in their name, only a range of values is provided, rather than specific values. Values provided for the SiO_2 content of JSC-1/2A are 46 to 49 weight percent for example. Further, although JSC-2A is the successor of JSC-1A and LHT-3M of LHT-2M it seems unrealistic, that the geochemical composition in both cases stayed exactly the same. Additionally, the manufacturer and provider of these simulants changed, which makes it even more unlikely that the simulants composition stayed exactly the same. No manufacturing standards are established in the field of simulants, thus manufacturers are not obliged to adhere to them. From this list and the issues pointed out, it is clear, that it will be required to analyse each simulant used prior to use, since else no reliable conclusion with respect to a simulants characteristics/composition can be drawn.

Table 2.3: Geochemical composition of selected regolith simulants, data provided by manufacturer showing weight percent

Simu.	**BP-1** [238]	**EAC-1** [239]	**FJS-1** [240]	**JSC-1A** [241]	**JSC-2A** [242]	**LHT-2M** [243]	**LHT-3M** [244]
SiO_2	43.0-47.2	43.7	49.1	46-49	46-49	46.7	46.7
Al_2O_3	16.4-18.0	12.6	16.2	14.5-15.5	14.5-15.5	24.4	24.4
Fe_2O_3	9-11.7	12.0	13.1	10-11.5	10-11.5	4.2	4.2
MgO	5.6-10.0	11.9	3.8	8.5-9.5	8.5-9.5	7.9	7.9
CaO	9.2-14.0	10.8	9.1	10-11	10-11	13.6	13.6
Na_2O	3.45	2.9	2.8	2.5-3	2.5-3	1.3	1.3
K_2O	0-1.1	1.3	1.0	0.75-0.85	0.75-0.85	0.1	0.1
TiO_2	-	2.4	1.9	1-2	1-2	0.4	0.4
MnO	-	0.2	0.2	0.15-0.20	0.15-0.20	0.1	0.1
P_2O_5	-	0.6	0.4	0.6-0.7	0.6-0.7	0.2	0.2

The lunar regolith simulant the most used mare simulants for publications and practical validations up to date is JSC-1A - for Johnson Space Center 1A. However, it is not being produced any more and the latest version manufactured by a different company is called JSC-2A. As shown in table 2.3, it is reported to have the same chemical composition (according to the manufacturer) than JSC-1A. In addition to changing simulant series and manufacturing company, also the manufacturing process was changed. A new process is applied to basaltic raw material, to obtain

JSC-2A - rather than just grinding the raw material. The novel apparatus used is described in patent [245]. This way of manufacturing is supposed to delivers a better representation of a regolith's grain size distribution and especially its grain shape. The fact that these two simulants are used frequently by the scientific community, and their supposedly high quality made them a first choice. Further, ideally it would be possible to compare results to the works of others.

The simulants LHT-2M and LHT-3M, also listed in table 2.3, are the two most commonly used lunar highland type simulants, and have thus been added to the list of simulants to be analysed. In addition to those four simulants, BP-1, EAC-1 and FJS-1 have been added to potentially increase the variety in geochemistry and mineralogy. This should ultimately lead to being able to test processes for their tolerance for different input materials. Further details on the selected simulants will be presented in the result section.

After briefly reviewing regolith and regolith simulants, a brief look was taken at basaltic glass, which may be contained in regolith, on the lunar surface, by up to 25.0 vol % as listed in table A.2.

2.2.3 Basaltic Glass

Basaltic glass can be formed by melting basaltic material and can occur naturally on both, the Earth and on the Moon. From the list of minerals abundant on the Moon (table A.2) it can be seen that the mare glass content (vol %) can get as high as 17 % and as low as less than 1 %. Similarly, the highland glass volume percent content can be observed in-between 5 and 25 %.

Compared to how well and long terrestrial glasses have been researched and used in manufacturing, the knowledge on manufacturing and processing basaltic glass is little. Some research was conducted in the field of lunar glasses [246, 247], terrestrial volcanic basalts [248] or mid-ocean ridge basalts [249, 250]. Moreover, studies of the crystallisation behaviour of basaltic glasses have been conducted in [251, 252], research on their chemical and physical properties in [253], and their magnetic properties in [254]. Further, basaltic glass has been used in practical applications such as immobilisation of transuranic wastes or to manufacture mirrors on basaltic glass manufactured from regolith simulant [255]. Some of these studies may prove to be helpful during attempting glass manufacture from regolith material.

Terrestrially manufactured glass, most often refers to soda-lime glass, has been used and researched for many centuries already [256, 257]. From the raw materials used in early glass production [258] to window glass of today, manufactured in the float glass process [259], many different types of glass have been manufactured on Earth. Working with glasses in general, has shown to pose certain challenges, for example, the avoidance of bubble formation [260], or proper relaxation of glass after manufacturing to release stress from the glass [261]. These challenges are likely to become relevant, when manufacturing devices by using basaltic glass as well. In

addition to that, in typical terrestrial glass fabrication, glass is recycled and used to produce new glass by combining it with raw materials, such as sand, for example. Old glass or previously melted material can be crucial to lowering energy required for processing by up to 13 % [262], and reduce the amount of new raw material required by about 17 % [263]. Thus, it may be possible, that glass contained in the regolith may have a similar effect on manufacturing basaltic glass. Hence, it will be important to gain a better understanding of the role basaltic glass content in regolith can play, when processing regolith into basaltic glass.

Understanding the composition and structure of (lunar) basaltic glass may be vital in gaining an understanding of processing temperatures, cooling and annealing behaviour while attempting to manufacture glass from regolith. Additionally, crystallisation of basaltic glasses during or after manufacturing may become relevant. Due to the lack of information on the characteristics of basaltic glasses manufactured from lunar regolith simulant, it will need to be investigated in more detail to aid manufacturing and processing.

2.2.4 Conclusion Regolith, Simulant and Glass

To be able to test manufacturing of potential lunar ISRU-made equipment on Earth, an analogue material to the one on the Moon needs to be found and tested. This comes down to selecting appropriate lunar regolith simulants, which are commercially available already, since developing a new simulant was deemed to be time and resource intensive. The composition of regolith at an actual landing site on the Moon will only be known, once a site has been selected. Hence, regolith manufacturing processes cannot be designed for a specific input material, but rather need to be able to process a variety of materials. To assure that processes are able to handle a variety of different input materials, multiple regolith simulants, with different compositions, were selected to be investigated. In this way, a maximum of practicability is assured but is, however, potentially increasing the complexity of the process. Prime simulants chosen for this study are BP-1 EAC-1, FJS-1, JSC-1/2A and LHT-2/3M. These simulants seem to have different geometric properties, as well as grain size distributions and chemical and mineralogical compositions. Further, all of them are easily accessible in quantities of about 10 kg. It is suspected that these simulants are provided with different characteristics compared to the manufacturers' data. Thus geochemical and mineralogical analysis of the simulants will be required, prior to any manufacturing and testing. This will need to be confirmed by detailed analysis of each simulant, once they arrive. Further, investigations on the behaviour of basaltic glasses during and after manufacturing are likely to be required as well.

2.3 Terrestrial and Lunar Purification Processes

For the goal of in-situ manufacturing of solar cells entirely on the Moon it needs to be determined, which elements or raw materials can be extracted from the lunar material. Purification, extraction or beneficiation will be required because building solar cells requires highly purified materials. Whether the quality of

the extracted material is a suitable stock material for the production of actual solar cells is of further relevance. As outlined in section 2.1.3 some potential resources on the Moon are, silicon, iron, aluminium and titanium [130], all occurring in their oxidised state. Being able to harness these elements could enable manufacturing using steel, aluminium and/or titanium alloys. Further using a purified or beneficiated version of the regolith could lead to manufacturing composites or more simple items like sintered regolith bricks or glass plates [264].

Most, other studies so far have focused on oxygen extraction [265–276] rather than extraction of elements such as silicon or iron. However, these oxygen reduction processes may produce metals and/or silicon as by-product of their reduction process. Unfortunately, not in all cases the quality/purity of these by-products acquired was assessed.

The main focus of this review on elemental extraction from regoliths will be based around the processes of silicon, extraction and purification, to be used for building silicon based solar cells. Therefore, before the quality of extract silicon can be assessed, it was necessary to establish what quality/purity of silicon is required to manufacture solar cells from it. Thus, first, terrestrial manufacturing of silicon in general was reviewed, before processes were reviewed which are applicable to the lunar regolith.

Processes available for elemental extraction which have been reviewed are; fluorine processing, carbothermal/hydrogen reduction, electrolysis, electromagnetic and bioleaching. Other processes like sulphuric acid reduction, or vapour phase pyrolysis are not discussed in detail, could however also be considered once their TRL is more advanced.

2.3.1 Terrestrial Purification

The most abundant element in Earth's crust is silica or silicon dioxide (SiO_2) with 45.2% oxygen and 27.2 % silicon out of the 100 % of all atoms in the Earth's crust [277], most commonly highly pure silica is found in the form of quartz sand. Whereas the sand known from the beaches on Earth is also mainly comprised of SiO_2, most of the times quartz rocks with even higher purity are used as a starting material for silicon extraction. Silicon can be purified from silica, and the purification industry can be divided into three categories depending on the level of purity [278]:

1. Metallurgical Grade Silicon (MG-Si) with approximately 99% pure silicon
2. Solar Grade Silicon (SG-Si) with approximately 99.999 9% (N6) pure silicon
3. Electronic Grade Silicon (EG-Si) with approximately 99.999 999 999% (N11) pure silicon

This evaluation will only look at the first two categories, MG-Si and SG-Si. However, an overview of silicon refining in general is provided in [279–281].

To synthesise MG-Si, most commonly first the oxygen is released from the silicon achieving approximately 98-99% pure silicon utilising the carbothermal reduction process (reaction (2.1)), working at around 1500 - 2000 $°C$.

$$SiO_2 + C \longrightarrow Si + CO_2 \tag{2.1}$$

The input materials (quartz) for this process are preferably sparse of aluminium, iron and other metals. The final product of this stage of purification is called Metallurgical Grade Silicon (MG-Si). At this stage, terrestrially produced MG-Si has impurities of alkali-earth, carbon, bromine, phosphorus, and transition metals. The transition metals are one of the main reasons why MG-Si seems not to be suitable for solar devices, or even more sophisticated electronic devices [282]. The price per kilogram MG-Si is in the area of a few \$/kg, and the energy necessary, to bring it to this level of purity, is about 14 - 16 $^{kWh}/_{kg}$ [283].

To achieve SG-Si purities of N6, two paths can be followed, recycling of EG-Si [284], or further refining of MG-Si. Since EG-Si silicon is not considered to be available on the lunar surface, the only viable option seems to be further refining MG-Si. Different processes of SG-Si production are highlighted in [285, 286], more recent in [287] and most up-to-date in [288] and can provide background information not covered in here. Establishing processes on the lunar surface, which are similar to the ones described in these works, would be desirable but seems unlikely for first return missions to the Moon. These processes are too energy intensive and the machinery and technology required too vast for the required amounts of silicon. Thus, reproducing traditional terrestrial processes on the lunar surface is not considered, and further details on terrestrial purification processes will not be discussed in this review. The required quality for SG-Si of 99.999 9% (N6) pure silicon, is the relevant purity level which needs to be achieved by an extraction process on the lunar surface.

2.3.2 Extraction/Purification Processes utilising Energy

Following the ISRU flow chart in figure 1.5, starting at the top of the chart, before any energy or additives can be applied to the raw regolith, it will be required to gather regolith first and transport it to a processing facility. At the facility, regolith can either be used directly or may need mechanical processing in the form of sieving or grinding first. The purpose of these processes is to either prepare the regolith for a more sophisticated second treatment and particularly for glass manufacturing, initial sizing by means of grinding is likely to be required.

After regolith is gathered and has been pre-processed, it will be ready to be used as starting material for processing. A general overview of recent advances in extraction of silicon (and oxygen) from lunar regolith are found in [289]. However, proposed in 1979 [290] already, extraction of aluminium, titanium, iron, magnesium, and oxygen from extra-terrestrial sources might be possible by utilising electric energy. Potential processes only using energy, which have at least partially shown to work are electrolysis, electromagnetic, and zone refining. These processes only require

electrical and/or thermal energy to extract elements. The following will review their potential for silicon extraction from lunar regolith.

Electrolysis

Electrolysis is a process breaking down substances into positively and negatively charged ions. These can than travel freely in a liquid to a positively or negatively charged electrode and accumulate or gas-off there. This has been tried using molten salt electrolysis [291–294], or molten regolith electrolysis [295–303]. Another method, similar to both described processes for elemental extraction, are ionic liquids [304], which have only received comparably little attention in the past. Molten salt electrolysis (shown in Fig. 2.4) has shown to produce a very pure (>99%) titanium-iron alloy from ilmenite.

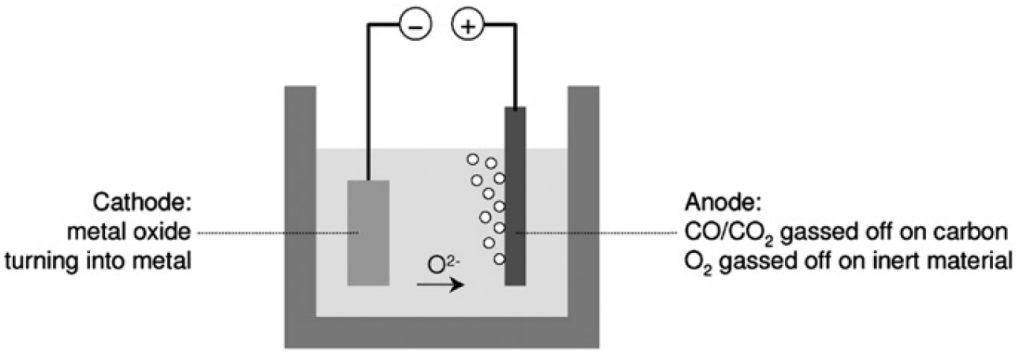

Figure 2.4: Schematic of the molten salt electrolysis process [292].

Molten regolith electrolysis has shown to reduce the oxygen from the regolith and leave behind a slag of iron, silicon, aluminium, titanium and remainder. Both processes are not separating the individual elements, but are rather stripping them of their oxygen. The leftover or slag of both processes could be used as a start for further processing. However, neither of the processes showed to produce elementally pure silicon close to the required N6.

Electromagnetic

A potentially simple process of extracting iron or ferromagnetic elements from the regolith is to use a magnetic field for extraction. The only work in this field found so far is the one in [305, 306], which could not definitely confirm that it is possible to separate minerals or elements contained in regoliths, by means of running regolith through a magnetic field. However, this process seems worthy of further investigation, due to its simple nature not requiring consumables or heat. Also possible are combinations of processes, such as contact charging or particle charging [307–309].

Zone Refining

Zone refining is shown in figure 2.6 and is a process based on utilising a concentrated heat source and translating a focused beam along a line. This at the same time

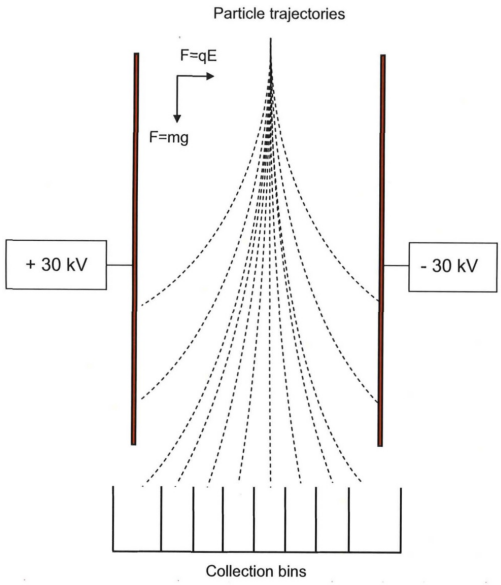

Figure 2.5: Schematic of the separator shows regolith falling from top through an electrostatic field into different collection bins [305].

frees oxygen and reduces the elements in the regolith. The technology has shown to be working but needs further investigation to improve the yield [310, 311].

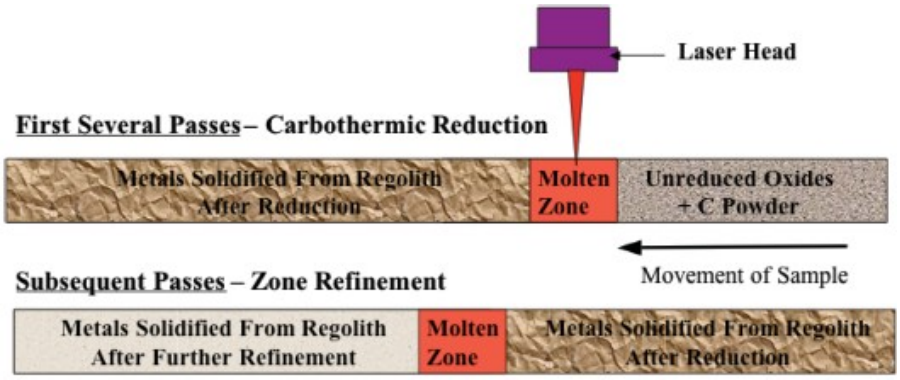

Figure 2.6: Utilising a laser to reduce oxide and zone refine regolith [310].

This technology utilises mainly power, similar to electrolysis and the electromagnetic field separation. However, it also requires carbon powder, to carbothermally reduce the regolith and free it of its oxygen. Since carbon is not abundant on the Moon, possibilities for recycling the carbon need to be investigated first to see whether this is a feasible technology to be deployed.

2.3.3 Extraction/Purification Processes Utilising Additives

The second type of extraction processes investigated are processes utilising additives to reduce elements from raw lunar soil. The processes analysed are carbothermic reduction, bioleaching and fluorine purification.

Carbothermic and Hydrogen Reduction

The carbothermal reduction is widely used on Earth for beneficiation of ores. The reaction to extract silicon from enstatite ($MgSiO_3$), for example, using methane, looks like this [312]:

$$\mathrm{MgSiO_3 + 2\,CH_4 \longrightarrow Si + MgO + 2\,CO + 4\,H_2} \tag{2.2}$$

Even a direct carbothermal reduction of silica to SG-Si [313] seems possible with this process. Most version of this process use methane (CH_4), which can be recovered running the formed carbon monoxide and the hydrogen through a nickel catalyst, to produce methane and water [314]. Other terrestrial processes reduce silica in nitrogen and a nitrogen-hydrogen mixture to achieve similar results [315]. A practical test of the carbothermal process applied to regolith is depicted in figure 2.7 [316] and shows JSC-1A regolith simulant after carbothermal reduction (left) and after being removed from the test bed (right). The centre of the sample shows a glass like appearance of the material and the surrounding "shell" seems to be made of sintered regolith simulant.

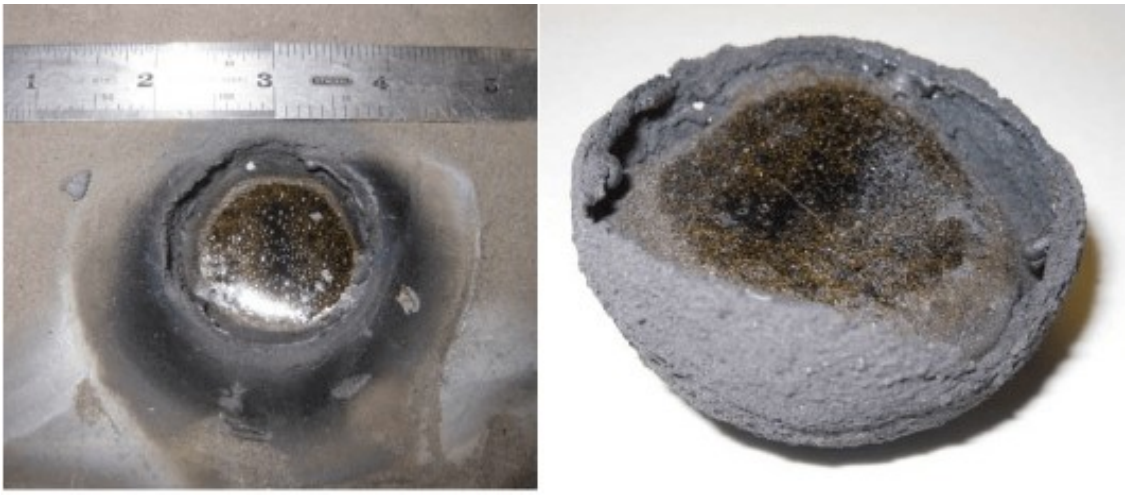

Figure 2.7: Regolith simulant (JSC-1A) sample after carbothermal reduction (left) and after being removed from the test bed (right) [316].

Other simulation and testing work carried out in the field of carbothermal reduction of regolith can be found in [317–320], and another interesting terrestrial application in [321]. As a source for the methane (consumable), either rocket fuel could be used (SpaceX's new engine generation) or polymers like packaging material could be recycled at a lunar outpost to produce methane [322].

Alternatively to carbon, hydrogen can be used as reactant to purify iron or titanium for example from ilmenite, glass [323], or directly from lunar regolith [273, 324]. Hydrogen required for this process could potentially be sourced on the lunar surface by capturing water from icy regolith via microwave heating and electrolysing that

water to hydrogen and oxygen [325, 326].

The benefits of carbothermal reduction are that it is comparably well understood and established on Earth, and it has proven to have good yields for removing oxygen from the target material. However, the need for consumables in form of a carbon source makes it difficult to utilise the carbothermal reduction process on the lunar surface. Hydrogen may offer an alternative, more viable option instead. Overall, it seems, however, much more practical to fly highly purified materials from Earth to the Moon, than a source of carbon for example. If, however, methane could be recycled on site, from either polymers or bioleaching, it would seem much more feasible to use carbothermal reduction. Although the discussed processes offer opportunities, none of them has provided silicon purities of 6N. Thus this extraction method is also not considered an option for silicon extraction from regolith.

Bioleaching

Bioleaching is a process reducing oxygen or metals from a raw material utilising bacteria and a nutritional solution. Terrestrial beneficiation of iron ore, via bioleaching, has received little attention in the last years but could offer an option for extraction [327, 328]. The reason for this lack of interest may be that raw iron ore mineral is comparably cheap and of good quality, thus bioleaching seems a lost cause on Earth. On the Moon, however, it could be an interesting solution [329] since the bacteria could work in a regenerative closed loop to extract iron ore and oxygen from the regolith using for example human waste or food waste as nutritional solution. Figure 2.8 shows quartz sand which has been freed of its iron ore by means of magnetic separation and a bioleaching treatment [330]. Recent development in the field can be found under [331] and [332]; a more outdated overview from 2004 under [333]. Bioleaching has the advantage that during the process methane might be produced as a waste product, which could be used in other applications.

Figure 2.8: Samples before treatment (left), after magnetic treatment (middle), and bioleaching with washing (right) [330].

Although bioleaching seems interesting for extracting iron from sands and regolith, no study was conducted using bioleaching for the extraction of silicon. Hence, also this extraction process is not deemed suitable for extracting silicon of N6 grade.

Potassium Fluoride Purification

This process uses a Potassium Fluorine (KF) salt to reduce primarily silicon and oxygen in a multi-stage process from the regolith as depicted in figure 2.9.

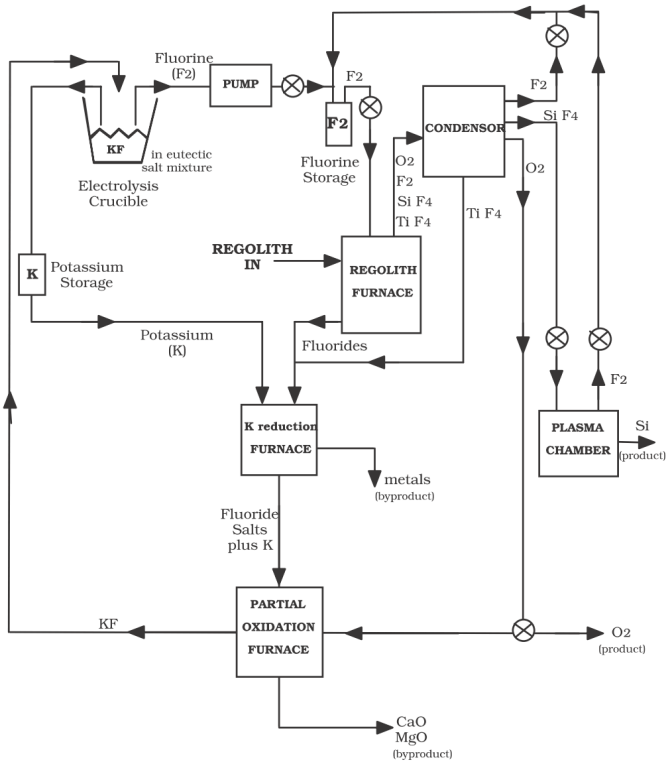

Figure 2.9: Silicon and oxygen reduction with potassium fluoride in a multi-step approach [334].

The potassium fluoride is split (equation (2.3)) up into potassium (K) and fluorine (F_2) which can reduce silicon (as shown in equations (2.4) and (2.5)), in a multi-step approach heating the mixture to different temperatures. For details on the process, temperatures, and energies required see [334, 335].

$$KF \longrightarrow 2K + F_2 \tag{2.3}$$

$$SiO_2 + 2F_2 \longrightarrow SiF_4 + O_2 \tag{2.4}$$

$$SiF_4 + 4K \longrightarrow Si{+}4KF \tag{2.5}$$

This process has several advantages: It is possible to reduce oxygen and silicon, and all other major elements contained in a mineral-mix like regolith. Moreover, the required maximum temperatures for the reactions to take place are less than 700 $°C$. This makes it a relatively energy efficient process, compared to the other processes operating at temperature above 1000 °C. The overall system requirements are, as proposed by [334]:

- 11 $^{kW}/_{h}$ electrical power
- A (solar) furnace operating at approximately 1200 °C
- A refrigerator for condensation operating at approximately -100 °C
- Plus infrastructure like gas tubing sensors, crucibles etc.

The biggest down side effect of this process is the fact, that during purification hydrofluoric acid (HF) could form, which is a highly hazardous liquid/gas for humans. No practical validation of this theoretical process has been carried out so far. Despite the theoretical possibilities of this process, purification using potassium fluoride are not considered for silicon extraction. This process is not matured enough yet and poses a high health and safety risk, which both render this extraction method unsuitable for silicon extraction.

2.3.4 Conclusion - Terrestrial and Lunar Purification

All processes discussed have shown to work to some degree, however, none of them have indicated to purify elements beyond 99% purity. For solar cell manufacturing on the Moon utilising local resources, solar grade silicon of 99.9999% (N6) or better is required which none of the processes seemed to be able to provide. In addition to the required purities of silicon, impurities in the range of parts per million (ppm) may already lead to a drastic decrease in performance of the cell [336], which suggests that a purity of only 99 % would potentially already be too contaminated, to be used to manufacture solar cells. Although ways to control and remove metal [337, 338] or phosphorus impurities [339] from silicon, as well as to upgrade silicon from metallurgic to solar grade silicon [340] have been researched, using these technologies would mean bringing even more equipment for purification to the lunar surface. Thus, purification of silicon on the lunar surface was deemed unrealistic at this point, and until further investigations prove otherwise, it is not considered for solar cell manufacturing.

As an alternative approach to in-situ extraction of silicon, the amount of ultra-pure silicon required to manufacture solar cells[3] capable of producing 250 kW of electrical power for a lunar base [77] was estimated. The amount of silicon required for such a scenario is in the range of 100 kg and therefore, it seems realistic to transport this amount of highly purified and readily doped silicon to the lunar surface from Earth to the Moon, rather than extracting silicon on the lunar surface.

2.4 Lunar Manufacturing

How to utilise the raw material on the Moon for manufacturing, has been investigated. The manufacturing techniques, microwave sintering, additive manufacturing, selective laser melting, a few other concepts and glass manufacturing in general have been evaluated.

[3] thin-film silicon solar cells, layer thickness 20μm, 10% efficiency

Potential materials for fabrication can be divided in three general categories which are metals, ceramics, and polymers. By combining two or all of these, a fourth category, composites is created [341, 342]. As outlined in section 2.1 almost all material that can be found on the lunar surface, appears to be basaltic sand, hence falls into the category of ceramics. Since regolith is the prime resource available on the lunar surface and the goal of this investigation is to determine whether it is possible to manufacture solar conversion devices from regolith, this part of the review is focused on manufacturing techniques for the basaltic sand and (basaltic) glass.

The idea of processing lunar materials into ceramics has been suggested before [343], as well as the use of melted regolith for ISRU applications [344, 345] and ISRU applications using 3D printing technologies [346]. Further, plans for entire "lunar industry plants" using regolith have been made [347] including a feed system for such plants [348]. Processing regolith and making it available in the form of basaltic glass will be an important step on the way to manufacturing mirrors or solar cells. Thus, finding a processing method, which allows to manufacture basaltic glass plates on the lunar surface, will be key to that.

2.4.1 Manufacturing Techniques

This section provides an overview about the manufacturing methods, which are of major importance for lunar surface manufacturing using ISRU. Prior to any manufacturing, the quality of the used raw material will need to be taken into account, since it may impact each processing technique differently [215]. Assessing the individual effect, the input material could have on each of the techniques reviewed, is beyond the scope of this work but will be conducted once a manufacturing technique is selected.

Additive Manufacturing

Additive manufacturing, often also called "3D Printing", is a technique that constructs a part layer-by-layer using a feedstock material like, for example, polymers. In terrestrial applications, these 3D printing techniques have already also been applied to glass and have shown to work [349] (More detailed in [350]). The system setup used for printing is schematically depicted in figure 2.10. Challenges faced printing glass are controlling solidification and annealing annealing temperatures as well as material incompatibilities leading to breakage or blockage of the extruder nozzle for example. Additionally, a similar approach has also already been using basaltic glass to print first structures [351]. Results of this research are depicted in figure 2.11, and show hollow dome structures printed from JSC-1A regolith simulant. The same challenges were faced printing regolith and additionally processing temperatures were higher for regolith than for soda lime glass.

In addition to using 3D printing technologies for building parts and structures made of glass, other fields of applications have been found in the past years [352, 353], as well as utilising regolith (prior to any beneficiation) as a stock material to build a

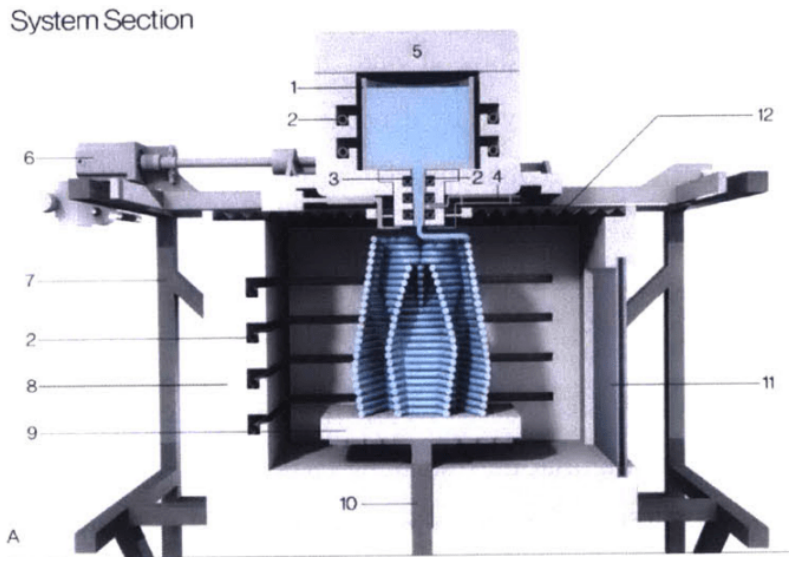

Figure 2.10: Schematic of setup for 3D printing optical transparent glass, detailed explanation of the system including the numbers depicted are found in the original source [350].

Figure 2.11: Free standing 3D printed dome structures made of regolith [351].

lunar base [75, 354, 355]. An overview of Automated Additive Construction (AAC) for additive manufacturing, in space, using in-situ resources, is provided by [356].

Further examples of additive manufacturing using regolith simulant can be found in [357–367]. From these examples, it seems viable to use AAC for augmenting a lunar mission in general. The possibility of these technologies reaches from manufacturing structural parts to entire buildings. Thus, ultimately using an AAC approach to manufacture solar conversion devices on the lunar surface seems possible. Hence, once glass manufacturing and glass characteristics are better understood in general, modifying an AAC process for building glass plates seems a next step.

Microwave Processing

Microwave processing is a promising technology being used more frequently also in terrestrial applications [368, 369]. It is consuming comparable little power, is rather small in size and simple in terms of how it is built. Microwaves are commonly known to be used to heat food, however, microwaves also affect silica sand, rocks, ceramics and metals [370–380]. With slight modifications in the form of utilising a susceptor martial based heating element, this technique may be called susceptor-assisted microwave heating [381], which, for example, has been used for activation of silicon dopants [382].

Applying these techniques to be used as an ISRU technology could look like the schematic depicted in figure 2.12, taken from [383]. The process depicted in figure 2.12 shows only a theoretical, non-susceptor assisted, 3D printing microwave heating approach. Other than this 3D printing approach using microwaves [383], concepts for long-term ISRU support [384] via microwave processing and microwave sintering of lunar soil, have been investigated [385, 386]. Additionally, computational models [387, 388] have been built to predict the dielectric behaviour of regolith. Since microwave processing of material happens at relatively high temperatures (> 1100 °C), high-temperature materials like carbon or silicon carbide [389, 390] need to be used as crucibles or protection materials. An interesting combination of microwave processing and carbothermic reduction of iron ores has been published in [391].

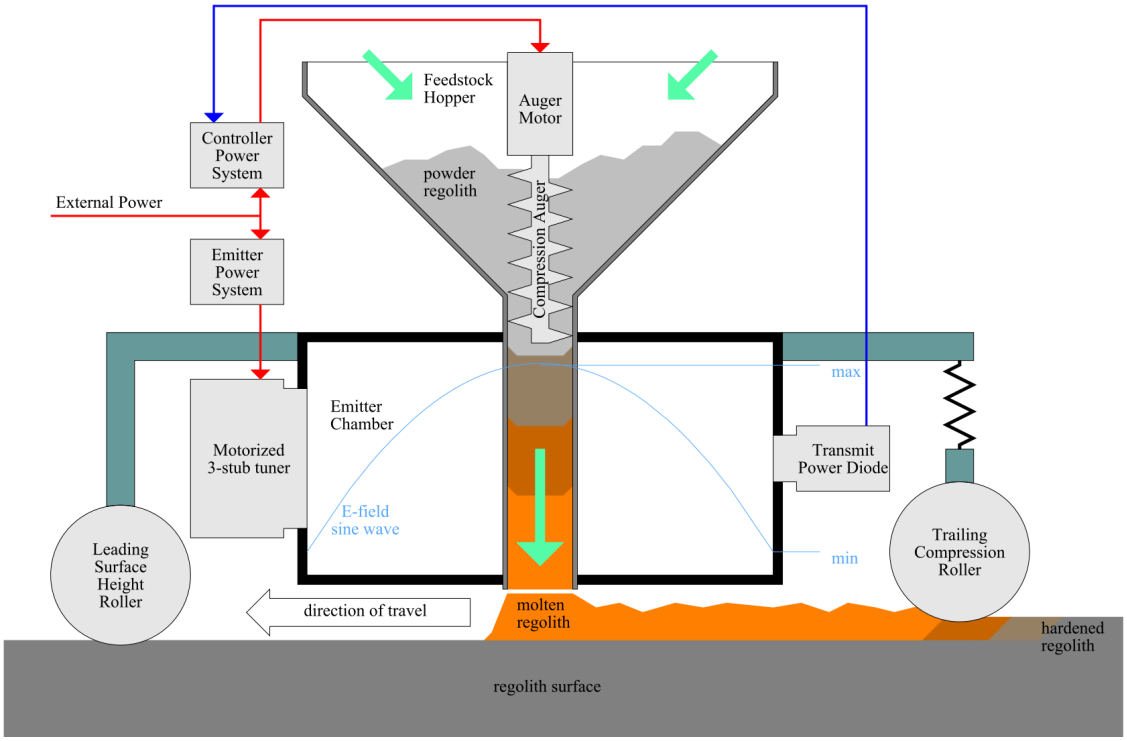

Figure 2.12: Microwave 3D printing concept utilising regolith as feedstock [383]

Using a susceptor assisted microwave approach for processing regolith offers the advantage of decoupling heating from the input material. In a regular microwave

oven/field, only susceptor materials will start to heat up. In a susceptor assisted microwave heating approach, the susceptor heating element will heat up, which will in turn heat any material close to it. Thus differences in the regoliths' composition, should in theory not, or only little, impact the heating process. This modification of the microwave heating process has the likely disadvantage of requiring more power, since thermal losses in the system will be increased.

Aiding the displayed concepts of microwave processing by means of the use of a susceptor seems highly interesting and novel, and could work for regoliths, since it has been used on rocks on Earth before. Developing such a susceptor assisted microwave heating approach and using it on regolith simulants is thus deemed worth exploring in this work.

Selective Laser Melting

Selective Laser Melting (SLM) is strictly speaking also an additive manufacturing process. It uses a high power laser to melt powdered material, based on 3D Computer Aided Design (CAD) data in a layer-by-layer fashion. Since the lunar regolith is already a very fine powder in its raw state, SLM seems to be an interesting option for manufacturing parts on the lunar surface. Before starting to work with SLM, influences on the process parameters need to be understood for terrestrial [392] and extra-terrestrial applications [393, 394].

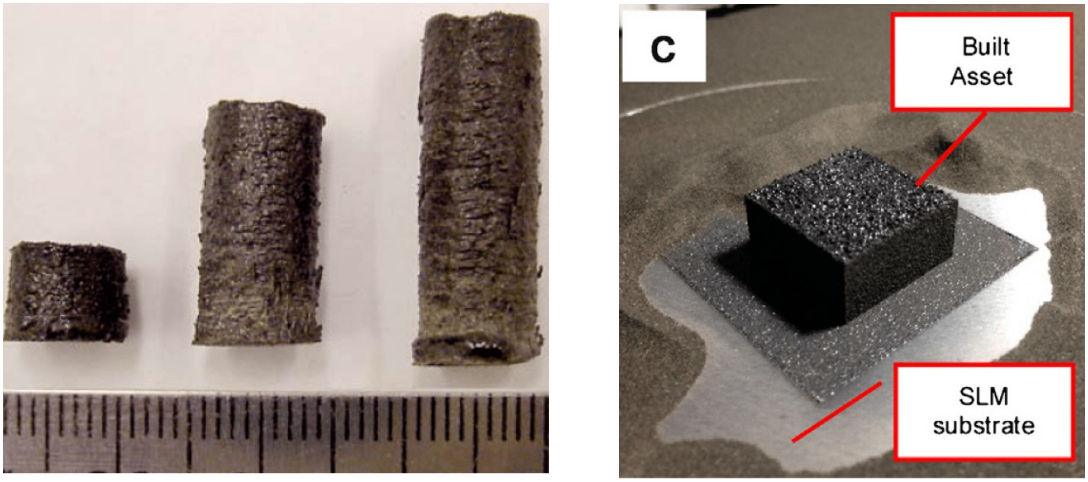

Figure 2.13: Left, laser melted regolith simulant [395]. Right, selective laser melted block of regolith simulant [360].

Terrestrial applications of melting soda lime glass [396] delivered first results, as well as multiple attempts of selective laser melting of regolith (figure 2.13) have been tried in the past, showing promising results [360, 395, 397]. Further, a combination of carbothermal reduction with SLM has been used to manufacture porous silica parts [398]. These works suggest that SLM could be another technique ultimately used to manufacture glass substrates and solar conversion devices. However, the challenge SLM faces are thermal stress introduced into the glass during manufacturing since

during manufacturing always only a small part of an entire part is heated/melted. The temperature gradients during manufacturing are likely to cause an issue, manufacturing larger parts. In conclusion, once basaltic glass manufacturing and its characteristics are better understood, it will be worth revisiting this technique.

Other Manufacturing Techniques

Figure 2.14: Building brick made of JSC-1A [399].

Other manufacturing techniques, which have been applied to lunar regolith simulant or could be adopted from terrestrial applications, include geo-polymers and composites. Simulations of regolith geo-polymer binder based cements, as a material for radiation protection, have shown that it might potentially be possible to protect a long term human mission to the surface of the Moon [400]. Preparation of lunar material based cements are depicted in figure 2.14 [399, 401, 402], and showed to work; further investigations showed that it is possible to do so with near-zero water consumption [403]. Cement is thought of being used as structural building material for bases, but also to build infrastructure. Whether it would be useful as solar cell or electronics substrate is yet to be determined (tbd). Other processes, which could augment a lunar base mission, are basalt fibre reinforced polymer composites (BFRPC). An overview of the state of the art of BFRPC is provided by [404–406]. Melting regolith, glass fibres can be produced on the lunar surface and used for composite production, which could be the solution for passive radiation protection [407]. Although basalt fibres can be produced on the lunar surface, the polymer part, like polyethylene (PE), would need to come from recycled from packaging foam, for example.

Last to be discussed is the possibility of using a solar furnace to heat and sinter/melt regolith on the lunar surface. Works of the past have successfully shown that solar energy can be used for 3D printing, much like SLM [408, 409]. Further, bricks have been sintered from lunar regolith simulant [410] and concepts for using solar thermal energy for manufacturing on the lunar surface have been proposed in [411–414]. The advantage of a solar concentrator system is that it requires little to no inputs, not even power. The only power which may be required is to reposition the sample and/or the concentrator mirrors, which is compared to other technologies very little. The biggest disadvantage of a solar furnace is that it is potentially large, bulky, heavy and fragile, thus the most difficult part will be to establish such a system on the lunar surface in first place. After such a solar furnace is established, it will likely be ideal for manufacturing glass and glass components.

2.4.2 Glass Manufacturing

Depicted in figure 2.15 is a failed experiment of Sir James Hall conducted in Edinburgh in the year 1798 (indicated by his note next to it). Over 220 years ago, he already tried to find out how rocks form inside volcanoes, by trying to reverse the processes of formation. He took basaltic rocks, from the Edinburgh castle and melted them in a clay crucible, heated by live coal in a blacksmith's workshop. Although he managed to melt the rocks into basaltic glass, he did not manage to form a rock from it or to fully separate it from the clay crucible again. Today, 50 years after humankind went to the Moon, we are still facing similar problems, when considering manufacturing basaltic glass on the lunar surface.

Figure 2.15: Historic sample of basaltic glass experiments, melting basaltic rock from Edinburgh Castle (UK) conducted by Sir James Hall in 1798. Shown are his laboratory notes on the left and a broken clay crucible containing basaltic glass on the right.

For building solar cells from basaltic glass, two major manufacturing steps have to be understood, substrate manufacturing and deposition on that substrate. Glass, produced of raw regolith, could therefore serve as a substrate or back-plate, since manufacturing glass from regolith only involves a small number of steps [334]. Soda-lime glass is the most common glass used on Earth, on the Moon, however, basaltic glass manufactured from lunar regolith and igneous rocks will be the only available option. Silicon dioxide makes up the bulk part of most terrestrially used glasses. Other oxides, such as CaO, for example, modify the glass behaviour and characteristics.

Using terrestrial expertise to manufacture basaltic glass on the Moon could provide a general raw material, not at least for solar cell production only. The area of lunar glass production seems to be highly novel and only very little work has been carried out in this field. However, in 1979 it was acknowledged already that a wider variety of glass can be useful on the Moon [415], and, for example, in 1986, fusing of lunar

materials by means of microwave melting has been simulated [416].

Generally, glass manufacturing can be described as a process sequence of three steps. Melting sand (raw material), shaping the hot and liquid glass and heat treating it. The three steps are depicted in figure 2.16 which are applicable to lunar glass fabrication as well, with the only difference that the raw material is limited to basaltic sands.

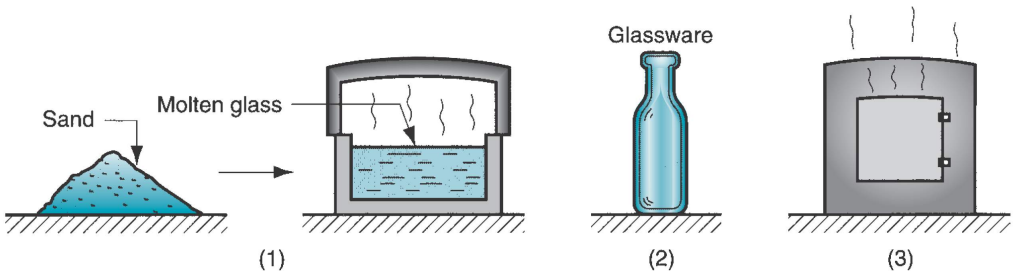

Figure 2.16: Process sequence of glass manufacturing process. Raw material and melting (1) shaping step (2) heat treatment (3) [417].

Basaltic glass in particular has been studied on Earth for a variety of applications such as recycling of sewage sludge [418], recycling of residues of basaltic quarries and ceramic wastes [419], as well as sintering it into thermal insulation blocks [420]. It has been structurally studied [421], and thermally characterised [422] for the JSC-1A simulant, and could potentially be manufactured using a solar furnace [423]. From these works it seems reasonable to try manufacturing basaltic glass substrates from regolith simulant.

Raw Material - Basaltic Sand

On the lunar surface, a different composition raw material (sand) will be available compared to Earth. This will influence the behaviour of the glass, which may behave more like a glass-ceramic system rather than just glass [424]. To better understand what are the differences between, using regolith or sand as input materials, research needs to be conducted.

As outlined in section 2.3 already, it is to some degree possible, to alter the composition of the lunar regolith, by means of extraction or beneficiation processes. This could in theory lead to quality improvements of the glass, with, for example, improved optical transparency. This would open its use up for cover and window glasses, for example, as well as many other applications. Investigations on how to affect the properties of glass by changing its composition have started in 1886 [425] and are still ongoing until the present day. For the Moon, however, it seems that the glass composition can typically only be altered under high energy/resource cost. Hence, it does only seem to be feasible, to explore possibilities of altering the composition of the glass, once the basic glass making process for lunar glass is understood and established. This leads to rather engineering the melting, shaping and heat treatment processes to be capable of handling the raw regolith without

geochemically altering it.

Despite it seeming impractical to alter the regolith's composition, its grain size distribution can be altered by simple means of grinding and sieving. The regolith can be sorted to only contain grain sizes from 0.1 to 0.6 mm, which is the optimum size for melting it [426]. Different methods of actual heating and melting regolith will be addressed later in this work.

Glass Shaping

Glass shaping can generally be categorised into four types; **spinning**, **pressing**, **blowing**, and **casting**. Utilising either of these, or a combination of multiple, historically different ways of manufacturing glass plates have been developed. Examples of the developed processes are; crown glass (spinning), sheet process (ribbon), cylinder process, glass casting, glass pressing (fig. 2.17), glass fusing and float glass (fig. 2.18). Summaries of these processes are provided in [417, 427], and an overview of scientific glass blowing is provided in [428].

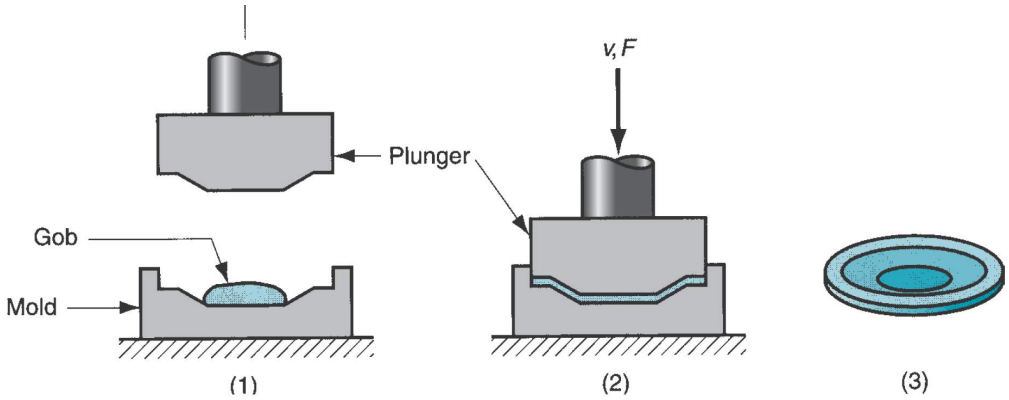

Figure 2.17: Pressing of a gob of hot glass into a flat plate. Insertion of hot glass (1), pressing (2), final shape of glass (3) [417].

Nowadays, window glass, for example, is most commonly manufactured utilising the float glass process. As depicted in figure 2.18 a stream of molten glass is poured onto a molten tin pool. Since the density of molten tin is much higher than the density of molten glass, the glass floats on top. By guiding the molten glass in a form of a river, the glass is flattened out and pulled into its final shape. A brief history review of float glass can be found in [259], and current innovation in the float glass industry in [429]. Float glass characteristics have been studied for many years already [430], and even details are well understood [431]. Although float glass in general produces a good quality glass sheet or substrate, the process involves rather big and bulky materials and it is unclear how well it will work under reduced gravity conditions. Hence, float glass manufacturing on the lunar surface is not deemed viable for early, small scale, surface missions.

Compared to float glass; other glass blowing, spinning, casting, and pressing techniques in general are older techniques. Some of which have been used for many

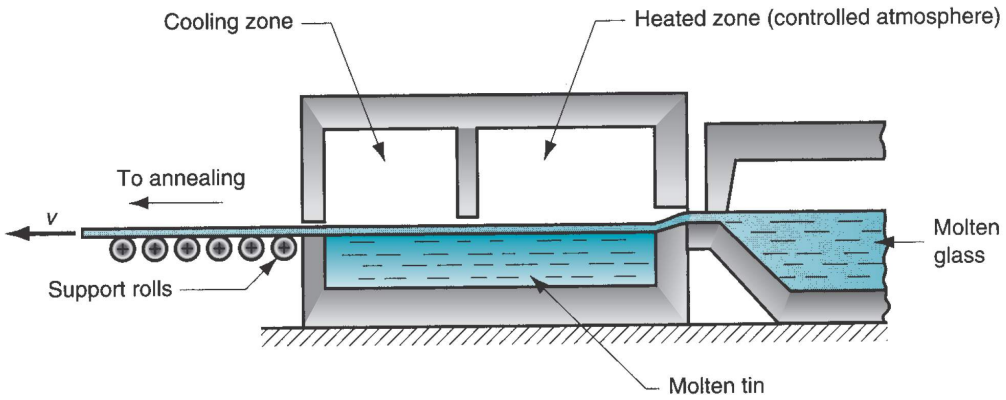

Figure 2.18: Schematic of the float glass process. Hot glass coming in from the right, poured onto the liquid tin bed ind the middle and pulled out on the left side [417].

centuries [259]. They can either be manual or fully automated processes, terrestrially conducted on an industrial scale, such as, for example, manufacturing of glass bottles. Possibilities and varieties of these processes are many and further investigations and testing will be required to determine which of these techniques will be the most suitable for basalt glass manufacturing, with the ultimate goal of lunar basalt glass production.

Glass Heat Treatment

Heat treatment for glass can be divided into two groups, **tempered glass** and **annealing** of glass. Annealing aims at releasing stress, which usually builds up inside the material during the manufacturing process. Tempering is introducing stress into the glass, for example, to increase the toughness of the glass. Especially the annealing process is a vital and time consuming process which can last up to several days or even months. If the thermal stress is not released from a piece of glass as, for example, a glass plate, this will lead to cracks. Manufacturing solar cells on glass plates, which are prone to crack, is not viable. Hence, special attention needs to be given to this last process step for the glass substrate.

To the knowledge of the author, little is known about the annealing behaviour of lunar basaltic glasses. Even looking at terrestrial applications, if research has been conducted into basalt glass annealing, it is in the context of waste capture [432], or quenched basaltic glass [433]. First studies on photovoltaic diodes on regolith glass substrates have also failed to address this point [77]. Additionally, as outlined in section 2.1, the thermal environment on the Moon is significantly different from Earth's. Hence, cooling will mostly happen through radiation rather than convection as it is the case on Earth. Determining the annealing behaviour for a variety of basaltic glasses will therefore be part of the research efforts proposed.

Glass Mirror Manufacturing

Understanding basalt glass manufacturing first, before attempting to manufacture mirrors on the lunar surface is essential. Such mirrors built on basaltic glass could

be used as solar concentrators or as telescope mirrors [434]. Producing mirrors requires a substrate and a reflective material to be deposited on its surface. Most commonly, aluminium is used for this purpose, and sometimes also silver and gold coated mirrors can be seen. Aluminium has high reflectivity in the whole visible spectrum, whereas silver is significantly worse below 400 nm [435] (see also, figure 2.19).

An overview of four different mirror coating materials is shown in figure 2.19. It shows the percentage of light each coating is capable of reflecting over a wavelength spectrum from 0.2 to 10 μm wavelength. It can be observed, that all materials reflect more than 90 % of the light at a wavelength above 1.1 μm. Aluminium reflects highest averaging over the shown wavelength range with most of the times more than 90 %. Aluminium and silver were deemed potentially suitable for attempting to build a mirror on basaltic glass and have therefore been selected for testing.

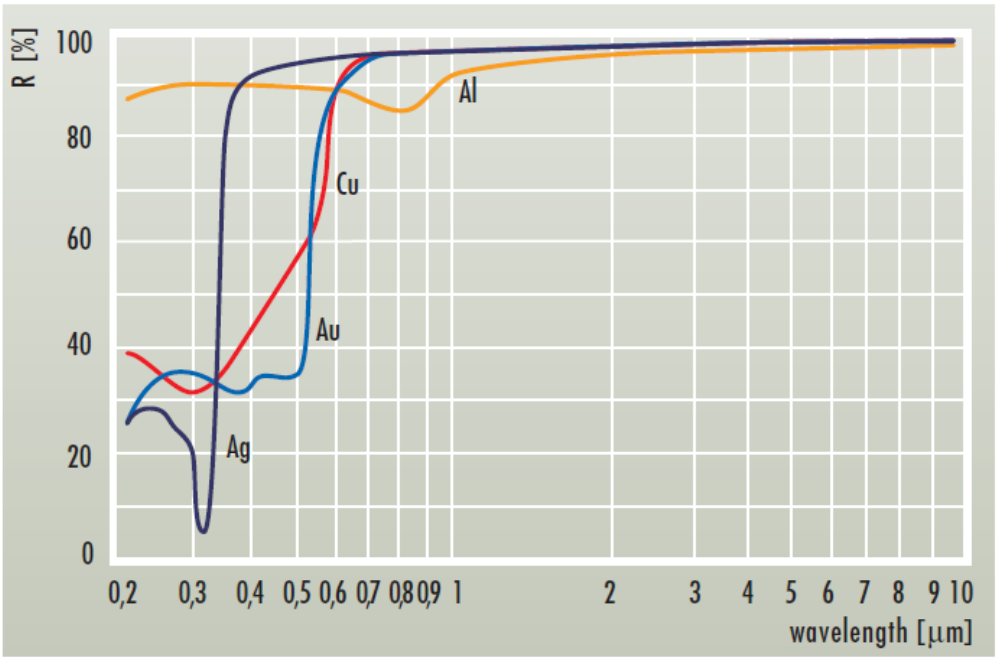

Figure 2.19: Percentage of light reflected (ordinate) over the wavelength spectrum (abscissa) of 0.2 - 10 μm of different materials: gold (Au), silver (Ag), copper (Cu), aluminium (Al). Credits: LAYERTEC GmbH

Using mirrors as solar concentrators, reflecting sunlight onto a solar cell, could influence the selection of a coating material as well. In this case, the absorption spectrum of the utilised solar cells will need to be taken into account as well, to maximize power output. As soon as it will be known, which specific wavelength range is of interest, further reading in the field of optics and mirrors can be found in [436–438].

To determine the ideal layer thickness for aluminium deposition, studies, which have been conducted on the connection between aluminium film thickness and

reflectivity, were reviewed. For aluminium layers on glass substrates, theoretical and empirical values presented in [439] suggest that aluminium layers > 15 nm achieve best reflectivity values. Other studies on gold (Au) and silver (Ag) suggest an ideal layer thickness of > 100 nm (Au [440]) and > 40 nm (Ag [441]). Further, a study conducted on deposition of aluminium on ceramic substrates manufactured from clays in Africa suggest best reflectivity for aluminium layer thickness of > 750 nm [442]. In conclusion, the layer thickness for thermal evaporation of aluminium onto a substrate manufactured from regolith simulant was set to be > 750 nm for substrates with $R_a > 100$ nm, and to ≈ 100 nm for substrates with $R_a < 100$ nm.

Using a required layer thickens (n_{Al}) of 100 nm as basis for an estimation of how much aluminium (density (ρ_{Al}) of 2700 $^{kg}/_{m^3}$ [443]) will be required lead to manufacture a surface Area (A) of 100 m^2, leads to,

$$A = 100m^2 \tag{2.6}$$
$$\rho_{Al} = 2700^{kg}/_{m^3} \tag{2.7}$$
$$n_{Al} = 100nm \tag{2.8}$$
$$m_{Al} = A \times n_{Al} \times \rho_{Al} \tag{2.9}$$
$$m_{Al} = 0.027kg \tag{2.10}$$
$$m_{Al} = 27g \tag{2.11}$$

, m_{AL} being the required mass of aluminium. Even considering losses in the evaporation/sputtering process for mirror fabrication, the amount of pure aluminium required to be flown from Earth to the lunar surface is in the few kg range. Hence, using aluminium brought from Earth for mirror manufacturing was deemed realistic. In addition to that, if aluminium extraction on the lunar surface becomes available, it will be more economically viable to use locally extracted aluminium.

2.4.3 Conclusion Fabrication Strategies

This review showed that a variety of different processing techniques are available, which have also been researched with respect to being able to process regolith (simulant). However, whether one of them would be suitable to produce a substrate, which can serve as a back-plate for a simple mirror, or even a fully functional solar cell, is yet to be determined. It is also possible that a combination of the reviewed processes will deliver the required quality of glass, or that of an intermediate glass product. If produced glass is not directly suitable for mirror and/or solar cell manufacturing, it may be suitable after post processing by means of grinding and polishing. From the reviewed manufacturing techniques, it should be possible to derive, suitable glass heating and shaping processes, as well as ways to manufacture glass substrates suitable for mirror and/or solar cell manufacturing. How the lunar environmental conditions will affect manufacturing and processing is still unclear since no work has been conducted so far, which tested manufacturing under lunar like conditions. Hence, once manufacturing on Earth works, it will need to be

tested under lunar conditions next.

The next and last section of this literature review will review available solar conversion devices, including their manufacturing techniques.

2.5 Solar Devices

Following the ISRU flow chart depicted in figure 1.5, this section reviews the final box, the application. Therefore, relevant information for building solar cells using basaltic glass made from regolith are reviewed. The basic background, of converting solar radiation via the photovoltaic effect, is established. Available solar cell types are reviewed, including to what extent they are useful for in-situ fabrication and lunar deployment. Constraints which will be imposed on manufacturing techniques depending on the solar cell type selected are pointed out.

For this research, solar devices are broken down into three categories; substrates, the active photovoltaic material (deposited on a substrate) and system components, such as, for example, wires, electrical contacts or cover glass. System components will only receive minor attention in this review, but it is clear that those will be relevant for any final system and will thus require further research once first working solar cells become available.

A review of recent trends in photovoltaic technologies in general is provided in [444], and a discussion about space solar arrays in general in [445]. However, the only actual work known to attempt building a sort of solar conversion device on the back of a substrate manufactured from regolith simulant is [446]. This suggests that little knowledge is available specifically to the task of manufacturing solar cells on basaltic glass substrates made from lunar regolith. Hence, terrestrially available solar cell types are reviewed and based on their suitability for the task, a type of solar cell will be selected for testing and manufacturing. Since silicon extraction, or elemental purification in general, was not considered an option, the type of cell defines, which materials for deposition have to be taken from Earth to the lunar surface.

2.5.1 The Photovoltaic Effect

The review of solar cells will require basic knowledge in the field of semiconductors, which can be found in [447, 448], for example, and will be assumed foreknowledge. Nevertheless, a brief introduction to the energy conversion by the photovoltaic effect is given and can simply be described as a two-step process. The generation of an electron-hole pair and the generation of electrical power. Electron-hole pairs are formed in a semiconductor material when a photon with sufficient energy (speed) is absorbed by the material. The hole and the electron are usually separated by the presence of an electric field, generated by the presence of a p-type (positively doped) and n-type (negatively doped) region of the semiconductor. The hole - swept across the junction - is attracted to/flows to, the positive contact, while the electron moves to the negative terminal and

current is generated, when the electron flows through an external circuit to meet again with the hole. This process is schematically depicted in figure 2.20. The figure is not accurate to scale, crystalline silicon cells, for example, typically have a layer thickness in the order of 300 μm, whereas thin-film solar cells and Gallium Arsenide (GaAs) have a layer thickness of several μm only. Additionally, the top of the cell might be covered with an anti-reflective coating [448], also not depicted here.

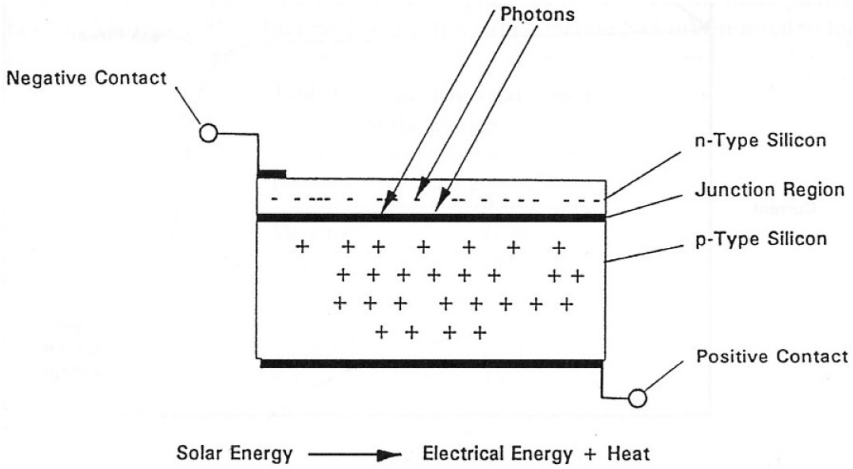

Figure 2.20: Principle of a Solar Cell: Incoming photons get absorbed in the p-n-junction, electron-hole pairs form creating a potential across the junction. If a circuit is connected current will flow. [449].

Photovoltaic cells are most commonly built with a single junction (one absorbing layer) as shown in figure 2.20. The type of material used, determines the wavelengths at which it can absorb photons. As shown in section 2.1, in space 1367 $^{W}/_{m^2}$ are available over the full wavelength spectrum. Every type of martial used to build junctions, absorbs light of a specific band (wavelength spectrum) and no material is capable of absorbing all wavelength at the same time by itself. As a logical consequence, that means that not all of the energy can be harnessed by just a single junction. For example, the wavelength spectrum that silicon absorbs light in, is in-between 360 - 1108 nm [450], unable to capture higher wavelengths effectively.

Solar cells with multiple layers (multijunction - MJ) of different materials target different areas of the solar spectrum at the same time, to maximise the power converted per surface area. This principle is highlighted in figure 2.21. The solar spectrum depicted on the right shows the wavelength ranges, at which each according layer of a cell (schematically depicted on the left) is able to absorb. The coloured AM1.5D line shows the irradiance at Earth's surface at an angle of 48.2°. The black AM0 line shows the available power in space with zero air mass attenuation. Note again the "valleys" in the coloured part which are caused by atmospheric interaction between the sunlight and the gases, such as water vapour and carbon dioxide.

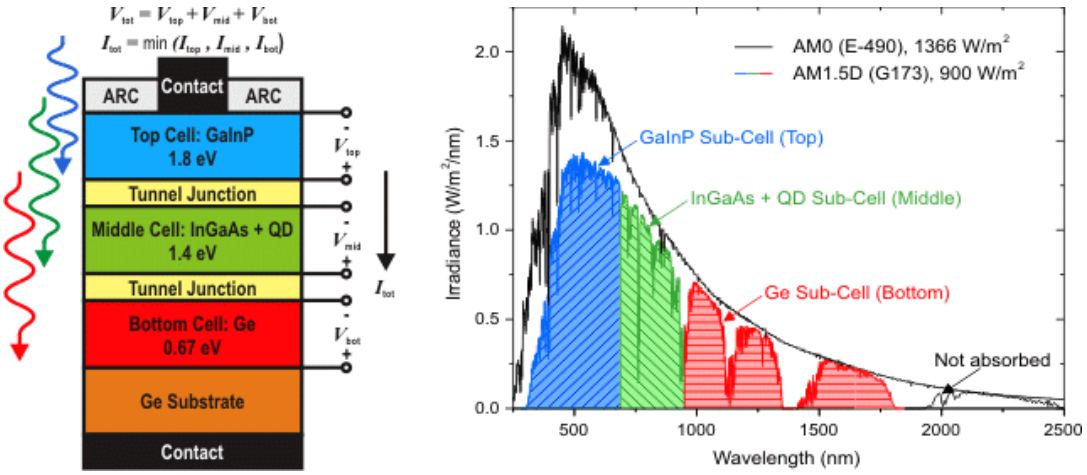

Figure 2.21: Multijunction solar cell and according solar irradiance bands [451].

The three colours, blue, red and green correspond to the different layers of the MJ cell and show which part of the solar light spectrum is absorbed by each layer. This schematically depicted triple junction cell is capable of harnessing almost all of the available energy, other than light in the wavelength > 1800 nm. Therefore, it can have a higher efficiency than a single junction silicon based solar cell.

In space, the full solar spectrum will be available and thus solar cells of any type may have an increased power output when used in space. Further details on different available solar cell types will be provided in the subsequent sections.

2.5.2 Solar Cell Types

Currently, worldwide, many different solar cell types are under investigation and a summary of the best research cells is depicted in figure A.1 in the appendix. The cells are categorised into four main categories: mutlijunction, crystalline silicon, thin-film technologies and emerging PV. They are presented as a function of the best, validated research cell efficiency and regularly updated on [452]. Best cell efficiencies (conversion of sunlight into electricity) can be achieved with multijunction cells, combined with solar concentrators, delivering a laboratory conversion efficiency of 47.1%. Moreover, best values in the other categories are 28.0 % for emerging PV, 27.6 % (with concentrators) for crystalline silicon cells, and 23.4 % for thin-Film technologies. More details on all SOTA efficiencies of solar cells can be found in [453]. Most of the emerging PV technologies are at low TRL at the moment, and are not yet sufficiently matured at terrestrial level. This rules out emerging PV technologies for space applications at the moment, however, the rapid progress in the field of perovskite cells, an emerging PV technology, in just a few years, suggests that this may change over the coming decade. Since the straight-forward manufacturing methods of perovskite cells may lend themselves to ISRU manufacturing. However, it is unlikely that many, of the necessary active materials for perovskite cells will be available on the Moon.

Choosing the most suitable solar cell technology, which can be (part-)built in-situ, for a future crewed mission to the Moon, is driven by four main factors.

1. Identifying cells with a high power-to-weight-ratio/specific power ($> 100\ ^{W}/_{kg}$ at array level).
2. Finding a suitable technology that can be entirely/partly-manufactured, but also mostly/partly sourced on the Moon.
3. Evaluating technologies with respect to their upgrade-ability or augmentation by means of ISRU.
4. Choosing a technology able to work under lunar/space environmental conditions.

Using these or similar criteria, a few examples of research conducted on high performance and/or lightweight solar cells can be found in [454–458]. Although some of the cell types listed on figure A.1 seem to be promising technologies for the future, only three types of cells have been identified which might fulfil (at least partially) the above listed criteria:

- Crystalline silicon cells
- Thin-film technologies
- Multijunction cells

Hence, the following provides a brief overview of these three technologies, using inputs from [448].

Crystalline Silicon Cells

Generally, crystalline silicon solar cells can be split into two categories, monocrystalline, poly- or multicrystalline both depicted next to amorphous silicon in figure 2.22. The actual form of the silicon dependents on the manufacturing method, which will be briefly shown in this section.

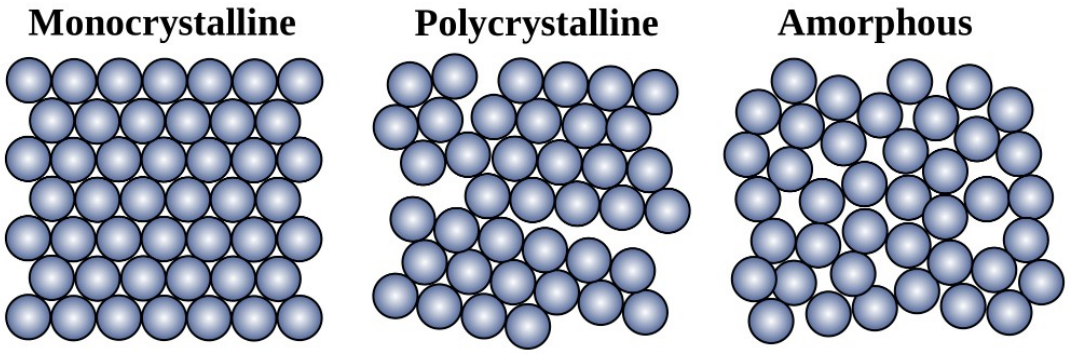

Figure 2.22: Schematic of allotropic forms of silicon horizontal plain [459].

Monocrystalline Silicon (CZ-Si) is grown in a process called *Czochralski Process* [4] and was accidentally discovered in 1915 [461, 462]. It is a method that uses a seed crystal that is dipped into a pool of molten material and by slowly raising it out of the melt - and at the same time turning it - a large, single crystal ingot can be

[4] after Jan Czochralski [460]

formed. This crystal is then sliced into wafers and used for solar cell manufacturing.

Polycrystalline Silicon (mc-Si) for solar cell applications can be obtained following two different paths [287]. The chemical route utilising trichlorosilane in the *Siemens* process to deposit silicon on an inverse u-shape hot filament [286], or the metallurgical route, which produces polycrystalline solar grade silicon directly from metallurgical silicon, and has shown to be up to five times more energy efficient than the Siemens process ($\approx 40\ ^{kWh}/_{kg}$) [463]. Independent of the method utilised, the formed polycrystalline material is then also cut into slices and used for solar cell manufacturing.

Crystalline Si (silicon) technology dominates the terrestrial PV market, accounting for > 95 % of modules sold. The biggest proportion of silicon wafers used for solar cell manufactured today are Czochralski, single crystalline and multicrystalline cells. In 2013 the distribution was 55 % mc-Si (25 % in 1995) and 45 % CZ-Si (60 % in 1995) [464].

When choosing between two crystalline Si technologies, one is faced with a trade-off in cost versus performance. Single crystal material provides higher conversion efficiency, a consequence of its better crystal quality, and purity, meaning generated electron-hole pairs can migrate more easily to electrodes. As a consequence of the multi-step approach[5] required for producing single crystalline wafers, manufacturing is more expensive. In multi-crystalline Si, compromises are made in purity and crystal quality, which results in a lower cost per cell, which is, however, also less efficient.

A downside of all crystalline silicon cells is that they are neither extremely efficient (compared to multijunction cells), nor are they light in terms of mass of the finished modules (compared to thin-film cells). On the upside, silicon based cells have been studied intensively over the course of the last decades and are well understood. As discussed, silicon is, after oxygen, the most abundant material on Earth and the Moon, which means, that if extraction methods become available, which can extract silicon from the lunar regolith, it might be possible to utilise them to manufacture solar cells on the Moon.

In section 2.3 it was established that extraction of silicon on the lunar surface is not an option, growing mc-Si or CZ-Si on the lunar surface is not considered for now. Further, the required amount of silicon wafers for crystalline silicon solar cells is rather high (large mass), transport of mc-Si or CZ-Si is also not considered an option. Adding to that, single junction silicon cells, have comparably low efficiencies to multijunction cells. As a result, crystalline silicon cells are not considered a suitable solar cell type for lunar manufacturing/use.

[5] which involves several purification processes prior to the Czochralski stage

Thin-Film Technologies

Thin-film solar cells are manufactured by depositing a thin (μm range) layer of semiconductor material on a supporting substrate. This is most commonly done by Chemical Vapour Deposition (CVD), which is an extremely well-established method for thin-film deposition across a number of applications. Several other thin-film technologies in this area have been demonstrated, such as sputtering, molecular beam epitaxy, atomic-layer deposition, ink-jet printing [465] or paste coating [466]. Typical substrates used are thin glass plates [467], flexible polymer substrates or even paper [468, 469]. Efficiencies of 10.2% [60], 11% [470], 11.6% [471], 12.4 % [472] and most recently up to 21.7% [473] have been reported for these devices. Further, due to their comparably low weight, their application in the space sector has been researched for some time now as well [474]. All thin-film solar cells are advantageous when it comes to their specific power where values (on cell level) of 2.0 $\pm$ 0.2 $^{kW}/_{kg}$ [60] can be achieved on Kapton®, or 1.68 - 1.84 $\frac{kW}{kg}$ on PI (Upilex-S) [475].

Typical semiconductor materials used as thin-films include amorphous-Si, Cadmium Tellurium (CdTe) and Copper Indium Gallium Selenium (CuInGaSe), both part of a group called CIGS (copper indium gallium selenide). A myriad of options have been proposed and tested [476] but these three cell types are highlighted since they have been commercially demonstrated for terrestrial applications, which was deemed an indication that they are suitably matured for potential applications in space. Other technologies are currently ignored, for the opposing reason.

Amorphous Silicon (a-Si) is silicon in non-crystalline or non-structured form, created by, for example, glow discharging in silane [477], Plasma-Enhanced Chemical Vapour Deposition (PECVD), H_2 diluted $SiH_4 + CO_2$ plasma [478], or electron cyclotron resonance microwave plasma chemical vapour deposition [479]. Amorphous silicon is most often used in thin-film technologies. As opposed to crystalline Si technologies it does not require such expensive material processing as the active PV material is deposited directly onto the substrate, rather than the substrate itself being made from Si. Largely because of its amorphous crystal structure, a-Si leads to cells with efficiencies less than crystalline technologies, similarity to mc-Si technologies.

CIGS cells have gained some market share of PV sales in the past seven years largely due to their commercialisation by a single manufacturer - First Solar. CdTe cells are significantly more efficient than a-Si cells. Moreover, by direct deposition of CdTe onto, radiation tolerant, flexible and cerium-doped micro-sheets of cover glass [455], the following specific power values could be calculated in table 2.4. Specific power are listed for entire modules, and CdTe exceed even triple-junction and Si cells:

This study shows that it is theoretically possible to achieve a specific power for a module as high as 8000 $^{W}/_{kg}$ on a large scale area for extra-terrestrial applications. Considering the requirement of NASA discussed in section 1.1, which was 500 $^{W}/_{kg}$, this technology is considered highly interesting. Further, this study highlights the most relevant advantage of thin-film solar cells; their comparable low weight.

Table 2.4: Specific power potential of CdTe, cell weight includes 80 μm thick cover glass for all 3 technologies. All values at BOL [455].

Technology	BOL Efficiency at AM0 in %	Cell Weight in $^{kg}/_{m^2}$	Specific Power in $^{kW_{peak}}/_{kg}$
TripleJunction	30*	1.06	0.38
Silicon	16.9*	0.52	0.44
CdTe	14**	0.24	0.80

*manufacturers' values, **projected efficiency

Nevertheless, they cannot entirely be manufactured on the Moon due to the lack of resources. This also goes for the latest and most efficient thin-film cell, which is $Cu(In, Ga)(S, Se)_2$ (CIGS)-based. Efficiencies higher than 20 % have been reported by multiple independent research institutes, as well as industrial companies (see [480] for an overview). These efficiencies where reported on a glass substrate, as well as polyimide.

In theory, this type of solar cell could also be built by recycling of spaceship material such as Multilayer Insulation (MLI) foil. MLI is usually made of several layers of coated Kapton®, which could already be coated in a way that it is useful for further manufacturing of thin-film solar cells, or solar cells can be built into the insulation material and be deployed on the lunar surface. Further, it might be possible to augment these lightweight cells with lunar resources and ISRU by building solar concentrators to increase efficiency. Whether thin-film cells could withstand the harsh lunar environment, and the increased heat load of concentrated sunlight, is yet to be demonstrated.

In conclusion, thin-film cells offer advantages such as they are light weight and hence need only little material to be built. Efficiencies are lower than other cells types but outweighed by their lower weight. Especially interesting is that thin-film cells can be built on a variety of substrates, including non-transparent substrates. All this, makes a thin-film based solar cell they most suitable type for ISRU manufacturing.

Multijunction cells

As mentioned in section 2.5.1, researchers and industry are aiming at converting as much of the available solar power into electricity. Pointed out from figure A.1 the best research cell efficiencies are achieved by multijunction cells. Each layer in a multijunction cell absorbs a certain wavelength range, as shown in schematic 2.21 on the left before. More information about high efficient multijunction solar cells can, for example, be found in [481].

The best multijunction cells in 2016 are shown in table 2.5. From these values it can be concluded that multijunction solar cell are with a maximum of 38.8 % the most efficient cells on the market. This gives them the distinct advantage of performing best in terms of power per surface area. However, since most of the cells are deposited on heavier substrates, these cells do not perform best in terms

of specific power. That said, it is likely that they could be substantially thinned for space applications. A study by [458] has shown that lightweight and flexible MJ cells are realisable by significantly thinning the Ge substrate on which they are formed. This led to only 1 % absolute reduction in cell efficiency, when compared to cells built on thicker Ge wafers.

Table 2.5: Confirmed terrestrial cell and submodule efficiencies measured under the global AM1.5 spectrum (1000 $\frac{W}{m^2}$) at 25 °C (IEC 60904-3: 2008, ASTM G-173-03 global) [453].

Classification	**Efficiency** in %	**Area** in cm^2	**Test Date**	**Description**
Five Junction Cell	38.8 ± 1.2	1.021 (ap)	7/13	Spectrolab [456]
InGaP/GaAs/InGaAs	37.9 ± 1.2	1.047 (ap)	2/13	Sharp [482]
GaInP/Si	29.8 ± 1.5	1.006 (da)	10/15	NREL
a-Si/nc-Si/nc-Si[6]	13.6 ± 0.4	1.043 (da)	1/15	AIST [483]
a-Si/nc-Si	12.7 ± 0.4	1.000 (da)	10/14	AIST [484, 485]

(ap) aperture area, (da) designated illumination area.

Certainly, materials for multijunction cells are not abundant on the Moon, while their structure is highly complex. This means that in-situ production of MJ cells on the Moon seems impractical. Despite the lack of raw resources on the Moon, their better efficiency per area is outstanding when considering their use with solar concentrators. Their use in this way is already well-established, as is their application in space settings. Importantly, ISRU can play a vital role in both, minimising the mass requirement, in terms of the amount of cells that are required to be taken, and in maximising the performance of the cells by augmenting a single cell with multiple ISRU-mirrors. This is achieved by pursuing the concept of concentrator-PV, whereby a large cell area is replaced by mirrors, which guide light from a large capture area onto a relatively small active PV device area. In parallel, concentration increases the photocurrent, and consequently, "Moon made" solar reflectors could increase the power harvested by a single cell by pushing the overall efficiency of the cell even higher.

Although manufacturing of MJ cells on ISRU substrates made on the Moon cannot be considered an option, using Earth-made MJ cells in combination with Moon-made mirrors, which form a concentrator, seems viable. Therefore such a combintation will be considered as a second solar conversion device option, next to thin-film manufacturing.

2.5.3 Solar Concentrators

Multijunction (MJ) cells are typically expensive, which is why they are usual candidates for being used together with solar concentrators terrestrially. This minimises the necessary cell area by focusing sunlight from a larger area onto a MJ cell. In figure 2.23 two possible setups for solar concentrators are depicted. The

one on the left is using two parabolic shaped mirrors (primary and secondary), and the right one simple flat mirrors on the sides.

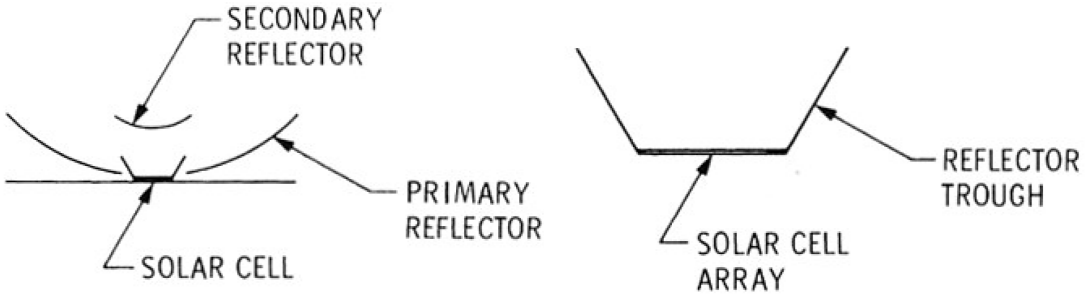

Figure 2.23: Schematic of two different concentrator types [34].

The possibility of manufacturing mirrors on the lunar surface is a more viable short term strategy, than manufacturing entire solar cell panels on the Moon, not least because none of the identified cell technologies is perfectly suited to be manufactured there. Although, thin-film solar cells were identified as the best type for lunar manufacturing, working cells will need to be manufactured first before they will be considered an actual option. Mirror manufacturing, compared to thin-film cells, will only require a substrate, ideally glass or glass-like, and a reflective coating, like silver or aluminium. As outlined earlier in section 2.4.2, reflective layers may be as thin as a few tens, or hundreds of nanometres and therefore only little material would be required from Earth. Both, glass and aluminium, can be found on the Moon as discussed in section 2.2.1. Further, in section 2.4.2 terrestrial applications of basaltic glasses were described, and although producing basaltic glasses is non-trivial [418], it is still considered a rather low-tech manufacturing process. Aluminium can be found on the Moon in large enough quantities to consider using it but, as shown in section 2.3, for now, it might be rather complex and energy intense to extract pure aluminium from the regolith. Fortunately, only very small quantities of approximately 27 grams per 100 m^2 - no losses considered - are required for mirror manufacturing. Therefore, manufacturing mirrors on ISRU basaltic glass substrates by bringing highly purified aluminium from Earth seems to be a practical solution. Equipment required for deposition - in the form of a simple evaporation system - also seems feasible to be transported to the lunar surface, as well as operating it there, since it is a straight-forward process.

This supports the finding made in the previous section, which is that MJ solar cells may be used in combination with mirrors made on the lunar surface. A simple setup such as depicted on the right in figure 2.23 seems the most straight-forward approach to that.

2.5.4 Terrestrial Manufacturing - Thin-Film Solar Cells

After reviewing three types of solar cells, one type was selected for potential manufacturing of solar cells on basaltic glass substrates. The type chosen is thin-film

deposition of solar cells and in the following, their terrestrial manufacturing will be reviewed with respect to their potential fabrication and use on the lunar surface.

Although different techniques for deposition exist, such as sputtering, pulsed laser ablation or evaporation, the most common deposition method for thin-film deposition is PECVD, a type of CVD method (schematically depicted in 2.24). Silicon thin-films are predominately deposited either from silane (SiH_4), or a mixture of silicon and hydrogen. Both are abundant on the Moon, however, concluded multiple times already, it seems more likely to bring these two as raw material from Earth, rather than relying on extracting them in required purities locally.

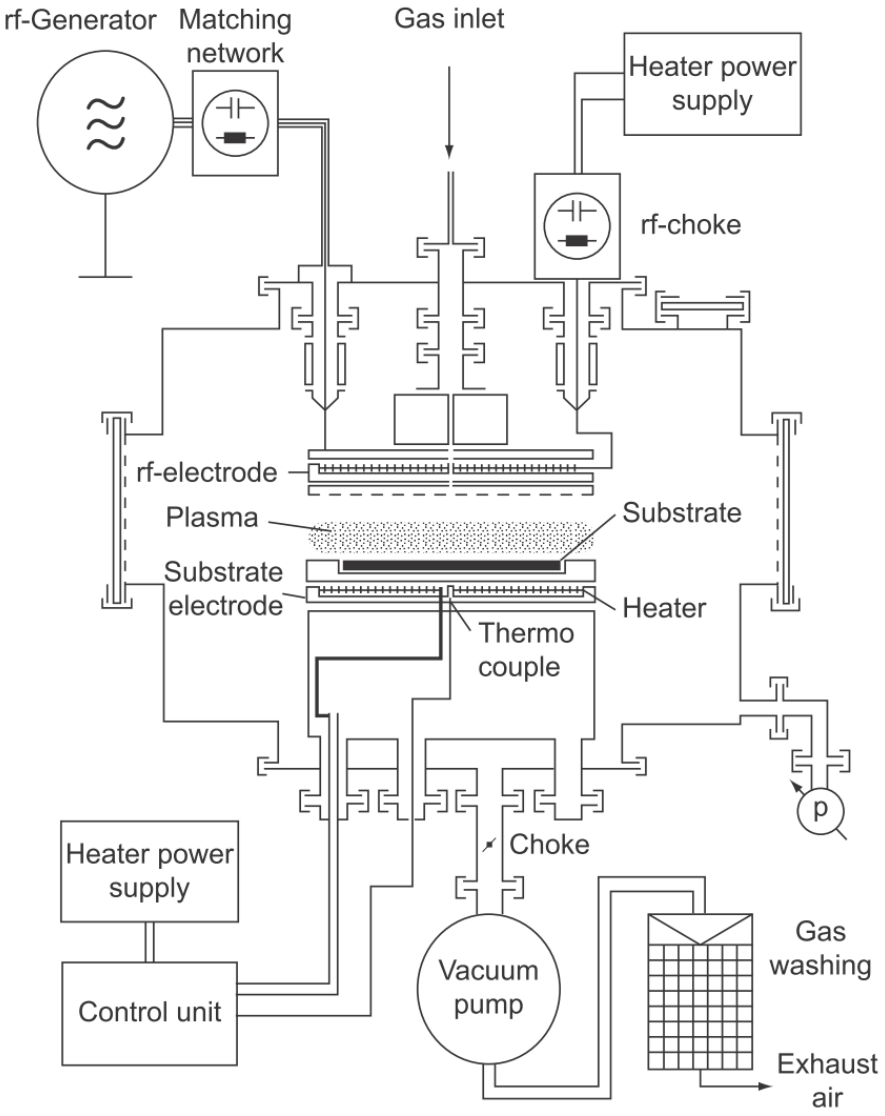

Figure 2.24: PECVD silicon deposition process [486].

Thin-film deposition will deliver micro-crystalline or amorphous silicon, and the 5 - 15 % of hydrogen, contained in the deposition mix, will passivate most of the built-in defects of these devices. Dopants are added in the form of phosphine (PH_3)

for n-type, or trimethylboron or TMB ($B(CH_3)_3$) for p-type [487]. The flexibility of the thin-film deposition process with respect to the production of devices is rather high, compared to others technologies [488]. At the same time the deposition rate of microcrystaline silicon (μc-Si) films is rather high [489]. The method of PECVD of silicon is very well established in the solar cell manufacturing industry [490, 491], and provides therefore the ideal tool for the task of manufacturing cells on "exotic" substrates. Hence, μc-Si thin-films are considered for deposition on basaltic glass substrates. Since silicon will not be considered to be extracted locally, first estimations suggest that manufacturing thin-film solar cells, capable of producing 250 kW of electrical power, would require about 100 kg[7] of ultra-pure silicon to be transported to the lunar surface [77]. This amount seems to be in a realistic range, considering the 6000 kg of payload-to-lunar-surface mass of a Saturn V rocket.

Whether regolith will be suitable to produce a suitable substrate, which can serve as back-plate for a working thin-film device (simple mirror or even a fully functional solar cell) is yet to be determined. Manufacturing a solar conversion device on basaltic glass is still challenging, since it has not been attempted other than in [77]. Therefore, building μc-Si thin-film cells is considered highly novel and of particular interest for this work.

2.5.5 Conclusion Solar Conversion Devices

After reviewing some of the available solar cell technologies, two options seem the most viable for augmentation of a lunar surface mission by means of ISRU. The first option is to take high efficiency multi-junctions cells, suitable for concentration, from Earth to the Moon. Mirrors may be built by using ISRU technologies to form a lunar solar concentrator, which would concentrate sunlight onto the cell and thus augment the MJ cell brought from Earth. The second possibility is, to manufacture glass substrates from lunar regolith and use these substrates as basis for thin-film μc-Si solar cell manufacturing.

As shown in this literature review, extracting silicon or aluminium on the lunar surface is not considered a viable option. Therefore, required high purity materials such as silicon or aluminium will need to be flown from Earth to the lunar surface. First estimations suggest that aluminium quantities of < 1 kg would be required to build mirrors with an area $> 100\ m^2$ and approximately 100 kg of silicon for building thin-film solar cells, capable of producing 250 kW of electrical power. Both of these requirements seem realistic for a future lunar surface mission which shall be augmented by means of ISRU. Both, thin-film cells and mirrors on basaltic glass are considered highly novel and both possess potential to realistically augment a future lunar surface mission.

[7] assumptions: layer thickness 20 μm, 10 % efficiency

2.6 Literature Review Conclusion

With respect to the idea of, manufacturing solar conversion devices on the lunar surface using in-situ resources, and the needs identified in NASA's TAs (chapter 1), the following areas were reviewed: Lunar environmental conditions and resources, regolith simulants, SOTA technologies in the field of ISRU elemental extraction and ISRU manufacturing and suitable solar conversion device types to be built on the lunar surface. After this review, conclusions can be drawn with respect to fulfilling the research objectives outlined in chapter 1.2:

Research Objective 1: - *Determine suitable raw materials for manufacturing and testing, using lunar surface like materials.*
From reviewing the work of researchers using regolith simulants, as well as information provided by simulant manufacturers, it became clear that prior to the start of manufacturing, the quality of potentially suitable raw materials (regolith simulants) needs to be assessed. As pointed out in this chapter, missing standardisation and quality assurance in the field of regolith simulants, make it impossible to use these materials off-the-shelf for manufacturing. Effects occurring during processing and manufacturing, which could be related to material compositions, cannot be identified by just using supplier data, since they are typically based on measurements taken from the bulk material and not from an individual shipment. Hence, geological and chemical analysis of regolith simulants will need to be conducted, prior to processing. Readily available regolith simulants chosen for this study are BP-1, EAC-1, FJS-1, JSC-1/2A and LHT-2/3M.

Research Objective 2 - *Demonstrate manufacturing of glass like substrates for use as back-plate, and cover glass for solar conversion device production.*
Works surveyed from the time of the Moon landing up until now, 50 years later suggest that little research has been conducted on using regolith to manufacture glass and make it available as a resource. Further, little research has been conducted on utilising basaltic glass to build substrates for solar conversion device manufacturing. Additionally, no research could be identified altering the composition of the regolith, by means of extraction or beneficiation, to impact the optical and/or mechanical properties of glass manufactured from regolith. Suitable technologies identified which could potentially help to fill these gaps in knowledge are, microwave processing and magnetic separation/beneficiation.

Research Objective 3 - *Demonstrate manufacturing of solar conversion devices from primarily lunar analogue material.*
Using lunar analogue material to build devices and equipment for lunar bases or structural elements has been researched in the past. However, the particular use of lunar resources to build solar conversion devices, in the form of reflector mirrors and/or solar cells, has only received little or no attention. Since the use of glass, manufactured from regolith, to build mirrors seems simple enough to be considered for an actual lunar mission, this particular field of research will receive special attention. Further, these lunar build mirrors, and their potential for augmenting

a lunar surface mission in form of a solar concentrator and/or solar furnace, are important to be explored in more detail. Once suitable substrates will have been manufactured from regolith simulant, thermal evaporation of reflective materials onto such substrates will form a mirror. Combining a number of mirrors, manufactured in the described way, into a solar concentrator via a suitable mount, will be the second step. Once these mirrors have successfully been built, building a μc-Si thin-film solar cell, on the back of a substrate by using PECVD methods, will be in focus.

Research Objective 4 - *Use experimental methods to determine the quality of the substrates and determine the performance of built solar conversion devices, corresponding to space exploration technology roadmaps.*
Once manufacturing of solar conversion devices has been demonstrated, testing and performance characterisation of the devices will be required. Tests identified will include testing optical properties, such as reflectivity and transmission, as well as exposure to simulated sun light on a solar simulator. The performance of working devices will be of interest to estimate the augmentation potential of such a technology for a future lunar mission.

Key gaps in knowledge identified from the review, which need solving to fulfill the outlined research objectives, are:

- Find an analogue material which can be used to demonstrate manufacturing of space power systems.
- Find a way to make glass from regolith and make it available as a resource.
- Investigate what glass quality (surface, geometry) is required to build solar conversion devices.
- Find a reproducible method to manufacture glass of determined quality.
- Find a way to make glass durable and last by developing a suitable heating and annealing strategy for basaltic glass.
- Find a method to manufacture mirrors and solar cells using glass made from regolith.
- Find a way to make basaltic glass (typically non-transparent) transparent to be used as cover glass (for solar cells).
- Determine the quality of manufactured devices by comparing them with Earth made devices. From the obtained results understand the feasibility of manufacturing such devices on the lunar surface.

3 Manufacturing of Substrates and Devices

After a review was conducted in all relevant fields to *Using Lunar In-Situ Resources for the Production of Solar Conversion Devices* and strategies for the fulfilment of the research objectives have been set, preparation and manufacturing of devices could commence. Thus, this section details what manufacturing techniques were utilised to prepare regolith, heat and melt it, anneal manufactured glass and post process that glass. After describing how suitable glass substrates were manufactured, solar conversion device manufacturing will be described.

3.1 Regolith Preparation and Beneficiation

Depending on the application, it was required to prepare or beneficiate a regolith simulant for manufacturing and/or analysis. The following sections will outline how utilised regolith simulants have been prepared prior to manufacturing.

3.1.1 Sieving

Grain size distribution of the regolith and regolith simulant is considered to be important for ISRU technologies since the grain size might have an impact on the heating/melting processes, as well as the quality of the final product. Hence, it is important to know the grain size distribution of each simulant selected, and if required, to target a certain grain size spectrum and separate it. By consecutively sieving regolith material trough sieves with decreasing sieve sizes, it is possible to separate regolith into different grain size distribution groups. Depicted in figure 3.1 is a sieve containing regolith gravel (1, left), a mechanical shaker-tower (2, middle) and a schematic of a sieve-shaker-tower shown on the right (3).

Either individual sieves can be used, to manually split the regolith into different groups, or an electrically driven sieve-shaker-tower. The latter option has the advantage of being faster and more thorough than manually sieving regolith. This is especially true for regolith amounts of more than 200 g. Additionally, sieving in general can be used to check a simulants grain size distribution curve, provided by the manufacturer, which was required due to differences in grain size distribution occurring in-between different shipments/batches. Sieving a part of each batch therefore delivered the actual grain size distribution received from the manufacturer.

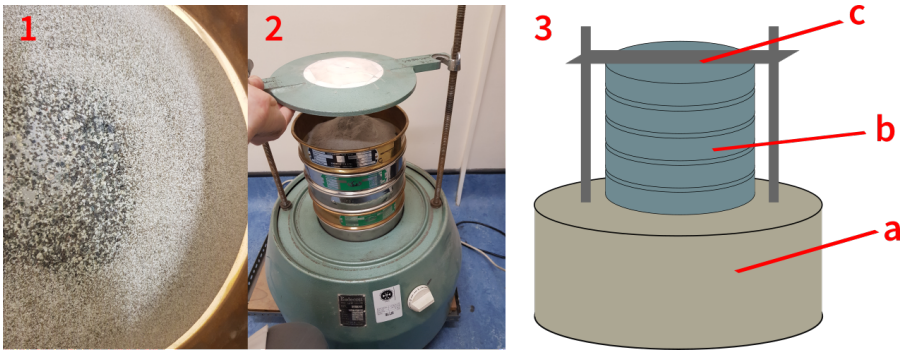

Figure 3.1: A sieve with regolith gravel shown on the left (1) the actual shaker-tower in the middle (2) and a schematic of a sieve-shaker-tower shown on the right (3). The shaker-tower consists of the electrically driven shaker base (a), a number of different sieves (b) and a mechanism to hold all sieves in place (c).

3.1.2 Grinding

To grind regolith into a powder ($< 38\ \mu$m) a mortar grinder called "Pulverisette 2" was utilised, which works at low speed and thus low thermal loads. Advantages of this machine were the brief (5 minutes) and reproducible grinding results. Moreover, its losses are rather little as well as its contamination potential. Up to 50 grams of regolith could be ground at one time.

Grinding of regolith was required to prepare regolith for measurements or a manufacturing process, which required a fine and/or homogenous powder. In addition to increasing the homogeneity of the regolith sample, grinding may have also released trapped gases and changed the mechanical characteristics of the simulant. The release of gases or volatiles may be relevant for manufacturing glass, since volatiles, released in a glass melt, will form bubbles, which lead to defects in the final substrates/glasses.

3.1.3 Drying

Figure 3.2 is showing a set of five samples, which have been prepared for a measurement. All of these samples have been ground in the mortar grinder, each for five minutes, then entered into petri dishes and placed inside an electrically heated and programmable kiln. Regolith was dried in this kiln at 220 °C for 2 hours, to remove residual moisture and volatiles.

Preheating of regolith was not only required prior to measurements conducted, but in some cases also prior to manufacturing. The goal of preheating the regolith was similar to grinding; releasing gases and/or volatiles. Again, these may have formed bubbles, which may have led to defects in the final substrates/glasses. Thus, removing gases and/or volatiles and/or moisture helped to improve measurements and/or manufacturing quality.

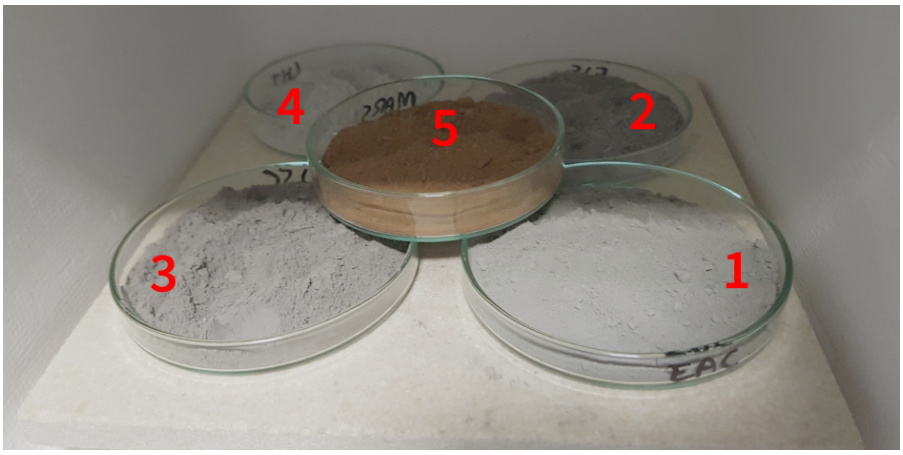

Figure 3.2: Drying regolith in an electrically heated kiln at 220 °C. Regolith simulants shown are EAC-1 (1), FJS-1 (2), JSC-2A (3), LHT-3M (4) and JSC-MARS-1A (5).

3.1.4 Magnetic Separation

A comparably simple beneficiation process, which was applied to the regolith for one set of experiments, was (electro)magnetic separation, using a device depicted in figure 3.3. This machine/process is commonly used in the field of geology to separate high density minerals such as apatite and zircon from the bulk sand. Prior to using the machine, depicted in figure 3.3, this method uses a hand magnet to separate highly magnetic materials in advance to running it through the machine. The use of this process allowed to split regolith up into five different groups of magnetic susceptibility. Although it would be possible to split regolith in more or less groups, since the electromagnet can be adjusted seamlessly, five was the number chosen for this experiment since the number of samples to be analysed was still manageable that way.

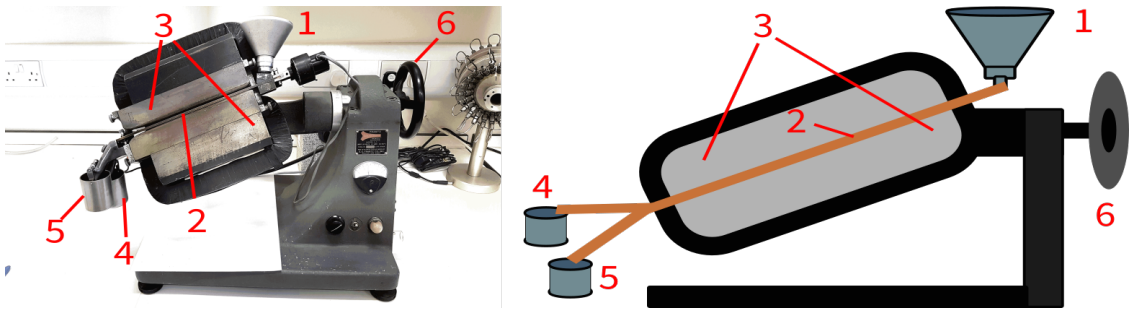

Figure 3.3: An electromagnetic mineral separator, the utilised system shown on the left and schematically on the right. Funnel to enter regolith material (1), electromagnet (3) with space at the centre for a cooper slide (2) to guide the regolith through the magnetic field. The slide has a separation wall at the end to split regolith in a bucket containing non-magnetic (4) and magnetic material (5). An adjustment wheel (6) allows to change pitch and roll angle.

Before regolith could be run through the system, each regolith needed to be separated into different grain size distributions via sieving. Each sample was separated into three groups, 63 to 125 μm, 125 to 250 μm and 250 to 500 μm. Each grain size distribution group had to be run through the electromagnetic system separately, to avoid clogging of the system. For each grain size distribution, the same procedure was repeated. First the sand was combed with a hand magnet (depicted in figure 3.4 on the left), then run through the electromagnetic separator three times, each time changing the power input to the electromagnet, leading to a change of the magnetic field and the regolith splitting again. At the end of the slide, leading through the centre of the electromagnet, regolith was separated at a fork (shown in figure 3.4 on the right) into a magnetic and a non- or less-magnetic bucket. White sand (non-magnetic regolith) can be seen on the left side of the fork in figure 3.4 and more brownish white regolith on the right side of the fork.

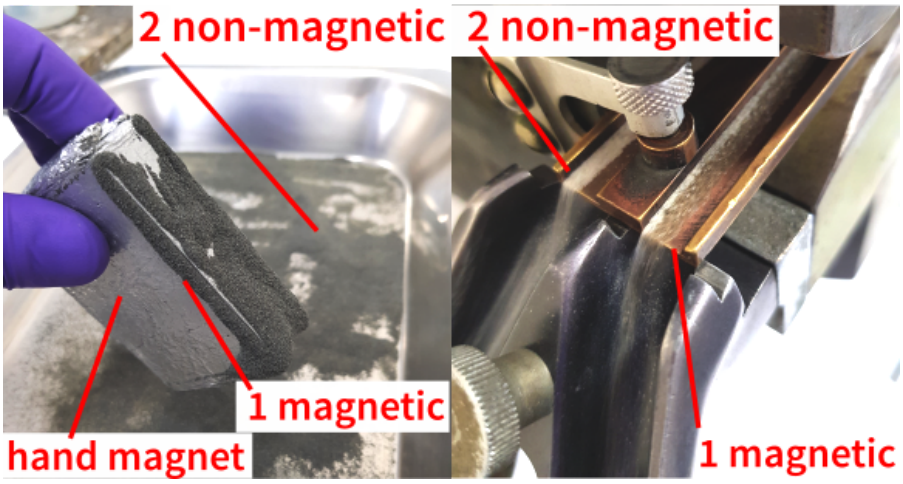

Figure 3.4: Two steps of magnetic separation, left separation utilising a hand magnet, and right the fork at the end of the cooper slide of the electromagnetic separator. Both sides show the magnetic fraction of each separation step (1) and the non-magnetic fraction (2).

This process was applied to six different simulants and proved to work for all of them. Due to the size of the electromagnetic separator, the amount of regolith, which can be filtered in a certain time, was limited, and running 200 grams of simulant through all stages of the system took about 4 to 5 hours. After processing 200 grams of simulant, in some cases, only about one gram (or less) iron sparse (non-magnetic) regolith was recovered. Hence, if amounts of non-magnetic regolith in the order of hundreds of grams or even kilograms are required, a larger system will be required to run a larger amount of regolith at the same time. The size of the system was, however, suitable to test whether this beneficiation process was working for regoliths, and enough material for measurements was gathered. Whether or not this process will work on the Moon, under the reduced gravity conditions and with the lack of atmosphere, will require research beyond this work. Further it seems possible to automate this process for the lunar surface, so processing time becomes less an issue and the system can operate autonomously after having been set up.

3.2 Basalt Glass, Regolith Heating and Annealing

As discussed in the literature review already, on Earth, glass is a widely used resource and throughout the history of humankind and opened up many new possibilities in manufacturing. Hence, the goal was to investigate how glass, in the form of basaltic glass, could be made available on the lunar surface, as a resource as well, to enable new manufacturing possibilities. Thus, determining what type of glass can be manufactured on the lunar surface, as well as defining heating and annealing parameters, was the first step.

After possible pre-processing of regolith, it was required to heat the regolith simulant above its melting point to form glass. By analysing available heating and shaping techniques, a process, utilising regolith as starting material for glass manufacturing, was designed and tested. Further, an annealing process was tailored to the basaltic glass, manufactured from the regolith.

The following sections elaborate on available and utilised heating and shaping techniques, suitable for melting regolith. Two of these techniques are detailed, and details on the developed annealing process are provided.

3.2.1 Baltic Glass as Resource

Glass, in form of "lunar highland" or "lunar mare" glass, naturally occurs on the lunar surface and can make up to 25 % of the overall regolith (table A.2). This glass is typically formed due to high velocity impacts of (micro) meteoroids, which (partially) melt the lunar regolith. When rapidly cooling, the melt forms basaltic glass on the surface. It is not required to extract such glass from the regolith for glass manufacturing, but the basaltic glass contained in the regolith may, however, be beneficial in manufacturing. In terrestrial processes old glass is mixed with new sand (input material) to form new glass. Adding this recycled or old glass lowers cost and production time by lowering the melting point and energy required for manufacturing. Thus, the actual glass content of a regolith material may be relevant for glass manufacturing once considering efficiency.

Good understanding of how to process lunar regolith (simulant), to form basaltic glass, is required to make basaltic glass a resource, potentially available on the lunar surface. Further, this requires heating, shaping and annealing of basaltic glass to be understood first, before considering the use of this basaltic glass as substrate for mirrors and semiconductor devices. The next sections will outline these three points further.

3.2.2 Available Heating and Shaping Methods

Basaltic glass melts could only be produced by using processes which were capable of achieving temperatures at around 1400 - 1600 $°C$. Although it was suspected that regolith simulants melt at around 1200 to 1250 °C, a system achieving significantly higher temperatures guaranteed that all simulant material was melted.

Before forming or shaping a substrate, and before any measurements on substrates could be attempted, a means of melting the raw regolith to form glass was required. Although it is desirable to find a process which is working (equally) on Earth and the Moon, it was not prioritised, since a general understanding of basaltic glass processing was required first. Hence, the key criteria selecting a suitable heating method for melting regolith simulant were:

- Efficiency
- Consumables required
- Complexity of the system and process
- Weight and size
- Maximum achievable temperature

Secondarily, it was required that the techniques could also be employed on the lunar surface, potentially with modifications/adaptations. The following shows a summary of the analysed means of heating, capable of heating (lunar) regolith beyond the required melting temperature. This work considered five techniques; gas heating, solar furnace, SLM, microwave heating and resistive heating. A more in depth analysis of most AAC technologies, available for ISRU processing/melting, can be found in [356].

Tradeoff Analysis of Heating Methods

All five technologies considered have been summarised in the tradeoff analysis table shown in table 3.1. After weighing the pros and cons of all technologies, microwave and resistive heating achieved the most positive points. The next best technology after these two is a solar furnace, which, once established on the lunar surface, would be an equal or even better solution. However, the effort of building and/or utilising such a system is comparably high to microwave and resistive heating. Gas heating and SLM did both not achieve positive points and are, referring to this analysis, less suitable for melting regolith.

Table 3.1: Tradeoff analysis for five different heating technologies capable of heating regolith

	Gas	Solar Furnace	SLM	Microwave	Resistive
Efficiency	+	++	-	+	o
Consumables	- - -	+++	+	+	+
Complexity	-	- -	-	++	++
Weight/Size	-	- -	o	+	+
Max Temp	++	+	+	-	o
Sum	-2	2	0	4	4

After the analysis of five techniques, suitable for melting regolith, was conducted, two techniques have been selected for this research. The first technique utilised was microwave heating due to its comparably low cost and good availability. The

second technique was resistive heating, which has proven to be a more reliable and controllable system than microwave heating. Which of these techniques is the best to be deployed will need to be tested by conducting lunar environmental testing. The vacuum environment may not affect any technique other than gas heating, the temperature environment on the other hand may affect all of them. Ambient temperature will impose constraints on cooling/annealing and therefore it will be key to understand thermal conditions better in order to prevent stress building up in the glass and to avoid cracking. Next, options on how to shape the molten glass have been analysed, and a suitable option has been selected.

Shaping of Regolith Melt

After a suitable method of heating the regolith into a glassy phase has been chosen, the next step was to manipulate the shape of the molten glass. Four techniques have been down selected based on section 2.4.2 and the following key criteria have been considered for their applicability to the project:

- Complexity of the system and process
- Weight and size
- Temperature stability
- Impact on shape

The more complex the process, the less likely for it to work or be deployed on the lunar surface. Most often, increased complexity means increased weight and size, both of which are not desirable for manufacturing on the lunar surface. Temperature stability of the process is important for two reason, first, that the glass is not solidifying before it has reached its final shape, and second that, no or little thermal stress can build up in the glass. An ideal process would additionally have full control over manipulating the shape of the glass to its desired form directly before cooling, so that it would require little to no post processing.

Tradeoff Analysis of Shaping Methods

All four processes considered have been summarised in the tradeoff analysis table shown in table 3.2. After weighing the pros and cons of all technologies, fusing scored the most points (5), followed by casting (3). Float glass and glass blowing are considered less suitable choices with -1 and 0 points.

As a result of these analyses both, fusing and casting have been selected as shaping techniques. Considering lunar conditions for this manufacturing step, those two techniques may work on the Moon as well, may however be impacted by reduced gravity (pouring, shaping), temperature (time to cast and cool) and vacuum (processing times and gas releases). Next, the selected glass heating and shaping techniques have been used to manufacture samples and are now described in more detail.

Table 3.2: Tradeoff analysis of glass shaping technologies

	Float Glass	Glass Blowing	Fusing	Casting
Complexity	- -	o	++	+
Weight/Size	- -	o	++	+
Temp. Stability	++	- -	++	-
Shaping	-	++	o	+
Surface Quality	++	o	-	+
Sum	-1	0	5	3

3.2.3 Microwave Heating

As discussed in the previous sections, microwave heating was considered a suitable heating method for melting regolith (simulant). In the literature review it was established that direct microwave heating is dependent on the regolith's susceptibility. Since different regoliths/simulants have different iron oxide contents, they showed different susceptibility to direct microwave heating. In order to decrease the dependency on the regoliths' susceptibility to microwaves, the microwave heating process was adapted. By introducing a so called microwave kiln into the microwave heating environment, microwave heating worked independent of the input material.

Passive Microwave Heating Using a Microwave Kiln

A schematic of the utilised microwave kiln system is depicted in figure 3.5. This kiln was entered into an off-the-shelf microwave oven operating at the 2.5 GHz standard. The microwave oven itself, was modified by a special company which cut a hole into the top of the oven to gain optical access to the processing chamber. The maximum power consumption of the used microwave oven was 1kW. For each use, the microwave kiln was entered into the centre of the microwaving chamber. Schematically depicted in figure 3.5 the microwave kiln used, hit by microwaves. When the microwaves hit a layer of susceptor material, they are converted into heat. Since the so formed heating element is contained inside a thermally insulated chamber, made of aluminium oxide foam, the temperature on the inside was increasing until thermal equilibrium was reached. Placing a crucible with regolith simulant inside the heating chamber led to heating and successful melting of the regolith.

Crucibles are available, made of a variety of high temperature materials, for example, aluminium oxide, clay or graphite, all of which have been tested for their use to melt regolith. Although regolith could be melted in all of them, the only crucible that allowed for removal of the sample (glass) after heating, was the crucible made of graphite. Hence, only by using graphite crucibles it was possible to obtain basaltic glass samples, which could further be used for processing. The first samples were manufactured using the fusing approach described earlier.

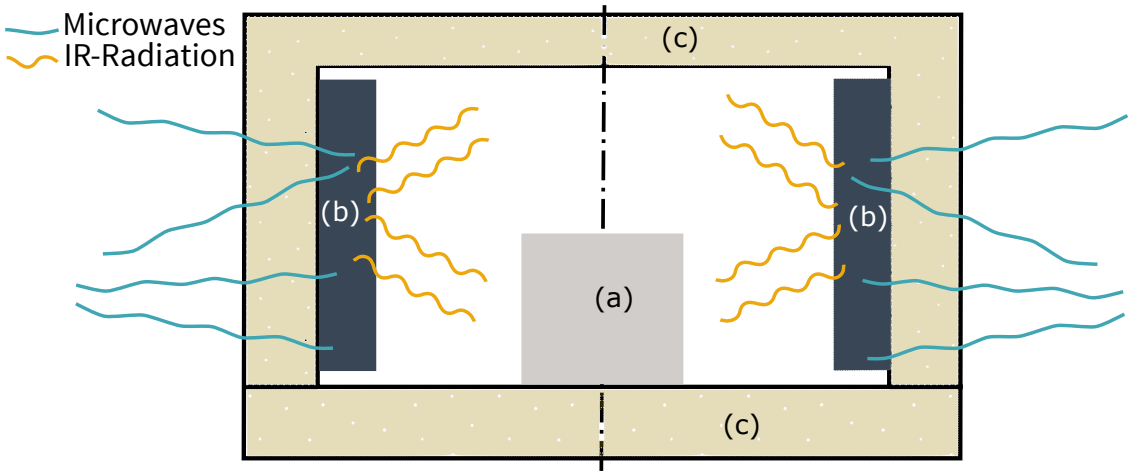

Figure 3.5: Cross section of a cylindrically shaped microwave kiln used for passive microwave heating, shown under operating conditions. A crucible (a) is surrounded by a susceptor material (b) (here: Magnetite-Graphite mix), which is contained in an alumina fire brick insulation chamber (c). Schematic published in own work [255] before.

On top of supporting the release of the sample from the crucible (after heating), graphite is a susceptor material [389, 390], which was supporting the heating process actively by acting as a second heating element. However, the downside of using a graphite crucible in an air atmosphere was, that the carbon seemed to react with the regolith. To confirm this, it would be required to conduct spot measurements on the obtained glass to see if any elemental material such as silicon or iron is found. For this research, this option was not further investigated and focus was put on removing gas from the melt. It is likely that carbon and regolith reacted in a carbothermal reaction, releasing the oxygen from the melted regolith in form of CO and/or CO_2. This led to bubbles forming in the melt, which in some cases led to a basaltic foam forming. Not in every case actual foam was formed, but in all cases bubbles were trapped in the melt, which led to voids forming after post processing a surface of the sample via grinding.

Rather than only fusing the regolith to glass by just keeping it in the crucible/mould, it was attempted to cast the regolith melt. Different variations and moulds have been tried, which mostly led to the same result, inhomogeneous shaped glass pieces, which were not suitable for manufacturing. Tests included but were not limited to, casting onto moulds made of clay, graphite and regolith itself. Although all cast samples had an odd shape, which was not ideal for manufacturing, casting allowed for the release of some bubbles. These had formed in the melt during heating, and casting seemed to have released them. Despite casting showing promising results, with respect to bubble release, it was not explored further while using microwave heating. The issue of the melt cooling too rapidly while casting could not be solved, and only oddly shaped glass samples could be manufactured. Since most of these samples were not suitable for processing, casting was not used until a better thermal stability could be ensured.

The processing temperatures during microwave heating were measured to be as hot as 1200 °C or more. This was determined by using a handhold remote sensing thermometer operating in a wavelength range of 8 to 12 μm, as well as using a pyrometer operating in-between 2.0 and 2.4 μm. Five different regolith simulants (BP-1, EAC-1, FJS-1, JSC-1A, JSC-2A) have been fully melted using the described passive microwave heating approach. One simulant (LHT-3M) could only partially be melted in the microwave kiln, since some of the contained minerals did not fully melt. Further analysis could show which minerals did not melt and what may have been the reasons for that. Although not all simulants used were fully melted, the passive microwave heating approach (similar to what was suggested by [384]) showed to work reliably and repeatedly on different simulants, and therefore showed advantages compared to a direct microwave heating approach described by [383] and [384].

After initial testing of the setup, two separate test runs have been conducted to test, whether substrates of good enough quality for mirror manufacturing could be produced. Test runs produced nine different glass-like substrates, five in the first batch and four in the second. Resulting samples are listed in table 3.3, and details on how they were manufactured will be discussed in the next section. Samples produced were stable under room condition (20 ° C), and did not shatter or break during processing.

Summary Initial Microwave Heating Tests

In summary the passive microwave heating process utilising a microwave kiln did homogeneously melted most simulants and after testing a variety of different manufacturing approaches, delivered first usable basaltic glass samples. The most likely reason for homogenous melting of the regolith was the heating element made of a susceptor material. This ring shaped element was contained in the thermally insulated chamber, and could therefore produce a homogenous heating environment. This environment led to fully melting all regolith contained in the crucible, unlike the direct microwave heating approach, which typically shows inhomogeneities since the microwave field, on the inside of a household microwave oven is inhomogeneous and has local hot and cold spots. This typically leads to samples either melting in the order of minutes or not at all. Even if samples melt, they only melt in a narrow area and the bulk part surrounding this area remains not melted.

The passive microwave heating process showed to be mostly independent of the simulants composition (listed in table 2.3), but it can not be excluded that the simulants composition does play a role using susceptor-assisted microwave heating. Iron and magnesium oxide do in general have an impact on the susceptibility of a material/regolith and thus impact the heating behaviour of a simulant. Hence, simulants with higher magnesium and/or iron oxide content are likely to heat faster, also under a microwave kiln. Independent of that, calcium oxide rich (anorthite rich) simulants will have a higher melting point than calcium oxide sparse simulants. Although this should not impact the heating processes as such, it will either take a longer time for these simulants to melt, or they will not fully melt at all, since

the melting point of the contained minerals will not be reached. This suggests that even if the heating process itself may not be impacted by composition, the process might not be capable of melting all input materials, since it cannot reach high enough temperatures.

The following sections will elaborate on the preparation of two independently manufactured basaltic glass sample batches. Both batches were heated using microwave heating and shaped either using fusing or casting.

Manufacturing Basaltic Glass Samples in two Batches

Microwave heating experiments have been split into two batches, a first initial batch using two regolith simulants types (JSC-2A and EAC-1), and a second using four different simulant types (EAC-1, FJS-1, JSC-2A, LHT-3M). Batch one consists of five samples, three made of EAC-1 and two made of JSC-2A, batch two consists of four samples one made of each simulant used. All samples of both batches have been processed at 1 kW input power to the microwave system. Experimental details are listed in table 3.3. Sample IDs show which batch a sample belonged to, indicated by the middle part of the ID, which is either *I* for the first batch or *II* for the second batch. Further information contained in the sample ID is the simulant type where EAC equals EAC-1, FJS equals FJS-1, JSC equals JSC-2A and LHT equals LHT-3M. The last number in batch one is the consecutive number of the sample in a batch. For batch two only one sample of each simulant was prepared, thus no last number was assigned. Other information listed in table 3.3 includes simulant type used, heating time and weight before heating, as well as for batch two only, the samples' weight after heating and the difference (delta) before and after heating.

All batch one samples have been heated for 40 minutes or less, and all, but one batch two sample, have been heated for 30 minutes with the exception of LHT-II, which was heated for 65 minutes. The JSC-I-2 sample was heated much longer than all other four samples, since it was cast after microwave heating. The extended heating period was intended to lead to a higher temperature of the melt and thus provide more time for casting before the temperature of the melt drops to the solidification point.

All but one sample showed to lose weight (table 3.3) from entering the raw regolith into the crucible to the final glass nugget. The only sample gaining 0.03 grams was JSC-II, which may be due to oxygen absorption of the iron (oxide) contained, or some interaction between the crucible and the sample. Weight loss on the other hand is most likely the loss of water and other volatiles evaporating during heating. To know more about mass losses in detail, further analysis such as mass spectroscopy of the released gases would be required, since it was not critical for this research, it was not investigated further.

Table 3.3: Overview of batch 1 and batch 2 samples manufactured using microwave heating

Sample ID	Simulant	Time (min)	Weight before Heating (g)	Weight after Mass (g)	Delta Mass (g)
EAC-I-1	EAC-1	20	15.00	-	-
EAC-I-2	EAC-1	30	15.00	-	-
EAC-I-3	EAC-1	15	15.00	-	-
JSC-I-1	JSC-2A	15	15.00	-	-
JSC-I-2	JSC-2A	40	15.00	-	-
EAC-II	EAC-1	30	14.97	14.51	-0.46
LHT-II	LHT-3M	65	19.97	19.86	-0.11
FJS-II	FJS-1	30	15.11	14.98	-0.13
JSC-II	JSC-2A	30	15.04	15.07	+0.03

Despite both batches having been conducted separately, both batches used the same susceptor-assisted microwave heating process utilising a microwave kiln. Both batches used graphite crucibles/moulds with cavities of 45 * 24 * 10 mm which led to an approximate sample size of 38 to 42 mm length, 22 mm width and 8 to 12 mm in height. Thus all samples have a size similar to the size of a domino brick. Next, differences in manufacturing the two batches will be outlined, as well as differences in-between manufacturing individual samples.

Microwave Heating - Batch 1

The first batch manufactured from regolith simulant was batch one. Two samples made of JSC-2A simulant and three made of EAC-1 have been manufactured which are all depicted in figure 3.6. For each sample, 15 grams of raw (unaltered) simulant were placed in the graphite crucible and entered into the microwave kiln, which was then placed inside the microwave chamber of the microwave oven. All samples have been manufactured with 1 kW input power and the experiment was run in air, further processing details are listed in table 3.3.

Figure 3.6: Batch 1 samples after cooling, samples from left to right (fltr): EAC-I-1 (top), EAC-I-1 (bottom), EAC-I-2 (bottom), EAC-I-3 (top), JSC-I-1 (top), JSC-I-1 (bottom), JSC-I-2 (top) and JSC-I-2 (bottom).

All three EAC-1 samples have been manufactured by fusing the simulant, hence, once the sample was entered in the crucible it remained in there until the sample was at room temperature again. The crucible of the sample with the ID EAC-I-1 was lined with a tungsten sheet (with the intention to reduce bubble formation), and the crucibles of the other two ECA-1 samples (EAC-I-2/3) were used without any lining. The JSC-2A sample JSC-I-1 was manufactured the same way as EAC-I-2/3 with the only difference that this sample did seem to be at the transition point of melting and sintering at the moment the heating stopped. Especially the top of the sample depicted in figure 3.6 (fifth from the left) shows that the top surface has rather the appearance of a brick than a glass nugget. The second JSC-2A sample, JSC-I-2 was manufactured by casting the hot regolith melt into another graphite crucible of the same size, by removing it from the microwave kiln first and casting it into the mould placed in another kiln. The other kiln was heated to 560 °C so that the mould was preheated and the thermal shock was minimised. After casting was finished the sample was allowed to cool to room temperature within an hour.

Microwave Heating - Batch 2

After the samples of the first batch were successfully manufactured, the second batch was manufactured based on the experiences gathered in the first batch. All four samples manufactured are shown in figure 3.7 and the most prominent sample of batch two is LHT-II with its apparent green colour. Taking a closer look at the sample revealed that it seemed that not all minerals/components of the sample have melted. However, the sample seemed to rather be a glass than a sintered brick. After the same 30 minutes of heating used for the other three simulants, the LHT-3M sample did not appear to be melted at all, which is why the heating time was increased to 65 minutes instead.

Figure 3.7: Batch 2 samples after cooling, images on the top show the top side of the samples and the images on the bottom show the bottom side. Sample pairs fltr: EAC-II, FJS-II, JSC-II and LHT-II.

Prior to processing, all samples seemed to have no bubbles smaller than 2 to 3 mm, however, up to three larger (> 3 mm) bubbles could be observed. Grinding and compressing (by hand) of the regolith may have lead to the reduced bubble formation. Some of these bubbles could be removed during post processing, but some of them were too big/deep to be removed by grinding entirely. All samples but JSC-II have been manufactured entirely the same way by entering simulant into

a crucible and fusing it. The sample JSC-II was manufactured the same way until heating stopped, then the microwave kiln lid was removed and the liquid glass was pressed on by using a metal spatula. The idea was to remove bubbles trapped in the melt. However, no obvious difference could be observed on the bottom side of the sample compared to the other three samples. The top of the sample, shown in figure 3.7, shows, however, groves cause due to compression.

3.2.4 Resistive Heating

After microwave heating was used for manufacturing the first sample generation, a heating technique was utilised which improved repeatability; resistive heating. The short comings of microwave heating were, its temperature limitations and reproducibility issues. Electric heating was employed as a second heating technique to overcome these issues and was comparably simple and more reliable than microwave heating. Further, it was possible to repeat experiments with the same outcome independent of the regolith simulant used. All samples produced by using resistive heating will be called "second generation" samples. Further, using resistive heating, another four batches were manufactured in total. These four batches of the second generation samples are independent from the two microwave heated sample batches.

Figure 3.8 shows the utilised resistively heated kiln (1), as well as the graphite moulds, on the hot plate being preheated for casting (2), and in their final casting position (3). Also shown are the platinum crucibles used before (4) and after (6) melting regolith simulant. Hot and freshly cast samples are shown in sub-figure (5), showing two JSC-2A glass samples at approximately 700 to 900 °C.

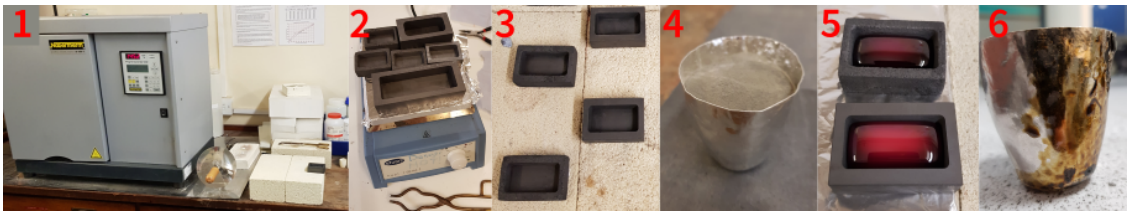

Figure 3.8: Resistive heating setup fltr: Resistive kiln (1) with firebricks next to kiln, preheated graphite moulds (2), moulds in casting position (3), platinum crucible filled with regolith (4), basaltic glass short after casting (in moulds) (5), platinum crucible after melting regolith (6).

For all samples prepared using the resistively heated kiln, the procedure was mostly the same. Regolith simulant was entered into a platinum crucible with about 50 ml capacity and approx. 1 mm wall thickness. The kiln was preheated to 1550 °C, the crucible containing the regolith was placed next to the kiln and by quickly opening the kiln the crucible was placed onto a fire brick inside the kiln. Entering the crucible into the kiln was always done with the utmost care and at the same time, as fast as possible, to avoid a large temperature drop in the kiln. Typically the temperature dropped about 50 °C by entering a sample into the kiln. The system

usually recovered the temperature within one minute. For all batches the crucible was kept in the kiln for 15 minutes, after that time all the regolith was molten in all cases. After the 15 minutes had passed, the crucible was swiftly removed from the kiln and directly cast into moulds right next to the kiln, which had been placed there shortly before casting. All sample, of all four batches manufactured, were cast, with the exception of three samples in batch four, which have been fused.

For the first two batches, moulds had been preheated to about 350 °C and only directly before removing the platinum crucible from the kiln (at 1550 °C) placed next to the kiln for casting. For all batches, the melt/glass was kept in the graphite crucibles for cooling in air at room temperature. For later batches, the crucibles were kept at room temperature prior to casting since the graphite crucibles seemed to provide enough buffer to avoid a thermal shock. This is likely due to graphite excellently conducting heat, thus fast adapting to the hot glass entered into the kiln. Further, no graphite mould cracked or broke during any of the experiments conducted for this work. Not breaking in combination with graphite not wetting by the regolith melt, made graphite the ideal mould material. It was possible to remove the samples from the crucibles after they have cooled since they never stuck to the graphite. After the samples were cold enough to be touched without gloves, they have been lined up for annealing, which will be detailed in the last section of this chapter.

As mentioned in the introduction to this section, a total of four independent batches has been prepared using the described resistive heating process. The first two batches only used JSC-2A simulant to manufacture 30 samples in the first batch and 25 in the second batch. The third batch produced 4 * 6 samples made of six different regolith simulants (BP-1, EAC-1, FJS-1, JSC-1A, JSC-2A and LHT-3M). The last batch 4, used magnetically beneficiated regolith, which was iron sparse, and led to the manufacture of transparent glass.

Resistive Heating - Batch 1

Depicted in figure 3.9 on the left are all thirty samples manufactured in the first batch as well as the top (right top) and bottom (right bottom) view of an individual sample prior to any processing. A full platinum crucible used, held enough material to fill three moulds with glass, hence produced three samples. The process was thus repeated 10 times to get a total number of thirty samples. All samples were cast into the same size crucibles and resulting sample sizes ranged from 36.1 to 42.4 mm in length, 20.9 to 21.9 mm in width and 7.6 to 11.1 mm in thickness. Average length of the samples was 41.6 mm, average width 21.2 mm and average thickness 8.6 mm.

Samples depicted in figure 3.9 were manufactured with the intent to be used for mirror manufacturing and testing. All 30 samples have been ground, polished and fully coated with aluminium on the polished side. Post processing and mirror

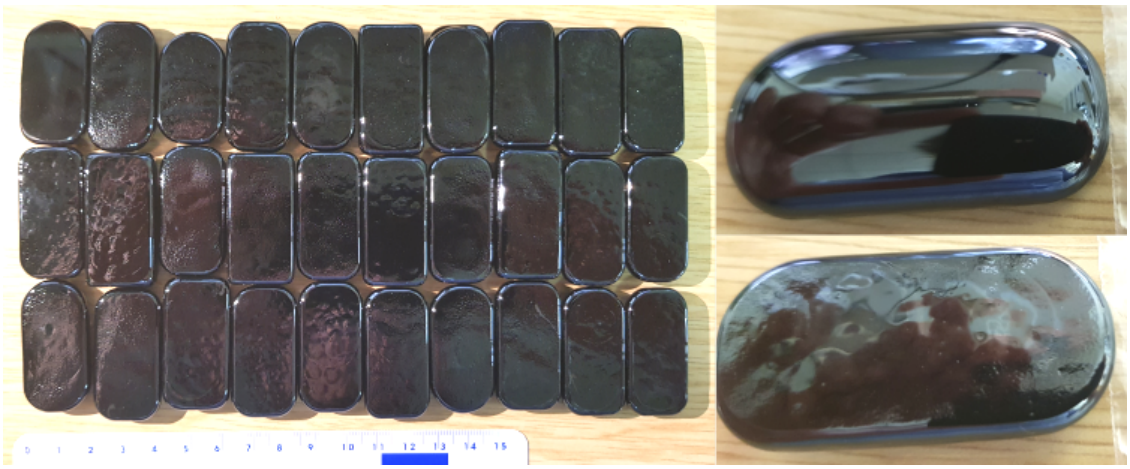

Figure 3.9: Raw (unprocessed) bottom sides of 30 basalt glass samples made from JSC-2A on the left and a close up of an individual sample top and bottom view on the right. Scale depicted on the left is in cm.

manufacturing will be described in the next chapters.

Resistive Heating - Batch 2

The second batch consisted of 25 samples manufactured in three different sizes. Samples were manufactured utilising moulds of three different cavity sizes (l * w * d), small (45 * 24 * 10 mm), medium (65 * 30 * 20 mm) and large (105 * 35 * 20 mm). A total of 18 small size samples and 5 (each) medium and large samples were manufactured with outer dimensions similar to the sizes of the moulds' length and width and all about 8 - 15 mm thick. The simulant used for all samples in batch two was JSC-2A. Figure 3.10 shows raw glass samples of all sizes (small, medium and large) on the left, and on the right in figure 3.10 a close up of a large sample's top (bottom) and bottom (top) view.

The medium and large samples were cast one, by one meaning only one sample was cast from one full crucible. Although it could have been possible to cast two medium samples from one crucible, the risk of running out of molten regolith whilst pouring the second sample was too high. Since this would have led to a smaller sample, also the large samples were cast one by one, which partially showed to "bend" up whilst cooling and form a slightly convex shape on the bottom and slightly concave on the top. Further, the large samples showed to be more flat and less drop like (convex) on top than the small samples. Large and medium samples were manufactured to potentially be used as substrates for solar cells, since the used PECVD process seemed to benefit from a larger sample size.

Resistive Heating - Batch 3

This was the first time other simulants than JSC-2A were used, to cast glass samples by using resistive heating. A total of six different sample types was

Figure 3.10: Raw basaltic glass samples made of JSC-2A, samples of small, medium and large size shown on the left and a close up of a large sample bottom (top) and bottom (top) side on the right. Scale on the right is in cm.

manufactured utilising the simulants BP-1, EAC-1, FJS-1, JSC-1A, JSC-2A and LHT-3M. Resulting samples are depicted in figure 3.11 and a total number of 4 * 6 samples was obtained. Samples shown in figure 3.11 were the first samples produced, which were not all as large as the cavity of the graphite mould. This was due to the use of a reduced amount of simulant for the first run to test whether the simulant will melt and whether the crucible will withstand the material. Further, since spilling molten glass inside the kiln is not favourable, this first run was conducted with only a minimum amount of regolith. Depicted in figure 3.11 are samples made of all six simulants used, each but FJS-1 depicted in top and bottom view. FJS-1 is only depicted from the top.

All other samples manufactured had the shape and size of the small samples produced in batch one and two. Samples depicted in figure 3.11 were used to determine the geochemistry of the glass and to compare the results to the geochemistry of the raw regolith. For this measurements it was required to break the samples up into smaller pieces, which surprisingly proved to be tougher than expected. After about 50 direct hits with a hammer and/or a centre punch the samples would break.

Noticeable about the samples shown in figure 3.11 is that all samples show the same colour to the human eye. Compared to the microwave heated samples, the LHT-3M now shows no green colour, as well as no sign of not melted mineral content.

Resistive Heating - Batch 4 Transparent Glass

The last batch manufactured using resistive heating was batch four, which was targeting the goal of manufacturing optically transparent glass. Prior to melting the regolith simulant in the kiln, the simulant had been magnetically beneficiated as described in the previous chapter. Only the iron sparsest fraction of the simulant was used to attempt to manufacture transparent glass samples. Only for beneficiated LHT-3M enough sample was available to fill a platinum crucible to a

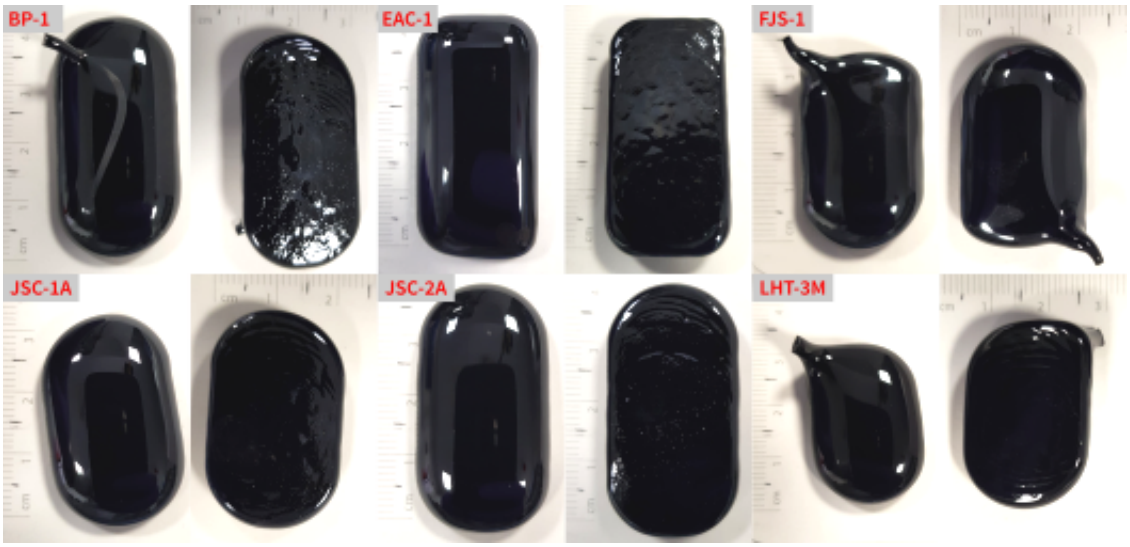

Figure 3.11: Raw (unprocessed) basaltic glass samples made of six different regolith simulants are depicted. From top left to bottom right, BP-1 top/bottom, EAC-1 top/bottom, FJS-1 top/top, JSC-1A top/bottom, JSC-2A top/bottom, LHT-3M top/bottom. Scale depicted are in cm.

typical level. For EAC-1, FJS-1 and JSC-2A only a few grams were available and for JSC-1A and BP-1, after conducting measurements on their geochemistry, none at all. Figure 3.12 shows two iron sparse regolith simulant samples on the left (1 and 4), iron sparse LHT-3M regolith next to crucible (2), after melting, cooling and compressing in the mould (3), and after removing the samples from the crucible (6). Subfigure 5 shows the entire available amount of iron sparse JSC-2A after heating and melting. The colour of the glass in the crucible was transparent with a colour appearing slightly blue to the human eye.

Three processable and transparent glass samples were manufactured from iron sparse LHT-3M, one utilising the same approach as described for the first three batches (resistive heating) and two more with a slight alteration to that process. These two samples were compressed right after the hot melt was entered into the mould. For compression, a graphite plunger the size of the mould's cavity was used. This led to the distinctly different shape of the two samples, depicted in subfigure 6 in figure 3.12. This approach allowed to manufacture two more useful samples despite the lack of material, since the little material remaining was spread flat over the entire bottom surface of the mould. The first sample manufactured had the same shape as all small samples of batch one, two and three had before.

No useful sample, made of one of the other three simulants, was manufactured. The available amount of sample was too little to processes it the same way as the other samples before. While attempting to cast the molten regolith from the platinum crucible into the graphite mould, the melt/crucible cooled too fast and the glass remained in the crucible. Subfigure 5 in figure 3.12 shows the result of that, the iron sparse JSC-2A sample remained in the crucible after an attempt to cast it. This was likely due to a too small thermal mass of the crucible/melt. In an attempt to

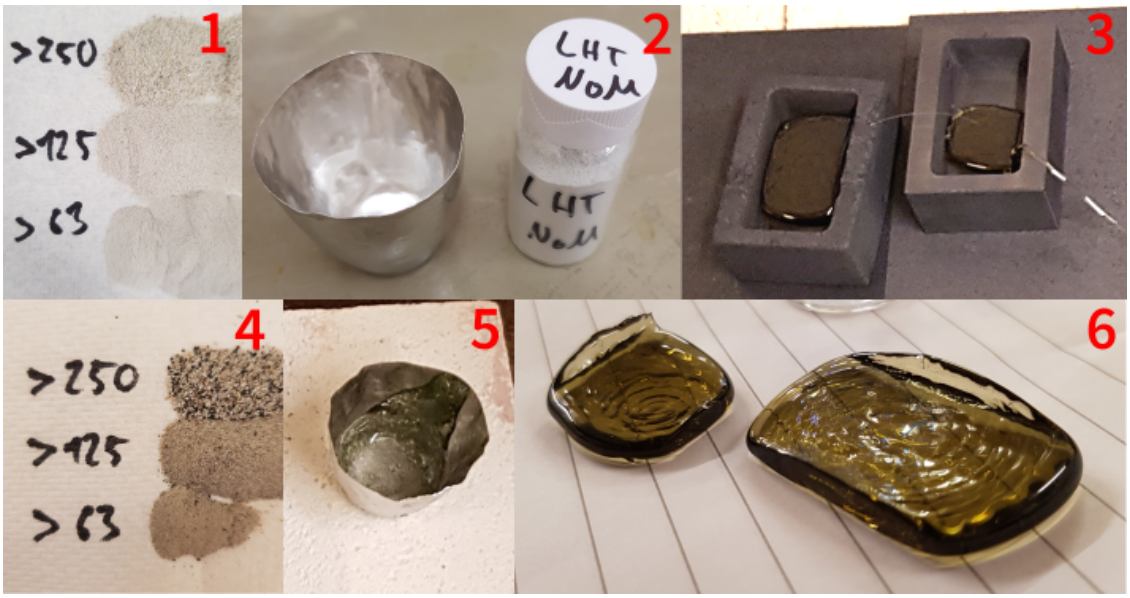

Figure 3.12: Iron sparse regolith (after magnetic beneficiation) on the left (1 - LHT-3M and 4 - JSC-2A), iron sparse LHT-3M regolith next to crucible (2), melted, cooled and compressed still in mould (3) and after removing the samples from the crucible (6). Melted and cooled iron sparse JSC-2A in platinum crucible without contamination depicted in 5.

still manufacture a sample from these simulants, the melted material was recovered from the platinum crucibles and entered into a graphite mould which was used as crucible and placed in the kiln at 1550 °C. The samples were kept in the kiln for only three minutes, but when removed from the kiln, already all samples showed visible signs of carbon contamination and had lost their transparent appearance.

Summary Resistive Heating

The resistive heating approach proved to be efficient and reproducible, as well as capable of melting all utilised simulant types. Combining resistive heating with the use of a platinum crucible completely eliminate the issue of bubble formation experienced by using microwave heating with fusing in graphite moulds/crucibles. Moreover, the platinum crucibles could be reused without any degradation. However, after each run, the remaining solidified glass had to be removed from the crucible by bending the crucible to crack off the glass from the walls. For (especially on the outside) removing the thin layer of basaltic glass, the platinum crucibles have been “rinsed” by reheating them with flux and then after cooling, they were entered in a sulphuric acid bath, which was kept at approx. 40 °C. Crucibles were kept in the bath for a minimum of eight hours, which removed residual basaltic glass, especially from the outside, which was important to avoid a damage to the inside of the kiln. Residual basaltic glass on the outside of the crucible (if not removed) could melt again when entered into the kiln and run down the sides of the crucible, until it hits the fire brick the crucible is resting on. Once hot regolith comes in contact with an alumina fire brick, it starts dissolving the brick rapidly

and may ultimately damage the kiln. Further, regolith/glass on the bottom of the crucible makes the crucible stick to the fire brick, when trying to remove the crucible from the kiln. In best case, this may lead to spillage and in worst case to ripping off the bottom of the softened platinum crucible, which leads to emptying of the entire crucible content inside the kiln (kept at 1550 °C).

The resistive heating process, in combination with a platinum crucible and a graphite mould did not cause complications for all experiments conducted. Further, a similar process may work on the lunar surface, in the lunar environment, as well. To understand how well the process would work on the lunar surface, the manufacturing process will require environmental testing first, before it can be considered for an actual lunar mission.

3.2.5 Annealing

Annealing of typical glasses used on Earth is crucial to release the thermal stress built up inside a glass piece during manufacturing. By removing that stress, potential cracking and shattering can be avoided and thus a potential total loss of the glass piece. Since annealing of basaltic glass is a field that little is known about, it was required to empirically determine the best annealing process and times for basaltic glass samples made of regolith simulant. Until the final annealing procedure was developed, different options have been tried first. Basaltic glass was observed to shatter and crack when cooled too fast or not annealed. Therefore an annealing process was designed to prevent that from happening.

All microwave heated samples have been annealed using one procedure. After samples had solidified and cooled to room temperature, they have been kept in their moulds and entered into a programmable resistively heated annealing kiln. This kiln was preheated to 560 °C and all samples were entered into the kiln. Once the kiln had compensated for the temperature drop, caused by opening the door and entering samples, the kiln was switched off. It was then allowed to naturally cool down to room temperature, which took about 2 hours. Lower starting temperatures and/or shorter cooling times did not allow for all stress to be released from the samples. Some of the test glass samples (used for testing the annealing process) would still crack and break after shorter times. All basaltic glass samples manufactured never exceeded masses of 20 grams for a small sample, and the largest samples were not heavier than 50 grams. This is why annealing times in the order of hours were chosen, and not of days or weeks, how it is typically done for larger glass pieces on Earth.

After finishing the microwave heating experiments, the annealing process was further adapted based on typical annealing processes used in glass blowing on Earth. The heating and cooling curve of the utilised annealing process is schematically depicted in figure 3.13. Major changes to the previously used annealing process for the microwave heated samples are that samples were now held at two different temperatures, 700 °C (for 1 h) and 550 °C (for 2 h). Further, samples have been entered into the annealing kiln at room temperature and heated to 700 °C at a rate

of 170 $^{\circ C}/_{h}$, cooled from 700 to 550 °C with a rate of 150 $^{\circ C}/_{h}$ and cooled back to room temperature with a rate of 60 $^{\circ C}/_{h}$. The kiln used for all annealing procedures was a Paragon Sentry Xpress 4.0.

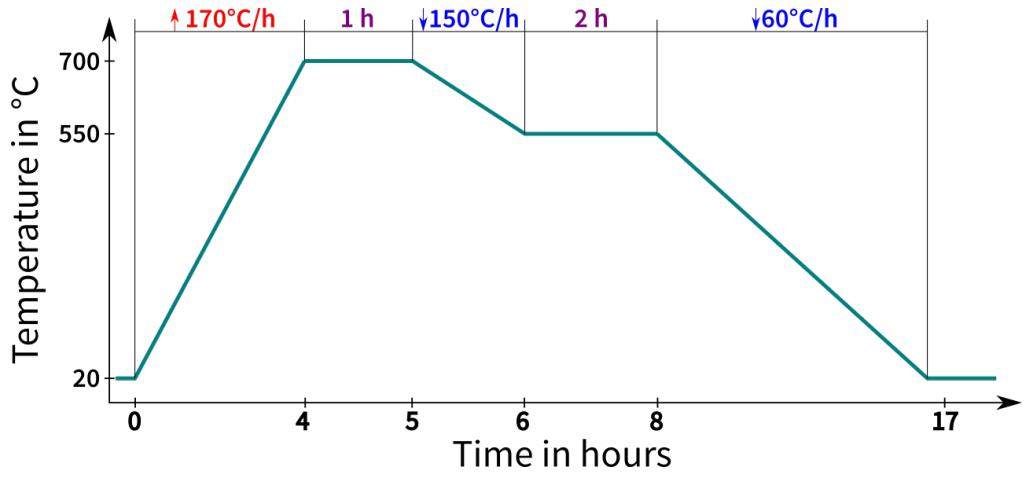

Figure 3.13: Schematic graph showing the annealing process for all second generation samples melted in the resistive heated kiln. Shown is one heating ramp, two holding points and two cooling slopes (Not to scale).

Increasing the start annealing temperature, compared to the microwave heated samples, to 700 °C seemed necessary due to the use of a variety of different simulants, with different compositions and thus melting points. A slow reheating of the samples, from room temperature to 700 °C at the start, proved to minimise cracking of samples by gradually releasing the stress from the samples during reheating. The same was true for controlled cooling of the samples at the end of the process. Care was taken to not choose the annealing temperature too high since the glass would have started to crystallise or even melt at one point.

Annealing on the lunar surface poses a larger challenge than on Earth, since the only heat transport mechanisms available on the lunar surface are radiation and convection. Based on the changed environment and conditions, a simulation of the thermal behaviour of hot basaltic glass on the lunar surface will need to be conducted prior to any mission design, utilising a basalt glass manufacturing system. Further, larger glass samples and therefore up-scaling will be another point to consider.

3.3 Post Processing

After pre-processing regolith and heating it, raw glass nuggets were formed. These raw glass nuggets were not suitable for use as mirror or for solar cell manufacturing. For microwave heated samples no surface was pristine and for resistive heated samples the top surface of the sample was shiny and pristine. However, the surface was convexly or oddly shaped in a way that this surface was not suitable for direct manufacturing. The bottom side of all samples, of all batches, was compared to the top, flat. The surface quality of the bottom side was, however, rather poor and

therefore also not suitable for direct manufacturing.

In order to be able to use the samples for manufacturing, three different processes were applied to the samples, which were all aiming at removing material off the sample to achieve a suitable surface quality for manufacturing mirrors and solar cells. These abrasive processes are split into grinding, lapping and polishing, and were applied in combination.

Polishing, grinding and lapping are processes well known and often used on Earth. Typical grinding materials/agents used are; silicon carbide (SiC) or diamond pastes/discs. Although these materials have also been used to process basaltic glasses manufactured from regolith simulant, ultimately a "lunar alternative" process was investigated. This was conducted in form of using regolith as an alternative grinding powder, to eliminate the need for consumables on the lunar surface. The following elaborates on the used postprocessing methods and materials and shows details on how each batch of basaltic glass samples was processed after heating and annealing.

3.3.1 Grinding

The first abrasive process described is grinding, which was used to roughly bring samples into shape and take of the bulk part of the material which needed removing. Two general grinding approaches can be differentiated, powder grinding and disc grinding.

Powder Grinding

Powder grinding uses an abrasive agent in the form of a lose powder to be mixed with a lubricant, such as water for example to form a slurry. After a slurry is formed, a basaltic glass sample was ground against a smooth hard surface, such as a glass plate, for example, and the slurry was kept in-between the sample and the plate. This process is schematically depicted in sub-figure *a* in figure 3.14. It shows a glass plate (2) and a basaltic glass sample (4), in-between both a slurry of a grinding agent and water (3).

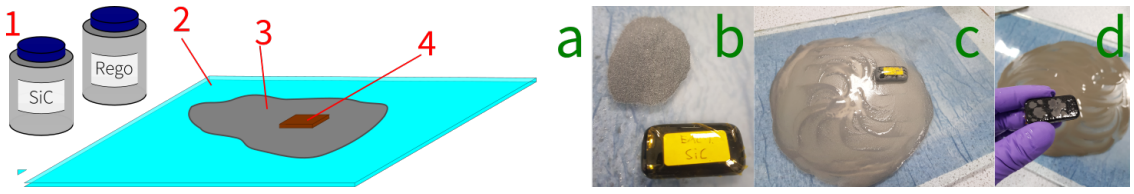

Figure 3.14: Schematic of powder grinding process (a), actual grinding setup at start (b) during grinding (c) and a sample in the middle of the grinding process (d). The schematic (a) shows a general powder grinding setup made of a grinding agent (1), a glass plate (2), a grinding slurry made of water and grinding powder (3) and a sample for grinding (4).

The most commonly used grinding agent is silicon carbide (SiC) powder which was used for most samples ground utilising powder grinding. Sub-figures *b* to *d* in figure 3.14 show a basaltic glass sample at the start of the grinding process (*b*) during the process (*c*) and the bottom side of the sample in the middle of the grinding process (*d*). This process was solely carried out manually, with no help or assistance of machines. To grind a sample in preparation for polishing, a series of different size powders was typically used. The larger the grain size distribution of the grinding power was, the more material was removed at the same time using a smaller grain size powder. Surface roughness of the sample after grinding was higher, the larger the grain size distribution was, further, it took longer to smooth out a surface with the next smaller grain size distribution. Typical sizes of SiC powder used were 220, 400, 600 and 1200, each number (grit size) corresponding to a distinct grain size distribution (sorted large to small).

As mentioned at the beginning of this chapter, by trying to find a lunar sourced grinding material, a study was conducted on whether or not it is possible to utilise regolith for powder grinding the same way than SiC powder. Figure 3.15 shows two basaltic glass samples made of JSC-2A before grinding (1) and after grinding (2). In the sub-figure two (right), the left sample has been ground using SiC powder and the left sample using JSC-2A simulant powder.

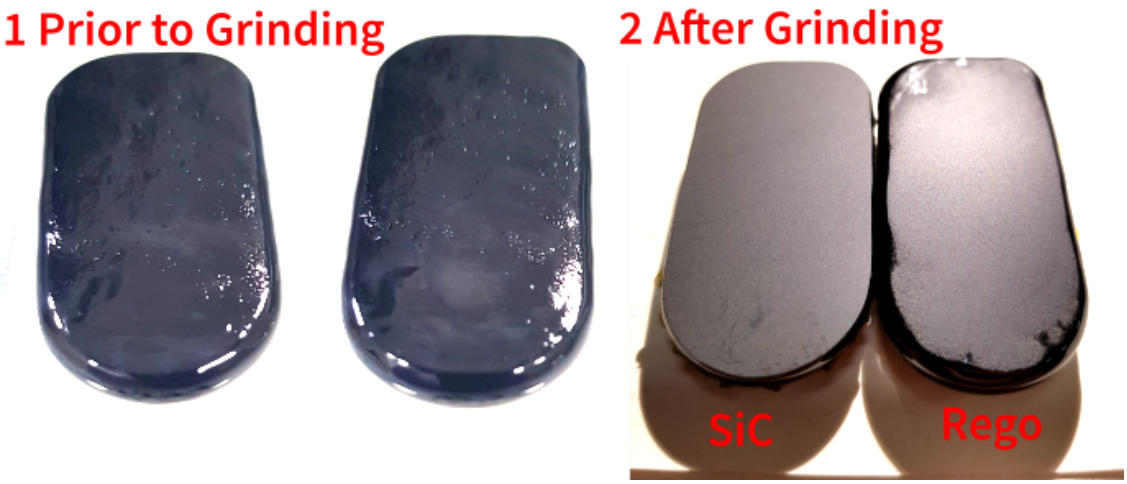

Figure 3.15: Comparison of JSC-2A basaltic glass samples after manufacturing on the left and after powder grinding on the right. The left sample shows the sample ground with SiC powder and the right, the sample ground with JSC-2A regolith simulant.

The final surface quality of the samples, after grinding with three different grain size distributions, for both SiC and regolith simulant, was similar. However, the regolith grinding process took about three to five times longer on average to remove the same amount of glass. This can be seen further by looking at the edges of the regolith ground sample on the very right in figure 3.15. At the edges of the sample, still the original surface after casting is visible. Since regolith does not take of as much material as SiC, the first round, which is typically about flattening the

bottom surface of the samples, was not seen through till the end. Thus, not the entire bottom surface was ground flat, before moving on to the next grain size. Hence, to avoid long grinding times on the Moon, a reasonably flat glass surface should be manufactured to start with.

Disc Grinding

The second technique used to grind samples was disc grinding. Schematically depicted in figure 3.16 is a disc grinding setup, showing a grinding wheel (4) with a grinding disc (3) attached to it. While the wheel/disc is rotating, water is streamed from the tap (1) over the surface to cool the sample and to take away the waste material to free up the grinding disc and the sample. The sample (2 in figure 3.16) can either be hold in place manually moving across the surface whilst the disc is spinning, or be mounted on a fixed holding mechanism. While statically holding a sample in place during grinding is convenient, it typically leads to unequal grinding of the sample and was therefore never used for a sample batch. When manually held in place, the sample needed to have a minimum thickness of approximately 6 mm.

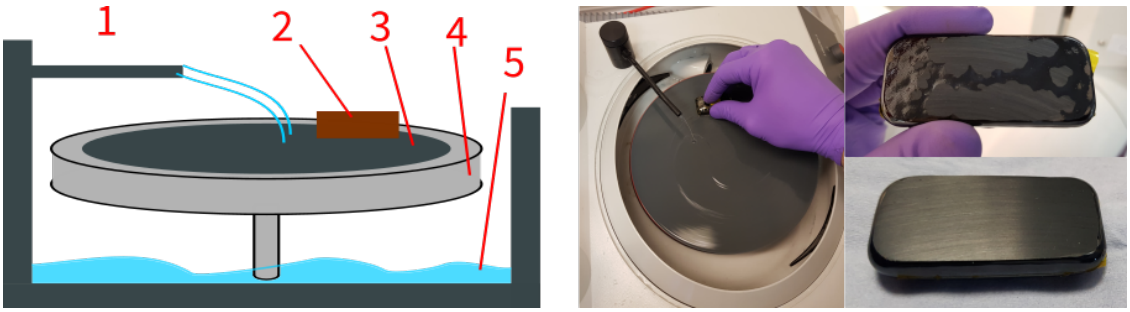

Figure 3.16: Schematic of disc grinding process on the left, actual grinding setup (middle), and a sample in the middle of the grinding process (right top), as well as after grinding (right bottom). The schematic on the left shows a general disc grinding setup made of a water tap (1), a sample (2) held in place by hand or a machine, a grinding disc (3) magnetically snapping on to the grinding wheel (4) and a reservoir (5) with a drain for the waste water.

Two types of grinding discs have been used for grinding basaltic glass samples, SiC discs and diamond discs. Discs coated with SiC powder of various grain sizes were one way to grind the samples to size. Although diamond discs are more expensive than SiC discs, the use of SiC discs was abandoned after the first batches, in favour of only using the diamond coated discs. Diamond discs are much harder than SiC discs, thus do not wear as fast as SiC discs and do not need to be replaced that often. Further they take off material much quicker than SiC in comparison. This was especially relevant for large size samples produced in the second batch of resistive heated samples. To ultimately use them for solar cell manufacturing, these large samples had to be ground down to a thickness of < 4 mm (from approx. 8 to 12 mm) to fit on the lapping machine for final sizing. Even by using diamond discs

grinding took several hours for a sample to prepare.

SiC disc girts utilised for experiments were 80, 220, 400, 800, 1200, 2000, 4000 and for diamond discs, 74, 20 and 10 μm average grain size. In general, the fastest, most reliable and most simple way of getting basaltic glass into rough shape was found by using diamond disc grinding. Thus the clear recommendation for processing basaltic glass (on Earth) are diamond discs. In space, only regolith seems economically viable, depends however on how long a diamond disc may last or how many square meters it can polish before it needs to be replaced.

3.3.2 Lapping

The second technique used to manipulate the shape of the basaltic glass samples was lapping. The machine used for lapping was a Logitech LP50 lapping machine, and to lapp a sample it needed to be mounted onto a glass slide as shown in figure 3.17 (all samples but the left). In order for the basaltic glass to stick to the glass-slide-mount, each sample needed to be ground into rough shape first. Although, it does not matter which grinding technique was used, diamond disc grinding is preferred, since it is the fastest way to bring the samples into a rough shape. In preparation for lapping, the shape of the samples needed to be particularly flat on at least one side, as well as reasonably parallel. If the surfaces are not parallel it may, for example, happen that corners break off during lapping, since unequal force will be applied to the samples surface.

Figure 3.17: Basaltic glass samples before and after lapping. Sample on the left prior to mounting on a glass slide, six samples mounted on such a glass slide in the middle, a sample after lapping (second from right) and mounted prior to machine polishing.

After samples are ground into shape (left sample in figure 3.17) they are stuck to a glass slide with a, at 80 °C thermally activated/liquified glue (glycol phthalate). Sample two to seven (from the left) in figure 3.17, are samples which have been prepared in the described way. All samples are surrounded by the transparent glue, which forms a solid bond between glass slide and basaltic glass at room temperature.

Lapping in general works similar to powder grinding and the process is schematically depicted in figure 3.18. The left side of that figure shows a close up view of the sample and the lapping disc. The sample (1) is held in place by a vacuum jig depicted in the right part of the figure (4). The lapping disc (5) is coated/flushed

with SiC slurry and the jig presses the sample down onto the rotating lapping disc. The slurry will enter in-between the sample and the lapping disc, and SiC particles in the slurry will grind the sample down over time. Removing one millimetre of sample took on average about 20 minutes, depending on the sample type and the number of samples mounted, as well as the rotational speed of the lapping disc.

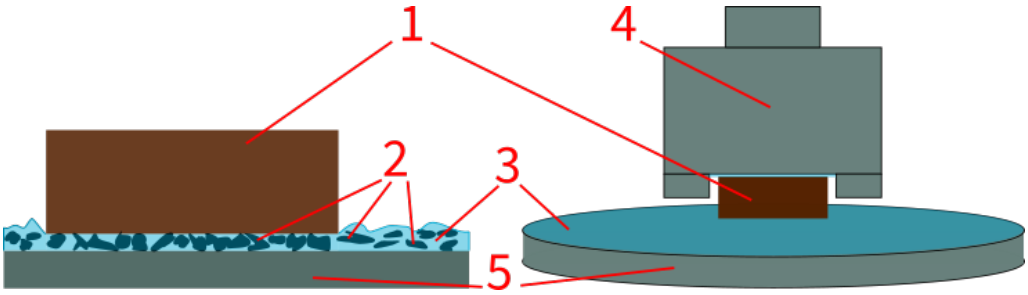

Figure 3.18: Schematic of lapping process in detail on the left, and overall on the right. Shown is a basaltic glass sample held in place (1) by a vacuum jig (4), lapping on a lapping disc (5), using a SiC(2)-water slurry (3) for lapping.

After lapping of a sample was finished, its surfaces were parallel and the sample had a constant thickness. Maximum thickness variations of 0.05 mm over a length of 40 mm could be observed for lapped samples. The glycol phthalate glue allowed for the samples to be removed from the glass slide after processing by reheating the sample-slide combination and pushing the sample off the glass. Once the glue was liquid again, it could be wiped of the sample and residual glue was removed by submerging the samples in acetone.

Lapping is an ideal technique to produce samples with flat and relatively parallel surfaces. Further, manufacturing samples in a size, which allows mounting samples on a lapping machine, also allows for the same samples to be mounted on a polishing machine. The process of polishing the samples surface to finish will be described next.

3.3.3 Polishing

After a sample was brought into shape by grinding and/or lapping, the samples surface was typically not smooth enough for analysis or coating, hence, polishing was required. In general, three different approaches have been used, polishing utilising pumice and rouge, diamond slurries or an aluminium oxide slurry.

Pumice and Rouge

A typical polishing setup used after blowing glass, is a spinning felt wheel, soaked with water and either pumice or a polishing agent called rouge. Pumice is typically used first and comes in powder form off-the-shelf. It was directly applied to the felt wheel and samples or objects were pressed into the vertically rotating wheel. The water pumice mix took off scratches and the second round, using rouge (an iron

oxide based polishing agent) instead of pumice, polished the samples surface to finish.

Using a felt wheel > 3 cm thick allows to polish uneven or oddly shaped samples better than a stiff material wheel. Since the felt wheel is adapting to the shape of the glass, uneven objects, such as the microwave heated samples, could be polished. Disadvantage of using a felt wheel were that edges tended to get rounded since more pressure was applied to them, and more material was taken off.

Diamond Slurry

Diamond slurries can be procured with many different average grain sizes. The ones used for this work are depicted in figure 3.19 and had average grain sizes of 14, 7, 3.5, 1.5 and 0.5 μm. These diamond slurries were used on laboratory filter papers, depicted at the bottom of figure 3.19, the round white circle shaped objects.

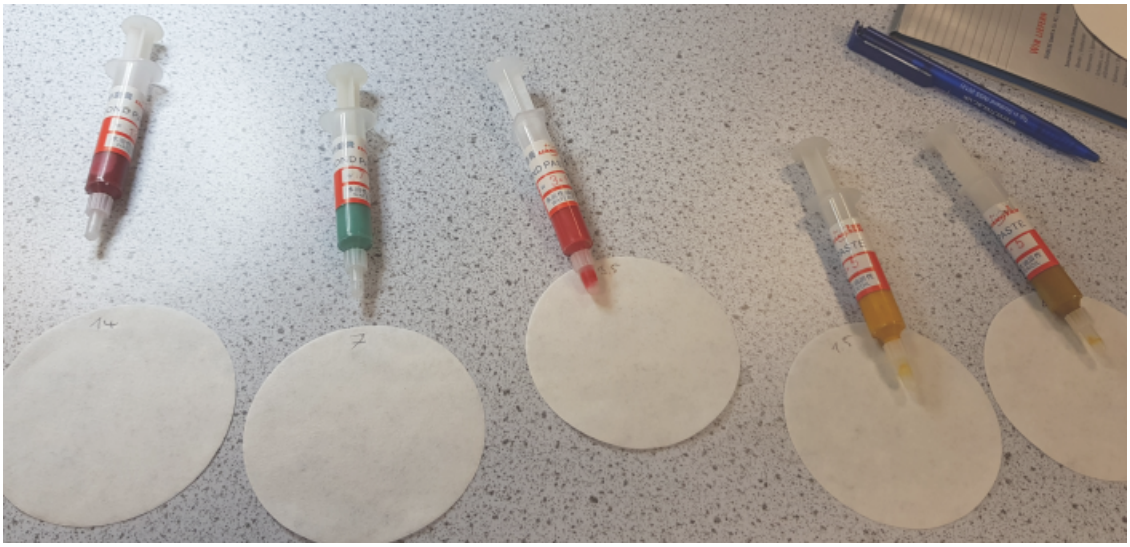

Figure 3.19: Polishing using different average grain sizes diamond slurries on filter paper. Average grain sizes from left to right are 14, 7, 3.5, 1.5 and 0.5 μm.

Samples requiring a very smooth surface finish, for analysis, for example, were processed using these slurries. To polish a sample, slurry was squeezed onto the centre of the filter paper and the sample was rubbed against the paper, with the slurry kept in-between sample and filter. The filter paper locked the diamonds, contained in the paste, in place and allowed therefore to grind the samples.

Aluminium Oxide

A widely used polishing agent is a slurry made up of aluminium oxide powder and water. For use, the slurry is entered onto either a neoprene or a linen disc, mounted on a rotating wheel. The wheel can be the same used for disc grinding described earlier. Both types of polishing discs can be used for holding the sample in place by hand. However, the linen disc made it much harder to hold a sample in place

than the neoprene disc did. Generally, the linen disc is more suited for machine polish and the neoprene for polishing by hand. Moreover, the neoprene disc has a similar effect on the samples as the felt wheel did. Hence, if the edges of a sample shall stay as sharp as possible, the use of a neoprene disc is not recommended.

If the sample size and geometry allowed for it, samples were polished using a robotic arm on a Buehler beta polishing machine with a vector polishing head. Samples were held in place on this machine via a robotic arm, with a planetary gear, capable of spinning and rotating the sample at the same time. Underneath the sample, mounted on the robotic arm, a linen disc was mounted and continuously covered with 0.3 μm average grain size aluminium oxide slurry. By rotating both, the sample and the disc at the same time, a homogenous surface quality was achieved. This process worked fastest and best on "small" size samples. Medium and large size samples did however, not fit on the machine directly but only with additional shortening of the samples. Hence large samples were ground on the linen fabric disc by hand at first, which was more complicated since the large samples need more time to be polished, especially in the centre part of their to-be-polished surface. Additionally, the large samples would easily stick to the disc (more often than the small ones), get carried away by the disc and thus made it hard to polish large samples.

3.3.4 Sample Batches Post-Processing

This last section of the post-processing chapter details the processes used to grind and/or lapp and/or polish each sample batch. Postprocessing of two microwave heated batches is described, as well as four resistively heated batches.

Microwave Heated Samples Batch 1

The five samples manufactured in the first batch using microwave heating, as described in the last chapter, were all processed the same way. First they have been ground flat by using a powder grinding process with successively using 220, 400 and 600 grit SiC powder. Then all samples were polished using pumice and rouge in combination with the felt wheel. All batch one samples, made of EAC-1 simulant, are depicted in figure 3.20, after grinding (left), and after polishing (right).

After polishing voids and bubbles from the melting process were clearly visible. The polishing process seemed to have worked fine on the samples and all surfaces were shiny after polishing, compared to being dull after grinding. Further, the samples' surfaces appeared to the human eye to be flat, with the exception of the voids on the samples' surfaces.

Microwave Heated Samples Batch 2

For the second batch of microwave samples a disc grinding process has been used. SiC grinding discs were used, of grit sizes of 80, 220, 400, 800, 1200, 2000 and 4000, in that order. These grit sizes correlate to average grain sizes from 201

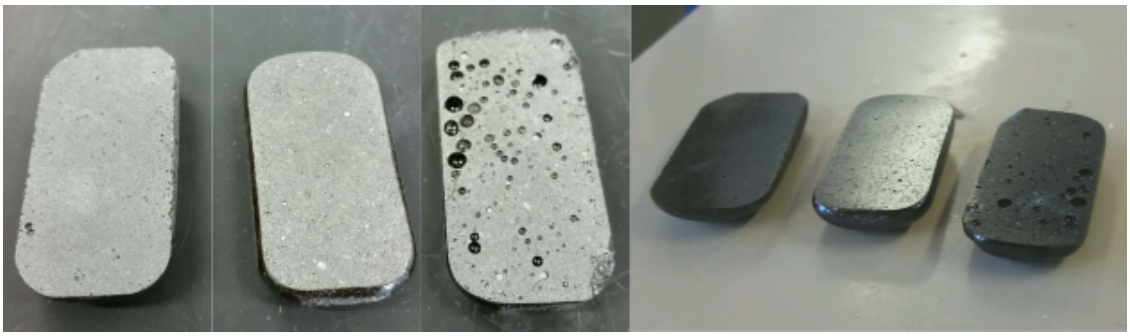

Figure 3.20: Ground samples, from left to right (fltr); EAC-I-2, EAC-I-3 and EAC-I-1 on the left and the same samples in the same order after polishing on the right.

to 5 μm. Since the last two stages of grinding paper were similarly fine than polish agents/slurries, and the surface quality seemed good enough, no additional polishing was applied. All four batch two samples are depicted in figure 3.21, shown in their polished state.

Figure 3.21: All four batch 2 samples after polishing, manufactured using microwave heating. Samples fltr are EAC-II, FJS-II, JSC-II and LHT-II, the scale is in centimeters, hence sample sizes are about equal.

All samples have been held in place during disc grinding/polishing by hand. After the first stages of SiC paper were used on the samples, voids were visible on the surface of these samples as well. However, in addition to the up to three large ($>$ 3 mm) bubbles, observed straight after cooling, only a few smaller bubbles could be seen additionally. The largest ($\approx$ 15 mm) bubble was visible on the sample made of FJS-1 (FJS-II) and exceeds all bubbles/voids observed on the first batch samples. The sample LHT-II did not show any large voids after grinding and polishing any more, but showed homogeneously distributed bubbles of less than 1 mm across its entire surface.

Resistive Heated Mirror Samples (Batch 1)

The first batch manufactured by using resistive heating was processed the same way as the second batch of the microwave heated samples. The only difference between processing these two batches was, that a final stage of polishing was applied to the resistive heated samples. For this additional final stage a neoprene disc was used, mounted on a grinding wheel, covered with aluminium oxide slurry (average grain size 0.3 μm). The end result after polishing is depicted in figure 3.22 showing seven samples prior to surface coating with aluminium.

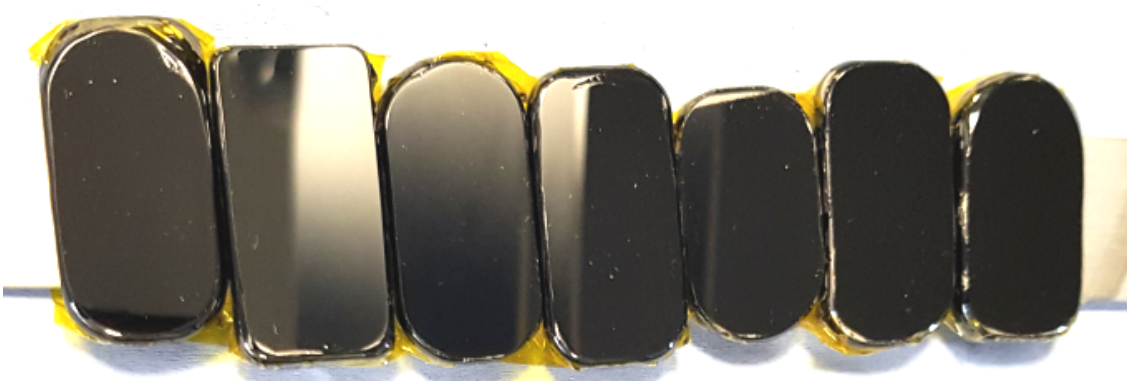

Figure 3.22: Polished basaltic glass samples made from JSC-2A, manufactured using resistive heating.

Samples did not show any visible surface features (to the human eye), hence, this first sample batch was considered a significant improvement compared to the microwave heated samples. Further, all samples are homogenous and appear consistently dark.

Resistive Heated Samples (Batch 2) for Solar Cell Manufacturing

Samples of the second batch were prepared in order to be used for different manufacturing experiments, than the first batch, and the microwave heated samples. These samples were manufactured with the intention to be used for solar cell manufacturing. Thus a total of three independently prepared sets of samples, for further experiments, was selected from all batch two samples. An additional set of sample was prepared form the batch two samples with the intention to be used for trying an alternative (ISRU) surface coating method - arcjet coating of basaltic glass using regolith as coating material.

Samples depicted in figure 3.23 were the first samples prepared for solar cell manufacturing. Two large samples have been ground to a thickness of less than 4 mm using a 74 μm average grain size diamond disc. Then, both have been further processed using diamond discs of 20 and 10 μm average grain size (in that order). The sample depicted second from the right in figure 3.23 was not further processed after grinding with a 10 μm average grain size diamond disc. The intention of stopping to grind/polish this sample after this step was, to have a rough surface for

the backside of the solar cell, which was supposed to reflect additional light back into the cell. The sample shown at the very right was further processed using a linen cloth disc with aluminium slurry (0.3 μm) and the sample was held in place manually. One sample was prepared with the best surface roughness value (R_a) as possible and the other sample was kept at the second best surface roughness. Achieved surface roughness was measured after polishing and will be detailed in chapter 5.2.

Figure 3.23: Fltr: Raw large basaltic glass sample top view, bottom view, coarsely polished and fine polished.

After first tests revealed that the odd outer shape of the samples, shown in figure 3.23, did not work for manufacturing solar cells, a second batch of two large samples and six small samples was prepared. The large ones were prepared similar to the first ones, but this time the sides of the samples have been ground off to achieve samples with a length of no more than 80 mm. This time the surfaces of both samples were polished fully (with aluminium slurry, 0.3 μm). The small samples have been processed by grinding them first, then mounting them on glass slides for lapping. After thinning the samples down to less than 6 mm, via grinding (diamond discs, 74 μm), lapping took them down further to 2 mm. After lapping, samples have been polished using aluminium slurry (0.3 μm) on linen fabric, mounted on the robotic arm. During the second attempt of manufacturing solar cells on the back of a basaltic glass, small samples have shown to be too small for thin-film cell deposition.

After second set of samples did not suffice for manufacturing solar cells again, a last third set was prepared using four medium and one large size samples from the pool of batch two samples. This time, the other glass geometry was manufactured to the specifications of the solar cell process and the glass samples' thickness was adjusted to be 500 μm and 1500 μm thick (two each for medium size and 1500 μm for large size).

The outer dimensions of the medium samples were approximately 50 * 30 mm and the large 80 * 40 mm. Further, these samples have been lapped prior to polishing,

which required all six sides (of the resulting brick) to be flat. Further, top and bottom surfaces were prepared to be as close as possible to parallel. After lapping all samples, they were already mounted the correct way to fit on the polishing machine as well. Thus samples have been machine polished on the linen cloth with aluminium oxide slurry. Although the surface quality was not significantly different from holding the samples in place by hand, the automated process guarantees homogeneity.

The last (independent from solar cell manufacturing) set of samples manufactured from samples of the batch two pool, were samples used for arcjet coating. Six of the small JSC-2A samples were ground, using a diamond discs, and lapped, temporarily mounted onto glass slides. By grinding the samples first, they have been thinned down to approximately 6 mm thickness and then mounted on the lapping machine to achieve a final thickness of 1.5 mm. After lapping, samples have been polished using aluminium slurry on linen fabric mounted on the robotic arm. One of the final samples is shown in figure 3.24.

Figure 3.24: Lapped and polished basaltic glass samples made of JSC-2A. Prepared for arjet coating of samples with regolith simulant. All three images show the same sample, left and middle normal exposure time and right extended time to make pattern on the substrate visible. Scale in cm

Depicted in figure 3.24 are three top views of the same sample at different angels and with different exposure times. The first two images (seen from the left) show an approximately 18 * 36 mm sized sample, which is 1.5 mm thick and has been ground, lapped and polished into its depicted form. No surface features such as bubbles or voids are visible, however, in the image to the right the exposure time was increased to visualise the pattern, which had formed on all samples processed. It is not clear what caused the pattern to occur, but it is strongly suspected that the pattern was formed during or before annealing, due to partial crystallisation similar as it was observed on the microwave heated samples before.

Resistive Heated Samples Made of Six Simulants (Batch 3)

From batch three, samples of each regolith simulant glass type were processed the same way as the samples prepared for arcjet coating have been processed. The results of the first try are depicted in figure 3.25.

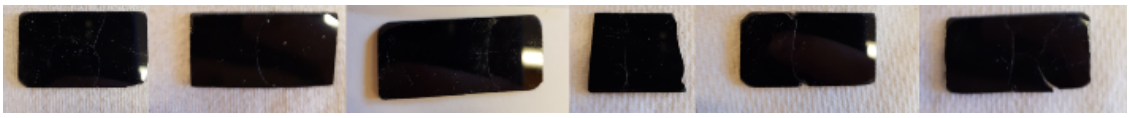

Figure 3.25: Basaltic glass plates made of (fltr): BP-1, EAC-1, FJS-1, JSC-1A, JSC-2A and LHT-3M. Samples lapped to a thickness of 2 mm and polished using aluminium oxide slurry.

All samples could successfully be processed into glass plates, independent of the regolith type. No differences between samples could be observed during processing. Thus grinding, lapping and polishing is considered to work for any type of basaltic glass the same way.

Resistive Heated Transparent Glass (Batch 4)

The last batch postprocessed was the transparent glass batch, which has been processed similar to the other small samples (batch 2 and 3) before. The difference for these samples was, that in this case it was required to machine polish both sides of the samples, rather than only one, to be able to conduct transmission measurements on the samples. Thus after the grinding (74 μm diamond disc), lapping ($\approx$ 1.5 mm thickness) and machine polishing (0.3 μm aluminium slurry) was finished, the samples have been removed of their sample holders (glass slides). After removing them, they have been cleaned of any residual glue and remounted on their polished side again, to this time expose the second (still rough) surface and lapp and polish it to finish as well. Figure 3.26 shows transparent glass samples mounted on glass slides prior to grinding (top). The bottom part of figure 3.26 shows all samples after grinding, lapping and polishing. All samples could be processed into a glass slide shape and three of six appeared transparent to the human eye after processing was finished.

3.4 Device Manufacturing

This last section of the manufacturing chapter shows techniques, used to; prepare measurement samples, manufacture mirrors and build solar concentrators and solar cells.

3.4.1 Surface Coating and Mirror Manufacturing

This section will detail techniques used to surface coat samples, as well as elaborate details of each sample batch and chosen standard processes for coating. As discussed in chapter 2.4, coating thickness for mirrors were chosen to be >100 nm. These have independently been confirmed with surface profilometry. Fore solar cell manufacturing, layer deposition followed a highly standardised process which has control over layer thickness deposition. The evaluation of the quality of the mirrors and solar cells will follow in chapter 5.3 and 5.4.1.

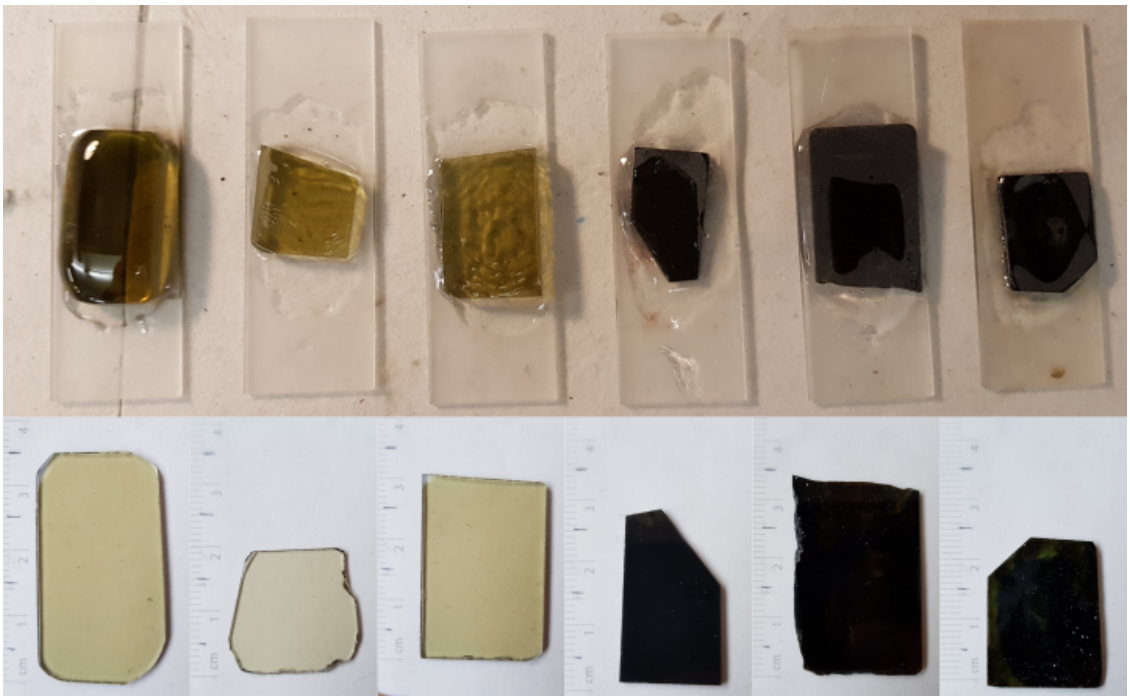

Figure 3.26: Fltr: LHT-3M samples 1, 2, 3, JSC-2A, FJS-1 and BP-1. The three samples on the right appear non-transparent due to partial carbon contamination. Top prior to lapping and polishing, and bottom, finished samples (scale in cm).

Physical Vapour Deposition

To coat a sample with a certain material/metal, Physical Vapour Deposition (PVD), a thin-film deposition method, was used. PVD either sputters or evaporates a source material onto a surface. For all samples prepared, only evaporation was used and no sputtering, hence, the following will describe evaporation only.

Figure 3.27 shows the actual system used for evaporation on the left and the schematic layout of a thermal evaporation system on the right. To coat a sample, a source material (1) (e.g. aluminium) is placed in an electrically heated filament (2) in a vacuum environment contained by a bell jar (3). The filament will melt the source material and ultimately evaporate it in the vacuum environment. Surfaces of the samples (4) held in place by sample holders (5), will start to accumulate evaporated material on their surfaces parallel to the source of evaporation.

For mirror manufacturing, thermal evaporation was chosen due to its simplicity despite other techniques possible being advantageous in terms of aluminium (back contact) deposition [492]. The layer deposition speed was kept as slow as possible to avoid an increase of surface roughness due to deposition [493]. Further, studies on aluminium thin-film deposition via sputtering on steel substrates suggests that surface roughness may increases at surface layers > 30 nm again since crystallisation takes place [494]. Increased surface roughness typically leads to increased diffuse reflection and decreased specular reflectance. Since a high specular reflectance is

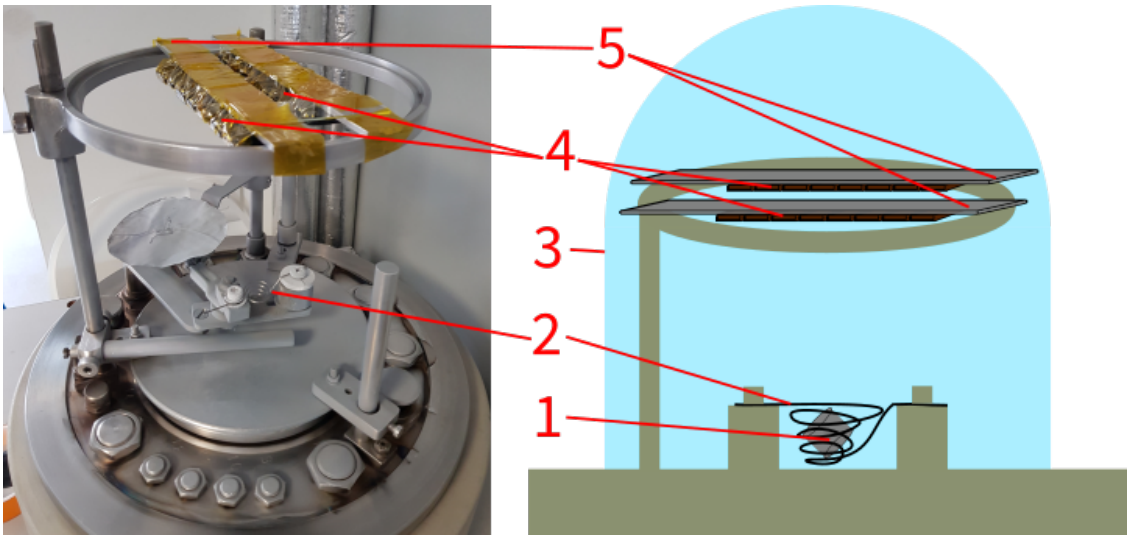

Figure 3.27: An actual thermal evaporation setup on the the left and a schematic of it on the right. Shown is the surface coating material bead (1), the filament (2), the vacuum bell jar (3), the samples to be coated (4) and the sample holder (5).

important for a mirror, it was intended to keep surface roughness of a final mirror as low as possible as well.

This process is considered to be rather simple compared to other processes, since only electricity is used to coat the surface of a sample and no other gases or materials than the source material are required. This system is capable of evaporating most source materials typically used, such as gold, silver, aluminium and others. Considering the use of this process on the lunar surface also seems possible, if not advantageous. Since the lunar surface already has a pressure of less than $3 * 10^{-15}$ bar (during night time), no vacuum chamber with its accompanying vacuum pumps would be required. The system when operating on Earth, operates around pressures of $1 * 10^{-6}$ bar which is almost ten orders of magnitudes higher than on the lunar surface.

A vacuum environment is crucial for the process to avoid contamination by dust or other particles, as well as to avoid the source material to react with gasses such as oxygen. In the case of aluminium, for example, evaporation in air would likely lead to an aluminium oxide coating forming on the samples' surface, which would be dull and less reflective than elemental aluminium.

Arcjet Coating

Materials with lower melting points than ceramics or regolith, can typically not be surface coated with ceramics since they need to be sintered onto a surface at above 1000 °C. For these materials an alternative was developed called Aerosol Deposition (AD), which is a method of spray coating surfaces with ceramic materials [495]. Fig-

ure 3.28 shows glass samples made of JSC-2A simulant coated with LHT-3M via AD.

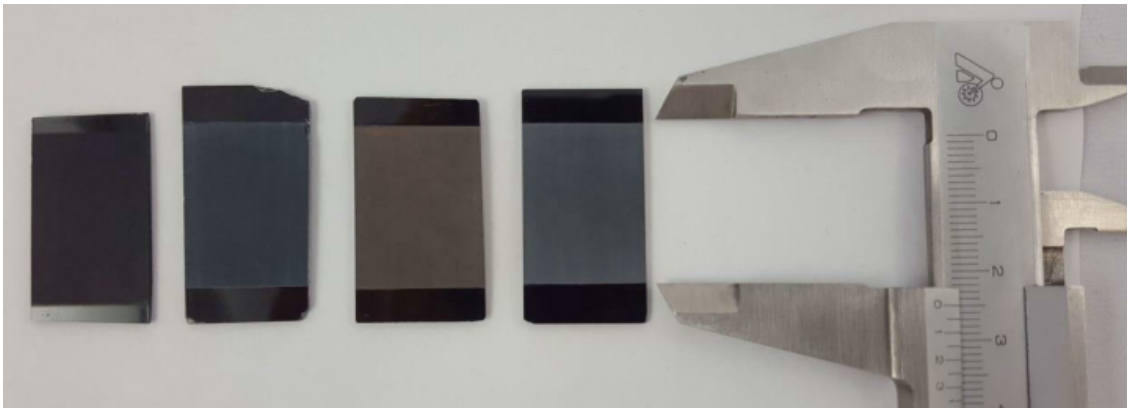

Figure 3.28: Aerosol Deposition (AD) on basaltic glass samples manufactured from JSC-2A regolith simulant and coated with ground LHT-3M simulant, caliper in cm.

While searching for a lunar alternative reflective material (100 % ISRU mirror), low iron bearing regoliths showed good reflective properties. Thus, ways of surface coating basaltic glass samples with this high reflective regolith were required. AD offered an opportunity to manufacture samples and test them. Details on the deposition process can be found in [495].

Microwave Heated Batches for Surface Coating

Using the described thermal evaporation method, microwave heated batches one and two were coated with aluminium/silver. The five batch one samples were coated with silver on one side and with aluminium on the other side, with a strip of blank (polished) glass in-between (depicted in figure 3.29, top). The bottom surfaces of the four batch two samples have been entirely coated with aluminium, before and after images are shown in figure 3.29, middle and bottom.

The source material layer thickness of batches, one and two, of all samples was > 750 nm for both, silver and aluminium. The thickness of the reflective layer was about six times more than what would have been required to achieve best reflectivity on an ideal substrate. This layer thickness was chosen, to potentially compensate for some of the surface features, as well as to avoid doubt about the reflectivity measurements conducted. For all samples the surface coating seemed to be even to the human eye, and all parts of the surface were covered, including the smaller and larger voids.

Resistive Heated Batches for Surface Coating

The same process used for batch one samples was used for batch two samples. The polished glass samples have been placed in a thermal evaporator, with their polished side facing the source. Samples were held into place by Kapton® tape

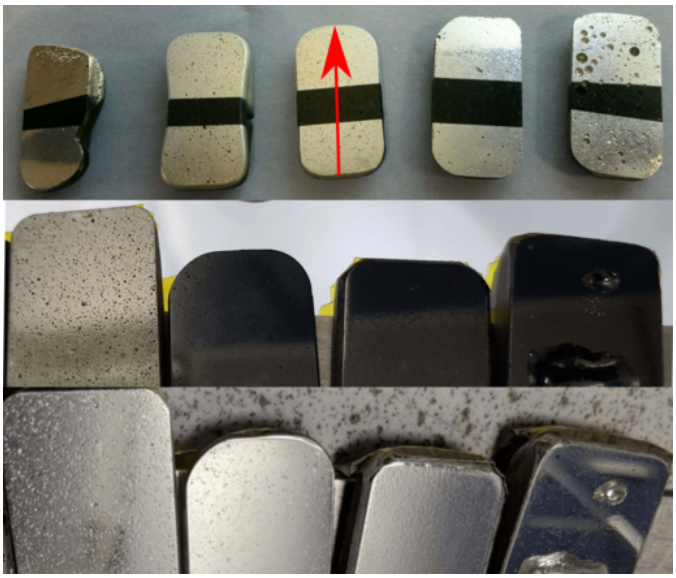

Figure 3.29: Microwave heated samples batch 1 shown on top, after deposition of aluminium (bottom side) on one side and silver (top side) on the other (centre remained uncoated). Batch 1 samples fltr: JSC-I-2, JSC-I-1, EAC-I-3, EAC-I-2, EAC-I-1. Batch 2 samples prior to (middle) and after (bottom) deposition of aluminium. Batch 2 samples fltr: LHT-II, EAC-II, FJS-II, JSC-II. The red arrow shown on sample EAC-I-3 indicates the measurement direction of batch 1 and 2 surface roughness measurements.

fixed to the samples and the sample mounts. The tape was fixed to the sample in a way that the entire polished surface could be coated with aluminium. The samples (at four manufacturing stages) are depicted in figure 3.30, from casting (top left) to the raw sample's bottom surface (top right) to the polished surface (bottom left) until the aluminium coated surfaces (bottom right).

A total of 30 samples was postprocessed (ground and polished), and surface coated in two evaporation batches (2 * 15 samples). This number was required to measure the reflectivity of a meaningful number of samples, as well as to select the best samples for a solar concentrator system, which required a minimum of 16 samples. A first proof of concept test was conducted assembling all thirty mirrors into an array of 3 * 10 mirrors with an overall surface area of approximately 214 * 128 mm (274 cm^2). These mirrors were mounted on a regular solar concentrator system instead of the normal mirror surface and exposed to sunlight in Dubai, United Arabic Emirates, where more constant and better solar exposure conditions made experiments more feasible. Although no actual quantitative measurements could be taken, the mirrors appeared to reflect sunlight in a similar fashion than the regular mirrors. After this proof of concept all mirrors have been measured in detail and results will be discussed in chapter 5. After these measurements were conducted, means of mounting these oddly shaped mirrors into a concentrator setup were required.

Figure 3.30: "Lunar" mirror manufacturing on basaltic glass made from JSC-2A simulant. Top left, after casting, top right raw surface after cooling, bottom left after grinding and polishing, bottom right after aluminium coating.

3.4.2 Basalt Mirror Mount for Solar Concentrator

To test the manufactured basaltic glass mirrors under laboratory conditions, a mount needed to be designed to hold the mirrors in place during the measurements. The chosen solution for testing the mirrors, was, as the literature review suggested, to arrange them into a solar funnel, as schematically depicted in figure 3.31.

Since every individual basaltic mirror was manufactured to rough dimensions of 42 mm in length and 21 mm, multiple mirrors needed to be combined to form a large enough surface for a solar reflector. Although all mirrors have similar width and length, their thickness varies from 7.6 to 11.1 mm. Since for an ideal reflector, all reflective surfaces need to be aligned in one plane, an ideal solution would require all mirrors to be front surface aligned.

Considering a thickness variation of 3.5 mm a design was required which could hold each mirror in the correct position by compensating for the thickness variation. One possible solution to arrange a number of mirrors with varying dimensions in a solar funnel geometry is depicted in figure 3.32. The image shows one of the four 3D printed mounts, depicted from three different angles. The mount is shown twice without mirrors and once with four basaltic glass mirrors mounted. These mounts were used to clamp 16 basaltic glass mirrors in a set of four of these mounts, which formed a funnel by placing one mount on each edge of a square shape solar cell.

The design parameters for the mounts were based on the case of using a set of two solar cells manufactured on basaltic glass substrates, each having a dimension of 40 * 20 mm. Putting the two cells next to each other, a square of 40 * 40 mm would be formed. Thus the length of the cell (l_{cell}) or cell area, was set to 40 mm. The length of the reflector/mount was determined by joining four mirrors at their long sides (approx. 4 * 21 mm), and adding space in-between and at the ends for

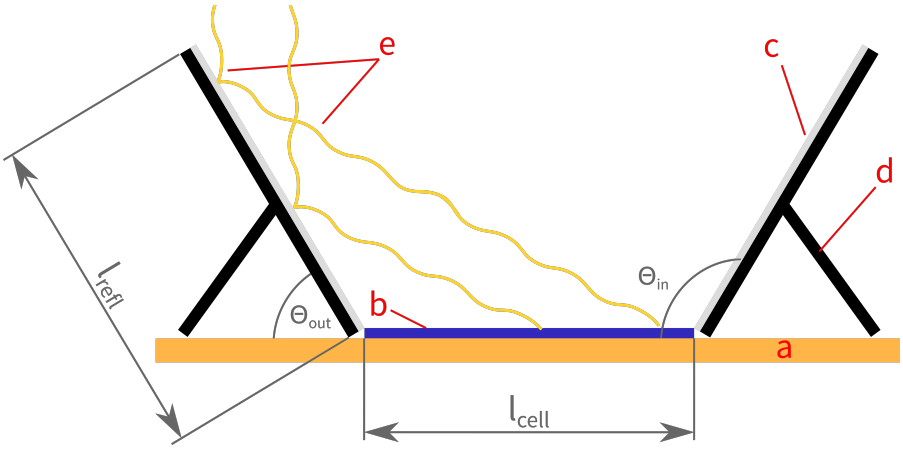

Figure 3.31: Schematic of a solar funnel comprised of a test bench (a), a solar cell (b), a reflective surface (c), a mount (d) and parallel light hitting the reflective surface under and angle of 90° (e). The light is emitted from a solar simulator with a solar spectrum of AM 1.5. Moreover, the solar cell length l_{cell}, the mount length l_{refl} and the inner (Θ_{in}) and outer (Θ_{out}) angles between the mount and the test bench are indicated in grey.

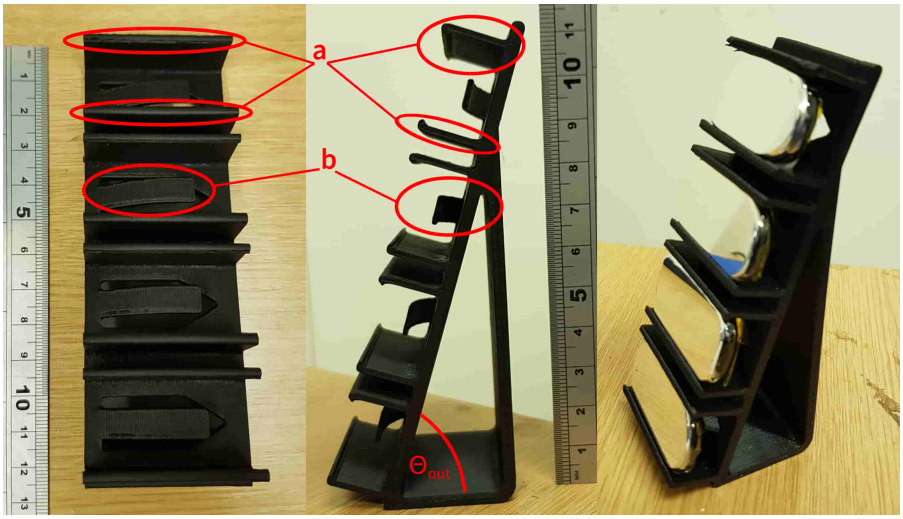

Figure 3.32: Front view (left) and side view (middle) of a 3D printed basaltic glass mirror mount. Each mount can hold 4 mirrors (right) in place, each pushed into the reflective plane by the back spring (b), and clamped in position by the side springs (a). The scale bars are in cm with mm separation dashes and Θ_{out} shows the angle in-between test bench and reflective surface.

mounts/springs as shown in figure 3.32. The design led to a total reflector mount length of 109.1 mm. Using these two values as an input, the angle in-between mount and test bench could be computed. From figure 3.31 the reflector length is defined as l_{refl} and the solar cell width as l_{cell}. The inner angle between the solar cell and the reflector is defined as Θ_{in} and the outer angle between the reflector and ground as Θ_{out}. This leads to:

$$\Theta_{in} = 90° + sin^{-1}\left(\frac{-l_{refl}}{4 * l_{cell}} + \frac{1}{4}\sqrt{\frac{l_{refl}^2}{l_{cell}^2} + 8}\right) \tag{3.1}$$

$$\Theta_{out} = 180° - \Theta_{in} \tag{3.2}$$

$$\Theta_{in} = 90° + sin^{-1}\left(\frac{-109mm}{4 * 40mm} + \frac{1}{4}\sqrt{\frac{(109mm)^2}{(40mm)^2} + 8}\right) \tag{3.3}$$

$$\Theta_{in} = 107 \tag{3.4}$$

$$\Theta_{out} = 180° - Theta_{in} \tag{3.5}$$

$$\Theta_{out} = 73° \tag{3.6}$$

Therefore the mount was designed with $\Theta_{out} = 73°$ as shown in figure 3.32. With this angle, all additional incident light from outside the solar cell surface area will be reflected only once, directly hitting the solar cell without bouncing of multiple times. Hence, losses due to secondary reflection are avoided. Furthermore, the reflected light hits the cell from one end to the other evenly, and therefore suggests a homogenous illumination of the cell from all four sides.

3.4.3 Thin-Film Deposition of Solar Cells

In section 2.5.2, different types of semiconductors were already outlined, which can be used to build solar cells. Although materials other than silicon may have better efficiencies or performances, silicon was chosen for this project. For the goal of manufacturing such a silicon solar cell on a basaltic glass substrate, plasma enhanced chemical vapour deposition (PECVD), a type of Chemical Vapour Deposition (CVD) method, was chosen. Solar cell manufacturing and characterisation was conducted at the "IEK5-Photovoltaik Forschungszentrum Jülich" in Germany, and further information on manufacturing techniques and principles of solar cells in general, can be found in the literature [448, 450, 462, 496, 497], and will be assumed foreknowledge.

Equipment and Processes Used for Test Cells Manufacturing

Built micro-crystalline silicon thin-film solar cells are schematically depicted in figure 3.33, which shows the layering of these cells, manufactured on basaltic glass. Each cell has been built by depositing three general layer types, Transparent Conducting Oxides (TCO), contact layers and multi-layered absorber layers. The brown coloured layer on the bottom in figure 3.33 shows the basaltic glass substrate which served as back-plate for deposition. The first layer deposited on the glass was a layer of TCO (1. TCO), then followed by a metal contact layer (2. Ag), another layer of TCO (3. TCO), the absorbing layer (4. Si) and finished by a TCO (5. TCO) layer topped by a front contact grid (6. Ag). The absorber layer is subdivided in three differently doped layers n, i and p.

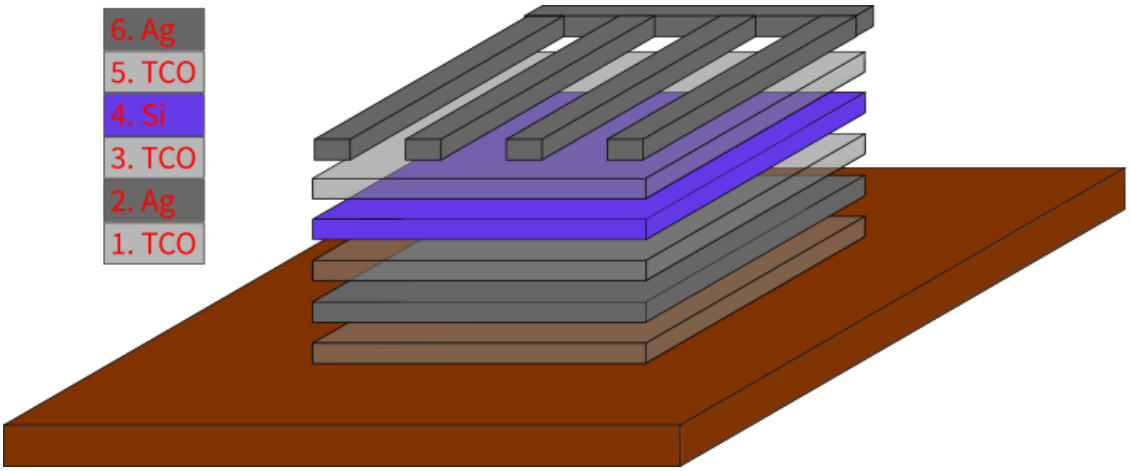

Figure 3.33: Schematic view of a silicon solar cell manufactured on basaltic glass made from regolith simulant. The brown layer at the bottom indicated the basaltic glass, built on the glass (layer-by-layer) 1. TCO, 2. Ag, 3.TCO, 4. Si, 5. TCO and 6. Ag.

For such a μc-Si:H solar cell, in n-i-p [498] configuration, non-transparent substrates can be used, rather than transparent substrates, which are typically used. For this cell, the top p-doped layer is covered with a TCO window layer to increase performance [499]. For all TCO layers, Aluminium doped Zinc Oxide (AZO) [500] was used and for all contact layers, silver was used. The AZO and silver layers were produced by Radio Frequency (RF) magnetron sputtering, at 150 °C, at a power of 250 W. To increase the reflectivity of the back contact, the first TCO layer (1. TCO) was etched [501] in Hydrochloric (HCl) acid solution for 40 seconds.

For the absorber layer deposition, an Ultra High Vacuum (UHV) six-chamber deposition system was used, to deposit micro-crystalline silicon solar cells in n-i-p configuration. By using a PECVD process, intrinsic (pure) semiconductor silicon thin-films were deposited, using silane (SiH_4) and hydrogen (H_2) at the same time. For p-type doping, TMB was added, and for n-type doping phosphine (PH_3) was added to the process gas.

Although the effects of doping are interesting, and may lead to significantly increased performance of a cell, for this study, dopants and dopant levels were not varied, since the primary goal was to achieve a working solar cell. For future lunar application it could, however, be considered to replace standard dopants, like boron (p-type) using lunar resources and extract rare p-type dopants such as aluminium, for example.

Structure of Test Cells Manufactured

Manufacturing solar cells was attempted in three runs with three different substrate types. First, large (approx. 90 * 40 * 4 mm) glass samples, depicted in figure 3.23, have been used. Next, small (38 * 20 * 1.5 mm) basaltic glass samples, as the ones depicted in figure 3.24, have been used. Finally, medium (50 * 30 * 1 mm) glass sam-

ples, similar to the ones depicted in figure 3.23, were used. The difference of the last samples to the first was that they were rectangular shaped, slightly shorter, much thinner, lapped and machine polished to finish. Only the final medium size sample delivered a working cell, since it was iteratively optimised to fit the PECVD process.

Key characteristics improved from first to the second run were surface quality/roughness due to machine polishing. From the second to the third, the samples' length increased to ≈ 50 mm, and their width to ≈ 30 mm. Despite the increase in size, the samples were still small enough to fit the machine-polish-mount. The last samples had the ideal size to fit the mounts of the lapping and polishing machine, as well as to fit the mounts on the PECVD system. The latter one allowed for accurate spacing between sample and electrode, which allowed for homogenous deposition. Thus, the last samples were ideal glasses for solar cell manufacturing.

Two types of cells have been manufactured on these glasses, one called 19B-015 and the other 19B-016. Each type has been deposited on a basaltic glass sample and reference glass during the same run. Although multiple different basaltic glass samples have been used in several attempts to manufacture a silicon thin-film solar cell, the layering of the cells was the same in all cases. The only layer which was altered for the two cell types 19B-015 and 19B-016, was the p-type layer, which had different doping levels. Details on the depositions of the layers schematically depicted in figure 3.33 are provided next.

Reflective Back Contact - AZO/Ag/AZO

First, the reflective back contact was manufactured, starting by cleaning the polished glass samples. Then, the first TCO layer (1. TCO), etched/textured[1] AZO, was deposited with 800 nm layer thickness. This layer was covered with an Ag/AZO sandwich, with 100 nm (2. Ag) and 80 nm layer thickness (3. TCO). The results of these reflective back contact layer depositions are depicted in figure 3.34 (left), showing small samples mounted on reference glass, coated with AZO/Ag/AZO. Although the deposition of the back contacts worked for the small samples, the layers were inhomogeneous, due to the different levels the basalt glass and reference glass were mounted on. This was solved in later stages by using the medium samples, which could be mounted at the same level than the reference glass.

Absorber Layer - n-i-p μc-Si:H

Next, after the back reflector deposition, a set of three μc-Si:H layers was deposited on top of the back reflector. Two cell types, 19B-015 and 19B-016, were deposited, both μc-Si:H in an n-i-p configuration. Thus, three layers were deposited, n - negatively doped with phosphorus, i - intrinsic (pure) semiconductor and p - positively doped with boron. The first two layers (n-i) are identical for both cell types (19B-015 and 19B-016), the third layer (p-doped) was different for both cells. These differences are described in the following, as well as details are provided on

[1] More details on texture-etched AZO layers and Ag/AZO sandwiches in [498].

all layers. N- and p-type layers were grown at excitation frequency of 13.56 MHz and a substrate temperature of 185 °C.

Layer 1, n-doped micro-crystalline silicon (μc-Si-n), two gases were used for deposition, PH_3 (2 %) in SiH_4 at 1 standard cubic centimetre per minute (sccm) rate, and H_2 at 200 sccm. Deposition duration was 8 minutes, deposition pressure 0.67 mbar, deposition power 25.3 W and substrate-electrode distance 20 mm. The layer thickness calculated to 35 nm, at a deposition rate of 0.73 $\text{Å}/s$ for 8 minutes and the concentration of phosphine is 2 %.

Layer 2, intrinsic micro-crystalline silicon (μc-Si-i) followed after layer 1, and used, SiH_4 at 5.1 sccm as well as H_2 at 98 sccm for deposition. Deposition duration was 130 minutes, first 4 minutes with SiH_4 at 4.5 sccm, then 5.1 sccm. The deposition pressure was 1.5 mbar, deposition power 24.3 W and substrate-electrode distance 12 mm. The layer thickness calculated to 2100 nm, at deposition rate of 2.7 $\text{Å}/s$ for 2 hours 10 minutes. This layer is intrinsic, thus not doped.

Layer 3a (19B-015), p-doped micro-crystalline silicon (μc-SiOx-p) followed after layer 1 and 2, 19B-015 used, SiH_4 at 0.83 sccm, H_2 at 500 sccm, TMB (1 %) in He at 0.31 sccm and CO_2 at 0.42 sccm for deposition. Deposition duration was 7.5 minutes, deposition pressure 4 mbar, deposition power 10.3 W and substrate-electrode distance 20 mm. The layer thickness calculated to 34 nm, at deposition rate of 0.75 $\text{Å}/s$ for 7.5 minutes and the concentration of TMB is 0.37 %.

Layer 3b (19B-016), p-doped micro-crystalline silicon (μc-Si-p) followed after layer 1 and 2, 19B-016 used, SiH_4 at 1.5 sccm, H_2 at 200 sccm and TMB (1 %) in He at 2 sccm for deposition. Deposition duration was 15 minutes, deposition pressure 4 mbar, deposition power 50.2 W and substrate-electrode distance 20 mm. The layer thickness calculated to 54 nm, at deposition rate of 0.6 $\text{Å}/s$ for 15 minutes and the concentration of TMB is 1.3 %.

All values are summarised in table 3.4. Figure 3.34 shows two small basaltic glass samples with back reflector (left), and n-i-p μc-Si:H layers on the right.

Table 3.4: Deposition parameters of individual layers summarised. Dopant gas flow TMB (p-type) and PH_3 (n-type) given in absolute values, in their dilution gases (1.0 % TMB in He and 2 % PH_3 in SiH_4)

	P	f	d_{el}	t_{depo}	p	T	SiH_4	H_2	CO_2	dopant
Series	W	MHz	mm	min	mbar	°C	sccm	sccm	sccm	sccm
μc-Si-n	25.3	13.56	20	8	0.67	185	1	8	-	1
μc-Si-i	24.3	13.56	12	130	1.5	185	5.1	98	-	-
μc-Si-p-a	10.3	13.56	20	7.5	4	185	0.83	500	0.42	0.31
μc-Si-p-b	50.2	13.56	20	15	4	185	1.5	200	-	2

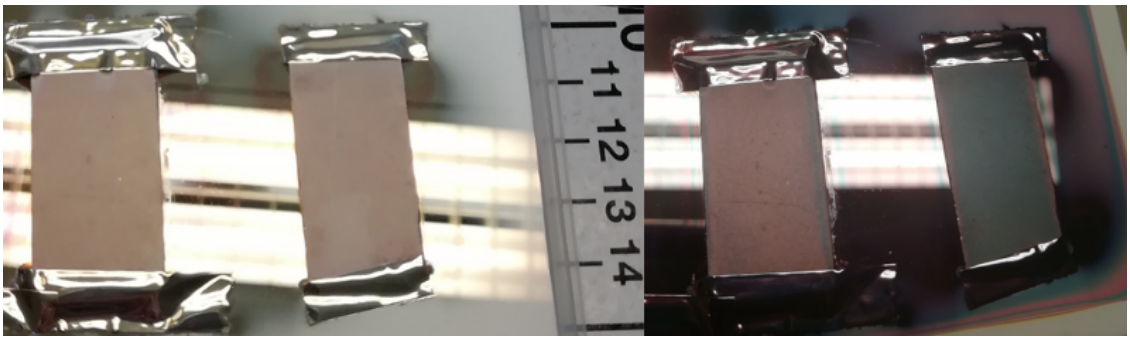

Figure 3.34: The image shows two basaltic glass substrates mounted on a reference glass. First coated with AZO/Ag/AZO (left), and then coated with n-i-p μc-Si:H (right). The scale depicted is in cm.

Front Contact AZO/Ag

After the absorber layer of the cell was finished by depositing the p-layer, it was covered with another AZO layer. This layer in combination with the last "layer", a silver grid, forms the front contact and allows the cell to be illuminated through the AZO layer. Actual samples, which have been deposited with these two layers, are shown in figure 3.35. The figure shows two basaltic (1 and 3) and two reference (2 and 4) solar cells. Samples in sub figure 1 and 2 are type-a (19B-015), and samples in sub figure 3 and 4 are type-b (19B-016). Type-a samples are named *Basalt 1* (sub figure 1) and *Reference 1* (sub figure 2) and type-b samples *Basalt 2* (sub figure 3) and *Reference 2* (sub figure 4). All solar cell samples (individual blue squares) consist of following layers: TCO/Ag/TCO/μc-Si:H/TCO, and some the cells are finished with an Ag grid on top.

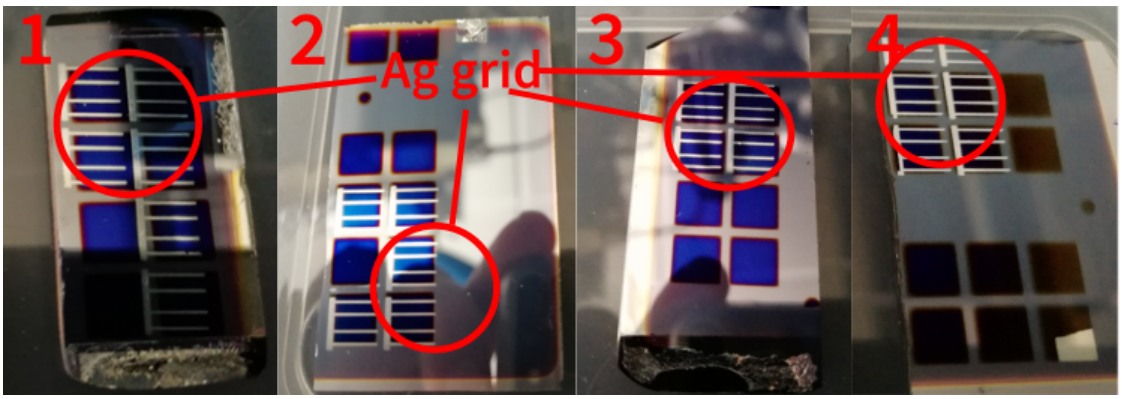

Figure 3.35: Two silicon thin-film cells built on basaltic glass substrates (1 and 3), and the corresponding two reference cells manufactured in the same run on reference glass (2 and 4).

After three separate manufacturing attempts were made to prepare a working solar cell on basaltic glass, finally, the last one was successful. A working cell was manufactured using a basaltic glass substrate, made from regolith simulant. A good surface quality and a suitable sample geometry, fitting all processes, was key for

that. Especially the correct geometry required for the machines and processes was important. This included a thickness of less than 0.5 mm and a difference in thickness between corners (partiality) of less than 50 μm (over a sample length off 40 mm or less). Further, manufacturing and annealing glass to withstands processing was key. Since the glass needs to be ground and polished into shape via mechanical processes, it needed to withstand the procedure to avoid cracking and the loss of the sample. Details on surface roughness of the used samples will follow in the results section.

4 Experimental Techniques, Methodology and Theory

Even before first devices were built from regolith simulants, a series of various tests was conducted to characterise samples, and to measure their performance. This chapter outlines the methods and experimental techniques utilised to determine the quality of lunar regolith simulants, as well as glasses, mirrors, concentrators and solar cells built of them.

This chapter splits analysing methods into three groups: geological and chemical analysis, optical analysis and physical analysis. The first section will therefore focus on techniques mostly used to characterise simulants, the second on optical assessments of simulants and products made of simulants, and the third mostly on the characterisation of the final products.

4.1 Geological and Chemical Analysis

Before actual devices could be tested, intermediate materials and processes, required for manufacturing, needed to be tested and validated. Different types of regolith simulant and basaltic glass manufactured from simulant have been analysed using the techniques described next. Actual selected simulants are discussed in chapter 5.1, but in general, seven simulants have been partially or fully analysed using the techniques EDX, XRD, XRF, CHN, DSC/TGA and Mösbauer Spectroscopy, which will be described in more detail next.

4.1.1 Energy-Dispersive X-Ray Spectroscopy (EDX)

To be able to reproduce results and to achieve comparability it is important to determine the exact chemical composition of the initial materials used, the regolith simulants. This ultimately helped to understand how tolerant the manufacturing processes were to fluctuations in the source material. It was possible to test the chemical and mineralogical composition of the regolith by means of a Scanning Electron Microscope (SEM) with Energy-dispersive X-ray Spectroscopy (EDX) [141]. Principles of SEM will be discussed in the next section and this section gives a brief overview of EDX.

Energy-Dispersive X-ray Spectroscopy (EDX), sometimes also called EDS or EDXA, is a technique, which allows to analyse elemental composition of a sample, in this case regolith simulant. EDX can detect X-rays emitted from a regolith sample during bombardment with an electron beam. The electron beam forces

out electrons from the inner shells of an atom, which are detected by a detector which allows the determination of the atomic number of atoms contained in a sample [502]. For all measurements conducted, using EDX or SEM, one of either of the two systems described next was used, depending on their availability. For the conducted EDX analysis no differences are expected to occur between the two different machines.

The first system used was a FEI Quant 650 FEG Scanning Electron Microscope (SEM), equipped with Oxford Instruments X-MaxN 150 mm energy dispersive X-ray (EDX) detector. This machine can operate in high and low vacuum mode as well as full environmental (environmental scanning electron microscope - ESEM) mode. These options allow to image most materials and conduct elemental analysis. Modes available for this machine were secondary electron (SE), backscattered electron (BSE), cathodoluminescence (CL) and electron backscattered diffraction (EBSD).

The second systems used for analysis of samples was a FEI/Philips XL30 environmental scanning electron microscope (ESEM), equipped with an Oxford Instruments X-Max 80 mm EDX detector. Fitted with a tungsten filament it has similar possibilities for analysis of samples than the first SEM/EDX system described, but is missing the EBSD mode. Both systems were used at the school of Energy, Geoscience, Infrastructure and Society at Heriot-Watt University.

To analyse regolith simulant using EDX, samples needed to be prepared for the measurements as depicted in figure 4.1. The left side of that figure shows 5 regolith simulant samples embedded in resin via vacuum impregnation. Vacuum impregnation was used to seal pores and bubbles in-between the grains and to hold the grains in place for the measurement.

After the resin was hardened, the regolith-resin cylinders have been turned to length using a lathe and after that, they have been ground flat using disc grinding. After finishing with a SiC paper of 2000 grit, the samples have been polished using diamond slurries, with 14, 7, 3.5, 1.5 and 0.5 μm average grain size (in that order).

Samples were mounted in the sample holder depicted in the middle in figure 4.1 and coated with a layer of gold (Au). Latter one was necessary to increase the conductivity of the samples, avoid charging and therefore increase the quality of the results. Samples have been measured using EDX and results are discussed in section 5.1.3. The sample mount allowed for all five samples to automatically be measured in the same run, since all the samples could be mounted at the same height and thus the system did not have to be refocused on the samples during EDX measurements.

4.1.2 X-Ray Powder Diffraction (XRD)

Basaltic sands and lunar regolith vary significantly in their mineral content as pointed out earlier in table A.2. Hence, it was also required to measure mineral

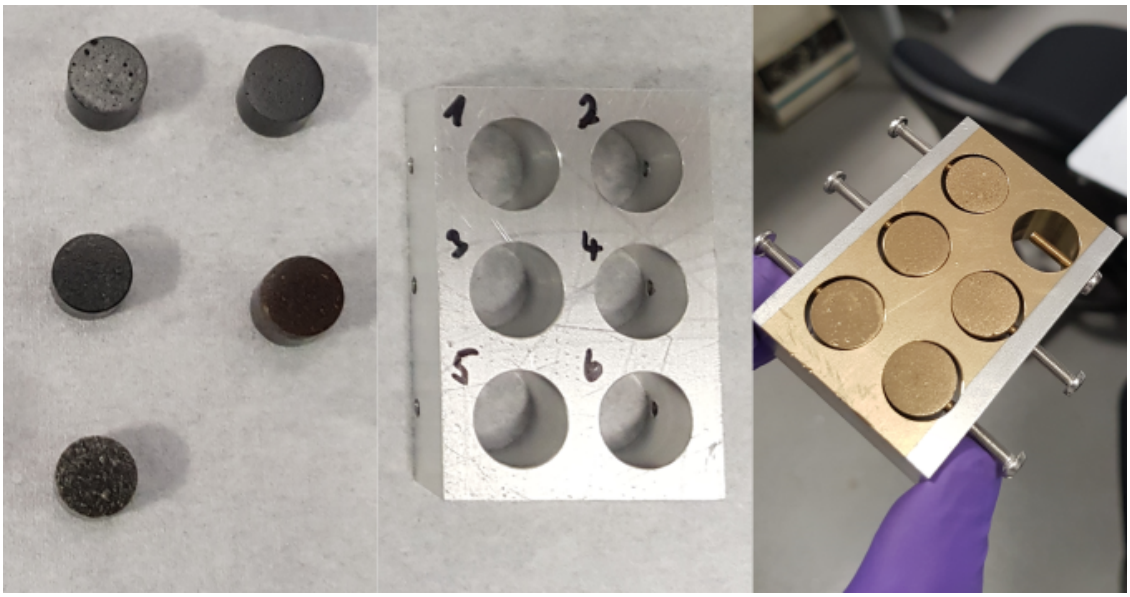

Figure 4.1: Regolith simulant prepared for EDX measurements, left side showing regolith simulants embedded in resin, middle the sample holder and right the mounted samples, readily coated with gold for the actual measurements.

contents of a simulant to determine differences. The technique used for this was X-Ray Defraction (XRD).

XRD is a typical analytical method used to identify minerals/phases in crystalline materials. Similar to EDX, also XRD is using X-rays to analyse samples by exposing a crystalline sample to monochromatic X-rays and measuring the resulting interference. For XRD, X-rays are generated (rather than only detected) via a cathode ray tube with filters attached, to radiate monochromatic radiation only. When the targeted beam hits a sample, diffracted X-rays are detected, which are processed, counted and ultimately refined using Rietveld refinement ([503]). To measure a sample (regolith simulant), it needs to be finely ground and ideally homogenous as well [504].

Regolith simulant samples were prepared for XRD measurements by first micro-grinding them and then spray drying them. Figure 4.2 shows some of the sample preparation steps. On the left, a microgrinding container is depicted which was equipped with 56 cylinders, made of aluminium oxide. Additionally approximately 20 grams of regolith simulant was ground and mixed with ethanol prior to entering it into the container.

The container was then attached at the right side of the microgrinder (depicted second from left in figure 4.2). Samples were ground for 10 minutes, after which no improvement to the process ability could be observed anymore, and then recovered from the microgrinding-chamber and stored in a vial. Next, the sample vials, with the regolith ethanol mix, have been attached to a spray nozzle depicted second from right, which was using air to form an aerosol of the regolith/ethanol mix.

Figure 4.2: Microgrinding and spray drying of regolith simulant samples in preparation for XRD. Left microgrinding-chamber with cylindrical grinding elements made of aluminium oxide, second from the left the microgrinder, second from the right the nozzle for spray drying and at the very right, the drying chamber. Images not to scale.

The regolith sample was sprayed into a heated chamber (right in figure 4.2) and the aerosol dried before it hits the ground, where it was recovered from a clean sheet. The sample was then ready to be pressed into pellets for XRD measurements.

The combination of microgrinding and spray drying minimises XRD measurement effects caused by crystal orientation in the sample. First the microgridning minimises the crystals size and then the spray drying forms ideally perfect spheres which assure random orientation of the crystals in the sample.

The actual system used was a Bruker D8 Advance, with a Sol-X energy dispersive detector. The machine is capable of quantitative and qualitative identification of crystalline materials via powder diffraction. The software used was Bruker Diffrac.EVA in combination with latest International Centre for Diffraction Data (ICDD) database. For the quantitative Rietveld analysis, the software TOPAS 3.0 was used.

4.1.3 X-Ray Fluorescence Spectroscopy (XRF)

X-Ray Fluorescence Spectroscopy (XRF) determines the elemental composition of a sample. Similar to EDX, also XRF uses the effect of ejected electrons from the inner shells due to high energy radiation such as X-rays hitting the atom. Characteristically emitted light of certain wavelengths is then used to determine the elemental composition [505]. The difference between XRF and EDX is that EDX uses a highly focused electron beam to expel electrons from an atom's core and XRF uses X-rays.

XRF was a technique, often used for this project, to determine elemental composition, and changes in elemental composition, by comparing two measurements (before and after). Most samples were analysed for 10 major and some for up to 14 trace elements. The machine used for most experiments was a Philips PW2404 wavelength dispersive sequential X-ray spectrometer at the School of GeoSciences at the University of Edinburgh. The system is fitted with a rhodium anode end

window X-ray tube. The XRF spectrometer is calibrated for major and trace element analysis using international standard samples. This instrument can be used for qualitative or quantitative analysis of geological materials, such as regolith simulants. It was possible to obtain a quantitative analysis for most relevant elements heavier than oxygen. Abundances which could be detected were in the range from 100 weight % (wt%) and one part per million (ppm).

To test different sample batches and to cross check results from the first machine, a second XRF machine was used, operated by Bernard Charlier at the department of Geology at the University of Liège (Belgium), was an ARL PERFORM-X 4200. This machine was also capable of measuring 10 major elements determined from samples manufactured into the form of lithium tetra- and metaborate fused discs, corrected by matrix corrections following the Traill-Lachance algorithm. Trace elements were measured on pressed powder pellets and the data was corrected for matrix effects by Compton peak monitoring. Approximately 100 samples of international standards were used for the calibration curves.

The effect of different regolith compositions on the glass and glass manufacturing/handling processes were analysed by investigating different regoliths in different forms (raw, ground, melted, beneficiated). Variations occurring in the regoliths due to beneficiation or processing are discussed in the results section 5. This section finishes by detailing sample preparation for XRF major and trace analysis.

Sample Preparation - Major Elements

Samples prepared for major element detection (for the machine in Edinburgh), were fused glass discs, prepared similar to the method described in [506]. Raw simulant powders were dried, as described in the previous chapter, overnight to remove moisture. Next, about one gram of sample powder was heated to 1100 °C in order to burn off carbonates and hydrous silicates. Carbonates burn off by forming CO_2 and hydrous silicates (e.g. clay minerals or micas) decompose to anhydrous equivalent products. This weight loss during that stage is called Loss On Ignition (LOI) and is measured in wt%.

A sample of a dried regolith simulant was weighed on precision scales (unfired) and entered into a crucible made of 90 % platinum (Pt) and 10 % Gold (Au). The entered sample was mixed with a borate flux (Johnson and Mathey Spectroflux 105 [1]) in a ratio of 1:5, sample:flux. Figure 4.3 shows a set of discs prepared from magnetically beneficiated BP-1 regolith simulant.

After moderate mixing, the flux-regolith-mixture was fused in a furnace at 1100 °C for 20 minutes to form glass. After removing the crucible from the furnace, the crucible was set aside to cool to room temperature (forming a solid glass in the crucible). After compensating for the weight loss of the flux during this firing, the

[1]Spectroflux 105 consists of a mixture of 47 % Lithium tetraborate , LI2b4O7, 37 % Lithium carbonate (Li2O) and 16 % of La2O3, Lanthanum oxide as a X-ray heavy absorber [507].

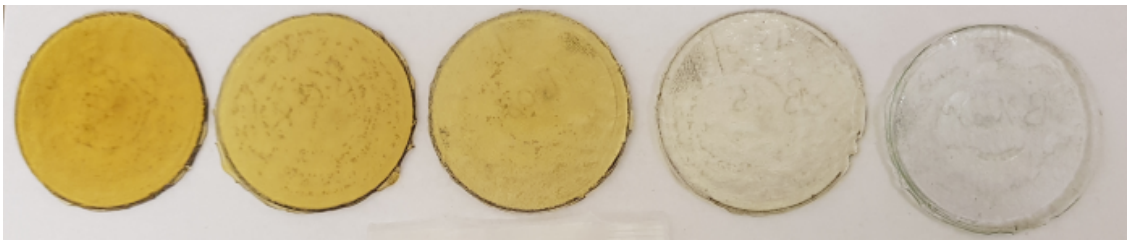

Figure 4.3: Glass discs prepared for XRF measurements from magnetically altered BP-1 regolith simulant. From left to right the amount of contained iron oxide is getting lower, diameter of discs was about 5 cm.

sample was fused a second time, this time using a Bunsen burner. Once the mix was homogenous and fully liquid again, the melt was poured onto a graphite disc and, by pressing down on the melt with an aluminium plunger, a glass disc was formed. Casting was carried out on a hot plate, pre-heated to 220 °C, where all graphite discs were kept to avoid thermal shock of the glass. After the glass discs had remained on the hot plate for ten minutes, they were removed from the plate and set aside to cool to room temperature, resulting in discs such as shown in figure 4.3.

Sample Preparation - Trace Elements

Samples for trace elemental analysis are not made into fused glass discs, but rather pressed powder pellets. Required were eight grams (± 0.1 g) of sample powder which was combined with eight drops of Poly-Vinyl Acetate (PVA) used as binder. The mix was entered into a tapered aluminium cup, pre-compressed by hand and machine compressed at eight tonnes for two minutes. After removing the pressed powder disc from the press, it was ready for XRF trace element analysis.

4.1.4 Carbon, Hydrogen and Nitrogen Analyser (CHN)

To determine "contamination" of the regolith simulants by materials which are not found on the lunar surface, a Carbon, Hydrogen and Nitrogen Analyser (CHN) was used. This machine determined the carbon, hydrogen and nitrogen content of a sample which in turn showed how much or whether at all a sample is contaminated by biological material (C, N) or water (H), for example. The system used was an Exeter CE-440 Elemental Analyser.

Sample preparation was straight forward and only less than a gram of ground regolith simulant was required for this measurement. The samples were entered in a crucible and combusted in oxygen atmosphere at about 1800 °C. Gaseous combustion products of the process were H_2O, N_2, NO_x, and CO_2, which were streamed through cylinders (some filled with copper oxide) where oxides were reduced to their elemental state. The created gas was measured by a detector which produced an electrical signal showing the concentration of carbon, hydrogen and nitrogen contained in a regolith [508].

4.1.5 Differential Scanning Calorimetry (DSC) and Thermogravimetric Analysis (TGA)

Simultaneous Differential Scanning Calorimetry (DSC) and Thermogravimetric Analyses (TGA) were conducted on regolith simulant samples, which measured weight changes and heat flow in the (crystalline) material at the same time; both as a function of time or temperature. Experiments were conducted in a controlled gas atmosphere and analysing both, DSC and TGA, at the same time, delivered supporting results. These allowed to separate endo/exothermic events from pure weight loss events. Further, simultaneous TGA/DSC measurements gave clues to the composition of multi-mineral systems such as regoliths are. They showed how reactive a material was with gases, how much volatiles (contamination) were released at low (< 200 °C) temperatures and helped to find melting, boiling and crystallisation points (transition temperatures) [509].

The DSC/TGA instrument used was a NETZSCH STA 449F1 and samples of regolith simulants were prepared by either grinding 10 grams of simulant or keeping it in "off-the-shelf-form". Fractions of these two sample types have then been entered into one platinum crucible for measurements, as well as another platinum crucible of same size was kept empty for reference. Since the sample melted during the measurement, the melt stuck to the platinum crucibles after the test was conducted. In order to be able to reuse the crucibles for multiple measurements, the same procedure needed to be carried out, used for cleaning the platinum crucibles, used for manufacturing. Reheating the DSC/TGA crucibles with flux and then entering them into a tempered sulphuric acid bath overnight, cleaned them out entirely and they were good to be used for the next measurements again.

4.1.6 Mössbauer Spectroscopy

To determine in more detail (after XRF and XRD) what amount of which type of iron oxide is contained in a simulant, Mössbauer spectroscopy measurements were conducted. These provided clues to which type of iron baring mineral was contained in a sample and what oxidisation state it was in.

The instrument used to analyse regolith samples was an Athena MIMOS II Mössbauer spectrometer, a portable backscattered Mössbauer instrument described in [510]. Graph 4.4 shows an example of curves obtained by measuring a regolith simulant (here: EAC-1) using Mössbauer spectroscopy. The curve indicated by "Curve 1" in this figure shows the measured data from the regolith simulant. The second curve, "Curve 2" shows a curve which was fitted to the measured curve by using reference data from potentially contained minerals/elements. All other curves ("Curve 3 - 6") are the characteristic curves of those individual minerals and were used to built "Curve 2".

An example of results obtained from such an analysis, depicted in figure 4.4, is shown in table 4.1. For some curves a supposed phase can be derived from the data and the oxidation state of the entire surface area could be determined from

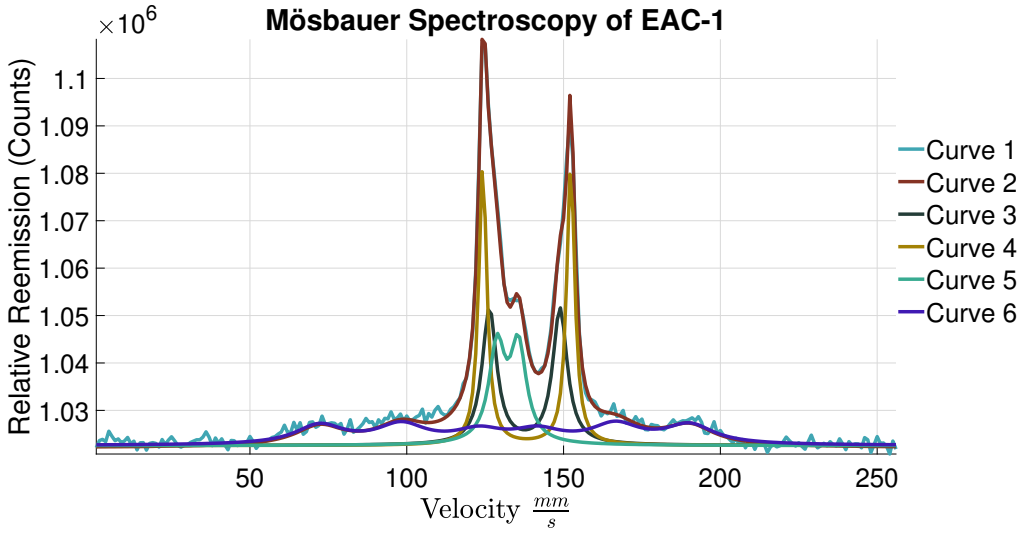

Figure 4.4: Mösbauer spectroscopy of a EAC-1 regolith simulant sample as analysed at the University of Stirling.

the obtained data. The velocity measurements "QS" and "IS" refer to the electrical quadrupole interaction which leads to an isomer shift (IS) and an electric quadrupole splitting/shift (QS), which are both effects used to determine the characteristics of the sample [510]. Ultimately these measurements provide an idea of how much of the surface area of a sample is covered with a certain type of iron oxide/mineral. The column "Area %" in table 4.1 refers only to the iron oxide content of a sample and not to other oxides contained.

Table 4.1: Results of Mösbauer spectra analysis of EAC-1

Curve	Phase	Ox. State	IS ($\frac{mm}{s}$)	QS ($\frac{mm}{s}$)	Area (%)
1	MB data				
2	Fit				
3*		Fe2+	1.05	2.33	24
4	olivine	Fe2+	1.12	2.91	28
5**		Fe3+	0.49	0.7	19
6***	ferric oxide	Fe3+	0.45	-0.13	30

*parameters not mineral specific, could be pyroxene or other silicate
**octahedral Fe3+, potentially Fe3+ in silicates or superparamagnetic Fe oxide
***parameters consistent with goethite

4.2 Optical Characterisation

Five different optical techniques have been used to characterise regolith simulants. Techniques used are optical microscopy, focus variation microscopy, scanning electron microscopy, a pyrometer and UV-Vis-NIR spectroscopy. Details are provided in the next subsections.

4.2.1 Microscopy

A technique typically used to analyse geological material, is thin section petrography. To analyse a sample, it needed to be prepared in the form depicted in figure 4.5, which shows a thinly sliced section of individual regolith simulant grains, lapped to a thickness of 30 μm and mounted onto a microscopy slide. By looking at these cross sections under Plain-Polarised Light (PPL) or Crossed Polars (XPL) it was not only possible to see the grains geometry, but also infer mineralogy.

Figure 4.5: Regolith simulant prepared for thin section analysis on a microscope using plain or crossed polarised light. Regolith embedded in resin, lapped to a thickness of 30 μm and mounted on a standard microscopy slide.

A Leica upright light microscopes was used to analyse thin section samples. The system had a digital camera attached to it and allowed for sample analysis with the human eye and digital photography at the same time. Using the PPL and XPL mode/filter and rotating the sample on the stage (rotatable 360 °C), digital images of thin section samples were taken to qualitatively determine a samples mineral content.

4.2.2 Focus Variation Microscopy

Surface topography images of basaltic glass samples made of regolith simulant, were created using the technique of focus variation microscopy (Alicona InfiniteFocus, Austria). The technique provides a measurement of areal surface topography based on optics with limited depths of field and vertical scanning. The technique is based on measuring the focal variation at different distances between the sample and the focal plane (z-positions). A vertical scan of the object's surface captures a stack of two-dimensional microscopic images thus creating a depth map of the sample due to the relation between the focus position and the specific distance. The data at various distances is then used to reconstruct the three-dimensional surface profile. These profiles provide information to display the surface roughness of the sample's surface [511–513].

4.2.3 Scanning Electron Microscopy (SEM)

Scanning Electron Microscopy (SEM) is working after the same principle than EDX does. It scans a beam of electrons along the surface of a sample and displays an enlarged image of the sample's surface. Samples are prepared either the same way as for EDX, or without coating the surfaces. An electron beam hits the samples surface, which was kept in a vacuum chamber, and was attracted by an anode consecutively being accelerated into an energetic beam. Via a set of electromagnetic coils, the electron beam can be focused and manipulated to move across the surface. When hitting the surface of the sample, the electrons got scattered and were detected by a detector which processed the signal into an image.

SEM is ideal to qualitatively analyse surfaces for features such as voids or ripples. Moreover, it can be used to detect changes in material composition or phases such as changes from the solid to crystalline phase. The actual systems used for analysis were described in EDX section 4.1 already and were used for SEM analysis as well.

4.2.4 Pyrometer and Emissivity

To determine the regolith's/melt's temperature remotely during processing, a pyrometer was used. The model used was a CALEX electronics limited PyroUSB 2.2 with Close Focus Optics (CF), with a 7.5 mm measurement spot diameter at 500 mm distance. The selected model used the High Temperature Rage (HT) from 450 to 2000 °C. The pyrometer was used in combination with the "CalexSoft 1.32" software and the device had a spectral response of 2.0 to 2.4 μm wavelength.

To non-invasively determine the temperature of the regolith simulant or glass melt, it was also required to understand the emissivity behaviour of the material in question. Little to nothing was done with respect to this point for regolith simulants and their melts. Hence, a series of tests - determining the emissivity of the regolith over a certain temperature and wavelength band - was conducted and will be discussed in chapter 5.2. After the emissivity behaviour of a material was known, the pyrometer allowed for non-invasive temperature measurements, which was in the case of microwave melting the only possible option.

This instrument was also used for the experiment designed to determine the emissivity of a simulant (discussed in detail in 5.2). By heating regolith simulant in a temperature controlled Paragon Sentry Xpress 4.0 kiln, its actual temperature was determined by a built-in thermocouple. Then, the emissivity value in the CalexSoft software was adjusted until the temperature displayed by the CALEX pyrometer matched the temperature of the thermocouple. Measurements have been taken in increments of 50 °C, from 500 to 1050 °C, and four simulants have been analysed.

4.2.5 UV-Vis-NIR Spectroscopy

Building devices, which were exposed to parts of the solar wavelength spectrum, required a good understanding of a device's optical properties, such as its reflectivity

and transmission. To determine these characteristics, a PerkinElmer Lambda 950 UV-vis-NIR spectrometer was used. The types of samples measured were; regolith simulants, basaltic glasses, mirrors built on basaltic glasses, transparent glasses made from regolith simulant and solar cells built on basaltic glass substrates.

The reflectivity, absorption and transmission represent by which part of the solar wavelength spectrum the glass was influenced. Depending on the use case of the glass, a high reflectivity (mirror) or a high transmission (cover glass) was useful. These parameters were not only influenced by the chemical composition of the glass, but also of its surface geometry and inner structure. Utilising the UV-vis spectrometer it was possible to measure relevant properties of the samples manufactured.

A solar concentrator's performance was mainly dependent on its ability to reflect light and to concentrate light. Therefore, reflectivity measurements were conducted first, before the entire system's concentration capacity was analysed on a solar simulator. These conducted physical measurements and the devices used for these measurement are described in the next and last section of this chapter.

4.3 Physical Characterisation

Tests, conducted to physically characterise samples, were surface roughness via surface profilometry, I-V Curve measurements of solar cells and a solar concentrator setups on a solar simulator, as well as External Quantum Efficiency (EQE) measurements on solar cells.

4.3.1 Surface Profilometry

Surface roughness and flatness were important parameters to be measured for all substrates (mirrors), since it was suspected that they correlate with the ability of a substrate to reflect sunlight, as well as they determine the suitability of a sample for solar cell manufacturing. To determine the surface roughness of a sample a Taylor Hobson Talysurf-5 stylus profilometer (modular system) was used.

The linear recorder of the system recorded the surface profiles of the samples onto electro-sensitive coordinate paper, which was synchronously driven by an electric motor. To measure a sample, it was placed with its to-be-measured surface on top, clamped by a vice and levelled. It was important for the sample to be parallel to the pick-up line/travel directly of the stylus, since else the recordings would exit the measurement paper rapidly. Vertical magnifications (V_v) and horizontal magnifications (V_h) were pre-selected on the profilometer depending on the samples supposed surface roughness and quality.

After the stylus measured a certain length across the surface, and the electro-sensitive coordinate paper had recorded the run, the plot was removed from the machine. Next, it was digitised by scanning it and importing the image into a software called GetData Graph Digitizer. This software allowed to digitise and

export the recorded lines as comma separated values (csv) and import them into a plotting software, such as Matlab® for example. An actual sample under the stylus of the profilometer is shown in figure 4.6.

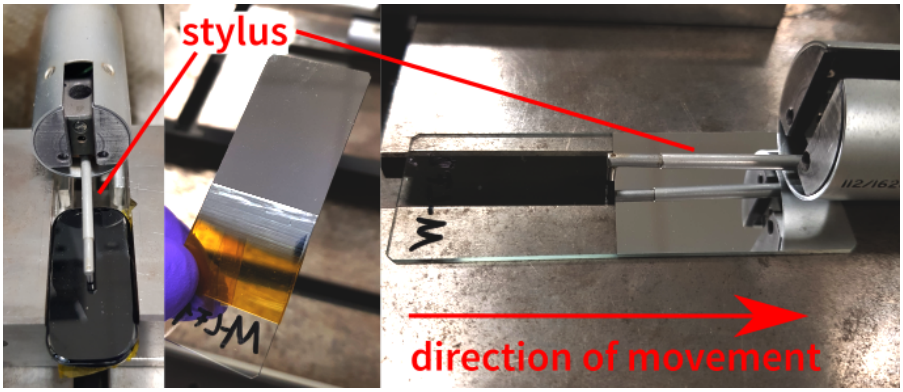

Figure 4.6: The setup of a sample clamped in a vice, under the stylus of the utilised profilometer (left). A reference microscopy slide after thermal evaporation coating of aluminium (middle) and after removing the tape (orange colour in middle image) and under the stylus (right).

The three images (in figure 4.6) show a polished basaltic glass sample, of the first batch of the resistive heated samples, every time depicted under the stylus of the profilometer. The sample was held in place, by clamping it into a vice. The stylus traversed across the sample's surface, parallel to the longest dimension of the sample. The middle of figure 4.6 shows a reference microscopy slide after thermal evaporation of aluminium. These samples were used to determine the layer thickness deposited on a sample's surface. By removing the Kapton® tape from the sample (right part of figure 4.6) the transition edge from uncoated glass to aluminium was exposed. By traversing over this transition zone perpendicular to the edge, the layer thickness could be determined.

Required Surface Quality for Use as Glass Substrate

At the beginning of the 20^{th} century researchers increased investigations on optical properties of surfaces, such as gloss for example [514]. These (gloss) measurements were aiming at determining how well a surface reflects light. In particular, the specular (directed or mirror-like) reflectivity, part of the gloss, was of interest and is one of the two contributors to the overall reflectivity. The other part is diffuse reflection, which is the amount of light, which gets scattered in other directions than the specular reflection. Specular reflection is thus the fraction of the light, which gets reflected at a symmetrical angle to its incident angel.

First investigations on the relation between surface roughness and specular reflectance have been conducted in 1961 and suggested that when measuring reflectivity, and not considering surface roughness, the measurement error is increased, the rougher a surface is [515]. This suggests that the amount of scattered light increases when the surface roughness increases. Experimentally determined

relationships between surface roughness and glossiness were conducted by [516] in 2004. Seven different materials have been analysed with five different surface roughness values each. These results show that the glossiness as well as the specular reflectance of a surface increases exponentially with a smoother surface. Further, surface roughness values of R_a smaller 100 nm showed highest reflectivity for all metallic surfaces and extrapolating these values suggest that maximum specular reflectance could be achieved at $R_a < 1$ nm.

Based on these works, surface roughness was identified to be a key characteristic for a substrate, relevant for manufacturing solar conversion devices, such as mirrors for example. Surface roughness is impacted by multiple factors, one of them is the surface finishing process [440], which can potentially even impact the reflectivity in a certain wavelength range only [517]. Further, substrate manufacturing processes are standardised in DIN ISO 10110, for example, and define, bubbles and inclusions, inhomogeneity, flatness, surface imperfections.

In conclusion, the aim for building glass substrates was to achieve a substrate with a low surface roughness value $R_a < 1$ nm, and as little as possible surface features, such as bubbles or voids, specified in DIN ISO 10110.

Hence, determining surface roughness of manufactures substrates was relevant to determine the suitability of a substrate for mirror manufacturing. Thus, based on the recorded surface profiles of a substrate, R_a the arithmetic average of the roughness profile, was determined. Figure 4.7 shows a surface profile in blue, which represents an actual surface profile recorded, the mean line (orange) and the R_a line in yellow. The mean line represents the mean deviation over the entire measurement length l_x and is always used as reference by putting it to zero. The arithmetic average (yellow R_a line) is the average roughness of the profile. The arithmetic average (R_a) was derived from,

$$R_a = (\frac{1}{l}) \int_0^l |y(x)|\, dx \tag{4.1}$$

with the numerical approximation of,

$$R_a = (|y(1)| + |y(2)| + ... + |y(n)|)/n \tag{4.2}$$

The measured distance on the surface is defined by l, the distance from the origin by x, the elevation of the surface profile at a particular distance to the origin is defined by $y(x)$, and the number of data points recorded by n.

In conclusion, the measured profiles by the profilometer have been digitised and used as a basis to determine the R_a value of a sample. R_a values of less than 1 nm have been found to be ideal for mirror and/or solar cell manufacturing.

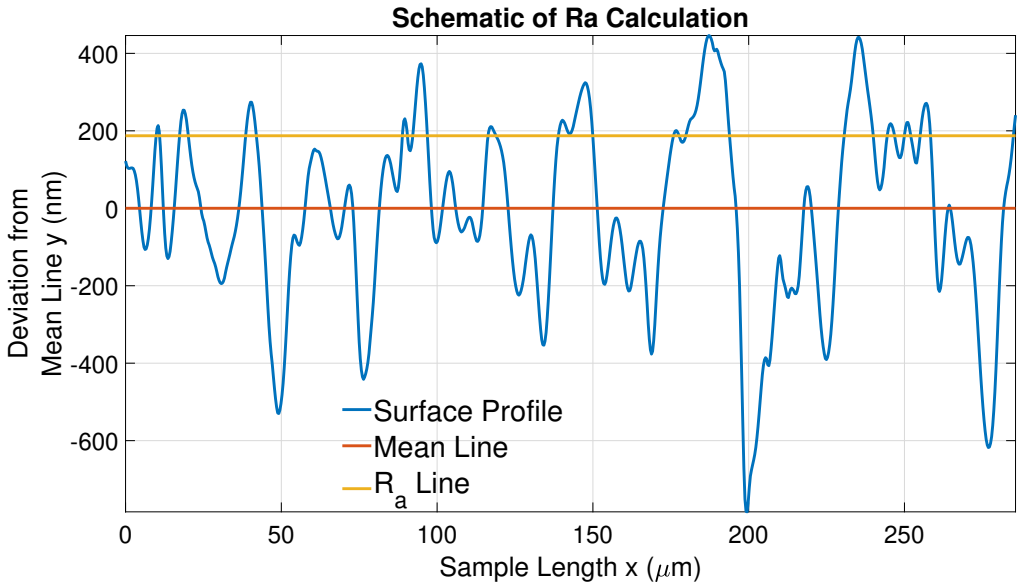

Figure 4.7: Schematic of arithmetic average (R_a) at the example of EAC-II's surface recorded via focus variation microscopy. The blue line shows the recorded surface profile, the orange the mean line and the yellow the arithmetic average.

4.3.2 Maximum Power Point (MPP) and I-V Curves

To determine the performance of a solar cell, current and voltage are measured from which I-V curves can be plotted. These curves can be used to determine the Maximum Power Point (MPP) of a solar cell. The MPP of a cell is typically indicated by P_{max}, measured in Watt and defined by $V_{MPP} * I_{MPP}$. The MPP voltage, V_{MPP}, and the MPP current, I_{MPP}, are both typically determined under standard illumination conditions AM1.5.

Additionally, the open circuit voltage V_{oc} of a cell, occurring when fully illuminated with no load attached, was of interest, as well as the short circuit current I_{sc}, measured when short circuiting a cell. Both of them represent the maximum achievable current or voltage output when the other value is at zero. In addition to that, the Fill Factor (FF), is a parameter which is used to determine the maximum power of a cell, in combination with I_{sc} and V_{oc},

$$FF = \frac{P_{MPP}}{V_{oc} * I_{sc}} \tag{4.3}$$

The FF is used to determine the efficiency η (measured in %) of a solar cell by,

$$\eta = \frac{FF * V_{oc} * I_{sc}}{Irradiance} \tag{4.4}$$

with the irradiance typically being 100 $^{mW}/_{cm^2}$ at standard AM1.5 test conditions. Further interesting to know about a cell are its shunt resistance R_{SH} and series resistance R_S. Both need to be low, to obtain a high efficiency. A high shunt

resistance suggests a larger number of manufacturing defects, a high series resistance suggests, a high (contact) resistance (between) of front and back contact.

For this project, two times I-V and MPP measurements were conducted. The first time on a off-the-shelf solar cell, using an ISRU solar concentrator system, the second time, on solar cells built on basaltic glass. The following provides details on both measurements.

Solar concentrator Testing

To measure the performance of the basaltic mirrors under laboratory conditions three separate measurements were conducted. First, a reference solar cell without reflector was measured, second a concentrator equipped with reference mirrors was measured and third a concentrator equipped with the basaltic glass mirrors. The test setup is depicted in figure 4.8. Shown is a schematic of the laboratory setup used to measure the performance of the basaltic glass mirrors versus the performance of reference mirrors.

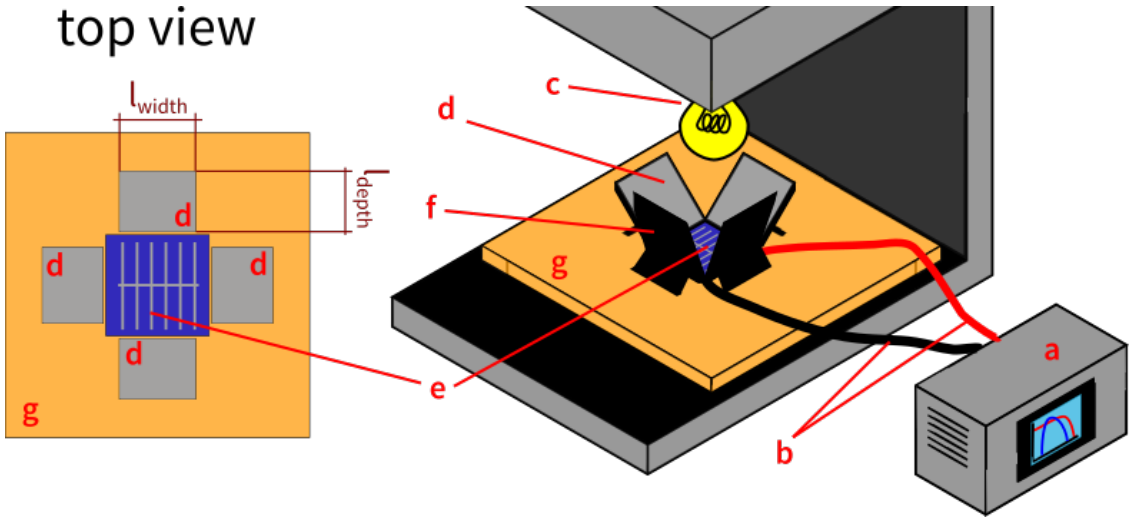

Figure 4.8: Shown in this schematic is a test setup used to analyse the performance of a solar concentrator equipped with basaltic glass mirrors. The performance of a solar cell (e) was measured with an RO3 (a), which was connected to the cell via two wires (b). Simulated sunlight (AM 1.5) hits the cell (e) as well as the mirrors (d). The setup was exposed from above (c) and the mirrors where held in place by 3D printed mounts (f). The entire setup was placed on a Kapton® tape covered test bench (g).

The used solar simulator for these experiments was an ABET Technologies Sun 2000 Solar Simulator with a field size of 160 * 160 mm, a 550 Watt lamp and irradiance of AM 1.5. The solar cell which was used as reference, was procured from RS components UK and was a SANYO Amorton AM-8701 cell, with an effective area of 54.3 * 53.0 mm. Its outer dimensions were 57.7 * 55.1 mm, its open circuit voltage V_{OC} was 6 Volts and its maximum output P_{max} was 190 mW

at AM 1.5 (100 $^{mW}/_{cm^2}$). The cell had an operational voltage V_{OP} of 4.6 V and an operational current I_{OP} of 41.2 mA. The device used to measure the I-V curves and the maximum power point was an RO3-series: I-V curve tracer with dynamic electrical load manufactured by TCS - Thermoelectric Conversion Systems. This system has a maximum continuous power dissipation in I-V Trace mode of 250 Watt, and input voltages ranging from 0 to 65 Volt (DC) as well as an input current ranging from 0 to 24 Ampere (DC). Its resolution for voltage measurements is 0.032 - 0.5 - 4 - 16 Volt (DC) and its voltage reading accuracy is ± 1 - 0.5 - 0.3 - 0.3 %.

The mirror mount design, discussed in section 3.4.2, was initially designed for the basalt glass mirrors, then adapted to fit reference mirrors procured from THOR labs as well. These reference mirrors where aluminium front coated, square shaped (2.54 * 2.54 cm) mirrors with a thickness of 3.2 mm. Since a single reference mirror by itself did not offer the same reflective surface area as a single basaltic glass mirror, two mirrors had to be mounted next to each other to form a large enough surface. The resulting increased surface area, which was larger than the basaltic glass mirror's, had to be blindfolded to adjust the reference mirrors surface area to exactly the surface of the basaltic glass mirrors. The modified design of the mirror mount for the reference mirrors is depicted in figure 4.9. All outer dimensions were kept the same as for the basalt glass mirror mount, to assure that the angle in-between mount and test bench remains the same and comparability was given.

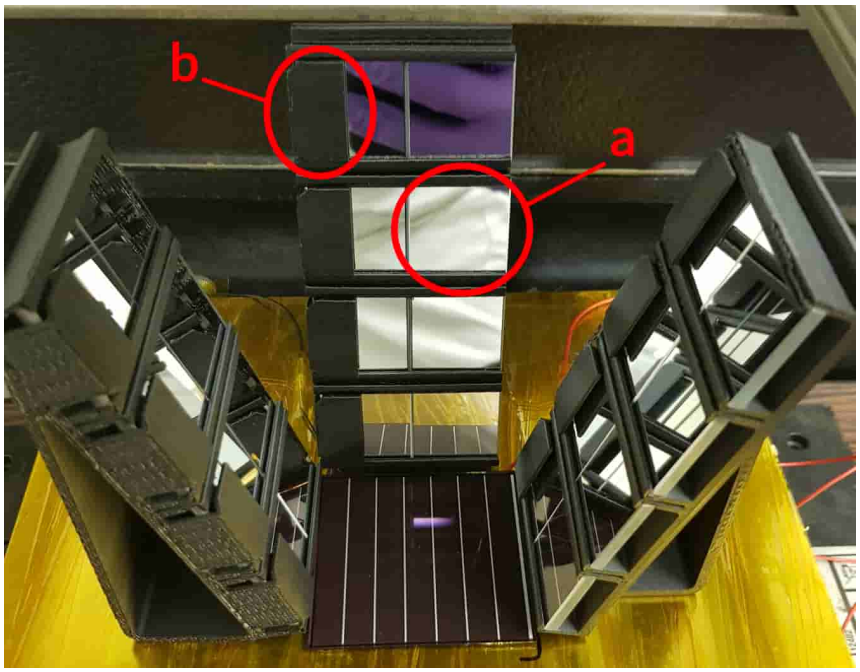

Figure 4.9: The image shows the test solar cell on the solar simulator surrounded by three sets of reference mirrors (a) mounted in the adapted mirror mount. The blindfold compensating for the difference in surface area is circled and marked (b).

The mirror surface area positioned next to the solar cell should increase the power output of the solar cell in the centre. To understand better how much the power output could be increased, the actual increase in surface area needs to be calculated. Using the calculated values from section 3.4.2, the dimension of the solar concentrator, seen by the solar simulator from on top (in figure 4.8 left), can be calculated. Using $l_{refl} = 109\ mm$ and $\Theta_{out} = 73°C$ can be calculated,

$$l_{depth} = cos\ \Theta_{out} * l_{refl} \tag{4.5}$$
$$l_{depth} = 31.87\ mm \tag{4.6}$$

l_{depth} indicated on the left in figure 4.8. Using this calculated depth and the width of the mirrors (l_{width}), a single concentrator element surface area $A_{element}$ is,

$$A_{element} = l_{depth} * l_{width} \tag{4.7}$$
$$A_{element} = 1275\ mm^2 \tag{4.8}$$
$$A_{concentrator} = 4 * 1275\ mm^2 \tag{4.9}$$
$$A_{concentrator} = 5100\ mm^2 \tag{4.10}$$

with the entire concentrator having four times the surface, thus $A_{concentrator}$. Since some of the surface area of the mirror is comprised of non-reflective black parts, the area needs to be adjusted. Out of $l_{refl} = 109\ mm$ only 4 * 21 mm = 84 mm is actual mirror surface area size. Hence, only 77 % of the length is made of mirror, the rest is black non-reflective. Adjusting the surface area accordingly leads to,

$$A_{concentrator} = 5100\ mm^2 * 0.77 \tag{4.11}$$
$$A_{concentrator} = 3930\ mm^2 \tag{4.12}$$

which is the surface by which the illuminated surface area should increase. Compared to the surface area of the solar cell A_{cell},

$$A_{cell} = 54.3\ mm * 53\ mm \tag{4.13}$$
$$A_{cell} = 2878\ mm^2 \tag{4.14}$$

this is an increase in surface area of approximately 137 %. This means that the solar cell surface is a 100 % and the mirror surface area adds additional 137%. In total, the illumination area is therefore increased to 237 %.

Solar Cell Testing

After the I-V performance of the solar concentrators has been determined, manufactured solar cells have been characterised the same way, using a solar simulator to conduct I-V trace measurements. Therefore, reference cells and cells built on basaltic

glass have been measured with a double source sun simulator [518] from Wacom (WXS-140S-super, Wacom Electric Co., Ltd., 541 Tanaka, Fukaya-Shi, Saitama, Japan), under standard illumination test conditions (class A spectrum, 100 $^{mW}/_{cm^2}$, 25 °C) [519–521]. Further details on the measurement process are provided in [522].

4.3.3 External Quantum Efficiency (EQE)

Standard testing for solar cells includes measurements of the Quantum Efficiency (QE), the conversion efficiency and reflectivity. The primary focus of the measurements was on single cell measurements, rather than overall modules or systems. However, determining the total losses of the system, including electronics and wiring, will be relevant once an overall system is designed using ISRU manufactured solar cells. Electric energy losses, due to conversion losses, or electric resistance losses, will occur in an actual solar cell power system, on the lunar surface. Thus each cell used/manufactured will need a minimum surface area, as well as efficiency to be practical and economically viable. Improving these two parameters was not the focus of this study, which focused on manufacturing a working solar cell in first place, since this has never been done before. This further included, that the losses of the entire solar power system, using solar cells for power generation, was neglected.

External Quantum Efficiency (EQE), the probability for an incident photon to generate an electron contributing to the short circuit voltage [523], was recorded on working cells. EQE is also called the incident photon-to-current efficiency [524] and is a measure of how good a cell absorbs and converts light into power. These measurements were dependent on the material deposited on the substrates and the wavelength of the simulated sunlight. For actual lunar cells, measurement using a solar irradiance of 1366 $^{W}/_{m^2}$ (AM0) will need to be used. On Earth however measurements under AM1.5 are more common, and therefore allowed for better comparability with other cells. Thus measurements were carried out under an AM1.5 exposure.

EQE measurements of the actual basaltic and reference solar cells were conducted with an interference filter setup[2] - incorporated into the optical path of the Wacom sun simulator [518], used for I-V characterisation already. Interference filters were necessary to reduce the monochromatic light from the solar simulator to only a fraction. For each cell, only small spots were measured, illuminated in-between the samples grids, to verify the I_{SC} values from the I-V measurements. Each of the four cells manufacture (2 basaltic, 2 reference) was measured with 0 V and -0.2 V reverse bias (to improve carrier collection), leading to a total of eight EQE curves. Further details of the utilised EQE setup are described in [522].

The following chapter 5, will detail performance results of all samples manufactured and measured using described methods and equipment.

[2] 21 interference filters, wavelength range 357 to 1103 nm, Full Width at Half Maximum (FWHM) $\approx$ 10 nm.

5 Experimental Results and Discussion

This section details experimental results of, regolith simulant analysis, physical and optical analysis of substrates manufactured from these regolith simulants and performance characteristics of the final solar conversion devices.

5.1 Utilised Raw Materials - Simulants

Since actual lunar regolith is not available on Earth for large scale manufacturing tests, regolith simulants have been utilised by scientists in the past. Each simulant aims to mimic certain properties of the actual lunar regolith, such as optical, geochemical or magnetic properties. Although a variety of simulants is commercially available, reliable characterisation data is not or only partially available. Therefore a thorough analysis of some of the available simulants was conducted. This includes analysis via methods of XRF, XRD, SEM/EDX, CHN, grain size distribution and microscopy of thin sections.

5.1.1 Overview of Selected Simulants

All regolith simulants that have been considered and analysed are depicted in figure 5.1, and their source and type is specified in table 5.1. The bulk part of all simulants chosen is silicon dioxide, since this is the case for most lunar rocks as well. However, simulants were designed with a comparably low silica content, compared to Earth's crustal material. Lava and/or scoria (lava sand) is, mineralogically seen, a good source material for simulants, since it is composed of igneous rocks, similar to lunar mare regolith. Since material on the lunar surface is not weathering due to rain, wind or frost, it has only been geochemically altered by space weathering over the last billion years, which is why rather young lava flows are preferred as a source in addition [231]. These flows usually show little or no alteration (geochemical modifications) compared with older flows.

Additional information on simulants are listed hereafter:

- **BP-1**: *Black Point 1* is sourced from the Black Point basalt flow (San Francisco Volcanic Field) in northern Arizona [238]. The igneous rock mined from that quarry is crushed to match the grain size distribution of the Apollo soil samples. It is mined close to the surface and was manufactured for the lunar surface lab at NASA Swamp Works. The sample for this research was provided by Rob Mueller at Swamp Works (KSC/NASA).

Figure 5.1: Overview of regolith types used and analysed. Fltr: BP-1, EAC-1, FJS-1, JSC-1A, JSC-2A, JSC-2A-TG, LHT-2M, LHT-3M (Scale in cm).

- **EAC-1**: *European Astronaut Centre 1* is sourced from a quarry called "Huehnerberg" located in the Eifel region south of Cologne, Germany. The igneous rock is mined close to the surface from that quarry and is crushed to match the grain size distribution of the Apollo soil samples. Samples were provided by the European Astronaut Centre, sourced from the "Rheinische Provinzial Basalt- und Lavawerke GmbH & Co. oHG". EAC-1 is made of Na and K rich basalt from the Miocene Epoch, and with an age of about 20 Ma, is a rather old material compared to most other simulants.
- **FJS-1**: *Fuji Japanese Simulant 1* was procured from the Shimizu Corporation, and sourced near Mount Fuji. The igneous rock mined from that quarry is crushed to match the grain size distribution of the Apollo soil samples. Two times two kilogram were ordered and both batches were made in 2007 and sourced from a approximately 10000 years old lava flow from Mount Fuji.
- **JSC-1A**: *Johnson Space Center 1A* is sourced from the volcanic ash field (San Francisco Volcanic Field, $35°19'29.6''N 111°17'03.0''W$) in northern Arizona. Igneous rock was crushed to match the grain size distribution of the Apollo soils range. JSC-1A is no longer commercially available, and a total of 14 metric tons have been produced. A detailed geochemical characteristiaion can be found in [525]. Although this batch was manufactured by Dr. James Carter, the sample for this research was provided by Rob Mueller at Swamp Works (KSC/NASA), who still had this type of regolith in stock.
- **JSC-2A**: *Johnson Space Center 2A*. The JSC-2A simulant is produced by and procured from Zybek Advanced Products in Westminster (CO), USA. It was manufactured to be similar to JSC-1A and was sold with the annotation "Bulk/Excavation Grade: crystal + glass; Approximately JSC1A" [526]. A bucket of 10 kg has been procured from this company.
- **JSC-2A-TG**: *Johnson Space Center 2A Technical Grade*. The JSC-2A simulant is produced by and procured from Zybek Advanced Products in Westminster (CO), USA. It was sold with the annotation "Technical Grade; crystal + glass + agglutinate"[526]. One kilogram of material was procured of this "technical grade" version.
- **NU-LHT-2M**: The NU-LHT-2M, simulant was designed and manufactured by the United States Geological Survey (USGS) as a follow-up of the NU-LHT-1M, which was a prototype. The name is a combination of **N**ASA/**U**SGS-

Lunar **H**ighland **T**ype - 2 **M**edium, and it was sourced from the Stillwater Mine ($45°23'26.9''N109°52'04.9''W$) in Montana (USA). Stillwater norite, anorthosite, hartzburgite, and twin sisters dunite was combined with partially and fully melted stillwater mill waste. Furthermore, version two contains ilmenite, synthetic whitlockite, natural fluor-apatite, and natural pyrite [527]. This batch was manufactured by USGS in about 2009, and is no longer available for sale. However, the sample (approx. 30g) was provided by Rob Mueller at Swamp Works (KSC/NASA) who still had this type of regolith in stock.

- **NU-LHT-3M**: Similar to NU-LHT-2M, but produced by Zybek Advanced Products in Westminster (CO), USA, rather than USGS/NASA, NU-LHT-3M, is also a lunar highland type simulant. It is supposed to be similar to NU-LHT-2M and was still commercially available in 2018, although their website stopped working in 2016 [526]. A total of 3 kilograms was procured in a batch of 1 kg and a second of 2 kg.

Table 5.1: List of analysed lunar regolith simulants and their sources

Regolith Simulants	Type	Source
BP-1	Mare	NASA KSC, Cape Canaveral USA
EAC-1	Mare	ESA EAC, Cologne Germany
FJS-1	Mare	CSP Japan Inc., Tokyo Japan
JSC-1A	Mare	NASA KSC, Cape Canaveral USA
JSC-2A	Mare	Zybek Advanced Products, Westminster USA
JSC-2A-TG	Mare	Zybek Advanced Products, Westminster USA
NU-LHT-2M	Highlands	USGS/NASA KSC, Cape Canaveral USA
NU-LHT-3M	Highlands	Zybek Advanced Products, Westminster USA

The simulants listed above have been chosen to be tested with respect to their relevant characteristics for manufacturing glass. This includes geotechnical analysis (chapter 5.1.2), as well as geochemical analysis (chapter 5.1.3). After analysis, a set of simulants has been chosen (chapter 5.1.4) for manufacturing solar conversion devices.

5.1.2 Geotechnical Features

Geotechnical features such as grain size distribution or grain shape may be relevant for a number of lunar research fields. Such mechanical features are most often relevant to determine soil mechanics for rover wheels, for example, or to determine the acoustic behaviour of the regolith. However, geotechnical features may potentially have impact on melting/manufacturing processes, as well as separation/purification methods used. The following determines these characteristics and compares them to the actual lunar regolith.

Regolith Grain Size Distribution

The grain size distribution of the regolith is different for each landing site on the Moon. Therefore, it seems only fitting that different regolith simulant types have different grain size distributions as well. These may impact how regolith can be

processed since simulants have a rather large fraction (> 45 %), which is very fine (< 63 μm) which may, for example lead to clogging. The distribution, for all simulants analysed, is achieved by sieving the raw regolith into categories and recombining these to a new grain size distribution. This is usually done by the manufacturer according to the costumers/community's specifications.

Figure 5.2 shows the grain size distribution of analysed regolith simulants, as well as four selected lunar soil samples from the Apollo mission analysed in the Lunar Soil Grain Size Catalog [155]. All regolith simulants shown in the graph show the grain size distributions of the simulant batches used for this work. The selected actual lunar soil samples are described further in [155], and are here as a reference. They do not, however, represent a mean or median distribution of the actual lunar soil, and are rather a spot analysis. A reference for average lunar grain size distribution can be found in [154].

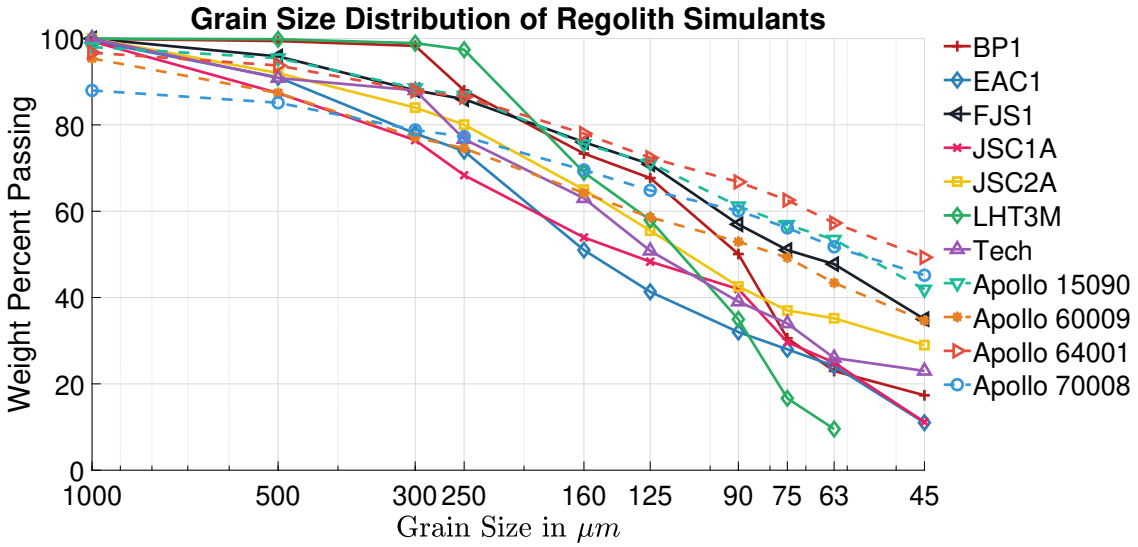

Figure 5.2: Grain size distribution of selected lunar regolith simulants. Detailed values are shown in table A.3 in the appendix. 15090: Apollo 15, subsample 15091, 1 - close to surface. 60009: Apollo 16, subsample 454 - drill core $\approx$ 29 cm below surface. 64001: Apollo 16, subsample 375 - drill core $\approx$ 59 cm below surface. 70008: Apollo 17, subsample 245 - drill core $\approx$ 60 cm below surface.

The comparison shows that the actual lunar soils (dashed lines) do contain more, larger particles (> 1 mm) and a larger fraction of fine particles (< 45 μm) than the simulants. The larger fraction in the samples is likely found, because the samples are taken from drill cores, which reached down into the lunar soil up to 60 cm. This shows that if the process requires larger particles, those could be found and sourced on the lunar surface. This shows that particles of grain sizes in-between 1 mm and 45 μm are abundant on the Moon and, therefore, if the process would require it, could be targeted specifically and gathered in quantities of multiple metric tons.

Grain size distribution is artificially chosen by the manufacturer and may or may not be close to what one can expect on the surface. For experimental purposes, it is

however, suitable to (if necessary) specifically target a certain grain size distribution and acquire it from the bulk regolith simulant. Considering the scenario of an actual lunar base, sieving equipment is comparably light to bring to the lunar surface, and has little power consumption as well as no consumables. Therefore, the grain size distribution can be altered according to the needs.

The aim of this project was to use a variety of regolith compositions, including a variety of different grain size distributions, to develop a manufacturing process, which is independent of the material composition and mechanical properties. As depicted in figure 5.2, the analysed simulants show such a variety in grain size distribution and were, therefore, considered suitable for the experiments. By using those regolith simulants with unaltered grain size distribution for most experiments, the process could be tested to work with a variety of input materials.

Grain Geometry

Lunar regolith simulants are sourced from cinder quarries (volcanic ash) or quarries mining basaltic deposits from igneous rock. After coarse sieving, either impact milling or a jaw crusher deliver the correct grain sizes to fit a specific grain size distribution. The manufacturing process, therefore, largely determines the grain geometry. Figure 5.3 and figure 5.4 show the grain geometry of all utilised simulants. Shown in figure 5.3 is an SEM scan of EAC-1, FJS-1, JSC-2A and LHT-3M simulant, with the grain size distribution of > 300 μm. Figure 5.4 shows the other four simulants (BP-1, JSC-1A, Tech and LHT-2M) in a 30 μm thick thin section of grain size distributions from 1 mm to 500 μm. The focus of this section is to analyse the grain geometry. Other characteristics, such as elemental composition or mineralogy, will be discussed in the next chapter.

The SEM images in figure 5.3 shows the silhouette of regolith grains as well as cross sections of the grains. The samples have been prepared as described in section 4.1.1. The black spots in the images mark bubbles in the resin or voids in the grains. Simulants EAC-1, FJS-1 and LHT-3M have probably been jaw-crushed to grain size specifications from raw material mined from their quarries. In figure 5.3, this can be seen by the sharp edges compared to JSC-2A, which has probably been impact-crushed rather than jaw-crushed. Impact crushing brakes down the mined material with itself, therefore the raw material particles impact with on themselves. This creates a more “Moon like” grain shape and minimises the metal contamination caused during processing. Jaw crushing uses a metal jaw to break the raw material into smaller pieces this leads to potentially sharper edges. In particular, EAC-1 shows larger, thin, sharp edged grains than other simulants, as depicted in figure 5.3.

Due to a long and thin geometry of the grains, with largest dimension of (in the case of EAC-1) more than 1 mm, grains may still fall through a 1 mm test sieve. Since their smallest dimensions/cross sections are smaller than 1 mm. As such, grain size distribution graphs merely show the grain size distribution with respect to the smallest cross section of the grains. This may be relevant for transport of regolith via tubes or funnels, since one dimension of the grain may be larger than

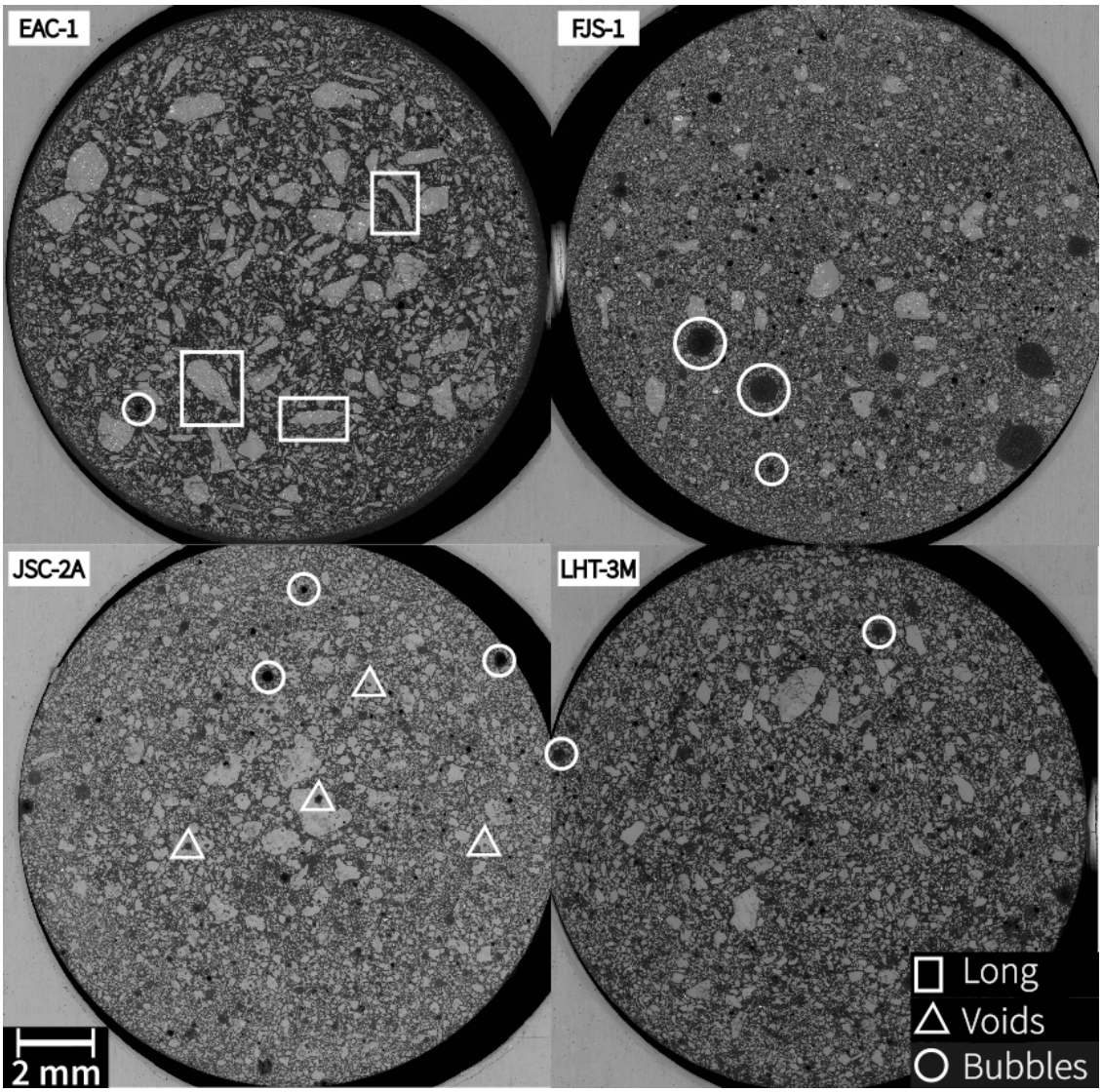

Figure 5.3: SEM image of four regolith simulants showing: EAC-1 (top left), FJS-1 (top right), JSC-2A (bottom left), and LHT-3M (bottom right) regolith simulant with a grain size distribution of > 300 μm. Black areas show the resin which surrounds all grains, dark grey to white areas are regolith grains. Red circles mark bubbles in the resin, green circles voids in the grain and blue squares comparably long and thin grains.

the pipe/funnel and lead to blockage. For this work, all systems have been designed with diameters larger than 1 mm and blockage was not encountered. However, for future projects/missions this may need careful consideration.

Looking at the actual lunar regolith's shape [528], it seems much more likely that the grain shape will look more like the one of JSC-2A. As shown in figure 5.3, in the image on the bottom left, JSC-2A grains seem to be more equant and rounded compared to the other three samples shown in this figure. On top of this, JSC-2A grains show larger voids within the grains than the other samples. This shape and these voids are typical for young erupted material from a volcano, and show indeed

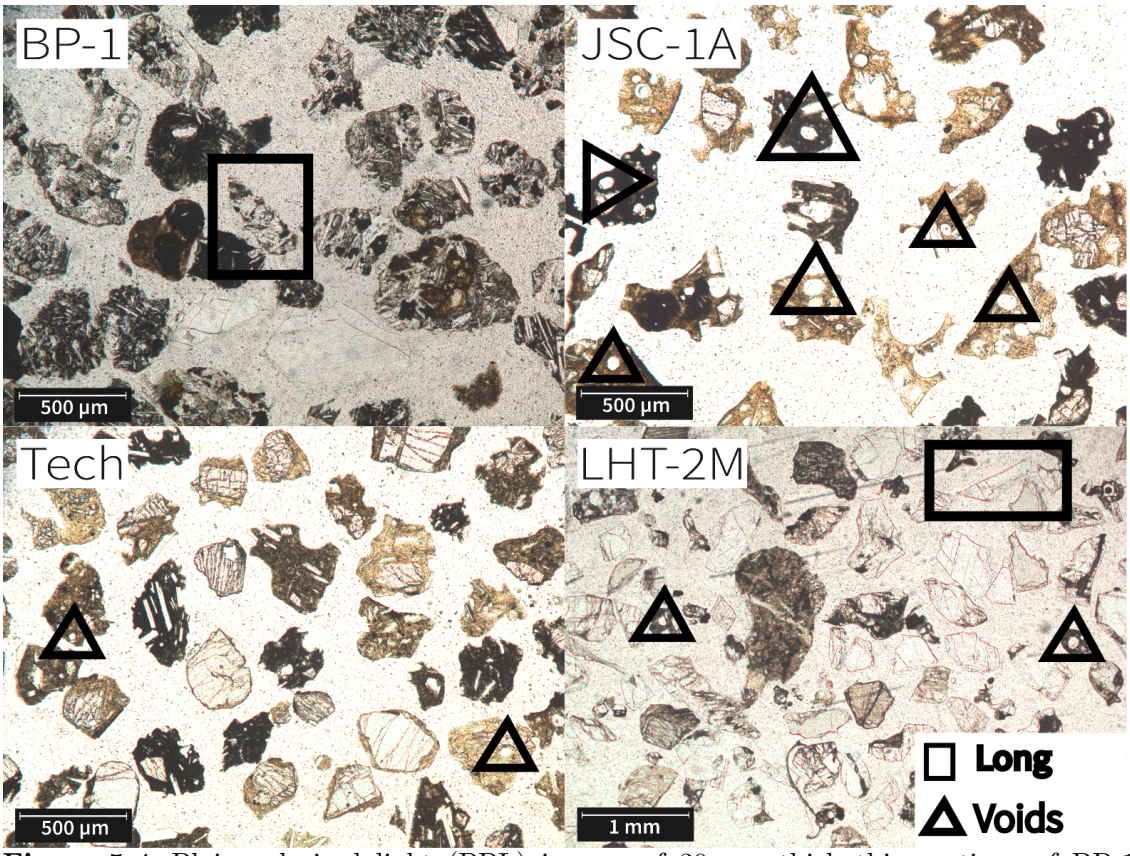

Figure 5.4: Plain-polarised light (PPL) images of 30 μm thick thin sections of BP-1 (top left), JSC-1A (top right), JSC-2A-Tech (bottom left) and NU-LHT-2M (bottom right) with grain sizes from 1 mm to 500 μm. Green circles indicate voids (resides or fluid inclusions) in the grain and blue squares comparably long and thin grains.

that JSC-2A has not been jaw-crushed. The porous structure of the JSC simulants leads to decreased grain stability when pressed or compacted, which could be observed during an experiment using regolith as grinding powder.

The thin sections shown in figure 5.4 also reveal grain shape. Simulant samples for this experiment were prepared as described in section 4.2.1 and the image in figure 5.4 shows PPL images of the four simulants. This way of visualising the grain geometry differs from SEM, shown in figure 5.3, and provides extra clues. Both in combination can be used to look at the grains geometry and learn more about it. One of the differences is that it is harder to see voids in the grains in just plain-polarised light, since some minerals appear transparent on these images. Hence, these minerals look much the same as voids, which are also transparent. However, putting an optical image of the grains next to an image taken under crossed polars (section 5.1.3) makes grains easier to distinguish.

Looking at BP-1 and NU-LHT-2M, similar shapes can be observed, sharp edges and a rather square shape. This is in line with the shape of the previously discussed crushed simulants and suggests that also BP-1 and NU-LHT-2M have been crushed

from larger rocks. Finally, JSC-1A and JSC-2A-Tech ("Tech") show voids in the grains, round edges and an overall rather equant, rounded grain shape. That makes them similar to JSC-2A (as shown in figure 5.3) and suggests that these two materials are also not crushed. Looking at the grains' voids of JSC-1A and JSC-2A, both show similar voids/bubbles, which have formed during eruption. JSC-2A-Tech on the other hand shows grains with only very small voids and although the outer shape of the grains is similar to JSC-1/2A the JSC-2A-Tech grains contain more solid minerals. In the thin section image, voids are indicated by transparent areas with no cleavage or streaks through them.

Overall, grain shape gives an indication to how the grains were processed and resulting from that, how the grains may behave during processing. Examples of process areas that may be impacted by the grain size and distribution are transport and mechanical processing, but also heating and melting. Melting can furthermore be impacted by volatiles, which may be trapped in the porous grains. If not compressed and/or ground probably before melting, bubbles can form in the melt and form a foam, rather than a solid glass.

Next, a closer look at the geochemistry and mineralogy will show further differences in-between the different simulants.

5.1.3 Geochemistry

The lunar regoliths' average composition was discussed in chapter 2.2.1, where a comparison of the average lunar regoliths' elemental composition with the average composition of Earth's Crust (table 2.2) showed that their composition is similar. This is why analogue materials to the lunar regolith can be found on Earth. These materials are, to some degree, similar to actual lunar material and may, therefore, be suitable for Earth based experiments on lunar regolith. The rock type being closest to the lunar mare composition is basalt, in its various forms. This is why it is common to use basalt/fresh volcanic rock as raw material for regolith simulants. How similar (and therefore suitable for this study) the selected regolith simulants are to lunar material, with respect to their geochemistry, will be discussed in the following.

Most lunar regolith simulants are sourced from (extrusive) igneous rock found near (past) volcanically active regions on Earth. Igneous rock is typically made up of the minerals listed in chapter 2.2.1, which make up about 95 % of a basalt, however, there are several subgroups of basalts which may contain for example larger amounts of olivine (olivine basalt) or feldspar than usual. As a reminder, a list of abbreviations of all minerals described in this thesis is found in the nomenclature at the beginning of the document and in the mineral overview table A.1 in the appendix.

Thin Sections

The theoretical background for this technique has been discussed in 4.1 thus, this section will show results obtained by applying this technique to all utilised regolith simulants. To analyse thin sections, a certain vocabulary is required to describe

morphological and optical properties, which will not be defined in here, since it is standard and contained in a number of sources [176, 529, 530]. Also, different colours and structures observed on the polarising microscope give clues to which minerals are contained in a sample. Since only basaltic materials are analysed, a certain set of minerals is expected to be found in the analysed samples. Hence, a brief summary of their appearance under the polarising microscope is given in the following before actual samples are discussed. This summary is derived from [530] and [531].

Clinopyroxene (CPx) *(e.g. Augite (Aug) or Pigeonite (Pgt))*: colourless or pale brownish or greenish, high relief, extinction angle 35 to 50 °, birefringence up to second order, twinning and zoning common. Very often contained in basic igneous rocks.

Orthopyroxene (OPx) *(e.g. Enstatite (En))*: pale green-pink (pleocroism), moderate to high relief, straight extinction, low to moderate birefringence up to first order, no twinning/zoning. Often contained in basic igneous rocks.

Plagioclase (Pl) *(Albite (Al), Oligioclase (Oli), Andesine (Ad), Labradorite (La), Bytownite (By), Anorthite (An))*: colourless, low relief, extinction angle -20 to -12° (Al), -12 to +12° (Oli), 12 to 28° (Ad), 28 to 39° (La), 40 to 52° (By), 52°+ (An) low birefringence, up to cream (Al,By), white (Oli,La), pale grey (Ad), or white/yellow (An), characteristic albite twins along the length as well as carlsbad and others. Bytownite and labradorite are often found in igneous rocks together with clinopyroxene and/or olivine.

Olivine (Ol) *(e.g. Forsterite (Fo) or Fayalite(Fa))*: colourless/pale green, moderate to high relief, although cleavage usually faint, straight extinction, very high birefringence up to third order, no zoning or twinning. Crystals often rounded with curving cracks, variably serpentinised. Very common in igneous rocks. Lack of colour and cleavage, and distinct birefringence make it easy to spot.

Oxide Mineral (OM) *(e.g. Titanomagnetite (TMag))*: opaque, no relief, no extinction; isotropic minerals have no birefringence, no zoning or twinning, characteristic octahedral crystal shape.

Alterations (Alt) *(e.g. Chlorite (Chl))*: green/brown, pleochroic, low relief, defuse/no extinction. Indistinct/Platy habit. Common in basic rocks as an alteration product with anomalous birefringence.

Depicted in figure 5.5 are thin section images of BP-1 simulant (left) and EAC-1 simulant (right). The top shows images with XPL and the bottom in PPL.

BP-1 one (left) shows thin white, needle like structures under XPL, which are transparent under PPL, indicating plagioclase. It seems most likely that plagioclase has intergrown with pyroxene, since next to the transparent plagioclase

grey/green minerals can be seen under the PPL. Under XPL these minerals are brown/orange/magenta colour, which would fit with pyroxene, likely CPx. Adding to that is the high relief under PPL. The green/brown mineral (XPL) at the bottom middle, which appears transparent in the bottom image, shows a rounded shape with curved cracks, typical for olivine. Black spots in both BP-1 images could be (titano)magnetite ((T)Mag), since it is opaque. At the bottom right of both images (XPL/PPL), brownish regions (Alt) are shown, which could be pyroxene alterations such as chlorite or mixed clay caused by water altering the original rock. The two circled areas in the XPL image could indicate microlitic plagioclase, possibly iron rich.

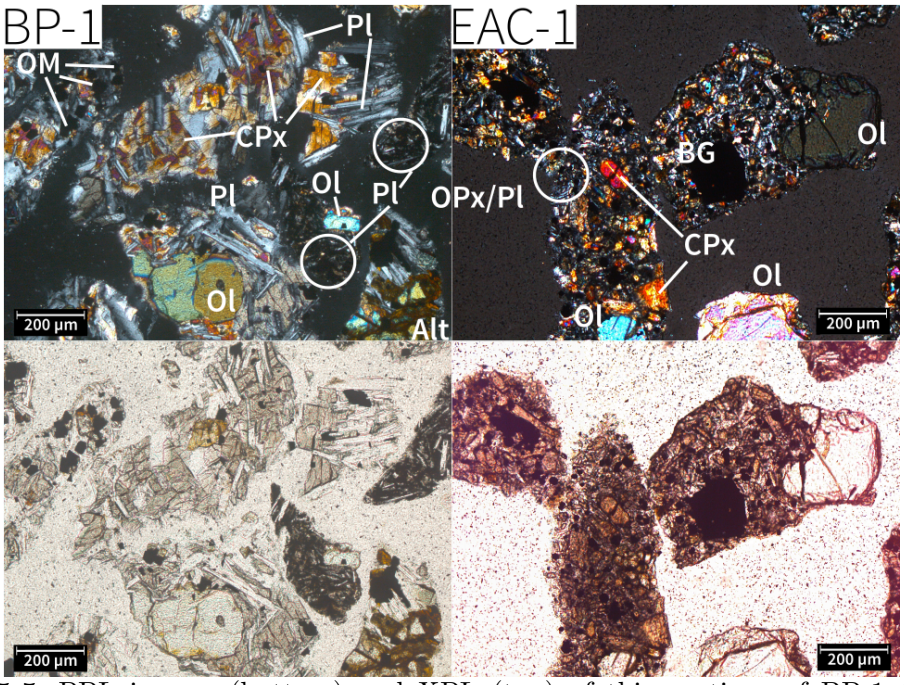

Figure 5.5: PPL images (bottom) and XPL (top) of thin sections of BP-1 (left) and EAC-1 (right). Grain sizes from 1 mm to 300 μm (EAC-1) and 1 mm to 500 μm (BP-1). Ol indicates olivine, (C/O)PX (Clino/Ortho)pyroxene, Pl plagioclase, OM oxide minerals, BG basaltic glass.

EAC-1 depicted in figure 5.5 on the right and in figure 5.6, shows black spots all over the depicted grains. Figure 5.5 shows one large grain in addition to the small ones. All EAC-1 images seem to show these oxide minerals which could be (titano)magnetite for example, since it just appears black in XPL/PPL independent of the angle. Further, it shows the typical octahedral or rhombic-dodecahedra crystal structure of Mag minerals. Other than the OM, in relation to BP-1 little can be seen what could be plagioclase in this sample. The grains rather show a very fine intergrowth of (probably) pyroxenes with olivines and (titano)magnetite. Looking at the PPL image at the bottom, almost no mineral is transparent other than the distinct olivine grains. The birefringence colour of the olivines contained suggest magnesium (Mg) rich olivine, since the pink/blue/yellow colour (XPL) is typical for Mg-rich olivine. With this unusually low plagioclase content and rather high pyroxene and olivine content, this could be an olivine basalt. The orange/red

crystals (indicated with CPx in the XPL) with distinct shape appear pale brownish in the PPL and could indicate clinopyroxene.

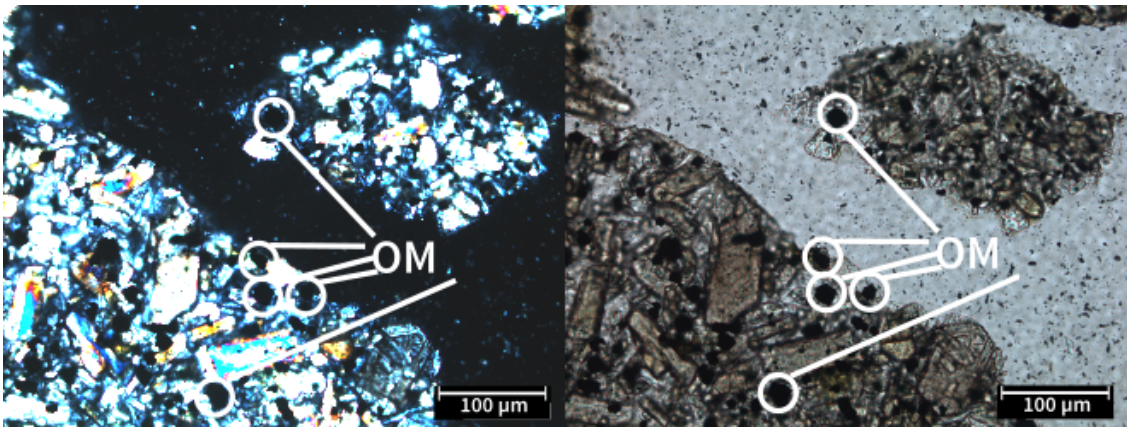

Figure 5.6: Thin section of regolith simulant EAC-1 grains, XPL (left) and PPL (right). White circles indicate possible locations for oxide minerals such as titanomagnetite for example.

Depicted in figure 5.7 are thin section images of JSC-1A simulant (left) and JSC-2A simulant (right). The top shows XPL images and the bottom PPL images.

JSC-1A displayed in the left two images in figure 5.7 shows sponge like grains with many voids. Furthermore, many of the grains seem to be made of amorphous glass in which a number of minerals are "trapped". Mostly seen is plagioclase with its typical twinning under the XPL and transparency under the PPL. Some of the grains appear darker than others, which suggest the presence of rather vesicular basaltic glass[1] with increased iron content. Other than glass, voids and plagioclase, olivine can be seen under the microscope, as well as some rare pyroxenes. The pyroxene circled in the top left image of figure 5.7 shows a possible clinopyroxene. It shows colours within the birefringence range of CPx, as well as twinning at two ends. Moreover, the PPL images shows high relief and distinct cleavage. Looking at the entire sample, pyroxenes are rare and the most dominant minerals are definitely plagioclase.

JSC-2A is shown on the right side of figure 5.7 and appears to show similar mineral content to the JSC-1A sample. Since JSC-2A is meant to be a replacement or follow-up of JSC-1A, this is to be expected. Also in this sample, voids, plagioclase and glass dominate the grains. Furthermore, olivine is present in some grains and is easier to find than pyroxenes. The potential large orthopyroxene crystal in the centre of the image, is also a rare find in JSC-2A. The pale blue colour (XPL) is within the first order or at the border to the second order on the birefringence chart. It shows a moderate to good relief and straight extinction with no zoning or twinning. Hence, in sum it appears to be an orthopyroxene. Also for JSC-2A, looking at the entire sample, pyroxenes are rare and the most dominant minerals

[1]Volcanic glass forms from lava which had a low crystal content.

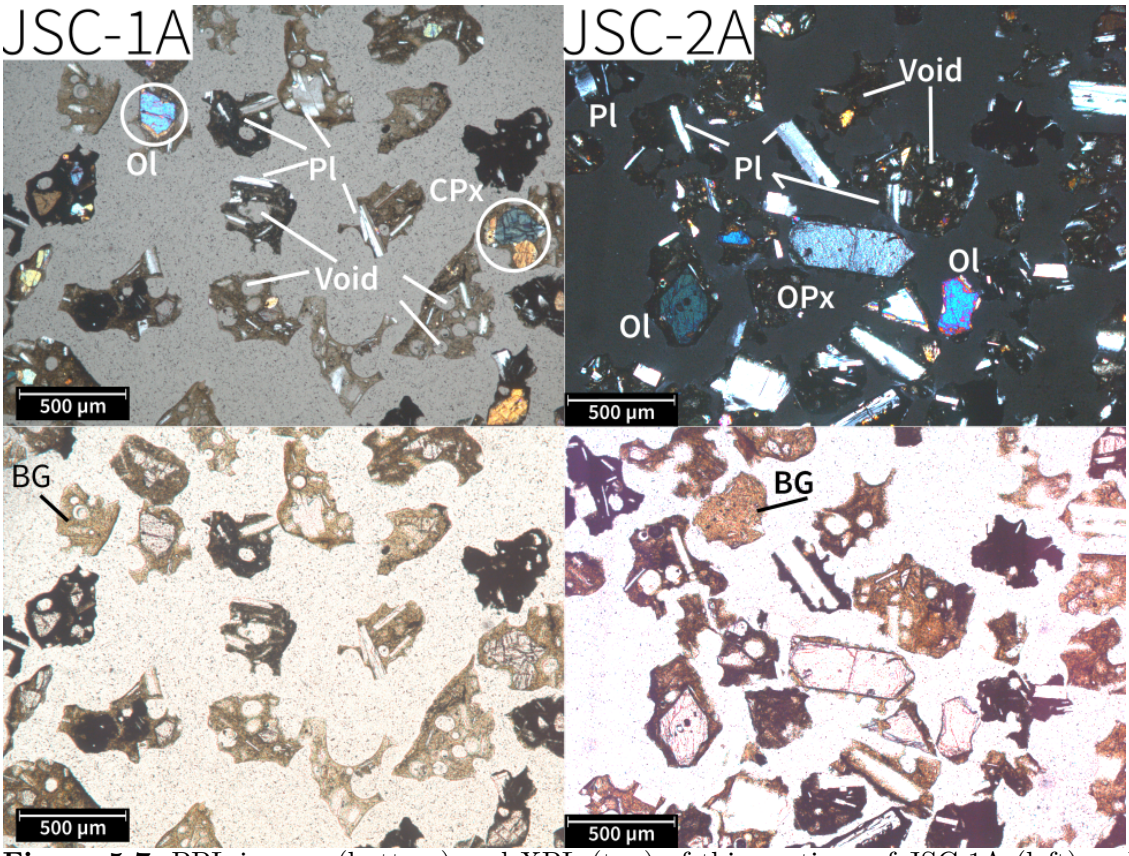

Figure 5.7: PPL images (bottom) and XPL (top) of thin sections of JSC-1A (left) and JSC-2A (right). Grain sizes from 1 mm to 300 μm (JSC-2A) and 1 mm to 500 μm (JSC-1A). Ol indicates Olivine, (C/O)PX (Clino/Ortho)pyroxene, Pl plagioclase, void empty spaces, and BG basaltic glass.

are definitely plagioclase minerals, followed by glass and olivine.

Depicted in figure 5.8 are thin section images of NU-LHT-2M simulant (left) and NU-LHT-3M simulant (right). The top shows XPL images and the bottom PPL images.

NU-LHT-2M is shown on the left side of figure 5.8, and at a first glance appears very similar to NU-LHT-3M depicted on the right. As for the JSC simulants, also here it makes sense, since LHT-3M is meant to be a replacement or follow-up of LHT-2M. The most prominent mineral in this sample is Pl with an estimated 50 - 60 area percent, followed by about 25 area percent of pyroxene. The plagioclase grains (indicated by *Pl*) show usual twinning in black and white with long parallel layers in XPL and are transparent in PPL. Two more specific examples of plagioclase feldspar have been highlighted in yellow and blue. Blue could be andesine (Ad) and yellow bytownite (By), this observation is based on their birefringent colour. It is, however, also likely that these grains are slightly thicker and could thus be different in colour. This is most likely true in case all plagioclase is from the same source, which should mean all plagioclase has the same composition. Indicated in red are potential orthopyroxenes (enstatite). Green marks an intergrowth of plagioclase

with pyroxene (possibly clinopyroxene (CPx)). In summary, this is not a simulant which is based on igneous rock as source material but rather plutonic rock, similar to the lunar highland regolith. Little to almost no intergrowth or mix of minerals is an indicator for this, as well as the grain shape (no voids, crushed from larger pieces) which is typical for non-volcanic rock. Due to high transparency of most grains, it is possible that this simulant is very iron sparse compared to the other samples.

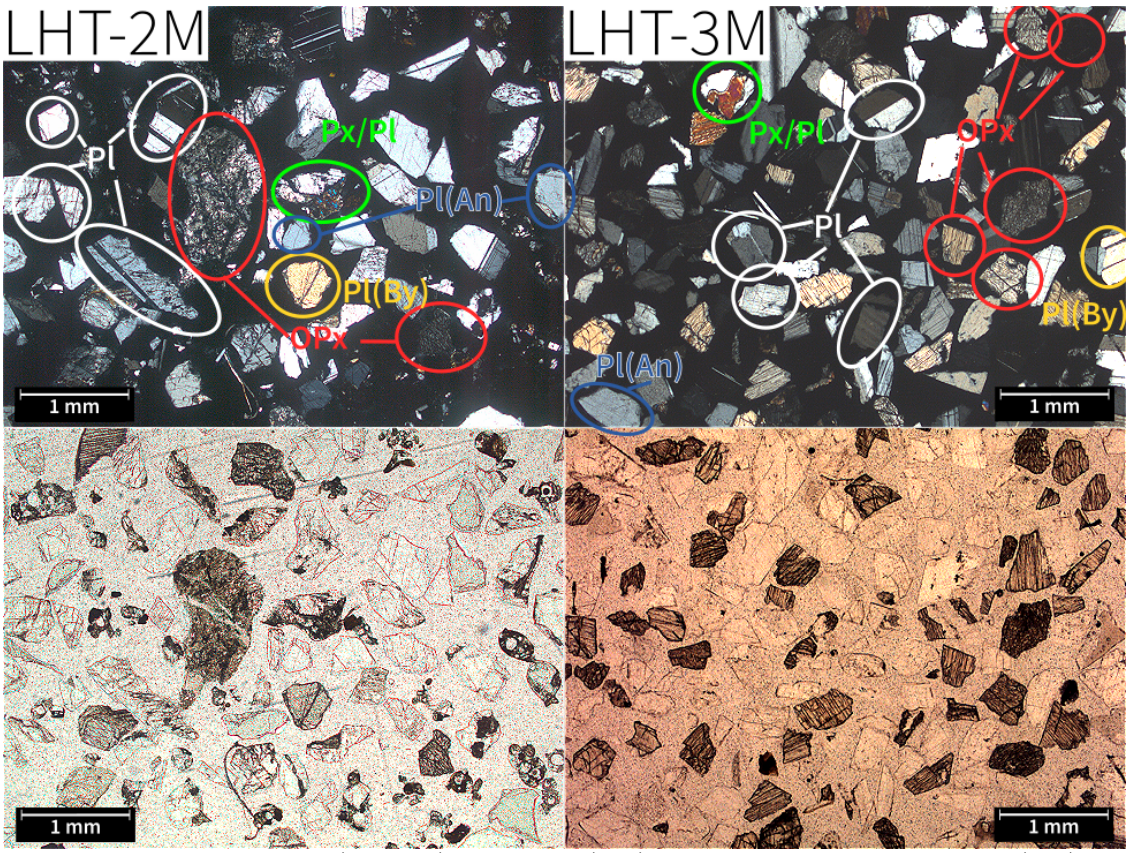

Figure 5.8: PPL images (bottom) and XPL (top) of thin sections of LHT-2M (left) and LHT-3M (right). Grain sizes from 1 mm to 300 μm (LHT-3M) and 1 mm to 500 μm (LHT-2M). (O)PX (Ortho)pyroxene, Pl(An/By) plagioclase (Anorthite/Bytownite).

NU-LHT-3M is shown on the right side of figure 5.8 and as discussed before, very similar to NU-LHT-2M depicted on the left. Also here, the most prominent mineral in this sample is plagioclase with an estimated 50 - 55 area percent, followed by about 30 area percent of pyroxene. Analogous to LHT-2M, the plagioclase grains (indicated by *Pl*) show usual twinning in black and white with long parallel layers in the XPL and are transparent in PPL. Specific plagioclase feldspar have also been highlighted here in yellow and blue, where blue could be andesine and yellow bytownite, basing the observation again on their birefringent colour. Indicated in red are potential orthopyroxenes (enstatite). This sample also contains multiple grains with intergrown plagioclase/pyroxene (possibly clinopyroxene) indicated in green. As LHT-2M, LHT-3M is not a simulant which is based on igneous rock, but

rather on plutonic rock. For the same reasons as LHT-2M, it is possible that this simulant is very iron sparse compared to the other samples.

Depicted in figure 5.9 are thin section images of FJS-1 simulant (left) and JSC-2A-Tech simulant (right). The top shows XPL images and the bottom PPL images.

FJS-1 is shown on the left side of figure 5.9. Typical for a basalt, about half the area is fine crystals of plagioclase, small long thin white/black twinned crystals, which seem to be the host in most cases for the other materials. About 20 percent of the sample could be pyroxene emended in the plagioclase host/ground mass. Although the XPL and PPL image show olivine as well as glass, both are rare in this sample. In fact, this was the only potential glass chip that was found on the sample slide. Olivine is not that rare but it occurs only in few small crystals.

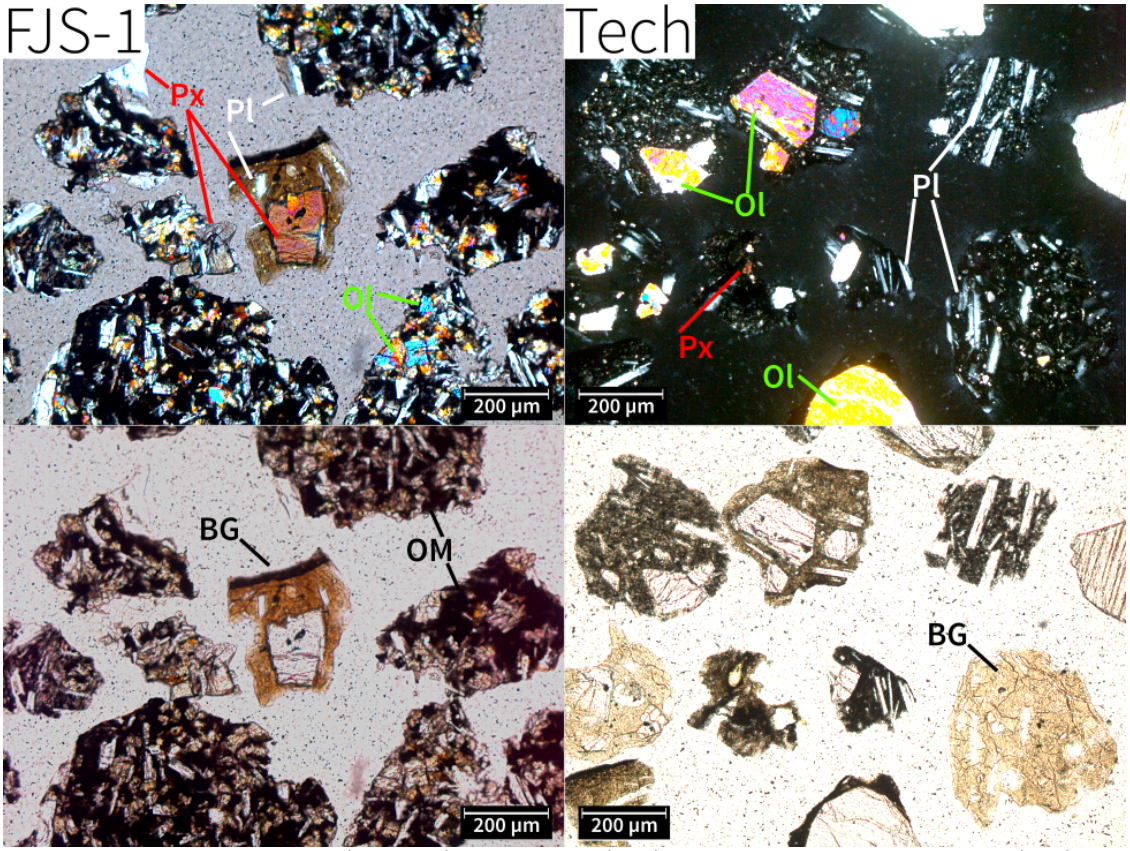

Figure 5.9: PPL images (bottom) and XPL (top) of thin sections of FJS-1 (left) and JSC-2A-Tech (right). Grain sizes from 1 mm to 300 μm (FJS-1) and 1 mm to 500 μm (Tech). Ol indicates Olivine, PX pyroxene, OM oxide minerals and BG basaltic glass.

JSC-2A-Tech shown on the right of figure 5.8 is a variation of JSC-2A. Compared to JSC-2A the "Technical Grade" version should, according to the manufacturer, have agglutinate (pyroclastic igneous rock) in addition to crystals and glass. However, this sample shows little to no difference to the JSC-2A sample, which may be a result of the sieving process, which removed larger particles, potentially include

agglutinate. As for the JSC series observed before, the main mineral is plagioclase feldspar, with smaller amounts of olivine and amorphous glass. Also here, very small minerals could be seen that resemble pyroxenes. Overall, fewer voids are observed in the grains, which may be a result of the modification process [245] applied to raw JSC-2A, or a less volatile-rich magmatic source with a lower degree of degassing. The apparatus [245] and method for producing a lunar agglutinate in these simulants involve hitting them with a plasma jet to create high temperatures. All in all this could/should be the most sophisticated lunar simulant; however, it does not appear to be significantly different in a way that would justify the 50 percent increased price. Moreover, JSC-2A was specifically engineered to mimic JSC-1A, which has been the standard in the scientific field of regolith simulants for years.

In conclusion, thin sections are useful to identify the bulk part of minerals contained in regoliths. What they cannot provide is an accurate quantitative analysis, but rather give only an estimate. In combination with techniques like SEM/EDX/XRD/XRF, the key of this analysis is to confirm the presence of a certain mineral or oxide detected by one of these methods. Once the mineral composition of a simulant or source material is known, it may be possible to relate manufacturing parameters to a source material composition.

SEM/EDX

Backscattered (BSE) SEM images individually are not quantitative measurements, but nevertheless give clues to what minerals may be contained (brighter spots may indicate high iron (Fe)), or at least what type of rock (igneous or pure mineral) a sample is made of. With the help of EDX (areal or spot analysis), SEM images can be more quantitative since EDX shows elemental composition on an SEM map.

The SEM images in figure 5.3 show different grain geometry looked at from a far distance. Zooming in on the image, individual grains can be examined for their composition. For each simulant a close up SEM image was taken and on that same frame, EDX measurements have been taken. These measurements lead to elemental maps and a combined phase map as, for example, shown in a compilation in figure 5.10 for EAC-1. These compilations have also been prepared for FJS-1, JSC-2A and LHT-3M and give clues to which minerals are contained in each sample. The phase map generated from the elemental maps has been enlarged to discuss spectra of similar coloured regions, which are composed of similar oxide/elemental compositions. Each colour's composition is listed and may point to a certain mineral being present in each particular regolith. Although maps do not give precise elemental compositions for given minerals contained in a simulant, they help constrain abundances/presence of certain minerals detected in the thin sections. Levels for Mn are too low to show up in areal analysis but are depicted in the elemental maps since small quantities are contained.

Main minerals to be expected here are again plagioclase feldspar, pyroxene and olivine alongside oxide minerals, such as magnetite, as well as alteration. Cross-

referencing this information with thin sections observations and the XRD and XRF results following allows a fuller picture of the mineralogy and geochemistry of the analysed simulants to be presented.

For each simulant, elemental maps of Oxygen (O), Silicon (Si), Aluminium (Al), Iron (Fe), Magnesium (Mg), Calcium (Ca), Sodium (Na), Potassium (K), Titanium (Ti), and Manganese (Mn) have been prepared and compiled in one figure, together with the BSE SEM image and the compiled phase map. Black areas indicate areas filled with resin or voids. The brighter a colour is displayed in a certain area, the higher the amount of that particular element contained at that spot. The colour is relative to the maximum amount of an element found in the displayed frame. Hence, if the largest concentration of titanium is 2.5 area percent (A %), the brightest spots will be those closest to that value. Area percent (A %) is not equal to weight percent (wt %). It is a measure of of how much area is occupied by a certain element rather than how much of the overall weight it constitutes. For more precise analysis of the minerals from EDX, further calculations would be necessary to determine the weight percent oxides as well as an endmember calculation. Since EDX is used here as a tool to confirm observations from the thin sections it is enough to look at the area percent results from the EDX to find out whether a certain mineral can be found in a simulant or not. A quantitative analysis of the mineral content is gained from the XRD results in the following section.

EAC-1 images are shown in figure 5.10 and 5.11. Latter one is an enlarged version of the phase map generated from the elemental maps shown in figure 5.10.

Figure 5.10 shows that all grains of the sample contain oxygen, although in different concentrations. This is not surprising since most of the material in Earth's crust is oxidised. Moreover, on the Moon, almost all materials found there are assumed to be fully oxidised. Looking at the silicon map, most but not all parts contain silicon. This means most but a few parts are likely to be silicates. The black spots within the grains here are no voids or bubbles but an absolute lack of silicon. Directly look at the iron and titanium chart next, the dark spots in the silicon map are brightly lit there. Together with oxygen, these are the only three maps, which show colour in these areas, and thus it is very likely that this may be an OM more specifically TMag. Looking at the Al-map, all areas lit in bright green (high aluminium content) are potentially Fsp. To determine which endmember the mineral is closest to, the Ca/Na/K-maps need to be crosschecked. Rich in Na, will probably be Albite (Al) rich; rich in Ca, probably An rich; and potassium rich will be an Alkalifeldspar (Afs). However, if the Ca-map does not show any overlap with the Na/Al-map, it is likely that these areas are Px. Checking with the Mg- and Fe-map, an idea can be gained whether or not this is true. Iron-, calcium- and magnesium-rich areas are likely to be CPx. Last, checking the bright areas in the Mg-map, clues to what could be olivine can be gained. The very bright (orange), homogenous grain towards the top left corner in the Mg-map is only lit in two more maps, silicon and oxygen plus a little bit in the iron map. This could be a Fo-rich Ol, as well as the areas with lower Mg and higher Fe could potentially be more

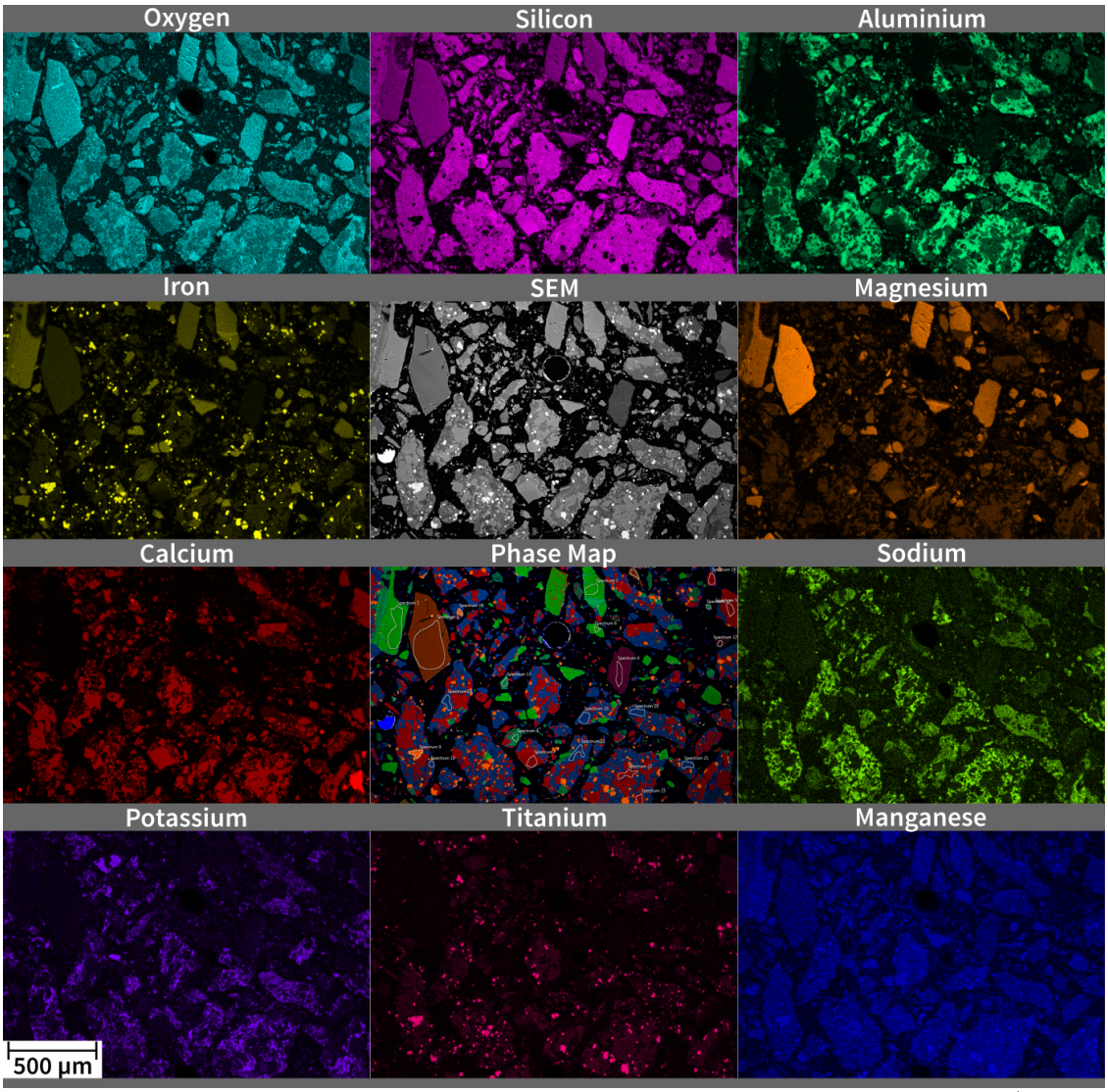

Figure 5.10: Elemental maps from EDX of EAC-1 plus the analysed SEM shot (middle-top) and a phase map (middle-bottom) compiled of the results from the elemental maps. All maps showing false colours.

Fa-rich olivines. Also supported by the fact that it has no Ca, Na, Ti, Mn. Figure 5.11 shows an enlarged version of the phase map included in the compilation of figure 5.10 as well. Followed by table 5.2 listing the EDX results for each spectra analysed.

Looking at table 5.2 it lists the mean elemental composition of an area circled in white in figure 5.11. The number indicates which spectra was analysed. The table is sorted by false colour groups according to the phase map (figure 5.11).

Starting from the top with the spectra coloured umber, the area percent values indicate the presence of O, Mg, Si and Fe in decreasing order. This composition is typical for olivines in particular very Fo-rich Ol, since the analysed areas show high Mg content. Similar for the purple series, most abundant elements are O, Si and

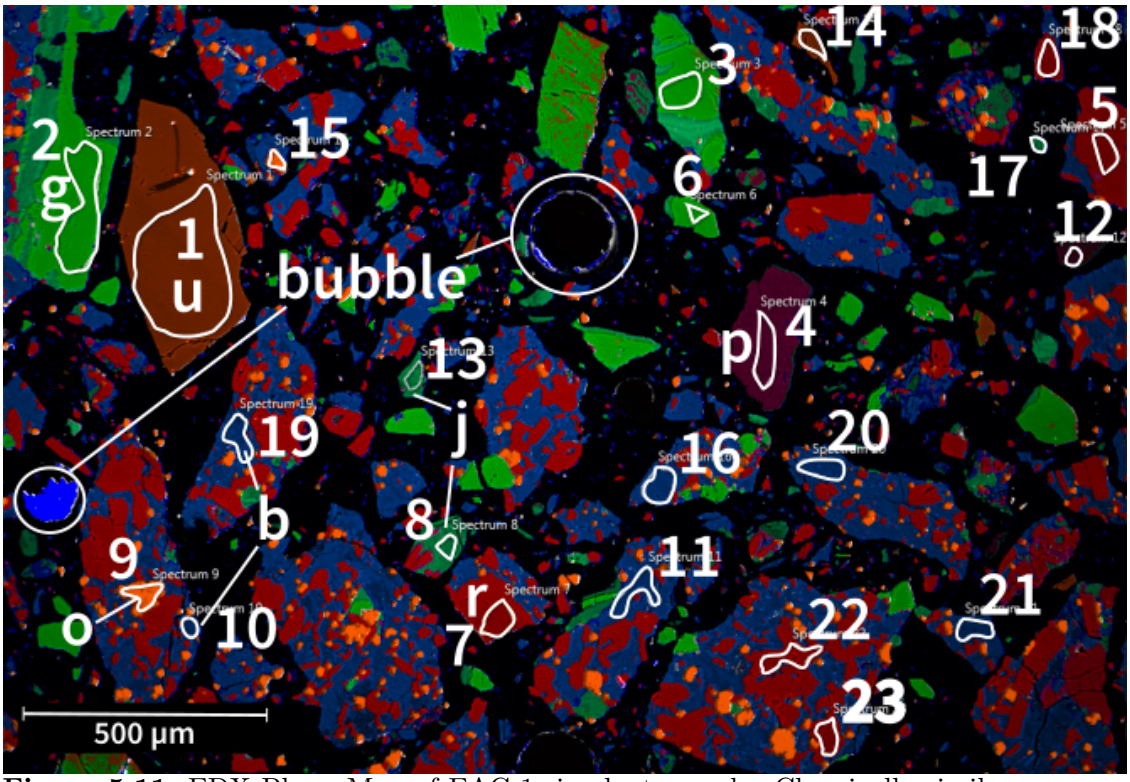

Figure 5.11: EDX Phase Map of EAC-1 simulant sample. Chemically similar areas are indicated in different (false) colours; blue (b), green (g), jade (j), orange (o), purple (p), red (r) and umber (u). Thin white circles indicate sampled areas.

Mg, with traces of Fe and Al for spectrum 4. The 1.1 A % Al found in spectrum 4 may be due to close proximity/embedded Pl, since Al is not common in Ol. Spectra shown in green on the phase map are as well likely to be Ol, this time with a rather high Fe content, although still smaller than the Mg content.

Next, the EAC sample shows hints that it may contain small particles of oxide minerals. Specifically titanomagnetite, which is suggested by zero silicon content as well as Fe, O and Ti being the only minerals detected. The shape, size and locations match the observations made in the EAC-1 thin sections in figure 5.5 (right side) and especially in figure 5.6. In the latter figure, the geometry of the grains does seem to be similar to the crystal shape of Mag or TMag. Solely judging from the results in table 5.2 the orange areas could also be Ilm ($FeTiO_3$).

Plagioclase is not as common in this sample as one could expect for a basalt. Although the blue areas indicate the presence of mostly An-rich Pl, it seems to be a little less abundant than for other basalts examined. Also traces of Mg (spectrum 20) and traces of Fe (spectra 11, 16, 19, 20, 21) suggest that the grains are an intergrowth of Pl and Px, typical in basalts. Red areas (spectra 5, 7, 18, 22, 23) show elements abundant in Px (Mg, Fe, Ca). Traces of Al show the same thing as the blue spectra, i.e. a potential intergrowth of Px with Pl. The traces of Ti could be due to small titanomagentite crystals contained in the areas, which the

Table 5.2: Elemental composition of EAC-1 spectra analysed on phase map shown in figure 5.11, values show A %

#	Colour	O	Si	Al	Fe	Mg	Ca	Na	K	Ti	Mn	Mi.	Prime
1	umber	32.6	17.9	-	7.3	28.1	-	-	-	-	-	Ol	Fo
14	umber	34	15.4	-	6.2	23.5	-	-	-	-	-	Ol	Fo
4	purple	37.7	25.9	1.1	2.4	15.9	-	-	-	-	-	Ol	Fo
12	purple	39.1	20.4	-	-	17.6	-	-	-	-	-	Ol	Fo
2	green	29.5	15.8	-	17.5	20.9	0.3	-	-	-	0.4	Ol	Fo
3	green	30.8	16	-	15	21.4	-	-	-	-	-	Ol	Fo
6	green	30.4	16.6	-	15.5	21.9	-	-	-	-	-	Ol	Fo
8	jade	35.2	22.3	2.9	10.1	12.6	-	-	-	-	-	Ol	FaFo
13	jade	33.2	20.6	-	12.2	12	-	-	-	-	-	Ol	FaFo
17	jade	34.1	13	3.4	14.3	9	-	-	-	-	-	Ol	FaFo
9	orange	19.7	-	-	53.4	-	-	-	-	11.5	-	OM	TMag
15	orange	20.7	-	-	46	-	-	-	-	10.8	-	OM	TMag
10	blue	35.6	28	15.1	-	-	5.5	5.5	3.3	-	-	Pl	An
11	blue	35.4	23.4	13.6	1.2	-	7.7	3.3	0.9	-	-	Pl	An
16	blue	35.6	22.9	13.7	0.8	-	7.6	3.3	0.8	-	-	Pl	An
19	blue	37.6	27.6	13.6	1.4	-	3.1	6	3.5	-	-	Pl	An
20	blue	35.5	23.5	12.3	1.8	1.2	4.2	3.7	2	-	-	Pl	An
21	blue	37.7	27	16	1.2	-	7.6	4.3	1.5	-	-	Pl	An
5	red	31.3	18.9	2.9	4.8	6.8	14.2	-	-	1.2	-	CPx	Aug
7	red	31	24.4	-	2.6	9.4	17.3	-	-	-	-	CPx	Aug
18	red	31.2	18.9	2.6	5.1	6.7	14.5	-	-	1.1	-	CPx	Aug
22	red	32.1	20.6	4.1	6	7	16.9	-	-	2	-	CPx	Aug
23	red	32.9	21.2	3.4	5.4	7.5	16.8	-	-	1.4	-	CPx	Aug

software then could have not been able to separate from the surrounding minerals. Furthermore, titanium does commonly occur in Ti-rich pyroxenes, hence the higher Ti could be genuine. Ti-rich pyroxene also give a slight purple/blue/green colour in XPL. If this is true, the overall iron content would also be lower than indicated. If titanium is detected, the value of Fe is increased compared to the non-titanium bearing (spectrum 7 for example). No BG could be detected, although it could potentially be contained. Reasons for that may be that the analysed area did not contain any, or the chosen grain size distribution does not contain glass. Furthermore, alteration is also not detected, which are observed on the thin section of EAC-1. The first reason might be the same as for glass, which is that no alteration was contained in the analysed spot, or alterations appear to be something else, such as pyroxene for example.

FJS-1 images are shown in figure 5.12 and 5.13. The latter is an enlarged version of the phase map generated from the elemental maps shown in figure 5.12.

Figure 5.12 shows an EDX analysis of FJS-1 in the same format as was shown for EAC-1. Once again, all grains analysed seem to contain oxygen, again in different concentrations. Black spots on the image are voids or bubbles in the surrounding resin. FJS-1 is a volcanic material from Earth's crust and thus most of the material is probably fully oxidised. Silicon is present in almost all parts of all the grains in this sample, with a few spots that are black (not containing Si). This sample

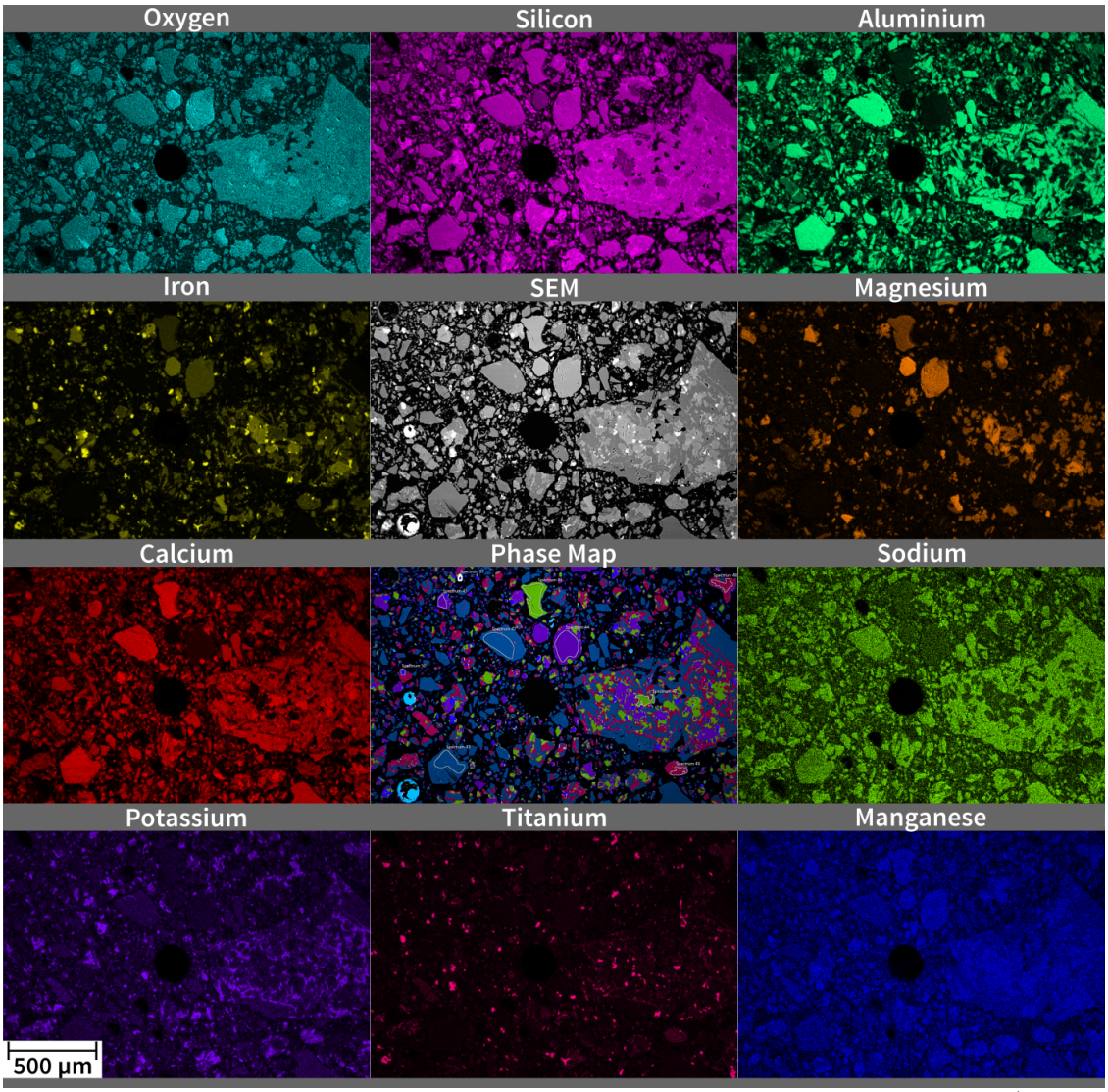

Figure 5.12: Elemental maps from EDX of FJS-1 plus the analysed SEM shot (middle-top) and a phase map (middle-bottom) compiled of the results from the elemental maps. All maps showing false colours.

therefore is also primarily composed of silicates. The black areas are more difficult to distinguish for FJS-1 than EAC-1, since those silicon sparse areas are partly close to voids, which by default appear black in all maps. Also in this case, directly crosschecking with the Fe/Ti-map, a comparably high concentration of Ti and Fe can be observed in these locations. Going back to the O-map, the location of these bright spots seems to contain oxygen. These areas are therefore iron and titanium rich and therefore likely an oxide mineral such as titanomagnetite or ilmenite.

The Al-map reveals all areas that could potentially contain Fsp (indicated in green). Again, combining this observation with the coloured areas in the Ca/Na/K-maps it can be differentiated which minerals are probably Al (Na-rich), An (Ca-rich); and Afs (K-rich). If Ca is contained but no or very little Al then it is more likely, that the mineral looked at is pyroxene. In addition, Mg- and Fe-rich areas also support the theory that pyroxene is present. To see whether FJS-1 contains Ol, a look at

the Fe- and Mg-maps shows that there are some bright grains on those two maps. These spots are darker on all other maps but Si and O, meaning those locations are likely to contain Ol. An enlarged version of the phase map for detailed discussion of results shown in table 5.3, is presented in figure 5.13 (also shown in fig. 5.12).

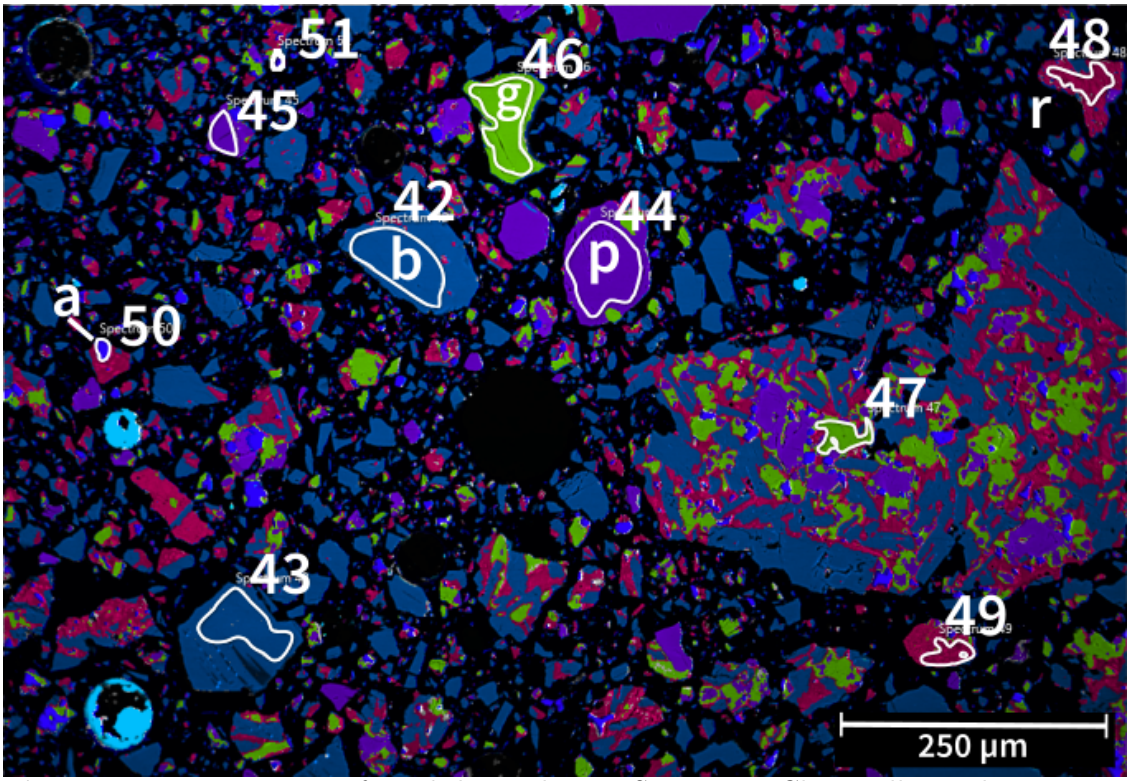

Figure 5.13: EDX image of regolith simulant FJS-1 grains. Chemically similar areas are indicated in different (false) colours; blue (b), green (g), purple (p), red (r) and azure (a). Thin white circles indicate sampled areas.

The mean elemental composition of analysed FJS-1 spectra (from figure 5.13) is summarised in table 5.3. Each spectrum has a specific number and was sorted by false colour groups in the table, according to the phase map (figure 5.13).

Blue coloured regions are high in Al and Ca, with small amounts of Na and Fe. This suggests presence of Pl, high in An. Purple areas are high in Mg and Fe and contain little to nothing else than Si and O. As stated before, those regions seem to be Ol rich, in this case potentially $Fo_{50}Fa_{50}$. Green areas are CPx-rich because they show increased Fe, Mg and Ca values, with very little Al and Ti (for spectra 46), hence likely to be CPx. Red contains Fe, Al, Ca, Mg/Na, Ti in decreasing order of A% seem to be no specific mineral but rather pieces of basaltic glass (BG). Although this assessment is not definite, a few pieces of glass have been observed in the FJS-1 thin sections; thus it could be possible that the red areas are indeed (amorphous) glass. Presence of glass also cannot easily be tested by XRD analysis, but might be indicated by broad background features in patterns.

Table 5.3: Elemental Composition of FJS-1 spectra analysed on phase map shown in figure 5.13. Values show A %

#	Colour	O	Si	Al	Fe	Mg	Ca	Na	K	Ti	Mn	Mi.	Prime
42	blue	38.5	19.2	14.3	0.7	-	9.2	1.9	-	-	-	Pl	An
43	blue	39.2	19.4	15.4	0.6	-	10.3	1.6	-	-	-	Pl	An
44	purple	37.2	20.2	0.9	11.2	12.9	1.3	-	-	-	0.3	Ol	FaFo
45	purple	34.5	14.7	-	17.8	18	-	-	-	-	-	Ol	FaFo
46	green	35.1	19.3	1.7	8	8	10.6	-	-	0.3	-	CPx	
47	green	34.6	19.4	1.5	8.6	8.5	10.2	-	-	-	-	CPx	
48	red	35.8	19.5	5.3	8.1	1.9	4.9	1.7	1.1	1.2	-	BG	
49	red	39.3	27.7	7.7	10.9	2.1	6.1	2.2	1.8	1.8	-	BG	
50	azure	23.6	2.3	-	49.7	-	-	-	-	9.7	-	OM	TMag
51	azure	23.1	3.6	-	45.8	-	-	-	-	6.9	-	OM	TMag

Lastly for this sample are the azure areas, which, similar to the case of EAC-1, may contain small particles of OM. This is again likely to be titanomagnetite, since it shows both, elevated levels of Fe and Ti with almost zero Si, and nothing else other than O. Including the thin section images (fig. 5.9) in this discussion, also in those two FJS-1 sections, one can see small black spots. However, these are not as distinct in shape and form as the ones observed in EAC-1, and ilmenite is another possibility.

Plagioclase (blue) is probably the most dominant mineral (colour) shown in figure 5.13 followed by Px (green), and BG (red), with small amounts of Ol (purple), and even less OM (azure). This seems to be a more classic distribution of minerals for a basalt than EAC-1.

JSC-2A SEM/EDX data depicted in figure 5.14 and 5.15. Figure 5.15 shows an enlarged version of the phase map constructed from the elemental maps shown in figure 5.14.

The EDX analysis of JSC-2A (fig. 5.14), presented the same way as EAC-1 and FJS-1, shows also O and Si to be the most abundant elements in this sample. Thus JSC-2A is also considered a silicate mineral rich simulant. Also, JSC-2A shows voids (black spots) although, not the distinct black spot pattern of the potential OM observed in EAC-1 and FJS-1 samples. Furthermore, the Ti/Fe- maps do not indicate clear spots as observed before, and hence suggest lower, if any, OM content in this sample.

JSC-2A shows, compared to EAC-1 and FJS-1, sharp edged crystals embedded in round grains. This can be seen particularly well in the SEM image and Al-map. The latter suggests that bright green (Al rich) areas are Pl. Low potassium, high calcium and average sodium, in combination with high Al suggest, An-rich Pl. Moreover, very small areas seem to be free of Al and show no Ca, suggesting the presence of olivine. Little to no areas can be seen that suggest Px. The hosting parts of the grains seem tougher to describe from the elemental map since it seems that all elemental maps show colour in these areas. Consistent with the thin sections,

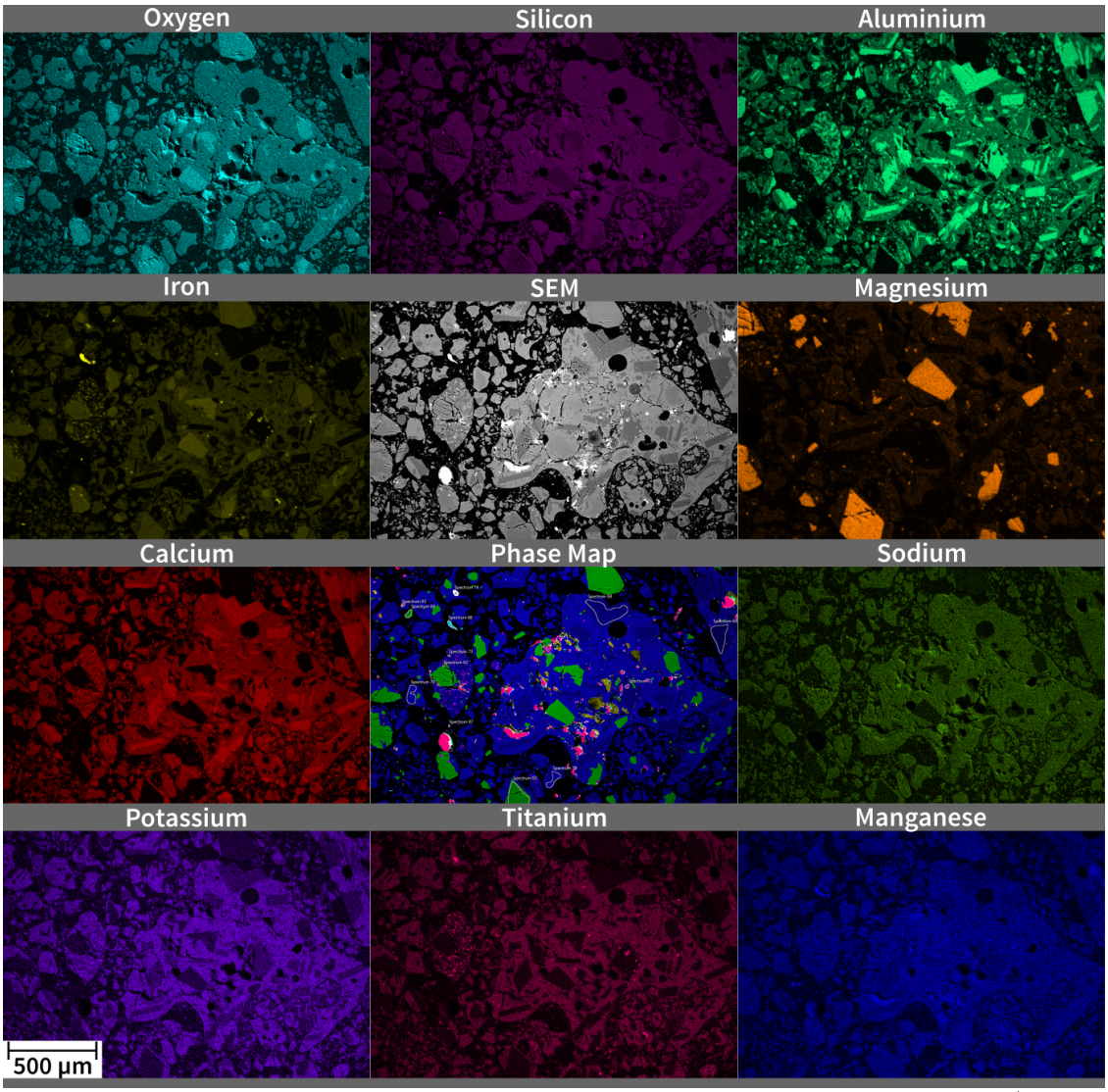

Figure 5.14: Elemental maps from EDX of JSC-2A plus the analysed SEM shot (middle-top) and a phase map (middle-bottom) compiled of the results from the elemental maps. All maps showing false colours. The Mg-map is zoomed in and thus not showing the full frame examined for JSC-2A. However, the entire SEM map was scanned for Mg and used to compile the phase map.

the only thing fitting that description is basaltic glass, which is a melt of all minerals contained in a basalt and thus contains all elements contained in those minerals.

The enlarged version of the phase map is shown in figure 5.15 and will, as before, be used to discuss results in table 5.4.

The elemental composition of the JSC-2A sample analysis are shown in table 5.4 and just focus on three areas (depicted in fig. 5.15), green, azure and blue. Yellow and pink areas are neglected since they show increased amounts of gold (Au). Au was used to form a conductive layer on the surface of the sample for SEM/EDX analysis. In regions of larger voids and bubbles, Au accumulated thicker than

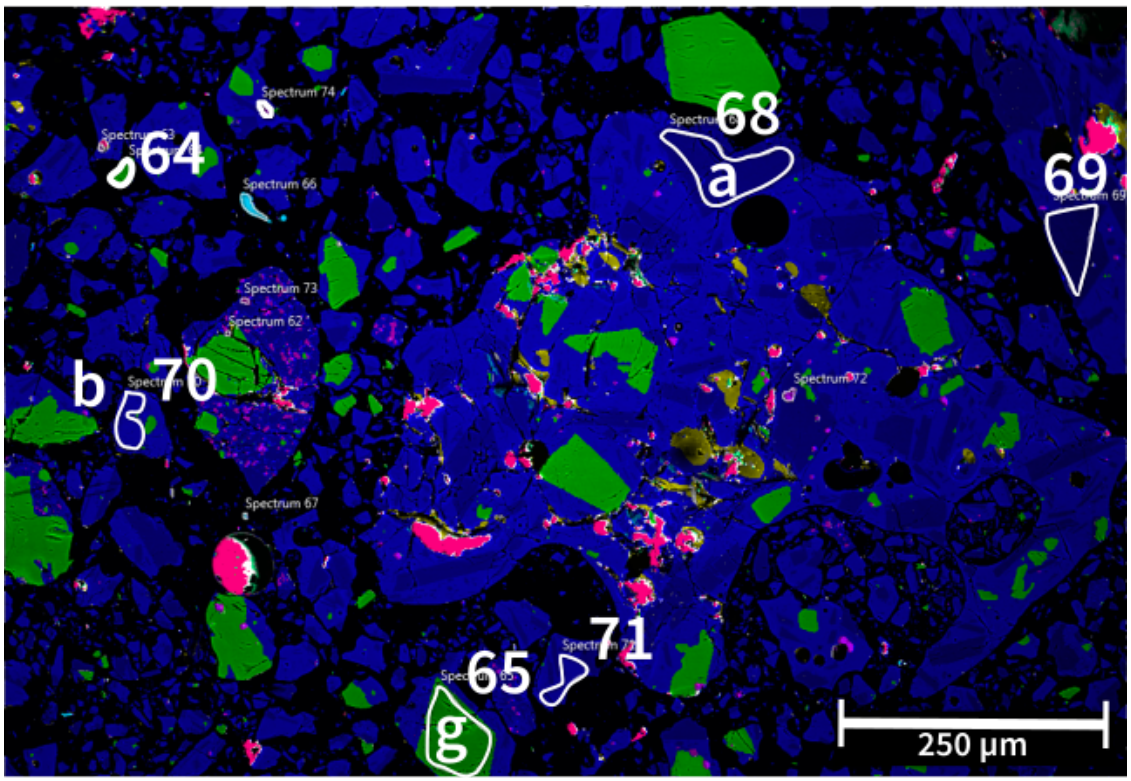

Figure 5.15: EDX image of regolith simulant JSC-2A grains. Chemically similar areas are indicated in different (false) colours; blue (b), green (g) and azure (a). Thin white outlines indicate sampled areas.

necessary and thus shows up in the analysis as gold.

Green regions are the ones showing O, Mg, Si and Fe and are once more Ol probably closer to Fo. Azure regions are likely Pl since they contain Al, Ca and Na (little trace of Fe). On top of that, the shape of these areas suggest Pl crystals as well. Overall this seems to be the most dominant fraction in this sample. Last, the blue regions show Fe, Al, Ca, Mg/Na, Ti K in decreasing order of A%. This is very similar to the results seen in FJS-1 and may indicate the presence of BG. Considering the thin sections discussed and analysed, this seems to match.

Table 5.4: Elemental composition of JSC-2A spectra analysed on phase map shown in figure 5.15. Values show area percent

#	Colour	O	Si	Al	Fe	Mg	Ca	Na	K	Ti	Mn	Mi.	Prime
64	green	38.7	14.4	-	11.7	19.9	-	-	-	-	-	Ol	Fo
65	green	39	13.7	-	10.2	21.1	-	-	-	-	-	Ol	Fo
68	azure	40.9	17.1	13.1	0.5	-	7.6	1.8	-	-	-	Pl	An
69	azure	41.1	16.6	13.1	0.5	-	7.7	1.9	-	-	-	Pl	An
70	blue	39.6	23.2	8.5	11.6	3.4	7	3.4	1.1	1.9	-	BG	
71	blue	40.5	23.5	8.3	11.1	3.2	7.1	3.1	1.1	1.9	-	BG	

For JSC-2A no specific areas could be clearly identified that contain Fe and Ti as for FJS-1 and EAC-1. Nevertheless, it is still likely that some OM might show up in the XRD analysis.

Plagioclase (azure) is likely the dominant mineral in JSC-2A and, together with Ol, mostly embedded in BG. Although no Px could be seen, it is likely that at least some is contained in JSC-2A as well.

LHT-3M SEM/EDX analysis is depicted in figure 5.16 with the phase map enlarged in 5.17. Results of aerial EDX analysis are shown in table 5.5.

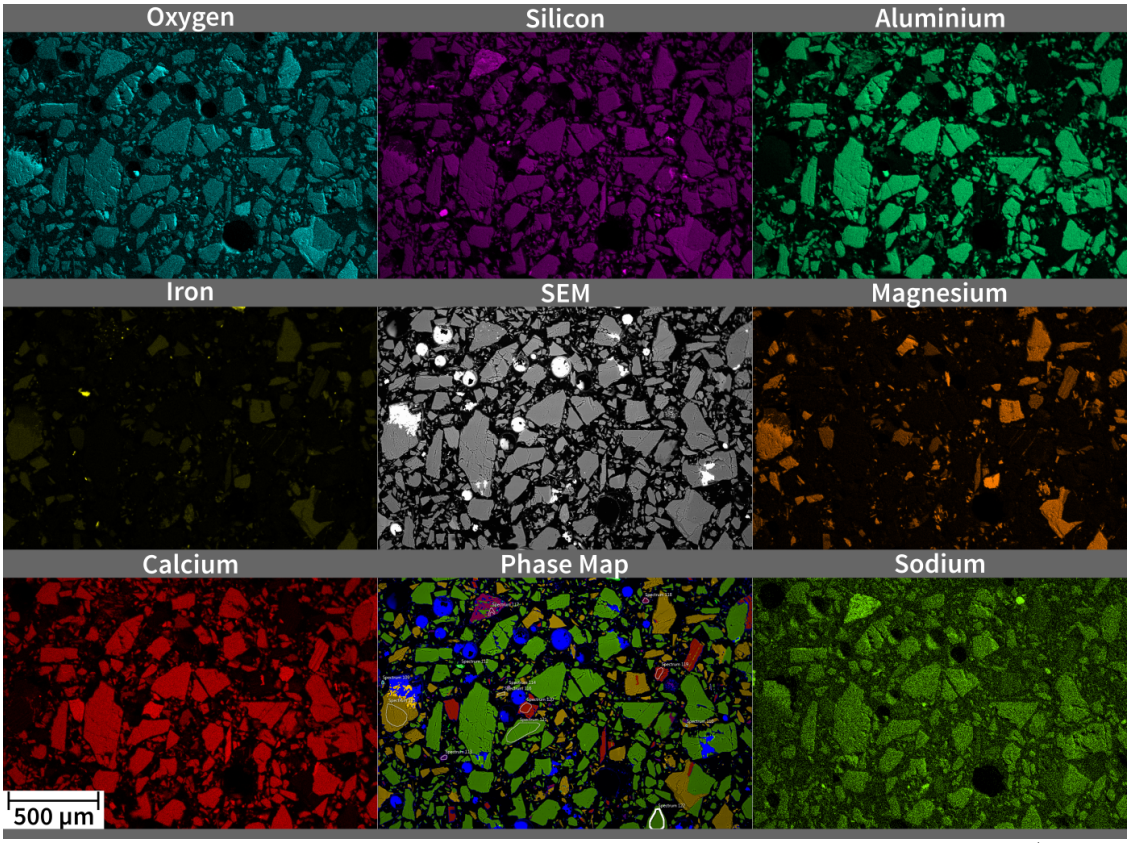

Figure 5.16: Elemental maps from EDX of LHT-3M plus the analysed SEM shot (middle-top) and a phase map (middle-bottom) compiled of the results from the elemental maps. All maps showing false colours.

The elemental analysis of LHT-3M is shown in figure 5.16 and looks distinctively different from the other three analysed samples. Each grain lit in the elemental maps is comparably homogenous and fully lit. For EAC-1, FJS-1 and JSC-2A this was not the case since most grains are a mix of different minerals. Here (LHT-3M) it seems that most grains are, in contrast, pure minerals. Moreover, values for Ti, K and Mn were so low that no elemental maps were generated. From the maps displayed, it seems that all minerals contain oxygen and silicon. Thus, all minerals should be silicates as expected. The Al-map shows Al being present in most grains and suggests the dominant mineral to be plagioclase. The regions not containing

Al show increased values of Mg, Fe, and Ca, which suggests pyroxene. As observed in thin sections, LHT-3M lacks olivine, and seems to be mostly made up of Pl and Px (70/30) with minor other minerals.

Taking a closer look at the LHT-3M phase map in figure 5.17, in combination with table 5.5, reveals whether the observations from the elemental maps match the measured values.

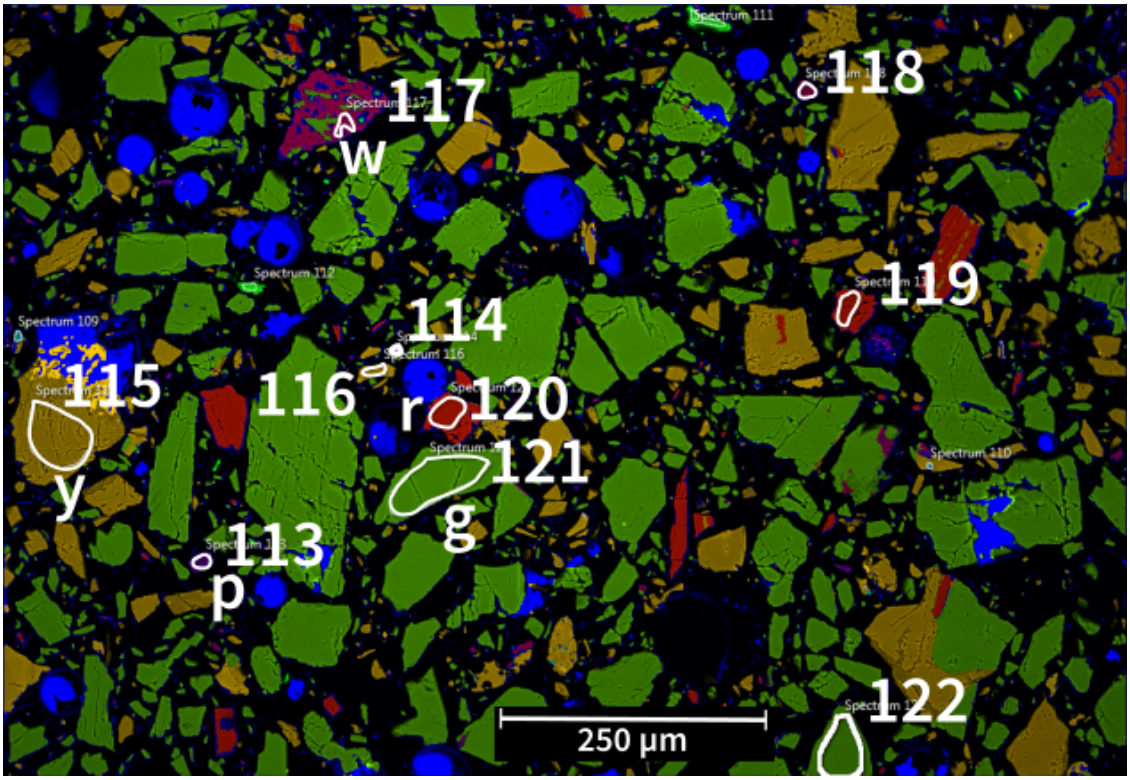

Figure 5.17: EDX image of regolith simulant LHT-3M grains. Chemically similar areas are indicated in different (false) colours; green (g), purple (p), red (r), yellow (y) and wine (w). Thin white circles indicate sampled areas.

Purple areas are very small and rare in the phase map (fig. 5.17) and coincide with the bright spots in the Si-elemental-map. Looking at the results in table 5.5, no elements but Si and O could be detected for those areas. This strongly suggests the presence of quartz, although in very small quantities. The yellow areas seem to be not as uniform as most other measurements shown. Where spectrum 115 shows elements usually contained in Px, spectrum 116 shows elements of both Pl and Px. This suggests that either a mixture of both, PL and Px, is contained in 116 or that, as the grain is comparably small, traces of the surrounding minerals have been picked up. Purple is more distinct than yellow when it comes to assigning a mineral type. Both areas seem to be feldspar, although 117 is alkali feldspar and 118 Pl probably fully consistent with Ab. 118 is lacking Na and K and only shows O, Si, Al and Na which suggest the plagioclase feldspar Albite. 117 on the other hand shows 4 A % of K, as well as Na, and Ca. Therefore it could be an

alkali feldspar. Red areas are typical for the pyroxene Augite with Fe/Mg/Ca and green areas typical for plagioclase feldspar anorthite. Blue areas are neglected since they are again areas with accumulated Au, which was also here used to form a conductive layer. Thus, blue regions (in the phase map) indicate voids and bubbles.

Table 5.5: Elemental composition of LHT-3M spectra analysed on phase map shown in figure 5.17. Values show area percent

#	Colour	O	Si	Al	Fe	Mg	Ca	Na	K	Ti	Mn	Mi.	Prime
113	purple	47.4	36.8	-	-	-	-	-	-	-	-	Qtz	
114	purple	46.5	27.9	-	-	-	-	-	-	-	-	Qtz	
115	yellow	41	19.9	-	8.6	14.7	1	-	-	-	-	Px	Aug
116	yellow	43.7	23.6	11.1	5.6	7	8.4	-	0.5	-	-	?	?
117	wine	46	33.9	9.2	-	-	2.2	3.4	4	-	-	Fsp	Afs
118	wine	43.7	22.4	8	-	-	-	6.3	-	-	-	Pl	Ab
119	red	37.8	19.6	-	3.3	8.2	12.7	-	-	-	-	Px	Aug
120	red	39.3	20.9	-	3.9	8.5	13.6	-	-	-	-	Px	Aug
121	green	41.4	17.4	15.3	0.3	-	10.7	0.9	-	-	-	Pl	An
122	green	40.7	18	15.7	0.3	-	10.6	1	-	-	-	Pl	An

For LHT-3M the presence of olivines and oxide minerals could not be confirmed. Moreover, the even colour distribution underlines observations, of the thin sections, that LHT-3M is composed of plutonic rock rather than sourced from igneous rock. The first observation, from the elemental maps, that LHT-3M is mostly made up of Pl can be confirmed by looking at the analysis of the spectra depicted in the phase map. The second largest fraction is Px, which was suggested by both thin sections and elemental maps.

The EDX analysis of EAC-1, FJS-1, JSC-2A and LHT-3M simulant confirmed most observations made from the thin sections. It also showed semiquantitative results for elements contained in each simulant, which in turn helped to form a hypothesis on which type of mineral is contained in which simulant. The analysis of the thin sections and the EDX analysis is, therefore, a good start for a further XRD analysis. Although XRD measures spectra of all minerals contained in a sample, it does not make sense to try to match each sample with all minerals (approx. 4000) in the database. This is because it would return partial matches for many of these minerals that may or may not be present in the mix, just because the crystalline structure of them is similar to each other. Hence, knowing what to look for, helps narrow down the contained minerals and improve pattern matching. A complementary technique to using EDX, to achieve more precise values for certain spots on the phase map, is to conduct spot measurements. By keeping the electron beam focused on one spot for a longer duration, more accurate readings can be achieved. Since it is not considered necessary to know the exact composition of a single grain in the simulant, nor its end member distribution, no spot measurements were conducted here.

XRD

To narrow down which minerals are contained in which quantity, X-ray powder diffraction (XRD) was conducted on EAC-1, FJS-1, JSC-2A and LHT-3M. The mineral composition - other than elemental/oxide analysis via XRF - gives clues to characteristics, such as melting behaviour. Olivines, for example, are amongst the first minerals to form when magma is cooling and crystallising. Depending on which olivine member is formed (forsterite or fayalite), these olivines will have different impact on the melting behaviour of regolith simulants. Knowing which minerals are contained in regolith (simulant) to be processed, will hence determine how suitable this raw material is for the application at hand.

The occurrence of pyroxene, feldspar, olivine, alterations and oxide minerals has been established by looking at the thin sections as well as the EDX results. From that, a list of minerals potentially contained in each simulant was compiled and applied when interpreting XRD data. Table 5.7 shows detailed results from the XRD analysis with Rietveld refinement, and table 5.6 a summary by group.

Groups of minerals detected (summarised in table 5.6) are alterations, K feldspar, mica, olivine, oxide minerals, plagioclase feldspar, pyroxene (ortho and clino), as well as glass. Latter one could not be detected actively but passively. How the glass content was determined will be described after a discussion of the contained minerals; followed by a discussion of the glass content of all simulants in comparison.

Table 5.6: XRD results overview, values for mineral groups are displayed in wt %

Group	BP1^{M}	EAC1	FJS1	JSC2A	LHT3
Plagioclase	57.7	13.82	55.94	45.67	66.58
K Feldspar	7.3	13.40	4.95	4.99	2.87
Pyroxene	13.8	35.48	26.26	6.83	24.37
Olivine	12.9	13.30	5.03	11.85	1.29
Oxide Minerals	8.3	2.01	1.52	0.62	0.26
Glass	na	14.35	0.70	23.86	0.00
Mica	na	3.31	3.18	1.77	0.87
Alteration	na	4.33	2.41	4.42	3.76
Sum	100.00	100.00	100.00	100.00	100.00

^{M} Manufacturer Data [238]

BP-1 was not measured, but manufacturer values were available for most of the minerals analysed. Although substantial variations in-between batches were reported in [238], the bulk part of BP-1 is clearly plagioclase, followed by pyroxene and olivine with almost similar amounts. The largest variations are found by analysing the calcite content for this simulant, since it differs from 0 to 9 wt %, and should not be contained in a lunar (basaltic) simulant, due to lack of calcite on the Moon. Moreover, the simulant shows 0 to 3 wt% quartz, which also should not be contained in a lunar simulant. Together with potential contamination, such as

sodium chlorite ($NaCl$), this renders this simulant a rather poor quality simulant, from a mineral point of view.

EAC-1 shows pyroxene, feldspar and olivine in descending order, as well as glass. This matches observations made earlier, where an unusually low content of plagioclase feldspar was detected for a basalt. This implies that EAC-1 is indeed an olivine basalt, especially comparing it with the other three analysed simulants. EAC-1 contains the largest amount of olivine of all four analysed samples, followed by JSC-2A, which, however, has a significantly lower pyroxene content. EAC-1 also has the second largest amount of alteration detected after JSC-2A, which seems logical since EAC-1 was mined close to the surface and is rather (geologically) old. This would have allowed water to penetrate to the rock and alter the minerals. Looking at the detailed mineral composition of EAC-1, analysed and listed in table 5.7, the largest amounts of a single mineral detected is CPx, followed by olivine. Where large pieces of the olivine were clearly seen in the thin section (fig. 5.5), large OPx was not observed in large quantities, but CPx is seen in the thin section. However, the surrounding host mineral could very well be OPx in a finer crystal structure, which makes it hard to observe in a thin section. Going back to the EDX results, what was shown red in the phase map in figure 5.11 looked like CPx by looking at the spectra in table 5.2. The red areas (CPx), together with the blue areas (Pl), also seem to be host for most other minerals contained. Thus, the results shown in table 5.7 seem to make sense. Furthermore, the XRD analysis confirms that potentially TMag is contained in small quantities. This is in line with the black spots observed in the thin sections and the orange spots in the phase map.

FJS-1 shows more than 55 % of plagioclase content (table 5.6), and more than a quarter of pyroxene, and is low in olivine and other minerals. This corresponds to the EDX results, where blue (phase map figure 5.13) seemed to show Pl (table 5.3), and the thin section results in figure 5.9 (left side), which showed a host of Pl, with chunks of Px and bits of Ol. Also here, TMag was detected, which seems to represent the black areas in the thin sections. Analysing the plagioclase content more in detail by using rietveld refinement, it turns out that more than 30 wt % are andesine (An 50). Adding another 10 % of bytownite and 5 % labradorite, for such FJS-1 seems to contain mainly calcium-rich plagioclase.

JSC-2A is composed of more than 45 % plagioclase and almost 12 % olivine. Pyroxene content is low compared to the other simulants, at only 7 %. JSC-2A potentially contains the highest amount of alterations of all four simulants with more than 4 %. This seems strange, as alteration is rarely found in the JSC-2A thin sections compared to EAC-1, where many and different types of alteration are visible. Also, JSC-2A is geologically much younger than EAC-1, and should thus not have weathered that much. One explanation may be connected to the potentially high glass content, which will be discussed at the end of the XRD section. Another explanation is, that alteration contained is too small, thus, is either not visible in the thin sections or, was removed during sieving in preparation for the thin sections sample preparation. Also, the largest alteration product,

Table 5.7: Mineral composition from XRD measurements with Rietveld refinement, values shown in wt %

Mineral	Group	EAC1	FJS1	JSC2A	LHT3
Chlorite	Alteration	2.40	0.66	1.32	1.16
Illite	Alteration	0.32	1.76	2.02	0.76
Kaolinite (BISH)	Alteration	1.61	na	na	0.64
Phlogopite	Alteration	na	na	1.08	1.19
Nepheline	Feldspathoid	5.41	1.86	0.00	na
Microcline maximum	K Feldspar	5.02	1.47	2.06	1.77
Orthoclase	K Feldspar	2.97	1.61	1.37	1.10
Sanidine Na0.07	K Feldspar	na	na	1.56	na
Annite Mica	Mica	na	na	0.27	na
Muscovite 2M1	Mica	3.31	3.18	1.50	0.87
Forsterite iron	Olivine	13.30	5.03	11.85	1.29
Ilmenite	Oxide Mineral	0.49	na	na	na
Titanomagnetite	Oxide Mineral	1.52	1.52	0.62	0.26
Albite	Plagioclase	0.00	3.37	2.16	3.48
Andesine An50	Plagioclase	5.61	31.13	20.10	14.01
Anorthite	Plagioclase	3.95	3.65	3.96	2.70
Bytownite An85	Plagioclase	1.77	10.42	13.56	36.41
Labradorite An65	Plagioclase	2.49	5.62	3.70	6.66
Oligoclase An16	Plagioclase	na	1.76	2.18	3.32
Aegirine	Pyroxene	1.91	2.28	0.82	0.76
Augite	Pyroxene	33.56	11.70	2.18	4.55
Diopside	Pyroxene	na	6.53	2.20	1.63
Enstatite	Pyroxene	na	2.64	1.62	16.64
Pigeonite	Pyroxene	na	3.10	na	0.79
Basaltic Glass	Glass	14.35	0.70	23.86	0.00

shown in table 5.7 is illite, which is hard to spot in thin sections, especially if it is contained in small crystals within a glass or plagioclase host.

LHT-3M has been identified as the most distinct simulant compared to other simulants analysed because it seems to be made up of crushed individual minerals, rather than igneous rock. EDX and thin section results showed clear single crystal grains with little to no intergrowth. Almost all of LHT-3M is made of just Pl (> 66 %), and Px (> 24 %), which together make up more than 90 % of the overall simulant and seems to be norite. In the plagioclase feldspar group, bytownite seems to be the dominant mineral (table 5.7) with >36 %, followed by andesine (14 %) and labradorite with more than 6 %. This makes LHT-3M a calcium-rich plagioclase simulant. Of further interest is the high content of OPx indicated by 16.64 %, of enstatite out of 24.37 % of Px, which suggests rather Mg-rich pyroxenes. With melting points of $1557°C$ for enstatite [532, 533] and anorthite [534], after [177, 535, 536], this suggests a rather high melting point compared to other simulants, which may melt at lower (around 1200°C) temperatures. More

details on melting points of the individual simulants will be discussed in section 5.2.

To determine the glass content of each simulant, a crystalline calcite spike of 15 % was added with a purity of 99.99 %. This artificially added spike required correction calculations to be applied to the measurements, to passively measure glass contained in the samples. The theory behind measuring glass passively with a calcite spike is, that if a certain amount of defined and pure spike (in this case 15% of 99.99% pure calcite) is added, and the XRD measurements return a value greater than that amount amorphous material, such as amorphous glass may be contained[2]. This is because the XRD can only measure crystalline constituents, and not non-crystalline ones, which leads to larger amounts of crystalline phases being detected. A schematic of how the correction was performed is shown in figure 5.18.

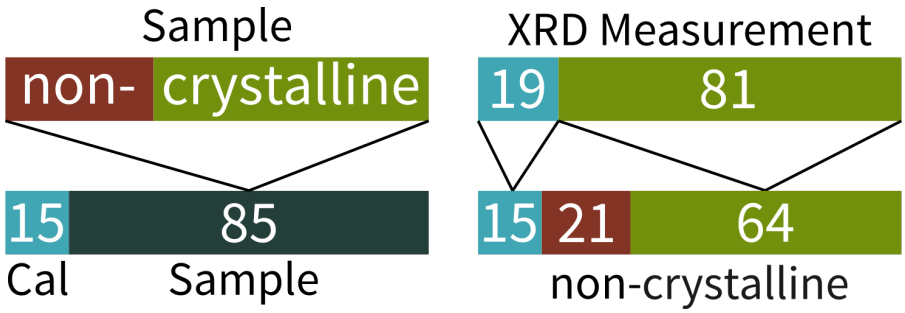

Figure 5.18: Calcite corrections for passive glass detection, schematic. Red indicates non crystalline parts of a sample and green crystalline, blue calcite content and black sample content. XRD can only detect crystalline parts and thus for an actual sample of 15 % Cal and 85 % sample it may detect 19 % Cal and 81 % sample. Knowing, that the actual Cal content is only 15 %, the measurements can be corrected and the actual crystalline part computes to 64 %. The remaining percentile is thus non-crystalline (here 21 %).

A calculation example is shown hereafter (all in wt %), where,

$$m_{spike_{real}} = 15\%, \tag{5.1}$$

and represents the actual amount of spike added to the sample. Moreover,

$$m_{sample_{real}} = 85\% \tag{5.2}$$

represents the percentile of regolith (original sample) in the regolith spike mix,

$$m_{spike_{measured}} = 19\% \tag{5.3}$$

is the amount of spike that the XRD detects, and

$$m_{crystalline_{measured}} = 100\% - 19\% \tag{5.4}$$

$$m_{crystalline_{measured}} = 81\% \tag{5.5}$$

[2]i.e. the presence of amorphous glass adds to the background of the pattern

is the percentile of the crystalline part of the regolith measured by the XRD. Using the ratio,

$$c = \frac{m_{spike_{real}}}{m_{spike_{measured}}} \tag{5.6}$$

$$c = 0.789 \tag{5.7}$$

the actual content of crystalline material contained ($m_{crystalline_{real}}$) in the sample can be determined by,

$$m_{crystalline_{real}} = \frac{m_{crystalline_{measured}}}{c} \tag{5.8}$$

$$m_{crystalline_{real}} = 63.9\% \tag{5.9}$$

and ultimately leads to the amount of glass contained (m_{glass}),

$$m_{glass} = 100\% - m_{crystalline_{real}} - m_{spike_{real}} \tag{5.10}$$

$$m_{glass} = 21.1\%. \tag{5.11}$$

Summing up the actual amount of spike and crystalline material, a percentage smaller than a 100% is the result, if the measured amount of spike is larger ($m_{spike_{measured}} > m_{spike_{real}}$) than the entered amount. Since for simulants it is unlikely to encounter large amounts of amorphous material other than glass, the entire amount is considered to be glass. However, if it is necessary, a closer look would need to be taken at the non-crystalline parts of the regolith in detail.

The amount of glass that may be contained in each regolith type varies from 0 % for LHT-3M to more than 23 % for JSC-2A (see tables 5.7 and 5.6). These amounts are engineered by the manufacture by source material selection and by mixing and manipulating it. These results are based on the calculation described before and assume that there is no other non-crystalline material contained in the sample but basaltic glass. This calculation does not consider, measurement errors and uncertainties and is therefore an indicator rather than an accurate measurement. However, the goal of this analysis is not to determine precise results for how much glass and minerals are contained in each regolith exactly, but to find out what types of materials are contained at all. What could also be gained is the approximate ratio of minerals and glass. This ratio and the occurrence and abundance of certain minerals, oxides or glasses will give clues to process-ability of the simulant, as well as characteristics of it, such as susceptibility to microwaves, reflectance etc. Therefore, it is in line with the observations made in the thin sections and EDX that FJS-1 and JSC-2A contain glass. For EAC-1, the thin sections showed material which could be basaltic glass, but the EDX measurements did not confirm this. Possibly, the analysed area did not contained glass, or the grain size distribution analysed was not the one bearing glass. Also, alterations and other parts, such as organic material could show up as non-crystalline.

Although it cannot be said for certain that the amount of glass passively detected is really contained in EAC-1, it seems likely that BG is contained. Furthermore,

it seems too little BG in FJS-1 (0.7 %) hence, further testing will be required, to test if, and if, how much, BG is contained. With respect to LHT-3M, it shows 0 % of glass contained and since it is artificially mixed and no glass was added, that assessment is likely to be true. Once more, the fact that glass is contained in a simulant is more important than knowing the exact amount. Since BG may impact the manufacturing processes in general, it is possible that other measurements, such as DSC may show the impact of that.

XRF

For any (scientific) application using regolith simulants of any type, it is imperative that results can be compared. Only with the possibility of assuring comparability and reproducibility, other research can be used and improved upon. In order to be able to do so, standards would be required, which are not in place yet. More specifically, even if multiple researchers use the same simulant, of a certain type provided, by the same manufacturer, it cannot be said, that those researchers use the same material. Fluctuations between batches make it impossible to assume that it is the same material. As a simple start, it would be helpful for the community to have a certain standard or minimum analysis, which would be required to publish anything related to simulants. X-ray fluorescence (XRF) measurements would be one possibility to take a step in that direction. Those measurements provide insights into the elemental composition of a simulant. They do, however, not provide details on a simulants mineral composition. Already only knowing, the elemental composition just by itself would assure a certain level of comparability, and thus, the possibility to rule out effects that might be caused by a significantly different elemental composition. Adding to that, each batch of regolith which is processed needs to be measured first before utilising it, in order to adjust process parameters according to actual elemental composition. This is especially true for actual missions on the lunar surface which would need to determine the regolith composition first, before the start of any manufacturing utilising regolith can commence. To point out differences in elemental compositions of regoliths, this section concludes the geochemical analysis of the utilised regolith simulants by presenting detailed XRF analyses.

The previous parts of this chapter 5.1.3 focused on grain geometry and mineralogy, which are both more qualitative than quantitative. Although the XRD provided numbers for the crystalline and non-crystalline parts of the regolith simulants, those results are not as accurate and reliable as XRF measurements. This section presents detailed measurements from two independent sources of all simulants used for this study. Results are compared with the manufacturer values, measurement sites are compared against each other, and different batches of regolith simulant are compared to each other. Furthermore, actual lunar regolith XRF measurements are compared to utilised simulants.

Figure 5.19 shows a graphical representation of lunar regolith compositions (Mare, Highland, AvgSurf) as well as lunar regolith simulants BP-1, EAC-1, FJS-1, JSC-1A/2A and LHT-2M/3M. The graph is based on data from table A.4, which

list average measurement results[3] for each simulant utilised. The graph does only show the 60 % of the regoliths' compositions, since all of them contain at least 40 % of SiO_2. For the actual lunar regolith, no measurements of TiO_2, MnO and P_2O_5 have been performed, which will also be contained in the "other" fraction of the according bars. Although significant differences between regolith simulants and the actual lunar soil can be seen, generally, all lunar simulants appear to be in the same frame. Lunar regolith simulants shown, can be split into two groups, highland and mare type simulants. The LHT series is considered a highland type simulant and the rest are mare simulants.

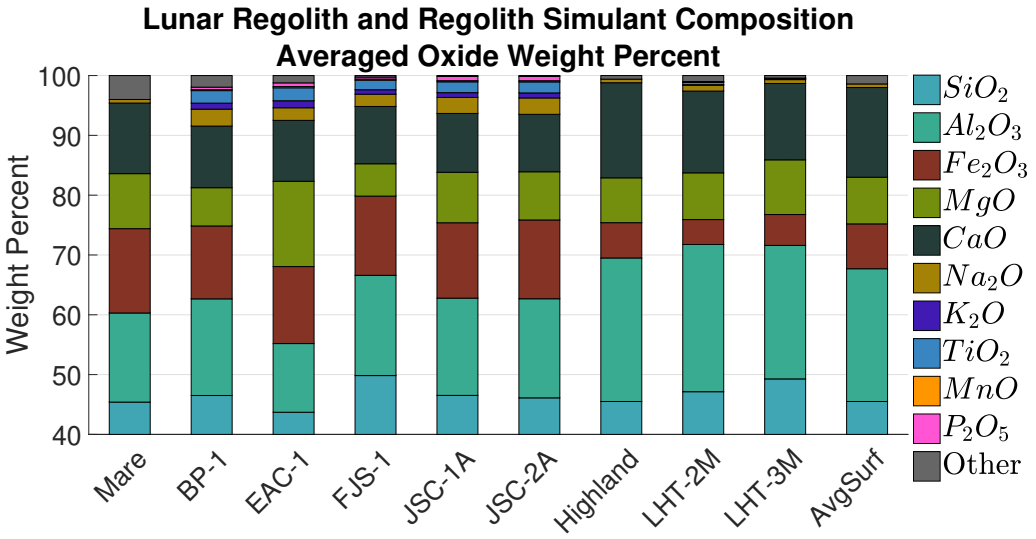

Figure 5.19: Regolith simulant and average lunar soil compositions. Comparison by weight percent and based on table A.4.

Highland simulants are characterised by a rather low iron, sodium and titanium content and a rather high aluminium and calcium content. The lack of iron compared to the other simulants is likely to cause it to be brighter in appearance than mare simulants. The same yields for actual lunar mare and highland regolith. The main impact on colour may be the iron content, but trace elements, such as chromium and titanium, for example, may colour the simulant different than white as well. In conclusion, judging from the measured elemental composition, compared with the average highland composition, it seems, that the LHT simulant series is a good simulants series since it is close to the actual lunar regolith. Hence, they will be chosen for all experiments as the lunar highland regolith representation.

Mare simulants are characterised by a higher iron and titanium content than highland simulants. Comparing the analysed samples with the average mare composition, the best elemental matches seem to be the JSC simulants, with the overall closest match, followed by BP-1 and EAC-1/FJS-1. Latter simulants differ more in Mg/Al content (EAC-1), and Si/Mg content (FJS-1) than others. All in

[3] values are averaged over batches (if applicable) and measurement results obtained in two locations, Edinburgh and Liège

all, all simulants analysed lie in areas which may be encountered when landing in a lunar mare region. This is however not showing the entire picture and components of actual lunar regolith such as sulfide or elemental iron are not considered for this work. However, the used simulants and results represent a good spread of potential elemental fluctuations, which could occur on the lunar surface as well. Thus they are suitable to test manufacturing processes for their tolerances against fluctuations in the input material.

In a next step, differences in-between manufacturer data and own measurements, differences between two simulant batches and differences between measurement facilities are pointed out. Elemental measurements via XRF show, quantitatively, the geochemistry of regoliths. Table 5.8 shows the entire data set available on all simulants measured, which are: BP-1, EAC-1, FJS-1, JSC-1A, JSC-2A, LHT-2M and LHT-3M. The superscript next to the simulant name in table 5.8 indicates the source of the data set. The three sources are "E" for School of GeoSciences at Edinburgh University, "L" for the Department of Geology at Université de Liège, and "M" for manufacturer data. Furthermore, simulants that are listed twice in a form, such as, for example, FJS-1-1 and FJS-1-2, are simulants procured from the same supplier but represent two different batches. All values shown in table 5.8 are showing wt %. LOI, the lost material, is usually a combination of H_2O and CO_2 and can indicate to which extent alteration may be contained in a sample.

Starting by comparing the obtained results from the School of GeoSciences at Edinburgh University and the Department of Geology at Université de Liège, table 5.9 was compiled and shows an absolute and relative comparison of their results listed in table 5.8. For the bulk part (SiO, Al_2O_3, Fe_2O_3, MgO, CaO) of all simulants, which usually makes up more than 90 % of the overall weight of regolith, the accuracy is about 4 % in-between Edinburgh and Liège. Moreover absolute and relative differences alter from positive to negative throughout the simulants for each oxide type.

This suggests normal measurement fluctuations and/or sample fluctuations[4], thus suggests reliable results for the bulk group of oxides. The most outstanding differences between measurements obtained in Edinburgh and Liège occurred measuring Na_2O. Results for Na_2O from Edinburgh are always reported higher (16 - 63%) than the results from Liège. This may have two reasons, the first may be the use of a different calibration standard for Na_2O, which may cause these differences. The second may be the sample preparation process and how samples were glassed. Since Na_2O may be contained in the flux used to fuse discs it needs to be compensated for. To achieve more reliable and accurate results for Na_2O, it should be measured from pressed powder pelts rather than fused glass discs. Differences for K_2O, TiO_2, MnO and P_2O_5 are again negative and positive throughout different simulants and suggest good measurements. High differences, such as 24/51% for K_2O and -125/-819 % for P_2O_5, for both LHT-3M simulant batches are explained with the absolute low values of 0.11 wt % or less. These are near the detection limit of the machine.

[4]e.g. how much sample was homogenised

Table 5.8: XRF analysis for major elements contained in different lunar regolith simulants and simulant batches conducted at the University of Edinburgh and the University of Liège

Simulant	SiO_2	Al_2O_3	Fe_2O_3*	MgO	CaO	Na_2O	K_2O	TiO_2	MnO	P_2O_5	SUM	LOI
BP-1^M	47.05	16.65	12.00	6.05	9.40	3.45	1.10	2.25	0.21	0.52	98.68**	
BP-1^E	46.13	15.91	11.96	6.31	10.28	3.08	1.011	2.041	0.171	0.395	99.32	2.04
BP-1^L	46.88	16.41	12.42	6.48	10.32	2.58	1.00	2.15	0.17	0.43	98.84	2.34
EAC-1^M	43.70	12.60	12.00	11.90	10.80	2.90	1.30	2.40	0.20	0.60	98.40**	
EAC-1^E	43.58	11.45	12.66	14.08	10.18	2.62	1.18	2.15	0.21	0.59	98.71	1.40
EAC-1^L	43.83	11.52	13.09	14.43	10.19	1.60	1.15	2.19	0.21	0.63	98.85	2.45
FJS-1^M	49.14	16.23	13.07	3.84	9.13	2.75	1.01	1.91	0.19	0.44	97.71**	
FJS-1-1^E	49.82	16.56	12.90	5.91	9.71	2.42	0.66	1.46	0.20	0.28	99.92	-0.25
FJS-1-1^L	49.73	16.91	13.03	5.97	9.67	1.64	0.64	1.47	0.19	0.29	99.54	0.33
FJS-1-2^L	49.97	16.80	13.83	4.35	9.36	2.08	0.94	1.86	0.20	0.41	99.78	-0.27
JSC-1A^M	47.50	15.00	10.75	9.00	10.50	2.75	0.80	1.50	0.18	0.65	98.63**	
JSC-1A^E	46.76	16.24	12.62	8.57	9.90	2.91	0.818	1.798	0.189	0.698	100.04	-0.46
JSC-1A^L	46.28	16.28	12.59	8.30	9.79	2.45	0.77	1.83	0.19	0.72	99.20	-0.34
JSC-2A^M	47.50	15.00	10.75	9.00	10.50	2.75	0.80	1.50	0.18	0.65	98.63**	
JSC-2A^E	46.28	16.63	13.18	7.98	9.65	3.11	0.82	1.83	0.20	0.71	100.38	-0.79
JSC-2A^L	45.94	16.50	13.17	8.14	9.56	2.38	0.86	1.85	0.19	0.72	99.32	-0.40
LHT-2M^M	46.70	24.40	4.16	7.90	13.60	1.26	0.08	0.41	0.07	0.15	98.73**	
LHT-2M^E	46.98	24.35	4.25	7.86	13.54	1.19	0.077	0.374	0.074	0.066	99.71	0.95
LHT-2M^L	47.29	24.89	4.08	7.77	13.81	0.82	0.06	0.38	0.07	0.08	99.23	0.96
LHT-3M^M	46.70	24.40	4.16	7.90	13.60	1.26	0.08	0.41	0.07	0.15	98.73**	
LHT-3M-1^E	49.34	21.59	5.56	9.49	12.54	1.04	0.08	0.11	0.09	0.02	99.85	0.12
LHT-3M-1^L	49.32	22.10	5.33	9.43	12.55	0.38	0.06	0.10	0.09	0.04	99.39	0.28
LHT-3M-2^E	49.24	22.61	4.90	8.77	13.05	0.72	0.043	0.083	0.085	0.004	99.94	0.43
LHT-3M-2^L	49.22	22.98	4.87	8.89	12.92	0.47	0.02	0.08	0.08	0.04	99.57	0.35

^{M} Manufacturer data, ^{E}University of Edinburgh, ^{L}University of Liège

$*$ Sum of FeO and Fe_2O_3, ** Sum of mean oxide contents

Table 5.9: Comparison of XRF measurements of major elements contained in regolith simulants. Absolute and relative comparison of results obtained by School of GeoSciences at Edinburgh University and the Department of Geology at Université de Liège

Simulant	SiO_2	Al_2O_3	Fe_2O_3	MgO	CaO	Na_2O	K_2O	TiO_2	MnO	P_2O_5
BP-1	-0.76	-0.51	-0.46	-0.16	-0.04	0.50	0.01	-0.11	0.00	-0.03
BP-1	-2%	-3%	-4%	-3%	0%	16%	1%	-5%	0%	-8%
EAC-1	-0.25	-0.07	-0.43	-0.35	-0.01	1.02	0.03	-0.05	0.00	-0.04
EAC-1	-1%	-1%	-3%	-2%	0%	39%	2%	-2%	2%	-6%
FJS-1-1	0.09	-0.35	-0.12	-0.06	0.04	0.78	0.02	-0.01	0.00	-0.02
FJS-1-1	0%	-2%	-1%	-1%	0%	32%	3%	-1%	1%	-6%
JSC-1A	0.48	-0.04	0.02	0.27	0.10	0.47	0.05	-0.03	0.00	-0.02
JSC-1A	1%	0%	0%	3%	1%	16%	6%	-2%	0%	-3%
JSC-2A	0.34	0.13	0.00	-0.16	0.09	0.73	-0.04	-0.02	0.01	-0.02
JSC-2A	1%	1%	0%	-2%	1%	23%	-4%	-1%	4%	-2%
LHT-2M	-0.31	-0.54	0.18	0.09	-0.27	0.37	0.02	-0.01	0.00	-0.01
LHT-2M	-1%	-2%	4%	1%	-2%	31%	22%	-2%	6%	-18%
LHT-3M-1	0.02	-0.51	0.24	0.06	-0.01	0.65	0.02	0.01	0.01	-0.02
LHT-3M-1	0%	-2%	4%	1%	0%	63%	24%	6%	9%	-125%
LHT-3M-2	0.02	-0.37	0.04	-0.12	0.14	0.25	0.02	0.00	0.00	-0.03
LHT-3M-2	0%	-2%	1%	-1%	1%	35%	51%	1%	1%	-819%

Elemental composition values provided by the manufacturer (see table 2.3 and A.5 in the appendix) seem never to be precise. This may be because manufacturers often describe the composition of their simulants in bulk. More specifically, the supplied regolith simulant may significantly differ from the values that the supplier provided, since the actual batch that is shipped is not specifically measured. In case of LHT-2M (made by USGS), and LHT-3M (made by Zybek) there is zero difference reported in elemental composition, according to the safety data sheets supplied by the manufacturer. However, a simulant mixed from individual minerals, manufactured by two different companies at two different locations is very unlikely to be composed of exactly the same elements.

By comparing the average results of the XRF measurements conducted in Edinburgh and Liège with the data supplied by the manufacturer, differences can be made apparent. Table 5.10 lists the absolute and relative differences to the supplier data, using the average measurement results obtained from each batch of simulant received as comparison. Most suppliers provide ranges rather than actual numbers for each oxide, hence the values used for this table are the ones shown in table 5.8 (indicated by ^{M}), which are the mean values of the ranges provided by the supplier and listed in table 2.3 and A.5 in the appendix. If an absolute/relative value is negative, it corresponds to less oxide measured compared to the supplier data and vice versa for positive values.

Overall, for the bulk part of the regolith (SiO, Al_2O_3, Fe_2O_3, MgO, CaO) the difference between the average measured values and the supplier data is between +29 % and -12 %. For Na_2O Edinburgh and Liège results differed the most, thus it is also to be expected that their average values, compared to manufacture data,

Table 5.10: Comparison XRF average major element measurement from Edinburgh and Liège vs. manufacturer data

Simulant	SiO_2	Al_2O_3	Fe_2O_3	MgO	CaO	Na_2O	K_2O	TiO_2	MnO	P_2O_5
BP-1	-0.55	-0.49	0.19	0.35	0.90	-0.62	-0.09	-0.15	-0.04	-0.11
BP-1	-1%	-3%	2%	5%	9%	-22%	-9%	-7%	-23%	-27%
EAC-1	0.00	-1.12	0.88	2.36	-0.61	-0.79	-0.13	-0.23	0.01	0.01
EAC-1	0%	-10%	7%	17%	-6%	-37%	-11%	-11%	6%	2%
FJS-1	0.70	0.53	0.18	1.57	0.45	-0.70	-0.26	-0.32	0.01	-0.11
FJS-1	1%	3%	1%	29%	5%	-34%	-35%	-20%	3%	-35%
JSC-1A	-0.98	1.26	1.85	0.43	-0.66	-0.07	-0.01	0.31	0.01	0.06
JSC-1A	-2%	8%	15%	5%	-7%	-3%	-1%	17%	4%	8%
JSC-2A	-1.39	1.57	2.42	-0.94	-0.90	-0.01	0.04	0.34	0.02	-0.09
JSC-2A	-3%	9%	18%	-12%	-9%	0%	5%	19%	10%	-12%
LHT-2M	0.44	0.22	0.00	-0.09	0.07	-0.26	-0.01	-0.03	0.00	-0.08
LHT-2M	1%	1%	0%	-1%	1%	-26%	-16%	-9%	3%	-108%
LHT-3M	2.58	-2.08	1.00	1.25	-0.84	-0.61	-0.03	-0.32	0.02	-0.12
LHT-3M	5%	-9%	19%	14%	-7%	-94%	-55%	-341%	20%	-477%

show the biggest differences. With -94% to 0%, Na_2O results differed the most and all other oxides maximum difference was -55% to 19% is. However, with the exception of ultra-low values for LHT-2M/3M for TiO_2 and P_2O_5. These numbers are higher compared to the differences between the measurements conducted in Edinburgh and Liège (+4 % to -4 % for bulk), thus a detailed look needs to be taken at individual cases:

BP-1 is showed the smallest difference (-3 % to +9 %) for bulk composition, further the rest of the oxides, were close (-27 % to - 7%) to the manufacturer values. However, the manufacturer data used in case of BP-1 is based on an average of only two measurements and not a large number of samples. This may be the reason why they are so close together. In conclusion, BP-1 manufacturer values are close to the actual values of the batch received, compared to other simulants.

EAC-1 is also shipped with single values for its oxide contents, rather than ranges. With differences of -37 % to 17 % (including Na_2O), it is one of the closest to the data provided by the supplier. Thus, it seems to be shipped with rather stable compositions in each batch (or at least for the batches studied here).

FJS-1 is, overall, a good match for the bulk part of the lunar regolith, other than MgO, which is off by 29 %. This may be due to averaging of measurements not only from two different sites but also two different batches. It also seems, that FJS-1 composition is rather stable.

JSC-1A is close to the measured values, other than for its iron oxide content. However, iron oxide is off, by 15 % in absolute terms, which is almost 2 wt % of the overall mix. Since iron is key to applications such as glass production or microwave susceptibility, this oxide measurement is probably more important than all other values, and it would be useful to know the accurate value. Moreover, the content

of Fe might be more variable if there are small oxides present, such as magnetite, for example. Since it is not possible to tell from the range of values provided by the manufacturer, individual measurements are essential. Thus, in any case, XRF measurements are required for all experiments conducted with this simulant since the manufacturer values are not good enough.

JSC-2A is the most used simulant in the scientific community after the initial JSC-1A batch ran out. Thus, it is of considerable importance to have precise values for its oxide content. However, as for LHT-2M (made by USGS) and LHT-3M (made by Zybek) also JSC-1A and JSC-2A have zero differences reported in elemental composition by the manufacturer. This suggests once more that no actual measurements were performed, but rather that the old values were taken instead. Looking at the results obtained measuring the received JSC-2A simulant, these results are closer to the manufacturer data than JSC-1A. However, also JSC-2A's composition was provided in a ranges rather than specific or average values. Hence, also here, XRF measurements are required for each batch received to be able to conduct experiments with this simulant.

LHT-2M is probably the best match out of all simulants analysed, with maximum differences of -1% to 1%. Unfortunately, this simulant is not available any longer and has been replaced by LHT-3M, not manufactured by USGS, but Zybek. Although this simulant seems to have a good quality (matching manufacturers data), it will not be used as a simulant, since it is no longer available.

LHT-3M; as pointed out before, the manufacturer likely took the elemental composition data for this simulant from LHT-2M, and did not actually perform measurements. This becomes more obvious by checking the discrepancy between the measured data and the manufacturer data. Where LHT-2M was very close to the supplier data for the bulk, LHT-3M is in-between -9 % to 19 % off. This makes it impossible for this simulant to be used without conducting individual measurements on each batch.

Detailed analysis showed that only in one case (LHT-2M) measured results were close ($\pm$ 1 %) to manufacturer data. All other simulants are in the same range but differ significantly in some cases. In conclusion, conducting XRF measurements is required for each simulant used in any scientific work. By doing so, a starting point is established which allows for comparability of works conducted using regolith simulants.

After looking at the difference between measured and supplier values, a closer look is taken at different batches of FJS-1 and LHT-3M. Table 5.11 shows the differences between two batches of FJS-1 and LHT-3M. Both batches of both simulants have been measured using the same machine in Liège. Both batches show significant differences for the bulk of up to 27 % (FJS-1), and 9 % (LHT-3M), as well as -47 % (FJS-1), and 66 % (LHT-3M) for the remaining oxides. This adds to the conclusion that it is necessary to measure each batch of simulant received, before utilising it

for an experiment, to assure that the actual composition of the simulant is known.

Table 5.11: Comparison of different simulant batches major elements absolute and relative

Simulant	SiO_2	Al_2O_3	Fe_2O_3	MgO	CaO	Na_2O	K_2O	TiO_2	MnO	P_2O_5
FJS-1 ^{L}	-0.24	0.11	-0.80	1.62	0.31	-0.44	-0.30	-0.39	0.00	-0.12
FJS-1 ^{L}	0%	1%	-6%	27%	3%	-27%	-47%	-26%	-1%	-40%
LHT-3M ^{L}	0.10	-0.88	0.46	0.54	-0.37	-0.08	0.04	0.02	0.00	0.01
LHT-3M ^{L}	0%	-4%	9%	6%	-3%	-22%	66%	18%	1%	14%

In addition to the major element analysis, a trace element analysis has been performed on the utilised simulants. This measurement has been conducted via XRF as well, but on pressed powder pellet samples rather than fused glass discs (preparation of both described in section 4.1.3). Results are shown in table 5.12 and show values for the elements Cu, Ni, R, Sr, Y, Zn, Zr, Cr and V. Many of these trace elements may be contained or trapped in minerals and often impact the colour of a mineral. It is for example likely, that chromium is responsible for a slight green colour of LHT-2M/3M.

Table 5.12: XRF analysis of trace elements contained in different lunar regolith simulants and simulant batches conducted at the University of Edinburgh and at the University of Liège. Results shown in ppm

Simulant	Cu	Ni	Rb	Sr	Y	Zn	Zr	Cr	V
BP-1^E	43.7	105.8	15.1	779.4	23.5	80.5	172.3	247.9	187.5
BP-1^L	58	46	22	719	25	71	169		
EAC-1^E	61	426	34	716	25	107	209	590	215
EAC-1^L	72	380	41	687	28	93	211		
FJS-1-1^E	188	145	12	362	28	104	90	346	390
FJS-1-1^L	214	53	18	352	28	89	95		
FJS-1-2^L	302	31	25	368	35	103	125		
JSC-1A^E	58.7	156.6	9.1	907.3	25.3	102.9	163.9	330.9	257
JSC-1A^L	73	83	16	814	26	95	157		
JSC-2A^E	63	220	10	925	25	111	160	461	260
JSC-2A^L	75	117	15	828	26	93	155		
JSC-2A-Tech^E	63	173.4	9.1	910	25.7	103.9	163.9	404.3	255.1
LHT-2M^E	30.8	426.1	2.7	107.2	1.5	14.3	16.1	991.6	49.1
LHT-3M-1^E	54	388	2	90	3	46	123	1459	69
LHT-3M-1^L	48	222	10	112	7	42	126		
LHT-3M-2^E	20.6	237.3	2	84.1	1.7	18.1	5.6	1108.3	60.2
LHT-3M-2^L	22	164	9	102	6	21	20		

*not enough material available to measure trace elements
^{E}University of Edinburgh, ^{L}University of Liège

A comparison between trace elements measured in Edinburgh and Liège (shown in table A.7), as well as a comparison between different batches (shown in table A.8), showed similar differences than the major elemental analysis, hence is not

discussed in detail. In summary, it is probably not necessary to measure trace elements for each simulant/batch before using it. However, it can not be said with certainty, especially since no work is know which conducted experiments on this point. Additionally, there may be potential experiments or applications that may require an accurate value for trace elements. In that case, trace element analysis is required, since also for trace elements there was no stable quantity detected from one batch to another.

CHN and LOI

To get a better idea of the quality of a simulant, CHN analysis was performed. This measurement determines hydrogen, carbon and nitrogen contained in a sample. None of these elements are expected to be found in a good quality simulant. Presence of carbon suggest organic material contamination, a presence of hydrogen that water is contained, and nitrogen contamination by nitrogenous vegetable and animal matter. Table 5.13 shows the wt % of C, H and N in JSC-2A, FJS-1, LHT-3M, EAC-1 and JSC-Tech.

Table 5.13: Carbon, hydrogen, and nitrogen content in mass percent

Sample	C	H	N
EAC-1	0.19	0.18	0.00
FJS-1	0.02	0.00	0.00
JSC-2A	0.02	0.00	0.00
JSC-Tech	0.28	0.04	0.02
LHT-3M	0.06	0.06	0.01

The error of this measurement is ±0.3 % and no sample showed levels of C, H and N higher than the error margin of the machine. Thus it is unlikely that any simulant contains large amounts of organic material (C + N) and/or water (H). An estimate of water potentially contained in EAC-1 based on the molecular weight of hydrogen and oxygen computes to:

$$m_H = 0.18\ wt\% \tag{5.12}$$

$$M_{H_2} = 2.016\ \frac{g}{mol} \tag{5.13}$$

$$M_O = 15.999\ \frac{g}{mol} \tag{5.14}$$

$$ratio = \frac{M_{H_2}}{M_O} \tag{5.15}$$

$$ratio \approx \frac{1}{8} \tag{5.16}$$

$$m_{H_2O} = \frac{m_H}{ratio} + m_H \tag{5.17}$$

$$m_{H_2O} \approx 1.62\ wt\% \tag{5.18}$$

with m_H and m_{H_2O} mass of hydrogen and water and with M_{H_2} and M_O being the molecular mass of hydrogen and oxygen. This means that about 1.62 wt % of water may be contained in EAC-1. This is in line with the LOI measured in table 5.8 with LOIs of in-between 1.40 and 2.45 % for EAC-1. In addition to water, probably also some carbon may have oxidised during the initial burn of the sample (1100 $°C$ before XRF) and added to the LOI.

Total Alkali-Silica (TAS) diagrams show the SiO_2 content of a geological sample versus the alkali-silica ($Na_2O + K_2O$) content in wt % and is used to classify samples based on bulk chemistry. A simplified version (based on [537]) of the diagram is depicted in figure 5.20 where all area names have been removed and all regolith simulants analysed have been entered based, on table A.4.

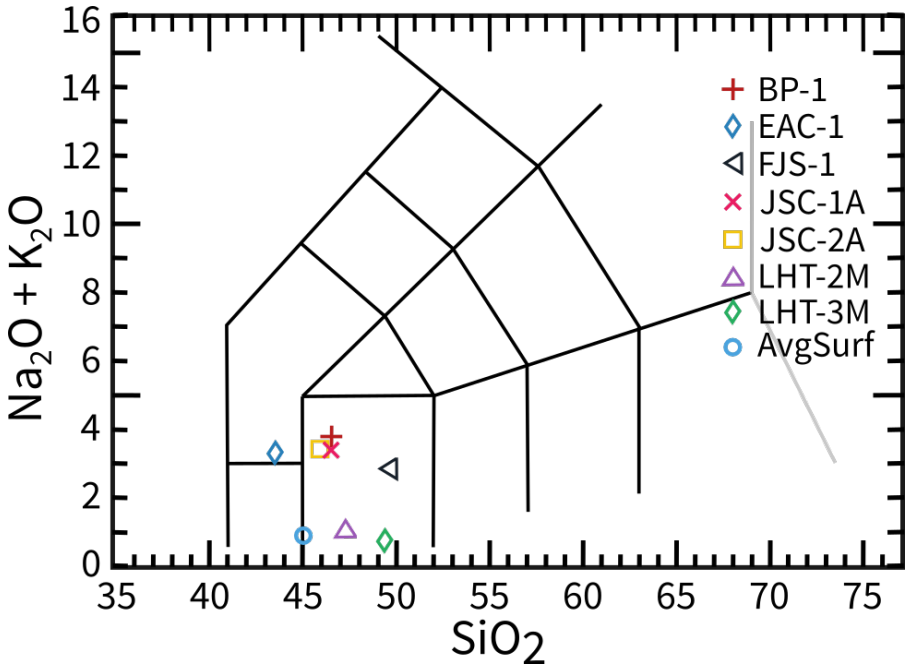

Figure 5.20: Total Alkali-Silica (TAS) diagram after [537].

All but one simulant lie in the "Basalt" region of the graph with the exception of EAC-1 which is in the "Tephrite Basanite" region, meaning that EAC-1 is considered undersaturated relative to silica. The Apollo mission returned undersaturated samples from the lunar surface, such as samples 12002, 12005, 70017 and 74220 with silica content of less than 44 wt% and alkali content of 0.45 wt % or less [538]. However, from what is know today it would be very unlikely to encounter non-basalts on the lunar surface, such as EAC-1. Furthermore, considering the average surface composition (blue circle "AvgSurf" in fig. 5.20) all simulants are within the same region but neither of them is at the same location than the average composition. Although, the measurements of the actual lunar surface material do not show values for K_2O, it is unlikely that they will. In turn this means that simulants containing K_2O are not appropriate simulants.

Geochemistry Conclusion

Detailed analysis of the geochemistry helps to understand how close a simulant is to lunar regolith and to detect differences in-between simulants. How thorough the analysis needs to be largely depends on the quality of information provided by the suppliers, as well as the use-case for the simulant. Most of the simulants (but one) analysed for this study were accompanied by poor data sets, as in particular shown with the XRF measurements. However, the conducted analyses on the to-be-utilised simulants are considered sufficient for this study, and the experimental applications of the simulant could commence.

Experiments will be centred on heating and melting regolith, as well as shaping manufactured basaltic glass. Thus, the elemental composition, as well as minerals contained are key in understanding the differences that may occur during processing. The results obtained from the XRD (+ thin sections) and XRF show, that all simulants analysed are suitably close enough to lunar regolith to be used. Furthermore, they also usefully represent a wide spread of material composition which may be encountered on the lunar surface. This helps to develop a process which tolerates a wide variety of input materials which in turn means that the process is lunar landing site independent.

5.1.4 Simulant Selection Summary

This chapter, chapter 5.1, showed some potential techniques which can be used to analyse regolith simulants. Thereby, these techniques were chosen based on their usefulness for the anticipated use-cases/manufacturing. There are further analytical techniques which can be applied to regolith simulants, and choosing a technique depends on which characteristic or parameter of the regolith simulants needs to be compared to actual lunar regolith. For example, if the simulant may be used to build a lunar base mock-up for public relation (PR) purposes, the main parameters of the simulant that are of relevance are optical appearance and its toxicity. Compared to that, if the simulant is to be used to test chemistry based extraction techniques, a thorough chemical analysis is required.

Working with (lunar) regolith simulants proved to be problematic, since not every user of a simulant is specialist in analytical techniques required to determine characteristics of a simulant. Thus, research conducted utilising regolith simulants is often more time consuming and unreliable than required. The extend of analysis conducted on regolith simulants for this work shows, it is a non-trivial matter to understand lunar regolith and to find a suitable analogue material to be used for manufacturing experiments.

A solution to this disconnect between the scientific community itself and the manufactures could be to define standard use-cases, accompanied by compulsory tests to be conducted, with according boundaries, which lead to different categories of simulants. Hence, each supplier knows which data to provide with their simulant and each scientist knows which simulant he/she can use for his/her use-case. A group

making a step in this direction is CLASS, the Center for Lunar and Asteroid Surface Sciences, a group of scientists at the University of Central Florida (UCF). They compiled the Planetary Simulant Database [539], a database of regolith simulants, which distinguishes four categories:

- **General purpose** manufactured to match a reference regolith's geotechnical, mineralogical and chemical composition. It is only used for simulants which are augmented or its mineralogy is a very close match to the reference.
- **Geotechnical/Physical** are simulants with the focus on physical and geotechnical properties. Mineralogy and chemistry are of secondary order of importance.
- **Spectral** is designed to mimic the optical appearance of a reference regolith by matching reflective properties.
- **Magnetic** means only the magnetic properties of a simulant are engineered to match a reference material.

For this work, a general purpose simulant is considered a high-fidelity simulant, a geotechnical/physical simulant is considered medium-fidelity, and spectral considered to be a low-fidelity simulant. Simulants chosen to be used for most experiments are:

- **BP-1**: medium-fidelity
- **EAC-1**: medium-fidelity
- **FJS-1**: high-fidelity
- **JSC-1A**: high-fidelity
- **JSC-2A**: high-fidelity
- **NU-LHT-3M**: high-fidelity

These six simulants chosen represent a spread of five lunar mare and one lunar highland type simulants. Moreover, their elemental composition differed around the elemental composition of the average lunar surface. Therefore these simulants, should allow for testing processes, for their input material tolerance.

In the field of regolith simulants, a first step has been made by CLASS at UCF to structure the field of experimental space sciences using simulants to demonstrate ISRU applications. Next steps will, however, require to make it useful for the entire community, by using the database as a starting point to develop international standards. These standards will define which categories are required, what type of tests each category will require and what limits and qualities are necessary. Further categories could include, for example, acoustic simulants or radiative simulants; a more detailed discussion can be found in [540]. Recommendations for production, usage and standardisation of lunar regolith simulants is discussed in [200]. By establishing standards, two things will be achieved: First, it will be possible to compare results in-between groups much better than at the moment, and second, scientists and groups do not necessarily need to understand all about a simulant before they can use it. Ideally, they would be able to procure a well characterised simulant of the category "manufacturing", for example, and use it straight away to test whether their process works with it or not. This saves time and reduces the turnaround time for testing and research in general.

5.2 Substrates Made of Regolith

After regolith simulants have been analysed in the previous chapter, this chapter shows detailed results on manufacturing basaltic glass substrates from regolith simulants. Manufacturing techniques used have already been described in chapter 3 and analytical methods in chapter 4. The first section describes basic parameters relevant to regolith processing and characterisation. The second and third sections show the two different approaches to substrate manufacturing used; microwave heating utilising a microwave kiln and graphite crucibles, and resistive heating utilising platinum crucibles. Section four and five in this chapter present improvements made on the substrate quality, based on the resistive heating approach. The last section of this chapter summarises the topic of substrate manufacturing from regolith.

5.2.1 Processing Parameters for Basaltic Glass Substrates

Before first substrates could be manufactured, melting regolith into glass needed to be understood, as well as what characteristics a glass substrates needs to have to qualify as substrate for mirror and later for solar cell manufacturing. To determine melting points of simulants, remote temperature measurements (with emissivity corrections), as well as DSC/TGA measurements have been conducted. After the discussion of these, a paragraph on substrate quality leads over to discussion of first actual substrates built.

Temperature Measurements

The basalt glass manufacturing process utilising microwaves to heat regolith simulants above melting point was described in section 3.2.3. The following will analyse and discuss measured temperature trends during processing, which are depicted in figure 5.21. Shown is the profile of heating six different regolith simulants by applying microwave heating, using the same process parameters. For each run, 15 g of regolith simulant have been entered in a new graphite crucible and heated for 1200 s (20 min), microwave power setting at 1000 W. The starting temperature for the conducted heating experiments was 20 °C.

The pyrometer was used to measure process temperatures which started recording at 450 °C. The lines in figure 5.21 show an initialisation phase (until crossing the threshold of 450 °C, a heating period (until 1200 s after start) and a cooling period (until temperature drops below 450 °C again).

Information on the heating behaviour of the substrates below 450 °C was not obtained. Although no values were recorded, information can be gained from the time it took to cross the 450 °C threshold (where the pyrometer started recording). The time was different for each simulant and table 5.14 summarises extrema found in figure 5.21, with t_{450} being the time it took for the simulant to heat from 20 to 450 °C. Additionally, T_{drop} indicates the temperature where a temporary drop in heating rate was observed, T_{max} the maximum end temperature after 1200 seconds heating,

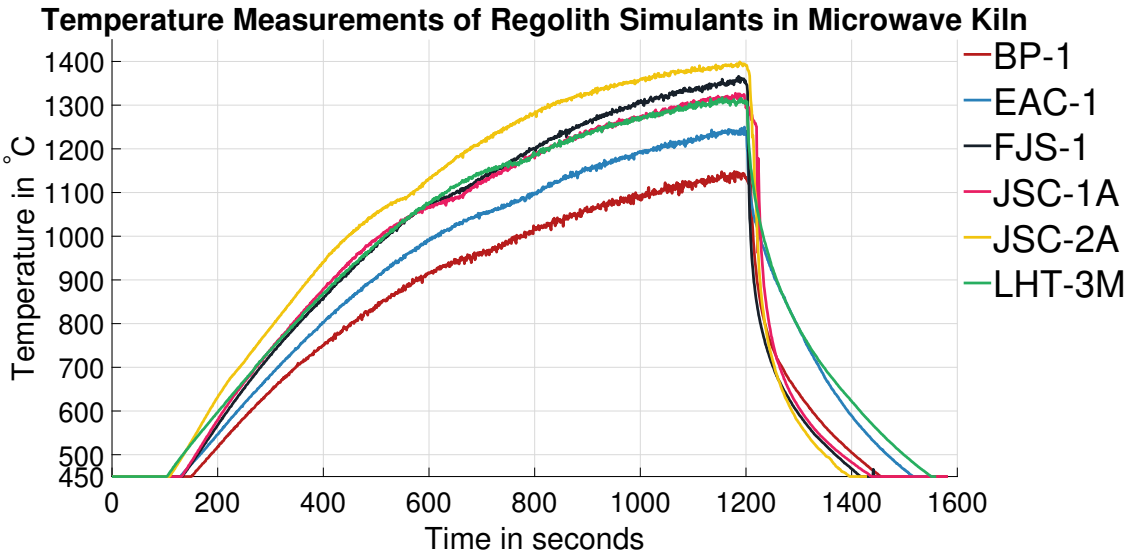

Figure 5.21: Regolith simulant temperatures in microwave kiln during a 20 minute heating period. Shown is recorded temperature from a pyrometer over time.

and $t_{cooling}$ the time it took for the sample to cool from 1200 (switching off) to 450 °C.

Table 5.14: Summary of extrema from figure 5.21

Sample	t_{450} in s	T_{drop} in °C	T_{max} in °C	$t_{cooling}$ in s
BP-1	151	956	1150	257
EAC-1	129	1081	1250	318
FJS-1	134	1086	1366	218
JSC-1A	131	1087	1327	239
JSC-2A	109	1090	1399	197
LHT-3M	105	1163	1318	351

With 151 seconds, BP-1 was the slowest to cross the threshold of 450 °C and with 105 seconds LHT-3M was the fastest, followed by JSC-2A with 109 seconds. BP-1 (simulant with the longest t_{450}) also had the lowest maximum temperature (T_{max}) of 1150 °C. From that it may seem like the two parameters could be connected but LHT-3M, which was the fastest to cross the threshold, only achieved the fourth highest maximum temperature with 1318 °C. The highest maximum temperature recorded during heating was for JSC-2A, with almost 1400 °C. From those results, reassessing processing temperatures, of all regolith simulants, their melting points seem to be located close to or above 1100 °C.

During a phase change from solid to liquid, for example, additional energy is required to break up solid bonds (crystals) to transition to the liquid state. For example, when salt ($NaCl$) hits water ice, the ice melts and the salt dissolves in the water. When measuring the temperature of the entire system before and after mixing, a temperature drop is recorded. This drop occurs since the salt takes

energy from the system, to dissolve. It does that in the form of energy taken, from the overall thermal energy of the system. The subtle drop in inclination of the regolith simulant heated in the microwave, which occurs around temperatures T_{drop}, was recorded for each simulant. It is thus likely the point where, similar to the salt example, the regolith undergoes a phase change from solid to liquid. This phase change could correspond to the drop in the temperature curve since the phase change will require additional energy from the system. Comparing process temperatures of the different simulants, depicted in figure 5.21 and listed in table 5.14, four of six simulants analysed show a drop of temperature increase within a window of 9 °C (1081 - 1090 °C). These drops occur after different starting times and thus seem independent of their heating rate. The only significant outliers are BP-1 with only 956 °C and LHT-3M with 1163 °C. The simulants cooling curve are similarly steep for BP-1, FJS-1, JSC-1A and JSC-2A (less than 260 s). Comparably slower cooling was recorded for EAC-1 and LHT-3M with a cooling time of more than 318 seconds. A connection between heating and cooling rate is not obvious from the results in figure 5.21, can, however, not be excluded either.

In general, for microwave experiments, the amount of susceptor material contained in a sample, heated in a microwave field, determines how well a material can absorb electromagnetic energy and convert it to heat. The goal of using a microwave kiln within a microwave field was, to eliminate the dependence on susceptor material contained in the regolith. Since all material could be heated in the kiln at a steady rate, this seem to be at least partially true, since iron sparse regolith such as LHT-3M usually tends not to heat up in a microwave field. Using a microwave kiln heating approach (as described in section 3.2.3), required two separate layers of susceptors. Both were used to aid the microwave process, in addition to the susceptor material contained in the simulant itself. The first layer being the silicon carbide ring in the microwave kiln, and the second the graphite crucible itself. Both materials are highly susceptible to microwaves and thus facilitate heating. This susceptor assisted heating approach therefore showed to offer a passive heating approach, which can be applied to a variety of input materials.

The downside of this approach is that all regoliths form large amounts of bubbles during the heating process. This effect is likely caused by the interaction of the graphite crucible with the regolith material itself. Carbon can react with the oxygen contained in the basaltic sands to form CO and/or CO_2 and thus reduce the elements contained in the simulant to their elemental state. Moreover, non-invasive measurements with a pyrometer can only determine the samples surface temperature, but not its core temperature. This suggests that a likely occurring temperature difference in-between the core of the regolith melt and the outside cannot be recorded.

For temperature measurements using a pyrometer, the emissivity of the measured regolith was set to 0.98 on the pyrometer for all measurements. Since it seemed likely that different simulants have different emissivities at different wavelength and temperatures an analysis of the regoliths' emissivity was conducted in order to be

able to compensate for these different emissivity values. What made it even more interesting to analyse the emissivity behaviour was that each simulant undergoes a phase change during heating, thus emissivity values are likely to be impacted even more.

Emissivity Corrections

Emissivity of a regolith simulant may be impacted by a simulant's chemical/mineral composition, its grain size distribution, and state of matter. To understand the impact of a regolith's emissivity on remote temperature measurements, an initial study was conducted based on the method described in section 4.2.4. All figures and analyses are based on measurement data listed in table A.6 in the appendix. Measurements were conducted as described in section 4.2.4.

Figure 5.22 shows the emissivity behaviour of four different regolith simulants, determined using the setup described in section 4.2.4 previously. The grain size distribution used for this measurement was the distribution the simulants have off-the-shelf, which was tested in figure 5.2 in section 5.1.2. Regolith simulants EAC-1, FJS-1, JSC-2A and LHT-3M have been measured over a range from 500 to 1050 °C and their according emissivity values have been recorded. Results in figure 5.22 show that FJS-1 has the highest emissivity values of all simulants analysed. This is true for the entire temperature range, and the emissivity of FJS-1 is slightly increased towards the highest recorded temperature. Hence, FJS-1 has the highest average emissivity (averaged over all temperatures measured) of all simulants with 0.94. It is followed by LHT-3M (0.90), JSC-2A (0.85) and EAC-1 (0.83) (details in table 5.15). The difference between the lowest and highest emissivity is $\Delta\epsilon = 0.11$, and is in-between FJS-1 (highest) and EAC-1 (lowest). JSC-2A seems to be the only simulant with large emissivity fluctuations (in-between 0.81 and 0.90), over the analysed temperature range, other simulants show smaller changes from 500 - 1050 °C. From these results it seems possible that remote temperature measurements obtained by an infrared pyrometer are prone to be impacted by emissivity fluctuations.

To better understand the impact, the grain size distribution of a regolith simulant may have on the emissivity, three different grain size distributions have been analysed and compared to the original grain size distribution. Figure 5.23 shows emissivity values for three (four) different grain sizes, and figure 5.24 a comparison of regolith with dull and shiny basaltic glass.

The grain size distribution used for the results depicted in figure 5.23 were:

- Raw: Unaltered regolith with grain size distribution as shown in figure 5.2
- Coarse: Grains larger than 300 μm
- Medium: Grains in-between 300 μm and $>$ 38 μm
- Fine: Everything smaller than 38 μm

Table 5.15 shows the average emissivity for each grain size distribution.

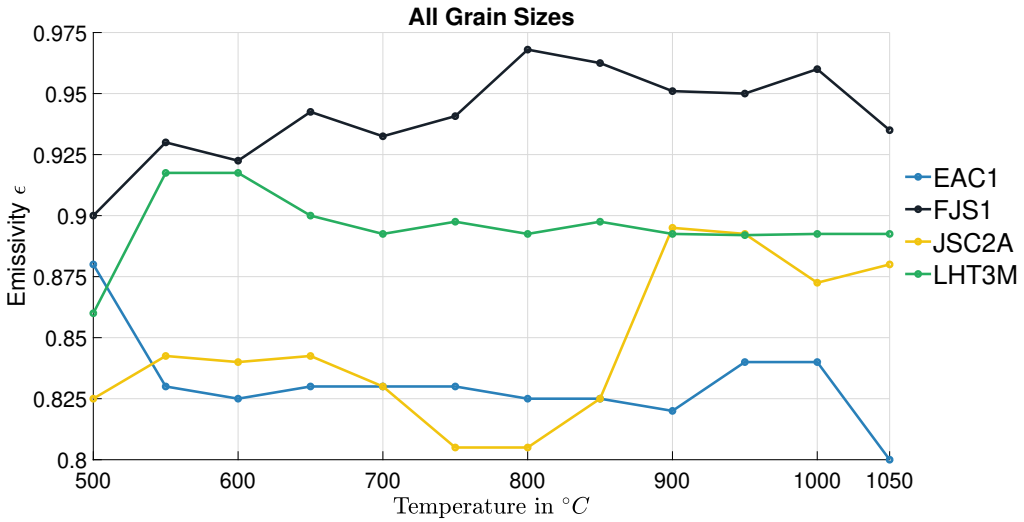

Figure 5.22: Regolith simulant emissivities recorded from 500 to 1050 °C for regolith containing a standard grain size distribution. The utilised pyrometer measured at 2 - 2.4 μm wavelength.

Table 5.15: Average emissivity of simulants dependent on grain size distribution

Simulant	Raw	Coarse	Medium	Fine
EAC-1	0.83	0.83	0.82	0.83
FJS-1	0.94	0.95	0.95	0.94
JSC-2A	0.85	0.85	0.85	0.85
LHT-3M	0.90	0.89	0.89	0.91

Although plots of the individual grain sizes' emissivity in figure 5.23 indicate small emissivity variations, the average emissivity does not differ more than 0.02 in-between different grain size distributions. The highest difference in average emissivity of 0.02 occurs in-between the coarse, medium and fine fraction of LHT-3M (table 5.15). Compared to the analysis of the emissivity of different regolith simulant types, grain size distribution seems to have a minor impact on the regoliths' emissivity.

The last factor analysed, which might impact the emissivity of a simulant, was the phase change. Therefore, measurements have been conducted determining the difference between raw regolith and basaltic glass made of regolith. Basaltic glass made of EAC-1 simulant has been compared with raw EAC-1 regolith simulant, results are depicted in figure 5.24. The figure shows emissivity measurements for two different types of glass ("dull" and "shiny"), as well as raw EAC-1 regolith simulant. The shiny version represents glass, which has been manufactured by heating and rapid cooling/quenching, thus, no or only little crystals could form and a shiny surface could be obtained. The dull version of the glass has been manufactured the same way, but has then been reheated to 1050 °C (and kept there for four hours) and likely lost its shine due to crystallisation effects taking place in the glass. To separate the effects, which surface quality and a phase change have

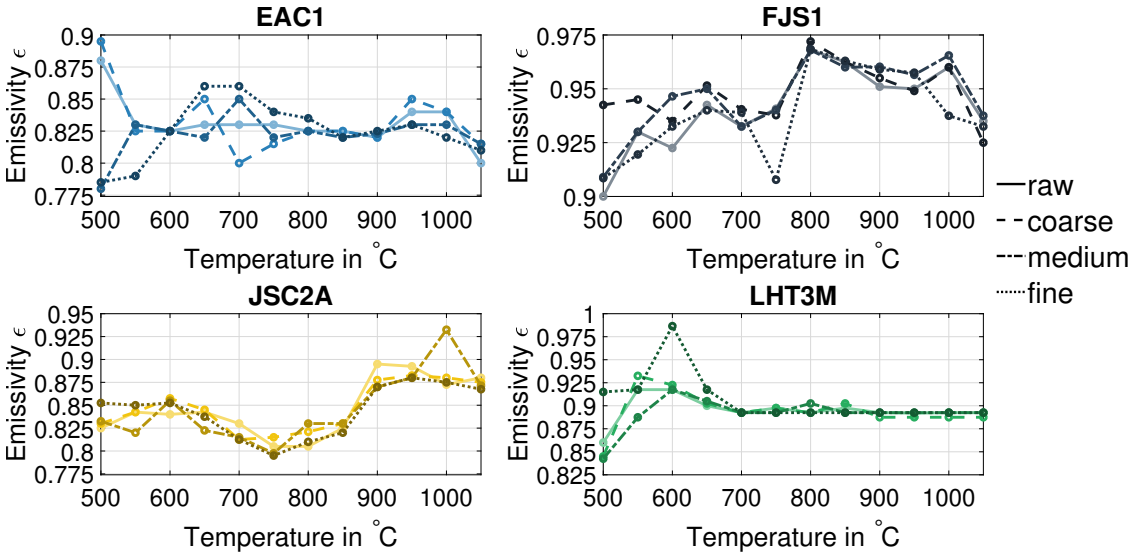

Figure 5.23: Regolith simulant's emissivities recorded from 500 to 1050 °C for four regolith simulant types (EAC1, FJS1, JSC2A, LHT3M). Each was measured with its standard grain size distribution (raw), > 300 μm (coarse), < 300 μm and > 38 μm (medium) and < 38 μm (fine). The used pyrometer measured at 2 - 2.4 μm wavelength.

on the emissivity measurements, was not possible with these experiments.

Figure 5.24 shows the emissivity results of the glasses and raw EAC-1 simulant. Differences in emissivity, in-between the two glass types, seem to be minor, since the absolute difference in average emissivity of the two glasses is 0.0071. Both glass curves follow the same downward trend, whereas the raw EAC-1 simulant seems to be steadier over the entire temperature range. The emissivity of both glasses drops absolute by 0.15 (shiny) and 0.16 (dull) over the course from 500 to 1050 °C. The emissivity of EAC-1 in comparison only drops by about 0.08 absolute. This may suggest, that once regolith is turned into glass, its emissivity may be more prone to fluctuations compared to raw, not melted regolith.

Concluding the observations of the regoliths' and basaltic glasses' emissivity behaviour, it seems that the emissivity of a regolith simulant itself in powder form remains rather stable over the examined temperature range from 500 to 1050 °C[5]. The average emissivity, however, differs significantly depending on which type of regolith is being measured, hence, each regolith type will require a different emissivity setting. This suggests, that once emissivity values are established for a simulant, measuring its temperature with a pyrometer should be reasonably accurate. Basaltic glass on the other hand seems to change its emissivity in an absolute range of about 0.15, thus will not show accurate results over a temperature range of 550 °C (from 500 to 1050 °C). Since, however, temperatures below 1050 °C are still below the actual melting point of most regolith simulants/basaltic glasses, it is unlikely that glass in its solid form needs to be measured during heating. What

[5]and in the measured wavelength spectrum of 2 - 2.4 μm

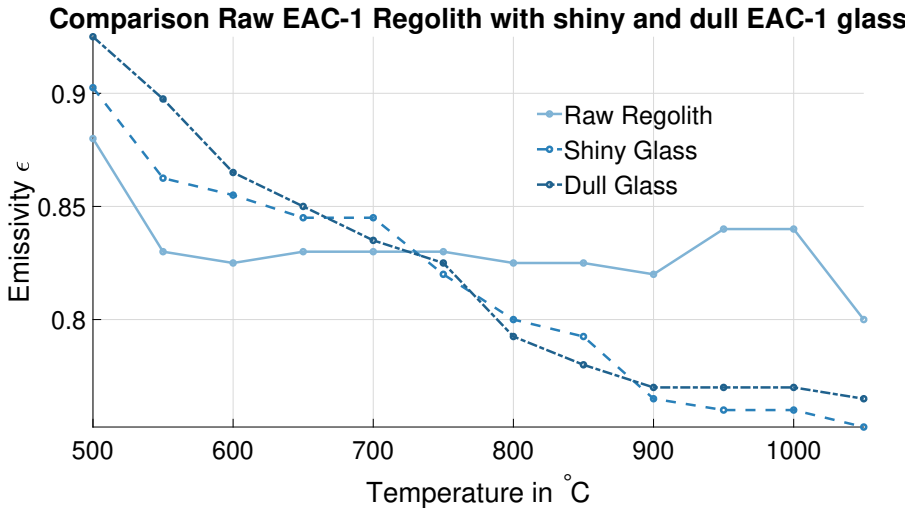

Figure 5.24: Emissivities of basaltic glass (dull/shiny) made of EAC-1 regolith simulant versus unprocessed EAC-1 regolith simulant. Temperature steps recorded from 500 to 1050 °C in increments of 50 °C, measured by a pyrometer from 2 - 2.4 μm wavelength.

seems, however, likely is that glass needs to be measured molten. With the utilised setup it was not possible to analyse the emissivity behaviour of molten glass, since the utilised kiln is limited to 1050 °C and therefore stays below melting point of the simulants. In case detailed measurements of hot glass will be needed, another set of experiments would be required.

With the obtained emissivity results an attempt was made to correct the results depicted in figure 5.21. The figure shows temperature measurements of six different simulants during heating and cooling, where the utilised pyrometer has not been set to the regolith simulant specific average emissivity. Instead, these measurements have been obtained utilising a constant emissivity of 0.98. Since all average emissivities are below this value, a correction for each simulants' curve seemed necessary and was attempted by utilising a simple correction approach described by [541]. This approach suggests, that a pyrometer is measuring two components, the radiation, emitted by the object's surface (E_{rego}), and the radiation, reflected by the background $E_{backgorund}$, where E in general is the radiant energy in $^{W}/_{m^2}$. This leads to a radiant energy detected by the pyrometer (E_{pyro}) of,

$$E_{pyro} = \epsilon * E_{rego} + (1 - \epsilon) * E_{backgorund}, \tag{5.19}$$

where ϵ is the emissivity of the measured regolith/object. Thus, if ϵ is different from its maximum of 1, a fraction of the background will be measured too. The following will attempt to correct the results shown in figure 5.21 by using the correct ϵ values for each measurement. Starting by converting from energy to temperature, equation (5.19) can be rewritten to,

$$\sigma * T_{pyro}^4 = \epsilon * \sigma * T_{rego}^4 + (1 - \epsilon) * \sigma * T_{backgorund}^4, \tag{5.20}$$

with σ the Stefan-Boltzmann constant ($5.67 * 10^{-8}$ W/m^2K^4), and T_{pyro} the according temperatures at the pyrometer, of the target (T_{rego}), and the background ($T_{backgorund}$) in Kelvin. The influence of the background can be neglected as long as the target area of the pyrometer is greater than the spot size described in the manufactures manual [542]. Since the pyrometer was setup focused on only the target, the background influence is set to zero which leads to,

$$\sigma * T_{pyro}^4 = \epsilon * \sigma * T_{rego}^4. \tag{5.21}$$

This leads to a correction approach of,

$$T_{rego}^4 = \frac{T_{pyro_{old}}^4}{\epsilon_{old}}, \tag{5.22}$$

$$T_{rego} = \frac{T_{pyro_{old}}}{\sqrt[4]{\epsilon_{old}}}, \tag{5.23}$$

with ϵ_{old} indicating the results depicted in figure 5.21 with $\epsilon = 0.98$ (constant for all measurements). All measured values (T_{pyro}) for EAC-1, FJS-1, JSC-2A and LHT-3M were accordingly divided by $\sqrt[4]{\epsilon_{old}}$, and lead to new ($_{new}$) temperatures $T_{pyro_{new}}$,

$$T_{pyro_{new}}^4 = T_{rego}^4 * \epsilon_{new}, \tag{5.24}$$

$$T_{pyro_{new}} = T_{rego} * \sqrt[4]{\epsilon}_{new}. \tag{5.25}$$

By inserting equation (5.22) into (5.25), $T_{pyro_{new}}$ following final equation can be written to,

$$T_{pyro_{new}} = \frac{T_{pyro_{old}}}{\sqrt[4]{\epsilon_{old}}} * \sqrt[4]{\epsilon}_{new}. \tag{5.26}$$

Using this correction approach a new figure, based on the corrected values, was plotted. It is depicted in 5.25 and it can be seen that the applied corrections lead to new extrema (drop and melting temperature as well as peak temperature). Those new values are summarised in table 5.16.

Overall, all values have decreased. Since no simulant had an emissivity as high as, or higher than 0.98 this is only logical. Moreover, the curve of JSC-2A and FJS-1, as well as LHT-3M show less space in-between their curves. This seems logical since all of them are a similar grade simulant. The largest change after correction can be observed at EAC-1's curve. Maximum temperature decreased from 1250 to

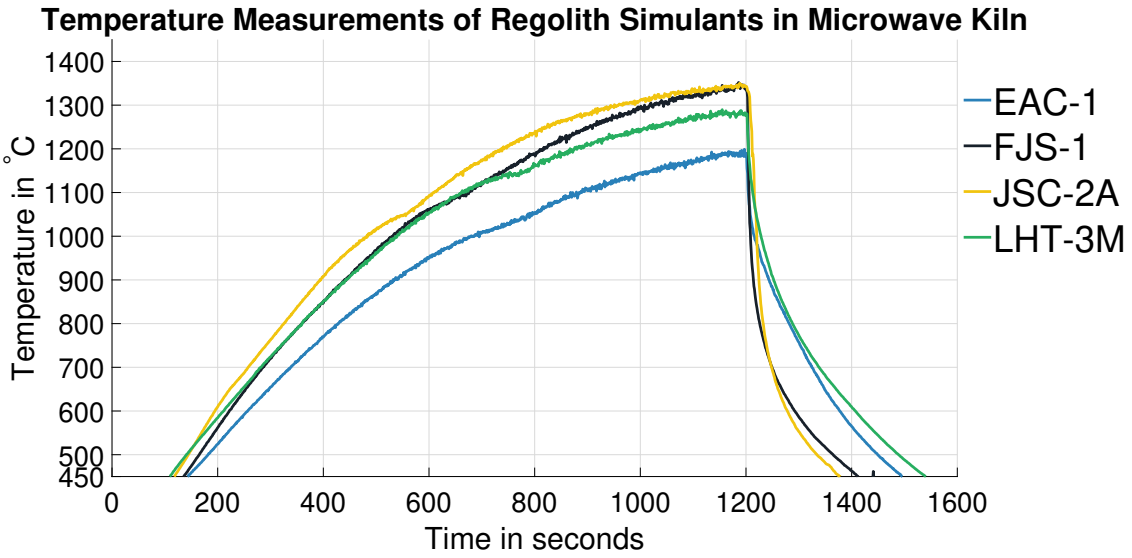

Figure 5.25: Corrected regolith simulant temperatures in microwave kiln.

1199 °C, which is a decrease of more than 4 %.

Table 5.16: Summary of extrema from figure 5.25

Sample	T_{drop} in °C	$\Delta T_{drop-abs}$ in °C	T_{max} in °C	$\Delta T_{max-abs}$ in °C
EAC-1	1023	- 58	1199	- 51
FJS-1	1082	- 4	1351	- 15
JSC-2A	1053	- 37	1350	- 49
LHT-3M	1144	- 19	1290	- 28

This attempt of correcting non-invasive temperature measurements of regolith simulant, conducted using a pyrometer, showed that it is non-trivial to measure the correct temperature. Although emissivity of an individual simulant does not seem to be impacted largely by its grain size distribution, but rather dependent on the regolith's composition. Another variable influencing the regoliths' emissivity was the phase change, which occurred during the measurements. It cannot directly quantitatively be said, how large the phase change impacts the emissivity, however, emissivity measurements conducted on solidified glass showed that glass[6] changes its emissivity rather largely compared to raw regolith. Hence, it is unclear how large the impact of the phase change is on the measurements, since there is reason to believe it may be significant. The sudden change of emissivity could also be reason for the drop, which was recorded in the temperature curves.

Studying the regoltih's emissivity behaviour in detail showed that a regolith's emissivity is impacted by a number of factors, which are not all fully understood yet. In turn, this makes remote temperature measurements by means of a pyrometer unreliable, and cooling and heating trends may only be discussed by considering the

[6]for temperature ranges from 500 - 1050 °C

uncertainty introduced by the emissivity. One possibility to improve the reliability of the results may be additional temperature measurements using for example thermocouples. Decreasing the heating rate will slow down overall heating, and thus leave more time for the sample to settle its temperature at each point, which may further increase the reliability. Due to most metals being susceptible to microwaves, it is non-trivial to introduce a standard temperature sensor into a microwave field, which is why in a first approximation the obtained measurement results shall be good enough to proceed with the experiments.

Differential Scanning Calorimetry and Thermogravimetric Analysis

To obtain further insights into the melting behaviour of regolith simulants, combined Differential Scanning Calorimetry (DSC) and Thermogravimetric Analysis (TGA) have been conducted. Results of the DSC are depicted in figure 5.27 and the TGA results are shown in 5.28. Each simulant has been run using the same procedure and parameters, starting at 25 °C and temperature was increased by 10.0 $^{°C}/_{min}$ to an end temperature of 1335 °C. The sample mass used for each run was in-between 7 and 30 mg (details in table A.9) and the results for DSC have been scaled to $^{mW}/_{mg}$ to compensate for the different amount of sample mass used. For each regolith type, a raw version (not ground) was analysed and for some also a ground version.

As basis for the discussion of the DSC and TGA results was [543], information provided by TA Instruments in [544] and a training video [545]. In general DSC and TGA results can show certain distinct characteristics, depicted in schematic 5.26. For regolith samples on the DSC, typically an exothermic peak can be observed at first, followed by an endothermic peak. Typically, an exothermic peak suggests crystallisation occurring and an endothermic peak, melting occurring. For TGA, three rather distinct phases can usually be observed, volatile evaporation at low temperatures, decomposition at medium temperatures and combustion at high temperatures. The terms low, medium and high refer to the characteristics of the material analysed and will drastically differ in-between for example polymers and rocks. The following paragraphs will analyse each simulant type in detail and point out potential regions/temperatures where certain phase changes may occur. Since all regolith simulants are composed of an inhomogeneous mix of different minerals/igneous rock, a clear crystallisation peak is not expected and may therefore not always be obvious. Next, each simulant will be individually discussed with respect to its DSC (figure 5.27) and the TGA results (figure 5.28).

BP-1 - DSC: The trend of both BP-1 lines (red full (raw) and red dashed (ground) in figure 5.27) is similar in shape. However, the ground curve is offset compared to the raw curve which suggests that the ground regolith is less exothermic (releases more heat) than the raw regolith. At about 660 to 670 °C a small (≈ 0.05 $^{mW}/_{mg}$) exothermic peak occurs which could mark the crystallisation temperature. Moreover, a small (≈ 0.1 $^{mW}/_{mg}$) endothermic peak occurs in the ground sample at around 1160 °C, which could mark the melting point (glass transition temperature).

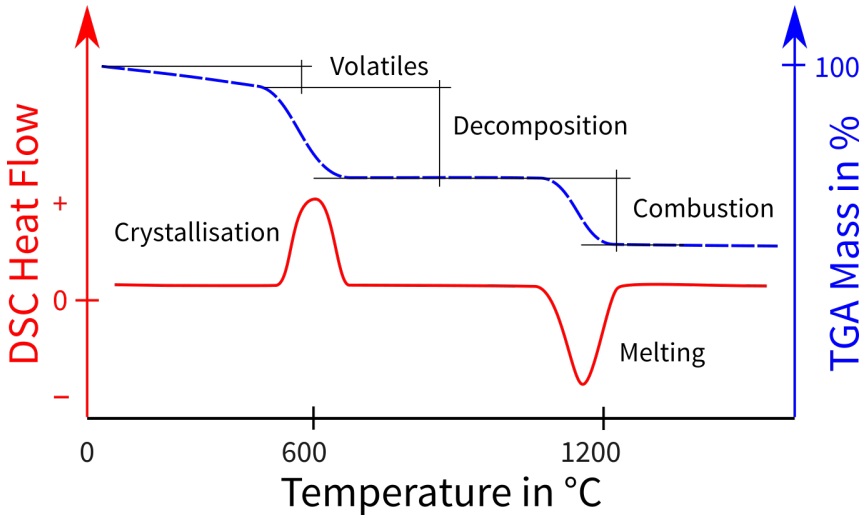

Figure 5.26: Schematic of DSC (red) and TGA (blue) results, indicating different transition zones.

BP-1 - TGA: In figure 5.28 the three areas, indicated in schematic 5.26, occur from 0 - 600 °C (volatiles), 600 - 700 °C (decomposition) and 1200 - 1350 °C (combustion). For both, ground and raw BP-1, this pattern shows to be similar with an offset in y direction ("lost mass") of about 0.5 %.
EAC-1 - DSC: Both, raw and ground EAC-1 lines (figure 5.27) are only about 0.1 $^{mW}/_{mg}$ apart and therefore much closer than JSC-2A or BP-1, for example. Both curves reach their highest point (most exothermic) at around 700 °C. Since no clear peak can be observed, it remains unclear whether this is the crystallisation temperature of EAC-1. The melting temperature may be indicated by a drop at around 1080 °C.
EAC-1 - TGA: From the TGA results depicted in figure 5.28 it seems that volatiles may be released from 0 to 400 °C and for ground and raw EAC-1 decomposition may occur from 400 to 800 °C. After a plateau of about 300 °C, combustion seems to occur from 1100 to 1330 °C. This is a similar region than where the highest exothermic heat flow can be observed for EAC-1 in the DSC graph.
FJS-1 - DSC: Crystallisation temperature for FJS-1 could be located around 750 °C and melting around 1160 °C. However, once more the crystallisation peak is rather broad and the melting peak distinct, but no larger than 0.05 $^{mW}/_{mg}$. No ground version of this simulant was analysed.
FJS-1 - TGA: Volatiles seem to be released until about 400 °C, after that no decomposition drop can be observed at all. Another drop occurs at around 1200 to 1350 °C, which seems to be the combustion drop rather than the decomposition drop.
JSC-1A - DSC: It has the highest exothermic heat flow of all raw regoliths, with about 1 $^{mW}/_{mg}$ at its peak point located around 750 °C. This also indicates the point where crystallisation is most likely to occur and melting seems to occur at around 1125 °C. Comparing JSC-1A and JSC-2A, their trend is similar but offset. This is not surprising since JSC-2A was engineered to be similar or even the same as JSC-1A. No ground version of this simulant was analysed.

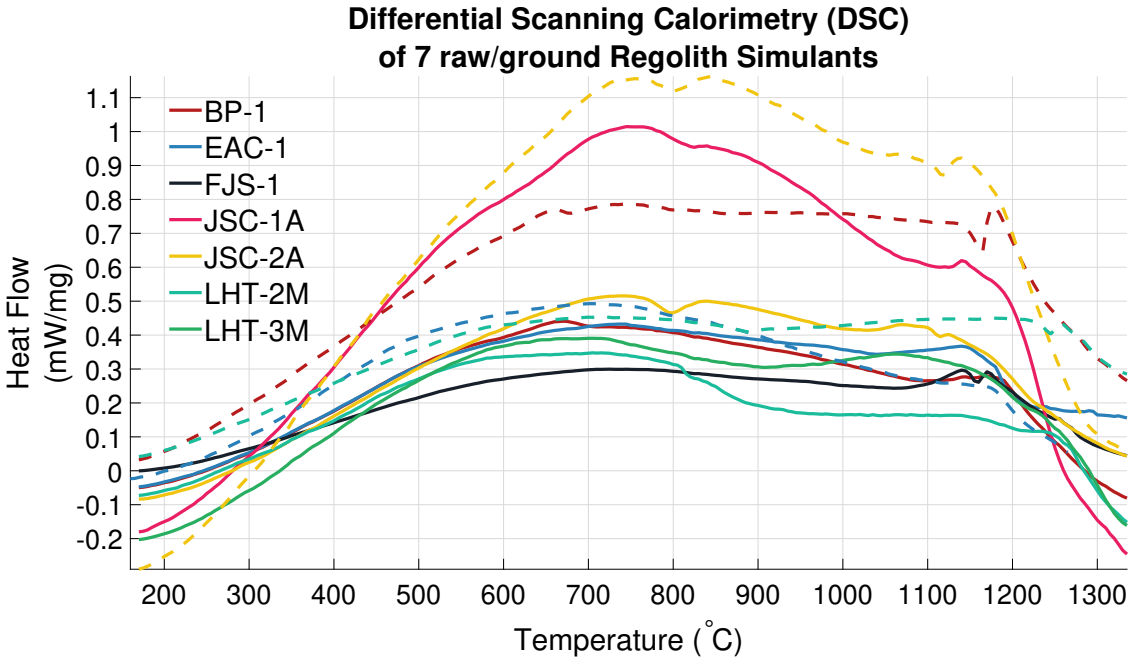

Figure 5.27: Differential Scanning Calorimetry (DSC) of raw regolith. The abscissa shows heat flow in $^{mW}/_{mg}$ and the ordinate temperature. Full lines show raw regolith, dashed ground (to smaller than < 38 μm) regolith.

JSC-1A - TGA: Volatiles contained in JSC-1A vaporise from 0 to 550 °C, followed by no clear decomposition drop but only a drop at 1150 to 1330 °C marking the combustion area.
JSC-2A - DSC: The DSC measurement for JSC-2A does not show a clear peak for crystallisation which happens probably from 750 to 850 °C. From the DSC results, it seems JSC-2A melts at around 1115 °C. Why JSC-2A raw has the highest shift of all simulants compared to its ground version is unclear an would need further investigations.
JSC-2A - TGA: The three zones of JSC-2A are 0 to 100 °C (volatiles), 650 to 750 °C (decomposition) and 1150 to 1300 °C (combustion). Compared to other simulants most volatiles seem to have vanished at rather low temperatures already, since the lost weight plateaus for 100 to 600 °C.
LHT-2M - DSC: This simulant is the predecessor to LHT-3M, thus shows a very similar trend to LHT-3M. Its crystallisation temperature seems to be around 700 °C and the melting point with around 1245 °C rather high compared to the other simulants.
LHT-2M - TGA: TGA curves for LHT type simulants show to be more shallow than curves of other simulants. This makes it more difficult to define distinct regions. The regions identified are 0 to 500 °C, 500 to 1000 °C and 1150 to 1300 °C for volatile evaporation, decomposition and combustion accordingly.
LHT-3M - DSC: As mentioned before LHT-3M is engineered to be similar in appearance and composition than its predecessor LHT-2M, thus its behaviour is close to LHT-2M as well. Its crystallisation temperature seems slightly higher with 720 °C and melting point slightly lower with 1220 °C. The melting temperature for

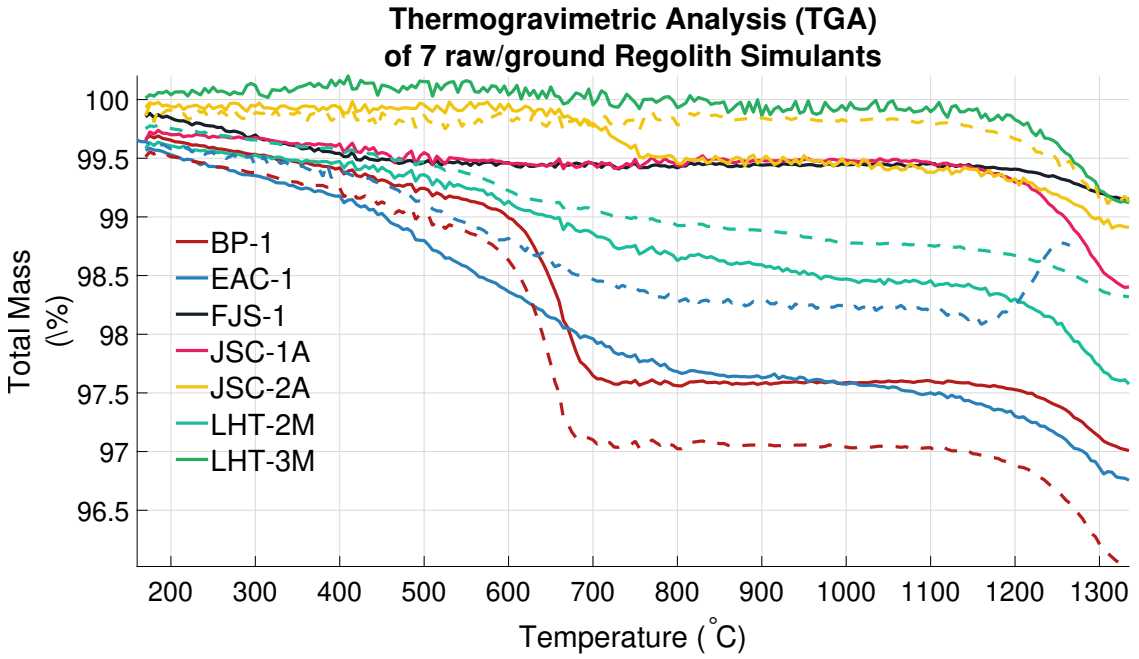

Figure 5.28: Thermogravimetric Analysis (TGA) of raw regolith. The abscissa shows total mass in % and the ordinate temperature. Full lines show raw regolith, dashed ground (to smaller than < 38 μm) regolith.

LHT-3M is therefore also rather high compared to all other "non-LHT" simulants. No ground version of this simulant was analysed.
LHT-3M - TGA: The TGA reading for raw LHT-3M is slightly off, since it shows values above 100 % at the beginning. The most likely reason for that is that little to no water/volatiles are contained in LHT-3M and instead of releasing volatiles, LHT-3M absorbs oxygen by oxidizing iron. Moreover, the only distinct region which can be identified is in-between 1200 and 1350 °C and should mark the combustion zone.

All estimated values for crystallisation, melting, volatile evaporation, decomposition and combustion are summarised in table 5.17. All values are taken from the raw simulant measurements. Comparing these values to the values measured during microwave heating (table 5.14), differences in supposed melting temperatures of in-between 57 to 78 °C can be observed. All temperature measurements obtained by the pyrometer show to be lower than the temperature values determined from the DSC/TGA measurements. This seems plausible since the temperature of the microwave samples was obtained remotely from the surface of the sample rather than their core. Since the temperature in the core, would likely have reached melting temperature earlier than on the outside, the phase change induced temperature drop would seem to occur at a lower temperature.

Two techniques helped to estimate the melting points of all simulants analysed, temperature measurements using a pyrometer and the presented DSC/TGA measurements. Further, DSC/TGA suggests crystallisation temperatures for all analysed simulants. Although both, crystallisation and melting, seem to occur

Table 5.17: Approximate transition temperatures of seven regolith simulants obtained from DSC and TGA measurements, values are in °C

Simulant	Crystallization	Melting	Volatiles	Decomposition	Combustion
BP-1	660-670	1160	0-600	600-700	1200-1350
EAC-1	700	1080	0-400	400-800	1100-1330
FJS-1	750	1160	0-400	n.a.	1200-1350
JSC-1A	750	1125	0-550	n.a.	1150-1330
JSC-2A	750-850	1115	0-100	650-750	1150-1300
LHT-2M	700	1245	0-500	500-1000	1150-1300
LHT-3M	720	1220	n.a.	n.a.	1200-1350

around similar temperatures (throughout all simulants), crystallisation temperatures seem to range from 660 to 850 °C and melting temperatures from 1080 to 1245 °C. These differences are likely caused by the differences in geochemistry (table A.4) and/or mineralogy (tables 5.6 and 5.7). Thus, determining exact temperatures, with either of the methods used, seems not possible and may be due to these inhomogeneities of the regoliths. All of them contain multiple different minerals, which all have different individual melting points. Thus, determined crystallisation and melting temperatures may, in combination with the mineralogical and geochemical analysis, of each simulant, provided to be useful to adjust the manufacturing processes.

After discussed process parameters (temperature and transition points) have been analysed, first manufacturing of samples was conducted. By heating, melting and cooling of regolith, basaltic glass samples were manufactured. The quality of the manufactured and processed samples is discussed next.

5.2.2 Microwave Manufactured Substrates

This section presents results of the first actual substrates built from regolith, utilising a microwave kiln and a standard household microwave oven to melt lunar regolith simulants. Presented are, surface features, surface roughness, topography and mineral content, as well as the substrates reflectivity. Microwave heating experiments have been conducted in two separate batches. The difference between those two batches is, that the first test batch used only two different simulants, EAC-1 and JSC-2A, the second batch utilised four simulants: EAC-1, FJS-1, JSC-2A and LHT-3M. Further details on manufacturing of the microwave heated samples can be found in section 3.2.3 and details on the samples are listed in table 3.3.

Surface Features

This section shows the results of the surface analysis of basalt glass samples manufactured from regolith by means of microwave heating. The results have been presented in a different form in [255] before. Surface feature analyses included optical analysis via SEM, mineralogical analysis via EDX, topographical analysis

via optical microscopy, and surface roughness analysis via profilometry.

Optical Analysis of Samples' Surfaces

Figure 5.29 shows an SEM image, as well as an optical microscope image of sample EAC-II (made of EAC-1), and figure 5.30 shows an SEM image of the polished surface of samples LHT-II, FJS-II and JSC-II (made of LHT-3M, FJS-1 and JSC-2A). Both figures show crystallised areas, as well as amorphous glass areas on the surface of all four samples. The crystallised areas are likely to have formed during cooling of the sample and led to partial recrystallisation of the glass melt, forming dendrites. These dendrites are shown in figure 5.29 in both images (left and right). A typical tree-like shape can be observed which is characterised by multi-branching off various points. On the right side of figure 5.29 areas with supposedly amorphous glass can be seen. These areas are likely to have cooled more rapid than the supposedly crystalline areas.

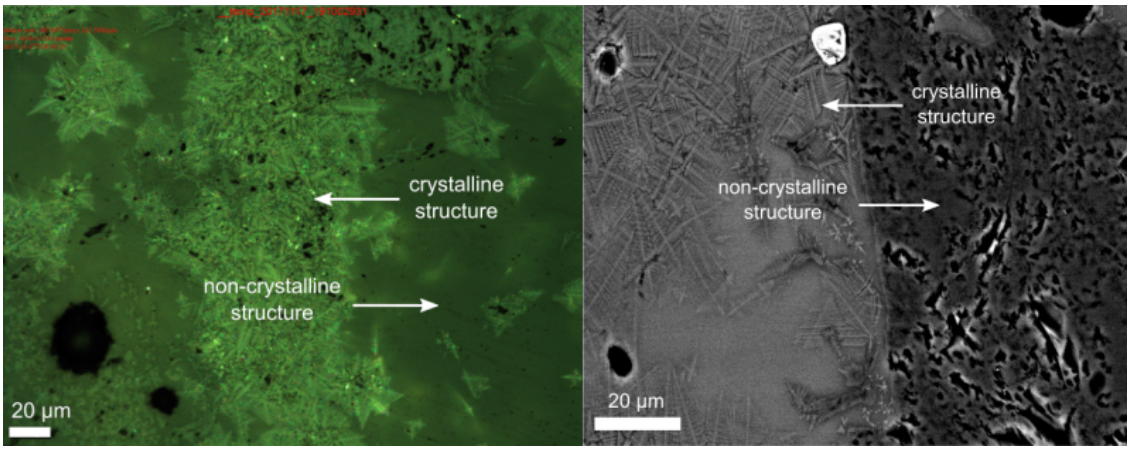

Figure 5.29: EAC-1 basaltic glass substrate (EAC-II) manufactured via microwave-heating. Focus variation microscopy image (left) and SEM image (right) with each showing mainly amorphous glass areas on their right vs. crystalline (dendrite) areas on their left.

During polishing of the surfaces, differences in behaviour, in-between the amorphous and crystalline areas, could not be observed. Thus, it seems that the level of crystallization has (if any) only a minor impact on the hardness of the sample and therefore on its grindability. Optically, however, this may be different since by looking at the samples, with the human eye, brighter and darker areas are visible, which coincide with the appearance of crystalline areas. The crystalline areas appear brighter to the human eye than the non-crystalline areas. An analysis of the optical properties of the polished glass surfaces was conducted and will be discussed in the next section, section 5.3.

The other three types of basaltic glasses (made of JSC-2A, FJS-1 and LHT-3M) also show beginnings of recrystallisation in the glass melt. Rectangular-shaped crystals can be seen in figure 5.30 on all three SEM images and appear all over the

samples surface. However, neither of these three samples shows crystals in form of dendrites as the sample made of EAC-1 does. Although the shape of the crystals is different from EAC-1 basaltic glass, the behaviour of the glasses during polishing was the same and the grindability did not seem to be impacted. These crystals may impact the reflectivity of the samples as well, thus may have influenced the optical properties of front coated mirrors manufactured on these substrates.

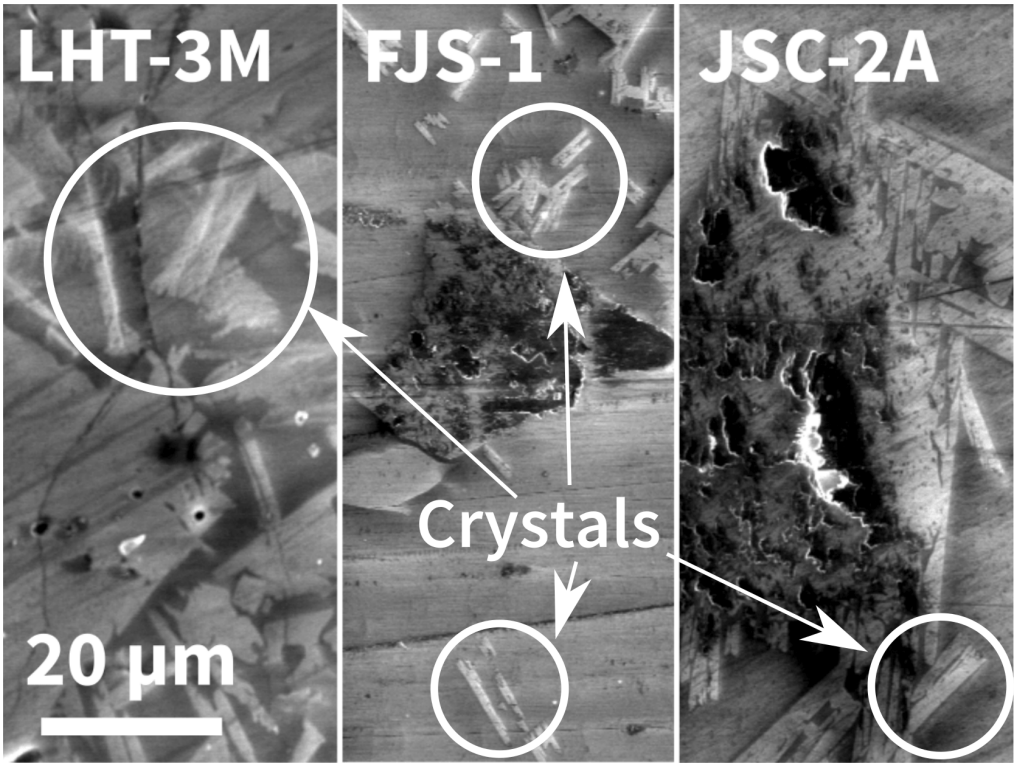

Figure 5.30: SEM (GSE) images of polished glass samples' surfaces of samples (left to right) LHT-II, FJS-II, JSC-II.

Mineralogical Analysis of LHT-3M Sample

By looking at the polished surface of the sample made of LHT-3M as depicted in figure 3.21 in chapter 3.3.4, the sample appears to have a different colour than all other samples. The colour of the sample can be described to be jade or pale green. By taking a closer look, different areas can be observed on the samples surface. These areas are depicted in figure 5.31 in an SEM image of the samples surface on the left and a false colour EDX image on the right. Darker grey areas (left figure) indicate areas where minerals have not melted and the distinct grain geometry is still intact. Lighter grey areas are surrounding these minerals and are likely to be composed of crystalline and amorphous glass. Crystals cannot be observed in this image as they can in figure 5.30 since the image is not zoomed in enough.

Next to the SEM image on the right side in figure 5.31, a composite elemental map, from energy-dispersive X-ray (EDX) analysis is shown. This image shows areas of different elemental compositions in different colours. Three distinct

colours/compositions were detected, blue, green and orange. Areas with light grey colour on the SEM image appear blue on the EDX false colour image, thus show the glass phase. The areas supposedly containing minerals are shown in green and orange. Both indicate two distinct minerals, which have not melted applying suceptor-assisted microwave heating. Detailed in table 5.18 are the average elemental compositions of all three areas (colours).

From the values obtained by EDX area measurements, shown in table 5.18, it seems that those minerals are mostly orthopyroxenes, clinopyroxenes or plagioclases (very anorthite rich). As discussed earlier, typically basalts (to a first approximation) can be defined as being a mix of these three, usually accompanied by variable amounts of olivine and/or amorphous basalt glass or other minerals. As the results in the geochemistry section 5.1.3 showed, LHT-3M is mostly comprised of orthopyroxene (16.64 % En), clinopyroxene (6.67 % Di + Aug + Pgt) and plagioclase (66.58 %). Moreover, a composition of such is typical for actual lunar samples as known from the Apollo [7] missions. An overview of the detected minerals:

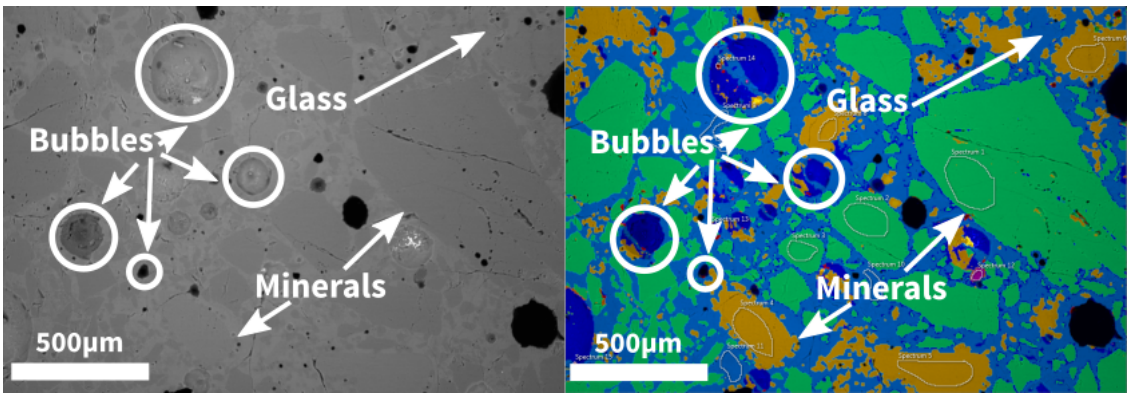

Figure 5.31: SEM image (left) of the LHT-3M glass and and EDX map of the same area on the right. Depicted are impairments in form of bubbles, surrounding glass as well as un-melted minerals. Three zones with different elemental compositions are indicated in green blue and orange in the EDX image on the right.

- *Plagioclase:* Likely the green areas - in the EDX image - are plagioclase feldspars, rich in calcium (9.83 %). This further suggests bytownite and labradorite, since both are rich in anorthite and matches the XRD measurement results with 36.41 % bytownite and 6.66 % labradorite. Such anorthite-rich minerals are also to be expected at temperatures, as high as 1200 °C or more since they can withstand those temperatures.
- *Clinopyroxene:* With contained aluminium as low as 2.58 % the orange areas could be pyroxenes. Moreover magnesium at 13.34 % and calcium at 1.84 % suggest augite (a clinopyroxene), a common mineral in basalts. From the XRD measurements in table 5.7 the amount of augite contained in LHT-3M is 4.55

[7] Table A.2 shows the composition of some Apollo mission samples containing more than 60% of pyroxene and plagioclase in total.

% and the overall clinopyroxene content is 6.67 %. This rather small amount combined with the elemental analysis of the orange area suggest the orange area to be clinopyroxene. Further, the orange areas occur less on the EDX image than the green areas. This observation matches the contained amount of clinopyroxene known from the XRD.

- *Orthopyroxene:* It forms at high temperatures and may occur in basalts. Although the orange area contains small amounts of aluminium, as well as calcium, it does not seem to be enough to be the mineral pigeonite. Moreover, the green area shows no magnesium and the orange areas shows iron, thus it is unlikely that either of these area would account for the 16.64 % of enstatite contained in LHT-3M.
- *Basaltic Glass:* The blue areas seem to be basaltic glass since it contains all elements but sodium.

Table 5.18: Elemental Compositions of the LHT-II Sample (Figure5.31) as detected by EDX area analysis

Element	Blue (wt%) Basaltic Glass	Green (wt%) Plagioclase	Orange (wt%) Clinopyroxene
O	50.2	53.03	49.86
Si	18.5	16.78	18.94
Al	8.65	13.80	2.58
Ca	6.58	9.83	1.84
Mg	5.48	-	13.34
Fe	3.7	0.48	6.2
Na	-	0.83	-
Total	93.11	94.75	92.76

Why clinopyroxene and plagioclase did not melt is not obvious. Considering the overall iron content of the simulant, LHT-3M has a total iron oxide content of 4.16 %. Compared to 10.75 wt % for JSC-2A, 12.00 wt % for EAC-1 and 13.07 wt % for FJS-1, LHT-3M is rather iron sparse. Due to coupled dielectric heating mode [384–386, 546], iron oxide is most susceptible to microwaves, thus, to microwave heating. Suggesting that LHT-3M (iron sparse material), has a reduced susceptibility and does not reach similar temperatures as hot as more iron rich materials. However, since the plagioclase (green) contains less than 1 % of iron, it may have had reduced susceptibility to microwaves. Which led to a decreased heating efficiency compared to minerals with a higher iron content, thus the green areas did not reach their melting point. Depending on how close the contained minerals are to either of the end members albite or anorthite, the melting point will be somewhere in-between 1100 °C (albite [185]) to 1550 °C (anorthite [186]). Since the EDX analysis suggests anorthite rich plagioclase for the green areas, it is likely that the melting point of those minerals indicated in green is close to 1550 °C. Since the maximum process temperature measured for any simulant does not exceed 1350 °C, and the maximum temperature measured for LHT-3M was even

lower than 1300 °C, it seems logical, that anorthite rich plagioclase could not melt.

As mentioned earlier, the LHT-3M sample has a jade appearance (figure 3.21) which makes it different from all other samples. One possibility for the different coloration (green) may be that LHT-3M contains a comparably high amount of the trace element chromium (1459 ppm, from table 5.12). Compared to the chromium content of, for example, 346 ppm for FJS-1, this trace element is significantly elevated and may be the reason for the samples colour. The 388 ppm nickel contained in LHT-3M (shown in table 5.12) could be a second possibility which can lead to green colour in samples. However, it is more likely to find this colour within olivines and LHT-3M is rather olivine sparse.

Whether the green appearance of the LHT-3M glass remains after all minerals have fully melted, cannot be said from this experiment and will require further tests. A portion of the iron contained in LHT-3M, is contained in the non-melted clinopyroxenes, which did not melt using the described microwave heating approach. Since the iron content of a glass typically primarily determines its colour, it remains to be seen what happens when the entire regolith simulant is melted and all iron oxide contained in LHT-3M is melted. It is therefore likely that LHT-3M when fully melted also forms a dark brown/black glass as was observed for all other simulants processed.

Surface Topography

After glass was manufactured, utilising microwave heating, the glass samples were ground flat and polished. Then, the surface structure of the samples was characterised by means of focus variation microscopy. The measurements depicted in figure 5.32 show examples for the dimensions of the macroscopic surface features found on the sample EAC-II. These results were obtained using focus variation microscopy which has been described in section 4.2.2.

The reconstructed surface created by the measurement software shows a top view of the sample EAC-II (figure 5.32, top). From that image/view, three surface profiles were extracted by measuring along the arrows indicated in white. The horizontally measured profiles are depicted in figure 5.32 at the bottom. Graphs (a), (b) and (c) show surface profiles of three different size surface features. Graph (c) shows the largest cavity with a maximum depth of about 40 μm. A medium size void is depicted in (b) and is about 5 μm deep. The actual surface roughness was measured along the arrow (a) and deviates 400 to -800 nm from the mean line. The profiles of two larger voids/bubbles (which have formed during melting) are depicted in subplots (b) and (c). These bubbles may have formed in the melt by surrounded air being trapped in the melt, outgassing of the regolith itself, or due to a chemical reaction of the regolith with the crucible material. In addition, as pointed out in the previous sections, the analysed sample made of EAC-1 shows partial crystallisation indicated in the 3D reconstructed image by brighter (crystalline) and darker green (non-crystalline) areas.

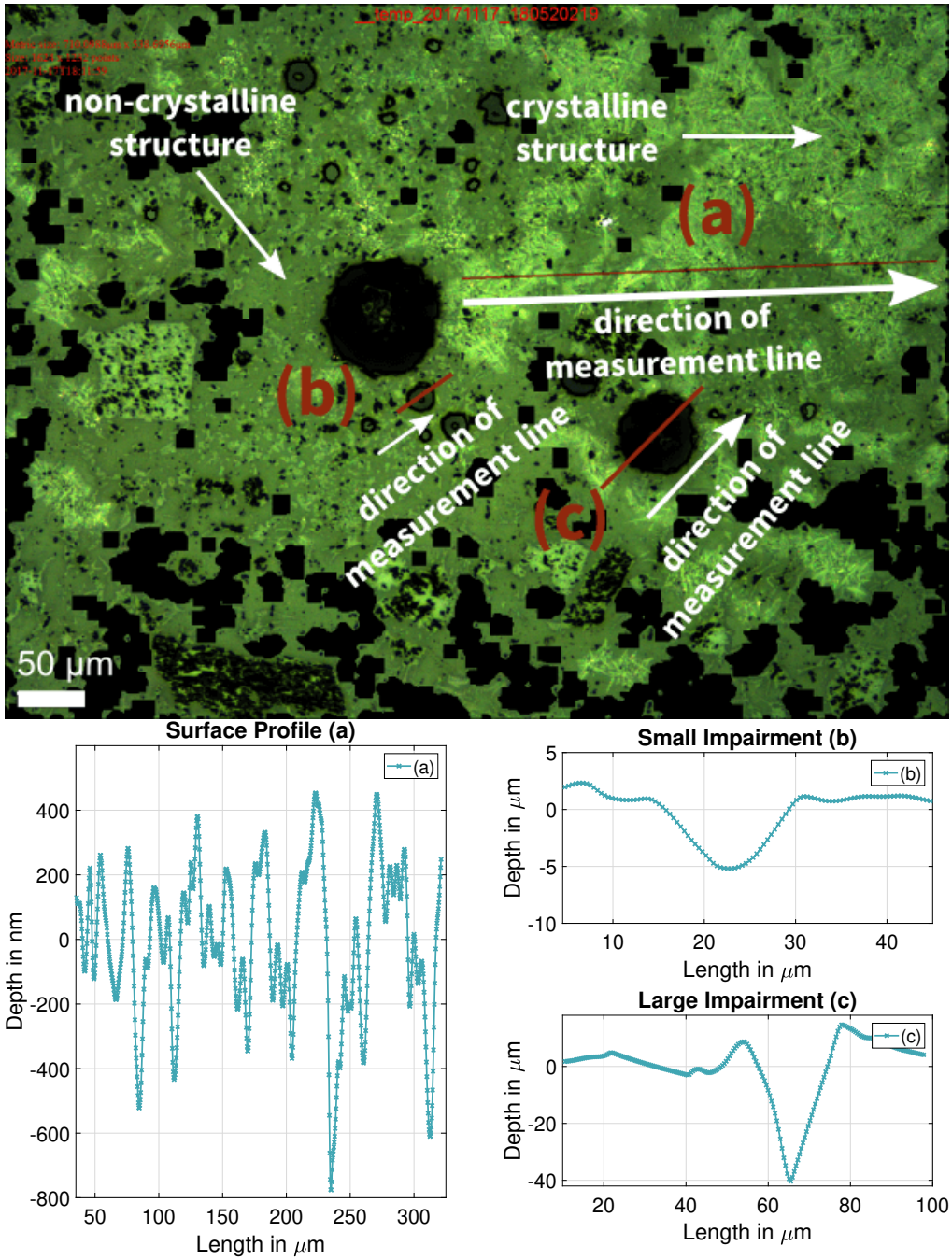

Figure 5.32: A 3-D reconstruction of the EAC-II glass sample is shown at the top, as measured by surface variation microscopy. The green-coloured areas represent areas where data could be recorded (black represents missing data). Red lines indicate the actual site of surface roughness measurements and the white lines the measurement direction. Non-crystalline areas are shown in dark green and crystalline in light green. The x-axes of graphs (a), (b) and (c), shown at the bottom, coincides with the measurement direction indicated by the white arrows. Three categories of surface features were measured, (a) the plane surface (b) a small impairment and (c) a large impairment.

Surface Roughness

For the characterisation of the surface quality of the substrates, a profilometer was used as explain in section 4.3.1. In addition to the nine batch one and two samples, a standard microscopy slide has been measured to be used as reference. All samples were placed under the stylus of the machine and measured across the surface as depicted by the arrow in figure 3.29. Vertical magnifications (V_v) used were x200 or x500 and the horizontal magnification (V_h) was set to x5 for all samples other than the microscopy slide which used x20. For batch one, the stylus was dragged along the surface for in-between 37 and 42 mm with the exception of JSC-I-2 which could only be measured for approximately 30 mm based on its geometry. Moreover, batch two samples LHT-II and EAC-II were measured for 40 to 42 mm and FJS-II and JSC-II for only 18 mm also due to their geometry.

An overview of the results is listed in table 5.19 showing the arithmetic average of the roughness profile (R_a) and the measured distance across the surface l_x. Two separate groups have been formed, a "macro" group and a "micro" group, which is to indicate whether the entire length on a sample's surface was used for the calculation of R_a, or only a part of it. The macro measurements show macroscopic features on the surface over the entire sample length. The micro group, compared to the macro group, shows the surface quality of the sample in-between the macroscopic voids/bubbles.

Table 5.19: Overview of surface roughness data, batch one and two

Sample ID	R_a macro (μm)	l_x macro (mm)	R_a micro (μm)	l_x micro (mm)
Batch 1 (avg)	26	37.6	1.5	3.0
EAC-I-1	16	41.2	0.5	2.7
EAC-I-2	17	40.5	1.4	2.7
EAC-I-3	13	37.7	2.6	3.5
JSC-I-1	26	38.0	2.6	2.6
JSC-I-2	57	30.7	0.4	3.8
Batch 2 (avg)	15	30.1	0.2	1.6
EAC-II	13	40.2	0.1	1.4
FJS-II	10	18.9	0.3	2.1
JSC-II	9	19.3	0.2	1.4
LHT-II	26	42.2	0.2	1.2
Other	-	-	(nm)	
EAC-II*	-	-	187	0.3
Microscopy Slide	-	-	15	5.6

*Focus Variation Microscopy
R_a: Arithmetic average of the roughness profile,
l_x: Measured length.

How the surface roughness was calculated was described in section 4.3.1. By looking at the R_a values it is possible to compare the surfaces quality of all samples. However, the values need to be understood first. The surface roughness (R_a) is influenced by different porosities/different number of voids/bubbles on a samples surface, as well as the smoothness of the areas in-between the voids. Batch one sample JSC-I-2, for example, shows the worst macroscopic surface roughness of all samples with 56.46 μm, but the best microscopic R_a value with 0.38 μm. This is because this particular sample has 3 deep voids/bubbles compared to the voids of the other samples. This leads to a large arithmetic average, measured across the entire surface. The areas in-between those large voids are, however, rather smooth, and free of smaller voids/bubbles. This leads to a small surface roughness (small R_a value). For all samples the polished glass areas in-between the voids are similar, compared to the macro scale values, since all samples were polished the same way. Differences may however occur, due to different hardness of the glasses, caused by deviations in the melting/annealing process and/or due to different chemical compositions. These lead to a different grindability and hence to a different surface roughness.

The sample showing the best macroscopic roughness, of all batch-one-samples, was EAC-I-3 with 13.46 μm, which was also the worst sample on the micro scale with 2.63 μm. Batch-two-samples showed an overall increase in surface quality with macroscopic values from 25.91 to 9.12 μm and microscopic from 0.26 to 0.13 μm. Average surface roughness for both batches has been calculated and are 26.04/1.49 μm for batch one and 14.60/0.19 μm for batch two. Suggesting that batch two has a better surface quality on average than batch one. Reasons for this improvement may be caused by changes in manufacturing and processing, such as the switch over from manual to semi-automated grinding for example.

Surface Roughness Batch One

Surface roughness curves recorded with the profilometer are depicted in 5.33 and show surface data for both batches, batch one on top, batch two at the bottom. The depicted data also shows the data points used for the calculation of the R_a values listed in table 5.19. Depicting the results in this format makes it easier to see the (magnified) surface features. From these plots it is obvious that the JSC-I-2 sample's surface is smoother for most parts than all other batch one samples. Further, the three comparably large voids (two at the beginning one at approx. 23 μm) are visible, which are responsible for a large macroscopic R_a value. Looking at this (JSC-I-2) sample with the human eye, it appears much smoother than JSC-I-1 or other samples. This is, however, not reflected by the values in table 5.19 (26.49 μm for JSC-I-1) vs. 56.64 μm for JSC-I-2). Looking at the raw data, these voids measure to be more than 250 μm deep and therefore, have a large impact on the surface roughness value calculation for sample JSC-I-2. However, comparing the microscopic values (2.55 μm for JSC-I-1 vs. 0.38 μm for JSC-I-2) they seem much closer to the subjective impression of the samples than the values calculated over

the entire length of the sample.

The largest voids found on JSC-I-2 are likely a result of manufacturing, in particular the casting of the sample into the mould. Possibly the first bit of molten glass that was poured out of the crucible, which hit the surface of the mould, trapped air under it and formed these bubbles. This, however, will not be the case on the Moon due to a lack of an atmosphere. Not only in the JSC-2A glass sample JSC-I-2, were bubbles observed, but also for all other samples although not that large. Size and amount of voids differ from sample to sample. Bubble depth/radius was in the range of 40 - 60 μm and in some cases even as large as several millimetres. Glass samples manufactured from EAC-1, shown in figure 5.33, show bubbles as deep as 40 - 60 μm. Nevertheless, no bubbles were deeper than 1 mm. For all batch one samples made of EAC-1, a larger number of bubbles in the range of 1 to 5 μm can be observed compared to the JSC-2A samples. In general, batch one samples made of EAC-1 show the smoother surfaces (with less surface features) compared to the JSC-2A samples.

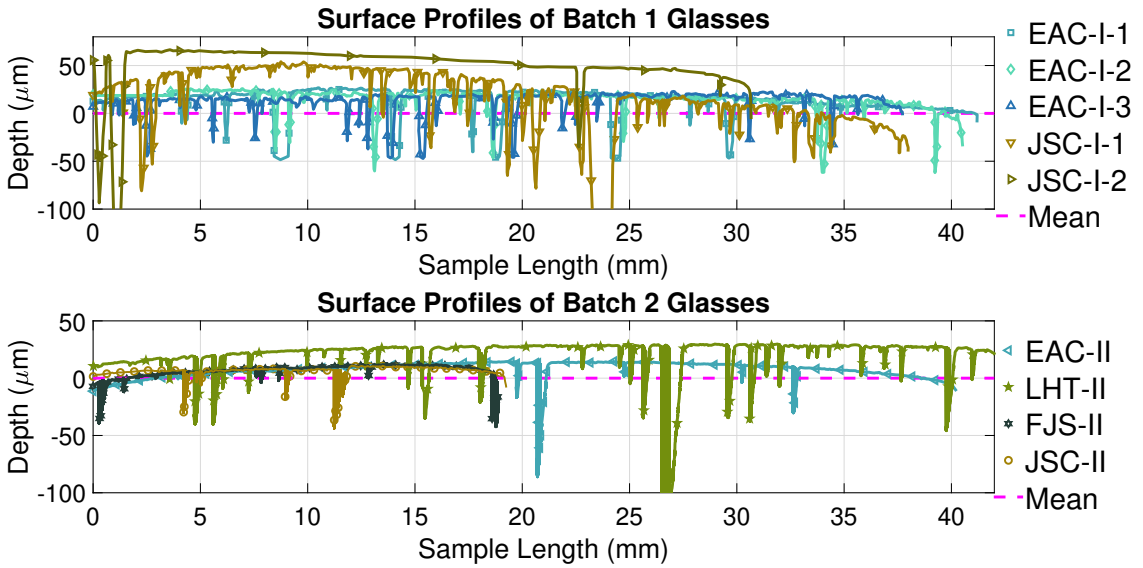

Figure 5.33: Surface roughness of batch one (EAC-I and JSC-I samples, top) and batch two (JSC-II, LHT-II, EAC-II and FJS-II samples, bottom).The abscissa shows length on the samples surface in mm, and the ordinate deviation from the mean line in μm. The dotted line in pink indicated by "Mean" shows the mean line, which is the same for each curve in each graph.

Surface Roughness Batch Two

All four batch two samples have been measured the same way as batch one samples. Moreover, their surface profiles have been plotted in the same fashion as those of batch one samples and are also depicted in figure 5.33 (bottom). The measured distance (approx. 18 mm in x-direction) of FJS-II and JSC-II was significantly shorter than for EAC-II and LHT-II which were measured for approximately 42 mm. Macroscopic surface features did not allow measurements over the entire

surface length on FJS-1 and JSC-2A samples.

As mentioned before, in general, the surface roughness of the second batch has increased compared to the first batch. JSC-I-2 could achieve the best microscopic surface roughness with 0.38 μm, which is still poor compared to even the worst batch two sample with 0.26 μm. Although improvements to the batch two samples were made, the new samples still show macroscopic surface features in the form of voids. This made it once more necessary to decouple macroscopic surface quality from microscopic surface quality. By looking at the plotted surface profiles depicted in figure 5.33, the quality of batch one and two samples can be compared directly. Comparing top and bottom graph in figure 5.33, the bottom lines seem smoother in-between the dips (voids) than the top profiles. This suggests a better surface quality in-between the voids, which was confirmed by the calculations of the R_a values in table 5.19.

Looking at the results of batch two in particular, LHT-II seems to have the largest/most voids compared to the other three samples. This also translates to the highest macroscopic roughness (for batch two) with a R_a value of 25.91 μm. Moreover, the batch two sample made of LHT-3M shows the largest number of microscopic voids (< 50 μm) on the surface which translates into the second roughest microscopic surface with 0.22 μm, and is only surpassed by FJS-II. One reason for the comparably high number of bubbles on LHT-II may have been the extended heating time, which was chosen for this simulant, to try to fully melt it. In turn this would have allowed the LHT-3M simulant to react with the graphite crucible for a longer time as well, which could have fostered outgassing, thus bubbles forming in the melt. To confirm a reaction in-between the graphite and the sample, EDX spot measurements would be required. In addition to that, since this simulant was not fully melted it is also likely that the melt could have had a higher viscosity compared to the other simulant melts. This would have hindered bubbles to escape from the melt. The smoothest looking sample in figure 5.33 seems to be either JSC-II or EAC-II. From table 5.19, the lowest arithmetic average of the microscopic roughness profiles of batch two has EAC-II with $R_a = 0.13$ μm, closely followed by JSC-II with $R_a = 0.15$ μm.

Comparison of Surface Roughness and Topography Results

Comparing results shown in figure 5.33 and figure 5.32, which both used different techniques to characterise the samples' surfaces, seem to be consistent. Comparing the order of magnitude of the macroscopic voids detected by focus variation microscopy to the profilometer results, both show voids of similar size. Profilometer voids (shown in figure 5.33 are in most but three cases in the range of -50 to -5 μm. Focus variation microscopy detected voids in the range from -40 to -5 μm as shown in (b) and (c) in figure 5.32. Hence, both observations match and confirm that voids in this range are presented on the measured samples.

Comparing both techniques on a microscopic scale, the detected range of surface features from the focus variation microscopy is as low as -800 nm to -400 nm (subplot (a) in figure 5.32). However, the magnification of figure 5.33 is not large enough to see surface features in the nanometer scale. At the depicted scale, however, visible microscopic features appear to be smaller than 2 to 3 μm. To be able to compare the results more quantitatively, surface roughness has been calculated from the focus variation microscopy results and was added in table 5.19. Accounting for the different units, the focus variation microscopy shows a surface roughness of $R_a = 0.19$ μm. This is close to the surface roughness (0.13 μm) calculated for another location on sample EAC-II. Hence, the observations seem to match, and the sample's surface roughness is in the order of less than a micrometer.

In a last step, the calculated surface roughness of the reference microscopy slide was compared to the basaltic glass samples. Results from the microscopy slide show the sample's roughness to be in the range of nanometers and at least one order of magnitude smoother than the basalt samples. With surface roughness of $R_a > 100$ nm substrates do not yet seem to be for manufacturing mirrors. Discussions in section 4.3.1 showed, that reflectivity of mirrors with roughness $R_a < 100$ nm, have the highest reflectivity values. Although modifications to the manufacturing process may improve the quality of the substrates further, it is unclear, how suitable substrates, manufactured using microwave heating, are for mirror manufacturing. The number and sizes (> 1 mm) of bubbles/voids determined on each sample seem to make solar cell manufacturing at best complicated.

Flatness

Flatness was estimated by extracting the largest and highest point from the surface profiles in figure 5.33. This was not considering voids, but rather the geometry of the entire surface as a whole. Maximum and minimum values determined are summarised in table 5.20 and are an estimate of how flat the samples are. Since all samples have been measured over different distances (in x-direction), results are hard to compare. Nevertheless, what can be gained from these values is that manufacturing and grinding lead to a consistently convex shape. This is due to increased material taken off closer to the edge during the grinding process.

Table 5.20: Maximum deviations of batch one and two samples with respect to flatness

Sample	Batch	Δ h in μm
JSC-I-1	1	85
EAC-I-3	1	15
EAC-II	2	25
JSC-II	2	12

Although it is not desirable for a concentrating mirror to be convex, the flatness of the samples' surfaces may still be enough to work as a reasonable mirror over

short distances (20 - 100 cm). Over such a distance, the diverging effects of the substrates' convex shape are considered minimal. For the use as solar cell, the flatness will probably have less impact than the surface roughness and the voids. Thus, if surface roughness can be decreased to a good enough level for solar cell fabrication, flatness should not be impacting the functionality.

Conclusion Microwave Manufactured Substrates

By utilising a susceptor assisted microwave heating approach, basaltic glass samples were manufactured from two (batch one) and four (batch two) different regolith simulants. The samples have been manufactured from simulant, melting it in a microwave environment, allowing the melt to cool lead to the formation of basaltic glasses. These substrate samples were ground and polished at their bottom surface and afterwards the samples' surface quality was analysed.

The samples' surface roughness was determined as well as its flatness. Their surface quality was analysed and, as discussed in section 4.3.1, with their surface roughness R_a larger than 100 nm, these substrates are not ideal for manufacturing mirrors. With respect to the flatness of the ground and polished side of the samples, all samples appear to be convexly shaped. Additionally, large surface features, such as voids and bubbles are not ideal for mirror manufacturing. Further, the voids by themselves seem to be enough reason why solar cell manufacturing would not work. Although it was possible to decrease the number of these voids from batch one to batch two, they could not be removed entirely. Further analysis showed, amorphous and crystalline phases in the glasses of both batches, which may impact optical properties of the glass, which further may impact mirror or solar cell manufacturing.

Although flatness, surface roughness and surface features (such as voids) suggest, that the substrates do not yet have the required surface quality to manufacture an ideal mirror on their back. However, aluminium deposition on low quality substrates, made from clay, showed to work as mirrors in the past, despite their "poor" surface quality [442]. Based on this, an attempt was made on trying to manufacture mirrors on the back of the substrates discussed in this section, despite them being of "poor" quality.

Recommendations

The utilised microwave manufacturing approach has shown to melt a variety of six different regolith materials, thus suggests that the utilised heating approach may be universally applicable to regolith types occurring on the lunar surface. Whether or not it is possible to deploy this method on the lunar surface needs to be determined in environmental tests (thermal, vacuum) first, before it can be considered as a manufacturing technique, which deserves further investigations.

The simple nature (no moving parts) of microwave heating would make it less prone to failure than other potential heating options (eg. solar furnace). Limitations of the utilised process setup are, limited maximum temperatures ($\approx$ 1350 °C),

complicated environment to take in-situ measurements, and materials which can be used inside the microwave field are limited, due to incompatibilities, such as graphite crucibles and regolith interacting.

However, the maximum temperature of the process can likely be increased by increasing the insulation of the microwave kiln. Material incompatibility could be eliminated by using a different crucible material (such as platinum for example). In-situ measurements might be taken via a temperature sensor made of a non-susceptive material. These suggested improvements could decrease the number of defects on the substrates' surface and increase the quality of the substrate. Whether the surface quality, for example, can be improved to an $R_a < 1$ nm is unclear and requires testing. Further, to improve the substrates surface quality, it will be required to understand the interaction between the regoliths' mineral compositions and the heating process.

5.2.3 Resistively Heated Substrates

As a next step, after the microwave heated substrate experiments, the next generation of basaltic glass substrates was manufactured utilising a resistively heated furnace. The utilised furnace's maximum temperature is 1750 °C and therefore by about 400 $°C$ hotter than the microwave kiln setup. The resistive heated furnace is capable of achieving more repeatable results due to better temperature control and readings. In addition to utilising a resistive heated furnace, the graphite crucible of the microwave experiments was swapped for a platinum crucible. The crucible allowed for temperatures up to 1800 °C, without chemically reacting with the simulant and without melting.

Manufacturing of second generation samples has been described in detail in chapter 3.2.4, this chapter will detail experimental findings. The quality of the samples surfaces was assessed optically, by means of SEM analysis and topographically by means of profilometry.

Surface Features

The 30 small samples of the second generation batch one (melted in a platinum crucible by means of resistive heating) have been gradually ground and polished and finished with diamond paste polishing by hand. The resulting surface, of the samples depicted in figure 3.22, was imaged by SEM and the samples surface is shown in figure 5.34. Compared to the microwave samples' surfaces shown in figure 5.30 in the previous section, the surfaces of these samples show almost no surface features. The samples' surface depicted in 5.34 shows one, of the comparably few, largest surface features. The void appears to be as large as 4.5 μm across its largest dimension and most other surface features are much smaller than 1 μm. Furthermore, the outer shape of the void indicates that the void is rather caused during grinding/polishing than during manufacturing. If the void occurred due to a trapped bubble in the glass, the void would be round. This void is sharp edged and elongated, thus likely to be caused by the grinding disc or agent. This

improvement, compared to the first sample batches, may make it possible to build not only a mirror but also a solar cell on such a substrate. Although voids do not seem desirable for solar cell manufacturing, they may be beneficial for mirror manufacturing since they could direct light from shallow angles towards a solar cell. To better understand the impact of bubbles/voids on the performance of a mirror, simulations and/or experiments would need to be conducted.

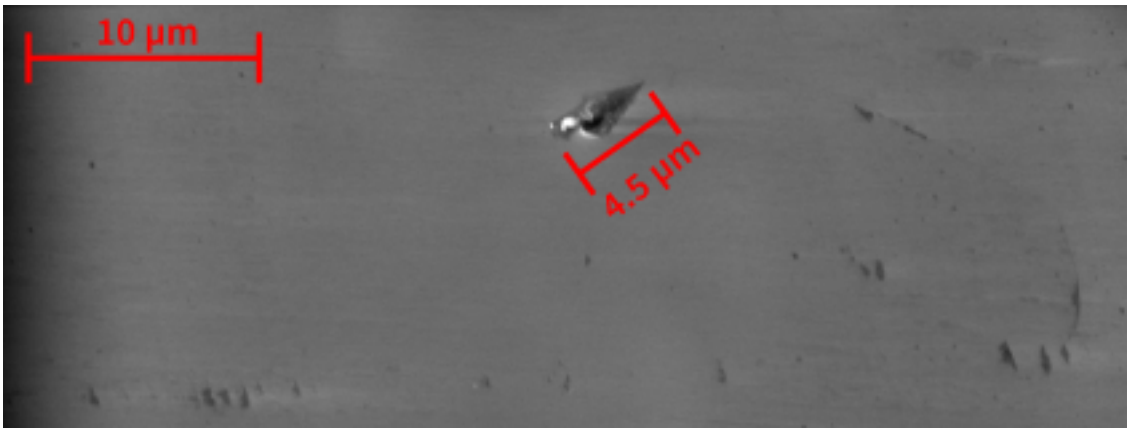

Figure 5.34: SEM image of basaltic glass, depicted is a small samples from the first batch (depicted in figure 3.22). Largest surface feature visible is located in the top middle of the image, measuring a width of approx. 4.5 μm. Other black dots in the image show smaller voids (< 1 μm).

Post processing of the large and medium size samples from batch two (depicted in figure 3.10) was discussed in section 3.3.4 and the two samples which have been prepared for solar cell deposition were shown in figure 3.23. Depicted in figure 5.35 are two SEM images of these two sample, next to each other, both showing the centre of the two large samples. The sample on the left has only been polished until the first stage (10 μm), the sample on the right with both stages (10 and 0.3 μm). The surface on the left shows many sharp edged irregularities compared to the surface on the right. Further, it does not appear to be smooth, only homogenous at this level of magnification. The right part of the image shows a surface which appears to be much smoother than the left. The largest void found on the right surface is indicated in red and measures approximately 10 μm.

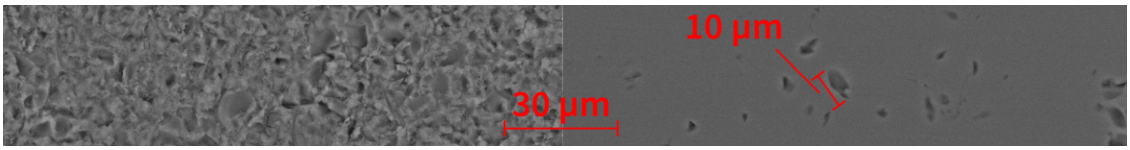

Figure 5.35: Comparison of coarse ground basalt glass sample (left) and fine polished glass (right). The fine polished sample shows voids on the surface which are of the order of 10 μm in their largest extent.

The two samples depicted in figure 3.23 were used to try to build a silicon thin-film cell. However, solar cell manufacturing on these substrates did ultimately fail. Most

likely the reason for that being the surface quality, which was simply too coarse in both cases. In addition to that, the top and all sides, other than the bottom of the basalt glass samples, were not processed at all. This made it difficult to mount the samples in the machine. Thus another option for grinding the samples needed to be found to increase the quality of the basalt glass even further.

Surface Roughness

The surface roughness and flatness of the first batch (30 basaltic glass samples) was assessed by measuring the surface roughness of 3 samples. These three samples were samples 5, 15 and 25. The higher the number the later in the batch the sample was manufactured. Thus three samples were measured representative for the entire batch. Other than the microwave samples, these three samples have been measured more in detail by conducting multiple measurements on the same sample. All three samples were measured on the same profilometer as the microwave samples and the same principle was applied to determine surface roughness. Figure 5.36 shows the measurement path of the stylus across the surface. Three measurements have been conducted in direction of the long dimension (L1, L2, L3 - red), four measurements have been conducted in the short dimension (S1, S2, S3, S4 - green) and one measurement was conducted to determine the microscopic surface roughness (blue) in the middle of the sample. Measurements L1 to L3 have been spaced apart 5 mm and S1 to S4, 10 mm.

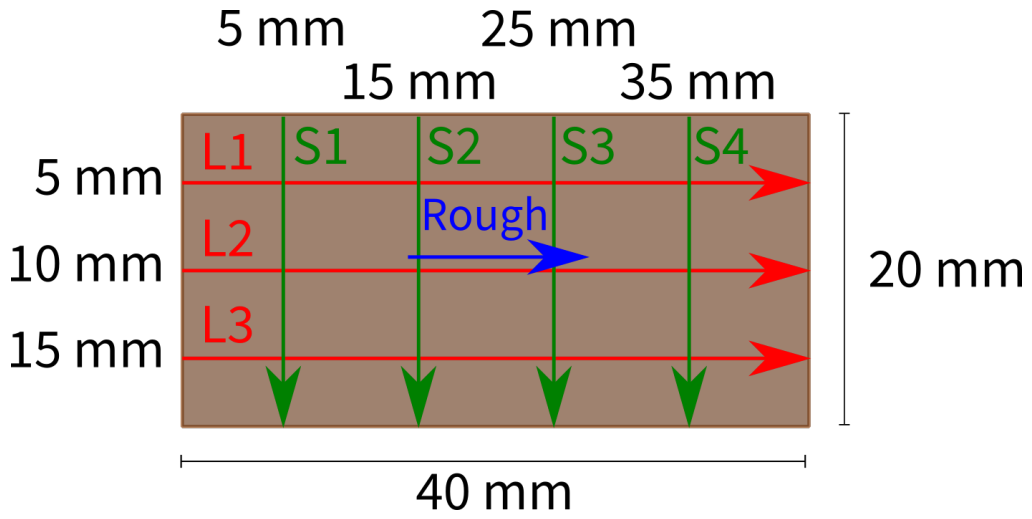

Figure 5.36: Schematic path of stylus across the surface of 2^{nd} generation substrate samples (brown coloured rectangle). Long dimension measurements (L1, L2, L3) are indicated in red, short dimension measurements (S1, S2, S3, S4) are indicated in green and microscopic surface roughness in the centre of the sample in blue.

Analysis of the macroscopic and microscopic roughness of the second generation samples' roughness measurements is listed in table 5.21. Comparing these values to the results from table 5.19 in the previous chapter, a decrease of macroscopic/microscopic surface roughness by approximately a factor 100 was achieved.

The second generation samples therefore may be suitable as substrates for solar cells, with best values of $R_a = 0.8$ nm (Sample 15, R1).

Table 5.21: Surface roughness values of the second generation samples

	Sample 5		Sample 15		Sample 25	
	R_a (nm)	l_x (mm)	R_a (nm)	l_x (mm)	R_a (nm)	l_x (mm)
L1	175	36	183	37	154	36
L2	203	37	98	41	155	38
L3	247	37	102	38	169	38
S1	137	16	113	18	136	19
S2	128	20	106	20	131	18
S3	110	18	124	20	102	18
S4	123	16	156	19	127	17
R1	1.3	1.1	0.8	0.3	2.2	0.9

Looking at the measured profiles in more detail, it can be seen that the measured length of the samples differed by up to approximately 4 mm. This is due to two factors, the samples overall shape and the shape of the bottom edges. The overall shape of the samples can be described similar to a domino brick. Some samples did not fully fill the entire cavity of the mould, hence, these samples may have more rounded edges and/or are shorter overall. This leads to slight differences in the long direction. Moreover, the edges of the sample on the bottom side are rounded to a certain degree. Depending on the mass/thickness of the sample, the sample may have more round (light samples) or sharp edges (heavy sample). The larger the radius at the bottom edge, the shorter the polished surface, which results in different lengths (l_x) measured.

Figures 5.37, 5.38 and 5.39 show plots of the recorded surface profiles. Measurements along the longest surface (L1 - L3) are depicted in figure 5.37, along the shortest (S1 - S4) in figure 5.38 and the microscopic surface profiles (R1) in figure 5.39. The most obvious difference to the macroscopic and microscopic surface profiles of the microwave heated samples (presented in the previous chapter) is the measurement frame. The second generation samples' macroscopic surface roughness presented in figures 5.37 and 5.38, as well as the microscopic results in figure 5.39 show a factor of about 100 smaller surface features. No macroscopic features as large as several microns can be found anymore in figures 5.37 and 5.38. Moreover, a maximum height difference of less than 1.2 μm can be observed. Compared to samples manufactured using microwave heating, which show surface features in the order of > 150 μm, the new samples' macroscopic surface feature size was reduced by two orders of magnitude.

Results of three surface roughness measurement runs (in the long dimension of the sample), are depicted in figure 5.37. Curves are shown for all three samples measured and all surface profile curves have been moved, to be centred around the

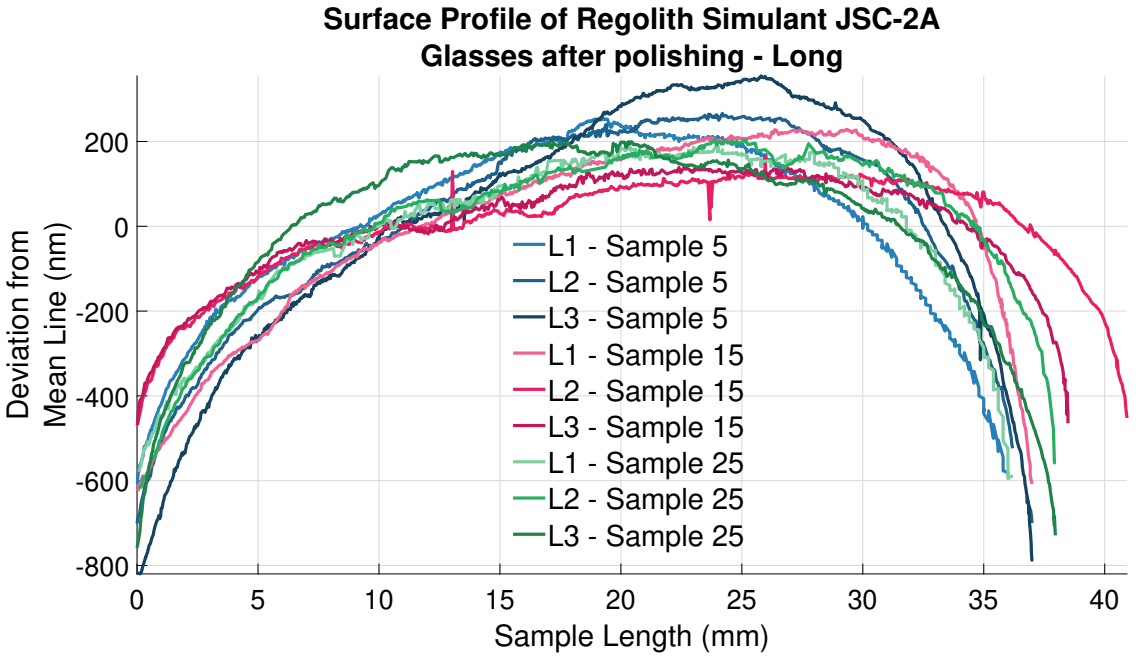

Figure 5.37: Surface roughness profiles of second generation samples 5 (blue), 15 (red) and 25 (green). Three measurement runs have been conducted, 5 mm from the edge (L1), 10 mm from the edge (L2) and 15 mm from the edge (L3). The abscissa shows length on the samples' surface in mm and the ordinate deviation from the mean line in nm.

mean line. An example for the largest macroscopic surface features found on these samples is a peak seen in the roughness plot of sample 15, L2 at about 24 mm. The peak is about 100 nm and suggests a cavity on the samples surface of about 100 nm depth. Although these are rare, they may have an impact on manufacturing when located at the wrong spot.

The overall flatness of these samples in the long direction can be assessed by looking at maximum differences in height. The largest difference can be observed from the surface plot of sample 5 run L3, and is about 1.2 μm. Compared to the best sample of generation one (microwave heated) with 12 μm (table 5.20), this is an improvement by a factor of 10. Some of the best samples with respect to flatness show differences in height from outside to inside of less than 0.6 μm.

Results of four surface roughness measurement runs (in the short dimension of the sample), are depicted in figure 5.38. Curves are shown for all three samples measured and all surface profile curves have been moved, to be centred around the mean line. The largest macroscopic surface features found on the surface profile measurements of the short side of the samples, is a peak seen in the roughness plot of sample 15, S4 at about 13 mm. It shows a delta in y direction of about 50 nm. The surface profiles of the short side depicted in figure 5.38 show even less and smaller surface features than the measurements in the longest direction. Hence, the second generation of samples seems indeed to have a much better quality compared

to the microwave heated samples.

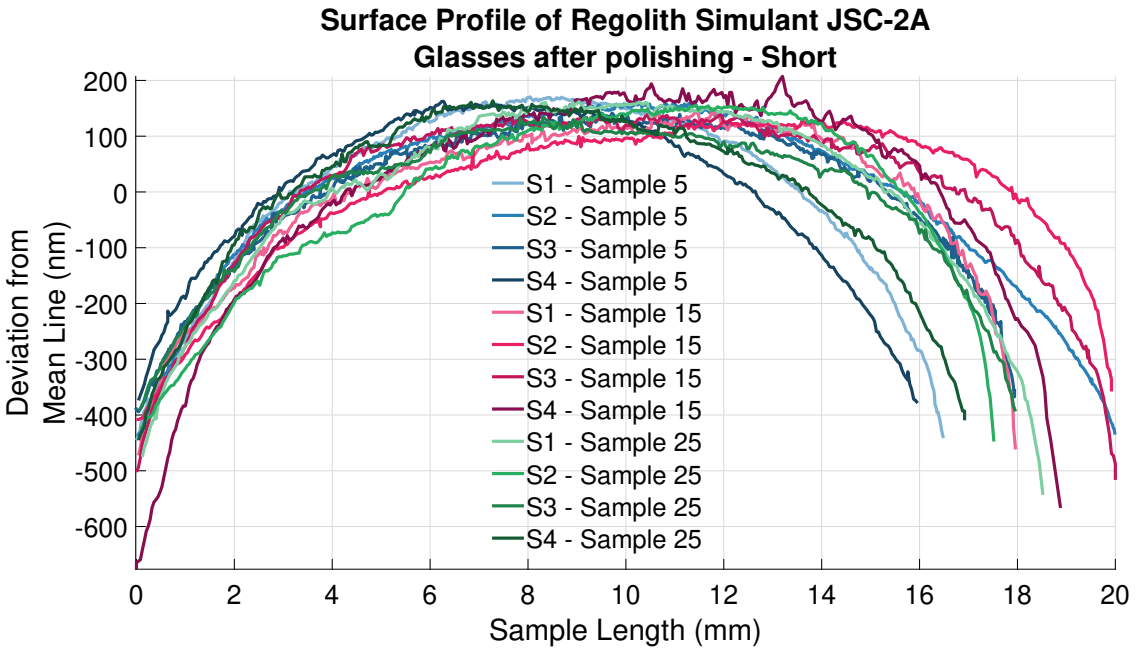

Figure 5.38: Surface roughness profiles of second generation samples 5 (blue), 15 (red) and 25 (green). Four measurement runs have been conducted, 5 mm from the edge (S1), 15 mm from the edge (S2), 25 mm from the edge (S3) and 35 mm from the edge (S4). The abscissa shows length on the samples surface in mm and the ordinate shows deviation from the mean line in nm.

The overall flatness of these samples in the short direction can be assessed by looking at maximum differences in height as well. The largest difference in height can be observed from the surface plot of sample 15 run S4 and shows about 0.9 μm difference. Comparing these results to the microwave batches directly does not work since the short direction for these samples was never assessed. However, the best sample of generation one (microwave heated) shows 12 μm (table 5.20) difference in height between outside and centre. Even if it can be expected that the short side shows a slightly smaller difference in height than the long side, the second generation samples are at least an order of magnitude flatter. Smallest differences in height along the short side are lower than 0.6 μm.

The microscopic surface roughness was assessed by measuring the surface roughness in the centre of each sample. A length of 200 - 1000 μm could be measured for all three samples (5, 15, 25). Based on these measurements the R_a values of the sample could be determined. Although the macroscopic R_a values give an indication of the overall roughness of a sample, they are heavily influenced by the flatness of the sample. Differences in height, between the outside and inside of the sample, will impact the calculation of the surface roughness largely, by using the method described earlier (figure 4.7). Thus, the actual surface roughness of the samples was determined by measuring a shorter distance on the samples surface, at a reasonably flat location. The centre of each sample therefore always seems to be the flattest

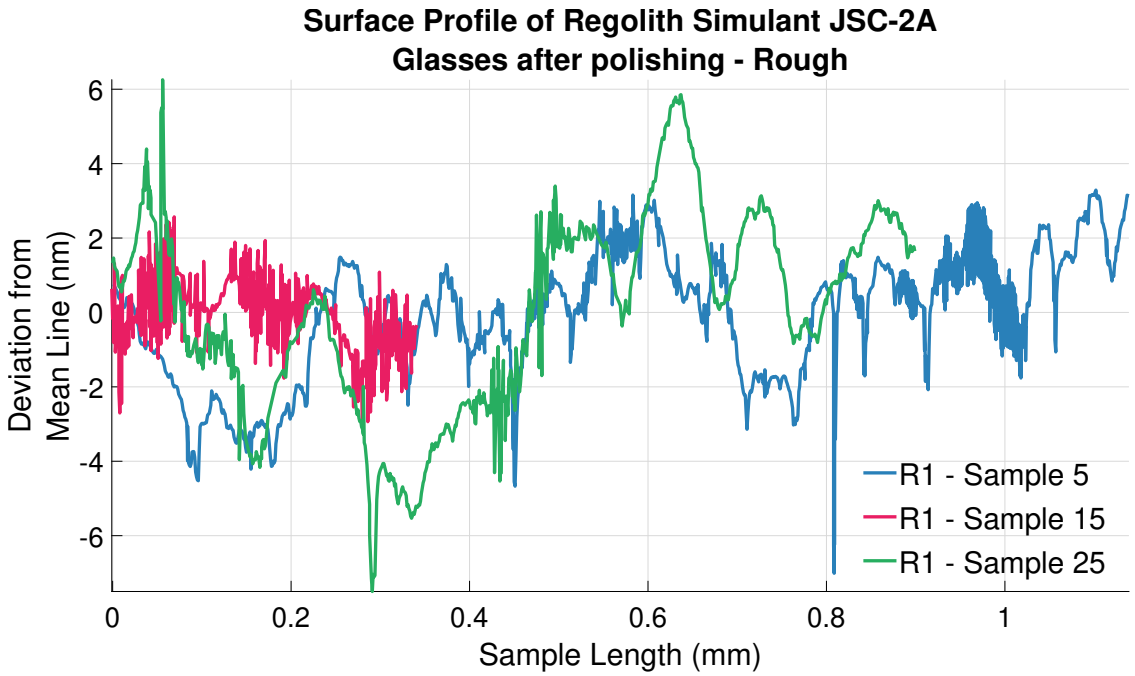

Figure 5.39: Surface roughness profiles of second generation samples 5 (blue), 15 (red) and 25 (green). All samples have been measured in the centre of the sample in direction of the longest side of the sample. The abscissa shows length on the samples surface in mm and the ordinate deviation from the mean line in nm.

region, least impacted by the overall flatness of the entire sample. However, the centre is typically also the area that is toughest to polish compared to the edges. Thus effects of flatness can be neglected and the results are likely to show the highest R_a values which can be measured on the surface.

Conclusion Resistively Heated Substrates

Utilising a resistive heating approach, basaltic glass samples were manufactured from JSC-2A regolith simulant. Basaltic glasses manufactured this way, showed increased quality compared to the samples manufactured using microwave heating. Surface roughness, on the macroscopic and microscopic scale, was decreased by two orders of magnitude, and flatness was improved by a factor of ten. Further, ground and polished sides of the samples now all appear to be less convexly shaped than for previous samples. Additionally, the overall number of large surface features such as bubbles, for example, could be minimised close to the point of being non-existent anymore.

Their surface quality now seems ideal for manufacturing mirrors, with a R_a smaller 100 nm. This improvement in quality further suggests that it may now even be possible to manufacture semiconductor devices, such as thin-film solar cells on the back of these samples. Next improvements and tests will show how well the manufacturing process works for different regolith simulants (other than JSC-2A) and how the substrates outer geometry can be improved.

5.2.4 Substrates from Six Different Simulants

After increasing the quality of the substrates by switching from the microwave heating setup (gen. 1) to the resistive heating setup (gen. 2), a new batch of samples was forged, batch three (gen. 2). This batch was aiming at trying to melt not only one simulant but a variety of six different regolith simulants.

The same manufacturing process used than for the second generation samples, this time to manufacture six different types of basaltic glass samples. The manufacturing process worked for all regolith samples alike and little to no difference in behaviour of the different simulants during manufacturing were observed. After basaltic glass samples were manufactured from regolith simulants BP-1, EAC-1, FJS-1, JSC-1A, JSC-2A and LHT-3M, XRF measurements were conducted to see if manufacturing changed the samples composition. The results of this XRF analysis are shown in table 5.22, which shows the elemental composition of each (raw) simulant vs. the composition of the basaltic glass samples after manufacturing.

Most prominent differences, for the bulk part oxides (SiO_2, Al_2O_3, Fe_2O_3, MgO, CaO), seem to occur in the simulant BP-1. This simulant shows relative differences of 6.09 % for SiO_2, and 8.41 % for CaO. However, these values are relative to the raw BP-1, which are not corrected for the LOI. Considering the LOI for each sample, and correcting it, will bring the two values (raw regolith and basaltic glass) even closer together. Changes in major oxide contents in general are rather little. The minor oxides (Na_2O, K_2O, TiO_2, MnO and P_2O_5) show, however, much larger relative differences in-between the raw regolith and the glass. This mostly seems so large (40 % + in some cases) because the absolute quantity of the oxides contained in the regolith/glass is very low and thus is closer to the detection limit of the XRF technique.

Overall, processing different regolith simulant types with the resistive heating approach, does not seem to alter the chemical composition of the material drastically from raw regolith to glass. Moreover, basaltic glass samples seem to be homogenous and melted entirely for all regolith simulant types. Thus, the method of using resistive heating for melting regolith simulants seems to work for a variety of materials. The resistive heating process still showed repeatable and good results. This made the comparison of different batches and samples possible since differences in the samples caused by manufacturing were found to be minor.

Table 5.22: XRF analysis comparison of unaltered regolith simulant versus basaltic glass manufactured from each simulant

Sample	SiO_2	Al_2O_3	Fe_2O_3	MgO	CaO	Na_2O	K_2O	TiO_2	MnO	P_2O_5	LOI	$Total$
BP-1	46.13	15.91	11.96	6.31	10.28	3.08	1.01	2.04	0.17	0.39	2.04	99.32
BP1-G	47.12	16.34	12.39	6.45	10.55	3.20	1.04	2.12	0.17	0.41	-0.11	99.68
Abs. Difference	1.00	0.43	0.43	0.14	0.27	0.13	0.03	0.08	0.00	0.01		2.50
Rel. Difference	6.09%	3.49%	6.64%	1.29%	8.41%	12.04%	1.30%	47.78%	-0.29%	-9.88%		
EAC-1	43.58	11.45	12.66	14.08	10.18	2.62	1.18	2.15	0.21	0.59	1.40	100.11
EAC1-G	44.28	11.56	12.85	14.50	10.30	2.31	1.20	2.15	0.21	0.59	-0.09	99.86
Abs. Difference	0.70	0.11	0.19	0.42	0.12	-0.31	0.02	0.01	-0.01	0.00		1.25
Rel. Difference	1.58%	0.93%	1.51%	2.91%	1.18%	-13.35%	1.33%	0.36%	-3.87%	-0.69%		
FJS-1	49.82	16.56	12.90	5.91	9.71	2.42	0.66	1.46	0.20	0.28	-0.25	99.67
FJS1-G	49.72	16.70	12.97	5.98	9.87	2.30	0.68	1.47	0.19	0.28	-0.11	100.05
Abs. Difference	-0.10	0.14	0.06	0.07	0.16	-0.12	0.02	0.01	0.00	0.00		0.24
Rel. Difference	-0.20%	0.81%	0.50%	1.25%	1.61%	-5.35%	2.90%	0.55%	-0.65%	-0.13%		
JSC-1A	46.76	16.24	12.62	8.57	9.90	2.91	0.82	1.80	0.19	0.70	-0.46	100.04
JSC1A-G	46.17	16.18	12.61	8.71	9.90	2.93	0.82	1.78	0.19	0.68	-0.16	99.80
Abs. Difference	-0.59	-0.06	0.00	0.14	0.00	0.01	0.00	-0.01	0.00	-0.02		-0.54
Rel. Difference	-1.28%	-0.36%	-0.01%	1.60%	-0.01%	0.45%	-0.02%	-0.78%	-2.00%	-2.48%		
JSC-2A	46.28	16.63	13.18	7.98	9.65	3.11	0.82	1.83	0.20	0.71	-0.79	99.59
JSC2A-G	45.75	16.41	12.99	8.09	9.68	3.01	0.83	1.81	0.19	0.70	-0.14	99.33
Abs. Difference	-0.53	-0.22	-0.18	0.11	0.03	-0.09	0.01	-0.02	-0.01	-0.01		-0.90
Rel. Difference	-1.15%	-1.35%	-1.40%	1.41%	0.34%	-3.04%	1.04%	-0.90%	-5.03%	-1.45%		
LHT-3M	49.34	21.59	5.56	9.49	12.54	1.04	0.08	0.11	0.09	0.02	0.12	99.97
LHT3M-G	49.59	22.70	5.04	9.11	13.24	0.83	0.06	0.09	0.09	0.01	-0.10	100.64
Abs. Difference	0.25	1.11	-0.52	-0.38	0.70	-0.21	-0.03	-0.02	-0.01	-0.01		0.89
Rel. Difference	0.51%	4.90%	-10.36%	-4.22%	5.31%	-24.92%	-45.00%	-20.45%	-10.90%	-		

201

Surface Roughness

In the same way the surface roughness was determined for the resistive heated JSC-2A samples, it was determined for the samples made of six different simulants. Samples have been ground semi-automated by using a grinding/polishing machine and holding the sample into place by hand. The samples were finished with an aluminium oxide slurry of 10 μm average grain size. All processing times and steps have been applied for the same time to each sample. Resulting R_a values are listed in table 5.23.

Table 5.23: Surface roughness of samples made of six simulants, machine polished

Simulant	R_a in nm	l_x in mm
BP-1	22	0.94
EAC-1	29	0.98
FJS-1	22	0.96
JSC-1A	20	1.08
JSC-2A	18	1.04
LHT-3M	39	1.03

It was possible to grind and polish all samples by using the same process used before. R_a values listed in table 5.23 further show R_a values of in-between 17.5 and 39.4 nm, which are similar to the previously ground samples. The samples were measured prior to lapping and machine polishing them with the last stage of aluminium oxide slurry, as depicted in figure 3.25. Thus, it is likely that the surface roughness was further improved, by polishing the samples with this finer slurry.

The grinding and polishing process was executed the same way for all samples, hence, differences in surface roughness are unlikely to be caused due to differences in the manufacturing process. Hence, different hardness of each glass could be an explanation by differences in surface roughness. Since JSC-2A, for example, is the seemingly smoothest, with an R_a of 17.54 nm, and LHT-3M the roughest, with an R_a of 39.42 nm, these two also seem to be the softest/hardest samples. To visualise the different surface roughness better, the actual surface profiles are depicted in figure 5.40.

Comparing the surface profile, of the seemingly softest material (JSC-2A/yellow), to the supposedly hardest (LHT-3M/green), both depicted in figure 5.40, their profiles look different. Where JSC-2A shows a profile with little macroscopic displacement (< 100 nm), LHT-3M shows drops and features of more than 250 nm. As discussed for the microwave heated samples at the beginning of this chapter, large surface features in the form of holes an voids will lead to a poor surface roughness value R_a. In turn, this means that the poor surface roughness value R_a of the LHT-3M glass, compared to the other five samples, could also be a result of the larger voids/features found on this sample. This would suggest that its hardness may not be increased. However, increased hardness might also lead to increase fragility and

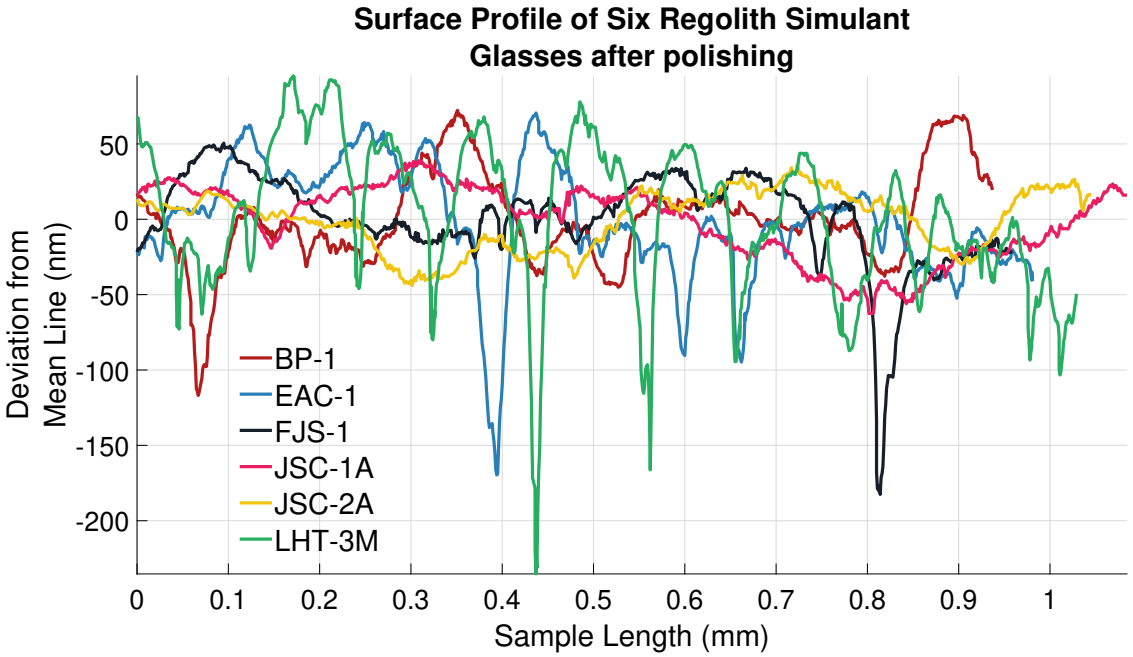

Figure 5.40: Surface roughness of polished substrates from six different regolith simulants. The abscissa shows length on the samples surface in mm and the ordinate deviation from the mean line in nm.

thus lead to increased amount of defects introduced during grinding.

Overall, it was possible to manufacture basaltic glass samples from six different regolith types and grind and polish them to a surface roughness (R_a) of tens of nanometres. All samples showed similar behaviour with small variations on the achieved ultimate surface roughness. This experiment suggests, that a variety of different regoliths from the lunar surface could be used for glass/substrate manufacturing. Thus the used process/technique should be rather landing site independent and therefore work at most places on the lunar surface, does however require a surface finish in the form of grinding and polishing.

Grinding Alternatives

After showing that it is possible to manufacture basaltic glass substrates from different regolith simulants, by using terrestrial methods, a lunar alternative was considered. Since grinding agents, such as silicon carbide (SiC) and/or aluminium oxide and/or diamond pastes, do not naturally occur pure on the lunar surface, it does not seem economically viable to fly these agents to the lunar surface. This is why lunar regolith was considered as a replacement for these grinding agents. Regolith is available everywhere on the surface of the Moon and could not only be used to manufacture basaltic glass, but also to grind this basaltic glass to a shiny finish.

To test whether regolith itself is a suitable grinding agent, three separate rounds of grinding have been conducted comparing SiC powder to regolith powder. A

powder grinding setup was used as described in section 3.3.1. After each round measurements of the samples surface roughness were taken and the surface roughness R_a was calculated. Each round of grinding was applied to a set of two times six basaltic glass samples, manufactured from six different regoliths. Moreover, each round used SiC powder and regolith powder of one grain size distribution, to grind each of the six samples. Despite the grain size distribution being the same for all regolith powders, each type of glass[8] was ground with the type of regolith it was made of.

In the first round, each sample ground by regolith was ground for a certain time before the entire grinding setup was reset. In total, each sample was started on a clean grinding setup for three times in round one, two times in round two and for one time in round three. Regolith grain sizes used where (in that order) 300 - 150, 125 - 60 and < 63 μm. The times each regolith sample was ground are listed in table 5.24.

For all samples ground with SiC powder (for all three rounds) the grinding setup has only been cleaned once at the start and not reset before each sample was finished. Each time, each sample was ground for 2 minutes, using 10 grams of SiC powder. Silicon carbide grit sizes used were (in that order) 220, 400 and 600, which have an average grain size of 220 = 68 μm, 400 = 35 μm and 600 = 25.8 μm accordingly.

Table 5.24: Processing time and amount of regolith powder used for grinding

Sample	300 - 150 μm weight in g	time in min	125 - 63 μm weight in g	time in min	< 63 μm weight in g	time in min
BP-1	124	30	56	13	38	16
EAC-1	80	45	50	10	33	14
FJS-1	72	20	55	15	44	15
JSC-1A	54	35	39	14	65	20
JSC-2A	61	35	57	12	52	12
LHT-3M	79	15	41	15	39	18

Compared to the SiC ground samples, the regolith ground samples needed longer time to be homogenous to the human eye. Moreover, especially the first stage, which required flattening the samples' surface, took significantly longer. Although the time, each sample was ground, was determined by the human eye rather than a surface roughness measurement, it is clear from the regolith amounts used for grinding (and the time), that using regolith for grinding is slower than using SiC. This study aimed at showing whether it is possible to grind basaltic glass samples made of regolith, with regolith. Thus the goal was not to compare how much regolith exactly is needed to achieve the same results as with SiC for example.

[8] BP-1, EAC-1, FJS-1, JSC-1A, JSC-2A, LHT-3M

To still quantify the effect, each grinding agent had on each sample, each sample's surface roughness has been measured after each round of grinding with a certain grain size. As for other samples' roughness discussed before, the roughness was measured using a profilometer and R_a values for each sample have been calculated. The results are shown in table 5.25, which show all 12 samples' surface roughness achieved after each round of grinding. Comparing R_a values for each round:

Table 5.25: R_a values of regolith grinding feasibility study. Three rounds of grinding using two sets of six samples made of six different regolith simulants. Grinding agents used were regolith simulants themselves and SiC powders. Over the course of three rounds of grinding three different grain sizes with consecutively shrinking grain sizes have been used.

Simulant	Agent	Round 1		Round 2		Round 3	
		R_a in μm	l_x in mm	R_a in μm	l_x in mm	R_a in μm	l_x in mm
BP-1	Rego	1.17	1.02	0.84	1.05	0.59	1.04
BP-1	SiC	4.97	1.05	1.59	1.06	0.61	1.00
EAC-1	Rego	0.96	1.00	1.34	1.08	0.78	1.00
EAC-1	SiC	3.26	1.00	1.24	1.08	0.70	1.01
FJS-1	Rego	1.34	1.03	0.67	1.01	0.51	1.01
FJS-1	SiC	3.95	1.03	1.16	1.01	0.60	1.15
JSC-1A	Rego	1.56	1.01	0.90	1.00	0.56	1.03
JSC-1A	SiC	3.00	1.00	1.39	0.99	0.55	1.00
JSC-2A	Rego	2.22	0.99	1.10	1.01	0.87	1.13
JSC-2A	SiC	3.31	1.01	1.43	1.07	0.67	1.03
LHT-3M	Rego	1.63	1.03	1.37	1.01	0.95	1.06
LHT-3M	SiC	2.78	1.04	1.19	1.06	0.55	1.04

1. Round (SiC220 vs. regolith 300 - 150 μm): After the first stage of grinding, SiC ground samples are about 3 - 4 times rougher than the regolith ground samples. This is likely due to the increased grinding time compared to the SiC powder as well as the lower hardness of the regolith compared to the SiC. Judging from the geometry of the regolith grains, as seen in chapter 5.1, most regolith powders seem porous, thus prone to crumble. This was also observed during grinding, after about a minute, most of the grains used for grinding have been crushed and a finer powder slurry was left over. This was also the reason why more regolith powder had to be used compared to the SiC powder. Only considering the results of the first round, it seemed already apparent, that samples can be ground with regolith instead of conventional grinding powders. Differences observed are higher consumption of grinding agent and longer grinding times for regolith based grinding agents. From the first round of grinding, it was not clear if the samples' surface can be ground to a smoother finish than displayed. Which is why a second round of grinding was conducted, using regoliths with a smaller grain size distribution.

2. Round (SiC400 vs. regolith 125 - 63 μm): The second round showed surface roughness to be smaller for each but one sample. The basaltic glass sample made of EAC-1, ground with regolith showed to be coarser than in round one. This is likely due to the long grinding time of 45 minutes in the first round versus 10 minutes in

the second run. However, a third round was required to see whether the roughness can be decreased for all samples even further.

3. Round (SiC600 vs. regolith < 63 μm): The third round was the final round conducted and measured. This time all samples showed an improved surface roughness compared to the second round and the first round. Surface roughness values in the order of < 1 μm could be achieved and all R_a values are in the range from 500 - 1000 nm. This is about one order of magnitude worse than the six samples which have been machine polished (table 5.23), and two orders worse than the fine polished JSC-2A samples (table 5.21). The decrease in roughness with decreasing grain size suggests, that it may be possible to grind the samples even smoother. In addition to that, this feasibility study was entirely conducted manual without any machine. Thus, the use of a polishing or lapping machine may decrease the roughness as well.

Overall, regolith seems to be a viable replacement for terrestrially available grinding agents and may therefore be considered a suitable alternative on the lunar surface. The increased amount of grinding agent required, when using regolith, is not considered to be a problem on the lunar surface, since it is available in almost unlimited quantities. However, the increased grinding time could be relevant since it may just take too long to polish a sample to finish. Despite that, it seems possible to manufacture a large surface mirror for, for example, a telescope on the lunar surface. This could be done by manufacturing basaltic glass, and grinding it, using regolith as a grinding agent. Therefore, it may be interesting to weigh the pros and cons of manufacturing large surface mirrors on the lunar surface against transporting them from Earth to the Moon.

Conclusion Substrates from Six Different Simulants

Initial tests showed that it is possible to use regolith materials with different geochemical/mineralogical compositions to manufacture potentially suitable substrates for mirror and/or solar cell manufacturing. Furthermore, all samples could be manufactured by utilising the same technique and processing parameters. This rather simple overall process does not require fine adjustment, based on input material, and is therefore lunar landing site independent. Nevertheless, by adjusting the processing temperature to the melting point of the utilised regolith material it may be possible to save energy and increase efficiency. Moreover, post processing of the basaltic glasses showed that it may be required to adjust processing times based on the input material, the manufactured basaltic glass. This is further supported by the results of the conducted feasibility study which analysed the use of local regolith material as a grinding agent. First results indicate, that it is possible to use regolith itself as grinding agent. Although it was possible to use it, the use of regolith as grinding agent increased processing times by up to 200 % compared to conventional grinding agents.

Findings suggest, it may be possible to land somewhere on the lunar surface with unknown regolith composition and start substrate manufacturing by using local

materials. Moreover, post processing these substrates by using regolith as a grinding agent seems viable. Manufacturing substrates on the lunar surface in the described way would be implementing an almost 100 % ISRU approach. Using local materials reduces the amount of material required to be brought form Earth, which in turn will reduce the cost of a lunar surface mission.

5.2.5 Cover Glass Made of Regolith

Up to this point, regolith was successfully melted using microwaves and resistive heating. Substrates of potentially good enough quality for mirror/solar cell manufacturing were produced. Manufacturing processes were applied to six different simulants which led to six different types of basaltic glass. However, no sample would be suitable as cover glass for a solar cell or a window for a lunar base, since no sample seemed optically transparent or translucent to the human eye. Only one sample showed partial translucency, which was a sample manufactured of LHT-3M, which was heated by microwaves. This sample is depicted in figure 5.41 and shows a type of green glass nugget with a large bubble formed underneath. Since the glass did solidify before the bubble burst, a thin layer of glass was formed on the top surface, which allows to see the background through the sample. Close up, it can be seen that not all material contained in the simulant was melted and that black appearing sand grains were floating in the melt before solidification occurred. This sample suggested that it is possible to manufacture transparent glass from regolith, which could be used as cover glass for example.

Figure 5.41: Semi-transparent microwave glass manufactured from LHT-3M regolith simulant by means of susceptor assisted microwave heating. Bottom view of not ground sample (left) and top view (right).

Of all chemical elements contained in a regolith, the element iron is most likely to account for a dark green-brow/black [547, 548] taint of a glass manufactured of it. Iron is contained in regolith, in mineral form, and depending on the contained

amount, it may determine a glasses colour. For example, glass with low-iron content ($\approx$ 0.01 % ferric oxide) are high-clarity glasses and are comparably as transparent as possible. Such a low iron content removes the colouration (blue-green), which a typical window glass ($Fe_2O_3 \approx 0.1$ %) may have, which becomes visible especially for thickness $>>$ 1 cm [549]. Another example are highly coloured glasses, which are grey-blue or green and typically used for applications such as car window or beverage bottles, where a low energy and light transmission is required. These glasses may have iron oxide (Fe_2O_3) contents of 1.4 to 4 % [550]. Iron is not the only element which could cause coloration of glass, chromium or iron sulphur may also lead to green-blue-brown colours, even in quantities smaller 0.1 % [547, 548]. However, iron is the only colour baring element, which is contained in quantities of more than 10 % for most simulants and was supposed to be the "main colour driver". Thus, the first step in trying to manufacture optically transparent glass from lunar regolith was to try to remove iron in the form of iron oxide and minerals from each simulant. The following describes how regolith simulants were freed of iron "contamination" to achieve a type of transparent glass which could be used as cover glass. The process included detailed iron content analysis, shaker separation, and magnetic separation, as well as XRF measurements for each step of the separation/preparation process. All utilised processes and methods were described in chapters 3 and 4.

5.2.6 Iron Content

The first step in removing iron was to determine in which form iron is contained in each simulant. In section 5.1 it was discussed that each simulant contains a different mix of minerals and/or igneous rock and it could be shown that the mineral composition of each simulant is different. Further suggesting, that simulants may contain different iron bearing minerals. To determine what type of iron and iron bearing minerals are contained in each simulant, Mösbauer spectra of each regolith simulants have been acquired (described in section 4.1.6). These are used to identify how much of the iron oxide contained in each simulant is in which oxidation state and contained in which mineral. Generally, it can be distinguished between iron(II) oxide or ferrous oxide (Fe2+, FeO), and iron(III) oxide or ferric oxide (Fe3+, Fe_2O_3)[181]. Most minerals will contain one or the other, but some like magnetite will contain both. Most prominent examples of (iron bearing) minerals found in basaltic sands are [551]:

- Ilmenite ($FeTiO_3$)
- Goethite ($FeOOH$)
- Hematite (Fe_2O_3)
- Magnetite (Fe_3O_4)
- Fayalite (Fe_2SiO_4)
- Kirschsteinite ($CaFeSiO_4$)
- Augite ($(Ca, Na)(Mg, Fe, Al, Ti)(Si, Al)_2O_6$)
- Nanophase Iron (Fe^0)

The overall iron contained in each simulant is listed in table 5.26 and was calculated as the average iron oxide content of the measurements obtained in Liège and Edinburgh, both listed in table 5.8. For all seven simulants analysed, values reach

from 4.16 % up to 13.17 %. Analysing simulants in more detail, using Mösbauer spectroscopy, gives clues to which minerals are harbouring the iron oxide contained in each simulant. This means that only, for example, the 13.17 % iron oxide content of JSC-2A will be analysed but not the remaining 86.83 %. As a result of that, a hundred percent in the Mösbauer spectroscopy results account (in the case of JSC-2A) only for the 13.17 % of iron oxide content measured by the XRF. Moreover, not all iron contained in regolith simulants is fully oxidised and Mösbauer spectroscopy gives clues to how much Fe2+ and/or Fe3+ is contained in a sample.

Table 5.26: Average iron content of regolith simulants averaged from XRF data measured in Liège and Edinburgh (from table 5.8)

Simulant	BP-1	EAC-1	FJS-1	JSC-1A	JSC-2A	LHT-2M	LHT-3M
Fe_2O_3	12.19	12.88	13.25	12.60	13.17	4.16	5.16

Information obtained from Mösbauer results also gives clues to which iron-bearing minerals could be found in each simulant. It can, however, only provide evidence of iron bearing minerals but not quantify the amounts of iron bearing minerals in the overall mix. Thus a combination of XRF, XRD and Mösbauer spectroscopy provides a more complete picture. Table A.11 shows the results of the Mösbauer spectroscopy conducted at Stirling University. It lists oxide states and their corresponding detected areas. Furthermore, from the detection patterns and the oxidation state, a potential mineral can be named which is fitting best. Since some iron bearing minerals are rather similar in their crystallographic structure, it is sometimes hard to to tell which mineral exactly is the one detected. Thus, the column "likely" indicates the most likely mineral rather than the exact mineral detected.

From the results in table A.11 it seems that all regolith simulants contain iron-bearing minerals in the form of olivines and/or pyroxenes and/or iron oxides. Thus a process needed to be found which could remove those minerals without removing the non-iron-bearing minerals.

5.2.7 Magnetic Separation

To remove the iron-bearing minerals, the magnetic separation process was used described in section 3.1.4, which is commonly used in the field of geology to separate apatite and/or zircon minerals which are non-magnetic minerals. Six simulants (BP-1, EAC-1, FJS-1, JSC-1A, JSC-2A, LHT-3M) have been processed using magnetic separation. Each sample was processed 4 times with different magnetic field strength levels. This lead to each simulant being split into 5 groups, "hm" (hand magnet), "high, "fair", "low" and "non", listed in supposed decreasing order of iron content. Each group of each simulant has been measured by means of XRF, which led to a total of 30 samples.

Each XRF measurement was corrected for the LOI listed in table 5.27. This was important since some of the samples showed losses higher than 20 wt %. The losses on ignition were especially high for the samples tagged "non", which is the

group supposedly containing the least amount of iron. One of the reasons for these comparably high LOIs is that all non-magnetic contaminants, such as polymers from packaging and/or bottling, as well as contained organic materials will collect in the non-magnetic group, which will then combust during XRF sample preparation at 1100 $°C$.

Table 5.27: Loss on ignition of magnetically altered samples

Sample	**BP-1**	**B-hm**	**B-high**	**B-fair**	**B-low**	**B-non**
LOI	2.04	0.88	2.22	3.76	9.11	9.80
Sample	**EAC-1**	**E-hm**	**E-high**	**E-fair**	**E-low**	**E-non**
LOI	1.40	1.19	1.74	1.08	6.05	20.31
Sample	**FJS-1**	**F-hm**	**F-high**	**F-fair**	**F-low**	**F-non**
LOI	-0.25	-0.19	-0.16	-0.37	-0.04	0.22
Sample	**JSC1A**	**J1-hm**	**J1-high**	**J1-fair**	**J1-low**	**J1-non**
LOI	-0.46	-0.46	-0.57	-0.67	-0.20	11.11
Sample	**JSC-2A**	**J2-hm**	**J2-high**	**J2-fair**	**J2-low**	**J2-non**
LOI	-0.79	-0.65	-0.64	-0.70	-0.46	14.05
Sample	**LHT-3M**	**L-hm**	**L-high**	**L-fair**	**L-low**	**L-non**
LOI	0.12	-0.36	2.22	0.21	0.26	0.25

Each of the 5 groups for each of the six simulants was analysed using XRF and compared to the raw regolith composition. Although the process was run for three different grain sizes as well, time and resources did not allow to prepare a total of 90 samples on the XRF. Thus samples with different grain size, but of the same simulant, and the same magnetic group, where combined into one sample to reduce the overall amount of samples to be prepared. Results of the analysis of these 30 samples are displayed in figures 5.42 to figure 5.47. These graphs have been plotted from the detailed results found in table A.10 in the appendix. Each simulant's groups overall composition is always shown on the left side of the figure and the amount of minor elements (Na_2O, K_2O, MnO, Ti_O2, P_2O_5) contained, on the right. The left most stacked bar, for both subplots left and right, always shows the regolith's composition as it comes off-the-shelf. Followed by, ftlr the groups of supposedly decreasing amount of iron oxide content. The left subfigure always only shows oxide content above 40 % since all regoliths contained at least 40 % SiO_2

BP-1, figure 5.42: The first sample depicted in figure 5.42 is BP-1. From "B-hm" (second from the left) to "B-non" the iron content is decreasing as expected. It is decreasing from about 14 % to less than 2 % of iron oxide, which is an absolute reduction of about 10 % and a relative reduction of more than 80 % compared to the raw regolith. As a side effect of this process the amount of Al_2O_3 in the "B-non" sample was increased from about 16 to about 21 % and the amount of MgO reduced from more than 6 % to almost 1 %. Furthermore, TiO_2 did decrease in a similar fashion to the iron oxide content from 2.1 % to 0.2 %. The most iron-bearing group for BP-1 is "B-hm", since it also was the first stage of removing iron, it seems logical, that this group would contain the highest amount of iron.

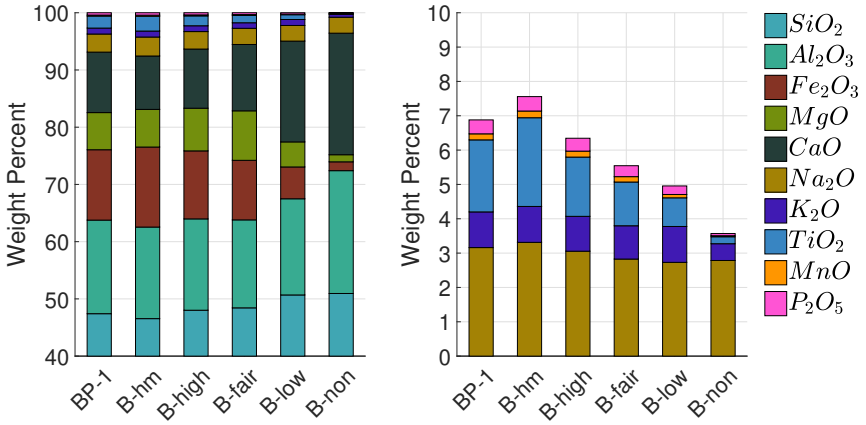

Figure 5.42: BP-1: Comparison of different stages of magnetic separation: BP-1 (unaltered regolith), B-hm, B-high, B-fair, B-low, B-non; after BP-1 in decreasing order of magnetic susceptibility. Left side shows the bulk of oxides contained and the right minor oxides only. Values below 40 wt % (left figure) are all $SiO2$ content.

EAC-1, figure 5.43: The next simulant presented in figure 5.43 is EAC-1. Also for EAC-1 the iron content could be reduced to less than 2 %, an absolute of $\approx$ 11 % and a relative reduction of $\approx$ 86 %. Moreover, TiO_2 content was decreased by about 2 % from 2.18 % contained in the raw regolith to 0.16 % in E-non. However, both Al_2O_3 and MgO were reduced, the first from 11.6 % (EAC-1) to 7.35 % (E-non) and to only 2.56 % for E-fair. MgO was reduced from 14.26 % (EAC-1) to 6.65 % in E-non. On the contrary, for E-non the amount of CaO contained was increased from 10.31 % (EAC-1) to 29.51 % and SiO_2 increased from 44.15 % (EAC-1) to 51.46 %.

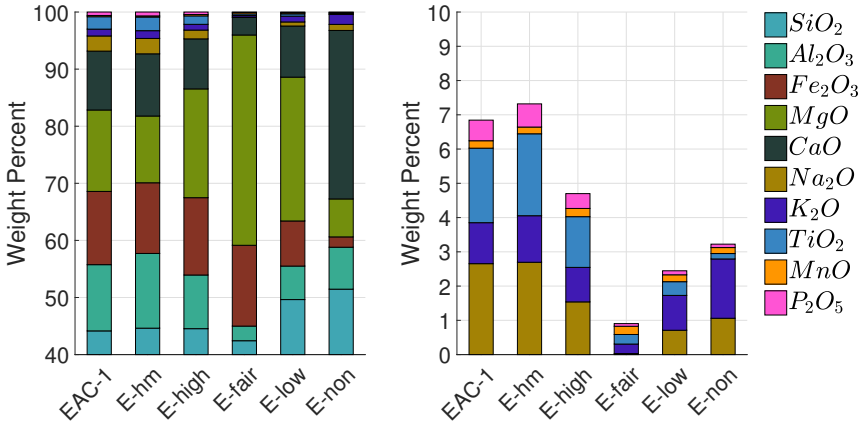

Figure 5.43: EAC-1: Comparison of different stages of magnetic separation: EAC-1 (unaltered regolith), E-hm, E-high, E-fair, E-low, E-non; after EAC-1 in decreasing order of magnetic susceptibility. Left side shows the bulk of oxides contained and the right side, minor oxides only. Values below 40 wt % (left figure) are all $SiO2$ content.

Although the E-non group sample contains the lowest quantity of iron oxide, the E-fair sample showed the highest iron oxide content with 14.16 %, an absolute

increase of approximately 1.5 % compare to the raw regolith. Typically it would be expected that the largest amount of iron oxide is found in the first or second group, here E-hm or E-high, but not in the third E-fair. Moreover, the E-fair sample shows to have the lowest content of Al_2O_3 (2.56 %), Na_2O (0.03 %) and CaO (3.12 %) as well as the highest amount of MgO (36.83 %) of all EAC-1 samples. Combining this observation with looking at the Mösbauer results in table A.11 and the XRD results in table 5.7, it seems likely that the E-fair sample does not contain any feldspar. Moreover, it seems likely that this sample mostly contains olivines, which is suggested by the high Mg and Fe content. Due to low Ca content it is unlikely that the clino-pyroxene augite is found in this sample.

FJS-1, figure 5.44: Also for FJS-1 the magnetic separation led to a gradual reduction in iron content and the iron sparsest sample F-non does show less than 2 % iron oxide, compared to 12.91 % contained in raw FJS-1. The amounts of TiO_2, MgO, MnO and P_2O_5 all decreased similarly than the iron oxide, meaning that 0.1 % or less can be found in the iron-sparsest sample F-non. The oxide content of Al_2O_3, Na_2O and CaO on the other hand increased for F-non which suggests an increased concentration of feldspar in the F-non sample.

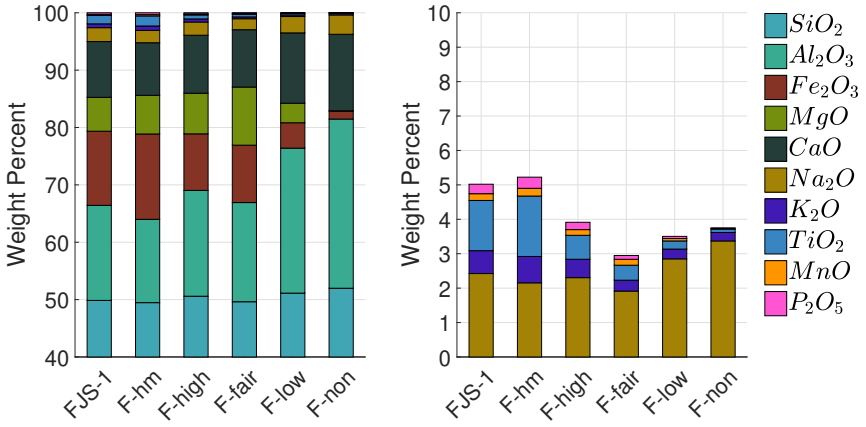

Figure 5.44: FJS-1: Comparison of different stages of magnetic separation: FJS-1 (unaltered regolith), F-hm, F-high, F-fair, F-low, F-non; after FJS-1 in decreasing order of magnetic susceptibility. Left side shows the bulk of oxides contained and the right side, minor oxides only. Values below 40 wt % (left figure) are all $SiO2$ content.

JSC-1A, figure 5.45: The composition of the JSC-1A samples does not change drastically for the first three steps of separation (hm, high, fair). Starting with J1-low, the iron and titanium oxide content decreases and finally goes to a minimum in the J1-non sample. Sample J1-non in turn shows increased values for CaO and Al_2O_3 and again suggests that the primarily present bulk mineral in J1-non is feldspar.

JSC-2A, figure 5.46: For JSC-2A, the overall oxide composition remains almost constant for all but one group, the final J2-non group. This last group shows a drop in iron and titanium oxide content (as observed for all tested simulants) and an increase from 9.61 % in calcium oxide content to 28.39 %. Accompanied by an

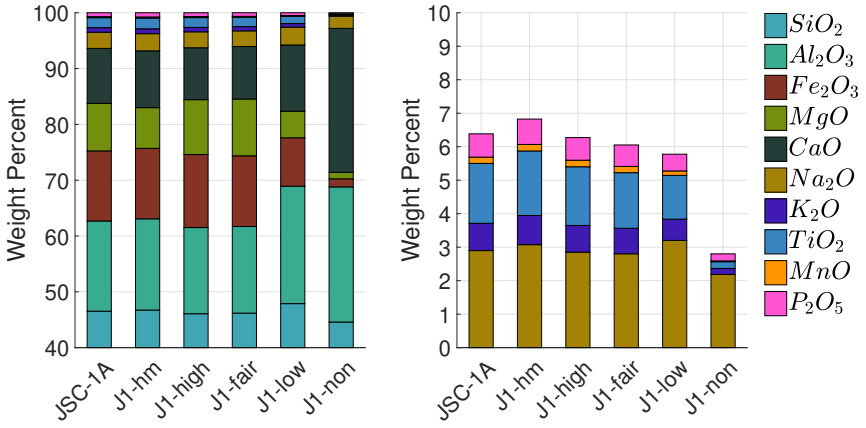

Figure 5.45: JSC-1A: Comparison of different stages of magnetic separation: JSC-1A (unaltered regolith), J1-hm, J1-high, J1-fair, J1-low, J1-non; after JSC-1A in decreasing order of magnetic susceptibility. Left side shows the bulk of oxides contained and the right side, minor oxides only. Values below 40 wt % (left figure) are all $SiO2$ content.

increase in aluminium oxide content this once more suggest the prime mineral to be feldspar in the iron sparsest sample J2-non.

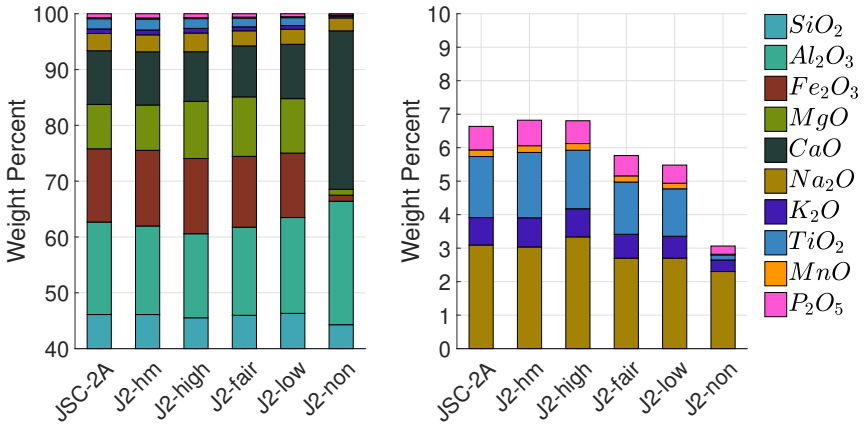

Figure 5.46: JSC-2: Comparison of different stages of magnetic separation: JSC-2A (unaltered regolith), J2-hm, J2-high, J2-fair, J2-low, J2-non; after JSC-2A in decreasing order of magnetic susceptibility. Left side shows the bulk of oxides contained and the right side, minor oxides only. Values below 40 wt % (left figure) are all $SiO2$ content.

LHT-3M, figure 5.47: The iron-sparsest simulant LHT-3M which is mainly composed of a mix of pure minerals rather than igneous rock, behaves different than all other analysed simulants. For LHT-3M the iron and titanium oxides content was gradually decreasing, but the content of MgO, CaO, Al_2O_3 and Na_2O behaved different from other simulants. MgO first increases and then decreases again over the course of the magnetic separation. CaO, Al_2O_3 and Na_2O behave exactly opposite to MgO. This would suggest an increase in pyroxene content until sample L-high,

followed by an increase of feldspar ending with a maximum reached at L-non.

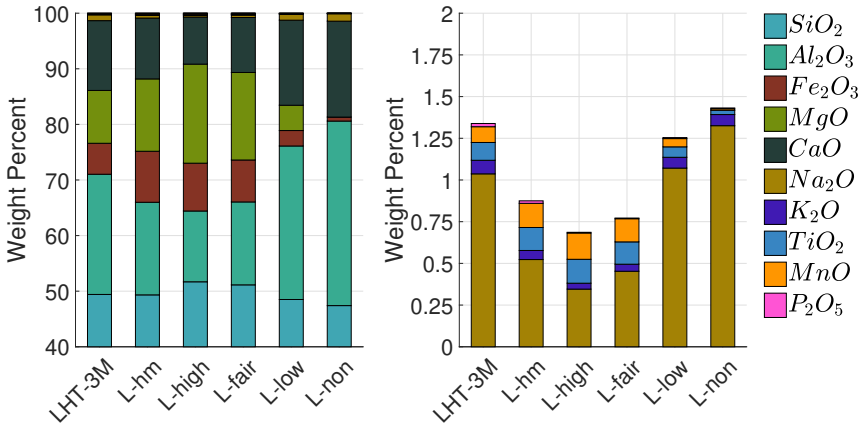

Figure 5.47: LHT-3M: Comparison of different stages of magnetic separation: LHT-3M (unaltered regolith), L-hm, L-high, L-fair, L-low, L-non; after LHT-3M in decreasing order of magnetic susceptibility. Left side shows the bulk of oxides contained and the right side, minor oxides only. Values below 40 wt % (left figure) are all $SiO2$ content.

The overall goal of this experiment was to remove most of the iron oxide to be able to manufacture transparent glass from regolith. Results obtained showed that the first step was successful for all simulants. All iron-sparsest samples indicated with "-non" contained less than 2 % of iron oxide for each simulant tested. As a side effect, the magnetic separation process also altered the elemental content by removing or increasing the amount of other oxides. This suggests the use of magnetic separation beyond iron removal, and may be a method which can be used to target certain minerals contained in (lunar) regolith. This further suggest that magnetic separation could be used as a comparably simple first beneficiation step, prior to any purification.

In addition to the discussed results, another experiment was conducted attempting to increase the amount of iron contained in a sample by repeatedly applying the hand magnet separation to the sample. This was conducted on LHT-3M samples and after repeating the procedure for 5 times, a XRF sample was prepared. The result of the XRF analysis of the supposedly iron enriched LHT-3M is shown in table 5.28. The first line ("L-hm") shows the results without correcting for the LOI of -18.0 wt % and the second ("corrected") the corrected. The unusually high negative LOI is likely caused by absorbing oxygen during initial firing of the sample (since not all iron contained in the LHT-3M must be fully oxidised) or release of sulfide. After correction, an iron oxide content of almost 60 % could be determined, this is an 53.46 % (absolute) increase compared to raw LHT-3M, and an almost ten times relative increase. Although no further tests have been conducted with this sample, such a large iron content may open up the possibility to use regolith as conducting material. This could potentially include the use of regolith for building wires from regolith on the lunar surface. These could then be used to transport electricity across the surface but may also be useful as conducting material for

building solar cells. Therefore, beneficiating regolith to increase its iron (oxide) content will need further attention to better understand its potential as conductor.

Table 5.28: XRF measurement of iron enriched LHT-3M sample

Sample	SiO_2	Al_2O_3	Fe_2O_3	MgO	CaO	Na_2O	K_2O	TiO_2	MnO	P_2O_5
L-hm	26.75	7.24	69.69	8.49	5.10	0.05	0.03	0.11	0.58	0.03
Corrected	22.66	6.13	59.03	7.19	4.32	0.04	0.02	0.09	0.49	0.02

In a final step a small study with only eight samples was conducted to see whether the grain size distribution of the processed regolith impacts how well it can be separated. Table 5.29 lists JSC-2A samples, which have been manually separated via a hand magnet (indicated by "hm"), and afterwards separated using an electromagnet at lowest settings (indicated by "high"). Moreover, four grain size distributions have been examined, 63 - 125, 125 - 250, 250 - 500 and 500 - 1000 μm.

Table 5.29: Impact of grain size distribution on magnetic separation

Sample	SiO_2	Al_2O_3	Fe_2O_3	MgO	CaO	Na_2O	K_2O	TiO_2
J-hm-63-125	46.68	16.94	13.86	6.72	9.97	3.08	0.90	2.02
J-hm-125-250	46.01	15.59	14.11	9.17	9.28	2.85	0.84	1.90
J-hm-250-500	46.08	15.71	13.35	9.28	9.38	2.84	0.83	1.84
J-hm-500-1000	46.42	16.55	12.63	7.78	9.95	2.94	0.83	1.86
J-high-63-125	46.77	17.07	12.61	7.10	9.94	3.18	0.88	1.91
J-high-125-250	45.66	14.83	14.01	10.96	8.75	2.71	0.80	1.78
J-high-250-500	45.52	14.65	13.80	11.61	8.62	2.75	0.77	1.70
J-high-500-1000	46.53	16.79	12.65	8.07	9.66	3.05	0.83	1.84

Both times (for "hm" and "high") the largest grain size (500-1000 μm) showed to contain the smallest amount of iron oxide. Moreover, the grain size distribution from 125 - 250 both times showed to have the largest amount compared to the other grain sizes. Only looking at the three largest grain size distributions analysed, the amount of iron oxide contained in a sample after separation is increased the smaller the grain size gets. This trend is broken by the finest grain size distribution used, reaching from 63 to 125 μm in grain size. It is likely that, the smaller the grains get, the iron oxide contained in the regolith is more accessible to the magnet, since it is not attached to as many other minerals, as the iron oxide of larger grains is. This causes the fine, iron oxide rich minerals to block the slide leading trough the electromagnet more frequently than for larger grain sizes. The smallest grain size distributions, separated by the hand magnet, show much higher values than the ones run through the electromagnet. It is, however, not possible to compare these two groups since the "hm" samples are a prior separation stage to the "high" stage. Meaning that they will have undergone a first separation process already. Therefore, the actual separation impact the hand magnet separation has on the

sample, prior to the electromagnet separation, is unclear. Thus, the values for the "high" samples are impacted by how much iron was removed via the hand magnet already before. Further, it may be possible that a different grain size distribution also has a different naturally occurring iron oxide content from the start. To exclude this being the case, samples of each grain size prior to the first separation stage need to be taken. Generally, it seems possible that a certain grain size distribution is favourable for iron extraction.

In conclusion, it can be reported that manipulating the iron oxide content, amongst other oxides and minerals, is definitely possible by means of magnetic separation. Further, an iron content lower than two percent for each of the utilised regolith simulants seems low enough to try manufacturing transparent glass from it. The biggest difficulty after removing the iron from the regolith was that the yield (shown in table 5.30) for the non-magnetic samples was less than 1 % for three simulants, and 2.5 and 5.8 % for two more, and only for one (LHT-3M) it was more than 34 %. Thus, gathering enough sample to be able to manufacture a glass sample was a challenge. Only four simulants delivered enough amount to measure samples on the XRF ($\approx$ 1 gram), and leave enough to try manufacturing a glass sample. The simulants used in the following to attempt to manufacture transparent glass are BP-1, FJS-1, JSC-2A and LHT-3M.

Table 5.30: Yield of six regolith samples magnetically separated from 63 to 500 μm grain size, split in five different levels of magnetic susceptibility, results shown in gram

500 - 63 μm	HM	high	fair	low	non	loss
BP-1	50.24	34.04	6.16	2.19	2.51	4.86
EAC-1	72.97	17.24	7.30	0.98	0.30	1.20
FJS-1	71.73	6.44	4.05	8.84	5.82	3.12
JSC-1A	21.96	43.57	29.66	2.27	0.44	2.10
JSC-2A	21.92	56.07	20.16	0.26	0.26	1.32
LHT-3M	2.08	13.18	38.78	10.95	34.23	0.77

5.2.8 Transparent Substrates

It was possible to manufacture transparent glass from magnetically beneficiated regolith simulant, one of the resulting samples is depicted in figure 5.48. The left side of the figure shows the raw glass nugget manufactured using the same resistive heating approach described earlier, and on the right the finished glass slide. In total three LHT-3M samples and one of each FJS-1, BP-1 and JSC-2A were manufactured. The two other LHT-3M samples turned out to be slightly smaller in dimension than the one depicted in figure 5.48, the three other samples were contaminated by carbon during manufacturing and are depicted in figure 5.49.

As discussed in section 3.2.4, for manufacturing only very little amounts of sample (3 - 5 grams) were available for BP-1, FJS-1 and JSC-2A, it was hard to manufacture

Figure 5.48: Transparent glass made from regolith simulant LHT-3M. Raw sample after casting (left) and ground and lapped glass slide (right).

a sample of it. Since the manufacturing procedure needed to be altered, it led to a contamination by carbon, penetrating into the glass melt. Figure 5.49 shows the three glass slides manufactured from these contaminated glass samples. Clear black lines can be seen where carbon entered the glass.

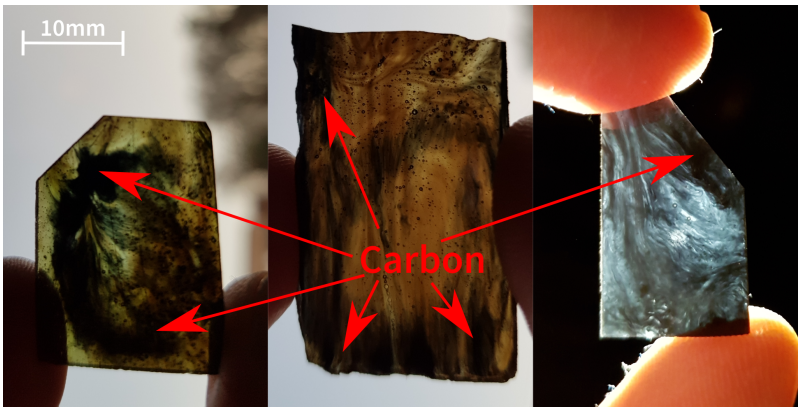

Figure 5.49: Transparent glass made from regolith simulant BP-1 (left), FJS-1 (middle) and JSC-2A (right). All samples appear partially transparent but show black lines of carbon contamination from the graphite crucible.

Although it was only possible to gather enough material from one regolith simulant (LHT-3M), to manufacture a good sample, this sample showed to be transparent to the human eye and was thus taken for further evaluation. Nevertheless, on all other (contaminated) samples optical measurements were performed as well. Even if the samples could not be manufactured as transparent as possible, they still show transparency to the human eye and thus it seems likely that transparent glass could be manufactured form a variety of regolith simulants.

Surface Roughness

All samples were lapped on the same machine with the same parameters. The surface roughness of three samples was measured, utilising the profilometer. Two LHT-3M

samples (L1, L2) as well as one microscopy slide (MS) were measured. The resulting plot is depicted in figure 5.50. The Surface roughness of the samples was calculated to $R_{aL1} = 7$ nm ($l_{xL1} = 0.7$ mm), $R_{aL2} = 6$ nm and ($l_{xL2} = 0.8$ mm) and $R_{aMS} = 3$ nm and ($l_{xMS} = 0.9$ mm). Thus, the samples are in the same surface roughness range as the microscopy slide.

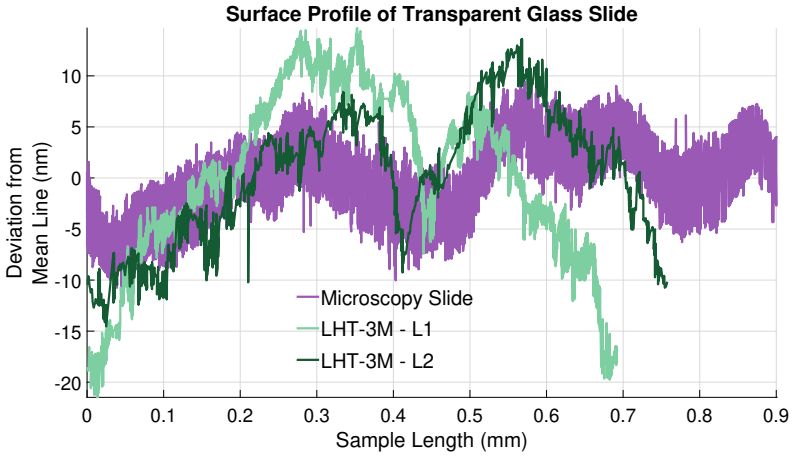

Figure 5.50: Surface roughness of polished transparent substrate made from LHT-3M which has been magnetically treated to remove iron oxide. The abscissa shows length on the samples surface in mm and the ordinate deviation from the mean line in nm.

5.2.9 Regolith Substrate Characterisation Summary

It has been a long way from thinking of using regolith simulant as a material to build substrates for solar conversion device manufacturing, to actually doing so. Figure 5.51 shows all iteration steps achieved during the entire project. A brief description of each step depicted in this figure:

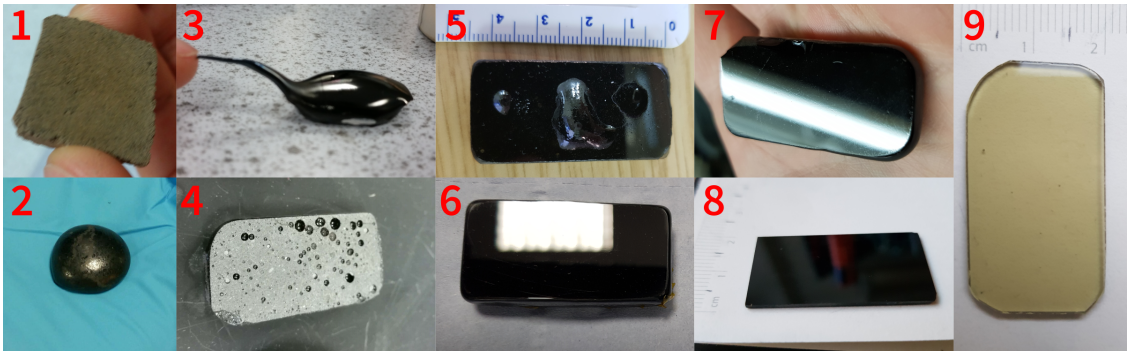

Figure 5.51: Substrate iterations (firsts): 1. Sintered EAC-1 2. Glass bead EAC-1 3. Cast Sample JSC-2A 4. Ground microwave heated sample EAC-1 5. Improved microwave heated sample JSC-2A 6. Bubble free glass JSC-2A 7. Polished bubble free glass - six simulants 8. Lapped glass slide JSC-2A 9. Transparent glass slide LHT-3M. Not to scale.

1. First samples were produced at the beginning of the project by entering EAC-1 simulant on a graphite sheet into a standard house hold microwave. The simulant did heat enough to sinter and form a 20 * 20 mm brick slide. Temperature was found to be too low to reach melting.

2. The first glass bead was produced by using a microwave kiln in combination with a graphite crucible. The bead did come off the crucible easily, but it was not possible to manipulate the glass into another shape than round/drop-like. Thus, a mould needed to be used.

3. It was possible to cast a sample into a clay mould, which showed promise to take the shape of the mould rather than the shape of a drop. Although the top surface of the sample was pristine for the first time, it was curved too much to build anything on its back. Moreover, the inside was filled with bubbles and the bottom side was not useful for manufacturing.

4. Continuous improvements to the process led to a first rectangular shaped sample, which could be ground and polished to see whether it could be used for further manufacturing steps. The entire bottom of the sample was covered in holes/bubbles, nevertheless it was possible to grind and polish the areas in-between and build first devices from these samples.

5. The last batch of microwave samples manufactured, utilised four different regolith simulants. All of the manufactured samples showed large bubbles on the bottom surface, which could, in most cases, be removed, by grinding the samples long enough. These samples' surfaces were analysed, and deemed to be better than the first batch of microwave samples. However, bubbles caused by interaction of the graphite (carbon) crucible, continued to cause trouble during manufacturing. As a result, the microwave heating approach was replaced in favour of resistive heating.

6. The first bubble free sample was produced, which was a milestone in the project. Bubble/void free glass enabled glass as a potential resource to be used for manufacturing, potentially also on the lunar surface. The process developed utilising a platinum crucible and resistive heating was then applied to various regolith materials.

7. Six different regolith materials were processed and all could successfully be shaped into rectangular bubble free glass nuggets. Moreover, 100 % ISRU manufacturing was successfully demonstrated by using raw regolith itself as grinding agent.

8. The manufactured bubble free glass nuggets where ground roughly into rectangular shaped glass slides, and then lapped to finish. After processing, glass slide samples with the approximate sizes of 38 * 20 * 1.3 - 1.5 mm were available.

9. In a final step the non-transparent glass manufactured until this point could be made relatively transparent by removing iron oxide contained in each regolith

simulant. This led to a transparent glass slide being manufactured, which could serve as window or cover glass on a lunar surface mission.

At the end of the described iteration process, on the way to finding out whether regolith can be a suitable substrate material, it can be concluded, that it can be. Although the effort of processing regolith into useful, and suitable glass substrates is much higher than, for example, terrestrial soda-lime glass, it may be a viable alternative for the Moon. Since on the lunar surface no other useful resource than regolith[9] can be found, it is the only locally available source material. Thus the comparably high temperatures, required to process the, comparably inhomogeneous raw material, may be worth exploring further. To use regolith as raw material for manufacturing glass, would only require processing/manufacturing equipment and initial power systems to be flown from Earth to the Moon once. After that, the system could manufacture glass continuously and by that, make it an available resource on the lunar surface.

The final stages of substrate manufacturing seemed good enough to start trying to build solar conversion devices on their backs. The first device, which was attempted to be built on the back of these samples was a mirror. The next chapter will detail results using basaltic glass substrates for optical applications/mirror manufacturing.

5.3 Mirrors Built on Basalt Substrates

Once a substrate with the desired surface specifications was built, building mirrors was attempted next. Manufacturing of mirrors was described in section 3.4.1 and the deposited layer thickness was determined in section 2.4.2. By designing mirrors on basaltic glass the described way, it was intended to maximise the mirrors' reflectivity. Ultimately, this would lead to maximising the efficiency of a solar concentrator system, using multiple mirrors, to reflecting more sunlight onto a solar cell, and thus increased its power output. This chapter will elaborate on each attempt to manufacture mirrors on substrates made of simulant, as well as analyse potentially transparent glass for its use as cover glass on a solar cell.

5.3.1 Microwave Substrate Mirrors

The first set of mirrors manufactured was built on substrates made of lunar regolith simulant manufactured by using microwave heating. To determine their performance reflectivity measurements have been conducted. First, the reflectivity of the uncoated samples' surfaces was measured to establish a reference to see how much surface coating can improve reflectivity. Next, the mirrors reflectivity has been measured for two cases, aluminium coating and silver coating.

Two batches have been manufactured for this first generation mirror fabrication. Batch one consists of five samples (EAC-I-1, EAC-I-2, EAC-I-3, JSC-I-1 and JSC-I-

[9] and possibly some water in form of frozen H_2O close to the poles

2), which have been made of EAC (3 samples) and JSC-2A (2 samples). Batch two consists of four samples (Sample IDs: EAC-II, FJS-II, JSC-II and LHT-II), each made of a different simulant. Simulants used for batch two samples were made of EAC-1, FJS-1, JSC-2A and LHT-3M.

Substrate Reflectivity

For all optical measurements conducted, the described UV-vis-NIR spectrometer described in section 4.2.5 was used with a detector handover at 860.8 nm and light bulb handover at 319.2 nm. Measurements close to these wavelengths show discontinuations in the recorded data around these wavelengths, which are system based and unlikely to be caused by the samples characteristics.

As mentioned, the first measurement required to determine the performance of a mirror is to know its substrate's reflectivity prior to coating. Figure 5.52 shows the results of a UV-vis analysis measured in the wavelength range from 300 to 1250 nm. Results of batch one samples are depicted in full lines and results of batch two samples in dotted lines. For most but one sample the reflectivity shows to be in-between 4 to 13 %. The one sample which stands out is the sample made of LHT-3M (LHT-II), which shows a peak reflectivity of approximately 28 % around 540 nm wavelength. To the human eye, this wavelength would appear as green since the green light spectrum is from 490 to 570 nm.

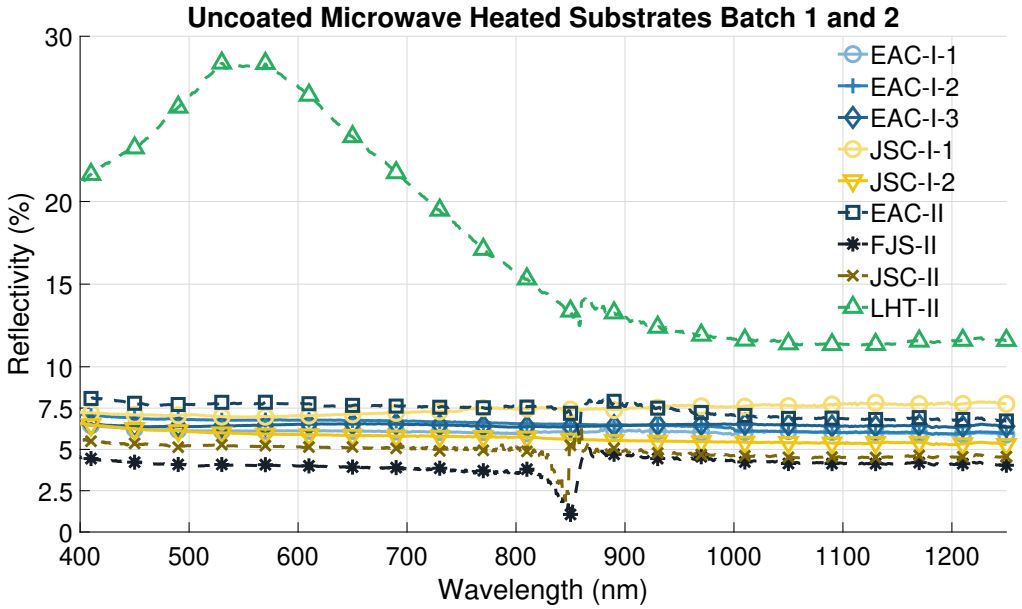

Figure 5.52: Reflectivity of uncoated microwave heated basaltic glass samples - batch 1 (EAC-I-1 to JSC-I-1) depicted in solid lines, batch 2 (EAC-II to LHT-II) in dotted lines. Shown is reflectivity over wavelength.

Looking at the results of batch one only, no sample seems to show a higher reflectivity than about 8 % and none a lower reflectivity than 5 %. Further, each sample's reflectivity stays rather constant over all wavelengths measured. These

results show that a polished basaltic glass substrate without any coating is a comparably bad reflector. Three samples (EAC-II, FJS-II and JSC-II) of batch two show similar reflectivity characteristics than all batch one samples and thus are not deemed suitable reflectors either. The only sample which may be of use as a reflector directly is the substrate made of LHT-3M regolith simulant (LHT-II). With an average reflectivity of 17.5 % (averaged over all wavelengths measured), its average reflectivity is about two to three times higher than that of all other samples. Still it is not a good reflectivity compared to a mirror which may have an average reflectivity, in the analysed wavelength range, of about > 90 % from 450 nm - 2000 nm [552]. Further, the reflectivity of this substrate may only be as high as it is since not all minerals were shown to have fully melted.

The reflectivity of EAC-II is slightly elevated compared to FJS-II and JSC-II. This may be due to the EAC-II sample showing crystalline areas on its surface which appear slightly brighter to the human eye than the other two samples do. If this sample's reflectivity is increased due to (partial) crystallisation, it may be favourable for a substrate to be crystallised, to improve its reflectivity.

A potential connection between surface roughness, listed in table 5.19, and its average reflectivity was analysed. To illustrate a potential connection, figure 5.53 (top) shows the samples' average reflectivity versus their surface roughness. The average surface roughness was taken from the R_a "micro" values in table 5.19, and the average reflectivity values, from figure 5.52. The results in figure 5.53 (top) do not suggest a direct connection between surface roughness and reflectivity.

However, a direct comparison in-between samples is only possible for samples manufactured from the same simulant. By attempting to compare samples manufactured from different simulants, their different geochemistry comes into play and makes it impossible to tell, whether a difference in reflectivity is caused by a sample's geochemistry or its surface roughness. Further, the overall number of samples is too low to see a clear trend, if existent. Lastly, other parameters such as crystallisation state and homogeneity might impact a sample's reflectivity as well, but it is impossible to decouple these effects from the measurements presented.

Another suspected potential dependency of reflectivity on substrate parameters is depicted in the bottom part of figure 5.53. Shown in this figure is average surface roughness versus the iron oxide content of each simulant. For each data point depicted, reflectivity of each substrate, made of a certain simulant type, has been averaged as well. Thus, the EAC-1 data point is an average of four samples and JSC-2A of three. For FJS-1 and LHT-3M only one sample was used. From the results in figure 5.53 (bottom), it seems that a connection between iron oxide content and reflectivity of a substrate is possible. To understand the connection between the two better, a study analysing a larger number of samples will be required. Further, since LHT-3M samples manufactured using resistive heating appeared as black as all the other samples to the human eye, it is likely that this connection does not hold up.

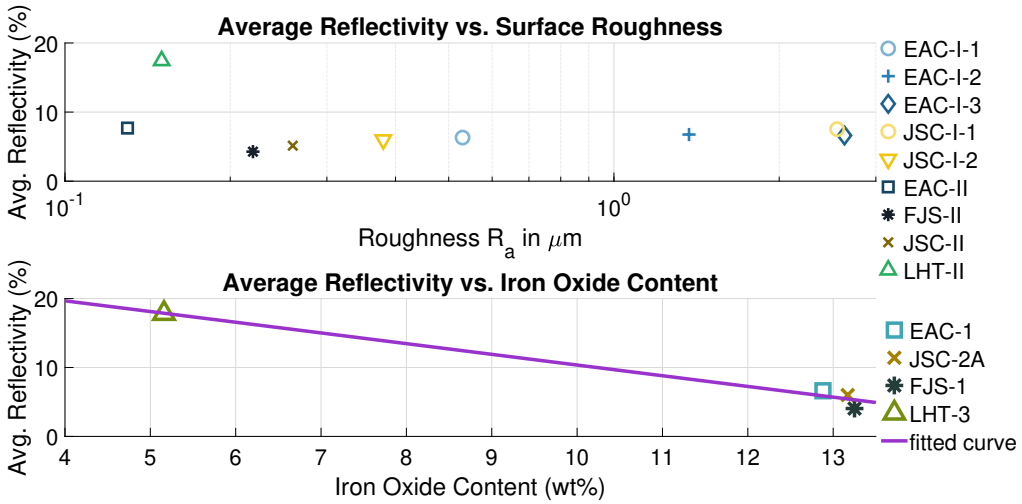

Figure 5.53: Reflectivity of uncoated microwave heated basaltic glass samples versus surface roughness (top - batch 1 and 2). Average reflectivity of uncoated EAC-1, LHT-3M, JSC-2A and FJS-1 samples (average of all samples batch 1 and 2) versus iron oxide content (FeO and Fe_2O_3 combined).

Silver-Coated Samples

After analysing the uncoated samples' reflectivity, batch one samples were coated with silver on one side to form a front coated silver mirror. Results from a UV-vis analysis of these samples is depicted in figure 5.54. By coating the samples with silver their reflectivity was increased to in-between 20 and almost 60 % for some wavelengths. This is a significant increase from the 5 to 8 % reflectivity the samples showed without coating. The best samples where EAC-I-1 to EAC-I-3, and the worst one was JSC-I-2.

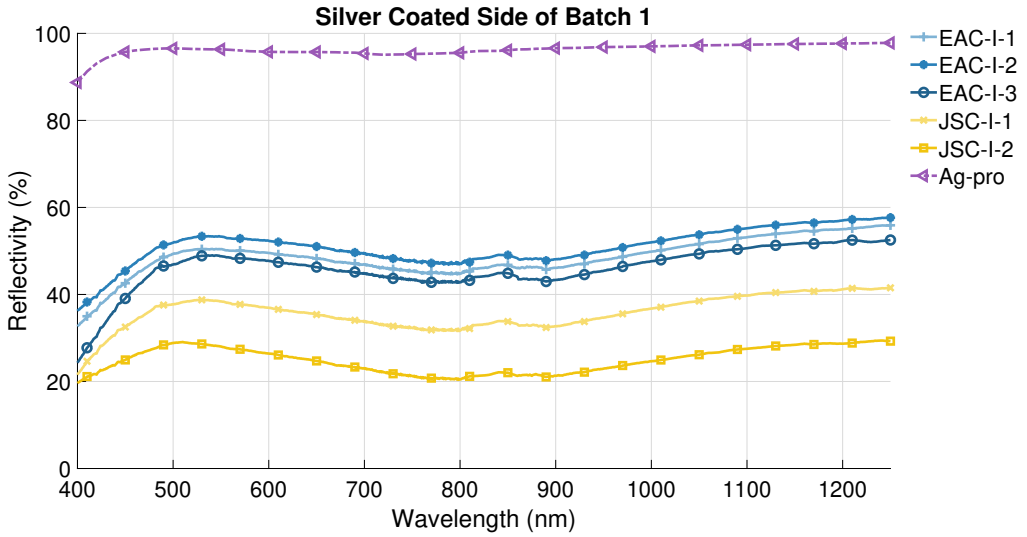

Figure 5.54: Reflectivity of batch 1 substrates coated with silver. Shown in violet (triangle markers) a THOR labs reference mirror also coated with silver with an additional protective layer on top.

This does not correspond to the samples microscopic surface roughness from table 5.19, but rather to the macroscopic roughness. JSC-I-2 showed the worst surface roughness and the lowest reflectivity for silver coating. Sample JSC-I-1 shows the second worst surface roughness and the second worst reflectivity. Although this connection seems true for JSC-2A samples, the EAC-1 samples do not match that observation. Considering the microscopic roughness for these samples, a connection seems more likely. Again, a larger number of samples will be required to establish a direct link between these two parameters. Since, however, it is understood from mirror manufacturing that a smoother surface leads to a better reflectivity, it is likely that a better surface roughness of a homogenous and void free sample should lead to a better reflecting mirror. As a last remark, since only one side of the batch one samples was covered with either silver or aluminium, there are geometrical differences of the sample itself which may cause differences as well. In case of JSC-I-2, the silver coated side contained a significantly larger amount of bubbles than the other side. Hence, it is to be expected that the other side will show better results since it is much smoother as indicated by the R_a micro results in table 5.19.

In addition to the results of the reflectivity measurements of the silver coated side of batch one samples a reference mirror was analysed. This mirror's results are depicted in figure 5.54 as a violet dash-dotted-line, bearing triangle markers. The reflectivity of this mirror shows, to be in-between 90 and 95 % reflectivity, for the largest part of the analysed wavelength spectrum. This suggests, that there is still a lot of room for improvement on the reflectivity of the silver coated mirrors built on regolith substrates. This improvement seems possible by increasing the surface quality of the substrates further.

Aluminium-Coated Samples

In addition to silver, the other side of batch one substrates has been front coated with aluminium. Moreover, all batch two samples have been covered entirely with aluminium. Aluminium shows, compared to all mirror materials considered for this work, the best average reflectance over a wide wavelength range. An additional side effect of selecting aluminium over gold or silver, is that aluminium is the cheapest and lightest material of these three, thus better suited for a space mission. Depending on the required amount to be carried to the lunar surface from Earth, the weight and price may play a relevant role in decreasing the cost of the mission.

The results of the reflectivity measurements of the aluminium coated sides are depicted in figure 5.55. The difference between batch one (full lines) and batch two (dotted lines) samples is rather clear. All batch one samples show similar reflectivity percentages than they showed for silver, from 25 to 55 %. Batch two samples in comparison show reflectivity values from 55 to 85 %. For both batches, the highest reflectivity was achieved around a wavelength of about 500 nm and above 1100 nm. Comparing batch two results to the results of the off-the-shelf front coated aluminium mirror (with an additional protective layer), plotted in violet in figure 5.55, most batch two mirrors perform similar. EAC-II and LHT-II even partially

outperform the reference mirror at wavelengths in-between 800 and 900 nm. This shows that it is possible to manufacture mirrors from lunar regolith simulant of similar quality than commercially available mirrors. Comparing the aluminium coating with the silver coating, aluminium showed higher reflectivity values for most parts of the measured wavelength spectrum. Silver, however, showed slightly higher values in the infrared (IR) wavelength ranges, which was expected from [553].

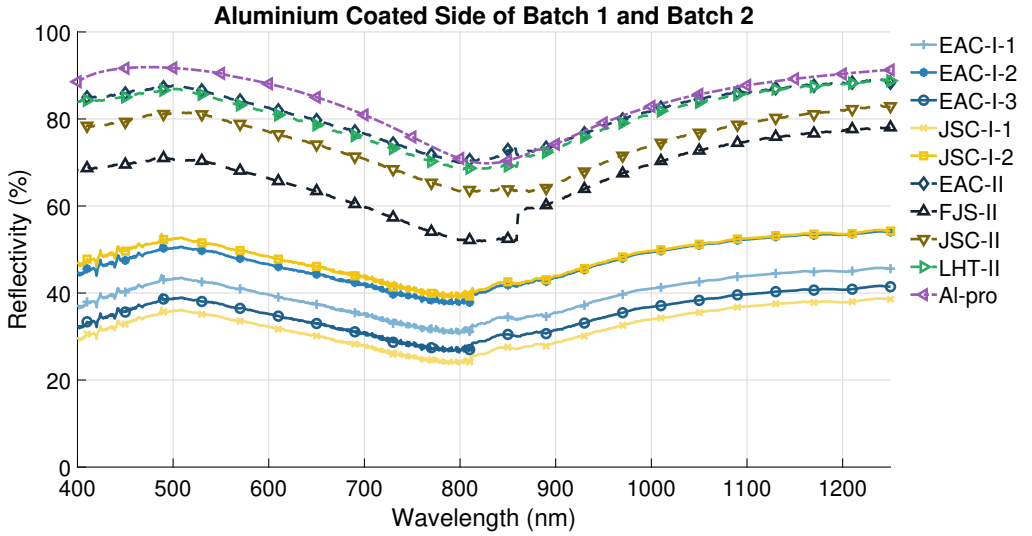

Figure 5.55: Reflectivity of aluminium coated side - batch 1 (full lines), batch 2 (dashed lines) and reference mirror (triangles).

Surface Roughness versus Average Reflectivity

Going back to batch one samples and considering the samples' surface roughness from table 5.19 again, JSC-I-2 now performed best. Closely followed by EAC-I-2, this again only partially matches the surface roughness observations. JSC-I-2 showed the smoothest microscopic surface with a R_a of 0.38 μm however, JSC-I-2 only showed the third smoothest surface with 1.37 μm. Since the impact of the voids/bubbles cannot be separated from the surface roughness effects in these measurements a direct conclusion cannot be drawn yet. When looking at the batch two samples' surface roughness vs reflectivity, a clear connection between them can also not be established. Although EAC-II has the lowest R_a with 0.13 μm and the highest reflectivity, JSC-II with the second lowest R_a value of 0.15 μm does only have the third highest reflectivity of the batch two samples.

To visualise a potential link between surface roughness and reflectivity of the mirrors, figure 5.56 was prepared. It shows each batch one and batch two sample with both, aluminium and silver, average reflectivity versus surface roughness. Reflectivity values used for this figure are based on the average reflectivity from reflectivity data depicted in figures 5.54 and 5.55. The violet line in the graph shows a potential trend calculated from the data points depicted. From this trend line it seems that with decreasing surface roughness of the substrate, the reflectivity is increasing. In addition to increasing reflectivity, with respect to surface roughness,

figure 5.56 also shows, that at a constant surface roughness, silver has a lower average reflectivity for the measured wavelength range.

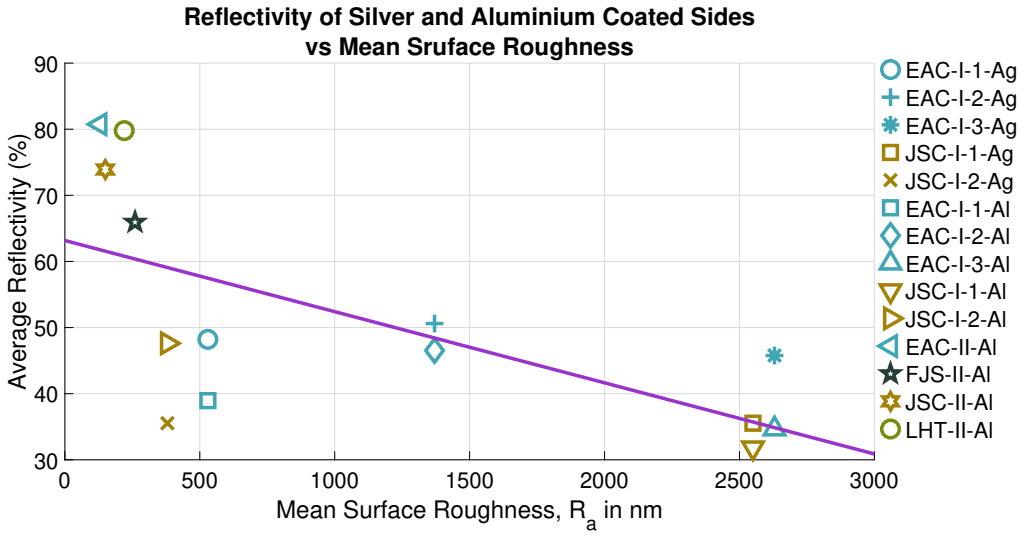

Figure 5.56: Average reflectivity in % of all batch 1 and 2 samples versus surface roughness R_a in nm. For batch 1 both sides, aluminium and silver covered sides are shown. Shown in violet is the trend line calculated from the data points and suggesting a correlation between surface roughness and average reflectivity.

Considering the entire first mirror manufacturing test run by looking at all batch one and two samples, this first experiment was a success. It was not only possible to manufacture front surface coated mirrors, but also to manufacture mirrors with similar reflectivity values than off-the-shelf mirrors. This is especially interesting since the substrate quality was not deemed to be good yet, considering the many voids contained on most samples, formed by bubbles in the melt. This further suggests, that even with comparably low quality substrates (rough surface and multiple voids), it is possible to build a comparably decent mirror.

All (but one) uncoated basaltic glass substrates made from lunar regolith simulant showed average reflectivity of about 4 to 8 %. The only exception was the batch two sample LHT-II, with an average reflectivity of more than 17 %, which was likely the result of the simulant not melting entirely. After coating, all of these samples' average reflectivity was increased to a minimum of 20 % up to more than 80 %. This shows a relative increase of five to ten times, comparing reflectivity after and before coating.

5.3.2 Resistively Heated Substrate Mirrors

After successfully manufacturing mirrors on top of basaltic glass substrates, manufactured from four different regolith simulants, the next step was to try to repeat the process on the second generation of basaltic glass samples. These samples were manufactured from JSC-2A regolith simulant and were heated using a resistively

heated furnace. Quality of second generation samples was improved by removing bubbles from the melt, due to the use of a combination of a platinum crucible with a graphite mould. As shown in the previous chapter, these samples had little to no surface defects compared to the samples manufactured using microwave heating. Thus, it was expected that building mirrors on top of these substrates will lead to increased reflectivity compared to the first generation samples.

Substrate Reflectivity

The uncoated substrates' surfaces reflectivity has been determined the same way as for the first generation samples. Results of the reflectivity measurements of the uncoated samples are depicted in figure 5.57. The reflectivity of the uncoated samples made of JSC-2A is within the range of 5 to 7 %, and therefore very similar to the results presented in figure 5.52 in the previous chapter. From the surface roughness measurements shown in tables 5.19 and 5.21, it is clear that the second generation samples have a lower R_a value and thus a better surface quality. The improved surface quality however did not lead to an improved reflectivity of the uncoated sample.

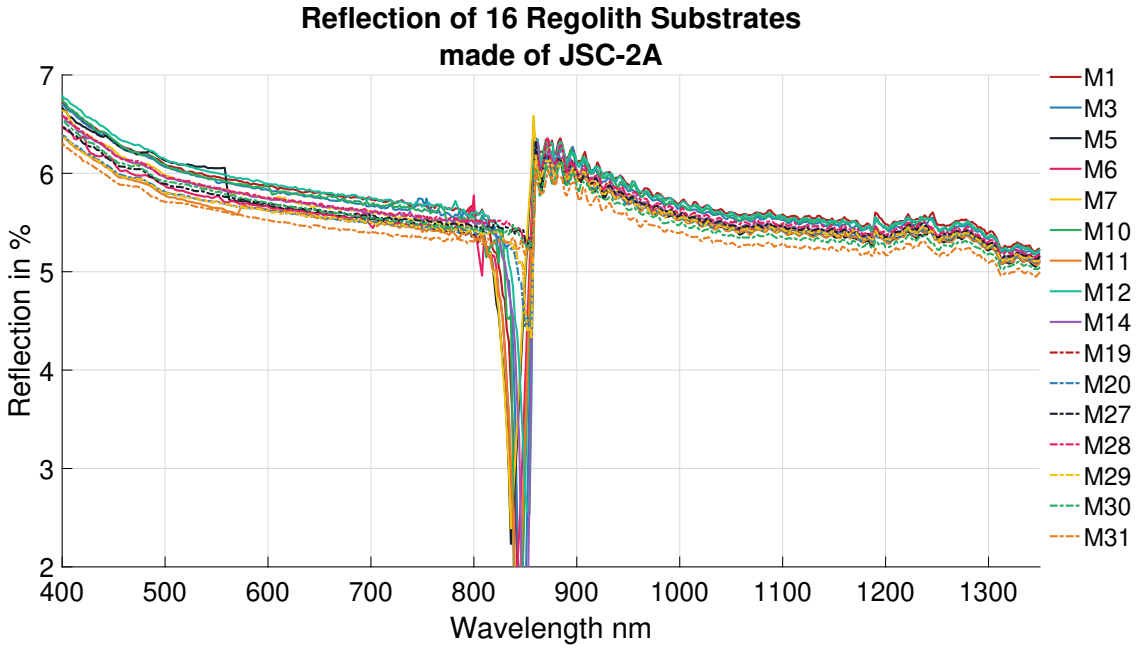

Figure 5.57: Reflectivity of 16 uncoated basaltic glass samples made of JSC-2A. The abscissa is showing wavelength in nm and the ordinate reflectivity in %.

Although the surface roughness did not seem to impact the reflectivity of the samples, there are differences of about 0.5 % reflectivity in-between the most reflective (M12) and the least reflective samples (M31). These differences may be a result of slight differences in the surface structure and/or different crystallisation state of the sample. Although crystallisation has not been observed, it is not excluded that the samples could have crystallised to a certain level during cooling. Since all results of all samples analysed are in a rather small corridor of about 0.5 %, sample differences were considered small enough to move on to coating the samples with aluminium.

Aluminium Coated Substrate Reflectivity

After coating all 16 samples with aluminium, their reflectivity has been measured and compared to two reference mirrors (Ref1, Ref2), also coated with aluminium. Results are depicted in figure 5.58 and show reflectivity of almost all mirrors to be in-between 82 and almost 100 %.

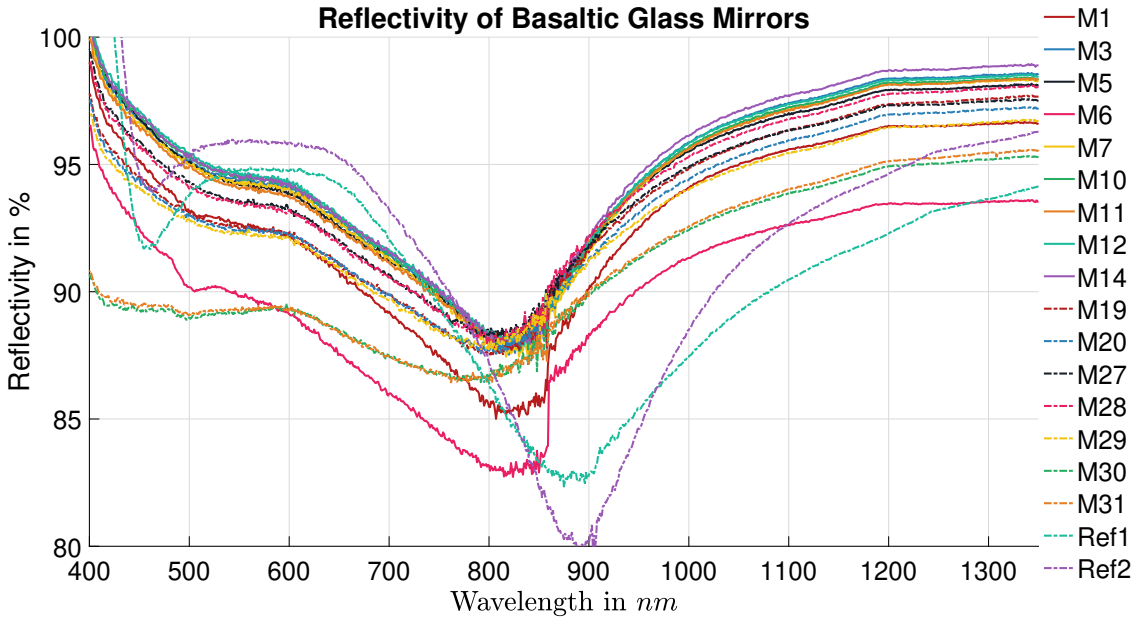

Figure 5.58: Reflectivity of aluminium coated substrates, manufactured from JSC-2A utilising resistive heating. The abscissa shows wavelength in nm and the ordinate reflectivity in %.

Despite 18 lines being depicted in figure 5.58, it can be seen that all basaltic glass mirrors perform similar, since they follow the same trend in a narrow corridor. Hence, it seems that melting, grinding, polishing and coating of the samples is reproducible. Calculating the average reflectivity of all 16 + 2 mirrors (from 400 to 1350 nm wavelength) resulted in table 5.31. The mirror performing the least best is M6 (90.0 %), and the one performing best is M14 (94.9 %). Moreover, the two reference mirrors analysed are showing average reflectivity of 91.0 and 92.2 %, thus shows a difference of 1.2 % in average reflectivity. Around 450, 900, and 1100 - 1350 nm the difference between the two reference mirrors is the most visible (in figure 5.58). However, these differences are within manufacturing tolerances for these mirrors. Comparing the trend of the basaltic glass mirrors to the trend of the off-the-shelf mirrors, the basaltic glass mirrors show a similar curve than the reference mirrors, and partially the basaltic glass mirrors outperform the reference mirrors. The most likely reason for that is, the protective layer of the reference mirrors, which prevents the mirrors from oxidisation and scratches, but also decreases their reflectivity. The basaltic glass mirrors do not have such a protective layer, which makes them more vulnerable to oxidisation, but increases the reflectivity.

Table 5.31: Average reflectivity (in %) calculated from the results depicted in figure 5.58. Averaged over wavelengths from 400 to 1350 nm

Sample	M1	M3	M5	M6	M7	M10	M11	M12	M14
Mean	92.8	94.7	94.5	90.0	94.5	94.7	94.5	94.8	94.9
Sample	M19	M20	M27	M28	M29	M30	M31	Ref1	Ref2
Mean	93.5	93.3	94.0	94.1	93.0	90.9	91.0	91.0	92.2

As observed from the table 5.31 the difference between the average reflectivity of the best and the worst basaltic glass mirrors is 4.9 %. Moreover, all basaltic glass mirrors achieved an average reflectivity above 90 %, matching observations made from figure 5.58. With an average reflectivity of 91.0 and 92.2 % the reference mirrors are within parameters provided by the manufacturer, which are *"THOR labs:...[reference mirrors] exhibit average reflectance in excess of 90 % in the 450 nm to 2 μm range..."*[554].

Comparing the results of mirrors built on the back of second generation basaltic glass samples, with the results of the first generation mirrors, an increase of about 30 to 75 % in reflectivity was achieved. Thus, it seems that the improved macroscopic and microscopic surface roughness have improved the mirrors reflectivity as well. In conclusion, it is expected, that mounting a set of 16 reference mirrors, as well as basaltic glass mirrors, in a solar concentrator setup, should lead to similar performance improvements of a solar cell for both setups. Thus, the next step of testing the analysed mirrors was to test them under a solar simulator, mounted in such a solar contractor setup.

5.3.3 Reflectivity of Substrates Made of Six Regoliths

After successfully building mirrors with reflectivity higher than 90 % (from 400 to 1350 nm wavelength) reflectivity of uncoated samples was analysed once more. This time, basaltic glass samples were analysed, which had fully melted and thus formed a homogenous glass. Further, these samples did not show any residuals of not melted regolith minerals and/or voids formed during the melting process. All samples were manufactured using resistive heating, a platinum crucible and a graphite mould. Moreover, all samples have been lapped to finish and were ground into the shape of a glass slide (samples shown in figure 3.26). All samples were measured on the same UV-vis-NIR machine than all other samples.

Substrate Reflectivity of Six Different Glasses

The results of the reflectivity analysis of basaltic glass samples made of six different regolith simulant, BP-1, EAC-1, FJS-1, JSC-1A, JSC-2A and LHT-3M are depicted in figure 5.59. The results show that after all samples have been melted and manufactured the same way, differences in-between the reflectivity of individual samples are within a corridor of less than 1 %.

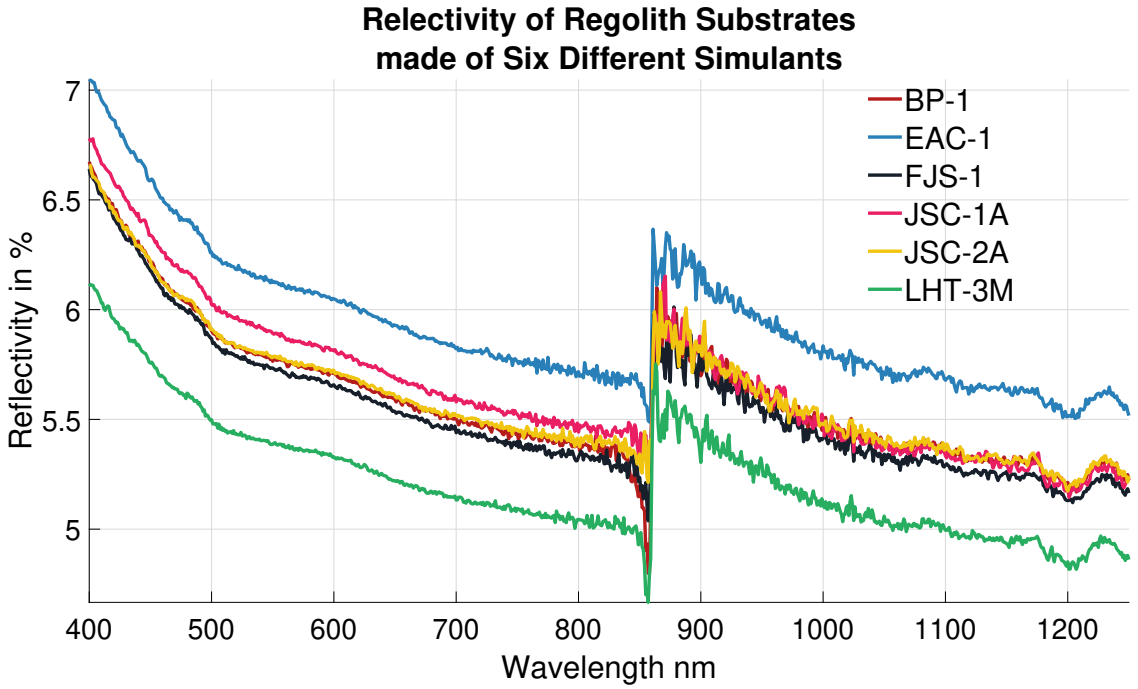

Figure 5.59: Reflectivity of uncoated basaltic glass substrates made of six (BP-1, EAC-1, FJS-1, JSC-1A, JSC-2A and LHT-3M) different regolith simulants.

Comparing the results of these homogenous samples to the results of the inhomogeneous samples shown in figure 5.52, the biggest difference is the behaviour of the sample made of LHT-3M. In figure 5.52 this samples achieved maximum reflectivity values of about 28 % and in figure 5.59 the LHT-3M sample shows reflectivity of mostly less than 6 %. Additionally it performed worst of all six samples analysed. This suggest, that a link in-between the iron oxide content of a simulant and the reflectivity of a basaltic glass sample, made of this simulant does not exist in the form suspected before. This seems to match the observation, that the LHT-3M sample (shown here in figure 5.59) is now homogenous and all minerals seem to have melted. This would have allowed iron and other glass-colour-impacting elements to taint the glass, as was the case for the other examined samples.

5.3.4 Arcjet Coating

After manufacturing substrates from different regolith simulants and coating them with different reflective materials, the possibility of a 100 % ISRU made mirror was investigated. The two most practical options for this are beneficiation and direct use of regolith. For beneficiation it would have been necessary to purify regolith to extract, for example, elemental aluminium. The extracted (and purified) material could then be used as reflective material to be deposited on a substrates surface. However, since the extraction of aluminium itself is a non-trivial process and requires additional equipment to be used (brought to the lunar surface), in a first test, a more simple approach was chosen: Arject coating of basaltic glass substrates with regolith powder as reflective material, as described in section 3.4.1.

Regolith Reflectivity

The first step in determining whether regolith may be a suitable reflective material replacement for aluminium, for example, was to analyse the reflectivity of different simulants. Since reflective properties of regolith are likely to be influenced by grain size and/or geochemistry and/or iron oxide content, reflectivity measurements of four different simulants were conducted. Each simulant was measured raw (off-the-shelf) and ground to a grain size of smaller than 38 μm. Figure 5.60 shows reflectivity values for these four simulants and two different grain sizes.

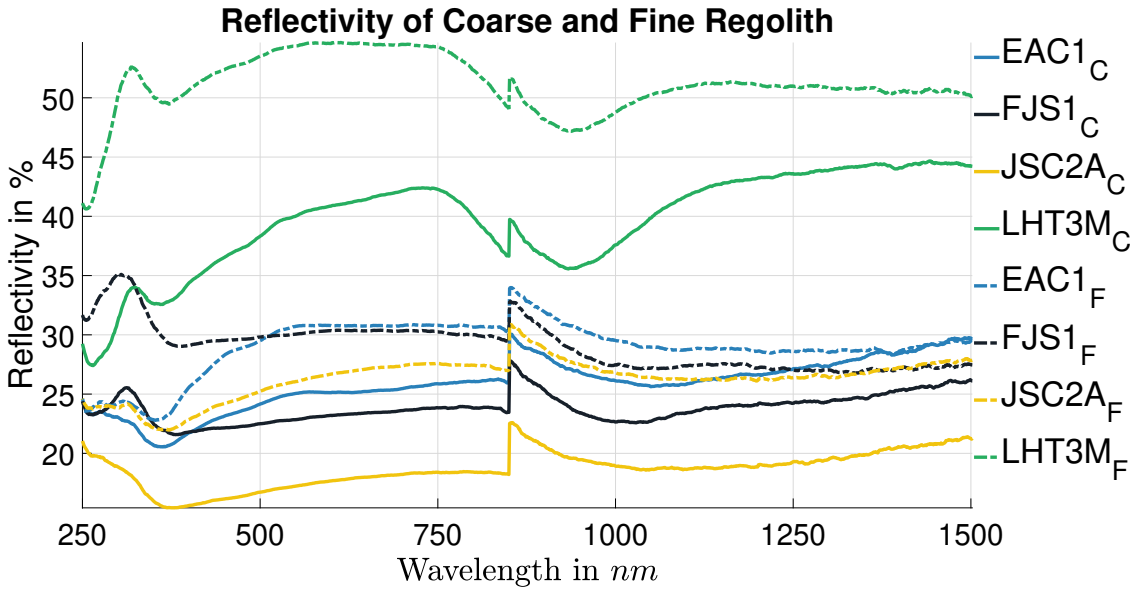

Figure 5.60: Regolith simulant reflectivity from 250 - 1500 nm for four regolith types (EAC-1, FJS-1, JSC-2A, LHT-3M) each measured with unaltered grain size distribution (full line) and fraction smaller 38 μm (dashed line).

Full lines in figure 5.60 show unaltered regolith and dashed lines ground regolith. For all four simulants the ground version showed higher reflectivity values than the unaltered regolith. JSC-2A not ground has the lowest reflectivity values with in-between 15 to 22 % reflectivity and LHT-3M ground has the best reflectivity with in-between 40 and 55 % reflectivity. Comparing these results to the reflectivity results of the six basaltic glass substrates analysed in figure 5.59, it can be seen that raw regolith is reflecting more light than basaltic glass. In case of comparing basaltic glass made of LHT-3M to ground LHT-3M, the difference is as high as about 40 %.

The shown results suggest once more that a more iron sparse simulant is reflecting more light than an iron rich simulant. Since LHT-3M has the highest reflectivity and the lowest average iron oxide content (from table A.10) with 5.57 %, and JSC-2A the lowest reflectivity and the highest iron oxide content with 13.13 %, this seems true. Further, taking the average iron oxide contents, of the other two simulants from table A.10, shows, that FJS-1 has the second highest average iron oxide content (12.91 %), and EAC-1 the third (12.83 %). This also corresponds

with their reflectivity, FJS-1 has the second lowest and EAC-1 the second highest. Considering the reflectivity of actual lunar regolith, depicted in figure A.2, taken from page 308 in [528], shows that actual regolith can also achieve reflectivity of 5 to 30 % (in a similar wavelength range). Comparing that to the results of the raw (not ground) samples, the results of the simulants seem to match this behaviour. Hence, it seems possible that also actual lunar regolith may be suitable as reflective material.

As a result of the reflectivity analysis of these four regolith simulants, LHT-3M (preferably ground) was selected as a potential reflective coating material. In a next step, it was tried to coat basaltic glass samples with this simulant to manufacture 100 % ISRU made mirrors.

Substrate Reflectivity - Coated vs. Uncoated

Four basaltic glass samples made of JSC-2A were lapped to finish and ground into glass slide shape. All four samples have been arcjet coated at the University of Bayreuth in Germany. Three different deposition batches were run on these four samples. All runs used LHT-3M simulant as coating material, which had to be treated prior to arject coating. Each batch used LHT-3M, which was treated differently:

- For batch 1, 130 g of LHT-3M regolith were treated by drying the simulant at 200 $°C$ prior to aerosol deposition.
- For batch 2, 70 g of LHT-3M were ground by high energy ball milling for 30 min in cylcohexane. After milling, the simulant was entered into a rotary evaporator to remove the cylcohexane before it was sieved through a 90 μm mesh. Finally, the simulant was dried, first at 120, then at 200 °C.
- For batch 3 also 70 g of LHT-3M were prepared the same way as for batch 2. The only difference being, that prior to all other treatments applied, simulant used for batch 3 was heat treated. For 10 hours the sample stayed at 700 °C in air atmosphere with a heating rate of 5 $^{K}/_{min}$.

Four substrates (Sub.), number, 6, 23, 27 and 28 were used to test the aerosol deposition (AD) process. All but substrate 6 could successfully be coated using AD. Substrate 6 only has an anchor layer, but no actual reflective layer deposition. Mean layer thicknesses achieved due to AD for the other three samples are 4.4 (Sub. 23), 3.8 (Sub. 27) and 8.3 μm (Sub. 28), which are typical thicknesses deposited on any carrier material using AD. The highest film thickness was measured on substrate 28 which was likely the result of a higher number of scans (100 instead of 80) and higher (approx. 30 instead of 18 g) feedstock amount used compared to the other samples.

Grinding LHT-3M simulant used for deposition of batch 2 and 3 layers improved processability and allowed for AD to work in first place. The heat treatment (batch 3), however, did not further improve deposition behaviour. The samples' roughness was measured before and after coating and results are listed in table 5.32. The R_a values of all samples before coating where 0.01 μm or smaller, and after coating,

roughness increased for all samples, due to the deposition of the LHT-3M layer.

Table 5.32: Surface roughness of substrates before and after coating (perpendicular and parallel to deposition direction). Results shown in μm.

	Substrate 6	Substrate 23	Substrate 27	Substrate 28
$R_{asubstrate}$	0.01	0.01	0.01	0.01
$R_{zsubstrate}$	0.1	0.08	0.06	0.14
$R_{afilm\perp}$	0.15	0.23	0.27	0.38
$R_{zfilm\perp}$	0.98	1.65	1.91	2.51
$R_{afilm\|\|}$	0.16	0.23	0.28	0.4
$R_{zfilm\|\|}$	1.06	1.53	1.86	2.6

Measurement directions compared to deposition direction:
$\perp$ = perpendicular, $||$ = parallel

In addition to the layer thickness, the reflectivity of each sample was determined prior to coating and after. Figure 5.61 shows the samples' reflectivity before (dark blue line) and after (light blue line) coating. Results show that the average reflectivity of all samples increased after AD.

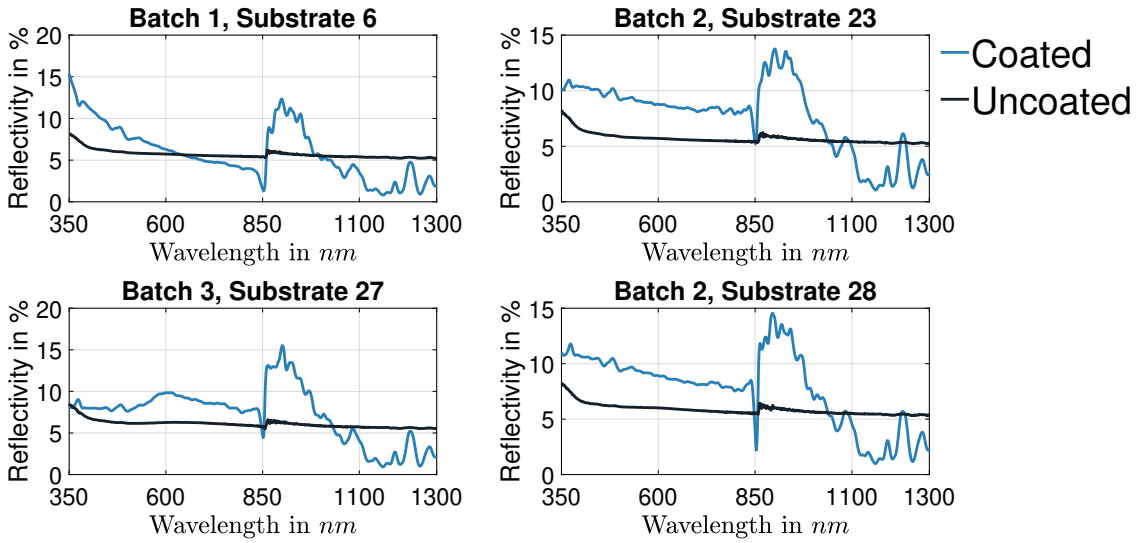

Figure 5.61: Reflectivity of uncoated vs arcjetcoated basalt glass. Reflectivity from 350 - 1300 nm for four batches. Each measured under same conditions and compared before (dark blue) and after coating (light blue).

Best results were achieved for batch 2 samples (Substrate 23/28) with ground LHT-3M. Although overall the reflectivity of all substrates was improved the reflectivity of the samples in the near infrared range decreased. This may be due to the increased surface roughness of the samples after coating. The increase of reflectivity in the visible range, however, is likely caused by the deposited LHT-3M (iron sparse material). Table 5.33 summarises average reflectivity of the substrates

before and after coating, as well as the absolute and relative changes.

Table 5.33: Average reflectivity of arcjet coated substrates

	Substrate 6	Substrate 23	Substrate 27	Substrate 28
Avg. uncoated	5.70%	5.70%	6.09%	5.86%
Avg. coated	5.90%	7.64%	7.25%	7.65%
Delta absolute	0.20%	1.94%	1.16%	1.79%
Delta relative	3.51%	34.04%	19.05%	30.55%

Best average reflectivity was achieved for substrates 23 and 28 with 7.64 and 7.65 % average reflectivity over the measured wavelength spectrum. Substrate 23 further showed the highest relative increase in reflectivity with 34.04 % compared to its uncoated surface. Overall, the reflectivity of the basaltic glass samples was increased due to AD of LHT-3M on basaltic glass samples made from JSC-2A. However, comparing the obtained results to the reflectivity of ground LHT-3M simulant powder, with about 50 % average reflectivity, it seems there is room for improvement. Further it seems likely that by increasing the layer thickness further, a full coverage of the the black glass substrate could be achieved, which may lead to improved reflectivity.

5.3.5 Optical Characteristics of Cover Glass

After analysing the reflectivity of substrates and mirrors built on non-transparent basaltic glass substrates, transparent substrates for the first time open up the possibility of conducting transmission measurements. Prior to the transparent glass samples manufactured for simulant which has been stripped of its iron oxide, no sample showed any transmission, but only absorption and reflectivity.

If the manufactured transparent samples shall be used as cover glass or lunar base windows, all their optical parameters (transparency, reflectance and absorption) will be of interest. This last section on optical, analysis of substrates made from regolith, will show how suitable the manufactured glass is as cover glass.

Substrate Reflectivity and Transparency

Samples which were available for analysis are listed in table 5.34. All glass samples made of iron reduced simulant were analysed, one sample each made of BP-1, FJS-1 and JSC-2A, three of LHT-3M (LHT-3M-1,2,3) and one reference microscopy slide ("micro"). Next to the samples names, table 5.34 lists the length and width of each sample, as well as all samples' thicknesses at four different locations, plus their average thickness. All samples have been prepared by lapping, and each individual sample shows differences in thickness across sides of less than 0.05 mm.

First, reflectivity measurements have been conducted for these samples, the same way as for all other samples before. Results are shown in figure 5.62 and show

Table 5.34: Dimensions of transparent glasses shown in mm

Sample	Length	Width	t_{LF^*}	t_{LB^*}	t_{RF^*}	t_{RB^*}	$t_{average}$
BP-1	24.2	18.1	1.353	1.346	1.323	1.32	1.336
FJS-1	33.7	21.1	1.314	1.343	1.303	1.322	1.321
JSC-2A	26.7	15	1.345	1.353	1.336	1.33	1.341
LHT-3M-1	34.5	19	1.391	1.391	1.412	1.404	1.400
LHT-3M-2	29.8	19.8	1.396	1.37	1.403	1.369	1.385
LHT-3M-3	18.9	19.6	0.833	0.838	0.839	0.843	0.838
Micro	75.8	21.9	1.077	1.073	1.074	1.075	1.075

* left front (LF), left back (LB), right front (RF) and right back (RB)

a similar reflectivity than the non-transparent samples measured in the previous chapters. Reflectivity measured is in-between 4 and 8 % from 350 to 1250 nm. The highest reflectivity was measured for the reference microscopy slide with about 9 % average reflectivity.

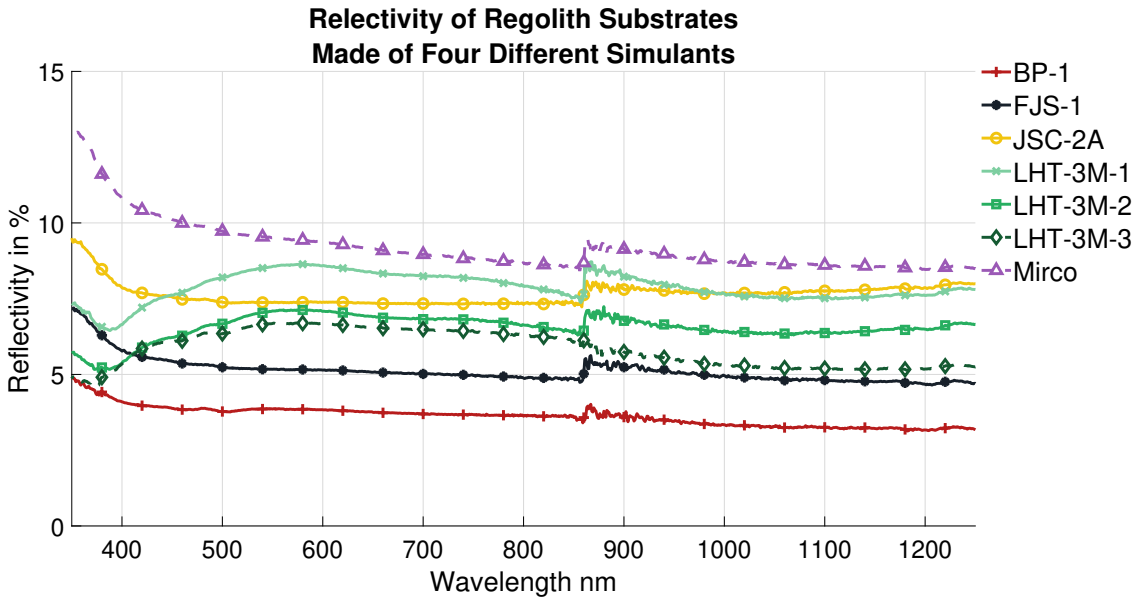

Figure 5.62: Reflectivity of transparent samples over a wavelength range of 350 to 1250 nm.

By only looking at the reflectivity measurements no or little difference to the black/non-transparent samples can be seen. Measuring the transmission of the samples, listed in table 5.34, plotting them and superimposing the AM0 spectrum onto them, led to figure 5.63. This figure shows that the sample with the best transmission is unsurprisingly the microscopy slide. However, it is closely followed by the LHT-3M-3 sample and next to that, offset by about 20 % (absolute) transmission, are LHT-3M-1/2.

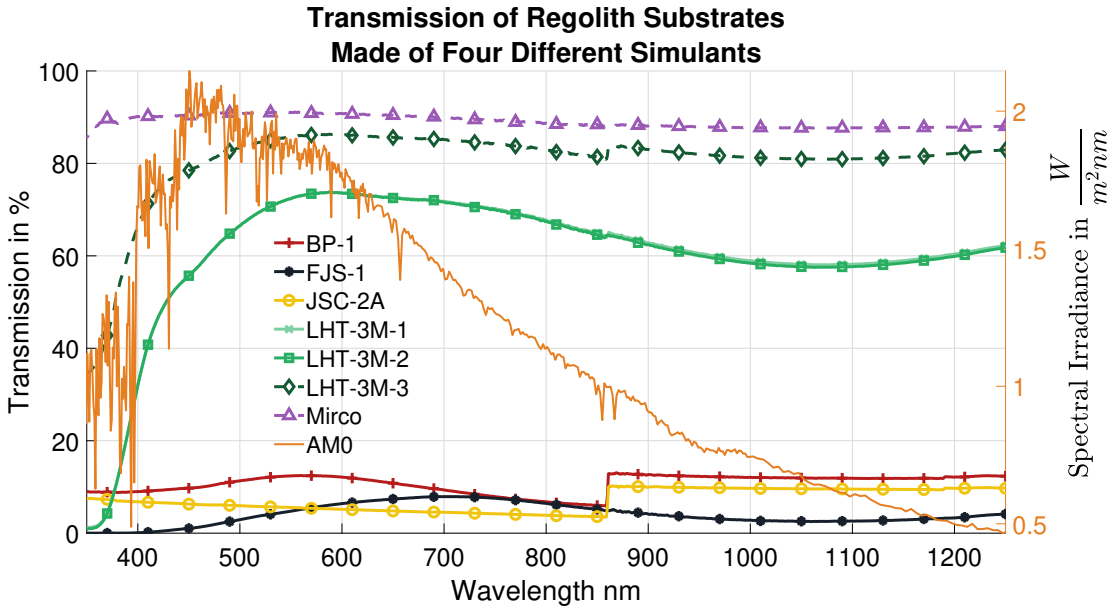

Figure 5.63: Transmission of transparent glass substrates superimposed by the solar spectrum AM0 which would be seen by a solar cell or a sample in space, in the vicinity of Earth. Lines of samples LHT-3M-1 and LHT-3M-2 coincide.

All three LHT-3M samples showed average transmissions of above 60 %, as listed in table 5.35. The most transparent sample, LHT-3M-3 was only 9 % less transparent than the reference microscopy slide. Looking at the superimposed AM0 spectrum, the LHT-3M-3 sample would allow for most of the energy of the sun, to pass through the glass. Especially in the areas of the highest spectral irradiance, around 450 nm, the sample still shows a transmission of about 80 %. Moreover, all LHT-3M samples stop most of the UV light (10 to 400nm), but let a large fraction of all light with higher wavelength (400 to 1250 nm) pass through. This should make it possible to use glass, made of iron reduced LHT-3M simulant (or iron reduced lunar regolith), as cover glass for a silicon solar cell. Additionally, the glass could not only act as cover glass, but also as filter. Since the glass also tends to block light in a certain wavelength range, it could be tailored to the solar cells in a way, that it will decrease degradation by UV light, as much as possible.

Table 5.35: Average transmission of transparent glasses

Sample	BP-1	FJS-1	JSC-2A	LHT-3M-1	LHT-3M-2	LHT-3M-3	Micro
Avg. Trans.	10.72 %	4.07 %	7.17 %	60.86 %	60.57 %	80.58 %	89.01 %

Looking at the supposedly transparent samples, BP-1, FJS-1 and JSC-2A, which have been contaminated with carbon, their transmission shows to be no higher than 15 % at best. At this level, they are unlikely to be suitable cover glasses. However, since the samples have been contaminated, the result cannot be used to determine the usefulness of these samples as cover glass or window. The results show however, that the samples are allowing for some part of the light to pass through the samples,

despite their contamination. Hence, it is very likely that the samples transmission can be increased by avoiding contamination during manufacturing. Further it is likely that, also more iron rich simulants/regolith, than LHT-3M, could be used as source material for cover glass or windows. Considering the achieved yield by magnetically separating iron oxide from regolith, iron rich regolith has a poor yield compared to iron sparse regolith (showed in table 5.30). Although it seems likely that it is possible to manufacture glass from any regolith, it is also likely that the amount of regolith, which needs magnetic treatment first, is much lower for iron sparse regolith. Thus, LHT-3M is considered the best simulant choice for manufacturing optically transparent glass.

The characteristics of the LHT-3M glasses seem to be determined by it thickness. Since the thinner (0.838 mm) glass LHT-3M-3 with almost half the thickness of the two other glasses LHT-3M-1/2 (1.385/1.400 mm) showed about 20 % higher transmission this seems true. Since the reflectivity values of all LHT-3M glasses only differed by about 3 %, it seems that the thicker glasses are, they must have a higher absorption than the thinner glasses. Knowing the reflectivity of the glasses, as well as the transmission, the absorption of the glass can be calculated (neglecting scattering effects) by subtracting transmission and reflectivity from 100 %. This leads to the absorption depicted in figure 5.64.

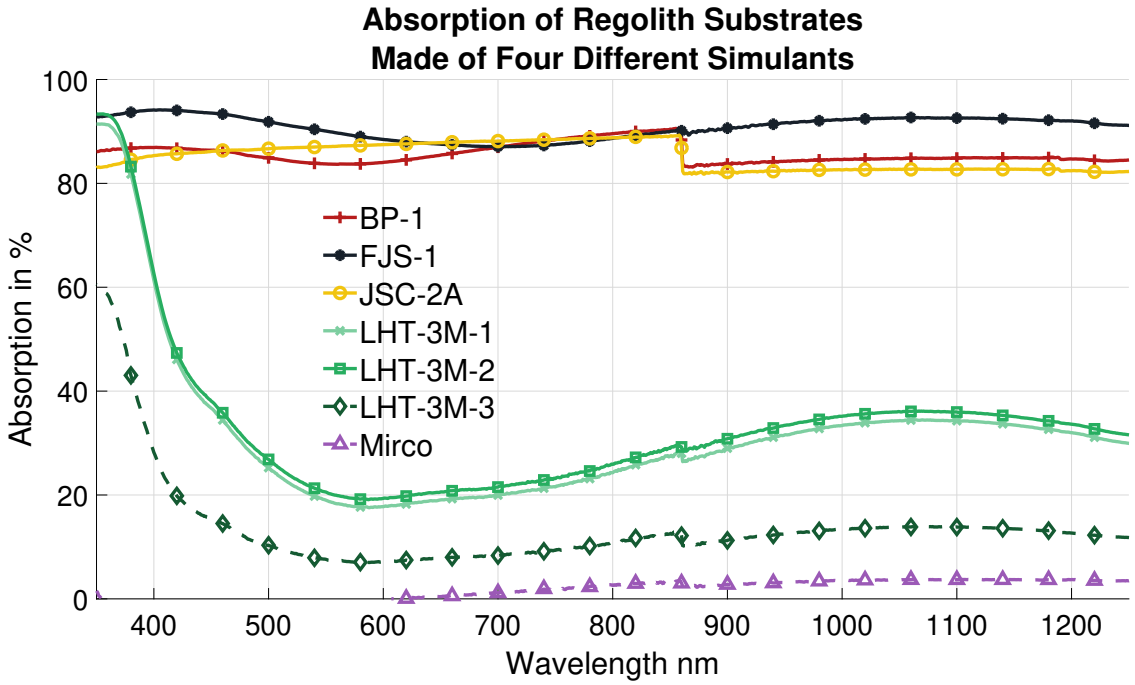

Figure 5.64: Absorption of transparent glass substrates, calculated from transmission and reflectivity measurements.

The microscopy slide did not absorb light or only little < 2 %. The thin LHT-3M sample number 3 absorbed about 15 % for most wavelength and the two other LHT-3M samples about 20 to 40 % of the incident light. Although this means that these glasses could indeed act as filters, it also means that they will absorb energy

which will be converted into heat. This will need consideration in the thermal design of such an ISRU solar cell, since it may lead to (over) heating of the system. This would increase the chance of failure and decrease the performance of the solar cell.

In conclusion, for the first time it could be shown that it is possible to reduce the iron oxide content in regolith, via a comparably simple magnetic separation method, only requiring electricity to work. Further, it was shown, that it was possible to manufacture optically transparent glass from the iron oxide reduced regolith. This glass showed transmissions of about 80 % for a wavelength spectrum from 450 to 1250 nm. This makes the glass potentially suitable as cover glass for a solar cell and opens up a variety of other uses, such as windows or other optical devices.

5.3.6 Optical Characterisation Summary

This chapter showed optical analysis of substrates made from raw regolith, mirrors built on those substrates and transparent glass made from magnetically altered regolith. It was shown that substrates manufactured from raw regolith, which formed black appearing glass, are suitable substrates for mirror manufacturing. The first generation of mirrors built on basaltic glass substrates showed already reflectivity of 20 to 80 %, and the second generation showed reflectivity of above 90 %. This showed that it was possible to build mirrors potentially suitable for a solar concentrator system.

Despite mostly regolith was used to build these mirrors, high purity (99.99 %) aluminium was used to coat the substrates and form a reflective layer on top. Since aluminium with such high purities is not naturally occurring on the Moon, alternatives were explored and an experiment using regolith powder itself as reflective layer was conducted. The results of this experiment showed that it is possible to increase the reflectivity of a substrate to a maximum of about 15% for some wavelength. However, the performance of these 100 % ISRU made “mirrors” is very poor compared to the performance of the second generation aluminium mirrors with > 90 % reflectivity. Further experiments may show that it is possible to increase the reflectivity of arcjet coated samples, but at the current state they are not deemed suitable mirrors for a solar contractor system or similar.

The final optical analysis of this chapter showed that manufacturing optically transparent glass, which is suitable as cover glass for solar cells, was a success. Average transmissions of 80 % were achieved for some samples which was very close to the 89 % transmission of the reference sample glass. These tests were the last step before assembling a solar concentrator system from the built mirrors and test it under a solar simulator.

5.4 ISRU Solar Conversion Devices Built on Basalt Substrates

In a last step, manufactured mirrors have been used to build a solar concentrator setup, as well as to build a thin-film solar cell on top of a basaltic glass substrate. This last result chapter shows the analysis of the performance of these systems.

5.4.1 ISRU Solar Concentrator

For building a solar concentrator setup in the form of a funnel, two types of mirrors have been used, reference mirrors bought off-the-shelf and basaltic glass mirrors manufactured from regolith simulant. How they were mounted and how their mount was designed, was explained in sections 3.4.2 and 4.3.2. Therefore, both, the basaltic glass mirrors and the reference mirrors have been mounted in such a concentrator and were tested under a solar simulator. Both types of mirrors have been fixed in four mounts each, and have been tested in two separate runs. Both times the entire setup (a solar cell and concentrator) have been placed under the solar simulator as shown in figure 5.65. In addition to these two runs, one run was conducted without either of the concentrators, but just with the solar cell itself. The results of this run were necessary to establish a baseline which served as reference for the two concentrator setups.

Figure 5.65: Left, the reference mirror concentrator setup, right, the basalt glass mirror setup.

The results from these test runs are shown in figure 5.66. They show the I-V curves (left) for both types of mirrors as well as the solar cell without a reflector. Next to it (right) the Maximum Power Point (MPP) curves are shown for all three measurements.

The I-V curves show that the solar cell itself (blue line) operates in-between 0 to 43 mA, and 0 to 6.1 V, at an irradiance of AM 1.5. Variations are expected, since the load across the cell is varied during the measurements. The reference mirrors (green), peak at 70 mA and 6.2 V and the basaltic glass mirrors (yellow), peak at 73 mA and 6.2 V. At a voltage of 4 V, the cell (without concentrator) delivers a current of 31.4 mA, the reference mirror concentrator setup increased the current output of the cell by 47.2 % to 46.2 mA, and the basaltic mirror setup by 50.8 % to 47.31 mA.

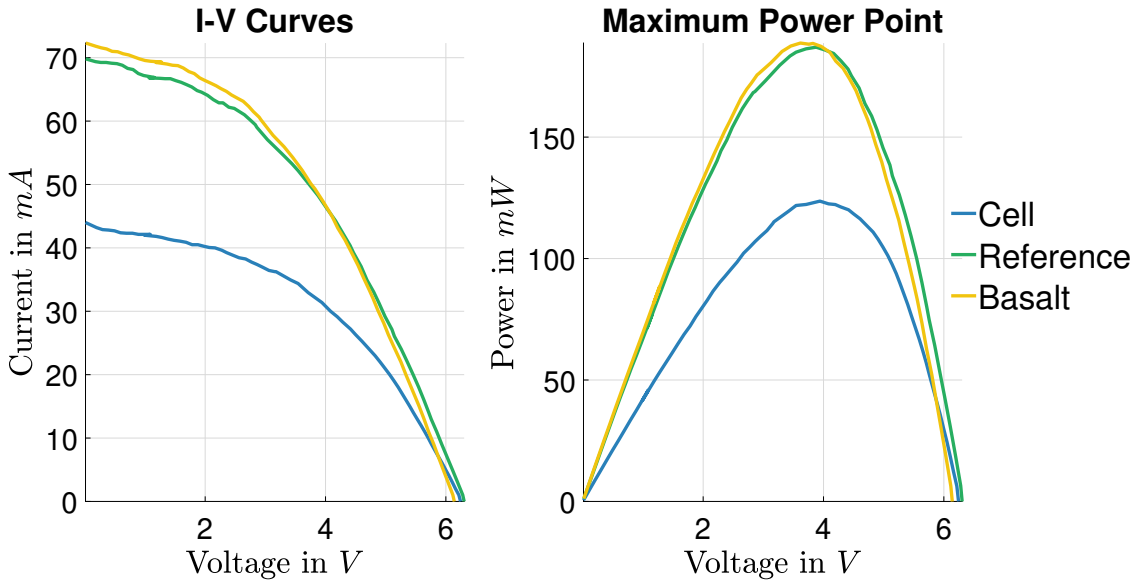

Figure 5.66: Basalt glass mirror performance vs reference mirror performance. Left, I-V curves, right, maximum power point curves, both recorded with an RO3. Solar cell indicated in blue, marks the performance of the solar cell without any mirrors but at the same illumination conditions. Green (reference) and blue (basalt) show the performance of the reference mirrors, and the basaltic glass mirrors.

These improvements are seen more clearly in the MPP graph, on the right side in figure 5.66. Peak performance of the cell (without concentrator) occurs at V_{MPP} of 3.94 V, with P_{max} of 123.6 mW. The reference mirror concentrator setup achieved P_{max} of 187.0 mW, at V_{MPP} of 3.88 V, and the basaltic mirror concentrator setup P_{max} of 188.7 mW, at V_{MPP} of 3.62 V. All values are summarised in table 5.36.

Table 5.36: Maximum performance values for a solar cell without, and with a concentrator. Two types of concentrators have been compared, basalt glass mirrors, as well as reference mirrors

Setup	P_{max} (mW)	V_{MPP} (V)	I_{MPP} (mA)
Cell	123.6	3.94	31.38
Reference	187.0	3.88	48.25
Basalt	188.7	3.62	52.19

Both reflector setups show increased power output at the cell, with a slightly better performance of the basaltic mirrors. This slight difference between reference and basalt mirrors may be explained due to geometrical differences. The reference mirror setup consists of four times two mirrors on each side of the solar concentrator. Thus, two reference mirrors needed to be joined together to form the same surface area than the basalt glass mirrors. The loss of light at the joining points may therefore be the reason for the slight difference in power output. All test have been repeated five times (every five minutes) and always achieved the same outcome, depicted in figure 5.66.

To calculate the theoretical power increase of the cell, two things are taken into account, the illumination surface area increase and the reflective losses of the mirrors. Considering a surface area increase of 137 %, determined in section 4.3.2, and calculating the average reflectivity losses of all the mirrors to about 10 %, from table 5.31, leads to a theoretical power increase of approximately 123 %. The measurements show an increase of power output of about 50 % which is 73% less than theoretically calculated. However, as listed in section 4.3.2 the maximum power output of the cell is 190 mW and it is likely that, with 187.0 and 188.7 mW both concentrators ran into this limitation. In that case, the cell would have been saturated and could therefore not produce more power. This suggests, that values closer to the theoretical values could still be achieved with a different solar cell. From just this experiment, it does not seem that the basaltic mirrors are under performing, compared to the reference mirrors, since both performed similar. However, only further experiments with a cell capable of taking of at least 1.5 times more sunlight can show the actual differences between the two mirror setups. Alternatively only part of the solar concentrator could be used on the same cell.

Another consideration are the losses of the mirrors, since they are likely to be higher than calculated only using their average reflectivity. When considering the actual reflectivity of the mirrors shown in 5.58, it can be seen that all mirrors show worst performance in-between 800 and 900 nm. Depending on the spectral sensitivity of the solar cell, this may lead to losses greater than only 10 %.

In summary, it seems likely, that basaltic glass mirrors are capable of achieving a similar performance as regular off-the-shelf mirror manufactured using traditional methods. Especially considering the reflectivity measurements discussed in section 5.4.1. Thus, it seems possible to utilise lunar regolith to augment a lunar mission by building such a solar concentrator device on the lunar surface. Moreover, this also opens up the possibility for the use of mirrors for other lunar applications such as telescopes, solar furnaces or optical relays as well.

5.4.2 Basalt Glass Solar Cell Characterisation

After successfully building solar cells on the back of a basaltic glass substrate, as described in section 3.4.3, the solar cells were characterised. This included haze evaluation of the back contact, MPP and EQE measurements, to determine efficiency,

and reflectivity measurements of the final solar cell. Two different deposition runs have been conducted, each depositing a thin-film cell on a basalt and a reference substrate. Thus, four samples were produced, *Basalt 1* and *Reference 1* in run one, and *Basalt 2* and *Reference 2* in run two. The following details the findings of all these measurements.

Haze Evaluation

After successful deposition of an AZO/Ag/AZO back contact, as described in 3.4, the basaltic glass sample and the reference glass sample have been taken for haze evaluation. Measurement results are depicted in figure 5.67 and show wavelength over haze. The haze evaluation shows how much light might be reflected back into the cell, after crossing the cell first without being absorbed in the absorption layer. The curve of the reference sample (blue line) shows a better reflection than the basalt glass sample (black line) from 300 nm wavelength to 1250 nm. After that, the basaltic glass becomes slightly better by about 2 %. However, for most of the analysed wavelength spectrum, the basaltic glass performs worse than the reference sample, with a maximum absolute difference of 45 %, at 500 nm. At this point, the basalt glass reflects about 47 % of the light with a wavelength of 500 nm and the reference glass 92 %. Although the performance of the basaltic glass is not ideal, compared to the reference sample, its back reflecting capability was still good enough to build a working cell on it.

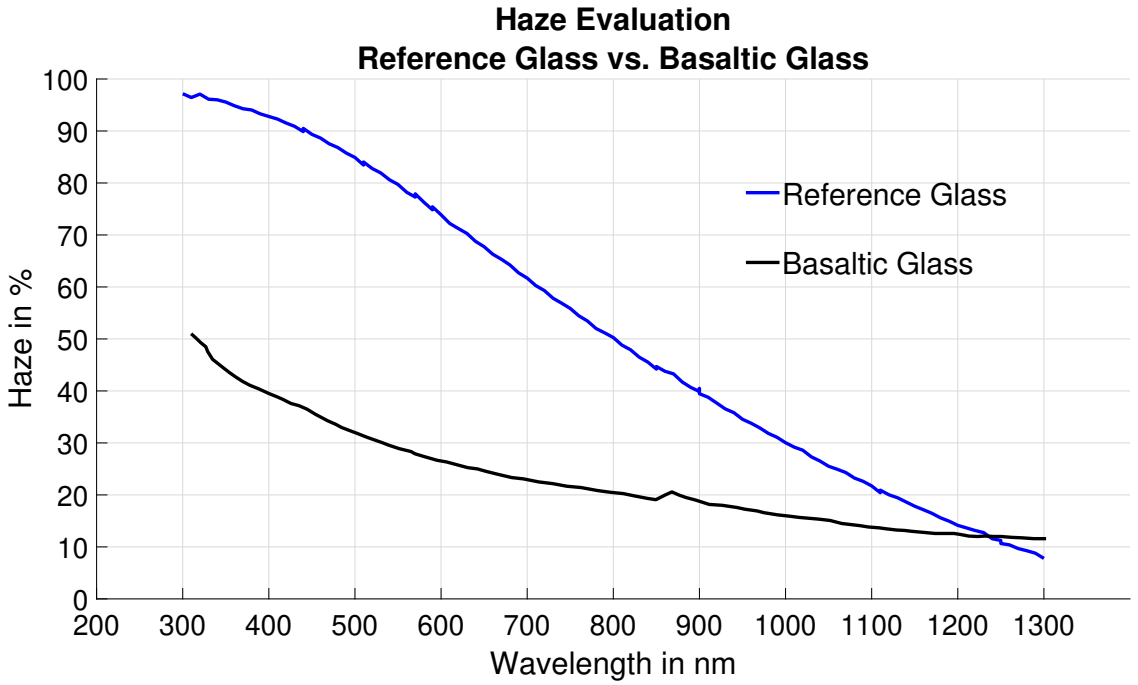

Figure 5.67: Evaluation of haze, the blue line shows the performance of the corning® reference glass, and the black line the performance of the basaltic glass sample. The abscissa shows wavelength in nanometres and the ordinate haze/reflection in percent.

The reasons for the underperformance of the basalt glass may be multiple, the two reasons, which may have the highest impact on the performance are estimated to be, surface quality and, maybe to a lesser extent, material composition. Latter would correspond with the haze evaluation since larger wavelength will penetrate deeper into the deposited layers, before they get absorbed. This in turn means, that light in the infrared range (> 700 nm) may penetrate the AZO/Ag layers and hit the actual substrate. Since normal borosilicate glass, for example, is transparent to most (approx. 90%) of the light in this wavelength, iron enriched glass, such as basaltic glass from regolith simulant, is rather non-transparent to light in this range. The underperformance of the basaltic glass, in the region from 300 nm wavelength to 1250 nm, may be explained by a higher surface roughness, than the reference glass, but may be compensated for wavelengths higher than 1250 nm, due to its geochemical composition.

EQE Measurements

For conducting EQE experiments on the final cells, only small spots (illuminated in-between the samples grids) were measured, to determine correct I_{SC} values. Thus EQE curves of four samples (two reference and two basaltic glass samples) have been conducted and seem to show valid data. Each cell was measured with 0 V and -0.2 V reverse bias (to improve carrier collection), leading to a total of eight EQE curves. The results of these measurements are depicted in figure 5.68. The achieved results were then used to correct the original I_{SC} values obtained from I-V measurements shown in figure A.3 in the appendix.

The corrected I_{SC} values, which have been determined via EQE measurements at AM1.5, and wavelengths from 350 to 1100 nm, are included in table 5.37, for both cases, with 0 V bias and with -0.2 V reverse bias. The EQE measurements removed the effect of the top contact silver grid, therefore, the values listed in table 5.37 can be compared against each other.

Detailed EQE results are depicted in figure 5.68, and only show significant fluctuations for one sample (Basalt 1), which are not realistic when measured with reverse bias at low (< 450 nm) wavelengths. However, it seems fine for long (> 450 nm) wavelengths. This means that the cell is unstable in the low wavelength range, likely due to quality issues. What exactly is the cause for it remains unknown until further investigations are conducted.

For the first deposition run (Basalt 1/Reference 1), I_{SC} values of around 16.5 $^{mA}/_{cm^2}$ were measured. For the second deposition run I_{SC} values of around 17 to 19 $^{mA}/_{cm^2}$ have been measured, for samples Basalt 2 and Reference 2. Effects of reverse bias are different for both runs, which is also reflected in differences in both, the short and long wavelength ranges in the EQE results (figure 5.68). These differences lead to a general shift of the curves of the second run compared to the first run. The EQE results of the second run are shifted towards the shorter wavelength, and have a lower peak point. These observations are true for both second run samples, the basaltic cell and the reference cell. The differences seem to match the variations

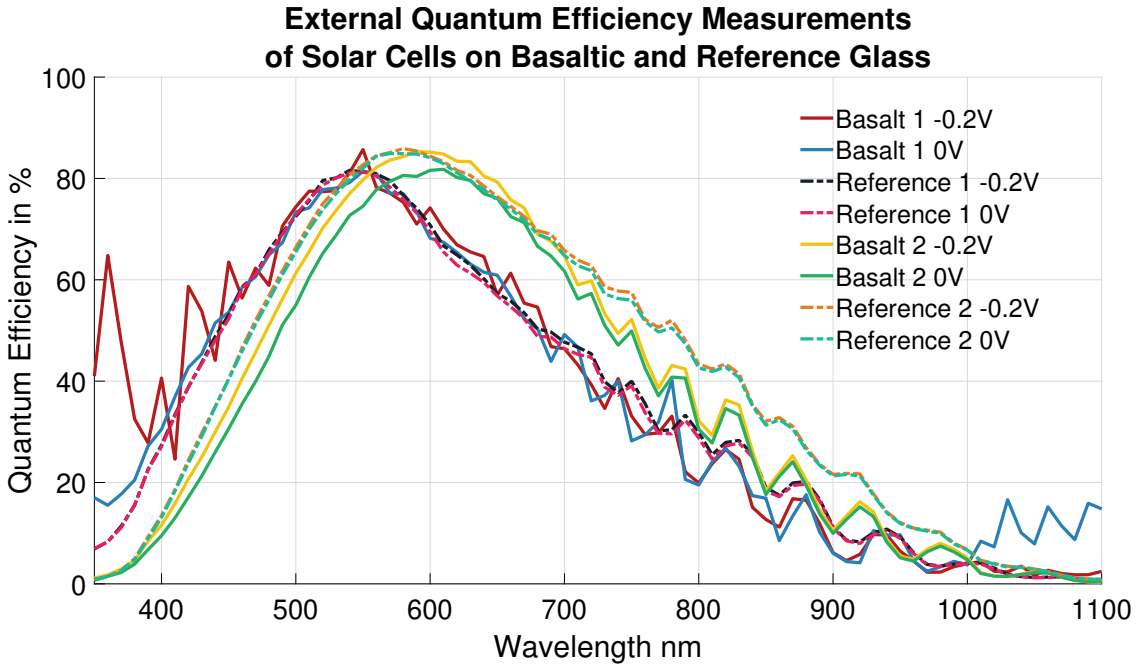

Figure 5.68: External quantum efficiency measurements of basaltic glass and reference solar cells. Each cell was measured with 0 V and -0.2 V reverse bias *Basalt 1* and *2* are basaltic glass cells, and *Reference 1* and *2* are the reference cells.

in the differently doped p-layers. One doped layer is thicker (54 vs. 34 nm), thus would result in a stronger field in the cell and hence reduced effect of reverse bias.

Key Performance Characteristics of Solar Cells

Two different types of cells have been manufactured (shown in figure 5.69), both following the same deposition principle; glass/TCO/Ag/TCO/Si/TCO/Ag, as described in the manufacturing chapter 3.4. As explained in detail in section 3.4.3, the two different types were manufactured using two slightly different p-type layers, thus it was expected, that the two cells show different results. Final cells are depicted in figure 3.35, and their performance data overview in table 5.37, as well as their I-V-Curves in figure A.3 in appendix.

Results in table 5.37 have been compensated for surface area, by using current density values, obtained by EQE measurements. The resulting short circuit currents I_{SC} are listed in table 5.37, for 0 V and -0.2 V reverse bias. Using the EQE short circuit current values at 0 V, and FF and V_{OC} from table 5.37, the efficiency could be calculated. By entering the values into equation (4.4), together with a standard irradiance of 100 $^{mW}/_{cm^2}$, the efficiencies of the cells were determined. All results are listed in table 5.37.

Results of the two different types of cells (19B-016 and 19B-017), deposited on two different substrates each, are all summarised in table 5.37 and can now be

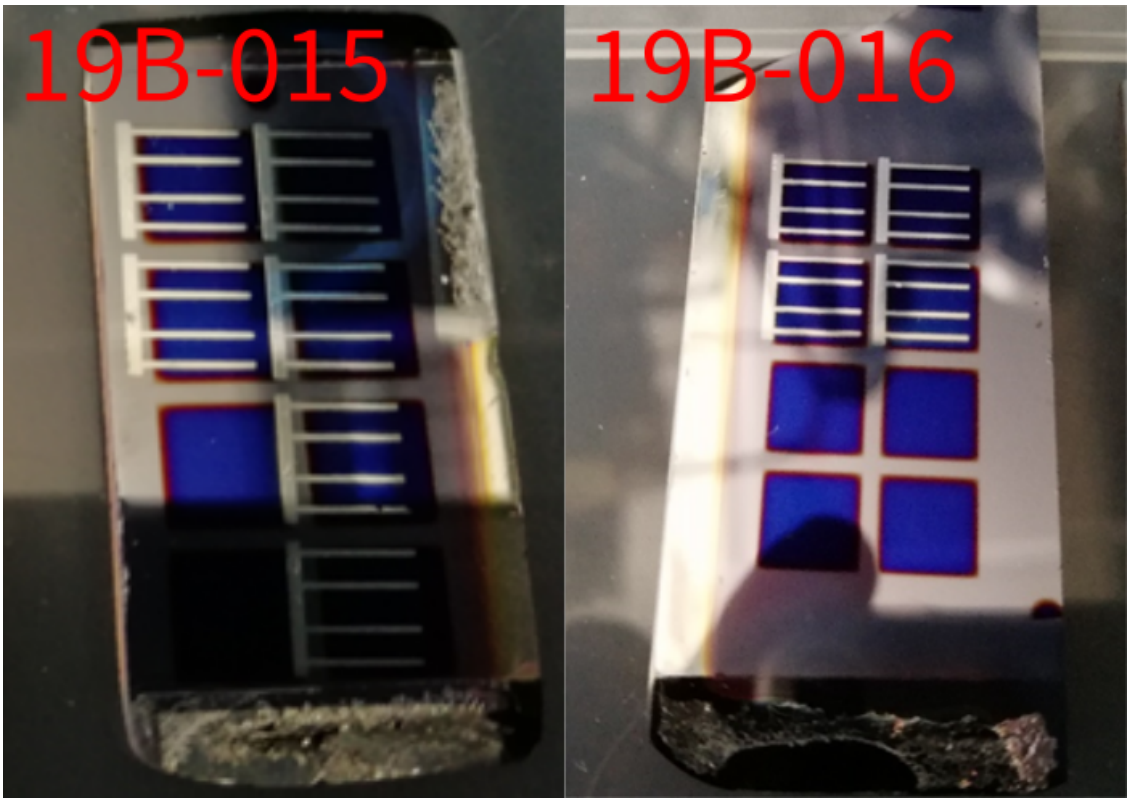

Figure 5.69: Two silicon thin-film cells built on basaltic glass substrates, left 19B-015 and right 19B-016.

compared. Considering the FF and V_{OC} values, both are lower for the solar cells built on basaltic glass, compared to reference cells built on reference glass. This was expected since the surface quality of the basaltic glass was expected to be worse than the quality of the reference glass. These differences in glass quality influence the silicon growth on a substrate in a negative way. Further, the efficiency values (η) of the basalt glass cell are, 3.31 % and 1.83 % respectively for both types, thus about 35 - 60 % lower than the efficiency values of their counter parts (reference cells) with 5.02 % and 4.51 %.

Table 5.37: Overview of key performance characteristics of solar cells built on basaltic glass

Sample	η	FF	P_{MPP}	V_{OC}	I_{SC0V}	R_{S-Voc}	R_{SH-Isc}
	in %	in %	in $\frac{mW}{cm^2}$	in V	in $\frac{mA}{cm^2}$	in Ω	in Ω
Basalt 1	3.31	44.1	3.31	0.454	16.53	7.9	82
Reference 1	5.02	63.9	5.02	0.481	16.33	7.74	na
Basalt 2	1.83	51.6	1.83	0.208	17.01	12.01	143
Reference 2	4.51	62.4	4.51	0.371	19.46	10.41	2519

Reflectivity of Solar Cells

The last characterisation step conducted was, to measure the cells' reflectivity. The reflectivity was determined by measuring TCO pads without silver grid. The results are depicted in figure 5.70 and show lowest reflection (< 20 %), for all cells, in the wavelength range from 500 to 650 nm.

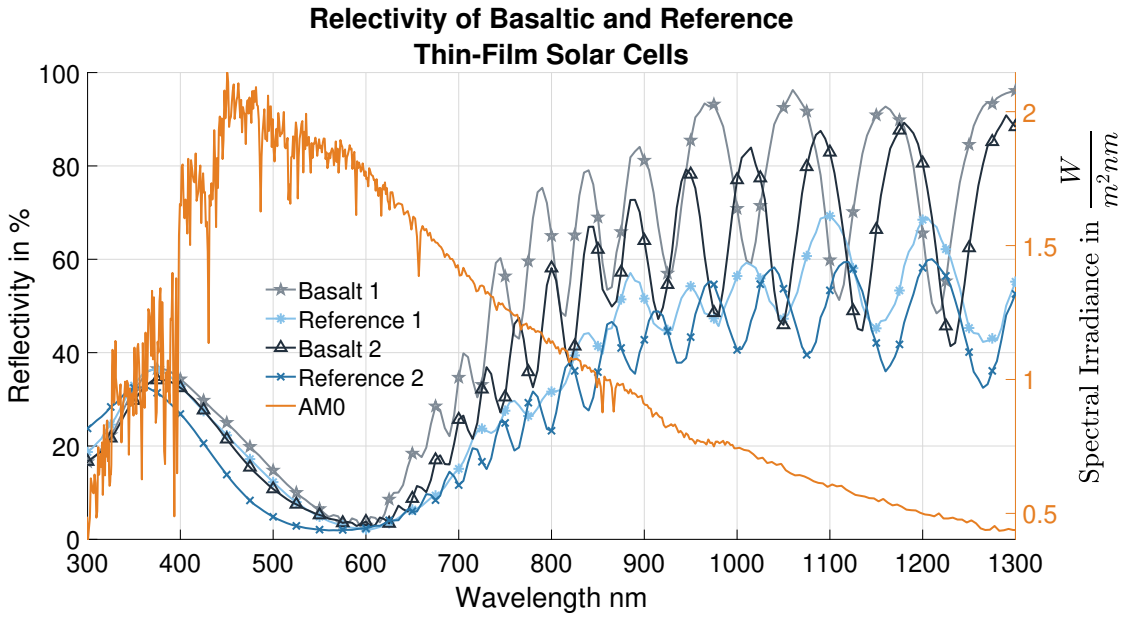

Figure 5.70: Reflectivity measurements of basaltic glass and reference solar cells, measured on a UV-vis spectrometer. *Basalt 1* and *2* are basaltic glass cells, and *Reference 1* and *2* are the reference cells, superimposed by the solar spectrum AM0, which would be seen by the solar cells in space, in the vicinity of Earth.

This corresponds to the EQE values measured prior, where the highest external quantum efficiency (> 60 %) was observed in the range from 450 to 700 nm. Although achieving a low overall reflectivity of the final cell, is desirable, the reflectivity will impact the thermal household of a solar cell system on the Moon. Hence, it may make sense for a cell to reflect light in the wavelength ranges, which cannot be converted into electricity by the cell type used. This would help to avoid overheating and/or performance decreases of the solar cells on the lunar surface. Reflectivity and the thermal household of a cell manufactured for the Moon should carefully be evaluated in practical measurements, and crosschecked by thermal simulations.

From the discussed results it seems possible, to build a working solar cell on basaltic glass, manufactured from lunar regolith simulant. Further, this may open up the possibility of building solar cells on the lunar surface, using lunar regolith. This work therefore, successfully demonstrated the practical application of an ISRU technique, theoretically proposed in works of others before. The first step to advancing the

TRL of manufacturing solar cells on the lunar surface is now taken and could open up the possibility to augment a future lunar mission.

5.4.3 Solar Conversion Devices on Basaltic Glass Summary

This last chapter of the results section showed how previously manufactured basaltic glass samples were successfully used to build two different types of solar conversion devices. One of the two was a working solar concentrator system, utilising mirrors built on basaltic glass substrates to form a solar funnel. By directing an increased amount of incident light onto a solar cell, the concentrator increase the solar cells output power. In comparison with traditionally manufactured off-the-shelf mirrors, this basaltic mirror concentrator system showed similar if not better performance. Since all basaltic mirrors reflected more than 90 % of the incident light in a wavelength range of 400 to 1350 nm those mirrors could further be used in other systems which require mirrors to work.

The second system successfully proved to work is a silicon thin-film solar cell which has been manufactured on the back of a basaltic glass substrate made of JSC-2A. Although it took about two years to get all parameters right, adjust the setup to the basaltic glass samples and the basaltic glass sample manufacturing process to the PECVD process, it was finally successful. First cells were built on mare regolith simulant, however, no evidence was found why it should not also work on glass made of a lunar highland simulant such as LHT-3M for example. However, only building cells on such simulant will ultimately prove this hypothesis. Working cells with efficiencies > 3 % were manufactured which also showed stable EQE results. Hence, building solar cells on the lunar surface, using lunar regolith, may be an ISRU technique which could augment a future lunar mission.

6 Conclusion and Future Work

The European Space Agency is aiming at establishing a permanent outpost on the lunar surface. Therefore, new technologies and equipment needs to be developed to enable and augment such a mission, as well as to make long-term planetary missions possible. The present study's research objectives aimed at determining the feasibility of *Using Lunar In-Situ Resources for the Production of Solar Conversion Devices*. A review of the latest literature in the fields of future space exploration, solar conversion devices, the lunar environment, extraction and purification processes, and manufacturing techniques was conducted. The review provided a start for the conducted works, which were aiming at fulfilling the research objectives.

To be able to test manufacturing of such structures, analogue materials to the regolith on the Moon were used. A variety of materials was tested and a process was engineered, which is capable of tolerating fluctuations in chemical and mineralogical compositions. Prime simulants chosen and analysed in detail for this study were BP-1, EAC-1, FJS-1, JSC-1A, JSC-2A, and NU-LHT-3M, since those have different geometric properties, grain size distributions and chemical and mineralogical compositions. Further, all of them were easily accessible in quantities of around 10 kg.

Before solar conversion device manufacturing was attempted, samples from up to six different lunar regolith types were successfully melted, first using a susceptor assisted microwave heating approach, then a resistive heating approach. After cooling and annealing, mostly amorphous glasses were formed, most of them in a size range of approximately 20 * 45 mm. These glass samples were ground and polished, and afterwards their reflective properties were measured.

Using these glass samples, mirrors were manufactured which were then used to build a solar concentrator system. First tests of this system were conducted in Dubai and afterwards it was characterised under laboratory conditions. Manufacturing of a required mount for the ISRU basaltic mirrors was conducted via means of 3D printing. Finally, the performance of the ISRU manufactured system has been compared to an off-the-self set of mirrors. A similar performance increase, of the tested solar cell, could be noted for both setups.

In addition to the tested solar concentrator system, manufacturing of thin-film solar cells on the back of the same "base" basaltic glass substrates has been explored. First tests showed promising results but delivered no working cells. Handling and manufacturing of thin basaltic glass slides needed to be developed and improved, to fit the needs of solar cell manufacturing methods. After the substrate quality was

finally good enough, a working μc-Si:H thin-film solar cell in an n-i-p configuration could be manufactured on the back of the basaltic glass substrates.

Concluding, it can be said, that melting lunar regolith, turning it into glass substrates and coating it with a reflective material has worked, and mirrors could be manufactured. Furthermore, assembling those mirrors into a solar concentrator, was successful, as well as testing such a system under solar illumination conditions. Additionally, working silicon thin-film solar cells have been manufactured on basaltic glass substrates made from regolith, which have also been tested under laboratory conditions. Results revealed an equal performance of the ISRU manufactured mirrors compared to reference mirrors. Further, the basaltic solar cells showed an about 35 % lower efficiency compared to the reference cells. This showed, that it may be possible to aid a potential future human surface mission on Earth's Moon by means of ISRU.

6.1 Fulfillment of Research Objectives

How research objectives, identified in section 1.2 in the first chapter, were fulfilled is detailed hereafter.

Research Objective 1: - *Determine suitable raw materials for manufacturing and testing, using lunar surface like materials.*

A variety of up to eight simulants has been analysed for this work, which is depicted in figure 6.1. After analysing the geochemical and mineral composition of these simulants, as well as geotechnical features, they were all considered suitable substrates for manufacturing and testing.

Figure 6.1: Overview of regolith types used and analysed. Fltr: BP-1, EAC-1, FJS-1, JSC-1A, JSC-2A, JSC-2A-TG, LHT-2M, LHT-3M (scale in cm).

However, some were "better" simulants than other, since they were deemed closer to actual lunar regolith, due to not containing alterations, for example. Six of the analysed simulants were used for most tests conducted of which four (FJS-1, JSC-1/2A and LHT-3M) were considered high-fidelity and two (BP-1 and EAC-1)

medium-fidelity. By characterising simulants and working with them, challenges were faced:
Poor quality of simulants and no standard tests conducted by suppliers. The type of available simulant did not fit the experiments needs. No characteristics data of a simulant was available and manufacturer data did not match the actual simulant. It was not possible to compare research and work despite using the supposedly same simulant. No standard for storage/shelf time exists. Categorisation and qualification of simulants was non-existent. These reasons led to conducting characterisation work on all simulants used. Further, due to these challenges it would have been impossible to conduct any scientific work, involving regolith simulants, without thorough analysis of the raw material prior to usage.

Research Objective 2 - *Demonstrate manufacturing of glass like substrates for use as back-plate, and cover glass for solar conversion device production.*

It was possible to demonstrate manufacturing of glass like substrates and cover glass from lunar regolith simulant. Figure 6.2 shows all iteration steps achieved during the entire project. A summarised description of each step depicted in this figure:

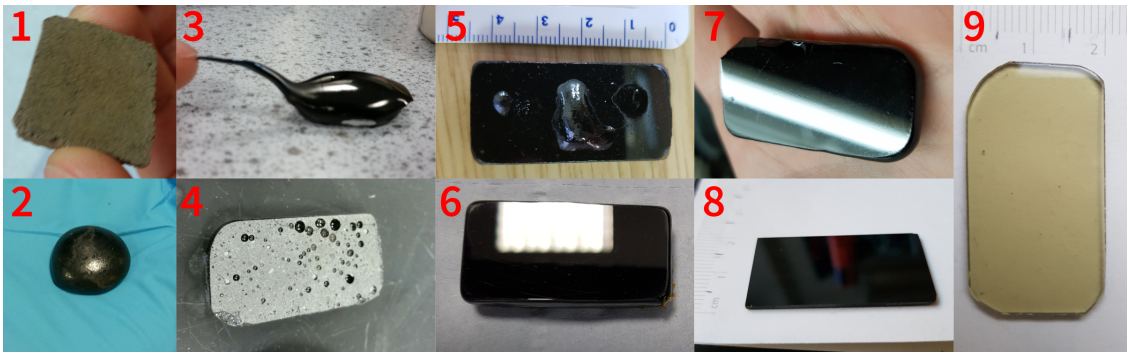

Figure 6.2: Substrate iterations: 1. Sintered EAC-1, 2. Glass bead EAC-1, 3. Cast Sample JSC-2A, 4. Ground microwave heated sample EAC-1, 5. Improved microwave heated sample JSC-2A, 6. Bubble free glass JSC-2A, 7. Polished bubble free glass - six simulants, 8. Lapped glass slide JSC-2A, 9. Transparent glass slide LHT-3M. Not to scale.

1. Sintered EAC-1 simulant brick slide, 20 * 20 mm.
2. Glass bead produced using a microwave kiln and a graphite crucible.
3. First successfully cast sample showed promises for casting approach.
4. First rectangular shaped sample, ground and polished.
5. Final microwave sample still showed large bubbles on the bottom surface.
6. First bubble free sample, a milestone in the project.
7. Substrate manufacturing successfully tested on six different regolith materials.
8. Bubble free glass nuggets in rectangular shape, slide sizes of 38 * 20 * 1.5 mm.
9. Final step, transparent glass slide.

In conclusion, manufacturing of glass like substrates for use as back-plate, and cover glass for solar conversion device production was successful. Although the effort of

processing regolith into useful and suitable glass substrates is much higher than, for example, terrestrial soda-lime glass, it may be a viable alternative for the Moon. Since on the lunar surface regolith is the only resource available, only processing and manufacturing equipment would need to be flown to the lunar surface to make glass a resource available on the Moon.

Research Objective 3 - *Demonstrate manufacturing of solar conversion devices from primarily lunar analogue material.*

It was successfully demonstrated how solar conversion devices have been manufactured from previously manufactured basaltic glass samples. Two different types of solar conversion devices have been built, which are both depicted in figure 6.3. On the left side, a solar concentrator system is shown and thin-film solar cells in the middle and on the right. Both devices have been built on substrates manufactured from lunar regolith simulant JSC-2A.

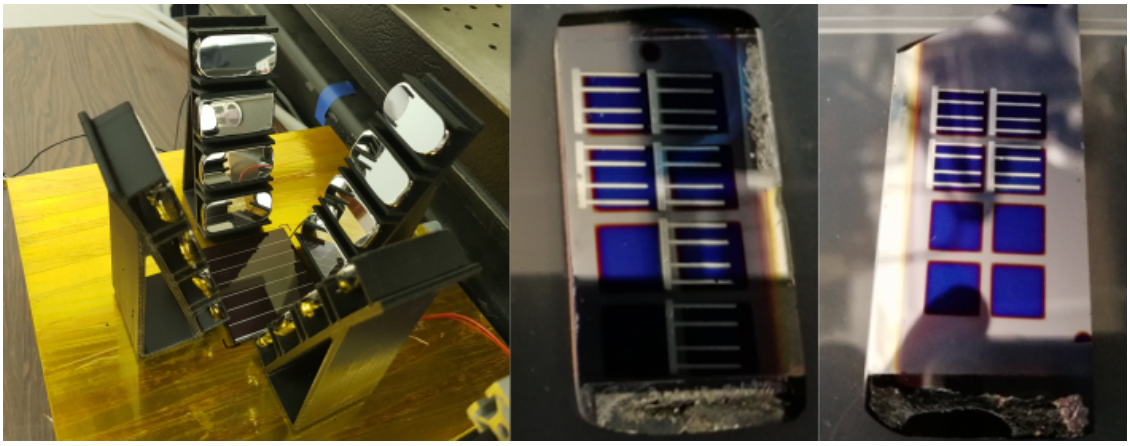

Figure 6.3: Solar concentrator built on basalt glass on the left and thin-film solar cells in the middle and on the right.

The solar concentrator system formed a solar funnel, which directed an increased amount of incident light onto a solar cell. Mirror mounts were manufactured using additive manufacturing of polymers, capable of incorporating mirrors with varying thicknesses. The silicon thin-film solar cells, also manufactured on the back of a basaltic glass substrate, took two years to build, due to adjusting the basaltic glass samples to the PECVD process.

These two demonstration devices may open up the possibility to investigate building solar conversion, on the lunar surface, using lunar regolith, as an ISRU technique augment an actual future lunar mission. Results achieved within this objective seem particularly drastic when considering that solar cells and mirrors depicted in figure 6.3 are made of the regoliths depicted in 6.1.

Research Objective 4 - *Use experimental methods to determine the quality of the substrates and determine the performance of built solar conversion devices,*

corresponding to space exploration technology roadmaps.

The most important metrics used to evaluate the quality of built substrates and the performance of devices were,

- Surface roughness
- Reflectivity/transmission
- I-V curves
- Efficiencies

First samples manufactured by microwave heating regolith achieved surface qualities of $R_a > 100$ nm and had a large number of voids and bubbles. The second generation of basaltic glass samples, heated and melted in a platinum crucible in a resistively heated kiln, and cast into a graphite mould, achieved surface roughness of $R_a < 100$ nm. Best samples showed R_a values of less than 1 nm and no voids larger than several microns.

Average reflectivity of first, uncoated samples was about 4 to 8 %, with one exception with more than 17 %. After coating with aluminium or silver, all samples' average reflectivity was increased to a minimum of 20 % and up to more than 80 %. Second generation samples showed average reflectivity of 5 to 7 %, similar to the results of the first batch. After aluminium coating, the average reflectivity of all basaltic glass mirrors was above 90 % and thus compared to 91.0 to 92.2 % average reflectivity of the reference mirrors. Hence, second generation samples show an increase of about 30 to 75 % in reflectivity compared to first generation samples. Reflectivity of uncoated transparent glass was measured in-between 5 and 8 %, thus despite transparent characteristics similar to the first and second generation samples. Transparent samples further showed average transmissions of above 60 %, with transmissions of up to about 80 % for the highest spectral irradiances around 450 nm.

The I-V curves measured for an ISRU built solar concentrator system have been compared with the performance of a cell without concentration and concentrators comprised of traditionally manufactured mirrors. At the irradiance of AM 1.5, the reference mirror concentrator setup increased the current output of the solar cell, from 31.4 mA (without), to 46.2 mA. The basaltic mirror setup from 31.4 mA, to 47.31 mA. This corresponded to an increased current output of 47.2 % and 50.8 % correspondingly. Peak performance of the cell (without concentrator) occurred at 3.94 V with P_{max} of 123.6 mW, the reference concentrator achieved P_{max} of 187.0 mW at 3.88 V and the basaltic concentrator setup P_{max} of 188.7 mW at 3.62 V accordingly.

Key performance parameters of solar cells built on basaltic and reference glass have been determined. Values from table 5.37 show that FF and V_{OC} values are lower for the solar cells built on basaltic glass, compared to reference cells built on reference glass. This was expected since differences in glass quality or glass roughness influences the silicon growth in a negative way. Further, also efficiency values (η) showed to be worse for basalt cells, with an efficiency of 3.31 % for one cell and 1.83 % for the other. This was about 35 - 60 % less efficient than the

reference cells[1], with 5.02 and 4.51 % respectively.

In summary, limitations encountered during manufacturing solar conversion devices from regolith simulant and how they could be resolved in the future are:

- No suitable and well characterised regolith simulant available off-the-shelf. *Potential solution:* Develop a simulant suitable for manufacturing and characterise it.
- Interaction/outgassing between graphite and regolith *Potential solution:* Study samples where bubbles formed, using EDX spot analysis.
- Rapid cooling of (regolith) melts due to small (<40 g) masses of regolith used. *Potential solution:* Increase mass (produce larger samples) to improve thermal stability for processing.
- Use of platinum instead of ceramic materials made crucibles reusable but only when cleaned with a lengthy procedure. *Potential solution:* Reuse same crucible or nozzle or search for a material that is releasing regolith melts/glass without wearing and/or cleaning and/or contaminating it.
- Unknown annealing behaviour of basaltic glass mixes. *Potential solution:* Conduct an empirical study to determine annealing behaviour of basaltic glasses.
- Excessive need for grinding and polishing for glass samples required *Potential solution:* Increase quality of glass by improving the samples' shape, resulting from manufacturing.
- The need for an additive manufactured mount made of polymer, required to hold mirrors in place is not suitable for the lunar surface *Potential solution:* Use regolith for 3D printing/sintering of mounts and/or investigate mounting mirrors on piled up regolith.
- Achieving glass surface quality on the Moon suitable for manufacturing solar cells seems too complex at the moment to be actually used on the Moon. *Potential solution:* Decrease complexity of glass and/or solar cell manufacturing by reducing manufacturing steps.

Conclusion Research Objectives

All four research objectives set out for this work were achieved. Suitable raw materials were chosen, thoroughly analysed and have shown to work as materials for testing lunar manufacturing. From these materials a variety of glasses was manufactured and back-plates and transparent cover glass plates were built. These plates have successfully been used to build mirrors, solar concentrators, solar cells and cover glass for solar cells, mainly manufactured from lunar analogue material. Experiments have characterised the glass plates, mirrors, concentrators and solar cells performances, and results indicate that built devices could be advanced to become technologies which could be used on an actual lunar mission.

However, before these devices can be considered for an actual lunar surface mission, their TRL needs to be improved further. What improvements and testing can help

[1]same type of cell, built in parallel to the basalt cell, only difference was that they were built on off-the-shelf glass

to advance the TRL of the devices built in the frame of this thesis, will be outlined in the last section 6.2, future work.

6.2 Future Work

Moon fly-bys are scheduled for the early 2020s and a crewed landing later in that decade. If an augmenting technology as the proposed one shall be used for testing on such a mission, it is important that the TRL of solar conversion devices built from lunar resources is advanced within the next years, something that this project has started. Moreover, this project was the first proof of ISRU-related solar conversion technologies working, and marks the starting point to integration of such technologies for future human exploration missions. By augmenting planetary missions with locally manufactured devices the number of re-supply flights required will be reduced, which will provide more freedom for mission designers. Since this approach can significantly reduce the overall weight necessary to be transported to the lunar surface, it will also reduce the cost of such an undertaking, potentially opening-up new approaches to mission design.

It is recommended, to further pursue and focus investigations, on basaltic glasses made of regolith (simulants), since in the opinion of the author, basaltic glass can realistically aid future lunar surface missions. In order to do so however, basaltic glasses, including their manufacturing and material properties, need to be understood better to assure safety and reproducibility. Following points could help to improve quality of the glass, and thus, devices build on or from these glasses, as well as to advance their TRL.

A field which will require improvements as well as movement from the international community are regolith simulants. The focus here should be put on establishing global regolith simulant standards to be adhered to by simulant manufacturers, researchers and companies. By creating categories of simulants, based on their use cases, and defining quality standards for each category, working with simulants can be more efficient and useful. One way of overcoming challenges in the field of regolith research may therefore be, to establish a form of simulant database which would ideally be maintained by an NGO and which is “peer-reviewed” by the ISRU community. The reason why an NGO would be best suited for this job is, that it is not so much influenced by politics/elections and thus agendas of individuals as a government is. This allows an NGO to constantly keep up a service to the public. This publicly available database could be the platform where all simulant base research/work is gathered, standards are published and issues can be discussed. Finding the best way to gather information, make it accessible and useful to the community as well as applicable to the work conducted using regolith simulants. Data collection for such a platform will be the next step before, introducing international standards to the international community.

Simulant manufacturers will benefit from the suggested approach, by knowing which specifications to manufacture to and which tests will be required for each

batch of simulant manufactured and shipped. Further, they will know what types of simulants are needed by the community, thus which will sell. Moreover, it will be possible to compare research conducted using simulants, due to a standard set of measurements being required for all simulants of a certain category. Additionally, manufacturing and testing, conducted using regolith simulant, will require much less research prior to selecting a suitable simulant. A company, for example, can chose a simulant based on its category such as "manufacturing" and it will be clear that it is suitable for construction work. Moreover, the selected simulant, of a certain category, will be shipped, with a regolith category specific set of characteristics, relevant for its category/field of work/research.

Next, to establishing standards on regolith simulants, research into links between mineral/geochemical composition and melting/processing temperatures of regoliths should be conducted. Only by better understanding the impact an input material, with different compositions has on the process, processes can be engineered to be efficient in terms of energy usage. Beyond processing/melting regoliths with different mineralogy and geochemical composition, regoliths' components will have an impact on mechanical and optical properties of the glass, as well as its crystallisation behaviour. Additionally, beneficiation and purification of regoliths may be able to alter the composition in beneficial ways. Better understanding compositional impacts and impacts beneficiation may have on a glass, will help to understand the value of glass as a resource on the lunar surface.

Understanding these differences will also help to increase lunar surface capabilities, and aid the susceptor assisted microwave heating process, used for in this work. Although this process seems to be mostly independent of the input material, it is not yet fully understood what the impact of the regolith materials composition is on the process. When these effects are understood susceptor assisted microwave heating may be an option for an energy efficient and universal heating method, which could be deployed on the lunar surface.

Independent of the manufacturing process used, whether it would be microwave or resistive heating or even using a solar furnace, processes will require to run mostly autonomous, since it is unlikely that humans, in form of astronauts, will be in the loop. Thus tested manufacturing processes and strategies will need to be adapted, to be performed autonomously by, for example, a rover with a robotic arm.

The suggested automation could further lead to a decrease of the number of defects on the substrates' surfaces, as well as a flat glass surface with R_a values < 1 nm prior to any post processing. This could maybe be achieved by finding or establishing processes which can manufacture glass sheet, similar to float glass.

At the same time of thinking of developing or researching a way to manufacture good quality glass sheets, directly without post processing, up-scaling could be considered. So far, sample sizes never exceeded 100 mm, for manufacturing large mirrors or solar cells, sheets in the order of 1 m^2 would be more useful. This would

require an up-scaling of about a factor of ten, which would increase the potential use of the discussed technologies and materials on the surface significantly.

In addition to improving and up-scaling the manufacturing processes, thermal aspects of glass manufacturing on the lunar surface will require thorough investigations. Basaltic glass manufacturing happens at temperatures at around 1500 °C and the surface temperature of the Moon may be lower than -150 °C at certain times of the lunar day/night. This leads to large temperature differences, which may cause problems to the machines, but also to the glass itself. Since heating, cooling and annealing of glass are non-trivial processes, thermal simulants and tests need to be conducted to decrease risk of failure.

In addition to thermal analysis, it will be relevant to determine whether or not it is possible to deploy a method on the lunar surface. This will need to be done in the form of environmental simulations and tests, which may include (but are not limited to); vacuum testing, radiation exposure testing, dust tolerance, sunlight exposure, magnetic susceptibility and testing under reduced gravitational conditions. Ideally a combination of multiple of these test will be conducted at the same time as, for example, testing in a solar-thermal-vacuum chamber. In addition to environmental testing, mechanical testing of glasses with different compositions, as well as electrical testing, will help to better understand the potential of glass as a resource in general.

In addition to all proposed research and testing, and in addition to using basaltic glass to build mirrors and solar cells, other applications of basaltic glass could be considered. Potential applications could include, for example, windows, thermal heat sinks, structural building materials, piping, storage tanks or a combination of other materials with glass, such as BFRPCs. Any potential basalt glass application will, however, benefit from basic research conducted on basaltic glasses, which will ideally lead to a well-defined glass being available on the lunar surface at one point.

References

[1] Albert Van Helden. *Measuring the universe: cosmic dimensions from Aristarchus to Halley*. University of Chicago Press, 2010.

[2] WA Baum, FS Johnson, JJ Oberly, C Cs Rockwood, CV Strain, and R Tousey. Solar ultraviolet spectrum to 88 kilometers. *Physical Review*, 70(9-10):781, 1946.

[3] Arthur P Cracknell and Costas A Varotsos. Editorial and cover: Fifty years after the first artificial satellite: from sputnik 1 to envisat. 2007.

[4] NASA. Nasa's great observatories. Online, 2004. last accessed 25.09.2019. URL: `https://www.nasa.gov/audience/forstudents/postsecondary/features/F_NASA_Great_Observatories_PS.html`.

[5] Jonathan P Gardner, John C Mather, Mark Clampin, Rene Doyon, Matthew A Greenhouse, Heidi B Hammel, John B Hutchings, Peter Jakobsen, Simon J Lilly, Knox S Long, et al. The james webb space telescope. *Space Science Reviews*, 123(4):485–606, 2006.

[6] Mitsunobu Tatsumoto. Age of the moon: An isotopic study of u-th-pb systematics of apollo 11 lunar samples-ii. *Geochimica et Cosmochimica Acta Supplement*, 1:1595, 1970.

[7] Joshua F Snape, Alexander A Nemchin, Jeremy J Bellucci, Martin J Whitehouse, Romain Tartèse, Jessica J Barnes, Mahesh Anand, Ian A Crawford, and Katherine H Joy. Lunar basalt chronology, mantle differentiation and implications for determining the age of the moon. *Earth and Planetary Science Letters*, 451:149–158, 2016.

[8] Claude J Allegre, Gerard Manhes, and Christa Göpel. The age of the earth. *Geochimica et Cosmochimica Acta*, 59(8):1445–1456, 1995.

[9] Robert C Reedy, James R Arnold, and Devendra Lal. Cosmic-ray record in solar system matter. *Annual Review of Nuclear and Particle Science*, 33(1):505–538, 1983.

[10] NASA. Lunar rocks and soils from apollo missions. Online, 2016. last accessed 25.09.2019. URL: `https://curator.jsc.nasa.gov/lunar/`.

[11] Bernhard Hufenbach, K Laurini, J Piedboeuf, B Schade, K Matsumoto, and F Spiero. International space exploration coordination group–the global exploration roadmap. In *62nd International Astronautical Congress*, 2011.

[12] ISECG. The global exploration roadmap, 2018. last accessed 25.09.2019. URL: `https://www.globalspaceexploration.org/wordpress/wp-content/isecg/GER_2018_small_mobile.pdf`.

[13] V Saturn. Flight manual sa507. *Revised Baseline Manual MSFC-MAN-507*, 1968.

[14] Mike Shafto, Mike Conroy, Rich Doyle, Ed Glaessgen, Chris Kemp, Jacqueline LeMoigne, and Lui Wang. Draft modeling, simulation, information technology & processing roadmap. *Technology Area*, 11, 2010.

[15] Bernhard Hufenbach, Thomas Reiter, and Elisabeth Sourgens. Esa strategic planning for space exploration. *Space Policy*, 30(3):174–177, 2014.

[16] Kurt Sacksteder and Gerald Sanders. In-situ resource utilization for lunar and mars exploration. In *45th AIAA Aerospace Sciences Meeting and Exhibit*, page 345, 2007.

[17] Gerald Sanders, William Larson, Kurt Sacksteder, and Carole Mclemore. Nasa in-situ resource utilization (isru) project: Development and implementation. In *AIAA SPACE 2008 Conference & Exposition*, page 7853, 2008.

[18] P. Turner. *True history and Lucius or the ass*. Midland Book, MB-175. Indiana University Press, 1974.

[19] Greg Grewell. Colonizing the universe: Science fictions then, now, and in the (imagined) future. *Rocky Mountain Review of Language and Literature*, pages 25–47, 2001.

[20] Jules Verne. From the earth to the moon. 1865. *Translated by J. and R. Baldick. Dutton, New York*, 1970.

[21] John Billingham, WP Gilbreath, Brian Oleary, and B Gosset. Space resources and space settlements. 1979.

[22] International Space Exploration Coordination Group. Benefits stemming from space exploration. resreport, International Space Exploration Coordination Group, September 2013. p. 4.

[23] Ian A Crawford. Introduction to the special issue on using extraterrestrial re-

sources to facilitate space science and exploration. *Space Policy*, 37:51, 2016.

[24] NASA. Nasa technology roadmaps. Online, 2015. last accessed 25.09.2019. URL: `https://www.nasa.gov/offices/oct/home/roadmaps/index.html`.

[25] NASA. Nasa strategic space technology investment plan. Last accessed 25.09.2019. URL: `https://www.nasa.gov/sites/default/files/atoms/files/2017-8-1_stip_final-508ed.pdf`.

[26] ESA. "exploring together" - esa space exploration strategy. Last accessed 25.09.2019. URL: `http://esamultimedia.esa.int/multimedia/publications/ESA_Space_Exploration_Strategy/`.

[27] MA Perino, F Fenoglio, S Pelle, P Couzin, J Thaeter, F Eilingsfeld, B Hufenbach, and A Bergamasco. Outlook of possible european contributions to future exploration scenarios and architectures. *Acta Astronautica*, 88:25–34, 2013.

[28] Kathleen C. Laurini, Bernhard Hufenbach, Juergen Hill, and Alain Ouellet. expanding human/robotic exploration mission collaboration opportunities. In *The golobal exploration Roadmap*. 66^{th} International Astronautical Congress, Jerusalem, Israel, 2015.

[29] Andrea EM Casini, Paolo Maggiore, Nicole Viola, Valter Basso, Marinella Ferrino, Jeffrey A Hoffman, and Aidan Cowley. Analysis of a moon outpost for mars enabling technologies through a virtual reality environment. *Acta Astronautica*, 143:353–361, 2018.

[30] Irene Lia Schlacht, Ms Orla Punch, EAC SpaceShip, Bernard Foing, Agata Kolodziejczyk, Aidan Cowley, and Giulio Ceppi. Design for the future: Flexhab project, the future lunar exploration habitat; mars; and exohab. *Update*, 2016.

[31] Samuel S Schreiner, Timothy P Setterfield, Daniel R Roberson, Benjamin Putbrese, Kyle Kotowick, Morris D Vanegas, Mike Curry, Lynn M Geiger, David Barmore, Jordan J Foley, et al. An overnight habitat for expanding lunar surface exploration. *Acta Astronautica*, 112:158–170, 2015.

[32] Eligar Sadeh, Willy Z Sadeh, Marvin Criswell, Eric E Rice, and Jenine Abarbanel. Inflatable habitats for lunar base development. *Living in Space*, page 165, 2009.

[33] Roger Alexander, Ryan Bechtel, Ted Chen, Tim Cormier, Sachin Kalaver, Mehmet Kirtas, Jung-Ho Lewe, Leland Marcus, Dave Marshall, Matt Medlin, et al. Moon-based advanced reusable transportation architecture the marta project. In *Third Annual HEDS-UP Forum, Human Exploration and Development of Space-University Partners*, page 206, 2000.

[34] M.D. Griffin and J.R. French. *Space Vehicle Design*. AIAA education series. American Institute of Aeronautics & Astronautics, 2004.

[35] Z Khan, A Vranis, A Zavoico, S Freid, and B Manners. Power system concepts for the lunar outpost: A review of the power generation, energy storage, power management and distribution (pmad) system requirements and potential technologies for development of the lunar outpost. In *AIP Conference Proceedings*, volume 813, pages 1083–1092. AIP, 2006.

[36] JF McElroy. Spe regenerative hydrogen/oxygen fuel cells for extraterrestrial surface applications. In *Proceedings of the 24th Intersociety Energy Conversion Engineering Conference*, pages 1631–1636. IEEE, 1989.

[37] Mohamed Gadalla and Sayem Zafar. Analysis of a hydrogen fuel cell-pv power system for small uav. *International Journal of Hydrogen Energy*, 41(15):6422–6432, 2016.

[38] V. Smil. *Power Density: A Key to Understanding Energy Sources and Uses*. MIT Press, 2015.

[39] P. Fortescue, J. Stark, and G. Swinerd. *Spacecraft Systems Engineering*. Wiley, 2003.

[40] Karl-Heinz Glassmeier, Hermann Boehnhardt, Detlef Koschny, Ekkehard Kührt, and Ingo Richter. The rosetta mission: flying towards the origin of the solar system. *Space Science Reviews*, 128(1-4):1–21, 2007.

[41] Xiaochen Lu, Rong Ma, Chao Wang, and Wei Yao. Performance analysis of a lunar based solar thermal power system with regolith thermal storage. *Energy*, 107:227–233, 2016.

[42] Yoshitsugu Sone. A 100-w class regenerative fuel cell system for lunar and planetary missions. *Journal of Power Sources*, 196(21):9076–9080, 2011.

[43] Joshua Freeh. Analysis of stationary, photovoltaic-based surface power system designs at the lunar south pole. In *AIAA SPACE 2008 Conference & Exposition*, page 7810, 2009.

[44] Sheila G Bailey and Geoffrey A Landis. Solar lunar power. 1994.

[45] J Mark Hickman, Henry B Curtis, and Geoffrey A Landis. Design consideration for lunar based photovoltaic power systems. In *Photovoltaic Specialists Conference, 1990., Conference Record of the Twenty First IEEE*, pages 1256–1262. IEEE, 1990.

[46] Dennis J Flood and Joseph Appelbaum. Photovoltaic power system considerations for future lunar bases. 1989.

[47] David J Brinker and Dennis J Flood. Advanced photovoltaic power system technology for lunar base applications. 1988.

[48] Dennis J Flood. Photovoltaics for high capacity space power systems. *Acta Astronautica*, 19(10):805–812, 1989.

[49] Timothy M Schriener and Mohamed S El-Genk. Thermal-hydraulics and safety analyses of the solid core-sectored compact reactor (sc-score) and power system. *Progress in Nuclear Energy*, 76:216–231, 2014.

[50] Mohamed S El-Genk. Space nuclear reactor power system concepts with static and dynamic energy conversion. *Energy Conversion and Management*, 49(3):402–411, 2008.

[51] Richard Welch, Daniel Limonadi, and Robert Manning. Systems engineering the curiosity rover: A retrospective. In *System of Systems Engineering (SoSE), 2013 8th International Conference on*, pages 70–75. IEEE, 2013.

[52] Jack Chan, Dennis Hill, Tim Hoye, and Douglas Leland. Development of advanced stirling radioisotope generator for planetary surface and deep space missions. In *Proceedings of the Sixth International Energy Conversion Engineering Conference (IECEC 2008)*, pages AIAA 2008–5768, 2008.

[53] Alfonso Delgado-Bonal, F Javier Martín-Torres, Sandra Vázquez-Martín, and María-Paz Zorzano. Solar and wind exergy potentials for mars. *Energy*, 102:550–558, 2016.

[54] RD Waldron. Unconventional systems for lunar base, power generation & storage. In *Proceedings of the 25th Intersociety Energy Conversion Engineering Conference*, volume 1, pages 434–439. IEEE, 1990.

[55] Aaron Valle Lozano. Development of a lunar regolith thermal energy storage model for a lunar outpost, 2016.

[56] Anthony J Colozza. Analysis of lunar regolith thermal energy storage. 1991.

[57] Hung D Nguyen and Gynelle C Steele. An overview of power, energy storage, and conversion efforts for 2014 sbir phases i and ii. 2016.

[58] Victor Christopher Elarde, Haruki Miyamoto, Ray Chan, Chris Stender, Chris Youtsey, Jessica GJ Adams, Andree Wibowo, Rao Tatavarti, Mark Osowski, and Noren Pan. (invited) fabrication and applications of high-efficiency, lightweight, multi-junction solar cells by epitaxial liftoff. *ECS Transactions*, 66(7):89–93, 2015.

[59] Christopher L Stender, Jessica Adams, Victor Elarde, Todd Major, Haruki Miyamoto, Mark Osowski, Noren Pan, Rao Tatavarti, Francis Tuminello, Andree Wibowo, et al. Flexible and lightweight epitaxial lift-off gaas multi-junction solar cells for portable power and uav applications. In *Photovoltaic Specialist Conference (PVSC), 2015 IEEE 42nd*, pages 1–4. IEEE, 2015.

[60] Kuen-Ting Shiu, Jeramy Zimmerman, Hongyu Wang, and Stephen R Forrest. Ultrathin film, high specific power inp solar cells on flexible plastic substrates. *Applied Physics Letters*, 95(22):223503, 2009.

[61] Tibor S Balint. Comparison of power system options between future lunar and mars missions. In *International Lunar Conference 2005 Proceedings*, pages 1–8, 2005.

[62] Xing Luo, Jihong Wang, Mark Dooner, and Jonathan Clarke. Overview of current development in electrical energy storage technologies and the application potential in power system operation. *Applied Energy*, 137:511–536, 2015.

[63] M Raja Reddy. Space solar cells - tradeoff analysis. *Solar energy materials and solar cells*, 77(2):175–208, 2003.

[64] Navid S Fatemi, Howard E Pollard, Hong Q Hou, and Paul R Sharps. Solar array trades between very high-efficiency multi-junction and si space solar cells. In *Photovoltaic Specialists Conference, 2000. Conference Record of the Twenty-Eighth*

IEEE, pages 1083–1086. IEEE, 2000.

[65] Roland Antonius Gabrielli, Johannes Mathies, Agnes Großmann, Georg Herdrich, Stefanos Fasoulas, Peter Schnauffer, Peter Middendorf, Miranda Fateri, and Andreas Gebhardt. Space propulsion considerations for a lunar take off industry based on regolith. In *ISSTS Conference Proceedings, presented at the 30th International Symposium on Space Technology and Science (Kobe, Japan,)*, 2015.

[66] Michael D Hogue, Robert P Mueller, Paul E Hintze, Laurent Sibille, and Daniel J Rasky. Regolith-derived heat shield for planetary body entry and descent system with in situ fabrication. In *Earth and Space 2012: Engineering, Science, Construction, and Operations in Challenging Environments*, pages 526–536. 2012.

[67] James Carpenter, Richard Fisackerly, and Berengere Houdou. Establishing lunar resource viability. *Space Policy*, 37:52–57, 2016.

[68] Jeremy Straub. In search of technology readiness level (trl) 10. *Aerospace Science and Technology*, 46:312–320, 2015.

[69] Daniel Andrews. Resource prospector (rp:) a lunar volatiles prospecting and in-situ resource utilization (isru) demonstration mission. 2016.

[70] Marianne Gonzalez, Jacqueline Quinn, Janine Captain, Josephine Santiago-Bond, and Stanley Starr. Regolith and environment science and oxygen and lunar volatile extraction (resolve): Lunar advanced volatile analysis (lava) capillary fluid dynamic restriction effects on gas chromatography. 2015.

[71] Hannah Bower, Kate Cryderman, and Janine Captain. Regolith and environment science and oxygen and lunar volatile extraction (resolve): Lunar advanced volatile analysis (lava) integration and testing-evaluation of lee valve. 2016.

[72] RC Anderson, LW Beegle, J Hurowitz, C Hanson, W Abbey, C Seybold, D Liminodi, S Kuhn, L Jandura, K Brown, et al. The mars science laboratory scooping campaign at rocknest. *Icarus*, 256:66–77, 2015.

[73] MH Hecht, JA Hoffman, and Moxie Team. The mars oxygen isru experiment (moxie) on the mars 2020 rover. In *Lunar and Planetary Science Conference*, volume 46, page 2774, 2015.

[74] Ewan Reid, Peter Iles, Jason Muise, Nick Cristello, Brad Jones, Michele Faragalli, Peter Visscher, Dale Boucher, Vincent Simard-Bilodeau, Dimi Apostolopoulos, et al. The artemis jr. rover: Mobility platform for lunar isru mission simulation. *Advances in Space Research*, 55(10):2472–2483, 2015.

[75] Giovanni Cesaretti, Enrico Dini, Xavier De Kestelier, Valentina Colla, and Laurent Pambaguian. Building components for an outpost on the lunar soil by means of a novel 3d printing technology. *Acta Astronautica*, 93:430–450, 2014.

[76] IL Ten Kate, EH Cardiff, JP Dworkin, SH Feng, V Holmes, C Malespin, JG Stern, TD Swindle, and DP Glavin. Vapor–volatile analysis by pyrolysis of regolith–an instrument for in situ detection of water, noble gases, and organics on the moon. *Planetary and Space Science*, 58(7):1007–1017, 2010.

[77] C Horton, C Gramajo, A Alemu, L Williams, A Ignatiev, and A Freundlich. First demonstration of photovoltaic diodes on lunar regolith-based substrate. *Acta Astronautica*, 56(5):537–545, 2005.

[78] CC Finlay, S Maus, CD Beggan, TN Bondar, A Chambodut, TA Chernova, A Chulliat, VP Golovkov, B Hamilton, M Hamoudi, et al. International geomagnetic reference field: the eleventh generation. *Geophysical Journal International*, 183(3):1216–1230, 2010.

[79] David R Williams. Moon fact sheet. *NASA Fact sheets*, 2006. last accessed 25.09.2019. URL: `http://nssdc.gsfc.nasa.gov/planetary/factsheet/moonfact.html`.

[80] CT Russell, PJ Coleman Jr, BR Lichtenstein, and G Schubert. The permanent and induced magnetic dipole moment of the moon. In *Lunar and Planetary Science Conference Proceedings*, volume 5, pages 2747–2760, 1974.

[81] Brett W Denevi, Mark S Robinson, Aaron K Boyd, David T Blewett, and Rachel L Klima. The distribution and extent of lunar swirls. *Icarus*, 273:53–67, 2016.

[82] DL Mitchell, JS Halekas, RP Lin, S Frey, LL Hood, MH Acuña, and A Binder. Global mapping of lunar crustal magnetic fields by lunar prospector. *Icarus*, 194(2):401–409, 2008.

[83] LL Hood, PJ Coleman, and DE Wilhelms. The moon: Sources of the crustal magnetic anomalies. *Science*, 204(4388):53–57, 1979.

[84] LL Hood and G Schubert. Lunar magnetic anomalies and surface optical properties. *Science*, 208(4439):49–51, 1980.

[85] NC Richmond and LL Hood. A preliminary global map of the vector lunar crustal magnetic field based on lunar prospector magnetometer data. *Journal of Geophysical Research: Planets*, 113(E2), 2008.

[86] M.G. Kivelson and C.T. Russell. *Introduction to Space Physics*. Cambridge atmospheric and space science series. Cambridge University Press, 1995. page 91-93.

[87] RM Skoug, JT Gosling, JT Steinberg, DJ McComas, CW Smith, NF Ness, Q Hu, and LF Burlaga. Extremely high speed solar wind: 29–30 october 2003. *Journal of Geophysical Research: Space Physics (1978–2012)*, 109(A9), 2004.

[88] Maxim L Khodachenko, Ignasi Ribas, Helmut Lammer, Jean-Mathias Grießmeier, Martin Leitner, Franck Selsis, Carlos Eiroa, Arnold Hanslmeier, Helfried K Biernat, Charles J Farrugia, et al. Coronal mass ejection (cme) activity of low mass m stars as an important factor for the habitability of terrestrial exoplanets. i. cme impact on expected magnetospheres of earth-like exoplanets in close-in habitable zones. *Astrobiology*, 7(1):167–184, 2007.

[89] Thomas N Woods, Francis G Eparvier, Juan Fontenla, Jerald Harder, Greg Kopp, William E McClintock, Gary Rottman, Byron Smiley, and Martin Snow. Solar irradiance variability during the october 2003 solar storm period. *Geophysical research letters*, 31(10), 2004.

[90] B McBreen and CJ Lambert. Interactions of high-energy (e> 5× 10 19 ev) photons in the earth's magnetic field. *Physical Review D*, 24(9):2536, 1981.

[91] MG Heaps. Parametrization of the cosmic ray ion-pair production rate above 18 km. *Planetary and Space Science*, 26(6):513–517, 1978.

[92] World Health Organization, International Commission on Non-Ionizing Radiation Protection, et al. Global solar uv index: A practical guide. 2002.

[93] Quincy F Johnson, Brad Gersey, Richard Wilkins, and Jianren Zhou. Radiation shielding of lunar regolith/polyethylene composites and lunar regolith/water mixtures. 2011.

[94] Jack Miller, L Taylor, Cary Zeitlin, L Heilbronn, S Guetersloh, M DiGiuseppe, Y Iwata, and T Murakami. Lunar soil as shielding against space radiation. *Radiation Measurements*, 44(2):163–167, 2009.

[95] AP Jordan, TJ Stubbs, JK Wilson, NA Schwadron, and HE Spence. The rate of dielectric breakdown weathering of lunar regolith in permanently shadowed regions. *Icarus*, 283:352–358, 2017.

[96] J-P Williams, DA Paige, BT Greenhagen, and E Sefton-Nash. The global surface temperatures of the moon as measured by the diviner lunar radiometer experiment. *Icarus*, 283:300–325, 2017.

[97] Ashwin R Vasavada, Joshua L Bandfield, Benjamin T Greenhagen, Paul O Hayne, Matthew A Siegler, Jean-Pierre Williams, and David A Paige. Lunar equatorial surface temperatures and regolith properties from the diviner lunar radiometer experiment. *Journal of Geophysical Research: Planets*, 117(E12), 2012.

[98] Zhen Ran and ZhenZhan Wang. Simulations of lunar equatorial regolith temperature profile based on measurements of diviner on lunar reconnaissance orbiter. *Science China Earth Sciences*, 57(9):2232–2241, 2014.

[99] Ramesh B Malla and Kevin M Brown. Determination of temperature variation on lunar surface and subsurface for habitat analysis and design. *Acta Astronautica*, 107:196–207, 2015.

[100] P Hager, R Haber, D Kraus, S Nogina, A Sievers, T Tattusch, and U Walter. *Dynamic thermal analysis for lunar surface operations: current status of the ThermoS approach*. Deutsche Gesellschaft für Luft- und Raumfahrt-Lilienthal-Oberth eV, 2013.

[101] Maria T Zuber, James W Head, David E Smith, Gregory A Neumann, Erwan Mazarico, Mark H Torrence, Oded Aharonson, Alexander R Tye, Caleb I Fassett, Margaret A Rosenburg, et al. Constraints on the volatile distribution within shackleton crater at the lunar south pole. *Nature*, 486(7403):378–381, 2012.

[102] Benjamin Vanoutryve, Diego De Rosa, Richard Fisackerly, Berengere Houdou, James Carpenter, Christian Philippe, Alain Pradier, Aliac Jojaghaian, Sylvie Espinasse, and Bruno Gardini. An anal-

ysis of illumination and communication conditions near lunar south pole based on kaguya data. In *Proceedings of International Planetary Probe Workshop, Barcelona*, 2010.

[103] David A Kring and Daniel D Durda. A global lunar landing site study to provide the scientific context for exploration of the moon. *Lunar and Planetary Institute. Contribution*, 1694:688, 2012.

[104] Ronald J White and Maurice Averner. Humans in space. *Nature*, 409(6823):1115–1118, 2001.

[105] RS Johnston, LF Dietlein, CA Berry, et al. Biomedical results of apollo (sp-368). *National Aeronautics and Space Administration, Lyndon B. Johnson Space Center, Houston, Texas*, 1975.

[106] R Margaria, GA Cavagna, and H Saiki. Human locomotion at reduced gravity. In *Proceedings of the 2nd Lunar International Symposium. Life Sciences Research and Lunar Medicine. Pergamon Press, Oxford and New York*, 1967.

[107] CE Carr, DJ Newman, and KV Hodges. Geologic traverse planning for planetary eva [sae technical paper 2003-01-2416]. In *33rd International Conference on Environmental Systems, SAE International, Warrendale, PA*, 2003.

[108] Sandra Wagner. The apollo experience lessons learned for constellation lunar dust management. 2006.

[109] DS McKay, BL Cooper, LA Taylor, JT James, K Thomas-Keprta, CM Pieters, SJ Wentworth, WT Wallace, and TS Lee. Physicochemical properties of respirable-size lunar dust. *Acta Astronautica*, 107:163–176, 2015.

[110] Dag Linnarsson, James Carpenter, Bice Fubini, Per Gerde, Lars L Karlsson, David J Loftus, G Kim Prisk, Urs Staufer, Erin M Tranfield, and Wim van Westrenen. Toxicity of lunar dust. *Planetary and Space Science*, 74(1):57–71, 2012.

[111] Roy Christoffersen, John R Lindsay, Sarah K Noble, Mary Ann Meador, Joseph J Kosmo, J Anneliese Lawrence, Lynn Brostoff, Amanda Young, and Terry McCue. Lunar dust effects on spacesuit systems: insights from the apollo spacesuits. 2008.

[112] James R Gaier. The effects of lunar dust on eva systems during the apollo missions. 2005.

[113] Hiroyuki Kawamoto and Noritaka Hara. Electrostatic cleaning system for removing lunar dust adhering to space suits. *Journal of Aerospace Engineering*, 24(4):442–444, 2010.

[114] Juan H Agui and Dennis P Stocker. Nasa lunar dust filtration and separations workshop report. 2009.

[115] Nima Afshar-Mohajer, Chang-Yu Wu, Jennifer Sinclair Curtis, and James R Gaier. Review of dust transport and mitigation technologies in lunar and martian atmospheres. *Advances in Space Research*, 56(6):1222–1241, 2015.

[116] CI Calle, CR Buhler, MR Johansen, MD Hogue, and SJ Snyder. Active dust control and mitigation technology for lunar and martian exploration. *Acta Astronautica*, 69(11):1082–1088, 2011.

[117] Cynthia M Katzan and Jonathan L Edwards. Lunar dust transport and potential interactions with power system components. 1991.

[118] H Kawamoto, M Uchiyama, BL Cooper, and DS McKay. Mitigation of lunar dust on solar panels and optical elements utilizing electrostatic traveling-wave. *Journal of Electrostatics*, 69(4):370–379, 2011.

[119] CI Calle, CR Buhler, JL McFall, and SJ Snyder. Particle removal by electrostatic and dielectrophoretic forces for dust control during lunar exploration missions. *Journal of Electrostatics*, 67(2):89–92, 2009.

[120] CI Calle, JL McFall, CR Buhler, SJ Snyder, EE Arens, A Chen, ML Ritz, JS Clements, CR Fortier, and S Trigwell. Dust particle removal by electrostatic and dielectrophoretic forces with applications to nasa exploration missions. In *Proc. ESA Annual Meeting on Electrostatics*, pages 1–14, 2008.

[121] Christiane Helling, R Giles Harrison, Farideh Honary, Declan A Diver, Karen Aplin, Ian Dobbs-Dixon, Ute Ebert, Shuichiro Inutsuka, Francisco J Gordillo-Vazquez, and Stuart Littlefair. Atmospheric electrification in dusty, reactive gases in the solar system and beyond. *Surveys in Geophysics*, pages 1–52, 2016.

[122] Travis Sarver, Ali Al-Qaraghuli, and Lawrence L Kazmerski. A comprehensive review of the impact of dust on the use of solar energy: History, investigations, results, literature, and mitigation approaches. *Renewable and Sustainable Energy Reviews*, 22:698–733, 2013.

[123] Carol J Riordan, Roland Hulstrom, and DR Myers. *Influences of atmospheric conditions and air mass on the ratio of ultraviolet to total solar radiation.* Solar Energy Research Institute, 1990.

[124] Fritz Kasten and Andrew T Young. Revised optical air mass tables and approximation formula. *Applied optics*, 28(22):4735–4738, 1989.

[125] Cutler J Cleveland and Christopher G Morris. *Handbook of Energy: Diagrams, Charts, and Tables*, volume 1. Newnes, 2013.

[126] M. Iqbal. *An Introduction To Solar Radiation.* Elsevier Science, 2012. p. 27.

[127] F Steinhilber, J Beer, and C Fröhlich. Total solar irradiance during the holocene. *Geophysical Research Letters*, 36(19), 2009.

[128] JA Duffie and WA Beckman. Solar engineering of thermal process, 2006.

[129] V. Badescu. *Modeling Solar Radiation at the Earth's Surface: Recent Advances.* Springer Berlin Heidelberg, 2008. p. 148.

[130] M Anand, Ian A Crawford, M Balat-Pichelin, S Abanades, W van Westrenen, G Péraudeau, R Jaumann, and W Seboldt. A brief review of chemical and mineralogical resources on the moon and likely initial in situ resource utilization (isru) applications. *Planetary and Space Science*, 74(1):42–48, 2012.

[131] Ian A Crawford. Lunar resources a review. *Progress in Physical Geography*, 39(2):137–167, 2015.

[132] Martin Elvis. What can space resources do for astronomy and planetary science? *Space Policy*, 37:65–76, 2016.

[133] Mary Fae McKay, David S McKay, and Michael B Duke. Space resources. volume 2: Energy, power, and transport. 1992.

[134] Katharine L Robinson, Jessica J Barnes, Kazuhide Nagashima, Aurélien Thomen, Ian A Franchi, Gary R Huss, Mahesh Anand, and G Jeffrey Taylor. Water in evolved lunar rocks: Evidence for multiple reservoirs. *Geochimica et Cosmochimica Acta*, 2016.

[135] Paul O Hayne, Amanda Hendrix, Elliot Sefton-Nash, Matthew A Siegler, Paul G Lucey, Kurt D Retherford, Jean-Pierre Williams, Benjamin T Greenhagen, and David A Paige. Evidence for exposed water ice in the moon's south polar regions from lunar reconnaissance orbiter ultraviolet albedo and temperature measurements. *Icarus*, 255:58–69, 2015.

[136] Anthony Colaprete, Peter Schultz, Jennifer Heldmann, Diane Wooden, Mark Shirley, Kimberly Ennico, Brendan Hermalyn, William Marshall, Antonio Ricco, Richard C Elphic, et al. Detection of water in the lcross ejecta plume. *science*, 330(6003):463–468, 2010.

[137] Craig Pitcher, Norbert Kömle, Otto Leibniz, Odalys Morales-Calderon, Yang Gao, and Lutz Richter. Investigation of the properties of icy lunar polar regolith simulants. *Advances in Space Research*, 57(5):1197–1208, 2016.

[138] Carle M Pieters, Joseph Boardman, Bonnie Buratti, Alok Chatterjee, Roger Clark, Tom Glavich, Robert Green, James Head, Peter Isaacson, Erick Malaret, et al. The moon mineralogy mapper (m3) on chandrayaan-1. *Curr. Sci*, 96(4):500–505, 2009.

[139] S Arivazhagan. Quantitative characterization of lunar mare orientale basalts detected by moon mineralogical mapper on chandrayaan-1. In *Planetary Exploration and Science: Recent Results and Advances*, pages 21–43. Springer, 2015.

[140] Bruce Hapke and Hiroyuki Sato. The porosity of the upper lunar regolith. *Icarus*, 273:75–83, 2016.

[141] Louise Alexander, Joshua F Snape, Katherine H Joy, Hilary Downes, and Ian A Crawford. An analysis of apollo lunar soil samples 12070, 889, 12030, 187, and 12070, 891: Basaltic diversity at the apollo 12 landing site and implications for classification of small-sized lunar samples. *Meteoritics & Planetary Science*, 51(9):1654–1677, 2016.

[142] J Mortimer, AB Verchovsky, and M Anand. Predominantly non-solar origin of nitrogen in lunar soils. *Geochimica et Cosmochimica Acta*, 193:36–53, 2016.

[143] Matthew A Pasek. Phosphorus as a lunar volatile. *Icarus*, 255:18–23, 2015.

[144] AB Sanin, IG Mitrofanov, ML Litvak, BN Bakhtin, JG Bodnarik, WV Boynton, G Chin, LG Evans, K Harshman, F Fedosov, et al. Hydrogen distribution in the lunar polar regions. *Icarus*, 2016.

[145] Dana M Hurley, Jason C Cook, Kurt D Retherford, Thomas Greathouse, G Randall Gladstone, Kathleen Mandt, Cesare Grava, David Kaufmann, Amanda Hendrix, Paul D Feldman, et al. Contributions of solar wind and micrometeoroids

to molecular hydrogen in the lunar exosphere. *Icarus*, 2016.

[146] Robert Mueller and Paul Van Susante. A review of lunar regolith excavation robotic device prototypes. In *AIAA SPACE 2011 Conference & Exposition*, page 7234, 2011.

[147] Martin Elvis. How many ore-bearing asteroids? *Planetary and Space Science*, 91:20–26, 2014.

[148] Grant Heiken, David Vaniman, and Bevan M French. *Lunar sourcebook: A user's guide to the Moon*. CUP Archive, 1991.

[149] Friedrich Hörz, Richard Grieve, Grant Heiken, Paul Spudis, and Alan Binder. Lunar surface processes. *Lunar sourcebook*, pages 61–120, 1991.

[150] C. Meyer. Lunar regolith. *Lunar Petrographic Educational Thin Section Set*, 2003. p. 46-47.

[151] Samuel S Schreiner, Jesus A Dominguez, Laurent Sibille, and Jeffrey A Hoffman. Thermophysical property models for lunar regolith. *Advances in Space Research*, 57(5):1209–1222, 2016.

[152] Guangfei Wei, Xiongyao Li, and Shijie Wang. Thermal behavior of regolith at cold traps on the moon' s south pole: Revealed by chang' e-2 microwave radiometer data. *Planetary and Space Science*, 122:101–109, 2016.

[153] Naoya Sakatani, Kazunori Ogawa, Yu-ichi Iijima, Masahiko Arakawa, and Satoshi Tanaka. Compressional stress effect on thermal conductivity of powdered materials: Measurements and their implication to lunar regolith. *Icarus*, 267:1–11, 2016.

[154] W David Carrier III. Particle size distribution of lunar soil. *Journal of Geotechnical and Geoenvironmental Engineering*, 129(10):956–959, 2003.

[155] John C Graf. Lunar soils grain size catalog. *NASA Reference Publication 1265*, 1993.

[156] DS McKay, RM Fruland, and GH Heiken. Grain size and the evolution of lunar soils. In *Lunar and Planetary Science Conference Proceedings*, volume 5, pages 887–906, 1974.

[157] W David Carrier III. Lunar soil grain size distribution. *The Moon*, 6(3-4):250–263, 1973.

[158] Bruce W Hapke. On the particle size distribution of lunar soil. *Planetary and Space Science*, 16(1):101–110, 1968.

[159] Grant Heiken and David S McKay. Petrography of apollo 17 soils. In *Lunar and Planetary Science Conference Proceedings*, volume 5, pages 843–860, 1974.

[160] JJ Papike, SB Simon, and JC Laul. The lunar regolith: Chemistry, mineralogy, and petrology. *Reviews of Geophysics*, 20(4):761–826, 1982.

[161] Grant Heiken, David Vaniman, and Bevan M French. *Lunar sourcebook: A user's guide to the Moon*. CUP Archive, 1991. Chapter 7.

[162] John F Lindsay. Lunar stratigraphy and sedimentology. *Amsterdam, Elsevier Scientific Publishing Co.(Developments in Solar System-and Space Science, No. 3), 1976. 315 p.*, 1, 1976. chapter 6 p. 227-287.

[163] NASA. Lunar sample and photo catalog. Online, 2016. last accessed 25.09.2019. URL: `https://curator.jsc.nasa.gov/lunar/samplecatalog/index.cfm`.

[164] Anthony L Turkevich. Average chemical composition of the lunar surface. *The moon*, 8(3):365–367, 1973.

[165] JC Laul and RA Schmitt. Chemical composition of apollo 15, 16, and 17 samples. In *Lunar and Planetary Science Conference Proceedings*, volume 4, page 1349, 1973.

[166] TH Prettyman, JJ Hagerty, RC Elphic, WC Feldman, DJ Lawrence, GW McKinney, and DT Vaniman. Elemental composition of the lunar surface: Analysis of gamma ray spectroscopy data from lunar prospector. *Journal of Geophysical Research: Planets*, 111(E12), 2006.

[167] R Jaumann, H Hiesinger, M Anand, Ian A Crawford, R Wagner, F Sohl, BL Jolliff, F Scholten, M Knapmeyer, H Hoffmann, et al. Geology, geochemistry, and geophysics of the moon: Status of current understanding. *Planetary and Space Science*, 74(1):15–41, 2012.

[168] George E Ulrich, Carroll Ann Hodges, and William R Muehlberger. Geology of the apollo 16 area, central lunar highlands. Technical report, USGPO: For sale by the Supt. of Docs, 1981.

[169] Deepak Dhingra, James W Head, and Carle M Pieters. Geological mapping of impact melt deposits at lunar complex craters jackson and tycho: Morphologic and topographic diversity and relation to the cratering process. *Icarus*, 2016.

[170] Philippe Lognonné, Jeannine Gagnepain-Beyneix, and Hugues Chenet. A new seis-

mic model of the moon: implications for structure, thermal evolution and formation of the moon. *Earth and Planetary Science Letters*, 211(1):27–44, 2003.

[171] C Meyer. Lunar sample mineralogy. *NASA Lunar Petrographic Educational Thin Section Set*, pages 8–9, 2003.

[172] Yann H Chemin, Ian A Crawford, Peter Grindrod, and Louise Alexander. Assessment of spectral properties of apollo 12 landing site. *PeerJ Preprints*, 4:e2124v1, 2016.

[173] Claire L McLeod, Alan D Brandon, Vera A Fernandes, Anne H Peslier, Jörg Fritz, Thomas Lapen, John T Shafer, Alan R Butcher, and Anthony J Irving. Constraints on formation and evolution of the lunar crust from feldspathic granulitic breccias nwa 3163 and 4881. *Geochimica et Cosmochimica Acta*, 2016.

[174] John Longhi. Petrogenesis of picritic mare magmas: Constraints on the extent of early lunar differentiation. *Geochimica et Cosmochimica Acta*, 70(24):5919–5934, 2006.

[175] John Longhi, Sedelia R Durand, and David Walker. The pattern of ni and co abundances in lunar olivines. *Geochimica et Cosmochimica Acta*, 74(2):784–798, 2010.

[176] R. Gill. *Igneous Rocks and Processes: A Practical Guide*. Wiley, 2011.

[177] Norman Levi Bowen. The later stages of the evolution of the igneous rocks. *The Journal of Geology*, 23(S8):1–91, 1915.

[178] Ralph Cusack. On the melting points of minerals. *Proceedings of the Royal Irish Academy (1889-1901)*, 4:399–413, 1896.

[179] DL Rickman and JE Edmunson. Reference images from thin sections of lunar regolith. In *Lunar and Planetary Science Conference*, volume 44, page 2503, 2013.

[180] AM Vance, R Christoffersen, LP Keller, EL Berger, and SK Noble. Evolution of shock melt compositions in lunar regoliths. 2016.

[181] Rochelle M Cornell and Udo Schwertmann. *The iron oxides: structure, properties, reactions, occurrences and uses*. John Wiley & Sons, 2003.

[182] Richard V Morris, Göstar Klingelhöfer, Randy L Korotev, and Tad D Shelfer. Mössbauer mineralogy on the moon: The lunar regolith. *Hyperfine interactions*, 117(1-4):405–432, 1998.

[183] Christian Schrader. Terrestrial and lunar geological terminology. 2009.

[184] Swapan Kumar Haldar. *Introduction to mineralogy and petrology*. Elsevier, 2013.

[185] Lawrence M Anovitz and James G Blencoe. Dry melting of high albite. *American Mineralogist*, 84(11-12):1830–1842, 1999.

[186] Julian R Goldsmith. The melting and breakdown reactions of anorthite at high pressures and temperatures. *American Mineralogist*, 65(3-4):272–284, 1980.

[187] Tsutomu Murase and Alexander R McBirney. Properties of some common igneous rocks and their melts at high temperatures. *Geological Society of America Bulletin*, 84(11):3563–3592, 1973.

[188] W Johannes, J Koepke, and H Behrens. Partial melting reactions of plagioclases and plagioclase-bearing systems. In *Feldspars and their Reactions*, pages 161–194. Springer, 1994.

[189] JS Huebner and AC Turnock. The melting relations at 1 bar of pyroxenes composed largely of ca-, mg-, and fe-bearing components. *American Mineralogist*, 65(3-4):225–271, 1980.

[190] PL Roeder and RFl Emslie. Olivine-liquid equilibrium. *Contributions to mineralogy and petrology*, 29(4):275–289, 1970.

[191] Carole McLemore. The need for lunar simulants. *LPI Contributions*, 1515:40, 2009.

[192] James L Carter, David S McKay, Lawrence A Taylor, and W David Carrier III. Lunar simulants: Jsc-1 is gone; the need for new standardized root simulants. 2004.

[193] Laurent Sibille. Lunar simulants, analogues, and standards: Needs and realities for mission technologies development. 2013.

[194] S Jayalekshmi and Pala Gireesh Kumar. Studies on the sinkages of rigid plain wheels and lugged wheels on tri-1 lunar soil simulant. *Journal of Terramechanics*, 82:35–42, 2019.

[195] L Sibille, P Carpenter, and RA Schlagheck. Toward a suite of standard lunar regolith simulants for nasa's lunar missions: Recommendations of the 2005 workshop of lunar regolith simulant materials. In *Space Resources Roundtable VII: LEAG Conference on Lunar Exploration*, volume 1287, page 81, 2005.

[196] Carole A McLemore, John C Fikes, and Joe T Howell. 2007 lunar regolith simu-

lant workshop overview. 2007.

[197] James R Gaier. The need for high fidelity lunar regolith simulants. 2008.

[198] Lawrence A Taylor and Yang Liu. Important considerations for lunar soil simulants. In *Earth and Space 2010: Engineering, Science, Construction, and Operations in Challenging Environments*, pages 106–118. 2010.

[199] Laurent Sibille and P Carpenter. Standard lunar regolith simulants for space resource utilization technologies development: Effects of materials choices. In *37th Annual Lunar and Planetary Science Conference*, volume 37, 2006.

[200] Laurent Sibille, Paul Carpenter, Ronald Schlagheck, and Raymond A French. Lunar regolith simulant materials: recommendations for standardization, production, and usage. 2006.

[201] P Carpenter, L Sibille, S Wilson, and G Meeker. Development of standardized lunar regolith simulant materials. *Microscopy and Microanalysis*, 12(S02):886–887, 2006.

[202] Douglas L Rickman. *Manufacture of lunar regolith simulants*. National Aeronautics and Space Administration, Marshall Space Flight Center, 2013.

[203] Sabhayu Sen, D Butts, CS Ray, GB Thompson, RA Morris, and JS O'Dell. Production of high fidelity lunar agglutinate simulant. *Advances in Space Research*, 47(11):1912–1921, 2011.

[204] Christian Schrader, Douglas Rickman, Carole McLemore, John Fikes, Douglas Stoeser, Susan Wentworth, and David McKay. Lunar regolith characterization for simulant design and evaluation using figure of merit algorithms. In *47th AIAA Aerospace Sciences Meeting including The New Horizons Forum and Aerospace Exposition*, page 755, 2009.

[205] J Edmunson, W Betts, D Rickman, C McLemore, J Fikes, D Stoeser, S Wilson, and C Schrader. Nasa lunar regolith simulant program. 2010.

[206] Lawrence A Taylor, Carle M Pieters, and Daniel Britt. Evaluations of lunar regolith simulants. *Planetary and Space Science*, 126:1–7, 2016.

[207] D.B. Stoeser, D.L. Rickman, and S. Wilson. Design and specifications for the highland regolith prototype simulants nulht-1m and -2m. 2010.

[208] Doug Rickman, Jennifer Edmunson, and Carole McLemore. Functional comparison of lunar regoliths and their simulants. *Journal of Aerospace Engineering*, 26(1):176–182, 2012.

[209] Yang Liu and Lawrence A Taylor. Characterization of lunar dust and a synopsis of available lunar simulants. *Planetary and Space Science*, 59(14):1769–1783, 2011.

[210] CM Schrader, DL Rickman, CA McLemore, and JC Fikes. Lunar regolith simulant user's guide. 2010.

[211] Kenneth W Street Jr, Chandra Ray, Doug Rickman, and Daniel A Scheiman. Thermal properties of lunar regolith simulants. In *Earth and Space 2010: Engineering, Science, Construction, and Operations in Challenging Environments*, pages 266–275. ASCE, 2010.

[212] Khalid A Alshibli and Alsidqi Hasan. Strength properties of jsc-1a lunar regolith simulant. *Journal of geotechnical and geoenvironmental engineering*, 135(5):673–679, 2009.

[213] Mehmet Murat Monkul and Amina Dacic. Effect of grain size distribution on stress-strain behavior of lunar soil simulants. *Advances in Space Research*, 60(3):636–651, 2017.

[214] DJP Donaldson Hanna, DJP Martin, KH Joy, JD Carpenter, NE Bowles, et al. Characterization of lunar highlands regolith simulants in preparation for drilling and sampling into the polar regolith by esa's prospect package. In *Lunar and Planetary Science Conference*, volume 48, page 1717, 2017.

[215] Thomas Gualtieri and Amit Bandyopadhyay. Compressive deformation of porous lunar regolith. *Materials Letters*, 143:276–278, 2015.

[216] Julie E Kleinhenz and R Allen Wilkinson. Development and testing of an isru soil mechanics vacuum test facility. 2014.

[217] Jeremiah N Mpagazehe, Kenneth W Street Jr, Irebert R Delgado, and C Fred Higgs III. An experimental study of lunar dust erosive wear potential using the jsc-1af lunar dust simulant. *Wear*, 316(1-2):79–91, 2014.

[218] Amrita Mukherjee. Micro-hollow cathode discharge analysis of lunar regolith simulants. 2012.

[219] Shawn M Allan, Brandon J Merritt, Brittany F Griffin, Paul E Hintze, and Holly S Shulman. High temperature microwave dielectric properties of jsc-1ac lunar sim-

ulant. 2011.

[220] Takashi Matsushima, Jun Katagiri, Kentaro Uesugi, Akira Tsuchiyama, and Tsukaka Nakano. 3d shape characterization and image-based dem simulation of the lunar soil simulant fjs-1. *Journal of Aerospace Engineering*, 22(1):15–23, 2009.

[221] Paul Greenberg, Kenneth W Street, and James Gaier. Structural, physical, and compositional analysis of lunar simulants and regolith. 2008.

[222] Hao Sun, Min Yi, Zhigang Shen, Xiaojing Zhang, and Shulin Ma. Developing a new controllable lunar dust simulant: Bhld20. *Planetary and Space Science*, 141:17–24, 2017.

[223] Hong Tang, Xiongyao Li, Sensen Zhang, Shijie Wang, Jianzhong Liu, Shijie Li, Yang Li, and Yanxue Wu. A lunar dust simulant: Clds-i. *Advances in Space Research*, 59(4):1156–1160, 2017.

[224] Eduardo Suescun-Florez, Stanislav Roslyakov, Magued Iskander, and Mohammed Baamer. Geotechnical properties of bp-1 lunar regolith simulant. *Journal of Aerospace Engineering*, 28(5):04014124, 2014.

[225] D Stoeser, D Rickman, and S Wilson. Design and specifications for the highland regolith prototype simulants nu-lht-1m and-2m. 2011.

[226] HA Oravec, X Zeng, and VM Asnani. Design and characterization of grc-1: A soil for lunar terramechanics testing in earth-ambient conditions. *Journal of Terramechanics*, 47(6):361–377, 2010.

[227] Melissa M Battler and John G Spray. The shawmere anorthosite and ob-1 as lunar highland regolith simulants. *Planetary and Space Science*, 57(14-15):2128–2131, 2009.

[228] CS Ray, ST Reis, S Sen, and JS O'Dell. Jsc-1a lunar soil simulant: Characterization, glass formation, and selected glass properties. *Journal of Non-Crystalline Solids*, 356(44-49):2369–2374, 2010.

[229] Yongquan Li, Jianzhong Liu, and Zongyu Yue. Nao-1: Lunar highland soil simulant developed in china. *Journal of Aerospace Engineering*, 22(1):53–57, 2009.

[230] Yongchun Zheng, Shijie Wang, Ziyuan Ouyang, Yongliao Zou, Jianzhong Liu, Chunlai Li, Xiongyao Li, and Junming Feng. Cas-1 lunar soil simulant. *Advances in Space Research*, 43(3):448–454, 2009.

[231] Hiroshi Kanamori, Satoru Udagawa, Tetsuji Yoshida, Shinji Matsumoto, and Kenji Takagi. Properties of lunar soil simulant manufactured in japan. In *Space 98*, pages 462–468. 1998.

[232] Caroline Smith, Sarah-Jane Gill, Kamini Manick, Giles Miller, Chris Jones, Mike Rumsey, Ludovic Duvet, and Dayl Martin. The european space agency exploration sample analogue collection (esa2c) and curation facility-present and future. In *42nd COSPAR Scientific Assembly*, volume 42, 2018.

[233] K Manick, S-J Gill, J Najorka, CL Smith, and L Duvet. Fundamental properties characterisation of lunar regolith simulants at the european space agency (esa) sample analogue curation facility. In *Lunar and Planetary Science Conference*, volume 49, 2018.

[234] Byung Chul Chang and Ki Yong Ann. Development of assessment methods of lunar soil simulants with respect to chemical composition. *Advances in Space Research*, 63(8):2584–2597, 2019.

[235] DL Rickman, CM Schrader, and JE Edmunson. Generation of requirements for simulant measurements. 2010.

[236] William M Cross and Gloria A Murphy. Characterization and evaluation of lunar regolith and simulants. 2010.

[237] Chunmei He. *Geotechnical characterization of lunar regolith simulants.* PhD thesis, Case Western Reserve University, 2010.

[238] DB Stoeser, DL Rickman, and S Wilson. Preliminary geological findings on the bp-1 simulant. *NASA NTRS*, 2010.

[239] Zentrallaboratorium Ochtendung. *Chemical Analysis of Tertiaer-Basalt Werk Huehnerberg.* Rheinische Provinzial Basalt- und Lavawerke GmbH & Co. oHG, Im Langacker 1, 56299 Ochtendung, Germany, October 2015.

[240] Inc. Shimizu Corporation/ CSP Japan. *Properties of Lunar Soil Simulants.* Shimizu Corporation/ CSP Japan, Inc., 5th Floor,Oshimaya Bldg. 2-22-5,Hatchobori, Chuo-ku,Tokyo 104-0032 Japan, 1998.

[241] Orbital Technologies Corporation. *Material Safety Data Sheet - JSC 1AF/1A/1AC Lunar Mare Regolith Simulant.* Orbital Technologies Corporation, 1212 Fourier Drive, Madison, WI 53717, USA, November 2007.

[242] Inc Zybek Advanced Products. *Material*

Safety Data Sheet - JSC 2AF/2A/2AC Lunar Mare Regolith Simulant. Zybek Advanced Products, Inc, 2845 29th Street, Boulder, CO 80301, USA, January 2013.

[243] USGS. *Material Safety Data Sheet - NU-LHT-2M*. USGS, Denver Federal Center, Building 20, Denver, CO, 80225, July 2008.

[244] Inc Zybek Advanced Products. *Material Safety Data Sheet - NU-LHT-3M*. Zybek Advanced Products, Inc, 2845 29th Street, Boulder, CO 80301, USA, January 2013.

[245] Michael Weinstein and Stephen A Wilson. Apparatus and method for producing a lunar agglutinate simulant, December 17 2013. US Patent 8,610,024.

[246] John W Delano. Pristine lunar glasses: Criteria, data, and implications. *Journal of Geophysical Research: Solid Earth*, 91(B4):201–213, 1986.

[247] D Stöffler. Glasses formed by hypervelocity impact. *Journal of Non-Crystalline Solids*, 67(1-3):465–502, 1984.

[248] Andrew D Saunders and John Tarney. Geochemical characteristics of basaltic volcanism within back-arc basins. *Geological Society, London, Special Publications*, 16(1):59–76, 1984.

[249] FA Frey, N Walker, D Stakes, SR Hart, and R Nielsen. Geochemical characteristics of basaltic glasses from theamar andfamous axial valleys, mid-atlantic ridge (36Â°–37Â° n): Petrogenetic implications. *Earth and Planetary Science Letters*, 115(1-4):117–136, 1993.

[250] Shen-Su Sun, Robert W Nesbitt, and Anatoly Ya Sharaskin. Geochemical characteristics of mid-ocean ridge basalts. *Earth and Planetary Science Letters*, 44(1):119–138, 1979.

[251] Dorothee JM Burkhard. Crystallization and oxidation of kilauea basalt glass: processes during reheating experiments. *Journal of Petrology*, 42(3):507–527, 2001.

[252] Senol Yilmaz, Osman T Özkan, and Volkan Günay. Crystallization kinetics of basalt glass. *Ceramics International*, 22(6):477–481, 1996.

[253] Jonathon E Ericson, A Makishima, JD Mackenzie, and Rainer Berger. Chemical and physical properties of obsidian: a naturally occuring glass. *Journal of Non-Crystalline Solids*, 17(1):129–142, 1975.

[254] AK Bandyopadhyay, Jerzy Zarzycki, P Auric, and J Chappert. Magnetic properties of a basalt glass and glass-ceramics. *Journal of Non-Crystalline Solids*, 40(1-3):353–368, 1980.

[255] Juergen Schleppi, Joseph Gibbons, Alexander Groetsch, Jim Buckman, Aidan Cowley, and Nick Bennett. Manufacture of glass and mirrors from lunar regolith simulant. *Journal of Materials Science*, 54(5):3726–3747, 2019.

[256] Seth C Rasmussen. Origins of glass: Myth and known history. In *How Glass Changed the World*, pages 11–19. Springer, 2012.

[257] Stefan Muthesius. Victorian glassworlds: Glass culture and the imagination 1830–1880 by isobel armstrong: Oxford: Oxford university press, 2008, pp. 472, 2010.

[258] Julian Henderson. The raw materials of early glass production. *Oxford Journal of Archaeology*, 4(3):267–291, 1985.

[259] Lionel Alexander Bethune Pilkington. Review lecture. the float glass process. *Proceedings of the Royal Society of London. Series A, Mathematical and Physical Sciences*, 314(1516):1–25, 1969.

[260] Varnakavi Naresh. Homogeneity: bubble formation in the manufacturing of glass. 03 2015.

[261] Yuan-Zheng Yue. Characteristic temperatures of enthalpy relaxation in glass. *Journal of Non-Crystalline Solids*, 354(12-13):1112–1118, 2008.

[262] LL Gaines and MM Mintz. Energy implications of glass-container recycling. Technical report, Argonne National Lab., IL (United States); National Renewable Energy Lab., 1994.

[263] M Kovacec, A Pilipovic, and N Stefanic. Impact of glass cullet on the consumption of energy and environment in the production of glass packaging material. *Recent Researches in Chemistry, Biology, Environment and Culture. Monteux, Switzerland*, 2011.

[264] Geoffrey A Landis. Materials refining for structural elements from lunar resources. In *Using in situ Resources for Construction of Planetary Outposts*, page 11, 1998.

[265] Andrea Jaime Albalat. Assessment of oxygen production on the moon through reduction of ilmenite. 2010.

[266] Julie E Kleinhenz, Kurt R Sacksteder, and Vedha Nayagam. Lunar resource utilization: Development of a reactor for volatile extraction from regolith. In *Aerospace Sciences Conference, Reno, NV*, 2007.

[267] PA Curreri, E Ethridge, S Hudson, and S Sen. Experimental demonstration of the

molten oxide electrolysis method for oxygen and iron production from simulated lunar materials. 2006.

[268] Lawrence A Taylor and W David Carrier. Oxygen production on the moon: an overview and evaluation. *Resources of near earth space*, page 69, 1993.

[269] Edgardo Santiago-Maldonado. Oxygen production system models for lunar isru. 2007.

[270] Donald M Burt. Lunar mining of oxygen using fluorine. In *Lunar Bases and Space Activities of the 21st Century*, pages 423–428, 1992.

[271] Samuel S Schreiner, Jesus A Dominguez, Laurent Sibille, and Jeffrey A Hoffman. A parametric sizing model for molten regolith electrolysis reactors to produce oxygen from lunar regolith. 2015.

[272] D Larry Clark, Bruce W Keller, and Joel A Kirkland. Field test results of the pilot hydrogen reduction reactor. *AIAA, Pasadena*, page 6475, 2009.

[273] Robert P Mueller and Ivan Townsend. Lunar regolith simulant feed system for a hydrogen reduction reactor system. In *47th AIAA Aerospace Sciences Meeting, Orlando, FL*, 2009.

[274] Diane Linne, Julie Kleinhenz, and Uday Hegde. Evaluation of heat recuperation in a concentric hydrogen reduction reactor. In *50th AIAA Aerospace Sciences Meeting including the New Horizons Forum and Aerospace Exposition*, page 636, 2012.

[275] Kristopher A Lee, Lara Oryshchyn, Aaron Paz, Mike Reddington, and Thomas M Simon. The roxygen project: Outpost-scale lunar oxygen production system development at johnson space center. *Journal of Aerospace Engineering*, 26(1):67–73, 2012.

[276] Michael A Gibson and Christian W Knudsen. Lunar oxygen production from ilmenite. In *Lunar bases and space activities of the 21st century*, page 543, 1985.

[277] Brian J Skinner. Earth resources. *Proceedings of the national Academy of Sciences*, 76(9):4212–4217, 1979.

[278] Buhle S Xakalashe and M Tangstad. Silicon processing: from quartz to crystalline silicon solar cells. *Chem Technol*, page 90 (8), 2012.

[279] Erwann Fourmond, Cyrille Ndzogha, David Pelletier, Yves Delannoy, Christian Trassy, Y Caratini, G Baluais, R Einhaus, Santo Martinuzzi, and Isabelle Perichaud. Refining of metallurgical silicon for crystalline solar cells. 2004.

[280] Arjan Ciftja. Refining and recycling of silicon: a review. 2008.

[281] Dawei Luo. Study on the preparation of solar grade silicon by metallurgical method. *New Research on Silicon: Structure, Properties, Technology*, page 55, 2017.

[282] S Pizzini and C Calligarich. On the effect of impurities on the photovoltaic behavior of solar-grade silicon i. the role of boron and phosphorous primary impurities in p-type single-crystal silicon. *Journal of the Electrochemical Society*, 131(9):2128–2132, 1984.

[283] Sergio Pizzini. Towards solar grade silicon: Challenges and benefits for low cost photovoltaics. *Solar energy materials and solar cells*, 94(9):1528–1533, 2010.

[284] S Pizzini, M Acciarri, and S Binetti. From electronic grade to solar grade silicon: chances and challenges in photovoltaics. *physica status solidi (a)*, 202(15):2928–2942, 2005.

[285] BG Gribov and KV Zinov'ev. Preparation of high-purity silicon for solar cells. *Inorganic materials*, 39(7):653–662, 2003.

[286] Peter Woditsch and Wolfgang Koch. Solar grade silicon feedstock supply for pv industry. *Solar energy materials and solar cells*, 72(1):11–26, 2002.

[287] AFB Braga, SP Moreira, PR Zampieri, JMG Bacchin, and PR Mei. New processes for the production of solar-grade polycrystalline silicon: A review. *Solar energy materials and solar cells*, 92(4):418–424, 2008.

[288] Yulia Meteleva-Fischer, Shadia Ikhmayies, Arief Suriadi Budiman, Prabhat Tripathy, and Guy Fredrickson. Preparation of solar grade silicon precursor by silicon dioxide electrolysis in molten salts. In *EPD Congress 2015*, page 209. John Wiley & Sons, 2015.

[289] Peter Schubert, Jeffrey Williams, Thomas Bundorf, and Alex Di Sciullo Jones. Advances in extraction of oxygen and silicon from lunar regolith. In *AIAA SPACE 2010 Conference & Exposition*, page 8703, 2010.

[290] D Bhogeswara Rao, UV Choudary, TE Erstfeld, Richard J Williams, and YA Chang. Extraction processes for the production of aluminum, titanium, iron, magnesium, and oxygen and nonterres-

trial sources. 1979.

[291] Derek Fray. Molten salts and energy related materials. *Faraday Discussions*, 2016.

[292] Carsten Schwandt, James A Hamilton, Derek J Fray, and Ian A Crawford. The production of oxygen and metal from lunar regolith. *Planetary and Space Science*, 74(1):49–56, 2012.

[293] Aimin Liu, Zhongning Shi, Junli Xu, Xianwei Hu, Bingliang Gao, and Zhaowen Wang. Preparation of al-si master alloy by electrochemical reduction of volcanic rock in cryolite molten salt. *JOM*, 68(6):1518–1524, 2016.

[294] KS Mohandas and DJ Fray. Ffc cambridge process and removal of oxygen from metal-oxygen systems by molten salt electrolysis: an overview. *Trans. Indian Inst. Met*, 57(6):579–592, 2004.

[295] Samuel S Schreiner, Jeffrey A Hoffman, Gerald B Sanders, and Kristopher A Lee. Integrated modeling and optimization of lunar in-situ resource utilization systems. In *2015 IEEE Aerospace Conference*, pages 1–11. IEEE, 2015.

[296] Laurent Sibille, Donald R Sadoway, Aislinn Sirk, Prabhat Tripathy, Orlando Melendez, Evan Standish, Jesus A Dominguez, Doru M Stefanescu, Peter A Curreri, and Sophie Poizeau. Recent advances in scale-up development of molten regolith electrolysis for oxygen production in support of a lunar base. In *Proc., 47th AIAA Aerospace Sciences Meeting*, 2009.

[297] PA Curreri, EC Ethridge, SB Hudson, TY Miller, RN Grugel, S Sen, and DR Sadoway. Process demonstration for lunar in situ resource utilization-molten oxide electrolysis (msfc independent research and development project no. 5-81). 2006.

[298] Laurent Sibille and Jesus A Dominguez. Joule-heated molten regolith electrolysis reactor concepts for oxygen and metals production on the moon and mars. In *50th AIAA Aerospace Sciences Meeting including the New Horizons Forum and Aerospace Exposition*, volume 2, page 6, 2012.

[299] Samuel S Schreiner, Laurent Sibille, Jesus Dominguez, J Hoffman, G Sanders, and A Sirk. Development of a molten regolith electrolysis reactor model for lunar in-situ resource utilization. In *8th Symposium on Space Resource Utilization*, page 1180, 2015.

[300] Samuel S Schreiner, Laurent Sibille, Jesus A Dominguez, and Jeffrey A Hoffman. A parametric sizing model for molten regolith electrolysis reactors to produce oxygen on the moon. *Advances in Space Research*, 57(7):1585–1603, 2016.

[301] Aislinn H Sirk, Donald R Sadoway, and Laurent Sibille. Direct electrolysis of molten lunar regolith for the production of oxygen and metals on the moon. *ECS Transactions*, 28(6):367–373, 2010.

[302] Donald R Sadoway, Aislinn Sirk, Laurent Sibille, Orlando Melendez, Dale Lueck, Peter Curreri, Jesus Dominquez, and Jonathan Whitlow. Advances in molten oxide electrolysis for the production of oxygen and metals from lunar regolith. 2008.

[303] Larry A Haskin. Oxygen production by electrolysis of molten lunar regolith. 1990.

[304] Mark Steven Paley, Laurel J Karr, and Peter Curreri. Oxygen production from lunar regolith using ionic liquids. 2009.

[305] Steve Trigwell, James Captain, Kyle Weis, and Jacqueline Quinn. Electrostatic beneficiation of lunar regolith: Applications in in situ resource utilization. *Journal of Aerospace Engineering*, 26(1):30–36, 2012.

[306] Steve Trigwell, John E Lane, James G Captain, Kyle H Weis, Jacqueline W Quinn, and Fumiya Watanabe. Quantification of efficiency of beneficiation of lunar regolith. *Particulate Science and Technology*, 31(1):45–50, 2013.

[307] Zoltán Sternovsky, Scott Robertson, Amanda Sickafoose, Joshua Colwell, and Mihály Horányi. Contact charging of lunar and martian dust simulants. *Journal of Geophysical Research: Planets*, 107(E11), 2002.

[308] Frank B Gross. Jsc mars-1 martian regolith simulant particle-charging experiments in the presence of ac and dc corona fields. *Journal of electrostatics*, 58(1):147–156, 2003.

[309] Frank B Gross, Sasha B Grek, Carlos I Calle, and Rupert U Lee. Jsc mars-1 martian regolith simulant particle charging experiments in a low pressure environment. *Journal of Electrostatics*, 53(4):257–266, 2001.

[310] Subhayu Sen, Elizabeth Schofield, Scott O'Dell, and Chandra S Ray. A viable scheme for elemental extraction and purification using in-situ planetary re-

sources. In *1 st Space Exploration Conference: Continuing the Voyage of Discovery*, pages 1–4, 2005.

[311] Subhayu Sen, Chandra S Ray, and Ramana G Reddy. Processing of lunar soil simulant for space exploration applications. *Materials Science and Engineering: A*, 413:592–597, 2005.

[312] Viorel Badescu. *Moon: Prospective Energy and Material Resources*. Springer Science & Business Media, 2012.

[313] Kenji Itaka, Takuya Ogasawara, Abderahmane Boucetta, Rabie Benioub, Masatomo Sumiya, Takuya Hashimoto, Hideomi Koinuma, and Yasubumi Furuya. Direct carbothermic silica reduction from purified silica to solar-grade silicon. In *Journal of Physics: Conference Series*, volume 596, page 012015. IOP Publishing, 2015.

[314] Sunhwan Hwang, Joongwon Lee, Ung Gi Hong, Jeong Gil Seo, Ji Chul Jung, Dong Jun Koh, Hyojun Lim, Changdae Byun, and In Kyu Song. Methane production from carbon monoxide and hydrogen over nickel–alumina xerogel catalyst: Effect of nickel content. *Journal of Industrial and Engineering Chemistry*, 17(1):154–157, 2011.

[315] Xiaohan Wan, Guangqing Zhang, Oleg Ostrovski, and Hal Aral. Carbothermal reduction of silica in nitrogen and nitrogen-hydrogen mixture. 2013.

[316] Robert J Gustafson, Brant C White, Michael J Fidler, and Anthony C Muscatello. Demonstrating the solar carbothermal reduction of lunar regolith to produce oxygen. *paper AIAA*, 1163:4–7, 2010.

[317] Ramaswamy Balasubramaniam, Suleyman Gokoglu, and Uday Hegde. Modeling of melt growth during carbothermal processing of lunar regolith. In *50th AIAA Aerospace Sciences Meeting including the New Horizons Forum and Aerospace Exposition*, page 638, 2012.

[318] R Balasubramaniam, S Gokoglu, and Uday Hegde. The reduction of lunar regolith by carbothermal processing using methane. *International Journal of Mineral Processing*, 96(1):54–61, 2010.

[319] Robert J Gustafson, Brant C White, and Michael J Fidler. Demonstrating carbothermal reduction of lunar regolith using concentrated solar energy. In *AIAA-2009-6476, AIAA SPACE 2009 Conference & Exposition, Pasadena, California, September*, 2009.

[320] R Balasubramaniam, U Hegde, and S Gokoglu. Carbothermal processing of lunar regolith using methane. 2009.

[321] Siu Chung Wong. *Kinetics of carbothermic reduction of natural aluminosilicates*. PhD thesis, University of British Columbia, 1995.

[322] Edgardo Santiago-Maldonado, Janine Captain, Robert Devor, and Jeremy Gleaton. Creating methane from plastic: Recycling at a lunar outpost. In *48th AIAA Aerospace Sciences Meeting Including the New Horizons Forum and Aerospace Expostion*, pages 2010–1551, 2010.

[323] Carlton C Allen, Richard V Morris, and David S McKay. Experimental reduction of lunar mare soil and volcanic glass. *Journal of Geophysical Research: Planets*, 99(E11):23173–23185, 1994.

[324] Julie Kleinhenz, Zengguang Yuan, Kurt Sacksteder, and John Caruso. Development of a reactor for the extraction of oxygen and volatiles from lunar regolith. In *47th AIAA Aerospace Sciences Meeting including The New Horizons Forum and Aerospace Exposition*, page 1203, 2009.

[325] Uday Hegde, Ramaswamy Balasubramaniam, and Suleyman Gokoglu. Analysis of water extraction from lunar regolith. In *50th AIAA Aerospace Sciences Meeting including the New Horizons Forum and Aerospace Exposition*, page 634, 2012.

[326] Edwin Ethridge and William Kaukler. Microwave extraction of water from lunar regolith simulant. In *AIP Conference Proceedings*, volume 880, pages 830–837. AIP, 2007.

[327] Peter J Williams and Thomas Eugene Cloete. Microbial community study of the iron ore concentrate of the sishen iron ore mine, south africa. *World Journal of Microbiology and Biotechnology*, 24(11):2531–2538, 2008.

[328] P Delvasto, A Ballester, JA Muñoz, F González, ML Blázquez, and C García-Balboa. Exploring the possibilities of biological beneficiation of iron-ores: The phosphorus problem. In *Proceedings of the 15th Steelmaking Conference, 5th Ironmaking Conference & 1st Environment and Recycling Symposium IAS*, pages 7–10, 2005.

[329] Bonnie P Dalton and Frank F Roberto. Lunar regolith biomining: workshop re-

port. 2008.

[330] Jaroslav Šuba and Darina Štyriaková. Iron minerals removal from different quartz sands. *Procedia Earth and Planetary Science*, 15:849–854, 2015.

[331] Katrin Pollmann, Sabine Kutschke, Sabine Matys, Sophias Kostudis, Stefanie Hopfe, and Johannes Raff. Novel biotechnological approaches for the recovery of metals from primary and secondary resources. *Minerals*, 6(2):54, 2016.

[332] Iveta Štyriaková, Alexandra Bekényiová, Darina Štyriaková, Katarína Jablonovská, and Igor Štyriak. Second pilot-plant bioleaching verification of the iron removal from quartz sands. *Procedia Earth and Planetary Science*, 15:861–865, 2015.

[333] Nalini Jain and DK Sharma. Biohydrometallurgy for nonsulfidic minerals-a review. *Geomicrobiology Journal*, 21(3):135–144, 2004.

[334] Geoffrey A Landis. Materials refining on the moon. *Acta Astronautica*, 60(10):906–915, 2007.

[335] Wolfgang Seboldt, Stephan Lingner, Stephan Hoernes, Wolfgang Grimmeisen, Reinhard Lekies, Ralf Herkelmann, Donald M Burt, JS Lewis, et al. Lunar oxygen extraction using fluorine. *Resources of Near Earth Space, U. Arizona Press, Tucson, AZ*, pages 129–148, 1993.

[336] J Hofstetter, JF Lelièvre, C Del Cañizo, and A del Luque. Acceptable contamination levels in solar grade silicon: From feedstock to solar cell. *Materials Science and Engineering: B*, 159:299–304, 2009.

[337] AA Istratov, T Buonassisi, MD Pickett, M Heuer, and ER Weber. Control of metal impurities in "dirty" multicrystalline silicon for solar cells. *Materials Science and Engineering: B*, 134(2-3):282–286, 2006.

[338] Noriyoshi Yuge, Kazuhiro Hanazawa, and Yoshiei Kato. Removal of metal impurities in molten silicon by directional solidification with electron beam heating. *Materials transactions*, 45(3):850–857, 2004.

[339] Buhle Sinaye Xakalashe. Removal of phosphorus from silicon melts by vacuum refining. Master's thesis, Institutt for materialteknologi, 2011.

[340] Jafar Safarian, Gabriella Tranell, and Merete Tangstad. Processes for upgrading metallurgical grade silicon to solar grade silicon. *Energy Procedia*, 20:88–97, 2012.

[341] DR Askeland. The science and engineering of materials pws-kent, 1989.

[342] David RH Jones and Michael F Ashby. *Engineering materials 2: an introduction to microstructures, processing and design*. Butterworth-Heinemann, 2005.

[343] BD Fabes, WH Poisl, D Allen, M Minitti, S Hawley, and T Beck. Melt-processing of lunar ceramics. 1992.

[344] Matthew Kallerud, Brian Nguyen, Timothy Paladin, and Anthony Wilson. In-situ resource utilization: Investigation of melted lunar regolith simulant jsc-1a. In *Proceedings of the Wisconsin Space Conference*, 2011.

[345] CA McLemore, JC Fikes, KS McCarley, JE Good, JP Kennedy, and SD Gilley. From lunar regolith to fabricated parts: technology developments and the utilization of moon dirt. In *Earth & Space 2008: Engineering, Science, Construction, and Operations in Challenging Environments*, pages 1–11. 2008.

[346] Athanasios Goulas, Jon GP Binner, Russell A Harris, and Ross J Friel. Assessing extraterrestrial regolith material simulants for in-situ resource utilisation based 3d printing. *Applied Materials Today*, 6:54–61, 2017.

[347] Roland Antonius Gabrielli, Jürgen Seelmann, Agnes Großmann, Georg Herdrich, Stefanos Fasoulas, Peter Schnauffer, Peter Middendorf, Miranda Fateri, and Andreas Gebhardt. System architecture of a lunar industry plant using regolith. In *30th International Symposium on Space Technology and Science, Kobe, Japan*, pages 6–10, 2015.

[348] Robert Mueller, Ivan Townsend, James Mantonvanni, and Philip Metzger. Evolution of regilith feed systems for lunar isru o2 production plants. In *48th AIAA Aerospace Sciences Meeting Including the New Horizons Forum and Aerospace Exposition*, page 1547, 2010.

[349] John Klein, Michael Stern, Giorgia Franchin, Markus Kayser, Chikara Inamura, Shreya Dave, James C Weaver, Peter Houk, Paolo Colombo, Maria Yang, et al. Additive manufacturing of optically transparent glass. *3D Printing and Additive Manufacturing*, 2(3):92–105, 2015.

[350] John Klein, Michael Stern, Giorgia Franchin, Markus Kayser, Chikara Inamura, Shreya Dave, James C Weaver, Peter Houk, Paolo Colombo, Maria Yang, et al. Additive manufacturing of optically transparent glass. mathesis, MIT, 2015.

[351] Robert P Mueller, Laurent Sibille, Paul E Hintze, Thomas C Lippitt, James G Mantovani, Matthew W Nugent, and Ivan I Townsend. Additive construction using basalt regolith fines. In *Earth and Space 2014*, pages 394–403. 2014.

[352] Andreas Gebhardt and Miranda Fateri. 3d printing and its applications, 2015.

[353] Xiling Yao, Seung Ki Moon, and Guijun Bi. Multidisciplinary design optimization to identify additive manufacturing resources in customized product development. *Journal of Computational Design and Engineering*, 2016.

[354] F Ceccanti, E Dini, X De Kestelier, V Colla, and L Pambaguian. 3d printing technology for a moon outpost exploiting lunar soil. In *61st International Astronautical Congress, Prague, CZ, IAC-10-D3*, volume 3, pages IAC–10–D3.3.5 Page 1 – 9, 2010.

[355] Niki J Werkheiser, Michael Fiske, Jennifer Edmunson, and Behrokh Khoshnevis. On the development of additive construction technologies for application to development of lunar/martian surface structures using in-situ materials. In *AIAA SPACE 2015 Conference and Exposition*, page 4451, 2015.

[356] Robert P Mueller, Scott Howe, Dennis Kochmann, Hisham Ali, Christian Andersen, Hayden Burgoyne, Wesley Chambers, Raymond Clinton, Xavier De Kestellier, Keye Ebelt, et al. Automated additive construction (aac) for earth and space using in-situ resources. In *Proceedings of the Fifteenth Biennial ASCE Aerospace Division International Conference on Engineering, Science, Construction, and Operations in Challenging Environments (Earth & Space 2016)*. American Society of Civil Engineers, 2016.

[357] Shannon L Taylor, Adam E Jakus, Katie D Koube, Amaka J Ibeh, Nicholas R Geisendorfer, Ramille N Shah, and David C Dunand. Sintering of microtrusses created by extrusion-3d-printing of lunar regolith inks. *Acta Astronautica*, 143:1–8, 2018.

[358] Athanasios Goulas, Jon GP Binner, Daniel S Engstrøm, Russell A Harris, and Ross J Friel. Mechanical behaviour of additively manufactured lunar regolith simulant components. *Proceedings of the Institution of Mechanical Engineers, Part L: Journal of Materials: Design and Applications*, 233(8):1629–1644, 2019.

[359] Adam E Jakus, Katie D Koube, Nicholas R Geisendorfer, and Ramille N Shah. Robust and elastic lunar and martian structures from 3d-printed regolith inks. *Scientific reports*, 7:44931, 2017.

[360] Athanasios Goulas, Russell A Harris, and Ross J Friel. Additive manufacturing of physical assets by using ceramic multicomponent extra-terrestrial materials. *Additive Manufacturing*, 10:36–42, 2016.

[361] A Cowley, J Salter, K Gutsche, L Barad, M Pedrazanni, M Fateri, and A Meurisse. In-situ resource-driven approaches to additive manufacturing using lunar regolith simulant. In *Annual Meeting of the Lunar Exploration Analysis Group*, volume 1960, pages No. 1960, id.5038, 2016.

[362] M Fateri, A Gebhardt, and AX Lester Bok. Investigation of the feasibility of mobile additive manufacturing systems powered by photovoltaic modules. *Additive Manufacturing (AM): Emerging Technologies, Applications and Economic Implications. Nova Publishers*, page 154, 2015.

[363] M Fateri, A Gebhardt, RA Gabrielli, G Herdrich, S Fasoulas, A Großmann, P Schnauffer, and P Middendorf. Additive manufacturing of lunar regolith for extraterrestrial industry plant, conference contribution for the 30th ists. In *34th IEPC & 6th NSAT Joint Conference, Kobe, Japan*, 2015.

[364] Behrokh Khoshnevis and Jing Zhang. Selective separation sintering (sss)-an additive manufacturing approach for fabrication of ceramic and metallic parts with application in planetary construction. In *AIAA SPACE 2015 Conference and Exposition*, page 4450, 2015.

[365] A Scott Howe, Brian Wilcox, Chris McQuin, David Mittman, Julie Townsend, Raul Polit-Casillas, and Todd Litwin. Modular additive construction using native materials. In *Earth and Space 2014*, pages 301–312. 2014.

[366] Luke Roberson, Paul Hintze, and Greg O'Connor. A conceptual study for the autonomous direct forming of lunar regolith into flexlock^{TM} geomats for lunar surface operations. In *47th AIAA Aerospace Sciences Meeting including The New Horizons Forum and Aerospace Exposition*, page 1013, 2009.

[367] Eric J Faierson, Kathryn V Logan,

Brian K Stewart, and Michael P Hunt. Demonstration of concept for fabrication of lunar physical assets utilizing lunar regolith simulant and a geothermite reaction. *Acta Astronautica*, 67(1-2):38–45, 2010.

[368] P Hartlieb, M Toifl, F Kuchar, R Meisels, and T Antretter. Thermo-physical properties of selected hard rocks and their relation to microwave-assisted comminution. *Minerals Engineering*, 91:34–41, 2016.

[369] J Alexander and BSM Augustine. The effect of combined thermal and microwave curing on mechanical properties and surface hardness of basalt/epoxy composites. *Middle-East Journal of Scientific Research*, 23(2):347–349, 2015.

[370] P Nekoovaght, N Gharib, F Hassani, et al. The behavior of rocks when exposed to microwave radiation. In *13th ISRM International Congress of Rock Mechanics*. International Society for Rock Mechanics, 2015.

[371] Wei Li, Jia Wei, Wei Wang, Dawei Hu, Yukun Li, and Jianguo Guan. Ferrite-based metamaterial microwave absorber with absorption frequency magnetically tunable in a wide range. *Materials & Design*, 110:27–34, 2016.

[372] AR Batchelor, DA Jones, S Plint, and SW Kingman. Deriving the ideal ore texture for microwave treatment of metalliferous ores. *Minerals Engineering*, 84:116–129, 2015.

[373] S Chandrasekaran, Tanmay Basak, and S Ramanathan. Experimental and theoretical investigation on microwave melting of metals. *Journal of Materials Processing Technology*, 211(3):482–487, 2011.

[374] Chenhui Liu, Libo Zhang, Jinhui Peng, Chandrasekar Srinivasakannan, Bingguo Liu, Hongying Xia, Junwen Zhou, and Lei Xu. Temperature and moisture dependence of the dielectric properties of silica sand. *Journal of Microwave Power and Electromagnetic Energy*, 47(3):199–209, 2013.

[375] R Subasri, Tom Mathews, OM Sreedharan, and VS Raghunathan. Microwave processing of sodium beta alumina. *Solid State Ionics*, 158(1):199–204, 2003.

[376] Joel D Katz. Microwave sintering of ceramics. *Annual Review of Materials Science*, 22(1):153–170, 1992.

[377] KJ Rao and PD Ramesh. Use of microwaves for the synthesis and processing of materials. *Bulletin of Materials Science*, 18(4):447–465, 1995.

[378] Ferri Hassani, Pejman M Nekoovaght, and Nima Gharib. The influence of microwave irradiation on rocks for microwave-assisted underground excavation. *Journal of Rock Mechanics and Geotechnical Engineering*, 8(1):1–15, 2016.

[379] R Meisels, M Toifl, P Hartlieb, F Kuchar, and T Antretter. Microwave propagation and absorption and its thermo-mechanical consequences in heterogeneous rocks. *International journal of mineral processing*, 135:40–51, 2015.

[380] Milithza Silva, Kurt Kyser, and Diane Beauchemin. Enhanced flow injection leaching of rocks by focused microwave heating with in-line monitoring of released elements by inductively coupled plasma mass spectrometry. *Analytica chimica acta*, 584(2):447–454, 2007.

[381] Madhuchhanda Bhattacharya and Tanmay Basak. A review on the susceptor assisted microwave processing of materials. *Energy*, 97:306–338, 2016.

[382] TL Alford, Mandar J Gadre, Rajitha NP Vemuri, and N David Theodore. Susceptor-assisted microwave annealing for activation of arsenic dopants in silicon. *Thin Solid Films*, 520(13):4314–4320, 2012.

[383] M Barmatz, D Steinfeld, M Anderson, and D Winterhalter. 3d microwave print head approach for processing lunar and mars regolith. In *Lunar and Planetary Science Conference*, volume 45, page 1137, 2014.

[384] Vibha Srivastava, Sungwoo Lim, and Mahesh Anand. Microwave processing of lunar soil for supporting longer-term surface exploration on the moon. *Space Policy*, 37:92–96, 2016.

[385] Lawrence A Taylor and Thomas T Meek. Microwave sintering of lunar soil: properties, theory, and practice. *Journal of Aerospace Engineering*, 18(3):188–196, 2005.

[386] A Cowley, T Haefner, JC Beltzung, and A Meurisse. Spaceship eac–fostering activities relevant to lunar exploration and isru. *LPI Contributions*, 1863:2037, 2015.

[387] Shawn Allan, Jeffrey Braunstein, Inessa Baranova, Nicholas Vandervoort, Morgana Fall, and Holly Shulman. Computational modeling and experimental microwave processing of jsc-1a lunar simu-

lant. *Journal of Aerospace Engineering*, 26(1):143–151, 2012.

[388] Shawn M Allan, Brandon J Merritt, Brittany F Griffin, Paul E Hintze, and Holly S Shulman. High-temperature microwave dielectric properties and processing of jsc-1ac lunar simulant. *Journal of Aerospace Engineering*, 26(4):874–881, 2013.

[389] Bernhard Gutmann, David Obermayer, Benedikt Reichart, Bojana Prekodravac, Muhammad Irfan, Jennifer M Kremsner, and C Oliver Kappe. Sintered silicon carbide: A new ceramic vessel material for microwave chemistry in single-mode reactors. *Chemistry–A European Journal*, 16(40):12182–12194, 2010.

[390] E Wuchina, E Opila, M Opeka, W Fahrenholtz, and I Talmy. Uhtcs: ultra-high temperature ceramic materials for extreme environment applications. *the electrochemical society interface*, 16(4):30, 2007.

[391] N Standish and W Huang. Microwave application in carbothermic reduction of iron ores. *ISIJ international*, 31(3):241–245, 1991.

[392] MD Viramgama and MC Karia. Study and investigation of influence of process parameters for selective laser melting-a review. 2016.

[393] Miranda Fateri and Andreas Gebhardt. Process parameters development of selective laser melting of lunar regolith for on-site manufacturing applications. *International Journal of Applied Ceramic Technology*, 12(1):46–52, 2015.

[394] Miranda Fateri, Andreas Gebhardt, and Maziar Khosravi. Experimental investigation of selective laser melting of lunar regolith for in-situ applications. In *ASME 2013 International Mechanical Engineering Congress and Exposition*. American Society of Mechanical Engineers Digital Collection, 2014.

[395] Vamsi Krishna Balla, Luke B Roberson, Gregory W O'Connor, Steven Trigwell, Susmita Bose, and Amit Bandyopadhyay. First demonstration on direct laser fabrication of lunar regolith parts. *Rapid Prototyping Journal*, 18(6):451–457, 2012.

[396] Miranda Fateri and Andreas Gebhardt. Selective laser melting of soda-lime glass powder. *International Journal of Applied Ceramic Technology*, 12(1):53–61, 2015.

[397] Athanasios Goulas, Daniel S Engstrom, Ross J Friel, and Russell A Harris. Investigating the additive manufacture of extra-terrestrial materials. 2016.

[398] Shuai Chang, Liqun Li, Li Lu, and Jerry Fuh. Selective laser sintering of porous silica enabled by carbon additive. *Materials*, 10(11):1313, 2017.

[399] Alessio Alexiadis, Federico Alberini, and Marit E Meyer. Geopolymers from lunar and martian soil simulants. *Advances in Space Research*, 2016.

[400] Carlos Montes, Kaylin Broussard, Matthew Gongre, Neven Simicevic, Johanna Mejia, Jessica Tham, Erez Allouche, and Gabrielle Davis. Evaluation of lunar regolith geopolymer binder as a radioactive shielding material for space exploration applications. *Advances in Space Research*, 56(6):1212–1221, 2015.

[401] Gabrielle Davis. Preparation of lunar regolith based geopolymer cement under heat and vacuum. 2016.

[402] Alessio Alexiadis, Federico Alberini, and Marit E Meyer. Geopolymers from lunar and martian soil simulants. *Advances in Space Research*, 59(1):490–495, 2017.

[403] Kai-tuo Wang, Qing Tang, Xue-min Cui, Yan He, and Le-ping Liu. Development of near-zero water consumption cement materials via the geopolymerization of tektites and its implication for lunar construction. *Scientific Reports*, 6, 2016.

[404] Vivek Dhand, Garima Mittal, Kyong Yop Rhee, Soo-Jin Park, and David Hui. A short review on basalt fiber reinforced polymer composites. *Composites Part B: Engineering*, 73:166–180, 2015.

[405] V Fiore, T Scalici, G Di Bella, and A Valenza. A review on basalt fibre and its composites. *Composites Part B: Engineering*, 74:74–94, 2015.

[406] Patrick Weichand and Rainer Gadow. Basalt fibre reinforced sioc-matrix composites: Manufacturing technologies and characterisation. *Journal of the European Ceramic Society*, 35(14):4025–4030, 2015.

[407] S Sen, E Schofield, JS O'Dell, L Deka, and S Pillay. The development of a multifunctional composite material for use in human space exploration beyond low-earth orbit. *JOM*, 61(1):23–31, 2009.

[408] Alexandre Meurisse, A Makaya, C Willsch, and M Sperl. Solar 3d printing of lunar regolith. *Acta Astronautica*, 152:800–810, 2018.

[409] D Urbina, H Madakashira, J Salini, S Govindaraj, R Bjoerstad, J Gancet, M Sperl, A Meurisse, M Fateri, B Imhof,

et al. Robotic prototypes for the solar sintering of regolith on the lunar surface developed within the regolight project. In *68th International Astronautical Congress (IAC), Adelaide, Australia*, pages 25–29, 2017.

[410] Luana Varela Miranda, Julio R Valdes, and Douglas D Cortes. Solar bricks for lunar construction. *Construction and Building Materials*, 139:241–246, 2017.

[411] Barbara Imhof, Diego Urbina, Peter Weissc, and Matthias Sperld. Advancing solar sintering for building a base on the moon. In *68th International Astronautical Congress (IAC), Adelaide, Australia*, 2017.

[412] John C Fikes, Joe T Howell, Harold P Gerrish, and Stephen L Patrick. Solar concentrator demonstrator for lunar regolith processing. 2008.

[413] Takashi Nakamura and Constance L Senior. Solar thermal power for lunar materials processing. *Journal of Aerospace Engineering*, 21(2):91–101, 2008.

[414] JR Pitts, CL Fields, JT Stanley, and BL Pallon. Materials processing using highly concentrated solar radiation. In *Proceedings of the 25th Intersociety Energy Conversion Engineering Conference*, volume 6, pages 262–267. IEEE, 1990.

[415] J Mackenzie and R Claridge. Glass and ceramics from lunar materials. In *4th Conference on Space Manufacturing Facilities Princeton University*, page 1381, 1979.

[416] DT Vaniman, TT Meek, and RD Blake. Fusing lunar materials with microwave energy. part ii: Melting of a simulated glassy apollo 11 soil. In *Lunar and Planetary Science Conference*, volume 17, pages 911–912, 1986.

[417] M.P. Groover. *Fundamentals of Modern Manufacturing: Materials, Processes, and Systems*. John Wiley & Sons, 2010.

[418] Mariona Tarrago, Irene Royo, Maite Garcia-Valles, and Salvador Martínez. Nucleation and crystallization of ca doped basaltic glass for the production of a glass-ceramic material. In *EGU General Assembly Conference Abstracts*, volume 18, page 15165, 2016.

[419] Gamal A Khater, Mamduh O Abu Safiah, and Esmat MA Hamzawy. Augite-anorthite glass-ceramics from residues of basalt quarry and ceramic wastes. *Processing and application of ceramics*, 9(2):117–123, 2015.

[420] Suna Cetin, Mauro Marangoni, and Enrico Bernardo. Lightweight glass–ceramic tiles from the sintering of mining tailings. *Ceramics International*, 41(4):5294–5300, 2015.

[421] MY Hassaan, HA Saudi, Hatem MH Saad, AG Mostafa, MA Ahmed, Y Iida, S Kubuki, and T Nishida. Structural study of glass and glass ceramics prepared with egyptian basalt. *Silicon*, 7(4):383–391, 2015.

[422] AS Pinheiro, ZM da Costa, MJV Bell, V Anjos, ST Reis, and CS Ray. Thermal characterization of glasses prepared from simulated compositions of lunar soil jsc-1a. *Journal of Non-Crystalline Solids*, 359:56–59, 2013.

[423] SQS Ahmad, RJ Hand, and C Wieckert. Use of concentrated radiation for solar powered glass melting experiments. *Solar Energy*, 109:174–182, 2014.

[424] Wolfram Holand and George H Beall. *Glass ceramic technology*. John Wiley & Sons, 2012.

[425] Charles R Kurkjian and William R Prindle. Perspectives on the history of glass composition. *J. Am. Ceram. Soc.*, 81(4):795–813, 1998.

[426] J Hlavae. Technology of glass and ceramics. 1983.

[427] P. Beveridge, I. Doménech, and E.P. Miró. *Warm Glass: A Complete Guide to Kiln-forming Techniques : Fusing, Slumping, Casting*. Lark Books, 2005.

[428] P.L. Pinnet. *Laboratory Scientific Glass-blowing: A Practical Training Method*. 2017.

[429] O. Uusitalo. *Float Glass Innovation in the Flat Glass Industry*. SpringerBriefs in Applied Sciences and Technology. Springer International Publishing, 2014.

[430] John S Sieger. Chemical characteristics of float glass surfaces. *Journal of Non-Crystalline Solids*, 19:213–220, 1975.

[431] Xiangqian Peng, Youping Chen, Wenyong Yu, Zude Zhou, and Guodong Sun. An online defects inspection method for float glass fabrication based on machine vision. *The International Journal of Advanced Manufacturing Technology*, 39(11):1180–1189, 2008.

[432] RO Lokken, LA Chick, and LE Thomas. Development and characterization of basalt-glass ceramics for the immobilization of transuranic wastes. Technical report, Pacific Northwest Lab., Richland,

WA (USA), 1982.

[433] Xiaoju Guo, John C Mauro, Marcel Potuzak, and Yuanzheng Yue. Structural relaxation in annealed hyperquenched basaltic glasses: Insights from calorimetry. *Journal of Non-Crystalline Solids*, 358(11):1356–1361, 2012.

[434] G Pareschi, E Giro, R Banham, S Basso, D Bastieri, R Canestrari, G Ceppatelli, O Citterio, M Doro, M Ghigo, et al. Glass mirrors by cold slumping to cover 100 m2 of the magic ii cherenkov telescope reflecting surface. In *SPIE Astronomical Telescopes+ Instrumentation*, pages 70180W–70180W. International Society for Optics and Photonics, 2008.

[435] The University of Arizona's Richard F. Caris Mirror Laborator. Frequently asked questions about mirror production. Online, 2016. Last accessed 25.09.2019. URL: `https://mirrorlab.arizona.edu/content/faq`.

[436] D. Korsch. *Reflective Optics*. Elsevier Science, 2012.

[437] E Hecht. Optics. 565p, 1974.

[438] J Eliasson and R Sandström. Applications of aluminium matrix composites. In *Key Engineering Materials*, volume 104, pages 3–36. Trans Tech Publ, 1995.

[439] Alexander E Kaplan. Metallic nanolayers: a sub-visible wonderland of optical properties. *JOSA B*, 35(6):1328–1340, 2018.

[440] R Steinkopf, A Gebhardt, S Scheiding, M Rohde, O Stenzel, S Gliech, V Giggel, H Löscher, G Ullrich, P Rucks, et al. Metal mirrors with excellent figure and roughness. In *Optical Fabrication, Testing, and Metrology III*, volume 7102, page 71020C. International Society for Optics and Photonics, 2008.

[441] J Domaradzki, D Kaczmarek, M Mazur, D Wojcieszak, J Halarewicz, S Glodek, and P Domanowski. Investigations of optical and surface properties of ag single thin film coating as semitransparent heat reflective mirror. *Materials Science-Poland*, 34(4):747–753, 2016.

[442] Robert Lugolole and Sam Kinyera Obwoya. The effect of thickness of aluminium films on optical reflectance. *Journal of Ceramics*, 2015, 2015.

[443] Joseph R Davis, Joseph R Davis, et al. *Aluminum and aluminum alloys*. ASM international, 1993.

[444] Mehreen Gul, Yash Kotak, and Tariq Muneer. Review on recent trend of solar photovoltaic technology. *Energy Exploration & Exploitation*, 34(4):485–526, 2016.

[445] Sheila Bailey and Ryne Raffaelle. Space solar cells and arrays. *Handbook of photovoltaic science and engineering*, pages 365–401, 2011.

[446] Alexandre Freundlich, Alex Ignatiev, Charles Horton, Michael Duke, P Curreri, and Laurent Sibille. Manufacture of solar cells on the moon. In *Conference Record of the Thirty-first IEEE Photovoltaic Specialists Conference, 2005.*, pages 794–797. IEEE, 2005.

[447] Leonhard Stiny. Grundlagen der halbleiter. In *Aktive elektronische Bauelemente*, pages 5–38. Springer, 2016.

[448] A. McEvoy, L. Castaner, and T. Markvart. *Solar Cells: Materials, Manufacture and Operation*. Elsevier Science, 2012. p. 4.

[449] Charles D Brown. *Elements of spacecraft design*. Aiaa, 2002.

[450] R. Brendel. *Thin-Film Crystalline Silicon Solar Cells: Physics and Technology*. Wiley, 2011.

[451] Karl Young. Do solar panels collect energy from the whole light spectrum or just focus on the red? Online, 2016. Last accessed 25.09.2019. URL: `https://www.quora.com/Do-solar-panels-collect-energy-from-the-whole-light-spectrum-or-just-focus-on-the-red`.

[452] National Renewable Energy Laboratory. Best research-cell efficiencies. Online, 2019. last accessed 25.09.2019. URL: `https://www.nrel.gov/pv/assets/pdfs/best-research-cell-efficiencies.20190802.pdf`.

[453] Martin A Green, Keith Emery, Yoshihiro Hishikawa, Wilhelm Warta, and Ewan D Dunlop. Solar cell efficiency tables (version 47). *Progress in Photovoltaics: Research and Applications*, 24(NREL/JA-5J00-65643), 2016.

[454] Aarohi Vijh. Lightweight, high-performance solar cells for high power-to-weight and deployable solar arrays. In *AIAA SPACE 2016*, page 5283. 2016.

[455] Daniel Ash Lamb, Stuart JC Irvine, Andrew James Clayton, Vincent Barrioz, Giray Kartopu, Mark A Baker, CI Underwood, Rossana Grilli, Rick Kimber, and James Hall. Lightweight and low-cost thin film photovoltaics for large area extra-

terrestrial applications. *IET Renewable Power Generation*, 9(5):420–423, 2015.

[456] PT Chiu, DC Law, SB Singer, D Bhusari, A Zakaria, XQ Liu, S Mesropian, and NH Karam. High performance 5j and 6j direct bonded (sbt) space solar cells. In *Photovoltaic Specialist Conference (PVSC), 2015 IEEE 42nd*, pages 1–3. IEEE, 2015.

[457] GFX Strobl, L Ebel, D Fuhrmann, W Guter, R Kern, V Khorenko, W Köstler, and M Meusel. Development of lightweight space solar cells with 30% efficiency at end-of-life. In *2014 IEEE 40th Photovoltaic Specialist Conference (PVSC)*, pages 3595–3600. IEEE, 2014.

[458] Daniel C Law, KM Edmondson, N Siddiqi, A Paredes, RR King, G Glenn, E Labios, MH Haddad, TD Isshiki, and NH Karam. Lightweight, flexible, high-efficiency iii-v multijunction cells. In *Photovoltaic Energy Conversion, Conference Record of the 2006 IEEE 4th World Conference on*, volume 2, pages 1879–1882. IEEE, 2006.

[459] Christophe Dang Ngoc Chan. Schematic of allotropic forms of silicon horizontal plain. Online, December 2016. last accessed 25.09.2019. URL: `https://en.wikipedia.org/wiki/Amorphous_silicon#/media/File:Schematic_of_allotropic_forms_of_silcon_horizontal_plain.svg`.

[460] Paweł Tomaszewski. Jan czochralski i jego metoda, jan czochralski and his method, 2003. p. 41.

[461] Jan Czochralski. Ein neues verfahren zur messung der kristallisationsgeschwindigheit der metalle. *Z. phys. Chemie.*, 92:219–221, 1918.

[462] T. Nishinaga. *Handbook of Crystal Growth: Fundamentals*. Handbook of Crystal Growth. Elsevier Science, 2014. p. 21.

[463] Eivind Øvrelid, Bart Geerligs, Aud Wærnes, Ola Raaness, Ingeborg Solheim, Roar Jensen, Kai Tang, Sven Santeen, and Benno Wiersma. Solar grade silicon by a direct metallurgical process. *Silicon for the Chemical Industry VIII, Trondheim, Norway*, 2006.

[464] A. McEvoy, L. Castaner, and T. Markvart. *Solar Cells: Materials, Manufacture and Operation*. Elsevier Science, 2012. p. 69.

[465] Wei Wang, Yu-Wei Su, and Chih-hung Chang. Inkjet printed chalcopyrite cuin x ga 1- x se 2 thin film solar cells. *Solar Energy Materials and Solar Cells*, 95(9):2616–2620, 2011.

[466] Jong Won Park, Young Woo Choi, Eunjoo Lee, Oh Shim Joo, Sungho Yoon, and Byoung Koun Min. Synthesis of cigs absorber layers via a paste coating. *Journal of Crystal Growth*, 311(9):2621–2625, 2009.

[467] Wendi Zhang, Ulrich W Paetzold, Matthias Meier, Aad Gordijn, Jürgen Hüpkes, and Tsvetelina Merdzhanova. Thin-film silicon solar cells on dry etched textured glass. *Energy Procedia*, 44:151–159, 2014.

[468] Andrei Salavei, Daniele Menossi, Fabio Piccinelli, Arun Kumar, Gino Mariotto, Marco Barbato, Matteo Meneghini, Gaudenzio Meneghesso, Simone Di Mare, Elisa Artegiani, et al. Comparison of high efficiency flexible cdte solar cells on different substrates at low temperature deposition. *Solar Energy*, 139:13–18, 2016.

[469] Kuan-Chun Tseng, Yu-Ting Yen, Stuart R Thomas, Hung-Wei Tsai, Cheng-Hung Hsu, Wen-Chi Tsai, Chang-Hong Shen, Jia-Min Shieh, Zhiming M Wang, and Yu-Lun Chueh. A facile chemical-mechanical polishing lift-off transfer process toward large scale cu (in, ga) se 2 thin-film solar cells on arbitrary substrates. *Nanoscale*, 8(9):5181–5188, 2016.

[470] A Romeo, G Khrypunov, F Kurdesau, M Arnold, DL Bätzner, H Zogg, and AN Tiwari. High-efficiency flexible cdte solar cells on polymer substrates. *Solar energy materials and solar cells*, 90(18):3407–3415, 2006.

[471] Yun Seog Lee, Talia Gershon, Oki Gunawan, Teodor K Todorov, Tayfun Gokmen, Yudistira Virgus, and Supratik Guha. Cu2znsnse4 thin-film solar cells by thermal co-evaporation with 11.6% efficiency and improved minority carrier diffusion length. *Advanced Energy Materials*, 5(7), 2015.

[472] J Perrenoud, B Schaffner, S Buecheler, and AN Tiwari. Fabrication of flexible cdte solar modules with monolithic cell interconnection. *Solar Energy Materials and Solar Cells*, 95:S8–S12, 2011.

[473] Philip Jackson, Dimitrios Hariskos, Roland Wuerz, Oliver Kiowski, Andreas Bauer, Theresa Magorian Friedlmeier,

and Michael Powalla. Properties of cu (in, ga) se2 solar cells with new record efficiencies up to 21.7%. *physica status solidi (RRL)-Rapid Research Letters*, 9(1):28–31, 2015.

[474] J Kuendig, M Goetz, X Niquille, A Shah, S Vaccaro, J Mosig, L Gerlach, P De Maagt, and E Fernandez. Thin-film silicon solar cells for space applications: radiation hardness and applications for an integrated solant (solar cell-antenna) module. In *Conference Record of the Twenty-Eighth IEEE Photovoltaic Specialists Conference-2000 (Cat. No. 00CH37036)*, pages 1079–1082. IEEE, 2000.

[475] Karsten Otte, Liudmila Makhova, Alexander Braun, and Igor Konovalov. Flexible cu (in, ga) se 2 thin-film solar cells for space application. *Thin Solid Films*, 511:613–622, 2006.

[476] KL Chopra, PD Paulson, and V Dutta. Thin-film solar cells: an overview. *Progress in Photovoltaics: Research and Applications*, 12(2-3):69–92, 2004.

[477] David E Carlson and Cristopher R Wronski. Amorphous silicon solar cell. *Applied Physics Letters*, 28(11):671–673, 1976.

[478] Liu Xiaojiao, Yin Junchuan, Zhang Jiawei, Li Ming, Yang Peizhi, and Hu Zhihua. Boron doped a-siox: H prepared by h2 diluted sih4+ co2 plasma. *Int. J. Electrochem. Sci*, 11:10827–10836, 2016.

[479] Kazuhiro Kobayashi, Masahiro Hayama, Satoru Kawamoto, and Hidejiro Miki. Characteristics of hydrogenated amorphous silicon films prepared by electron cyclotron resonance microwave plasma chemical vapor deposition method and their application to photodiodes. *Japanese journal of applied physics*, 26(2R):202, 1987.

[480] Thomas Feurer, Patrick Reinhard, Enrico Avancini, Benjamin Bissig, Johannes Löckinger, Peter Fuchs, Romain Carron, Thomas Paul Weiss, Julian Perrenoud, Stephan Stutterheim, et al. Progress in thin film cigs photovoltaics–research and development, manufacturing, and applications. *Progress in Photovoltaics: Research and Applications*, 2016.

[481] Frank Dimroth and Sarah Kurtz. High-efficiency multijunction solar cells. *MRS bulletin*, 32(03):230–235, 2007.

[482] Sasaki K and Agui T, editors. *9th International Conference on Concentrating Photovoltaics Systems, Miyazaki, Japan*, 2013. p. 22.

[483] Hitoshi Sai, Takuya Matsui, Takashi Koida, Koji Matsubara, Michio Kondo, Shuichiro Sugiyama, Hirotaka Katayama, Yoshiaki Takeuchi, and Isao Yoshida. Triple-junction thin-film silicon solar cell fabricated on periodically textured substrate with a stabilized efficiency of 13.6%. *Applied Physics Letters*, 106(21):213902, 2015.

[484] T. Matsui and H. Sai, editors. *Development of Highly Stable and Efficient Amorphous Silicon Based Solar Cells*, 2013. p. 2213-2217.

[485] Hitoshi Sai, Keigo Maejima, Takuya Matsui, Takashi Koida, Michio Kondo, Sachiko Nakao, Yoshiaki Takeuchi, Hirotaka Katayama, and Isao Yoshida. High-efficiency microcrystalline silicon solar cells on honeycomb textured substrates grown with high-rate vhf plasma-enhanced chemical vapor deposition. *Japanese Journal of Applied Physics*, 54(8S1):08KB05, 2015.

[486] J Heemeier, M Rostalsky, F Gromball, N Linke, and J Muller. Thin film technology for electron beam crystallized silicon solar cells on low cost substrates. In *Photovoltaic Specialists Conference, 2002. Conference Record of the Twenty-Ninth IEEE*, pages 1310–1313. IEEE, 2002.

[487] RC Chittick, JH Alexander, and HF Sterling. The preparation and properties of amorphous silicon. *Journal of the Electrochemical Society*, 116(1):77–81, 1969.

[488] F Meillaud, A Feltrin, D Dominé, P Buehlmann, M Python, G Bugnon, A Billet, G Parascandolo, J Bailat, S Fay, et al. Limiting factors in the fabrication of microcrystalline silicon solar cells and microcrystalline/amorphous ('micromorph') tandems. *Philosophical magazine*, 89(28-30):2599–2621, 2009.

[489] D Hrunski, F Mootz, A Zeuner, A Janssen, H Rost, R Beckmann, S Binder, E Schüngel, S Mohr, D Luggenhölscher, et al. Deposition of microcrystalline intrinsic silicon by the electrical asymmetry effect technique. *Vacuum*, 87:114–118, 2013.

[490] Axel Metz, Dennis Adler, Stefan Bagus, Henry Blanke, Michael Bothar, Eva Brouwer, Stefan Dauwe, Katharina Dressler, Raimund Droessler, Tobias Droste, et al. Industrial high performance

crystalline silicon solar cells and modules based on rear surface passivation technology. *Solar Energy Materials and Solar Cells*, 120:417–425, 2014.

[491] Christiane Becker, Daniel Amkreutz, Tobias Sontheimer, Veit Preidel, Daniel Lockau, Jan Haschke, Lisa Jogschies, Carola Klimm, Janis J Merkel, Paul Plocica, et al. Polycrystalline silicon thin-film solar cells: Status and perspectives. *Solar Energy Materials and Solar Cells*, 119:112–123, 2013.

[492] Tina Wahl, Jonas Hanisch, and Erik Ahlswede. Comparison of the al back contact deposited by sputtering, e-beam, or thermal evaporation for inverted perovskite solar cells. *Journal of Physics D: Applied Physics*, 51(13):135502, 2018.

[493] Kirill Bordo and Horst-Günter Rubahn. Effect of deposition rate on structure and surface morphology of thin evaporated al films on dielectrics and semiconductors. *Materials Science*, 18(4):313–317, 2012.

[494] Hayk Khachatryan, Sung-Nam Lee, Kyoung-Bo Kim, and Moojin Kim. Deposition of al thin film on steel substrate: The role of thickness on crystallization and grain growth. *Metals*, 9(1):12, 2019.

[495] Dominik Hanft, Jörg Exner, Michael Schubert, Thomas Stöcker, Paul Fuierer, and Ralf Moos. An overview of the aerosol deposition method: Process fundamentals and new trends in materials applications. *J. Ceram. Sci. Technol*, 6(3):147–182, 2015.

[496] T. Dittrich. *Materials Concepts for Solar Cells (Second Edition)*. World Scientific Publishing UK Limited, 2018.

[497] K.L. Chopra and S.R. Das. *Thin Film Solar Cells*. Springer US, 2013.

[498] W Böttler, V Smirnov, J Hüpkes, and F Finger. Texture-etched zno as a versatile base for optical back reflectors with well-designed surface morphologies for application in thin film solar cells. *physica status solidi (a)*, 209(6):1144–1149, 2012.

[499] Wanjiao Böttler, Vladimir Smirnov, Andreas Lambertz, Jürgen Hüpkes, and Friedhelm Finger. Window layer development for microcrystalline silicon solar cells in n-i-p configuration. *physica status solidi c*, 7(3-4):1069–1072, 2010.

[500] FK Mugwang'a, PK Karimi, WK Njoroge, and O Omayio. Characterization of aluminum doped zinc oxide (azo) thin films prepared by reactive thermal evaporation for solar cell applications. *J Fundam Renewable Energy Appl*, 5(170):2, 2015.

[501] Oliver Kluth, Gunnar Schöpe, Jürgen Hüpkes, Chitra Agashe, Joachim Müller, and Bernd Rech. Modified thornton model for magnetron sputtered zinc oxide: film structure and etching behaviour. *Thin solid films*, 442(1-2):80–85, 2003.

[502] Daisuke Shindo and Tetsuo Oikawa. Energy dispersive x-ray spectroscopy. In *Analytical Electron Microscopy for Materials Science*, pages 81–102. Springer, 2002.

[503] JE Post and DL Bish. Rietveld refinement of crystal structures using powder x-ray diffraction data. *Modern Powder Diffraction*, 20:277–308, 1989.

[504] Vitalij Pecharsky and Peter Zavalij. *Fundamentals of powder diffraction and structural characterization of materials*. Springer Science & Business Media, 2008.

[505] B Kanngießer, N Langhoff, R Wedell, et al. Handbook of practical x-ray fluorescence analysis. *Beckhoff, B., Kanngiesser, B., Langhoff, N., Wedell, R., Wolff, H., Eds*, pages 433–474, 2006.

[506] Keith Norrish and JT Hutton. An accurate x-ray spectrographic method for the analysis of a wide range of geological samples. *Geochimica et cosmochimica acta*, 33(4):431–453, 1969.

[507] THermoFIscher SCIENTIFIC. *Product Specification Spectroflux 105*, September 2019.

[508] Wolfgang Kirmse. *Organic elemental analysis: Ultramicro, micro, and trace methods*. Elsevier, 1983.

[509] Michael Ewart Brown. *Introduction to thermal analysis: techniques and applications - Chapter 4*, volume 1. Springer Science & Business Media, 2001.

[510] Goestar Klingelhoefer, Richard Van Morris, Bodo Bernhardt, D Rodionov, PA de Souza Jr, SW Squyres, J Foh, E Kankeleit, U Bonnes, R Gellert, et al. Athena mimos ii mössbauer spectrometer investigation. *Journal of Geophysical Research: Planets*, 108(E12), 2003.

[511] Reinhard Danzl, Franz Helmli, and Stefan Scherer. Focus variation–a new technology for high resolution optical 3d surface metrology. In *The 10th International Conference of the Slovenian Society for Non-Destructive Testing*, pages 484–491, 2009.

[512] Leach R. Helmli F. *Focus Variation In-*

struments in Optical measurement of surface topography, volume 14. Springer, 2011.

[513] Wojciech Kapłonek, Krzysztof Nadolny, and Grzegorz M Królczyk. The use of focus-variation microscopy for the assessment of active surfaces of a new generation of coated abrasive tools. *Measurement Science Review*, 16(2):42–53, 2016.

[514] Richard S Hunter et al. Methods of determining gloss. *NBS Research paper RP*, 958, 1937.

[515] HE Bennett and JO Porteus. Relation between surface roughness and specular reflectance at normal incidence. *JOSA*, 51(2):123–129, 1961.

[516] Makiko Yonehara, Tsutomu Matsui, Koichiro Kihara, Hiroaki Isono, Akira Kijima, and Toshio Sugibayashi. Experimental relationships between surface roughness, glossiness and color of chromatic colored metals. *Materials Transactions*, 45(4):1027–1032, 2004.

[517] Akanshu Sharma, Prabhat Ranjan, Dibakar Datta, and Ratna Rueban Balasubramaniam. A comparative study on the reflectivity of metallic mirrors finished by deterministic and random processes. *All India Manufacturing Technology, Design and Research Conference (AIMTDR 2014)*, 2014.

[518] Thomas Kirchartz, Kaining Ding, and Uwe Rau. Fundamental electrical characterization of thin-film solar cells. *Advanced characterization techniques for thin film solar cells*, pages 33–60, 2011.

[519] Iec 60904-1-1:2017, photovoltaic devices - part 1-1: Measurement of current-voltage characteristics of multi-junction photovoltaic (pv) devices, May 2017.

[520] Iec 60904-3:2019, photovoltaic devices - part 3: Measurement principles for terrestrial photovoltaic (pv) solar devices with reference spectral irradiance data, February 2019.

[521] Iec 60904-9:2007, photovoltaic devices - part 9: Solar simulator performance requirements, October 2007.

[522] Andreas Lambertz, Friedhelm Finger, Ruud EI Schropp, Uwe Rau, and Vladimir Smirnov. Preparation and measurement of highly efficient a-si: H single junction solar cells and the advantages of μc-siox:h n-layers. *Progress in Photovoltaics: Research and Applications*, 23(8):939–948, 2015.

[523] R. Brendel. *Thin-Film Crystalline Silicon Solar Cells: Physics and Technology*. Wiley, 2011. p 53.

[524] C.J. Brabec, V. Dyakonov, J. Parisi, and N.S. Sariciftci. *Organic Photovoltaics: Concepts and Realization*. Springer Series in Materials Science. Springer Berlin Heidelberg, 2013. p. 263.

[525] Xiangwu Zeng, Chunmei He, Heather Oravec, Allen Wilkinson, Juan Agui, and Vivake Asnani. Geotechnical properties of jsc-1a lunar soil simulant. *Journal of Aerospace Engineering*, 23(2):111–116, 2009.

[526] Sheryl M. Genco. Lunar simulants and custom synthetics. online, May 2016. Last accessed 20.05.2016. URL: `https://web.archive.org/web/20160520171433/www.zybekap.com/LunSyn22Pricing.php`.

[527] Xiangwu Zeng, Chunmei He, and Allen Wilkinson. Geotechnical properties of nt-lht-2m lunar highland simulant. *Journal of Aerospace Engineering*, 23(4):213–218, 2010.

[528] David S McKay, Grant Heiken, Abhijit Basu, George Blanford, Steven Simon, Robert Reedy, Bevan M French, and James Papike. The lunar regolith. *Lunar sourcebook*, pages 285–356, 1991.

[529] J. Reinhardt M.M. Raith, P. Raase. *Guide to thin section microscopy - second edition*. ISBN 978-3-00-037671-9 (PDF), 2012.

[530] W.S. MacKenzie and A.E. Adams. *A Color Atlas of Rocks and Minerals in Thin Section*. Wiley, 1997.

[531] John Faithfull. Identification tables for common minerals. 1998.

[532] FR Boyd, JL England, and Brian TC Davis. Effects of pressure on the melting and polymorphism of enstatite, mgsio3. *Journal of Geophysical Research*, 69(10):2101–2109, 1964.

[533] H.R. Wenk and A. Bulakh. *Minerals: Their Constitution and Origin*. Cambridge University Press, 2004.

[534] C. Klein and A. Philpotts. *Earth Materials*. Cambridge University Press, 2016.

[535] Navrotsky A. Weill D.F., Hon R. The igneous system camg-siao6-caa12si208 : variations on a classic theme by bowen. *Hargraves RB (ed) Physics of magmatic processes. Princeton University Press, Princeton, pp 49-92*, 1980.

[536] Alexandra Navrotsky, Papu Maniar, and

Richard Oestrike. Energetics of glasses in the system diopside-anorthite-forsterite. *Contributions to Mineralogy and Petrology*, 105(1):81–86, 1990.

[537] MJ LE BAS, RW LE Maitre, Arthur Streckeisen, Bruno Zanettin, and IUGS Subcommission on the Systematics of Igneous Rocks. A chemical classification of volcanic rocks based on the total alkali-silica diagram. *Journal of petrology*, 27(3):745–750, 1986.

[538] Charles Meyer. The lunar petrographic educational thin section set. Technical report, Astromaterials Curation NASA Lyndon B. Johnson Space Center Houston, Texas 77058, 2003.

[539] Lunar and Asteroid Surface Science (CLASS). Planetary simulant database. Online, 2019. last accessed 25.09.2019. URL: `https://sciences.ucf.edu/class/planetary-simulant-database/`.

[540] Stephen Covey Metzger Philip, Daniel Britt and John Lewis. Results of the 2015 workshop on asteroid simulants. *Earth and Space 2016: Engineering, Science, Construction, and Operations in Challenging Environments*, page 94, 2016.

[541] Campbell G.S. & Diak G.R. Net and thermal radiation estimation and measurement. *Micrometeorology in Agricultural Systems*, pages 59–92, 2005.

[542] Calex electronics limited, PO Box 2, Leighton Buzzard, Bedfordshire, England LU7 4AZ. *CALEX PyroUSB 2.2 Series Operators Guide*, first edition edition, November 2011.

[543] Sergey Vyazovkin, Nobuyoshi Koga, and Christoph Schick. *Handbook of thermal analysis and Calorimetry: Recent Advances, techniques and applications*, volume 6. Elsevier, 2018.

[544] TA Instruments. How to interpret the unexpected transitions in dsc results. Online, July 2015. last accessed 25.09.2019. URL: `https://www.azom.com/article.aspx?ArticleID=12101`.

[545] Robert Jones and Jazmin Ley. Dsc traces, university of texas rio grande valley. Online, video, April 2016. last accessed 25.09.2019. URL: `https://www.youtube.com/watch?v=Sig7X5PD19Q`.

[546] Lawrence A Taylor and Thomas T Meek. Microwave processing of lunar soil. *Science and Technology Series*, 108:109–123, 2004.

[547] K.J. Rao. *Structural Chemistry of Glasses*. Elsevier Science, 2002. page 448.

[548] H. Bach and N. Neuroth. *The Properties of Optical Glass*. Schott Series on Glass and Glass Ceramics. Springer Berlin Heidelberg, 2012. pages 170-175.

[549] JK Yang, XH An, YL Liu, and HL Zhao. Analysis and calculation of melting performance for the low-iron glass. *J. Mater. Sci. Eng*, 4:034, 2009.

[550] Pierre Combes, Jean-Jacques Massol, and Pedro C Alvarez. Colored glass compositions and glazings produced therewith, October 4 1994. US Patent 5,352,640.

[551] Dariusz Malczewski, Martyna Jeleń, Jerzy Żaba, Artur Błachowski, Krzysztof Ruebenbauer, and Maria Dziurowicz. Identification of iron-bearing minerals in basalts and pillow lavas of the kaczawa mountains using 57fe mössbauer spectroscopy. *Nukleonika*, 62(2):145–148, 2017.

[552] THORLABS. Protected aluminum mirrors. Online, 2019. last accessed 25.09.2019. URL: `https://www.thorlabs.com/NewGroupPage9_PF.cfm?ObjectGroup_ID=890`.

[553] Georg Hass. Filmed surfaces for reflecting optics. *JOSA*, 45(11):945–952, 1955.

[554] THORLABS. Square protected aluminum mirrors: 450 nm - 2000 nm. Online, 2019. last accessed 25.09.2019. URL: `https://www.thorlabs.de/newgrouppage9.cfm?objectgroup_id=264`.

[555] Jaakko Siivola and Rolf Schmid. List of mineral abbreviations. 2007.

[556] JC Laul, JJ Papike, and SB Simon. The lunar regolith-comparative studies of the apollo and luna sites. chemistry of soils from apollo 17, luna 16, 20, and 24. In *Lunar and Planetary Science Conference Proceedings*, volume 12, pages 389–407, 1982.

[557] JC Laul, OD Rode, SB Simon, and JJ Papike. The lunar regolith: Chemistry and petrology of luna 24 grain size fractions. *Geochimica et Cosmochimica Acta*, 51(3):661–673, 1987.

A Appendix

Table A.1: Abbreviation of mineral names based on [555], plus additional minerals

Mineral Name	Abbreviation	Mineral Name	Abbreviation
Agerine	Aeg	Illite	Ill
Albite	Ab	Ilmenite	Ilm
Alkalifeldspar	Afs	Kaolinite	Kln
Andesine	Ad	Labradorite	La
Annite	Ann	Magnetite	Mag
Anorthite	An	Mica	Mca
Apatite	Ap	Microcline	Mc
Augite	Aug	Muscovite	Ms
Basaltic Glass	BG	Nepheline	Ne
Bytownite	By	Olivine	Ol
Calcite	Cal	Oligoclase	Oli
Chlorite	Chl	Orthoclase	Or
Clinopyroxene	CPx	Orthopyroxene	OPx
Diopside	Di	Oxide Mineral	OM
Enstatite	En	Phlogopite	Phl
Fayalite	Fa	Pigeonite	Pgt
Feldspar	Fsp	Plagioclase	Pl
Ferrosilite	Fs	Pyroxene	Px
Forsterite	Fo	Quartz	Qtz
Haematite	Hem	Sanidine	Sa
Hedenbergite	Hd	Titanomagnetite	TMag
Hornblende	Hbl	Zircon	Zo

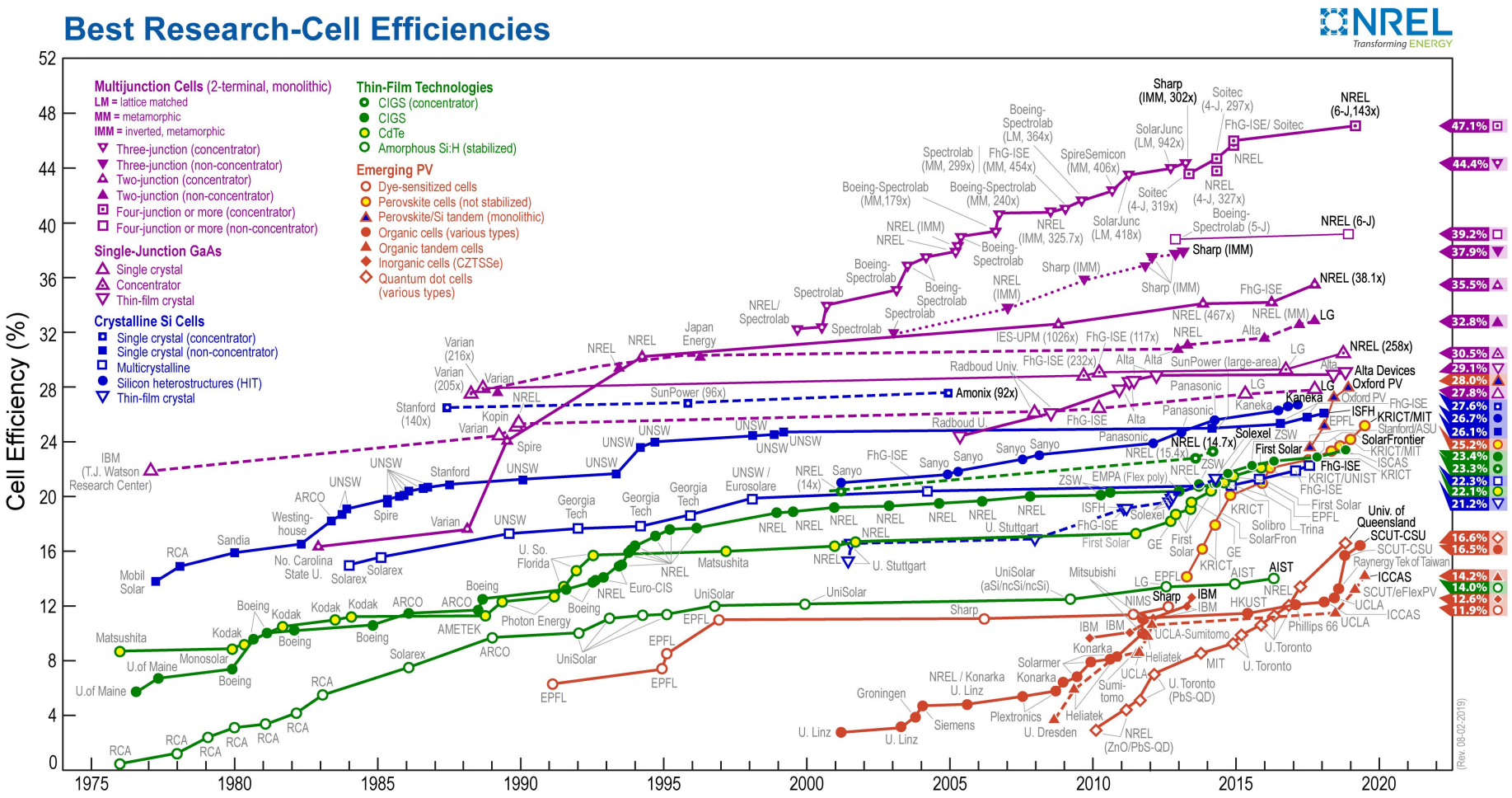

Figure A.1: Best research-cell efficiencies by NREL [452]. Shown is cell efficiency over year of accomplishment.

284

Table A.2: Modal proportions of minerals and glasses in soils from the Apollo (A) and Luna (L) sampling sites in volume % (90 - 20 μm fraction, not including fused-soil and rock fragments). Taken from page 123 in the Lunar Source Book [148] originally from [160, 556, 557]

Mineral	**A-11**	**A-12**	**A-14**	**A-(H)**	**A-(M)**	**A-16**	**A-(H)**	**A-(M)**	**L-16**	**L-20**	**L-24**
Plagioclase	21.4	23.2	31.8	34.1	12.9	69.1	39.3	34.1	14.2	52.1	20.9
Pyroxene	44.9	38.2	31.9	38.0	61.1	8.5	27.7	30.1	57.3	27.0	51.6
Olivine	2.1	5.4	6.7	5.9	5.3	3.9	11.6	0.2	10.0	6.6	17.5
Silica	0.7	1.1	0.7	0.9	-	0.0	0.1	-	0.0	0.5	1.7
Ilmenite	6.5	2.7	1.3	0.4	0.8	0.4	3.7	12.8	1.8	0.0	1.0
Mare Glass	16.0	15.1	2.6	15.9	6.7	0.9	9.0	17.2	5.5	0.9	3.4
Highland Glass	8.3	14.2	25.0	4.8	10.9	17.1	8.5	4.7	11.2	12.8	3.8
Other	-	-	-	-	2.3	-	-	0.7	-	-	
Total	99.9	99.9	100.0	100.0	100.0	99.9	99.9	99.8	100.0	99.9	99.9

(H) Denotes highland, (M) Denotes mare.

Table A.3: Grain size distribution of selected lunar regolith simulants

Size	**BP1**	**EAC1**	**FJS1**	**JSC1A**	**JSC2A**	**LHT3M**	**Tech**	**15090**	**60009**	**64001**	**70008**
1000	99.9	99.5	100.0	99.3	100.0	100.0	100.0	98.0	95.4	96.7	88.0
500	99.4	91.0	95.9	87.4	92.0	99.8	90.9	95.5	87.4	93.8	85.1
300	98.3	78.0	88.0	76.5	84.0	98.9	88.0	88.5	77.1	87.9	78.8
250	88.0	73.9	86.0	68.3	80.1	97.4	76.7	86.8	74.6	86.5	77.3
160	73.4	51.0	76.0	53.9	65.0	69.0	63.0	75.6	64.2	78.0	69.5
125	67.7	41.3	70.9	48.3	55.5	57.9	50.8	71.2	58.6	72.4	64.8
90	50.1	32.0	57.0	42.0	42.6	34.9	39.0	61.2	52.9	66.8	60.1
75	30.6	28.0	51.0	29.7	37.0	16.6	34.0	56.9	49.3	62.6	56.1
63	23.0	24.2	47.8	24.9	35.2	9.5	26.0	53.4	43.4	57.3	51.8
45	17.35	11	35	11.17	28.97	NaN	23	41.9	34.6	49.3	45.2

285

Table A.4: Average geochemical compositions from all conducted XRF measurements. Values for "Mare", "Highland" and "Avg. Surf." are taken from the literature and are not altered

Simulant	SiO_2	Al_2O_3	Fe_2O_3*	MgO	CaO	Na_2O	K_2O	TiO_2	MnO	P_2O_5	$Other$
Mare	45.40	14.90	14.10	9.20	11.80	0.60	-	-	-	-	4.00
BP-1	46.50	16.16	12.19	6.40	10.30	2.83	1.01	2.10	0.17	0.41	1.94
EAC-1	43.70	11.48	12.88	14.26	10.19	2.11	1.17	2.17	0.21	0.61	1.22
FJS-1	49.84	16.76	13.25	5.41	9.58	2.05	0.75	1.59	0.20	0.33	0.25
JSC-1A	46.52	16.26	12.60	8.43	9.84	2.68	0.79	1.81	0.19	0.71	0.15
JSC-2A	46.11	16.57	13.17	8.06	9.60	2.74	0.84	1.84	0.19	0.71	0.15
Highland	45.50	24.00	5.90	7.50	15.90	0.60	-	-	-	-	0.60
LHT-2M	47.14	24.62	4.16	7.81	13.67	1.00	0.07	0.38	0.07	0.07	1.00
LHT-3M	49.28	22.32	5.16	9.15	12.76	0.65	0.05	0.09	0.09	0.03	0.42
Avg. Surf.	45.50	22.20	7.50	7.80	15.00	0.60	-	-	-	-	1.40
JSC-1A-M	40.40	22.62	16.86	3.33	5.76	1.50	0.49	3.67	0.29	0.85	4.23

* All iron contained considered to be fully oxidised

Table A.5: XRF data of lunar simulants from suppliers, values in wt%

Simulant	SiO_2	Al_2O_3	Fe_2O_3	MgO	CaO	Na_2O	K_2O	TiO_2	MnO	P_2O_5
BP-1	47.05	16.65	12.00	6.05	9.40	3.45	1.10	2.25	0.21	0.52
EAC-1	43.7	12.6	12.0	11.9	10.8	2.9	1.3	2.4	0.2	0.6
FJS-1	49.14	16.23	13.07	3.84	9.13	2.75	1.01	1.91	0.19	0.44
JSC-1A	46-49	14.5-15.5	10-11.5	8.5-9.5	10-11	2.5-3.0	0.75-0.85	1-2	0.15-0.20	0.6-0.7
JSC-1A-M	34.5-44	18.5-23.5	11.5-15.5	2.5-3.5	5-6	2-2.5	0.5-0.6	3-4	0.2-0.3	0.7-0.9
JSC-2A	46-49	14.5-15.5	10-11.5	8.5-9.5	10-11	2.5-3	0.75-0.85	1-2	0.15-0.20	0.6-0.7
LHT-2M	46.7	24.4	4.16	7.9	13.6	1.26	0.08	0.41	0.07	0.15
LHT-3M	46.7	24.4	4.16	7.9	13.6	1.26	0.08	0.41	0.07	0.15

286

Table A.6: Emissivity values of regolith simulants with different grain size distributions, as well as glass manufactured of regolith simulant EAC-1

Temp.	**EAC-1 in μm**				**FJS-1 in μm**				**JSC-2A in μm**				**LHT-3M in μm**				**EAC-1 Glass**	
in °C	all	> 300	300-38	< 38	all	> 300	300-38	< 38	all	> 300	300-38	< 38	all	> 300	300-38	< 38	Polished	Dull
500	0.88	0.90	0.78	0.79	0.90	0.94	0.91	0.91	0.83	0.83	0.83	0.85	0.86	0.85	0.84	0.92	0.90	0.93
550	0.83	0.83	0.83	0.79	0.93	0.95	0.93	0.92	0.84	0.84	0.82	0.85	0.92	0.93	0.89	0.92	0.86	0.90
600	0.83	0.83	0.83	0.83	0.92	0.94	0.95	0.93	0.84	0.86	0.86	0.85	0.92	0.92	0.92	0.99	0.86	0.87
650	0.83	0.85	0.82	0.86	0.94	0.95	0.95	0.94	0.84	0.85	0.82	0.84	0.90	0.90	0.91	0.92	0.85	0.85
700	0.83	0.80	0.85	0.86	0.93	0.94	0.93	0.94	0.83	0.81	0.82	0.81	0.89	0.89	0.89	0.89	0.85	0.84
750	0.83	0.82	0.82	0.84	0.94	0.94	0.94	0.91	0.81	0.82	0.80	0.80	0.90	0.90	0.89	0.89	0.82	0.83
800	0.83	0.83	0.83	0.84	0.97	0.97	0.97	0.97	0.81	0.82	0.83	0.81	0.89	0.89	0.90	0.89	0.80	0.79
850	0.83	0.83	0.82	0.82	0.96	0.96	0.96	0.96	0.83	0.83	0.83	0.82	0.90	0.90	0.89	0.89	0.79	0.78
900	0.82	0.82	0.82	0.83	0.95	0.96	0.96	0.96	0.90	0.88	0.87	0.87	0.89	0.89	0.89	0.89	0.77	0.77
950	0.84	0.85	0.83	0.83	0.95	0.95	0.96	0.96	0.89	0.88	0.88	0.88	0.89	0.89	0.89	0.89	0.76	0.77
1000	0.84	0.84	0.83	0.82	0.96	0.96	0.97	0.94	0.87	0.88	0.93	0.88	0.89	0.89	0.89	0.89	0.76	0.77
1050	0.80	0.82	0.82	0.81	0.94	0.93	0.94	0.93	0.88	0.88	0.87	0.87	0.89	0.89	0.89	0.89	0.75	0.77
Med.	0.83	0.83	0.82	0.83	0.94	0.95	0.95	0.94	0.84	0.84	0.83	0.85	0.89	0.89	0.89	0.89	0.81	0.81
Avg.	0.83	0.83	0.82	0.83	0.94	0.95	0.95	0.94	0.85	0.85	0.85	0.84	0.90	0.89	0.89	0.91	0.8133	0.8204

287

Table A.7: Comparison XRF trace element measurements from Edinburgh vs. Liège. Results shown in ppm

Simulant	Cu	Ni	Rb	Sr	Y	Zn	Zr
BP-1	-14	60	-6	60	-2	10	3
BP-1	-32%	57%	-43%	8%	-8%	12%	2%
EAC-1	-12	46	-7	28	-2	14	-2
EAC-1	-19%	11%	-21%	4%	-9%	13%	-1%
FJS-1-1	-26	93	-6	10	0	15	-5
FJS-1-1	-14%	64%	-50%	3%	0%	14%	-6%
JSC-1A	-14	73	-7	94	-1	8	7
JSC-1A	-24%	47%	-73%	10%	-3%	8%	4%
JSC-1A-M	-6	19	-6	137	8	44	57
JSC-1A-M	-39%	43%	-60%	16%	14%	34%	12%
JSC-2A	-12	102	-5	97	0	18	5
JSC-2A	-19%	47%	-56%	10%	-2%	16%	3%
LHT-3M-1	6	166	-8	-22	-4	5	-2
LHT-3M-1	10%	43%	-399%	-24%	-147%	10%	-2%

Table A.8: Comparison different simulant batches, major elements absolute and relative. Results shown in ppm

Simulant	Cu	Ni	Rb	Sr	Y	Zn	Zr
FJS-1	-88	22	-6	-16	-7	-14	-30
FJS-1	-41%	42%	-33%	-5%	-25%	-16%	-32%
LHT-3M	26	58	1	10	1	21	105
LHT-3M	54%	26%	13%	9%	15%	50%	84%

Table A.9: Sample mass for DSC/TGA runs

Simulant	Raw Mass in mg	Ground Mass in mg
BP-1	16.58	10.01
EAC-1	17.97	14.16
FJS-1	29.34	
JSC-1A	8.75	
JSC-2A	16.67	7.21
LHT-2M	10.16	20.47
LHT-3M	9.67	

Table A.10: XRF analysis results of magnetically altered regolith simulant samples

Sample	SiO_2	Al_2O_3	Fe_2O_3	MgO	CaO	Na_2O	K_2O	TiO_2	MnO	P_2O_5
BP-1	47.41	16.35	12.30	6.49	10.57	3.16	1.04	2.10	0.18	0.41
B-hm	46.55	16.00	13.98	6.58	9.33	3.31	1.05	2.58	0.20	0.42
B-high	48.02	15.96	11.88	7.46	10.34	3.06	1.02	1.73	0.17	0.37
B-fair	48.43	15.37	10.41	8.65	11.59	2.83	0.97	1.27	0.16	0.32
B-low	50.69	16.80	5.56	4.38	17.61	2.73	1.04	0.83	0.10	0.25
B-non	50.94	21.46	1.54	1.24	21.24	2.78	0.49	0.20	0.03	0.06
EAC-1	44.15	11.60	12.83	14.26	10.31	2.65	1.20	2.18	0.22	0.60
E-hm	44.63	13.09	12.38	11.69	10.89	2.70	1.36	2.39	0.20	0.68
E-high	44.54	9.40	13.54	19.05	8.76	1.54	1.01	1.48	0.24	0.43
E-fair	42.43	2.56	14.16	36.83	3.12	0.03	0.28	0.28	0.24	0.08
E-low	49.64	5.87	7.90	25.19	8.96	0.71	1.02	0.40	0.20	0.12
E-non	51.46	7.35	1.81	6.65	29.51	1.06	1.73	0.16	0.17	0.10
FJS-1	49.86	16.58	12.91	5.91	9.72	2.42	0.66	1.46	0.20	0.28
F-hm	49.47	14.52	14.88	6.74	9.16	2.15	0.77	1.76	0.22	0.32
F-high	50.59	18.45	9.86	7.08	10.11	2.30	0.53	0.70	0.17	0.21
F-fair	49.63	17.29	10.00	10.13	10.00	1.91	0.32	0.44	0.17	0.11
F-low	51.13	25.27	4.43	3.41	12.26	2.85	0.28	0.24	0.07	0.06
F-non	51.98	29.49	1.43	0.01	13.34	3.37	0.25	0.10	0.02	0.02
JSC1A	46.53	16.16	12.55	8.52	9.85	2.90	0.81	1.79	0.19	0.69
J1-hm	46.73	16.35	12.62	7.29	10.18	3.08	0.87	1.93	0.19	0.76
J1-high	46.08	15.44	13.08	9.83	9.30	2.85	0.80	1.75	0.20	0.68
J1-fair	46.18	15.52	12.66	10.18	9.40	2.80	0.76	1.66	0.19	0.64
J1-low	47.88	21.04	8.66	4.76	11.88	3.20	0.64	1.31	0.13	0.50
J1-non	44.59	24.20	1.45	1.16	25.79	2.19	0.18	0.20	0.02	0.21
JSC-2A	46.11	16.57	13.13	7.95	9.61	3.09	0.82	1.82	0.20	0.70
J2-hm	46.10	15.87	13.55	8.11	9.54	3.04	0.87	1.95	0.20	0.76
J2-high	45.53	15.06	13.48	10.24	8.89	3.34	0.84	1.75	0.20	0.68
J2-fair	45.97	15.78	12.69	10.66	9.13	2.70	0.71	1.56	0.18	0.61
J2-low	46.31	17.17	11.54	9.76	9.73	2.70	0.65	1.42	0.17	0.54
J2-non	44.28	22.12	1.09	1.05	28.39	2.30	0.34	0.15	0.02	0.25
LHT-3M	49.41	21.62	5.57	9.50	12.55	1.04	0.08	0.11	0.09	0.02
L-hm	49.34	16.66	9.17	13.02	10.94	0.52	0.05	0.14	0.14	0.02
L-high	51.69	12.73	8.60	17.82	8.47	0.35	0.04	0.14	0.16	0.00
L-fair	51.14	14.91	7.55	15.74	9.89	0.45	0.04	0.13	0.14	0.00
L-low	48.50	27.61	2.78	4.55	15.30	1.07	0.06	0.06	0.05	0.01
L-non	47.41	33.19	0.72	0	17.25	1.33	0.07	0.03	0.01	0.01

Table A.11: Summery of Mösbauer Spectroscopy results

Simulant	Area %	Ox. State	Phase	Likely
BP-1	28	Fe2+	Pyroxene*	Augite
	28	Fe2+	Olivine	Fayalite
	20	Fe3+	Ferric oxide	Magnetite
	15	Fe3+	**	
	7	Fe2.5+	Magnetite	
	3	Fe3+	Hematite	
EAC-1	30	Fe3+	Ferric oxide	Goethite
	28	Fe2+	Olivine	Fayalite
	24	Fe2+	Pyroxene*	Augite
	19	Fe3+	**	Basaltic Glass
FJS-1	41	Fe2+	Pyroxene*	Augite
	28	Fe2.5+	Ferric oxide	Magnetite
	18	Fe2+	Olivine	Fayalite
	6	Fe3+	**	
	5	Fe3+	Ferric oxide	Magnetite
	2	Fe2.5+	Ferric oxide	Magnetite
JSC-1A	33	Fe2+	Pyroxene*	Augite
	24	Fe2+	Olivine	Fayalite
	24	Fe3+	**	
	20	Fe2+	Pyroxene*	Augite
JSC-2A	34	Fe2+	Silicate*	Basaltic Glass
	22	Fe2+	Olivine	Fayalite
	22	Fe3+	**	
	11	Fe2+	Pyroxene*	Augite
	11	Fe3+	Ferric oxide	
LHT-2M	57	Fe2+	Pyroxene*	Augite
	23	Fe3+	**	
	19	Fe2+	Olivine	
	2	Fe2+	Ferric oxide	Ilmenite
LHT-3M	73	Fe2+	Pyroxene*	Augite
	17	Fe2+	Pyroxene*	Augite
	10	Fe3+	**	

$*$ parameters not mineral specific, could be pyroxene or other silicate

$**$ octahedral $Fe3+$, potentially $Fe3+$ in silicates or superparamagnetic Fe oxide

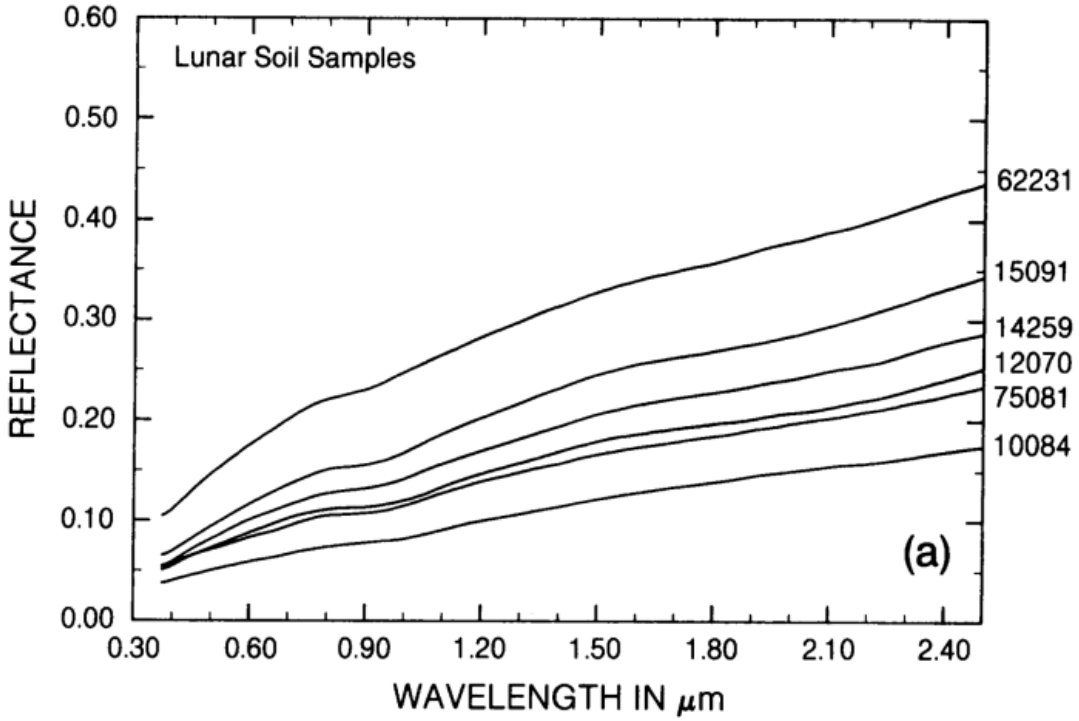

Figure A.2: Reflectivity of actual lunar regolith taken from page 308 in [528].

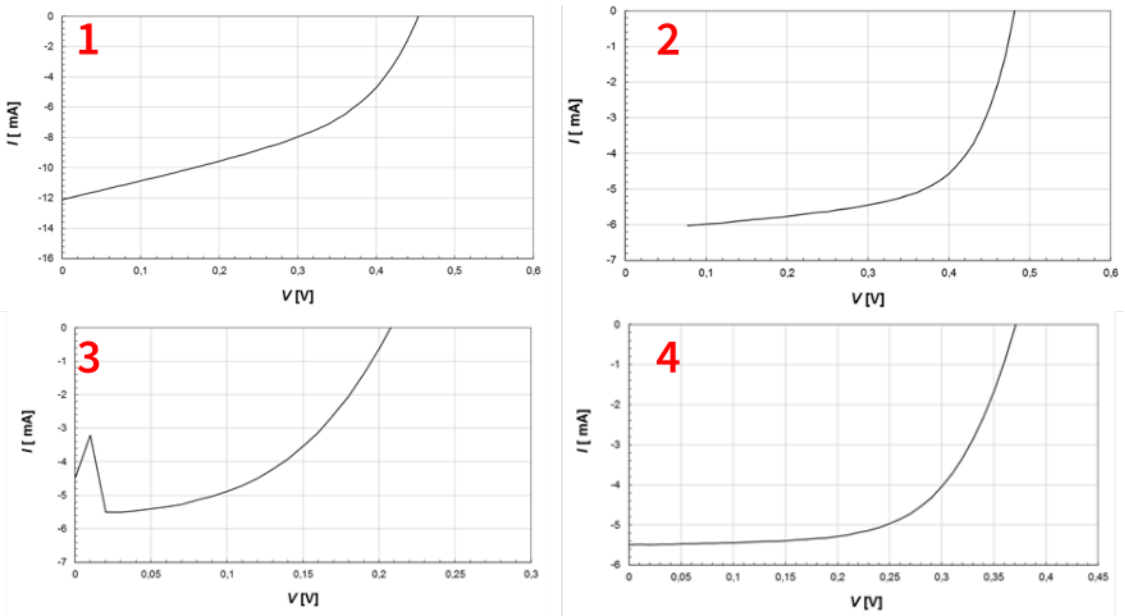

Figure A.3: I-V-Curves basaltic glass and reference solar cells. Numbers match figure 3.35, graph 1 and 3 are basaltic glass cells, and 2 and 4 are reference cells.